Physics of the Solid State, Vol. 44, No. 5, 2002, pp. 799–803. Translated from Fizika Tverdogo Tela, Vol. 44, No. 5, 2002, pp. 769–773.

METALS AND SUPERCONDUCTORS

Superstructural Ordering and Electronic-Density Modulation in Oxide HTSC Systems

N. V. Anshukova*, A. I. Golovashkin*, L. I. Ivanova, and A. P. Rusakov****

** Lebedev Physical Institute, Russian Academy of Sciences, Leninskiĭ pr. 53, Moscow, 119991 Russia*

*** Moscow Institute of Steel and Alloys, Leninskiĭ pr. 4, Moscow, 117936 Russia*

Received June 14, 2001

Abstract—New experimental data obtained on the lattice and spin modulation in oxide HTSCs are explained in terms of superstructural ordering in the CuO_2 planes without invoking the stripe model. The effect of doping on superstructural ordering in HTSCs is considered. The shape of the Fermi surface in oxide HTSCs and its variation with doping are also explained. © *2002 MAIK "Nauka/Interperiodica".*

The doping of oxide HTSCs has been experimentally observed to produce superstructural lattice and spin ordering [1–3]. This superstructural modulation is most clearly pronounced in $La_{2-x-y}Nd_ySr_xCuO_4$. The results of these and other experiments on lattice and spin ordering provided a basis for the model of electron ordering termed the stripe model [4]. This theoretical model rests on the assumption that the electron density in a metal rigidly follows the atomic displacement even on a local level. There appears to be no direct experimental evidence in support of such an electronic redistribution (which is certainly correct for dielectrics); therefore, for metals, the validity of the stripe model cannot be considered to be proved.

We will show that the observed atomic and spin modulation in HTSCs has its origin in the specific features of their band structure, which are due to the existence of CuO_2-type conducting planes. Another consequence of the same features in the HTSC band structure is an electronic-density modulation, which differs strongly from the hypothetical stripe model. The results of our treatment compare favorably with new experimental data and allow for their interpretation.

We will focus our attention here on the $La_{2-x}Sr_xCuO_4$ (LSCO) and $La_{1.6-x}Nd_{0.4}Sr_xCuO_4$ (LNSCO) systems, because it is on these systems that most of the experimental data on lattice and spin modulation are available. Most theoretical studies of stripes deal with these compounds.

To study the processes occurring in HTSCs under doping, we have first to address the nature of the insulating state without doping. In particular, for the LSCO and LNSCO systems, it corresponds to $x = 0$. Theoretical calculations suggest that the initial state of a system without doping ($x = 0$) should be metallic. The corresponding metal is called the praphase. As shown by us earlier [5], the CuO_2 planes in the praphase contain oxygen ions in two charge states, O^{2-} and $O^{1.5-}$. This corresponds to $Cu–O^{2-}$ ionic and $Cu–O^{1.5-}$ ionic-covalent bonds. The ordering of such "covalent" $Cu–O^{1.5-}$ bonds doubles the lattice period of this metallic praphase in the CuO_2 plane in the [100] and [010] directions. In other words, an electronic charge density wave forms and the state with free conduction electrons is replaced by the insulating state. A dielectric energy gap E_g forms (in the oxide HTSCs, $E_g \sim 2$ eV). Thus, one observes the insulating phase rather than the metallic praphase. To discriminate this covalent charge density wave on the oxygen sublattice of an insulator from charge density waves (CDW) forming under doping, we shall denote it as CCDW.

The $Cu–O^{1.5-}$ covalent bonds in adjacent CuO_2 planes should order in two mutually perpendicular directions, [100] and [010]. It is this type of ordering that yields the largest gain in energy when a dielectric energy gap forms. This dielectric gap is produced not only in the CuO_2 plane but also in the *c* direction. The result is a new unit cell which contains, in addition to the O^{2-} ions, four $O^{1.5-}$ ions. The insulating compound La_2CuO_4 with such a doubled cell can be presented as

$$La_{16}^{+3}Cu_8^{+1.75}O_4^{-1.5}O_{28}^{-2}. \quad (1)$$

The $O^{1.5-}$ ions being coupled more weakly to the lattice than O^{2-}, their electronic states lie closest to the chemical potential of the insulator; i.e., they are at the top of a complex valence band. The above ordering of these weakly coupled $O^{1.5-}$ ions in a crystal also produces a narrow, practically purely oxygen, valence band lying above a broad mixed (copper–oxygen) $Cu–O^{2-}$ band, as shown schematically in Fig. 1a. This scheme conforms to the available experimental data. Some of the energies obtained experimentally [6] are shown for comparison in the same figure. The narrowness of the upper oxygen band is accounted for by the relatively small overlap of the $2p$ states of $O^{1.5-}$, because the unit cell contains only four such ions

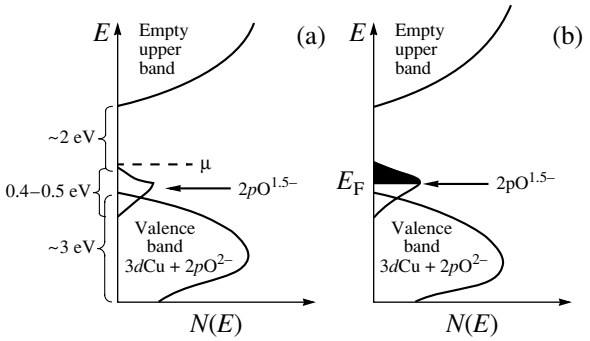

Fig. 1. Energy band diagram of cuprate HTSC systems (a) in the insulating state without doping and (b) in the metallic state under optimum doping. The arrow specifies a narrow, purely oxygen band, which is derived from the $O^{1.5-}$ states. E is the energy, μ is the chemical potential, E_F is the Fermi level, and $N(E)$ is the electronic density of states. The energies were taken from experimental data of [6]. The filled area specifies the hole states created by doping.

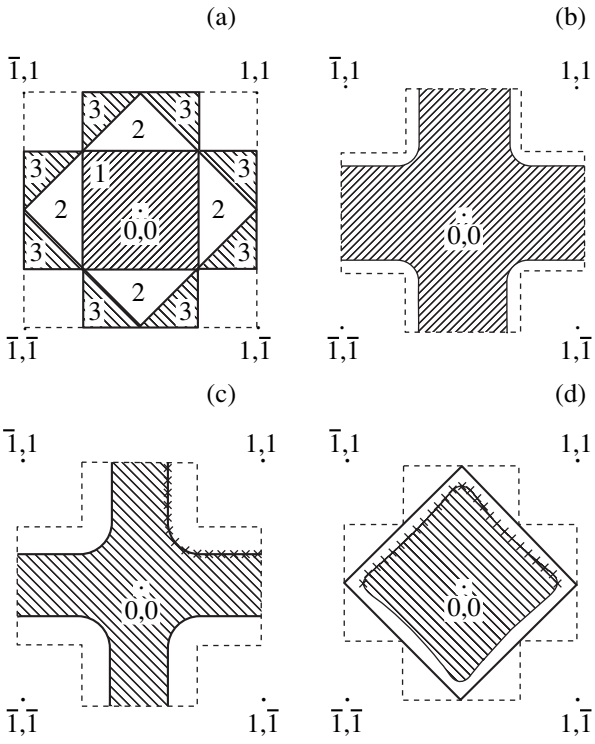

Fig. 2. Brillouin zones and the shape of the Fermi surface for cuprate HTSCs constructed for different doping levels. Crosses are experimental data obtained by ARPES [8, 9]. (a) The first three filled Brillouin zones (numbered) for the plane doubled CuO_2 lattice corresponding to the insulating state, $x = 0$. The dashed line shows the first Brillouin zone for the plane CuO_2 lattice without unit-cell doubling. The coordinates of points are in units of π/a, where a is the minimum Cu–Cu distance. (b) Fermi surface under light hole doping ($x \approx 0.05$–0.1, solid lines). The dashed line specifies the boundary of the third Brillouin zone. The filled electronic states are hatched. (c) Fermi surface under optimum doping corresponding to the half-filled third Brillouin zone. (d) Fermi surface under heavy doping ($x = 0.3$, $p > 0.25$). Dashed line specifies the boundaries of the second and third Brillouin zones.

against 28 O^{2-} ions. The latter ions form a broad (~3 eV) valence band together with the Cu 3*d* states.

The doubled unit cell [see Eq. (1)] contains four $O^{1.5-}$ oxygen ions. Thus, the upper narrow (0.4–0.5 eV) oxygen band has $4 \times 1.5 = 6$ electrons per unit cell. These electrons fill three Brillouin zones of a plane quasi-two-dimensional lattice made up of two CuO_2 planes. Because of the oxygen $O^{1.5-}$ states being coupled, these two planes can be considered to be a unique quasi-two-dimensional structure. The three filled Brillouin zones for a plane lattice in an insulator are shown in Fig. 2a. The third Brillouin zone is identified with two electrons; i.e., there are $2/8 = 0.25$ electrons per one copper ion in a formula unit of Eq. (1).

We now consider the doping process. Weak doping with strontium forms hole states at the valence-band top, as shown in Fig. 1b (filled area). The Fermi surface thus formed is close to the boundaries of the third Brillouin zone, as depicted in Fig. 2b (solid lines).

Optimum doping (corresponding to the maximum value of T_c) is reached for the half-filling of the oxygen band by holes. Indeed, taking into account the three-dimensional nature of the coupling, the half-filling of this band corresponds to the maximum in the density of states $N(E)$, as shown in Fig. 1b. In the Brillouin zone diagram, this corresponds to the third Brillouin zone being half-filled by holes. Thus, the half-filling is reached at a hole concentration $p_{opt} = 0.25/2 = 0.125$ per Cu ion in a formula unit of Eq. (1). Taking into account the trapping of a part of the holes δp [3, 7] due to deep impurity levels of Sr and Nd, optimum doping is reached for $x = x_{opt} = p_{opt} + \delta p \approx 0.15$–$0.16$. Figure 2c illustrates the case of optimum doping. The crosses refer to ARPES experimental data [8, 9]. Note that the Fermi surface crosses the boundaries of the Brillouin zones. If the electron energies undergo noticeable jumps at these boundaries, the Fermi surface in the extended band scheme should reveal breaks at these crossing points; however, experiments are apparently still not sensitive enough for them to become observable.

Electron depletion (strong doping $x \geq 0.25$) of the third Brillouin zone moves the Fermi surface close to the boundaries of the second Brillouin zone (Fig. 2d). This was also borne out by the ARPES measurements [8] (denoted by crosses).

The results presented in Fig. 2 are obtained by straightforward band-structure calculations. The results of these calculations made for the dispersion $E(\mathbf{k})$ of the upper valence bands can be fitted by the following relation obtained in the tight-binding approximation [10–12]:

$$E(\mathbf{k}) = -2t(\cos k_x + \cos k_y) - 4t'\cos k_x \cos k_y - 2t''(\cos 2k_x + \cos 2k_y) - t_\perp(\cos k_x - \cos k_y)^2/4, \quad (2)$$

where $\mathbf{k} = (k_x, k_y)$ is the wave vector of a quasi-two-dimensional reciprocal lattice; t, t', t'' are the overlap integrals with the first-, second-, and third-nearest neighbors, respectively; and $t_\perp$ is the overlap integral for coupling between the adjacent CuO_2 planes. The t, t', t'', and $t_\perp$ parameters are derived by fitting the calculations to the ARPES experiments. The parameters obtained for the $Sr_2CuO_2Cl_2$ insulator, for which the most complete experimental data are available, are as follows [11]: $t = 386$ meV, $t'/t = -0.272$, $t''/t = 0.223$, and $t_\perp = 150$ meV. The calculated valence-band maxima were found to coincide with the Brillouin zone boundaries (Fig. 2a), exactly as predicted by our oxygen-ordering model. The large magnitude of the parameters t' and t'' stresses the significance of taking into account long-range coupling in the insulating or weakly doped states of HTSC systems. This coincidence argues for the validity of the lattice-period-doubling model under consideration.

The calculations made for the case of doping yield the Fermi surfaces shown in Figs. 2b–2d. For instance, in the case of optimum doping (Fig. 2c), i.e., for the band being half-filled, the parameters are $t = 0.5$ eV, $t'/t = -0.3$, $t''/t = 0.2$, and $t_\perp = 0.15$ eV [10]. In the case of heavy doping (Fig. 2d), i.e., for a totally depleted third Brillouin zone, we have $t' = t'' = 0$. Thus, when the hole concentration is sufficiently high ($p \geq 0.25$), long-range interaction is screened efficiently.

For further discussion, the extended-band scheme is more appropriate. This scheme is shown in Fig. 3 for the case of close-to-optimum doping. The solid lines show the Fermi surface to be cut by the $z = 0$ plane in accordance with Eq. (2). The hatched area is the region occupied by electrons. The dashed lines bound the third Brillouin zone. The coordinates of the points are in units of π/a. $\mathbf{G}_L = 2(\pi/a)[1\ 0\ 0]$ (or $\mathbf{G}_L = 2(\pi/a)[0\ 1\ 0]$) is the reciprocal lattice vector for the direct lattice without doubling (we assume, for the sake of simplicity, that the lattice periods in the CuO_2 planes are the same in both directions and equal to a). Hence, vector $\mathbf{G}_L$ is the translation vector of the copper ion sublattice. Vector $\mathbf{G}_0 = \mathbf{G}_L/2$ is the reciprocal-lattice vector of the doubled-period direct lattice; in other words, it is the translation vector of the oxygen sublattice of the $O^{1.5-}$ ions, which form a narrow valence band near the Fermi level. We denote by ε the distance between the boundary of the third Brillouin zone and the Fermi surface (Fig. 3). Vector $\mathbf{Q}_n = \mathbf{G}_0 - 2\varepsilon$ (Fig. 3) is the nesting vector connecting nearly parallel (congruent) parts of the Fermi surface. It is well known [13] that nesting gives rise to a Peierls instability accompanied by the formation of a dielectric energy gap on the Fermi surface, with the corresponding modulation of the electron density and ion distribution density in the lattice. For the case under study here (Fig. 3), this means there is modulation along the [100] and [010] directions in the direct lattice. For an arbitrary value of ε, $\mathbf{Q}_n$ is an incommensurate

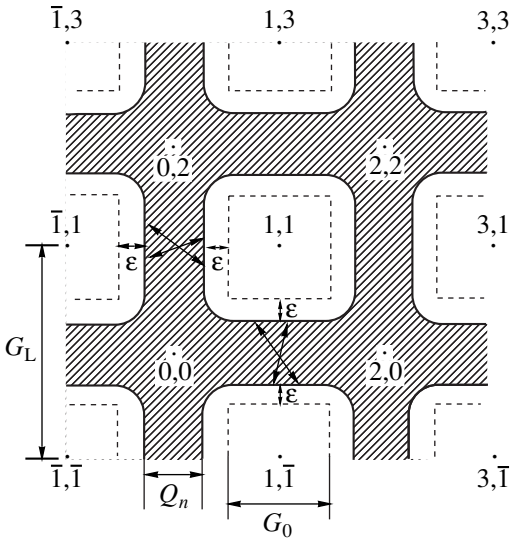

Fig. 3. Fermi surface in the extended-zone scheme constructed for the case close to optimum doping (solid lines). Dashed lines specify the boundaries of the third Brillouin zone. The electron-occupied region of states is hatched. ε is the distance between the boundary of the third Brillouin zone and the Fermi surface. See text for the notation of vectors $\mathbf{G}_L$, $\mathbf{G}_0$, and $\mathbf{Q}_n$.

vector of the reciprocal lattice. As a result, the neutron diffraction pattern should contain, in addition to the main reciprocal-lattice Bragg reflections, superstructural reflections separated by $\pm 2\varepsilon$ from the $\mathbf{G}_L$ vectors in the [100] and [010] directions, as shown in Fig. 4. This conclusion as to the superstructural lattice modulation is borne out by neutron-diffraction and x-ray measurements [1–3].

Because the formation of the superstructure also involves the Cu ions, which have a magnetic moment, their antiferromagnetic interaction produces an antiferromagnetic ordering whose period is twice that of the lattice modulation (in the direct lattice). Accordingly, superstructural reflections of the reciprocal lattice will be separated from the antiferromagnetic Bragg vectors $\mathbf{G}_{AF} = (\pi/a)[\pm 1, \pm 1, 0]$ by one half this distance (i.e., by $\pm\varepsilon$, Fig. 4). Thus, antiferromagnetic superstructural reflections should be observed for $\mathbf{G}_{AF} \pm \varepsilon$. This conclusion has also been confirmed experimentally [1–3].

As the doping is increased, the Fermi surface moves away from the boundary of the third Brillouin zone and, as seen from Fig. 3, this entails a growth in ε. Vector $\mathbf{Q}_n$ becomes commensurate with vector $\mathbf{Q}_0$ for $\varepsilon = 0.25(\pi/a)$; i.e., vector $\mathbf{Q}_n = \mathbf{Q}_0 - 2\varepsilon = (\pi/a)[1\ 0\ 0] - 0.5(\pi/a)[1\ 0\ 0] = 0.5\ (\pi/a)[1\ 0\ 0] = 0.5\mathbf{Q}_0 = 0.25\mathbf{Q}_L$. Thus, for $\varepsilon = 0.25(\pi/a)$, the lattice period quadruples in the CuO_2 plane.

As the doping is increased still further, the Peierls gap Δ^*, forming as a result of nesting over substantial parts of the Fermi surface, will decrease because of the congruence conditions breaking down in the [100]

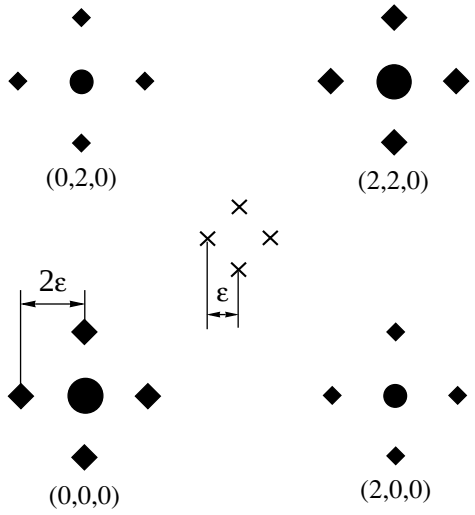

Fig. 4. Reflections and their splitting for the reciprocal lattice of oxide HTSCs. Circles are Bragg reflections for the lattice without superstructural modulation (the large and small symbols refer to the high and weak reflection intensity due to the crystal symmetry, respectively); diamonds are Bragg reflections of a lattice with superstructural modulation (±2ε); crosses are Bragg reflections for antiferromagnetic ordering with modulation (±ε).

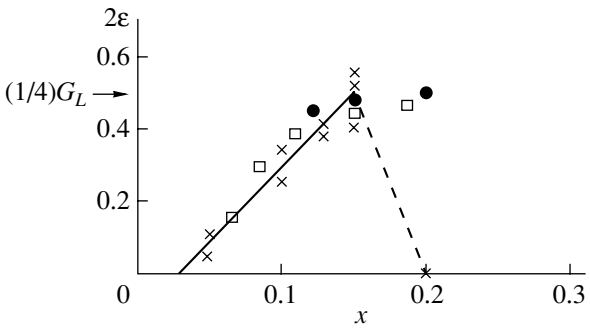

Fig. 5. Superstructural-modulation parameter ε plotted vs. acceptor doping level *x*. Solid line is an estimation using Eqs. (2)–(4); crosses are data from [14] (the dashed line connects the data points); circles are data for $La_{1.6-x}Nd_{0.4}Sr_xCuO_4$ [2]; and squares are data for $La_{2-x}Sr_xCuO_4$ [2] (these data are obtained from dynamic measurements).

directions (Fig. 2). It is known that the Peierls gap reaches a maximum in the quasi-one-dimensional case where there is a small contribution from two- or three-dimensional coupling, which suppresses fluctuations. In other words, the gap is maximum under light doping, where the Fermi surface is nearly parallel to the boundary of the Brillouin zone [Fig. 2b, Eq. (2)], and decreases under doping because of the Fermi surface curvature and an increasing contribution from two-dimensional interactions. As follows from Eq. (2), for small ε, the $E(\mathbf{k})$ relation is strong only in one direction. It is this quasi-one-dimensional behavior that results in the existence of nearly parallel parts of the Fermi surface close to the boundary of the third Brillouin zone. Under doping ($x \geq 0.15$), the $E(\mathbf{k})$ relation becomes two-dimensional to a greater extent. This results not only in a decrease in the energy gap Δ* but also in a decrease in the amplitude of superstructural modulation of both the electronic and ionic densities. This makes superstructural modulation unobservable. This conclusion has been borne out experimentally [14]. It was shown in [14] that for $x = 0.2$, the distribution of electronic density in the CuO_2 plane becomes uniform.

As seen from Fig. 2, the Fermi surface changes dramatically as one crosses over from the insulating state ($x = 0$) to a heavily doped metal ($x \approx 0.3$). This change, with increasing hole concentration *p*, can be described in the tight-binding approximation by introducing the dependence of the parameters t' and t'' on *p* in the form

$$t' = t_0'(0.25 - p)/0.25, \quad (3)$$

$$t'' = t_0''(0.25 - p)/0.25, \quad (4)$$

where t_0' and t_0'' are the parameters for the insulating state ($p = 0$). The maximum value of *p* corresponding to complete depletion of the third Brillouin zone is 0.25.

Equations (2)–(4) can be used to construct the ε(*p*)relation. Figure 5 shows the dependence of the quantity 2ε on the doping level $x = p + \delta p$ (solid line). The results obtained agree qualitatively with [1–3, 14]. The measurements reported in [14] were made not of ε but rather of the line halfwidth under superstructural ordering, which is related to ε. Therefore, the data from [14] are presented, for the sake of convenience, in arbitrary units normalized against the value of ε for $x = 0.15$ which was taken from [2]. Significantly, the superstructural modulation reported in [14] was observed only for $x < 0.2$ and disappeared at $x = 0.2$.

It is thus obvious that the new available experimental data from [1–3] find a natural and straightforward explanation in terms of the oxygen-ordering model without any need of invoking the stripe model. The model of oxygen ordering also predicts other experimental observations. It can be shown that the Peierls gap Δ* discussed above has the same properties (dependence on temperature, doping level, etc.) as the well-known pseudogap observed at temperatures below T^*. The narrowing of the Peierls gap with increasing doping level and the onset of the insulating state when the superconductivity is destroyed by a strong magnetic field for $x < x_{opt}$ [15–17] suggest that it is the Peierls gap that one observes experimentally as a pseudogap.

Another consequence of the model under consideration is possible superconducting carrier pairing at congruent parts of the Fermi surface. As seen from Fig. 3, $\mathbf{G}_0$ is the translation vector for oxygen states in the narrow upper valence band. Thus, the points $(\pi/a)(0, \pm 1)$ and $(\pi/a)(\pm 1, 0)$ can be considered to be the origin in the reduced-zone scheme. Hence, carrier pairing can

take place on the Fermi surface, as is shown by the arrows in Fig. 3, and condensation of superconducting pairs with zero momentum relative to these points is possible.

The existence of congruent sections on the Fermi surface makes nesting favorable for both Peierls (insulating) and superconducting pairing [13]. Under light doping, only the Peierls gap occurs. When the doping is increased, the feature in the density of states $N(E)$ for the Peierls gap smears out. This results from the increasing influence of the two- and three-dimensionality effects. This smear in the Peierls density of states can initiate the superconducting state. This conclusion is buttressed by tunneling measurements [18], which reveal both the superconducting gap and the density-of states singularities due to the Peierls gap at higher energies.

ACKNOWLEDGMENTS

This study was supported by the Russian Foundation for Basic Research (project no. 01-02-16395) and the Scientific Council "Topical Issues in Condensed-Matter Physics" (subprogram "Superconductivity").

REFERENCES

1. J. M. Tranquada, B. J. Sternleb, J. D. Axe, *et al.*, Nature **375**, 561 (1995).
2. J. M. Tranquada, J. D. Axe, N. Ichikawa, *et al.*, Phys. Rev. B **54**, 7489 (1996).
3. N. Ichikawa, S. Uchida, J. M. Tranquada, *et al.*, Phys. Rev. Lett. **85**, 1738 (2000).
4. U. Löw, V. J. Emery, K. Fabricius, and S. A. Kivelson, Phys. Rev. Lett. **72**, 1918 (1994).
5. A. I. Golovashkin and A. P. Rusakov, Usp. Fiz. Nauk **170**, 192 (2000).
6. *Electronic Properties and Mechanisms of High T_c Superconductors*, Ed. by T. Oguchi, K. Kadowaki, and T. Sasaki (Elsevier, Amsterdam, 1992).
7. N. V. Anshukova, A. I. Golovashkin, L. I. Ivanova, and A. P. Rusakov, Kratk. Soobshch. Fiz., No. 8, 16 (2000).
8. A. Ino, C. Kim, T. Mizokawa, *et al.*, J. Phys. Soc. Jpn. **68**, 1496 (1999).
9. A. Ino, C. Kim, Y. Nakamura, *et al.*, Phys. Rev. B **62**, 4137 (2000).
10. A. I. Liechtenstein, O. Gunnarsson, O. K. Andersen, and R. M. Martin, Phys. Rev. B **54**, 12505 (1996).
11. O. P. Sushkov, G. A. Sawatzky, R. Eder, and H. Eskes, Phys. Rev. B **56**, 11769 (1997).
12. T. Mishonov and E. J. Penev, J. Phys.: Condens. Matter **12**, 143 (2000).
13. Yu. V. Kopaev, in *Problems in High-Temperature Superconductivity*, Ed. by V. L. Ginzburg and D. A. Kirzhnits (Nauka, Moscow, 1977), p. 205.
14. E. S. Bozin, G. H. Kwei, H. Takagi, and S. J. L. Billinge, Phys. Rev. Lett. **84**, 5856 (2000).
15. S. Ono, Y. Ando, T. Mirayma, *et al.*, Phys. Rev. Lett. **85**, 638 (2000).
16. G. S. Boebinger, Y. Ando, A. Passner, *et al.*, Phys. Rev. Lett. **77**, 5417 (1996).
17. P. Faumier, Y. Wang, and G. M. Stocks, Phys. Rev. Lett. **81**, 4720 (1998).
18. V. M. Krasnov, A. Yurgens, D. Winkler, *et al.*, Phys. Rev. Lett. **84**, 5860 (2000).

Translated by G. Skrebtsov

Physics of the Solid State, Vol. 44, No. 5, 2002, pp. 804–810. Translated from Fizika Tverdogo Tela, Vol. 44, No. 5, 2002, pp. 774–779.

SEMICONDUCTORS AND DIELECTRICS

Optical Properties of Semiconductors under Strong Pumping in the *M*-Band Region and Two-Photon Probing of the Biexciton State

P. I. Khadzhi, A. V. Korovaĭ, and D. V. Tkachenko

Dniester State University, ul. 25-ogo Oktyabrya 128, Tiraspol, MD 3300 Moldova

e-mail: tdsu.@tirastel.md

Institute of Applied Physics, Academy of Sciences of Moldova, Chisinau, MD 2028 Moldova

Received May 15, 2001; in final form, July 12, 2001

Abstract—The behavior of the semiconductor dielectric susceptibility under the action of a strong laser pulse in the range of the luminescent *M* band and two-photon probe of a biexciton level is investigated. It is shown that the pronounced Autler–Towns effect occurs at the two-photon transition. The position of the absorption peaks is essentially determined by the amplitude and frequency of the pump field. © *2002 MAIK "Nauka/Interperiodica".*

1. INTRODUCTION

The optical Stark effect is one of the most striking nonlinear optical effects in the exciton spectral range. This effect has been studied in a number of experimental and theoretical works [1–11]. Experimentally, the optical Stark effect is manifested by a shift of the exciton level under the action of an ultrashort laser pulse and by its returning to the initial position after the pulse action is terminated. Theoretical works have made it possible to investigate the peculiarities of the behavior of exciton systems in semiconductors affected by strong coherent laser radiation, which leads to macroscopic coherent polarization of the medium. In [3], this effect was interpreted in terms of the exciton Bose–Einstein condensation induced by external coherent laser radiation. It turned out that the filling of the phase space by virtual electrons and holes results in a change in the internal exciton structure. These phenomena are similar to those occurring upon spontaneous exciton Bose–Einstein condensation [8]. The bands of the absorption and amplification of a weak probing beam in the presence of Bose-condensed excitons, which appear under nonequilibrium conditions due to the field of coherent laser radiation, were investigated in [9, 10]. It was shown that instabilities, which essentially affect the absorption of a probing beam, occur in the spectrum due to the real emergence of two laser photons and their conversion into two noncondensate particles.

In connection with those investigations, the pump–probe method acquired special significance in the experimental investigation of semiconductor optical properties in the exciton spectral range at high excitation levels of the crystal. This method uses two beams of laser radiation: a strong pump and a weak probing beam. The weak beam probes the changes in the optical properties of the crystal caused by the action of the pump beam. These changes are determined by the amplitude and frequency of the field and by the parameters of the crystal.

A pump–probe investigation of the optical properties of media composed of two-level atoms revealed a number of nonlinear optical effects [12]. Application of these experimental techniques to solid-state systems is very promising. For example, the pump–probe method was used to investigate the kinetics of the radiative biexciton recombination, nonlinear response of a high-density system of excitons and biexcitons, red and blue shifts of the exciton band under picosecond pumping, and the analog of the Autler–Towns effect on biexcitons in CuCl [12].

In recent years, many efforts have been made to develop a satisfactory theory of the pump–probe method for high-density systems of excitons and biexcitons [9, 10, 13, 14]. It has been shown [14] that in the presence of elastic exciton–exciton interaction, the susceptibilities of a semiconductor in the exciton spectral range reveal bistable behavior depending on the frequency and intensity of the pump pulse and on the frequency of the probing pulse.

Below, we present the results of the theoretical studies of the behavior of the semiconductor dielectric susceptibilities in the pump–probe regime. These studies were initiated by the experimental investigation of the Stark effect on excitons and biexcitons in CuCl [12], in which the splitting of the biexciton absorption band into two lines was observed at high excitation levels between the Z_3-exciton polariton and biexciton state. Knowing the amount of splitting, the authors of [12] determined the corresponding transition dipole moment in the *M*-band range. We experimentally found

1063-7834/02/4405-0804$22.00

that the spectra of the two-photon absorption bands are essentially determined by the pumping intensity and the frequencies of the pump and probe pulses.

2. STATEMENT OF THE PROBLEM AND BASIC EQUATIONS

Let us investigate the behavior of the real and imaginary parts of the semiconductor dielectric susceptibility in the case of stationary excitation by a strong pump beam in the *M*-band (optical exciton–biexciton conversion band) range and two-photon probing of the biexciton state by a weak laser beam (Fig. 1). The formulation of the problem corresponds to the experimental conditions in [12]. The biexciton state, which is a bound state of two excitons (two electrons and two holes), was observed in the spectra of different semiconductors by using either two-photon excitation from the ground state of the crystal or the optical conversion of excitons into biexcitons in the *M*-band range [15]. These processes are characterized by giant oscillator strengths. The nonlinear optical process associated with the biexciton formation can be described in terms of the three-level model of the semiconductor (Fig. 1). If the frequency of the strong coherent pump pulse is equal to the transition frequency between the exciton and biexciton states, then these states are mixed due to photon-induced exciton–biexciton transitions and the so-called dressed states of the exciton and biexciton occur (the polariton states of the system "exciton + photon and biexciton" [16, 17]). These states can be probed in the range of two-photon excitation of biexcitons from the ground state of the crystal by a weak pulse whose frequency is equal to half the biexciton transition frequency.

We consider the case where a strong monochromatic coherent laser radiation (pump beam) with amplitude E_0 and frequency $\omega_l = \Omega_0 - \omega_0$ and a weak monochromatic laser radiation (probe pulse) with amplitude E and frequency $\omega \approx \Omega_0/2$ are incident on a semiconductors; Ω_0 and ω_0 are the eigenfrequencies of the biexciton and exciton states, respectively. The pump photons mix the exciton and biexciton states, and photons of the second pulse probe these changes in the spectral range of two-photon excitation of biexcitons from the ground state of the crystal. Using the resonance approximation, which contains the terms responsible for the optical exciton–biexciton conversion by the field of the strong pulse E_0 and for two-photon excitation of biexcitons by the field of the weak pulse E, we write the interaction Hamiltonian in the form (Fig. 1)

$$\begin{aligned} H &= -\hbar\sigma(E_0^- a^+ b e^{i\omega_l t} + E_0^+ b^+ a e^{-i\omega_l t}) \\ &\quad -\hbar\mu(b^+ E^+ E^+ e^{-2i\omega t} + b E^- E^- e^{2i\omega t}), \end{aligned} \tag{1}$$

where a and b are the amplitudes of excitonic and biexcitonic polarization waves of the medium, respectively; $E_0^+(E^+)$ and $E_0^-(E^-)$ are the positive- and negative-frequency components of the pump (probe) radiation; and σ and μ are the constants characterizing the optical exciton–biexciton conversion and two-photon excitation of biexcitons from the ground state of the crystal, respectively [15, 17, 18].

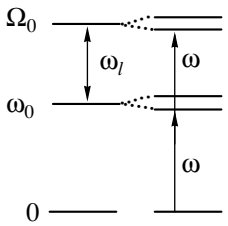

Fig. 1. Schematic diagram of the energy levels (0 is the ground state of the crystal and ω_0 and Ω_0 are the exciton and biexciton states, respectively) and quantum transitions under the action of a pump field with frequency ω_l and two-photon probing of the biexciton level by a pulse with frequency ω.

Using Eq. (1) and assuming the exciton, biexciton, and photon states to be macroscopically filled, we can easily obtain the Heisenberg (material) equations for the amplitudes a and b:

$$i\dot{a} = \omega_0 a - i\gamma_1 a - \sigma E_0^- b e^{i\omega_l t}, \tag{2}$$

$$i\dot{b} = \Omega_0 b - i\gamma_2 b - \sigma E_0^+ a e^{-i\omega_l t} - \mu E^+ E^+ e^{-2i\omega t}, \tag{3}$$

where γ_1 and γ_2 are phenomenological parameters characterizing exciton and biexciton damping, respectively, due to exciton and biexciton transitions from the coherent to incoherent modes.

Let us calculate the response of the system to all orders in the perturbation expansion in the pump pulse amplitude E_0 and to the second order in the amplitude E of the weak pulse in the stationary regime. We seek a solution to Eq. (2) in the form of a sum of terms with the exponential factors $\exp(-i\omega_l t)$ and $\exp(-i\omega t)$ and a solution to Eq. (3) in the form of a sum of terms with the factors $\exp(-2i\omega_l t)$ and $\exp(-2i\omega t)$, which oscillate with the frequencies of the strong and weak pulses. In this case, the nonlinear parts of these equations lead to the appearance of resonant terms. In Eq. (2), these terms are proportional to $\exp(-2i\omega_l t + i\omega t)$ and $\exp(-2i\omega t + i\omega_l t)$, and those in Eq. (3) are proportional to $\exp(-i\omega t - i\omega_l t)$ and $\exp(-3i\omega_l t + i\omega t)$; the frequencies of these terms are close to the frequencies of the corresponding transitions. Thus, we seek solutions to Eqs. (2) and (3) in the form

$$\begin{aligned} a = a_0 e^{-i\omega_l t} + a_0^* e^{i\omega_l t} + A_1 e^{-i\omega t} + A_1^* e^{i\omega t} + A_2 e^{-i(2\omega-\omega_l)t} \\ + A_2^* e^{i(2\omega-\omega_l)t} + A_3 e^{-i(2\omega-\omega_l)t} + A_3^* e^{i(2\omega-\omega_l)t}, \end{aligned} \tag{4}$$

$$b = b_0 e^{-2i\omega_l t} + b_0^* e^{2i\omega_l t} + B_1 e^{-i(\omega_l+\omega)t} + B_1^* e^{i(\omega_l+\omega)t} + B_2 e^{-2i\omega t} + B_2^* e^{2i\omega t} + B_3 e^{-i(3\omega_l-\omega)t} + B_3^* e^{i(3\omega_l-\omega)t}, \quad (5)$$

where a_0, A_1, A_2, A_3, and b_0, B_1, B_2, B_3 are time-independent amplitudes. Substituting Eqs. (4) and (5) into Eqs. (2) and (3) and equating the coefficients of the identical exponentials, we obtain the following system of nonlinear equations to the lowest order in the amplitudes E, A_i, and B_i ($i = 1, 2, 3$) in the stationary regime:

$$\begin{aligned}
(\omega_l - \omega_0 + i\gamma_1)a_0 &= -\sigma E_0^- b_0,\\
(\omega - \omega_0 + i\gamma_1)A_1 &= -\sigma E_0^- B_1,\\
(2\omega - \omega_l - \omega_0 + i\gamma_1)A_2 &= -\sigma E_0^- B_2,\\
(2\omega_l - \omega - \omega_0 + i\gamma_1)A_3 &= -\sigma E_0^- B_3,\\
(2\omega_l - \Omega_0 + i\gamma_2)b_0 &= -\sigma E_0^+ a_0,\\
(\omega_l + \omega - \Omega_0 + i\gamma_2)B_1 &= -\sigma E_0^+ A_1,\\
(2\omega - \Omega_0 + i\gamma_2)B_2 &= -\sigma E_0^+ A_2 - \mu E^+ E^+,\\
(3\omega_l - \omega - \Omega_0 + i\gamma_2)B_3 &= -\sigma E_0^+ A_3.
\end{aligned} \quad (6)$$

From these equations, we obtain $a_0 = b_0 = A_1 = B_1 = A_3 = B_3 = 0$ and

$$B_2 = -\frac{\mu E^+ E^+}{2\omega - \Omega_0 + i\gamma_2 - \dfrac{\sigma^2 E_0^2}{2\omega - \omega_l - \omega_0 + i\gamma_1}}. \quad (7)$$

The probing pulse induces the polarization of the medium P corresponding to the two-photon transition from the ground state of the crystal into the biexciton state, which is determined by the equation $P = 2\hbar\mu b E^- = \chi E^+ E^+ E^-$. Taking this into account and using Eqs. (5) and (7), we obtain the following expression for the complex dielectric susceptibility of the medium $\chi \equiv \chi^{(3)}$:

$$\chi = -\frac{2\hbar\mu^2}{2\omega - \Omega_0 + i\gamma_2 - \dfrac{\sigma^2 E_0^2}{2\omega - \omega_l - \omega_0 + i\gamma_1}}. \quad (8)$$

This formula shows that the dielectric susceptibility χ is a nonlinear function of the amplitude E_0 of the field of the strong pump pulse ($\sigma E_0 = \omega_R$ is the Rabi frequency) and a complicated function of the frequencies ω_l and ω of both pulses. To understand the results that follow, let us consider the dependence of the dielectric susceptibility on the frequency ω of the probe radiation in the limit of zero damping constants. In this case, we have

$$\chi(\omega) = -\frac{2\hbar\mu^2(2\omega - \omega_0 - \omega_l)}{(2\omega - \Omega_0)(2\omega - \omega_0 - \omega_l) - \sigma^2 E_0^2}. \quad (9)$$

It follows from Eq. (9) that $\chi(\omega)$ diverges if the frequency of the probing pulse equals $\omega = \omega_\pm$, where

$$\omega_\pm = \frac{1}{4}(\Omega_0 + \omega_0 + \omega_l \pm \sqrt{(\omega_l + \omega_0 - \Omega_0)^2 + 4\sigma^2 E_0^2}). \quad (10)$$

It should be noted that a similar formula was used in [12, Eq. (1)] to interpret the experimental data.

If the frequency of the pump pulse is in exact resonance with transitions in the M-band range, then we have

$$\omega_\pm = \frac{1}{2}(\Omega_0 \pm \sigma E_0). \quad (11)$$

If the detuning between the frequency of the strong pulse and the transition frequency is significantly larger than the Rabi frequency, then

$$\omega_+ = \frac{1}{2}(\omega_0 + \omega_l), \quad \omega_- = \frac{1}{2}\Omega_0. \quad (12)$$

The frequencies $\omega_\pm$ are the eigenfrequencies of the renormalized states. The pump field mixes two states of the same energy: the biexciton state and the combined state of the exciton and a pump photon. The coherent coupling of these states leads to the renormalization of the semiconductor energy spectrum. We can see from Eqs. (10) and (11) that the eigenfrequencies of the new states ω_+ and ω_- are determined by the amplitude of the pump pulse E_0. The splitting between these states $\omega_+ - \omega_-$ grows with increasing E_0.

Using Eq. (9) and the formula $c^2k^2/\omega^2 = \varepsilon_\infty + 4\pi\chi|E|^2$ (ε_∞ is the background dielectric function and E is the amplitude of the probe field), we can derive the dispersion law $\omega(k)$ for the probe photons in the presence of a strong pumping pulse (Fig. 2). It is seen from Fig. 2 that the dispersion law consists of three branches. We

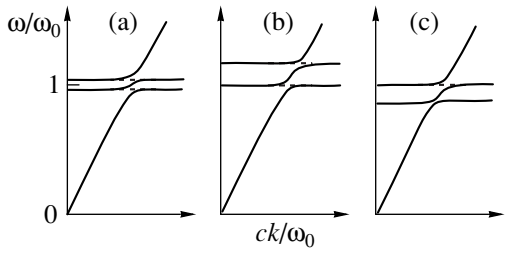

Fig. 2. The dispersion laws for the probing photons in the presence of a strong pump pulse, which mixes the exciton and biexciton levels, at different frequencies ω_l of the pump pulse: (a) $\omega_l + \omega_0 = \Omega_0$, (b) $\omega_l + \omega_0 > \Omega_0$, and (c) $\omega_l + \omega_0 < \Omega_0$.

explain this dispersion as follows. The pump field splits the biexciton level into two sublevels with frequencies ω_+ and ω_-. Under the conditions of two-photon excitation of biexcitons from the ground state of the crystal, the interaction between the probe photons and these levels results in polariton-like branches of the dispersion law of the weak pulse. With increasing pump field amplitude E_0, the region of existence of the middle branch broadens (Fig. 2). There are also two longitudinal modes, whose frequencies are determined by the condition $\varepsilon = 0$.

The real χ' and imaginary χ'' parts of the susceptibility $\chi = \chi' + i\chi''$ can be found to be

$$\chi' = -\frac{2\hbar\mu^2\left(2\omega - \Omega_0 - \dfrac{\sigma^2 E_0^2(2\omega - \omega_l - \omega_0)}{(2\omega - \omega_l - \omega_0)^2 + \gamma_1^2}\right)}{\left(2\omega - \Omega_0 - \dfrac{\sigma^2 E_0^2(2\omega - \omega_l - \omega_0)}{(2\omega - \omega_l - \omega_0)^2 + \gamma_1^2}\right)^2 + \left(\gamma_2 + \gamma_1\dfrac{\sigma^2 E_0^2}{(2\omega - \omega_l - \omega_0)^2 + \gamma_1^2}\right)^2}, \tag{13}$$

$$\chi'' = \frac{2\hbar\mu^2\left(\gamma_2 + \gamma_1\dfrac{\sigma^2 E_0^2}{(2\omega - \omega_l - \omega_0)^2 + \gamma_1^2}\right)}{\left(2\omega - \Omega_0 - \dfrac{\sigma^2 E_0^2(2\omega - \omega_l - \omega_0)}{(2\omega - \omega_l - \omega_0)^2 + \gamma_1^2}\right)^2 + \left(\gamma_2 + \gamma_1\dfrac{\sigma^2 E_0^2}{(2\omega - \omega_l - \omega_0)^2 + \gamma_1^2}\right)^2}. \tag{14}$$

It follows from Eqs. (13) and (14) that the susceptibilities χ' and χ'' are nonlinear functions of the amplitude E_0 of the strong pump pulse and depend on the frequencies ω_l and ω of both pulses. When the frequencies of each pulse are in exact resonance with the corresponding transitions (with frequencies $\omega_l = \Omega_0 - \omega_0$ and $\omega = \Omega_0/2$), we have $\chi' = 0$ and

$$\chi'' = \frac{2\hbar\mu^2/\gamma_2}{1 + \dfrac{\sigma^2 E_0^2}{\gamma_1\gamma_2}}. \tag{15}$$

It follows from Eq. (15) that under the conditions of exact resonance, the susceptibility χ'' quickly saturates with increasing pump intensity. If the pump photons are in resonance with the frequency of transitions in the *M*-band range ($\omega_l = \Omega_0 - \omega_0$), then the absorption component χ'' of the susceptibility, as a function of the probing pulse frequency, is symmetrical with respect to the frequency $\omega = \Omega_0/2$. If the pump amplitude is such that $\sigma^2 E_0^2 \le \gamma_1^3/(2\gamma_1 + \gamma_2)$, then the spectral dependence of χ'' has a maximum at $\omega = \Omega_0/2$. In the opposite case of $\sigma^2 E_0^2 \ge \gamma_1^3/(2\gamma_1 + \gamma_2)$, it has a minimum at $\omega = \Omega_0/2$ and two symmetrical maxima at the frequencies

$$\omega = \frac{1}{2}\left(\Omega_0 \pm \sqrt{\left(2 + \frac{\gamma_2}{\gamma_1}\right)\frac{\sqrt{\sigma^2 E_0^2 + \gamma_1\gamma_2}\left(\sigma^2 E_0^2 - \dfrac{\gamma_1^3}{2\gamma_1 + \gamma_2}\right)}{\left(1 + \dfrac{\gamma_2}{\gamma_1}\right)\sigma E_0 + \sqrt{\sigma^2 E_0^2 + \gamma_1\gamma_2}}}\right). \tag{16}$$

Introducing the normalized quantities

$$\delta = \Delta/\gamma_1, \quad \delta_l = \Delta_l/\gamma_1, \quad s = \gamma_2/\gamma_1,$$
$$f_0 = \sigma E_0/\gamma_1, \quad \chi_0 = 2\hbar\mu^2/\gamma_1, \tag{17}$$

where $\Delta = \omega - \Omega_0/2$ and $\Delta_l = \omega_l - (\Omega_0 - \omega_0)$ are the detuning of each pulse from resonance, we can represent Eqs. (13) and (14) in the form

$$\frac{\chi'}{\chi_0} = -\frac{2\delta - \dfrac{(2\delta - \delta_l)f_0^2}{(2\delta - \delta_l)^2 + 1}}{\left(2\delta - \dfrac{(2\delta - \delta_l)f_0^2}{(2\delta - \delta_l)^2 + 1}\right)^2 + \left(s + \dfrac{f_0^2}{(2\delta - \delta_l)^2 + 1}\right)^2}, \tag{18}$$

$$\frac{\chi''}{\chi_0} = \frac{s + \dfrac{f_0^2}{(2\delta - \delta_l)^2 + 1}}{\left(2\delta - \dfrac{(2\delta - \delta_l)f_0^2}{(2\delta - \delta_l)^2 + 1}\right)^2 + \left(s + \dfrac{f_0^2}{(2\delta - \delta_l)^2 + 1}\right)^2}. \tag{19}$$

Here, f_0 plays the role of the Rabi frequency in the spectral range of the optical exciton–biexciton conversion. It follows from Eqs. (18) and (19) that $\chi'(-\delta_l, -\delta) = -\chi'(\delta_l, \delta)$ and $\chi''(-\delta_l, -\delta) = \chi''(\delta_l, \delta)$.

3. DISCUSSION

It follows from Eq. (19) that at $\delta_l = 0$ (at exact resonance with respect to the pumping), the function $\chi''(\delta)$ is a Lorentzian with the maximum at $\delta = 0$ and half-width γ_2. With an increase in f_0, the Lorenzian is distorted gradually; at the critical field $f_0 = f_{0c} = (2 + s)^{-1/2}$, a dip appears in the center of the $\chi''(\delta)$ curve which becomes deeper with increasing f_0; and at $f_0 > f_{0c}$, the $\chi''(\delta)$ curve transforms into two Lorentzians located symmetrically about $\delta = 0$. In this case, the absorption of the probing pulse is associated with two exciton sublevels split by the pump pulse. Evidence of the formation of new polariton states is found in the splitting in the spectrum of two-photon probing in the region of biexciton resonance. Figure 3 shows the spectrum of the absorption component of the susceptibility as dependent on the detuning of the resonance δ for the probe pulse at $\delta_l = 0$ for different amplitudes of the pump field f_0. It is clearly seen that as the pump field increases, splitting of the biexciton line occurs and monotonically increases and the absorption at the center of the absorption band decreases quickly. The calculated peaks of the absorption spectrum of the weak probing pulse are consistent with those observed in the experiment [12, Fig. 2]. At high excitation levels, the pedestal of the absorption bands is determined by the parameter s. At $f_0 \gg f_{0c}$, we have $\chi'' \sim f_0^{-2}$.

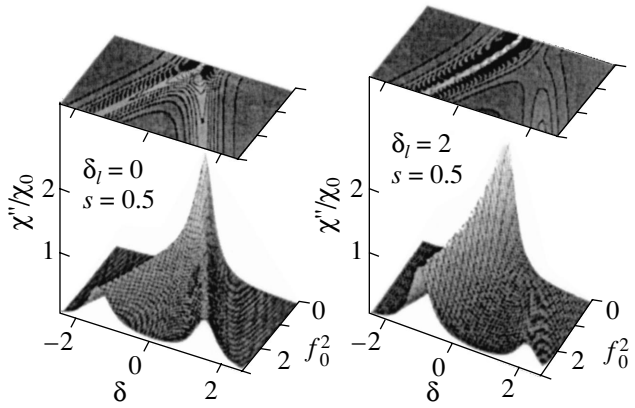

Fig. 3. Dependence of the absorption component χ''/χ_0 of the susceptibility on the detuning of the resonance δ of the probe pulse and on the field amplitude f_0 of the pump pulse at two values of the detuning of the resonance δ_l for the frequency of the pump pulse.

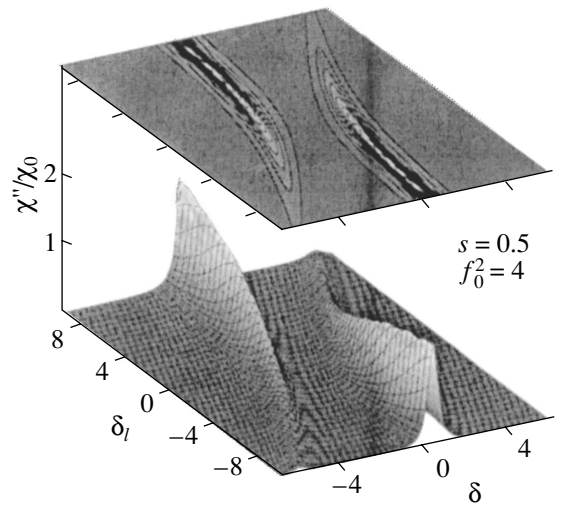

Fig. 4. Dependence of the absorption component χ''/χ_0 of the susceptibility on the detuning of the resonance of the pump pulse δ_l and of the probe pulse δ at a fixed value of the pump field amplitude f_0.

The absorption spectrum also depends essentially on the difference δ_l between the frequency of the pump field and the transition frequency in the *M*-band region. It is seen from Fig. 3 that the absorption band acquires an asymmetric form. At $\delta_l > 0$, the long-wavelength absorption peak for the probe radiation is stronger than the short-wavelength peak. In this case, the latter peak initially increases with a growth in the excitation level, then reaches its maximum value, and decreases, whereas the long-wavelength peak decreases quickly after its appearance. This occurs because at $\delta_l > 0$, the upper polariton-like branch of the system "exciton + pump photon and biexciton" is biexciton-like to a smaller extent; that is, it contains a dominant electromagnetic and a feebly marked mechanical component, which leads to suppression of the two-photon absorption of the probe radiation. At $\delta_l < 0$, the situation is opposite. These results also agree well with the experimental data [12, Fig. 3]. The upper part of Fig. 3 shows contour lines of equal susceptibility which are symmetrical (with respect to $\delta = 0$) at $\delta_l = 0$ and asymmetrical at $\delta_l \neq 0$. The larger δ_l, the more pronounced one of the two absorption peaks and the weaker the other.

Figure 4 shows the $\chi''(\delta_l, \delta)$ spectra depending on the resonance detuning of both pulses at a fixed excitation level. In the vicinity of $\delta_l = 0$, the function $\chi''(\delta)$ has a symmetrical two-peak structure. At $|\delta_l| \gg f_0$, the absorption spectrum becomes essentially asymmetrical. For example, at $\delta_l \gg f_0$, there is a strong long-wavelength and a weak short-wavelength absorption peak. The spectral position of the strong peak is virtually independent of δ_l and is determined by the frequency ω_- of the renormalized energy spectrum of the semiconductor, whereas the spectral position of the weak peak is determined by the frequency ω_+. At $\delta_l \gg f_0$, we have $\omega_+ \sim \delta_l/2$; i.e., the weak peak rapidly shifts to shorter wavelengths with increasing δ_l. The amplitudes of these peaks are different, because the split polariton-

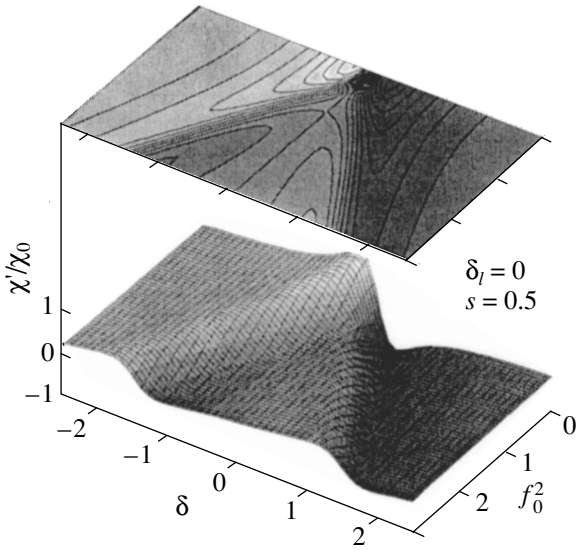

Fig. 5. Dependence of the dispersion component χ'/χ_0 of the susceptibility on the detuning of the resonance δ of the probe pulse and on the pump pulse amplitude f_0 at $\delta_l = 0$.

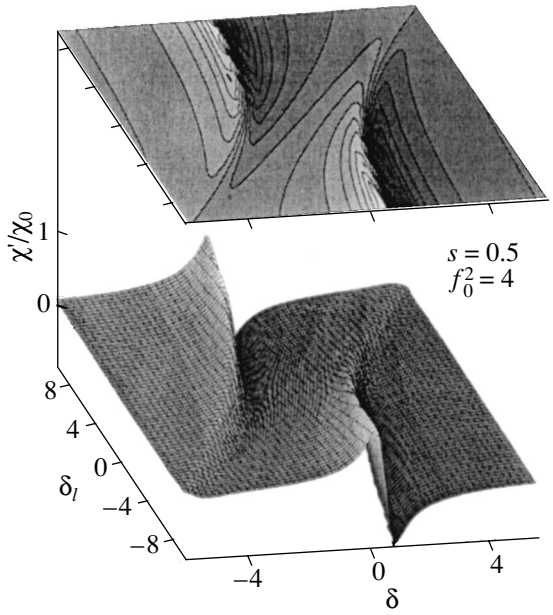

Fig. 6. Dependence of the dispersion component χ'/χ_0 of the susceptibility on the detuning of the resonance of the pump pulse δ_l and probing pulse δ at a fixed value of the pump field amplitude f_0.

like states formed by the field of the strong pulse have different fractions of the mechanical component.

It should be noted that at low temperatures, when $\gamma_1 \longrightarrow 0$ and $\gamma_2 \longrightarrow 0$, the absorption band of the probe radiation consists of two pronounced, δ-function-like peaks at the frequencies ω_+ and ω_-. The larger the amplitude of the pump field E_0, the larger the distance between these peaks. With increasing temperature, the peaks broaden and their amplitudes decrease.

It should also be noted that the absorption component χ'' is always positive. Therefore, upon any changes in the intensity and frequency of the pumping pulse, the probing pulse is absorbed; it cannot be amplified, in contrast to the case where there is elastic exciton–exciton interaction [14].

Precision measurements of the absorption peak positions can provide detailed information on the parameters of the optical transitions.

It should be noted that only the behavior of the absorption component of the susceptibility was studied in [12]. Nevertheless, the behavior of the dispersion component χ' of the susceptibility is of great interest. It is seen from Eq. (18) that χ' also essentially depends on the amplitude of the pump pulse f_0 and on the frequencies of both pulses. Figure 5 shows the $\chi'(\delta, f_0)$ dependence at $\delta_l = 0$. It can be seen that at $f_0 \gtrsim 0$, the $\chi'(\delta)$ graph has a typical form with a maximum and a minimum symmetrically located about $\delta = 0$. As the excitation level grows, the extrema of the $\chi'(\delta)$ curve shift to longer and shorter wavelengths, respectively, and their amplitudes decrease. At a certain value of the pump field amplitude f_0, an additional maximum and minimum appear; therefore, the $\chi'(\delta)$ dependence has two regions of anomalous dispersion in this case. These results are in complete agreement with those for the function $\chi''(\delta)$ shown in Fig. 3.

Figure 6 shows the $\chi'(\delta, \delta_l)$ dependence at a fixed value of f_0, which also demonstrates changes in the semiconductor energy spectrum due to a strong pump pulse. At $\delta_l \gg f_0$, there is a long-wavelength region of dispersion with a sharp change in $\chi'(\delta)$ and a distant short-wavelength region of feebly marked dispersion. These features are also consistent with those in the behavior of the function $\chi''(\delta)$ (Fig. 4).

4. CONCLUSION

Thus, the results of the experimental investigations [12] of the peculiarities of two-photon probing of the biexciton state of a semiconductor excited by a strong laser pulse in the absorption *M*-band region associated with optical exciton–biexciton conversion are explained theoretically. The dispersion and absorption components of the semiconductor dielectric susceptibility depending on the frequency of the probing pulse, as well as on the amplitude and frequency of the pump pulse, are calculated. It is shown that the form of the two-photon absorption band for a weak probing pulse is essentially determined by the frequency and amplitude of the pump field and acquires a pronounced doublet structure as the excitation level grows. This paper gives additional information on the dynamics of the absorp-

tion component of the susceptibility that can be used in further experiments. The calculated dispersion component of the susceptibility can also be useful in explaining experimental results and gives a more comprehensive understanding of the physical processes involved.

REFERENCES

1. W. H. Knox, D. S. Chemla, D. A. B. Miller, *et al.*, Phys. Rev. Lett. **62**, 1189 (1989).
2. C. Klingshirn, Semicond. Sci. Technol. **5**, 457 (1990); Semicond. Sci. Technol. **5**, 1006 (1990).
3. S. Schmitt-Rink, D. S. Chemla, and H. Huag, Phys. Rev. B **37**, 941 (1988).
4. M. Combescot, Phys. Rep. **221**, 167 (1992).
5. V. R. Mis'ko, S. A. Moskalenko, and M. I. Shmiglyuk, Fiz. Tverd. Tela (St. Petersburg) **35**, 3213 (1993) [Phys. Solid State **35**, 1580 (1993)].
6. A. L. Ivanov and L. V. Keldysh, Zh. Éksp. Teor. Fiz. **84**, 404 (1983) [Sov. Phys. JETP **57**, 234 (1983)].
7. A. L. Ivanov and H. Haug, Phys. Rev. B **48**, 1490 (1993).
8. L. V. Keldysh and A. N. Kozlov, Zh. Éksp. Teor. Fiz. **54**, 978 (1968) [Sov. Phys. JETP **27**, 521 (1968)].
9. S. A. Moskalenko, V. G. Pavlov, and V. R. Mis'ko, Fiz. Tverd. Tela (St. Petersburg) **40**, 924 (1998) [Phys. Solid State **40**, 850 (1998)].
10. S. A. Moskalenko and D. W. Snoke, *Bose–Einstein Condensation of Excitons and Diexcitons and Coherent Nonlinear Optics with Excitons* (Cambridge Univ. Press, Cambridge, 2000).
11. S. E. Harris, J. E. Field, and A. Kasapi, Phys. Rev. A **46**, R29 (1992).
12. R. Shimano and M. Kuwata-Gonokami, Phys. Rev. Lett. **72**, 530 (1994).
13. G. S. Agarwal, Phys. Rev. A **51**, R2711 (1995).
14. P. I. Khadzhi and D. V. Tkachenko, Fiz. Tverd. Tela (St. Petersburg) **40**, 934 (1998) [Phys. Solid State **40**, 860 (1998)]; in Proc. SPIE **3405**, 406 (1997).
15. P. I. Khadzhi, *The Kinetics of Recombination Radiation of Excitons and Biexcitons in Semiconductors* (Shtiintsa, Kishinev, 1977).
16. P. I. Khadzhi, S. A. Moskalenko, and S. N. Belkin, Pis'ma Zh. Éksp. Teor. Fiz. **29**, 223 (1979) [JETP Lett. **29**, 200 (1979)].
17. P. I. Khadzhi, *Nonlinear Optical Processes in System of Excitons and Biexcitons in Semiconductors* (Shtiintsa, Kishinev, 1984).
18. E. Hanamura, Solid State Commun. **12**, 951 (1973); J. Phys. Soc. Jpn. **39**, 1506 (1975).

Translated by A. Poushnov

Physics of the Solid State, Vol. 44, No. 5, 2002, pp. 811–815. Translated from Fizika Tverdogo Tela, Vol. 44, No. 5, 2002, pp. 780–784.

SEMICONDUCTORS AND DIELECTRICS

Study of Birefringence in Porous Silicon Layers by IR Fourier Spectroscopy

L. P. Kuznetsova, A. I. Efimova, L. A. Osminkina, L. A. Golovan', V. Yu. Timoshenko, and P. K. Kashkarov

Moscow State University, Vorob'evy gory, Moscow, 119899 Russia

e-mail: kuzl@vega.phys.msu.su

Received June 28, 2001

Abstract—Birefringence in porous silicon layers prepared with different etching currents on a (110) substrate is studied by IR Fourier spectroscopy. The spectra exhibit beats in the intensity of transmitted and reflected radiation due to the summation of the intensities of the ordinary and extraordinary waves interfering in the porous layer. An analysis of the spectra shows the layers to exhibit properties of a negative uniaxial crystal with the optical axis lying in the layer plane. The difference between the refractive indices of the ordinary and extraordinary waves for a layer with a porosity of 80% reaches 18%. The experimental data are in agreement with the calculations based on the effective-medium approximation, which takes into account the anisotropy of silicon nanocrystal arrangement in a porous layer. © *2002 MAIK "Nauka/Interperiodica"*.

1. INTRODUCTION

Due to its remarkable electronic and optical properties, porous silicon (PS) has been attracting considerable interest over the past decade. In particular, high-porosity PS exhibits efficient photoluminescence in the visible range [1], which may be considered to result from quantum size effects due to confinement of the photoexcited carriers in silicon nanocrystals [2]. As the nanocrystal dimensions are much less than the wavelength in the optical region, the optical properties of PS are characterized by an effective dielectric permittivity (DP). The latter differs considerably from that of crystalline silicon because most of the material has been removed [3]. The optical properties of PS have been reported in many publications (see, e.g., [1–4]). Only quite recently, however, was it established that PS exhibits a noticeable optical anisotropy [5–7].

It is known that crystalline silicon has cubic symmetry and is isotropic; however, the nanostructure formed in the growth of pores gives rise to optical anisotropy. The reason for this lies in the pores growing preferentially along the [100] crystallographic directions [2]. PS layers prepared on (100) substrates are optically isotropic under normal incidence but exhibit birefringence when light strikes the surface at an angle, which is interpreted as form birefringence [5]. PS layers prepared on low-symmetry substrates, for instance, (110)-oriented plates, exhibit strong birefringence under normal light incidence [6, 7]. At present, there is no consistent theory describing the birefringence phenomenon in PS layers. In [7], this phenomenon is attributed to spatial distribution of silicon nanocrystals with different filling factors in two main directions in the (110) plane. The DP tensor of a system of cylindrical nanocrystals is considered theoretically in [8]. However, the applicability of the latter model to real PS layers requires substantiation. To develop an adequate model which would describe PS birefringence, one would obviously have to obtain new experimental data, in particular, the dependence of the DP anisotropy of this material on its porosity. One should also learn whether PS is a positive or a negative crystal.

This work was aimed at a comprehensive study of the birefringence phenomenon in (110)-oriented PS layers of different porosity. The IR Fourier spectroscopy method employed permits one to investigate the reflectance and transmittance of PS layers at various angles of light incidence over a broad spectral range.

2. EXPERIMENTAL TECHNIQUE

PS layers were prepared by electrochemical etching of (110)-oriented single-crystal plates of p^{++}-Si : B (electrical resistivity 1.5 mΩ cm) in a 1 : 1 solution of HF (48%) in ethanol. The etching current density was varied from 10 to 100 mA/cm^2, which corresponds to a porosity of 60–80%. The etching time was varied from 5 to 35 min, and the layer thicknesses thus obtained were 10–50 μm. The film was exfoliated from the substrate by sharply increasing the current density up to 500 mA/cm^2 for a few seconds. The thickness of the exfoliated PS layers was measured with an optical microscope.

A Perkin–Elmer Spectrum RXI FT-IR (Fourier Transform Infrared) spectrometer was used in measuring the IR spectra. The IR transmittance and reflectance spectra were obtained in the range from 500 to 6500 cm^{-1} (1.54–20 μm) with a resolution of 4 cm^{-1}.

1063-7834/02/4405-0811$22.00

The reflectance spectra were taken at a close-to-normal incidence angle. The transmittance spectra were studied at different incidence angles. The experiments were carried out in air at room temperature.

3. EXPERIMENTAL RESULTS AND DISCUSSION

Figure 1 presents typical reflectance and transmittance spectra of (110)-oriented PS layers obtained with polarized IR radiation. The transmittance spectra feature lines corresponding to absorption by Si–H_x (2050–2150, ~910, 610–630 cm^{-1}) and Si–O–Si bonds (1070–1190 cm^{-1}) [3]. The spectra exhibit clearly pronounced periodic intensity oscillations associated with interference in the thin layer. The amplitude of these oscillations is modulated by beats, whose period is the same in transmission and reflection. No such beats were observed on reference PS layers prepared on a (100)-oriented substrate. The onset of beats in (110) layers can be accounted for by the ordinary and extraordinary waves interfering in the porous layer.

The observed beats can be characterized by a short ($\Delta\nu_1$) and a long ($\Delta\nu_2$) period (Fig. 1). The beat periods can be readily connected with the refractive indices for the ordinary and extraordinary waves. Indeed, in the case of a uniaxial crystal with the optical axis lying in the layer plane, the intensities of two waves, an ordinary and an extraordinary one, each of which interferes in the thin film, will add to produce beats. Thus, under normal incidence,

$$\Delta\nu_1 = \frac{1}{d(n_o + n_e)}, \qquad (1)$$

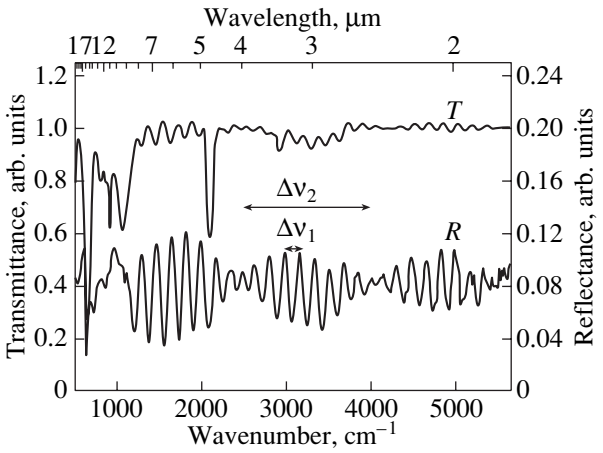

Fig. 1. IR transmittance (*T*) and reflectance (*R*) spectra of a porous silicon layer prepared on a (110)-oriented substrate. The spectra were obtained with nonpolarized radiation. The etch current density was $j = 50$ mA/cm^2, and the layer thickness was $d = 16$ μm.

$$\Delta\nu_2 = \frac{1}{2d|n_o - n_e|}, \qquad (2)$$

where d is the layer thickness and n_o and n_e are the refractive indices for the ordinary and extraordinary waves, respectively. Straightforward estimates made using Eqs. (1) and (2) yield $n_o = 1.76$ and $n_e = 1.58$ for the layers formed at a current density of 50 mA/cm^2. For d varying from 10 to 60 μm, the refractive indices did not depend on the layer thickness. The samples exhibited stable optical properties for several months after their preparation.

Note that although measurements with unpolarized light do allow determination of n_o and n_e, relating these quantities to the crystallographic directions in the original silicon crystal is possible only by using polarized radiation. Polarization measurements were conducted in the spectral region 4000–6000 cm^{-1} (1.66–2.5 μm). No beats were present in the transmittance spectra obtained with polarizers, which made it possible to determine the refractive indices for different polarization directions. Thus, we succeeded in establishing that the refractive index for the light polarized along [001] is minimum, whereas along the $[1\bar{1}0]$ axis, it is maximum.

Fast Fourier transform is a more precise method of determining n_o and n_e by analyzing the beat pattern in a PS layer. We used reflectance and transmittance spectra differentiated with respect to wave vector, which made it possible to eliminate the invariable component and to reduce the contribution due to the absorption lines originating from surface molecular groups. The frequencies of the corresponding Fourier components $\omega_{o,e}$ are related to the refractive indices through a simple expression, $\omega_{o,e} = 4\pi d n_{o,e}$. This permits one to easily find the values of n_o and n_e.

Figure 2 shows Fourier-analyzed transmittance spectra obtained at different incidence angles. The sample was rotated about the $[1\bar{1}0]$ crystallographic axis. The data obtained in the Fourier analysis were used to derive the refractive indices, with due account made of the dependence of the Fourier component frequencies on the angle of light incidence θ on the sample: $\omega_{o,e} = 4\pi d(n_{o,e}^2 - \sin^2\theta)^{1/2}$. We readily see that the Fourier component corresponding to the smaller refractive index shifts toward larger values of the refractive index with increasing incidence angle. It is known that the phase velocity and, hence, the refractive index n_e of the extraordinary wave depend on the wave-vector direction in the crystal. Therefore, one may conclude that the smaller refractive index corresponds to the extraordinary wave, in other words, that the birefringent film under study exhibits properties of a negative crystal whose optical axis coincides with the $[00\bar{1}]$ crystallographic axis. Note that the Fourier component corresponding to the extraordinary wave disappears at suffi-

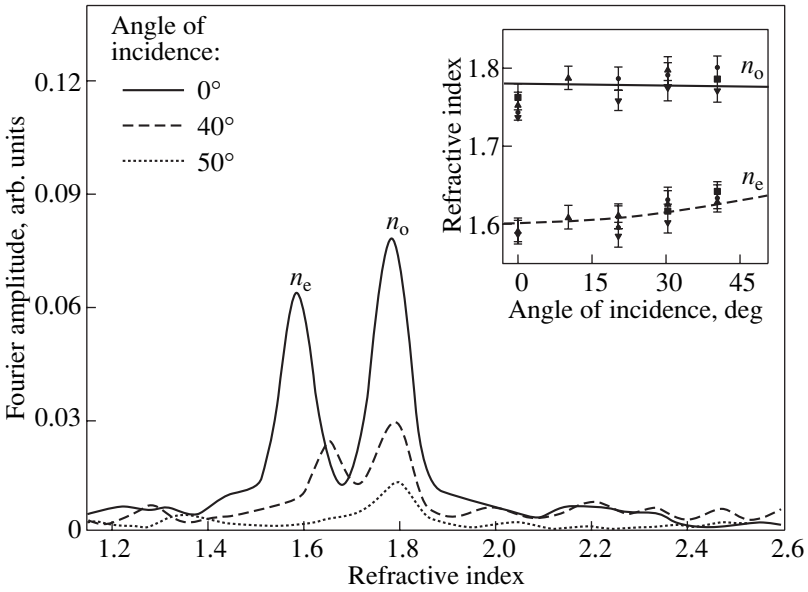

Fig. 2. Fourier analysis of IR transmittance spectra of a porous silicon layer (d = 48 μm, j = 50 mA/cm^2) obtained by rotating the layer around the direction perpendicular to the optical axis. Inset: points are experimental refractive indices for the ordinary and extraordinary waves plotted vs. incidence angle; lines are theoretical calculations of n_o and n_e made using the effective-medium model.

ciently large angles of light incidence on the sample ($\theta \approx 50°$). This observation finds ready explanation in that θ approaches the Brewster angle. Indeed, because the sample rotates around the $[1\bar{1}0]$ axis, the extraordinary wave is *p*-polarized and, hence, the reflectance drops with increasing θ; this results, in turn, in a decrease of the corresponding Fourier component in amplitude [9].

The inset to Fig. 2 shows the values of n_o and n_e determined experimentally for different incidence angles. We readily see that the refractive index of the ordinary wave does not change in magnitude to within experimental accuracy, whereas that of the extraordinary wave increases with the angle of light incidence on the sample. Note that the error in the experimental data obtained in such a processing is determined by the half-width of the corresponding Fourier component.

The dashed line in the inset to Fig. 2 presents a plot of the refractive index for the extraordinary wave against the angle of incidence, which was calculated using the expression [10]

$$n_e(\theta_{in}) = \frac{n_e n_o}{\sqrt{n_e^2 \sin^2\theta_{in} + n_o^2 \cos^2\theta_{in}}}, \qquad (3)$$

where θ_{in} is the angle the wave vector in the PS layer makes with the surface normal. We observe good agreement of the calculated $n_e(\theta)$ dependence with experimental data, which quantitatively corroborates the earlier conclusion that the layer under study is a negative uniaxial crystal.

The anisotropy of a PS layer depends, obviously, on its porosity. To study this dependence, we used PS samples prepared with different etch current densities and, hence, having different porosities. Figure 3a plots the refractive indices of the ordinary and extraordinary waves, and Fig. 3b shows their difference $\Delta n = n_o - n_e$ as a function of current density j. The decrease in the refractive indices n_o and n_e with increasing j is obviously associated with the increasing PS layer porosity. Estimates of the layer porosity made using the data from [3] are given in Fig. 3 for several values of j. An increase in the current density also entails a growth in the refractive index difference Δn, which reaches, in the spectral region 1.5–8 μm, a value of 0.24 for an average refractive index $\langle n \rangle = (n_o + n_e)/2 = 1.3$ for j = 100 mA/cm^2. These values of Δn indicate that the PS layers under study have an extremely large anisotropy. The relative difference between the refractive indices of the ordinary and extraordinary waves $\delta n = \Delta n/\langle n \rangle$ reaches 18% for j = 100 mA/cm^2, which is substantially larger than, for instance, that for Iceland spar ($\delta n \sim 9\%$ in the same spectral region [11]).

By applying a Fourier transform within comparatively narrow IR intervals, one can determine the refractive index dispersion. The wavelength dependence of the quantity $n_o - n_e$ for samples prepared with two different etch currents is presented in Fig. 4. The PS layers are seen to have normal dispersion. We carried out simulation of Δn in the effective-medium approximation. We used Bruggeman's theory of the DP of a disordered heterogeneous mixture [12], which relates the effective DP of such a system ε_{eff} to the DP

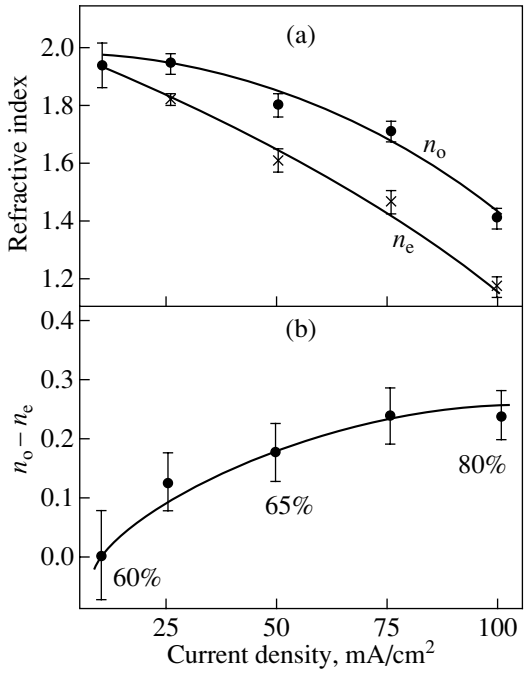

Fig. 3. (a) Refractive indices of the ordinary and extraordinary rays in porous silicon layers plotted vs. the etch current density. (b) Refractive index difference $\Delta n = n_o - n_e$ for porous silicon layers plotted vs. the etch current density; the figures adjacent to the experimental points are the porosities of the PS layers under study taken from review [3]. The lines were drawn to aid the eye.

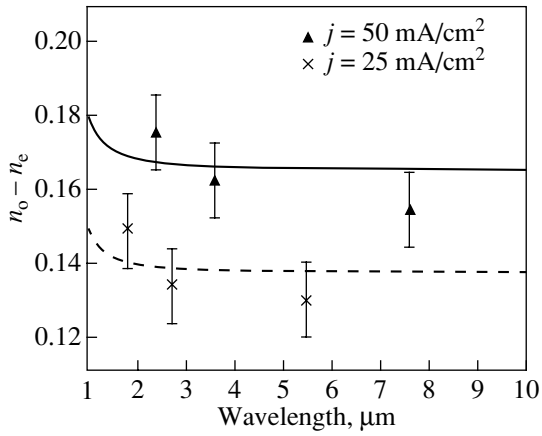

Fig. 4. Dispersion relations for the refractive index difference $\Delta n = n_o - n_e$ in porous silicon layers prepared at different etch current densities j. The experimental points were obtained by Fourier-analyzing transmittance spectra of nonpolarized light. The analysis was made within the ±750 cm^{-1} region of the experimental points. The lines are theoretical calculations making use of the effective-medium approximation, which were carried out for $f_o = 0.38$, $f_e = 0.32$ (solid line) and $f_o = 0.447$, $f_e = 0.4$ (dashed line).

of silicon ε_{Si} and that of the dielectric filling the pores ε_d; in our case, the pores are filled by air and $\varepsilon_d = 1$:

$$(1 - f)\frac{\varepsilon_d - \varepsilon_{eff}}{\varepsilon_d + 2\varepsilon_{eff}} + f\frac{\varepsilon_{Si} - \varepsilon_{eff}}{\varepsilon_{Si} + 2\varepsilon_{eff}} = 0, \qquad (4)$$

where f is the filling of the medium by silicon nanocrystals, $f = 1 - p$, and p is the porosity. The different in-plane refractive indices, which correspond to electric vector vibrations along and perpendicular to the optical axis, were simulated by accepting different filling factors f_e and f_o, respectively. The condition $(f_o + f_e)/2 = 1 - p$ was imposed. Next, using Eq. (4) and the dispersion of the DP of crystalline silicon ε_{Si} [13], we calculated n_e and n_o and their difference Δn. Figure 4 displays the spectral dependence of Δn for samples of two porosities (solid and dashed curves). We readily see that Δn grows weakly with decreasing wavelength within the interval from 2 to 10 μm, which agrees with the experimental data.

Thus, our results show that the birefringence in the PS layers under study is so large that it considerably exceeds the change in the refractive index due to normal dispersion of the material. This situation differs radically from that typical of most semiconductors, which opens new possibilities for the application of anisotropic porous media in nonlinear optics. In particular, their birefringence can be used for phase matching of the nonlinear optical processes occurring in such media. Indeed, as we discovered recently [14], the efficiency of second harmonic generation in (110)-oriented anisotropic PS layers is substantially higher than that in PS layers prepared on substrates with another orientation, for instance, (100). This effect was attributed to having met the phase matching conditions for the birefringent PS layers. Moreover, it was established that the second harmonic is polarized in the plane containing the [001] axis and the propagation vector. It is known [10] that in negative crystals, the phase-matched second harmonic is always polarized in the optical-axis plane. This is in accord with the fact that the (110) PS layer is a negative uniaxial crystal with the optical axis along the [001] direction.

4. CONCLUSION

Thus, our study shows that infrared Fourier spectroscopy is a very efficient tool for analyzing birefringence in PS layers. In particular, the beats observed in the reflected and transmitted light intensities provide a convincing argument for the existence of birefringence in (110)-oriented PS layers. Fourier analysis of IR spectra permits one to determine the refractive indices of the ordinary and extraordinary waves, as well as their dispersion. It has been established that the refractive index difference between the ordinary and extraordinary waves reaches as high as 18% in the region of transparency of PS, which attests to this material possessing a strong optical anisotropy. An analysis of the transmit-

tance spectra obtained at various angles of incidence on a sample suggests that the birefringent PS layer under study is a negative uniaxial crystal whose optical axis lies in the (110) plane and coincides with the [001] direction. The experimental results are in good agreement with the conclusions drawn using the effective-medium approximation, which assumes anisotropic distribution of silicon nanocrystals in space.

ACKNOWLEDGMENTS

The authors are indebted to D. Kovalev, A.M. Zheltikov, and M.G. Lisachenko for valuable discussions.

This study was supported by the Ministry of Industry, Science, and Technology of the RF (program "Semiconducting Nanostructures") and CRDF (grant no. RP2-2275).

REFERENCES

1. C. Pickering, M. I. J. Beale, D. J. Robbins, *et al.*, J. Phys. C **17**, 6535 (1984).
2. A. G. Cullis, L. T. Canham, and P. D. J. Calcott, J. Appl. Phys. **82**, 909 (1997).
3. W. Theiβ, Surf. Sci. Rep. **29**, 91 (1997).
4. D. Kovalev, H. Heckler, G. Polisski, and F. Koch, Phys. Status Solidi B **215**, 817 (1999).
5. M. E. Kompan, J. Salonen, and I. Yu. Shabanov, Zh. Éksp. Teor. Fiz. **117** (2), 368 (2000) [JETP **90**, 324 (2000)].
6. O. G. Sarbey, E. K. Frolova, R. D. Fedorovich, and D. B. Dan'ko, Fiz. Tverd. Tela (St. Petersburg) **42** (7), 1205 (2000) [Phys. Solid State **42**, 1240 (2000)].
7. D. Kovalev, G. Polisski, J. Diener, *et al.*, Appl. Phys. Lett. **78**, 916 (2001).
8. A. V. Ghiner and G. I. Surdurovich, Braz. J. Phys. **24**, 344 (1994).
9. M. Born and E. Wolf, *Principles of Optics* (Pergamon, Oxford, 1970; Nauka, Moscow 1973).
10. F. Zernike and J. E. Midwinter, *Applied Nonlinear Optics: Basics and Applications* (Wiley, New York, 1973; Mir, Moscow, 1976).
11. *Tables of Physical Quantities*, Ed. by I. K. Kikoin (Atomizdat, Moscow, 1976).
12. D. A. G. Bruggeman, Ann. Phys. (Leipzig) **24**, 636 (1935).
13. C. D. Salzberg, J. Opt. Soc. Am. **47**, 244 (1957).
14. L. A. Golovan, V. Yu. Timoshenko, A. B. Fedotov, *et al.*, Appl. Phys. B **B73**, 31 (2001).

Translated by G. Skrebtsov

Physics of the Solid State, Vol. 44, No. 5, 2002, pp. 816–822. Translated from Fizika Tverdogo Tela, Vol. 44, No. 5, 2002, pp. 785–791.

SEMICONDUCTORS AND DIELECTRICS

Self-Compensation of Metastable Centers in Semiconducting Chalcogenide Glasses

N. T. Bagraev*, L. N. Blinov, and V. V. Romanov****

**Ioffe Physicotechnical Institute, Russian Academy of Sciences, ul. Politekhnicheskaya 26, St. Petersburg, 194021 Russia*

***St. Petersburg State Technical University, ul. Politekhnicheskaya 29, St. Petersburg, 195251 Russia*

Received July 12, 2001

Abstract—The temperature dependences of magnetic susceptibility are employed for the first time to study the self-compensation of metastable centers with negative correlation energy in the As_2S_3 chalcogenide glass. The one-electron states of the metastable centers manifest themselves in the Curie paramagnetism at high temperatures, whereas for $T \le 77$ K, one observes an enhancement of antiferromagnetism as a result of spontaneous dissociation of these states $2D^0 \longrightarrow D^+ + D^-$. The observed self-compensation of the paramagnetic centers is similar to the spin-Peierls instability of magnetic lattices, which is supported by the existence of a double peak in the temperature dependence of inverse magnetic susceptibility. This peak identifies the spontaneous dissociation of two different metastable centers for $T \le 77$ K. A comparative analysis of the data on magnetic susceptibility, optically induced absorption, and ESR shows that the one-electron paramagnetic states of these metastable centers (D^0) represent native hole and electronic defects formed by the chalcogen and arsenic dangling bonds, respectively. The self-compensation of the two types of metastable centers is enhanced in successive cooling runs 300 K $\longrightarrow$ 3.5 K $\longrightarrow$ 300 K $\longrightarrow$ 3.5 K … accompanied by optical pumping at an energy close to the Urbach absorption edge, which is reflected in a decrease in the Curie paramagnetism and an enhancement of the van Vleck paramagnetism of two-electron states with negative correlation energy (D^-). © *2002 MAIK "Nauka/Interperiodica".*

1. INTRODUCTION

Interpretation of the results obtained in studies of ESR, optical absorption, photoluminescence, and photoconductivity in chalcogenide glasses is based on different models of native defects with deep levels lying in the band gap [1, 2]. The one-electron models of deep defects in amorphous semiconductors [1, 2] predict a high density of localized states near the Fermi level, which is supported by electrical and optical measurements [3, 4]. However, the concentration of unpaired spins in chalcogenide glasses residing in thermodynamic equilibrium was not found by ESR to be anywhere near noticeable, an observation which practically unambiguously indicates the absence of one-electron localized states in the band gap [5]. To remove this controversy, the concept of negative correlation energy was put forward [6–9], within which the one-electron deep center (D^0) dissociates spontaneously to form a two-electron (D^-) and an empty (D^+) state as $2D^0 \longrightarrow D^- + D^+ + |U|$, where U is the Hubbard correlation energy [6].

Actually, the deep-center models proposed are based on the effective Hubbard attraction of two electrons at a defect as a result of the Coulomb repulsion being cancelled by electron–vibration coupling; this is what accounts for the absence of the Curie paramagnetism and for the Fermi level pinning in the band gap of chalcogenide glasses. In other words, the two-electron deep-center states with an inverse level order (negative-U centers) represent counterparts of Cooper pairs with a short correlation length.

A direct consequence of the formation of negative-U centers in chalcogenide glasses is the possibility of generation of paramagnetic one-electron states in nonequilibrium conditions, for instance, through the optical injection of electron–hole pairs $D^- + D^+ + h\nu \longrightarrow D^- + D^+ + (e + h) \longrightarrow 2D^0$. Such paramagnetic centers have been observed in ESR studies performed under optical pumping with monochromatic light with its photon energy near the Urbach optical absorption edge in chalcogenide glasses α-Se, As_2Se_3, and As_2S_3 [10]. An increase in the concentration of the electronic and hole paramagnetic centers localized at arsenic and chalcogen atoms, respectively, was accompanied by quenching of the intrinsic photoluminescence and the generation of optical absorption, which was due to optical transitions between the deep one-electron states and the conduction band [10, 11]. Subsequent optical pumping by monochromatic light with its photon energy corresponding to the induced-absorption spectrum produced optical dissociation of the one-electron paramagnetic states, $2D^0 + h\nu \longrightarrow D^- + D^+$ [12], which may be considered an additional argument for the intrinsic defects having a negative correlation energy in chalcogenide glasses.

However, no models of two-electron states of these defects were identified and their possible role in photostructural transformations initiated in chalcogenide

glasses under prolonged optical pumping was not discussed. This work is the first attempt at solving these problems by measuring the temperature dependences of the magnetic susceptibility.

2. EXPERIMENTAL

The objects chosen for the study of the temperature dependences of the magnetic susceptibility in chalcogenide glasses were bulk As_2S_3 samples prepared from 99.999%-pure constituents using a standard technology. ESR studies carried out in stationary conditions (in the absence of optical pumping) did not reveal residual impurities in anywhere near noticeable concentrations, in particular, of iron centers, which usually form during the preparation of chalcogenide glasses [12].

The temperature dependences of the magnetic susceptibility were obtained in the range 3.5–300 K by the Faraday method using an MGD312FG magnetic balance. This method is based on measuring the force with which the sample under study interacts with an external magnetic field having a characteristic gradient dB/dx along a chosen direction:

$$F = m\chi B\frac{dB}{dx}, \qquad (1)$$

where χ is the specific magnetic susceptibility and m is the sample mass. Note that the MGD312FG instrument provides a high sensitivity of magnetic susceptibility measurements (10^{-9}–10^{-10} emu), which is reached through stabilization of the BdB/dx product by using pole pieces of a special profile. The BdB/dx values were calibrated on samples of pure indium phosphide, whose magnetic susceptibility ($\chi = 313 \times 10^{-9}$ cm^3/g) did not vary with temperature within the above range. This calibration permitted us to determine the range of BdB/dx variation within the magnetic-field range used (0.05–1.1 T) from 0 to 15 T^2/m.

The optically induced enhancement of the paramagnetic component in the magnetic susceptibility and the red shift of the absorption spectrum of the As_2S_3 samples were studied in the course of preliminary optical pumping by monochromatic light with its photon energy near the Urbach edge ($\alpha \sim 100$ cm^{-1}). This was done with a 4*H*-SiC-based laser diode operating at a wavelength of 0.53 μm at a power level of ~1 mW/cm^2. The induced paramagnetism was subsequently optically bleached and the initial spectral response of absorption was recovered by irradiation with IR light of wavelength 1.55 μm and intensity ~1 mW/cm^2 generated by an InGaAsP–InP heterojunction laser diode. In addition, the samples were optically pumped with a photon energy near the Urbach absorption edge in successive cooling runs 300 ⟶ 3.5 ⟶ 300 ⟶ 3.5 K … to study the changes in the paramagnetic properties of the As_2S_3 chalcogenide glasses building up in the course of slow photostructural transformations.

3. RESULTS AND DISCUSSION

The temperature dependence of the magnetic susceptibility recorded in an As_2S_3 sample under cooling exhibits Curie paramagnetism only at high temperatures (Fig. 1). As the temperature is lowered, the $1/\chi = f(T)$ plot reveals two characteristic peaks below 100 K, which signal spin instability of two different paramagnetic centers.

The temperature bleaching of the paramagnetic properties observed in As_2S_3 is similar to the spin-Peierls doubling in magnetic lattices [13] and is apparently due to the formation of singlet states of the negatively charged chalcogen and arsenic dangling bonds caused by their self-compensation, $2D_0 \longrightarrow D^- + D^+$. Therefore, the temperature dependence of χ can be described by the expression

$$\chi = \frac{\mu_B^2 g^2 |S(S+1)|^2}{3kT} N_0 + 2\frac{\mu_B^2 g^2 N_-}{3kT}\frac{\sum_S S(S+1)\exp\left(-\frac{aS(S+1)}{2kT}\right)}{\sum_S \exp\left(-\frac{aS(S+1)}{2kT}\right)}, \qquad (2)$$

where the first term relates to the Curie paramagnetism of neutral dangling bonds and the second describes the van Vleck paramagnetism of the negatively charged dangling bonds in the singlet state, which is manifested in their transition to the excited triplet state through exchange interaction; a is the exchange constant. The

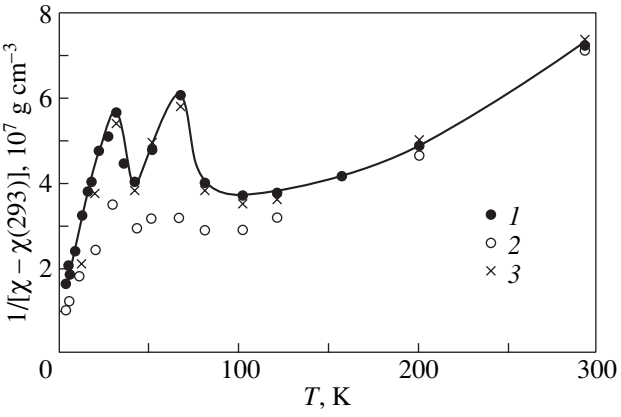

Fig. 1. Temperature dependence of the magnetic susceptibility of As_2S_3, which shows self-compensation of the neutral paramagnetic hole and electronic centers of the chalcogen and arsenic, respectively. (*1*) Cooling in the dark, (*2*) after irradiation by a monochromatic light of wavelength 0.53 μm carried out at $T = 3.5$ K and (*3*) after subsequent irradiation by 1.55-μm monochromatic light at $T = 3.5$ K.

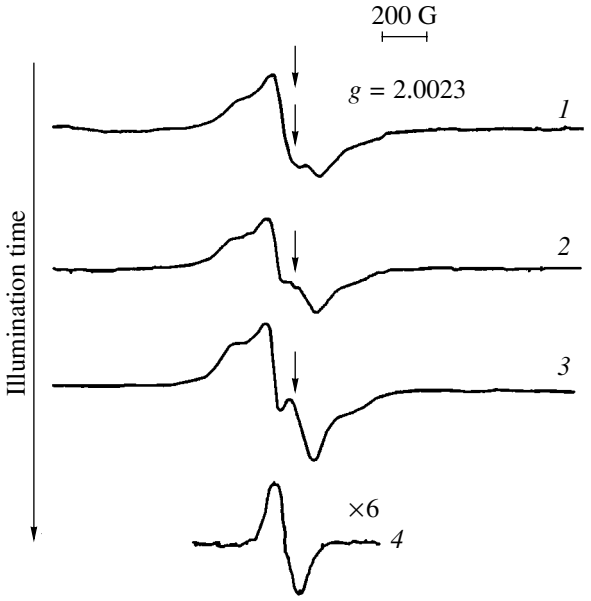

Fig. 2. ESR spectra induced optically in As_2S_3 at $T = 3.5$ K under irradiation by monochromatic light of wavelength 0.53 μm. Curves *1–3* reflect the variation in the concentration of the electronic centers of arsenic (broad resonance line) and the hole centers of the chalcogen (narrow line) with pumping time. Curve *4* relates to the chalcogen hole center forming in the early stage of the optical pumping by monochromatic light (0.53 μm).

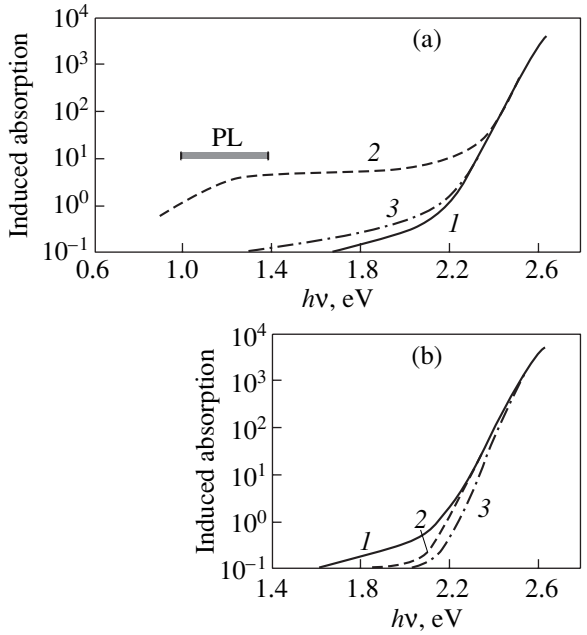

Fig. 3. Spectral response of the absorption coefficient of As_2S_3 obtained at $T = 3.5$ K. (a) (*1*) After sample cooling to 3.5 K, (*2*) after irradiation by monochromatic light of wavelength 0.53 μm at $T = 3.5$ K, and (*3*) after subsequent irradiation by 1.55-μm monochromatic light at $T = 3.5$ K. (b) (*1*) After sample cooling to 3.5 K and (*2, 3*) after two and three consecutive cooling runs 300 ⟶ 3.5 ⟶ 300 ⟶ 3.5 K, respectively, performed under irradiation by monochromatic light of wavelength 0.53 μm.

concentrations of neutral (N_0) and negatively charged (N_-) dangling bonds depend on the sample cooling rate, which was revealed in the corresponding temperature hysteresis of the magnetic susceptibility for $T < 100$ K.

Note that the bleaching of the paramagnetic component of the magnetic susceptibility observed to occur in As_2S_3 at low temperatures apparently accounts for the attempts at ESR detection of dangling bonds in the absence of optical pumping being unsuccessful. Accordingly, at high temperatures ($T > 100$ K), where unpaired dangling bonds dominate (Fig. 1), no noticeable ESR spectra were observed because of the fast electron spin–lattice relaxation.

It is known [12] that ESR spectra of dangling bonds in chalcogenide glasses are produced as a result of optical generation of their neutral states ($D^- + D^+ + h\nu \longrightarrow 2D^0$), which was reached in this work through irradiation by monochromatic light with a wavelength of 0.53 μm, which corresponds to the Urbach absorption edge in As_2S_3 (Fig. 2). The growth of the ESR signal with optical-pumping duration is accompanied by an enhancement of the paramagnetic component of the magnetic susceptibility, whose temperature dependence becomes closer in shape to the Curie law (Fig. 1). Moreover, the red shift of the absorption spectral response revealed after irradiation with 0.53-μm light indicates unambiguously that the optically induced paramagnetic centers D^0 create deep levels in the As_2S_3 band gap (Fig. 3a).

An optically induced ESR spectrum is a combination of a narrow high-field line and a broad low-field line belonging to a hole and an electronic center formed at the chalcogen and arsenic atoms, respectively [12]. The neutral dangling bonds localized at the arsenic atoms require a longer optical pumping for their formation than the paramagnetic chalcogen centers, which is accounted for by the metastable properties of the latter. Therefore, the high-temperature peak in the temperature dependence of $1/\chi$ is apparently due to self-compensation of the chalcogen dangling bonds, which becomes fixed at $T \approx 77$ K as a result of their metastability. By contrast, spontaneous dissociation of the arsenic neutral paramagnetic centers is observed to occur only for $T < 40$ K, which accounts for their much weaker metastability, with the latter also becoming manifest in the stability of the corresponding peak in the temperature dependence of $1/\chi$ to optical pumping at 0.53 μm (Fig. 1).

It should be pointed out that the partially resolved ESR multiplet forming under prolonged optical pumping at 0.53 μm is apparently due to the arsenic D^- singlet state transforming to a paramagnetic center with spin $S = 1$. Such transitions were observed in Frenkel pair systems with nonequidistant components on the III–V sublattices [14], which gives one grounds to associate the observed ESR spectrum of chalcogenide

glasses with exchange interaction of the D^- centers with the photoinduced D^0 paramagnetic centers.

ESR spectra of distant $(D^+ - D^-)$–D^0 pairs can be simulated by means of the Hamiltonian [14]

$$H = \beta B\mathbf{g}S + D\left[S_z^2 - \frac{1}{3}S(S+1)\right] + E(S_x^2 - S_y^2), \quad (3)$$

assuming the **g** tensor to take into account all possible D^0 configurations with respect to the D^+–D^- axis, along which the self-compensation of arsenic dangling bonds is the strongest. Note that the line separation in a photoinduced ESR spectrum ($S = 1$), which reflects the magnitude of the exchange coupling, increases with optical-pumping time, which is most probably associated with the creation of ever closer $(D^+ - D^-)$–D^0 pairs.

As follows from a comparative analysis of ESR data and magnetic susceptibility measurements, the self-compensation processes in As_2S_3 can be described by models of metastable centers with a negative correlation energy proposed within the Anderson Hamiltonian approach [6, 15]:

$$\begin{gathered} H = P^2/2M + \kappa Q^2/2 + E_0(n_\uparrow + n_\downarrow) + Un_\uparrow n_\downarrow - FQ, \\ F = (F_0 + \delta F)\beta_0 + F_1\beta_1 + (F_2 - \delta F)\beta_2, \\ \beta_n^2 = \beta_n, \quad n = 0, 1, 2, \quad \beta_0 = (1-n_\uparrow)(1-n_\downarrow), \\ \beta_1 = n_\uparrow + n_\downarrow - 2n_\uparrow n_\downarrow, \quad \beta_2 = n_\uparrow n_\downarrow, \quad \delta F = eE\cos\theta, \end{gathered} \quad (4)$$

where P and Q are the canonical momentum and the center coordinate, respectively; M and κ are the center mass and the corresponding force constant; E_0 and U are the one-electron energy and the interelectron interaction at a center; F is the electron–vibration coupling constant; n_σ are the occupation numbers for electrons with spins $\sigma = \uparrow, \downarrow$; β_n are the projection operators for the center charge states with the total electron number n; δF is the Stark-induced change in the electron–vibration coupling constant at a deep center placed in an electric field E; and θ is the angle between the electric field and the coordinate Q.

Diagonalization in the defect charge states permits one to determine the adiabatic potentials for different values of $n = n_\uparrow + n_\downarrow$ in an explicit form (Fig. 4a):

$$\begin{gathered} E_0(Q) = \kappa(Q - Q_0 - \delta Q)^2/2 \longleftrightarrow D^+\text{-center}, \\ E_1(Q) = -I_1(E) + \kappa(Q - Q_1)^2/2 \longleftrightarrow D^0\text{-center}, \\ E_2(Q) = -I_2(E) + \kappa(Q - Q_2 + \delta Q)^2/2 \longleftrightarrow D^-\text{-center}, \end{gathered} \quad (5)$$

where the one- and two-electron ionization potentials [$I_1(E)$ and $I_2(E)$, respectively] of a point center can be identified with the change that the correlation energy $U(E)$ undergoes in the capture of a background and a correlated electron $D^+ \longrightarrow D^0 \longrightarrow D^-$ (Fig. 3); $Q_0 = F_0/\kappa$, $Q_1 = F_1/\kappa$, $Q_2 = F_2/\kappa$, $\delta Q = \delta F/\kappa$, $Q_0' = Q_0 + \delta Q$, $Q_2' = Q_2 - \delta Q$; and

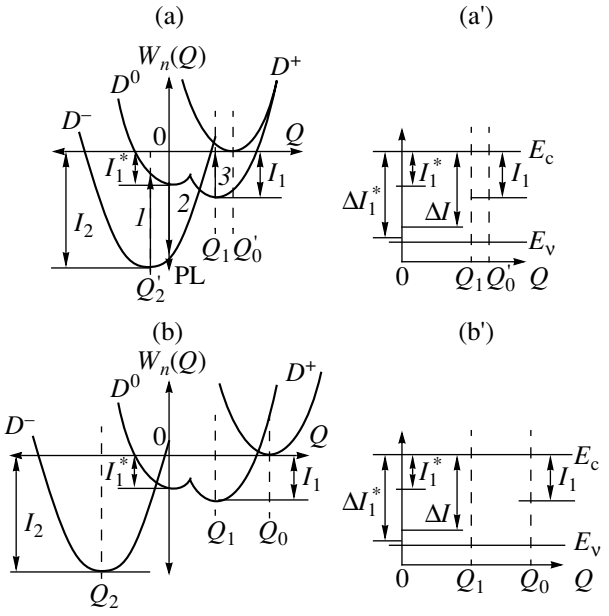

Fig. 4. (a, b) Adiabatic potentials and (a', b') equivalent one-electron band diagrams of centers with negative correlation energy present in the metastable state in As_2S_3 (a, a') as a result of a built-in electric field inducing a Stark shift $\delta Q \neq 0$ and (b, b') with the built-in electric field self-compensated, $\delta Q = 0$. Arrow *1* corresponds to photoionization of the D^-center, which stimulates the formation of a neutral paramagnetic state; arrow *2* identifies photoluminescence with a Kondo shift; and arrow *3*, photoionization of the D^0 center with subsequent self-compensation produced by two-electron capture ($2D^0 + h\nu \longrightarrow D^- + D^+$).

$$\begin{gathered} I_1(E) = I_1 - F_0\delta F/\kappa, \quad I_1 = -[E_0 + (F_0^2 - F_1^2)/2\kappa], \\ I_2(E) = I_2 - F_0\delta F/\kappa, \\ I_2 = -[2E_0 + U_0 + (F_0^2 - F_1^2)/2\kappa], \\ U(E) = 2I_1(E) - I_2(E) = U - [E_0\delta F + (\delta F)^2], \\ U = 2I_1 - I_2 = U_0 + (2F_1^2 - F_2^2 - F_0^2)/2\kappa. \end{gathered} \quad (6)$$

Thus, the change in the local effective correlation energy resulting from electron capture by neutral paramagnetic centers ($D^0 \longrightarrow D^-$) is caused by the polaron energy shift $W_1 = (F_1^2 - F_2^2)/2\kappa$.

The two-electron adiabatic potentials (Figs. 4a, 4b) and the equivalent one-electron band diagrams (Figs. 4a', 4b') offer a revealing explanation for the spontaneous dissociation of one-electron dangling-bond states in chalcogenide glasses observed to occur under cooling, where their metastable properties are

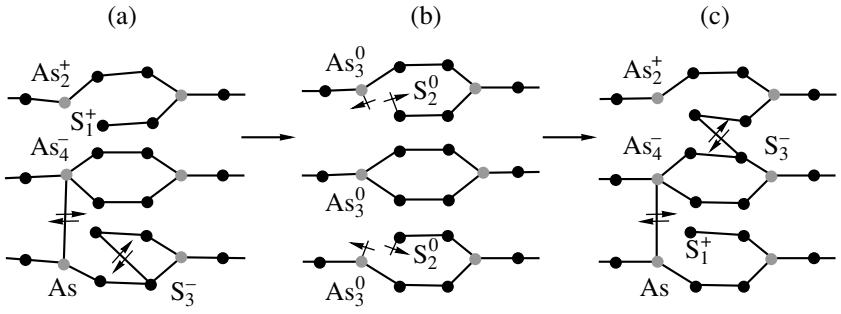

Fig. 5. A fragment of the As_2S_3 chain, which demonstrates the electric dipoles formed by centers with negative correlation energy for the cases of (a) parallel and (c) antiparallel orientation, as well as (b) the neutral paramagnetic states of these centers forming at $T = 3.5$ K under irradiation by monochromatic light at 0.53 μm. The arrows specify various stages in the transformation of the parallel to the antiparallel orientation of dipoles subjected to successive cooling runs 300 ⟶ 3.5 ⟶ 300 ⟶ 3.5 K under irradiation by monochromatic light of wavelength 0.53 μm.

governed by the height of the energy barrier between their two-electron and neutral states, which can be overcome only at high temperatures; this results, in particular, in the thermal generation of paramagnetic neutral states ($D^- \longrightarrow D^0$), which manifests itself in Curie paramagnetism (Fig. 1). However, the intense reverse transitions ($D^0 + e \longrightarrow D^-$ or $D^0 + D^+ + e \longrightarrow 2D^0 \longrightarrow D^+ + D^-$), combined with the short electron spin–lattice relaxation time due to exchange interaction, do not allow observation of the ESR of neutral paramagnetic centers at high temperatures. In addition, the energy barrier separating the D^0 and D^- states stabilizes (at low temperatures) the one-electron paramagnetic state, which is generated under the 0.53-μm optical pumping ($D^- + D^+ + h\nu \longrightarrow D^- + D^+ + (e + h) \longrightarrow 2D^0$).

The model proposed here (Figs. 4a, 4b) also allows interpretation of the optical bleaching of photoinduced paramagnetic centers in As_2S_3 under optical pumping performed at 1.55 μm, $2D^0 = h\nu \longrightarrow D^- + D^+$ (Fig. 1), which is accompanied by the recovery of the photoluminescence and edge absorption spectra (Fig. 3a). Note that the energy of photoionization ($D^- \longrightarrow D^0$) and the kinetics of carrier trapping by neutral paramagnetic centers ($D^0 \longrightarrow D^-$) depend on the magnitude of the polaron energy shift $W_1 = (F_1^2 - F_2^2)/2\kappa$ and can vary substantially in the presence of an external and an internal electric field (Figs. 4a, 4b).

It should be pointed out that the internal electric field, which induces the Stark shift δQ accounting for the metastable properties of the hole and electronic chalcogen and arsenic centers, is apparently due to the formation of electric dipoles of the type $As_2^+ - As_4^-$ and $S_1^+ - S_3^-$ in the course of their self-compensation (Fig. 5a). When oriented parallel to one another, the dipole centers can produce a fairly strong electric field (~10^7–10^8 V cm^{-1}), which in the case of Stark-shifted charge states of the chalcogen and arsenic dangling bonds, produces an Urbach tail ($\alpha \sim 100$ cm^{-1}) in the spectral response of the absorption coefficient (Figs. 3a, 3b) [16]:

$$\alpha(\omega) = \alpha_0 \exp[2(\hbar\omega - E_{1g})/\kappa(Q_2 - Q_1 - \delta Q)^2], \quad (7)$$

where the band gap E_{1g} does not include the effects of disorder. It appears only natural to assume that the parallel orientation of the dipoles (Figs. 4a, 5a) formed by centers with negative correlation energy is nonequilibrium and sets in only in the course of chalcogenide glass preparation. Therefore, the possibility of controlling the optical properties of chalcogenide glasses by bleaching the Urbach tail stimulates interest in the investigation of the mechanisms underlying self-compensation of the built-in electric field through transfer of electric dipoles to the antiparallel state with a lower energy.

In this work, such bleaching was observed to occur in successive As_2S_3 cooling runs 300 ⟶ 3.5 ⟶ 300 ⟶ 3.5 K …, which were followed by optical pumping at 0.53 μm (Fig. 3b). The temperature dependence of the magnetic susceptibility measured in these runs reveals a decrease in the concentration of the paramagnetic component, as well as stabilization of the two-electron singlet state of the chalcogen and arsenic dangling bonds (Figs. 6, 7), which are manifested in the Curie law breaking down at high temperatures and in an enhancement of van Vleck paramagnetism in the low-temperature domain, respectively. It was found that after the completion of the above cyclic cooling procedure, the formation of paramagnetic neutral states under 0.53-μm optical pumping at low temperatures ($D^- + D^+ + h\nu \longrightarrow 2D^0$) was suppressed, which was signaled by the corresponding stabilization of the temperature dependence of magnetic susceptibility (Figs. 6c, 7).

Thus, successive cooling runs applied to As_2S_3 suppress the metastable properties of centers with negative correlation energy and stimulate sample bleaching as a result of a disappearance of the Urbach tail in the edge absorption spectrum. The results obtained are treated in

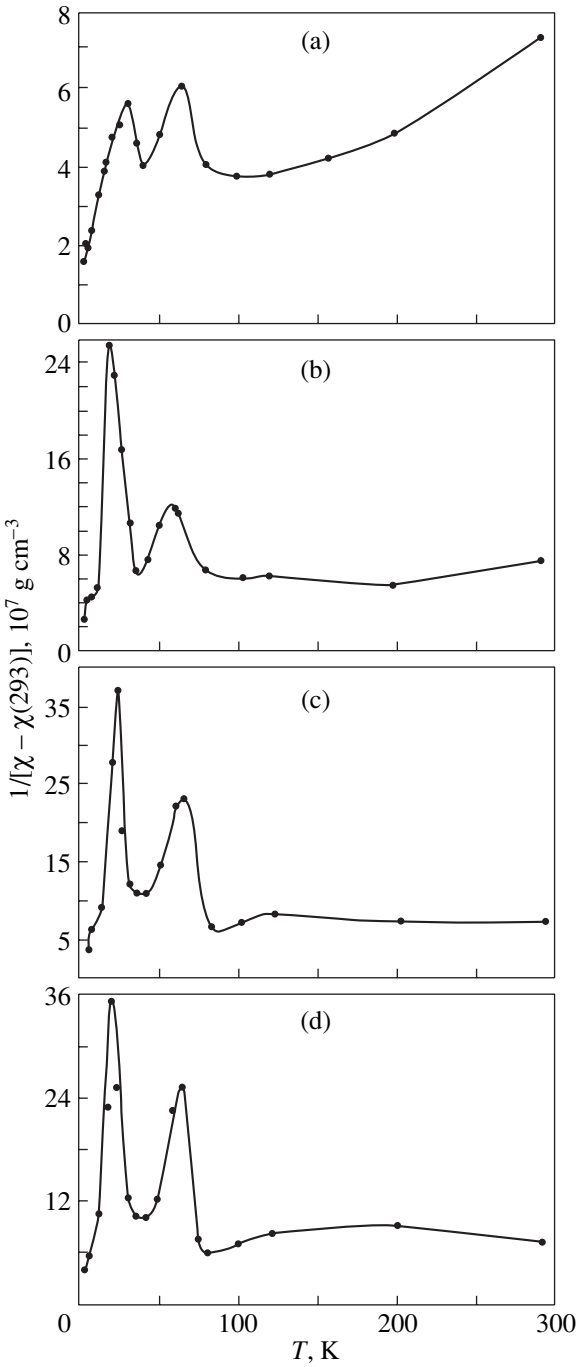

Fig. 6. Temperature dependence of the magnetic susceptibility of As_2S_3 obtained on a sample (a) cooled in the dark and after (b) two and (c) three successive cooling runs 300 ⟶ 3.5 ⟶ 300 ⟶ 3.5 K under irradiation by monochromatic light of wavelength 0.53 μm and (d) after subsequent irradiation by 0.53-μm monochromatic light at 3.5 K.

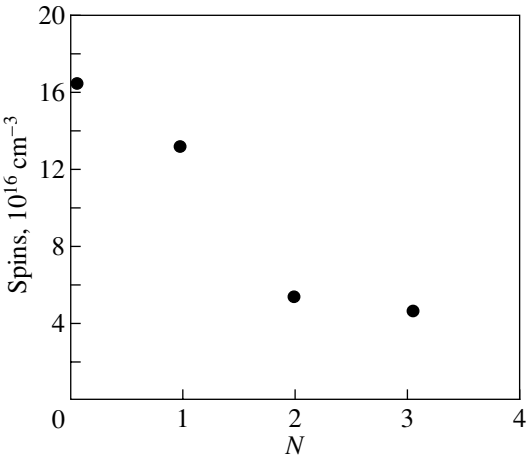

Fig. 7. Decrease in the concentration of the neutral arsenic paramagnetic centers derived from the temperature dependence of the magnetic susceptibility of As_2S_3 obtained in the course of successive cooling runs 300 ⟶ 3.5 ⟶ 300 ⟶ 3.5 K under irradiation by monochromatic light of wavelength 0.53 μm. N is the number of the run.

terms of the proposed model of a deep metastable center, because the magnitude of the Stark shift δQ decreases strongly with increasing number of cooling runs (Fig. 4b). The explanation of such a decrease in the Stark shift revealed in the spectral response of absorption (Fig. 3b) lies apparently in the self-compensation of the built-in electric field occurring as the electric dipoles cross over gradually to the antiparallel state (Fig. 5c).

4. CONCLUSION

To sum up, our study of the temperature dependence of magnetic susceptibility has permitted identification of the metastable properties of centers with negative correlation energy created by chalcogen and arsenic dangling bonds in the As_2S_3 chalcogenide glass. The observed reactions of optical bleaching and recovery of the neutral paramagnetic states of negative-U centers showed that the metastable chalcogen and arsenic dangling bonds undergo self-compensation with the formation of electric dipoles, which are responsible for the Urbach edge in the spectral response of absorption. The transformation of the parallel to antiparallel oriented electric dipoles, which was realized in the course of successive cooling runs and was identified with changes in the temperature dependence of the magnetic susceptibility, resulted in self-compensation of the built-in electric fields, a process revealed in the observed disappearance of the Urbach tail in the edge absorption spectra.

REFERENCES

1. N. F. Mott and E. A. Davis, *Electronic Processes in Non-Crystalline Materials* (Clarendon, Oxford, 1971; Mir, Moscow, 1974).
2. H. Fritzsche, J. Phys. Soc. Jpn., Suppl. A **49**, 39 (1980).
3. A. E. Owen and J. W. Robertson, J. Non-Cryst. Solids **2**, 40 (1970).

4. W. E. Spear and P. V. LeComber, J. Non-Cryst. Solids **8–10**, 727 (1972).
5. S. C. Agarwal, Phys. Rev. B **7**, 685 (1973).
6. P. W. Anderson, Phys. Rev. Lett. **34**, 953 (1975).
7. P. W. Anderson, J. Phys. (Paris) C **4**, 339 (1976).
8. R. A. Street and N. F. Mott, Phys. Rev. Lett. **35**, 1293 (1975).
9. M. Kastner, D. Adler, and H. Fritzsche, Phys. Rev. Lett. **37**, 1504 (1976).
10. S. G. Bishop, U. Strom, and P. C. Taylor, Phys. Rev. Lett. **34**, 1346 (1975).
11. S. G. Bishop, U. Strom, and P. C. Taylor, Phys. Rev. Lett. **36**, 543 (1976).
12. S. G. Bishop, U. Strom, and P. C. Taylor, Phys. Rev. B **15**, 2278 (1977).
13. V. A. Grarzhulis, V. V. Kveder, and Yu. A. Osipyan, Phys. Status Solidi B **103**, 519 (1981).
14. K. Brower, Phys. Rev. B **14**, 872 (1976).
15. N. T. Bagraev and V. A. Mashkov, Solid State Commun. **51**, 515 (1984).
16. A. V. Kolobov and S. R. Elliott, Adv. Phys. **40**, 625 (1991).

Translated by G. Skrebtsov

Physics of the Solid State, Vol. 44, No. 5, 2002, pp. 823–830. Translated from Fizika Tverdogo Tela, Vol. 44, No. 5, 2002, pp. 792–798.

SEMICONDUCTORS AND DIELECTRICS

Thermopower of $CeNi_5$ with Strong *f*-Electron Instability: Band Effects

M. D. Koterlin[1, 2], O. I. Babich[1], and R. I. Yasnitskiĭ[1]

[1] *Lviv National University, Lviv, 79005 Ukraine*

e-mail: koterlyn@mail.lviv.ua

[2] *K. Wielkiego Academy of Bydgoshch, Bydgoshch, 80064 Poland*

Received July 13, 2001

Abstract—Numerical calculations of the thermopower component S_d that is associated with the fine structure of the density of *d* states near the Fermi level are carried out for $CeNi_5$ and its La analog. The estimates, together with earlier experimental data on the transport coefficients in $Ce(M_xNi_{1-x})_5$ solid solutions with M = Ga, Cu ($0 \le x \le 0.4$)), are used to analyze the behavior of the thermopower component S_f originating from the Ce valence instability. It is shown that as Ce crosses over from the state of its usual intermediate valence to the saturated-valence state, the feature near the Fermi energy, which represents a Lorentzian-shaped peak of the density of *f* states, transforms to a double-humped structure. The possibility of formation of a strongly correlated band of *f* states in $Ce(M_xNi_{1-x})_5$ in the crossover to the Ce saturated-valence state, accompanied by the opening of a quasi-gap $\Delta \sim 400$ K, is discussed. © *2002 MAIK "Nauka/Interperiodica".*

1. INTRODUCTION

Despite the considerable interest expressed in metallic systems with electronic instability of *f* states, known as intermediate-valence (IV) systems, heavy fermions, or Kondo lattices (KLs), the microscopic nature of the Ce *f* states in condensed phase remains unclear [1–4]. This is particularly true for the formation of electronic states near the Fermi level E_F under strong *f*-electron instability or for the so-called saturated-valence (SV) state of Ce. The Ce saturated-valence state can apparently be considered to be a nonmagnetic KL with a high characteristic temperature $T_K \sim 10^3$ K [1]. There are, however, calculations and experimental data [3–6] which suggest that *f* electrons in the valence-instability regime can be treated essentially as itinerant, which disagrees, to some extent, with the description of their properties in the Kondo model. The difficulties associated with this problem are aggravated by the fact that the Ce saturated-valence state occurs primarily in compounds characterized by a high density of *d* states at the Fermi level [7, 8]. In such cases, detection of the Ce SV effects in their "pure" form becomes substantially complicated by correlation interactions in the narrow *d* bands.

Of particular interest among the Ce saturated-valence compounds is $CeNi_5$ (hexagonal $CaCu_5$-type structure), in which, in addition to spin fluctuation effects in the narrow *d* band [7, 9], a certain effect of *f*-electron instability on conduction-band states near the Fermi energy E_F can be detected [10, 11]. This was revealed in the presence of a high-temperature maximum in the thermopower S_{max2} ($T_{Smax2} \approx 700$ K), which is sensitive to the Ce valence state [10]. However, the maximum S_{max2} stands out unusually weakly against the $S(T)$ dependence ($S_{max} \approx 2$ μV/K [10, 11]). It is well known that in most Ce intermediate-valence compounds, the characteristic values of thermopower exceed those observed in conventional metals of the type of copper by 10–100 times. The $S(T)$ relation in such compounds has a positive extremum and can quite frequently be satisfactorily fitted by the relation $S \approx aT/(T^2 + b)$, which indicates strong electron scattering in transitions from the broad *sd* conduction band to the narrow *f* band forming a Lorentzian density-of-states peak near the Fermi level [12–14]. Note that the temperature position of the S maximum correlates qualitatively with T_K and the Ce *f*-state occupation number ($T_{Smax} \sim T_K \sim \langle n_f \rangle^{-1}$) [14].

To date, it has not been established whether the fact that the characteristic dependence $S \approx aT/(T^2 + b)$ does not hold in $CeNi_5$ is caused by the masking action of specific features in the structure of the *d* states or by the Ce *f* states at E_F not being described by a Lorentzian density-of-states peak. Analysis of all the earlier data as a whole [7, 9–12] suggests that the total $CeNi_5$ thermopower can be written as

$$S \approx S_{ph} + S_{mag} + S_d + S_f,$$

where S_{ph} is the phonon-drag component of thermopower, S_{mag} is the magnetic contribution originating from spin fluctuations in the narrow *d* band, S_d is the Mott contribution due to scattering in *s–d* transitions, and S_f is the contribution from *f* states of the valence-unstable Ce. The main components of the total ther-

mopower of $LaNi_5$, which is used frequently as an analog, can differ in magnitude from those of $CeNi_5$. This applies particularly to the component S_d, which is associated with structural details of electronic states near E_F. Band calculations suggest that $CeNi_5$ and $LaNi_5$ have a nearly identical density-of-states structure in the conduction band, with the exception of a narrow energy interval (~0.2 eV) in the vicinity of E_F [15–18]. The component S_{mag} in $LaNi_5$ can apparently be neglected. The components S_{ph} and S_{mag} contribute noticeably to the total thermopower of $CeNi_5$ for $T < 300$ K but are strongly suppressed for low substitutional-impurity concentrations (<5 at. %) on the nickel sublattice (Ni ⟶ Cu, Ga, Al, Si, Ge) [7, 10–12, 19]. Spectroscopic studies [20, 21] show that atomic substitutions made within these limits do not affect the Ce valence state substantially. Hence, the component $S_f(T)$ in phases with saturated Ce valence can be estimated if data on Mott's component $S_d(T)$ are available.

We present estimates of the contributions due to the band structure and local *f* states to the total thermopower of the $Ce(M_xNi_{1-x})_5$ solid solutions (M = Ga, Cu; $0 \le x \le 0.4$) containing Ce in amounts corresponding to the SV–IV transition. We used the phenomenological approach developed by us earlier [12–14] to describe the transport coefficients of systems with intermediate Ce valence in order to analyze the behavior of the thermopower component $S_f(T)$ associated with saturated Ce valence. It is shown that the fine structure in the density of *f* states near the Fermi level is due to a Kondo-type *s*(*d*)–*f* correlation interaction. The Ce transition to the SV state is accompanied by a quasi-gap formation in the *f* spectrum, which may imply the formation of strongly correlated itinerant *f* states.

2. MOTT COMPONENT OF THE THERMOPOWER IN RNi_5 (R = La, Ce)

Calculations of the $N(E)$ curves relating the density of states to energy for RNi_5 (R = La, Ce) made using various band-structure approaches yield fairly similar results [7, 15–18]. The total density of states $N(E)$ is derived primarily from states of the *s* and *d* type. The $N(E)$ curves for these compounds agree well within a broad energy range of conduction-band states, except in the energies closely adjoining the E_F level. In the case of $CeNi_5$, a narrow peak of the density of *d* states appears. Remarkably, this peak forms not as a result of additional *d*–*f* hybridization but rather because of the *f* states being expelled out of the conduction band into the region of positive energies [18]. The specific features seen in the $N(E)$ curve suggest that the band component of thermopower is connected primarily with carrier scattering in transitions from the *s* to *d* states, and it can be estimated using Mott's model [22]. In this model, the relaxation time $\tau(E)$ is inversely proportional to the density of *d* states. The density of *s* states being comparatively low, one usually assumes $\tau(E) \sim 1/N(E)$.

Although calculated $N(E)$ curves are frequently used to estimate the temperature dependences of the electronic properties of a metal [23–27], no clear-cut criteria of the applicability of this approach to a realistic thermopower estimation have thus far been elaborated. An analysis of such estimates [25, 26] suggests that calculation of the transport coefficients should take into account the smearing of the $N(E)$ fine structure, which is caused by the finite lifetime of electrons in a metal due to their scattering. For this purpose, one frequently employs the electrical resistivity ρ of the crystal. In this case, the half-width of the Lorentzian broadening function is found from the relation $\sigma = h/\tau$, where $\tau = m/ne^2\rho$ [25]. This method of estimation of σ can, however, produce an overestimated broadening of the $N(E)$ structure if applied to transition metals and their alloys [27]. Application of the transport relaxation time to determination of the parameter σ is apparently not fully justified, and the problem of calculation of the density-of-states broadening is far from trivial.

In our calculation of the thermopower component S_d, the parameter σ was considered variable. This is particularly convenient if one takes into account the sensitivity of the absolute values of S_d to the particular choice of σ, which is usually high. The calculations of thermopower with inclusion of the broadening of the structure was done using our earlier calculations of the energy spectrum of RNi_5 by a modified LCAO method [15, 16]. To take into account the effect of conduction electron scattering on the overall pattern of $N(E)$, a density-of-states histogram was constructed taking into account the weight of each computational point of the Brillouin zone in k space by means of not the δ function, as was done in [15, 16], but of the Lorentzian broadening function of the half-width σ.

Figures 1 and 2 present $N(E)$ curves calculated for RNi_5 [15, 16] within a narrow energy interval about E_F with due account of the variable broadening σ, as well as similar density-of-states curves obtained in [18] without the inclusion of broadening. Also shown are the diffusion components of thermopower $S_d(T)$ calculated from the relation [22]

$$S_d(T) = -\frac{1}{|e|T}\frac{I_1}{I_0},$$

$$I_n = \int_{-\infty}^{\infty} E^n \frac{dF}{dE} N(E)^{-1} dE, \quad n = 0, 1,$$

where $F(E)$ is the Fermi–Dirac distribution function. In estimating $S_d(T)$, one may limit oneself to integration within an energy interval ±1 eV about the Fermi energy $E_F(0) = 0$.

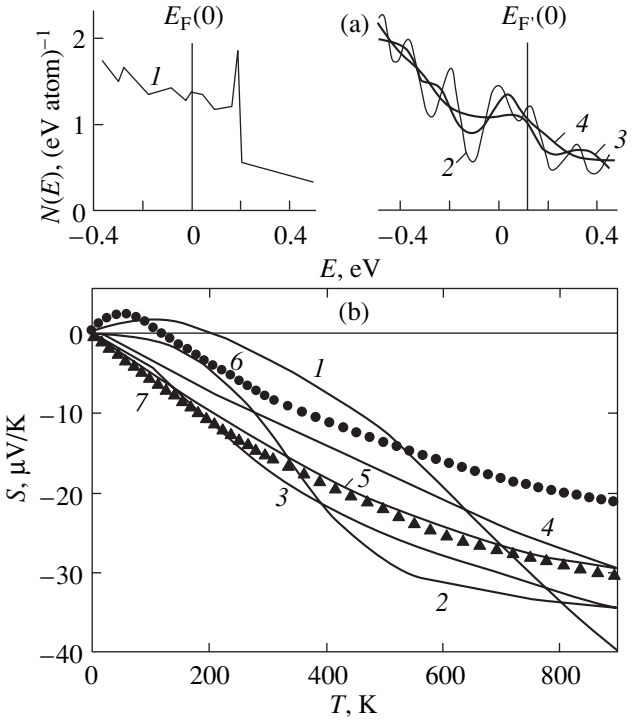

Fig. 1. (a) Density-of-states functions of $LaNi_5$ near the Fermi level obtained (*1*) in [18] and (*2*) in [15] with the inclusion of broadening σ = 0.02, (*3*) 0.05, and (*4*) 0.1 eV, and (b) the corresponding temperature dependences of thermopower calculated for the starting Fermi level displaced by (*1*) 0 and (*2–4*) 0.1 eV. Curve 5 was obtained by taking into account the temperature dependence of broadening $\sigma = \sigma_0 + bT$ ($\sigma_0 = 0.05$ eV, $b = 1.5 \times 10^{-4}$ eV K^{-1}) and displacement $E_{F'}(0) = 0.1$ eV. Also shown for comparison are the experimental thermopower plots for (*6*) $LaNi_5$ and (*7*) $LaNi_4Cu$.

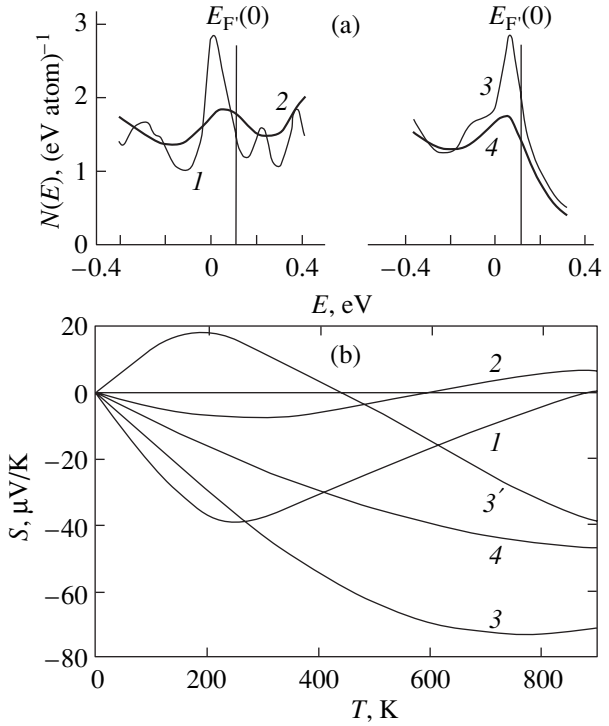

Fig. 2. (a) Density-of-states functions of $CeNi_5$ near the Fermi level obtained in [16] with inclusion of broadening σ equal to (*1*) 0.02 and (*2*) 0.1 eV, (*3*) in [18], and (*4*) in this work, and (b) the corresponding temperature dependences of thermopower calculated for the starting Fermi level displaced by (*3'*) 0 and (*1–4*) 0.1 eV.

For comparison, Fig. 1 also presents experimental $S(T)$ relations obtained for $LaNi_5$ and an $LaNi_4Cu$ solid solution [10, 12]. The deviation from linearity $S \sim T$ and the additional positive contribution to the thermopower of $LaNi_5$ for $T < 200$ K are due predominantly to phonon drag [7]. In the case of $CeNi_5$, this positive contribution is considerably enhanced ($S_{\max 1} = 5$ μV/K for $T_{S\max 1} = 100$ K) [7, 10]. Note that no additional positive contribution to the thermopower appears already in the case of Ni being substituted by ~2–5 at. % Cu or Ga, Al, Si, Ge, irrespective of the actual type of the *R* element [7, 10–12, 19]. This means that the experimental $S(T)$ curve for $La(M_xNi_{1-x})_5$ can be identified with the component $S_d(T)$. Despite the thermopower being slightly dependent on the content of the substituting element, the character of the $S_d(T)$ dependence is retained virtually without chang over a broad temperature range [12] and follows the pattern of curve *7* in Fig. 1b. Because of the existence of an additional component S_f associated with the Ce intermediate valence, a similar estimate of the thermopower $S_d(T)$ can be made only by calculations.

Taking into account the inaccuracy with which the Fermi energy at $T = 0$ K is determined in band-structure calculations, $S_d(T)$ was computed for a number of $E_{F'}(0)$ values displaced from the starting level $E_F(0) = 0$ in steps of 0.02 eV within ±0.2 eV. For $LaNi_5$, the magnitude of thermopower and the character of the calculated curves were found to depend radically on the choice of σ and $E_{F'}(0)$. The calculation approaches the experiment most closely only when the starting Fermi level is displaced to positive energies by 0.1 eV and the broadening is taken to be σ = 0.1 eV. For such a broadening σ, however, the $S_d(T)$ dependence becomes almost linear throughout the temperature interval covered (curve *4* in Fig. 1b). It is seen that a certain nonlinearity in the $S_d(T)$ dependence for $LaNi_5$ similar to the one observed experimentally can be obtained in the approach [18] made without invoking a broadening function and Fermi level displacement or in the calculation [15, 16] performed with the parameters σ = 0.02 eV and $E_{F'}(0) = 0.1$ eV (curves *1* and *2* in Fig. 1b, respectively). With such parameters, however, the $S_d(T)$ curve disagrees with experimental values at high temperatures. To rec-

oncile the calculated thermopower with experimental values throughout the temperature range studied, one should take into account the dependence of σ on temperature. Assuming a linear growth of the broadening parameter by the relation $\sigma \approx \sigma_0 + bT$ ($\sigma_0 = 0.05$ eV, $b = 1.5 \times 10^4$ eV K^{-1}), one can obtain a fairly good fit to the experimental thermopower for the $LaNi_4Cu$ alloy (curve *5* in Fig. 1b).

As follows from the above estimates, the calculated thermopower S_d agrees well with experimental values for La $(Cu_xNi_{1-x})_5$, if one neglects the S_{ph} contribution for the composition with $x = 0$. In doing this, one should correct the starting position of the $E_F(0)$ level in the calculated density-of-states of $LaNi_5$, which is frequently done in such estimates of the electronic characteristics of metals [24, 27].

Determination of the component S_d for $CeNi_5$ by using band-structure calculations [18] results in a temperature dependence (curve *3*' in Fig. 2b) that differs slightly from the one obtained for $LaNi_5$. This can be traced, in the case of $CeNi_5$, to the formation of a distinct fine structure in the density of *d* states at the E_F level. The presence of this feature is supported experimentally by the onset of spin fluctuations in $CeNi_5$ [9]. A more realistic estimation of the $S_d(T)$ dependence should be based on the fitting to experiment done for $LaNi_5$. As expected, if the Fermi level displacement $E_{F'}(0) = 0.1$ eV and the broadening $\sigma = 0.1$ eV are taken into account, the calculated thermopower components $S_d(T)$ for $CeNi_5$ (curves *3*, *4* in Fig. 2b) and for $LaNi_4Cu$ (curves *3*, *5* in Fig. 1b) follow approximately the same course. Note the fundamentally different behavior of $S_d(T)$ at high temperatures ($T > 300$ K) obtained when using the band structure calculations presented in [16, 18]. This is due to the $N(E)$ curves behaving differently in the region of positive energies (Fig. 2a). In the calculations reported in [18], the band of the itinerant *f* states lies slightly higher above the E_F level (by ~0.5 eV) in comparison to the data from [16]. As a result, the hybridization of the *f* and *sd* states in [18] is weaker, thus producing a steeper $N(E)$ falloff within the interval $E_F < E < 0.5$ eV. The discrepancy between the calculations originates from the fact that the *f*-orbital contribution to $CeNi_5$ band states is taken into account in [16] in a somewhat simplified manner. For this reason, the high-temperature part of the $S_d(T)$ dependence represented by curve *3* in Fig. 2b is preferable. Taking nonzero σ into account primarily affects the magnitude of the thermopower and does not influence its temperature behavior in any way.

To include the broadening of the peak in the density of *d* states near E_F and the steep decay of $N(E)$ for $E > E_F$, we calculated the $S_d(T)$ relation using the model density of states $N(E)$ (curve *4* in Fig. 2a). Curve *4* corresponds to the calculation made in [16] with a broadening $\sigma = 0.1$ eV for $E < E_{F'}(0)$ (curve *2* in Fig. 2a) and to the calculation in [18] for positive energies $E > E_{F'}(0)$ (curve *3* in Fig. 2a). This is probably the most appropriate model of the density of states for estimation of the component $S_d(T)$ for Ce $(M_xNi_{1-x})_5$ alloys with small *x*. We readily see that the magnitude of thermopower and the nature of the $S_d(T)$ relation (curve *4* in Fig. 2b) agree satisfactorily with similar estimates made for La alloys (curves *3*, *5* in Fig. 1b).

Thus, the calculations show that taking the fine structure in $N(E)$ and the high-energy shift of the $E_F(0)$ level into account is sufficient for a realistic evaluation of the thermopower component $S_d(T)$ for alloys of the type $R(M_xNi_{1-x})_5$ with small values of *x*. Treated within the one-electron band approach, the *f* states are not directly involved in the formation of an additional structure in the total density of states near E_F. Whence one may conclude that the $S_d(T)$ relations follow approximately the same behavior for the Ce and La alloys and that $La(M_xNi_{1-x})_5$ can be used as an analog to determine the contribution from the valence-unstable Ce to the total thermopower of $Ce(M_xNi_{1-x})_5$.

3. CONTRIBUTION FROM *f* STATES OF VALENCE-UNSTABLE Ce TO THE TOTAL THERMOPOWER OF $Ce(M_xNi_{1-x})_5$ (M = Ga, Cu)

Data on the thermopower *S* and the electrical resistivity ρ of $Ce(M_xNi_{1-x})_5$ alloys with M = Cu, Ga and of the corresponding La analogs obtained within a very broad temperature range (4–900 K) can be found in [7, 10–12, 19].

Figures 3 and 4 present the temperature dependences of the *f*-state contribution (S_f) of the valence-unstable Ce to the total thermopower of $Ce(M_xNi_{1-x})_5$ alloys (M = Ga, Cu) calculated using the Gorter–Nordheim relation [22]

$$S_f = [\rho(\mathrm{Ce})S(\mathrm{Ce}) - \rho(\mathrm{La})S(\mathrm{La})]/[\rho(\mathrm{Ce}) - \rho(\mathrm{La})],$$

where ρ(Ce), ρ(La) and S(Ce), S(La) denote the total electrical resistivity and thermopower of alloys of the same composition with Ce and La, respectively. The component S_f for the $x = 0$ composition is seen to additionally contain S_{mag} and S_{ph} contributions. This manifests itself clearly in the $S_f(T)$ dependence in the form of a positive contribution peaking at $T \approx 120$ K (Fig. 3). The additional contribution is very sensitive to composition and vanishes completely in Ga alloys even for $x = 0.035$ (curve *2* in Fig. 3) or in Cu alloys with $x > 0.02$ [7]. As follows from these examples, $Ce(M_xNi_{1-x})_5$ alloys (M = Ga, Cu) with small substitutional-impurity concentrations on the Ni sublattice ($x < 0.1$) appear to be particularly convenient subjects for studying the Ce SV phenomenon.

The temperature behavior $S_f(T)$ of $Ce(M_xNi_{1-x})_5$ alloys differs from that usually observed in systems with intermediate Ce valence [1] in the presence of a negative contribution for $T < T_{Sf\max}$, which passes

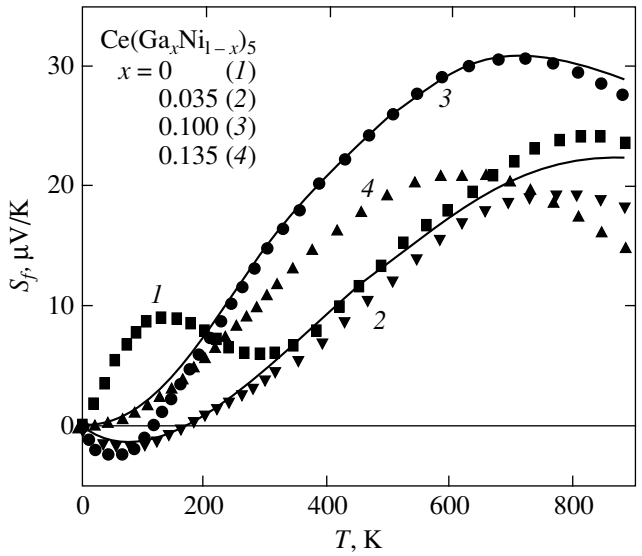

Fig. 3. Temperature dependences of the contribution of Ce *f* states to the total thermopower of $Ce(Ga_xNi_{1-x})_5$. Solid lines plot the thermopower calculated from Eq. (3).

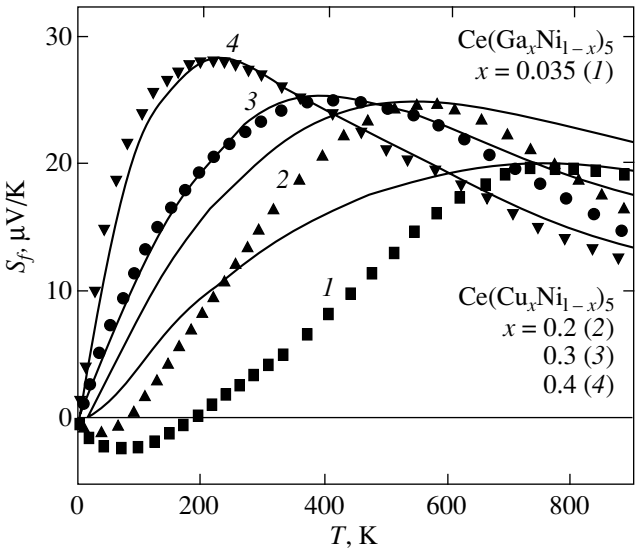

Fig. 4. Temperature dependences of the contribution of Ce *f* states to the total thermopower of $Ce(M_xNi_{1-x})_5$ with *M* standing for (*1*) Ga and (*2–4*) Cu. Solid lines plot the thermopower calculated from Eq. (2).

through a minimum at $T \sim 50$–100 K. As x increases, the region of the negative contribution becomes progressively narrower, resulting in the appearance of a linear region in the thermopower ($S = aT$, $a > 0$) at low temperatures, which is characteristic of conventional systems with intermediate Ce valence. Spectroscopic measurements of the occupation numbers $\langle n_f \rangle$ [20, 21] suggest that the Ce^{3+} state becomes stable with increasing x. The increase in $\langle n_f \rangle$ is ~10% for $Ce(Ga_xNi_{1-x})_5$ ($0 \le x \le 0.135$) and ~40% for $Ce(Cu_xNi_{1-x})_5$ ($0 \le x \le 0.4$). The temperature $T_{Sf\max}$ for both alloys correlates qualitatively with the *f*-state population ($T_{Sf\max} \sim \langle n \rangle^{-1}$), which is in agreement with general ideas concerning the relation of thermopower to the intermediate-valence state of Ce [14].

The thermopower of systems with intermediate Ce valence has been studied most comprehensively within the Anderson model with strong *f*-orbital degeneracy in [28–30]. However, analytic relations which would permit a comparison of the theory with experiment over a broad temperature range have not been obtained thus far. The phenomenological approach proposed by us [12–14] for consideration of transport effects in systems of this type appears to be the most convenient for this purpose. It is assumed in [12–14] that the main contribution to thermopower in the case of the intermediate Ce valence is due to electron scattering in transitions from the broad *sd* conduction band to a strongly correlated *f*-like band with a Lorentzian-shaped density of states $g_f(E)$:

$$g_f(E) = W_f/[(E - E_f)^2 + W_f^2],$$

where E_f and W_f are the position of the *f* band relative to the E_F level and its width, respectively. Now, one can readily derive the following expression for the thermopower component $S_f(T)$ [12]:

$$S_f = \frac{2}{3}\pi^2 \frac{k_B}{|e|} \frac{T\varepsilon_f}{(\pi^2/3)T^2 + \varepsilon_f^2 + \Gamma_f^2}, \qquad (1)$$

where $\varepsilon_f = E_f/k_B$ and $\Gamma_f = W_f/k_B$ (k_B is the Boltzmann constant). The $S_f(T)$ relation passes through an extremum,

$$S_{f,\,\mathrm{extr}} = \frac{\pi}{\sqrt{3}} \frac{k_B}{|e|} \frac{\varepsilon_f}{\sqrt{\varepsilon_f^2 + \Gamma_f^2}}, \quad T_{Sf,\,\mathrm{extr}} = \frac{\sqrt{3}}{\pi}\sqrt{\varepsilon_f^2 + \Gamma_f^2}.$$

Equation (1) satisfactorily describes the temperature dependences of thermopower for most systems with intermediate Ce valence even regardless of the possible temperature dependence of the parameters ε_f and Γ_f [14]. In the case of strong orbital degeneracy of *f* states ($N_f \gg 1$), which occurs in systems with intermediate Ce valence, it is appropriate to use the well-known relation connecting the parameters ε_f, Γ_f, and T_K ($\varepsilon_f = T_K$, $\Gamma_f = \pi T_K/N_f$ [29]). Then, in place of Eq. (1), we obtain a more convenient expression,

$$S_f = \frac{2}{3}\pi^2 \frac{k_B}{|e|} \frac{TT_K}{(\pi^2/3)T^2 + (1 + \pi^2/N_f^2)T_K^2}, \qquad (2)$$

with only one fitting parameter T_K.

Systems with saturated Ce valence exhibit a maximum orbital degeneracy $N_f = 2J + 1 = 6$, and the calculated maximum $S_{f\max}$ lies at $T \approx 0.62T_K$. This means that if the experimentally found thermopower follows the

$S = aT/(T^2 + b)$ relation, Eq. (2) can be used to determine the characteristic temperature T_K.

Figure 4 presents $S_f(T)$ curves (solid lines) calculated from Eq. (2) under the assumption of a temperature-independent T_K and fitted to experimental data by matching their maxima. For convenience of comparison with experimental values, the calculated thermopower was normalized using a coefficient $p = S_{f\max,\,exp}/S_{f\max,\,calc}$, where $S_{f\max,\,exp}$ and $S_{f\max,\,calc}$ denote the maxima in the experimental and calculated relations, respectively. For $Ce(Cu_xNi_{1-x})_5$ alloys, the fitting is reached at T_K = 880, 640, and 368 K for the compositions with x = 0.2, 0.3, and 0.4, respectively. The curve calculated for an x = 0.035 Ga alloy was obtained with T_K = 1200 K. The best fit to experiment was obtained for a Cu alloy with x = 0.4, in which Ce is close to the trivalent state [20]. Alloys with $x < 0.2$ exhibit substantial disagreement with experimental values at low temperatures ($T < T_{Sf\max}$) because of the appearance of an additional negative component. In this range of compositions, Ce is in the SV state [20, 21]. The negative contribution to thermopower for $T < T_{Sf\max}$ is seen to increase as Ce approaches the SV state. As for a certain disagreement of the calculations with experimental values at high temperatures ($T > T_{Sf\max}$), this can be attributed to a possible temperature dependence of T_K. $Ce(Cu_xNi_{1-x})_5$ alloys with $x \geq 0.2$ exhibit a noticeable stabilization of the Ce^{3+} state with increasing temperature [20]. Hence, one may expect a decrease in T_K at high temperatures and a steeper falloff of the calculated thermopower for $T > T_{Sf\max}$.

The character of the deviation of the experimental $S_f(T)$ relation from calculations made using Eq. (2) suggests the possibility of formation of an additional density-of-states peak below the E_F as Ce transfers to the SV state. The behavior of $S_f(T)$, in this case, can be qualitatively described with the relation

$$S_f = \frac{2}{3}\pi^2\frac{k_B T}{|e|}\sum_i \frac{\varepsilon_{fi}}{(\pi^2/3)T^2 + \varepsilon_{fi}^2 + \Gamma_{fi}^2}, \qquad (3)$$

where ε_{fi} and Γ_{fi} denote the parameters of the $g_{f1}(E)$ and $g_{f2}(E)$ peaks. Figure 3 plots normalized $S_f(T)$ relations (solid lines) calculated from Eq. (3). Curve *2*, calculated for the x = 0.035 composition, agrees well with the experiment. Agreement is reached for ε_{f1} = 316 K, Γ_{f1} = 1510 K and ε_{f2} = –52 K, Γ_{f2} = 542 K. In the case of compositions with $x > 0.035$, agreement with the experiment is not reached over the whole temperature range if only ε_{fi} and Γ_{fi} are used as fitting parameters. Matching the curves at high temperatures ($T > 300$ K) does not yield a distinct minimum and consistent values of $T_{Sf\max}$ in the low-temperature part of the $S_f(T)$ relation (curve *3*, calculated with ε_{f1} = 316 K, Γ_{f1} = 1232 K and ε_{f2} = –39 K, Γ_{f2} = 453 K). Whence it follows that the $g_{f1}(E)$ and $g_{f2}(E)$ peaks may approach a Lorentzian shape only for an x = 0.035 alloy and that they exhibit a stronger energy dependence of the density of states near E_F for alloys with $x > 0.035$. This situation can be identified qualitatively with the formation of a quasi-gap $\Delta \approx |\varepsilon_{f1}| + |\varepsilon_{f2}| \approx 400$ K in the energy spectrum of $CeNi_5$ in the vicinity of E_F. Total disappearance of the quasi-gap and the formation of only one $g_f(E)$ peak in $Ce(M_xNi_{1-x})_5$ solid solutions are observed to occur when Ce transfers from the SV to its usual intermediate-valence state.

4. DISCUSSION OF RESULTS

Judging from the fine-structure parameters of $g_f(E)$ and from their sensitivity to the Ce valence state, the fine structure forms primarily by the Kondo mechanism. This conclusion is buttressed by estimates of T_K made in terms of Anderson's impurity model with inclusion of strong orbital degeneracy [29]. This can be done conveniently by using the relation connecting T_K with the band structure characteristics

$$T_K = D(\Gamma/\pi|E_f|)^{1/N_f}\exp(\pi E_f/N\Gamma), \qquad (4)$$

where D is the conduction-band half-width, E_f is the binding energy of the f states to band states, and Γ is the hybridization-induced broadening of an f level in the single-particle approximation. Band-structure calculations [16, 18] and spectroscopic measurements [31] suggest the following values of the parameters: D = 2.5 eV, Γ = 0.3 eV, and E_F = –1.5 eV. Then, Eq. (4) yields T_K = 1330 K, a value close enough to that derived from the $S_f(T)$ relation (T_K = 1200 K). One may also conveniently use the expressions relating T_K to parameters allowing experimental determination [29],

$$T_K = C\langle n_f\rangle/\chi_f(0) \qquad (5)$$

or, invoking the paramagnon model of systems with intermediate Ce valence [32],

$$T_{sf} = C/2\chi_f(0), \qquad (6)$$

where C is the Curie constant for the principal Ce^{3+} configuration ($4f^1$, J = 5/2), which is 0.807 emu K/mol Ce, and $\chi_f(0)$ is the low-temperature part of the paramagnetic susceptibility associated with f states. The f-state occupation number for $CeNi_5$ is known from spectroscopic measurements ($\langle n_f\rangle$ = 0.6 [20]). $\chi_f(0)$ can be estimated using data on the magnetic susceptibility of $CeNi_5$ and $LaNi_5$ at 300 K in order to avoid the effect of impurities and of the additional paramagnon susceptibility component connected with spin fluctuations in

the *d* band of $CeNi_5$. Using the data quoted in [12, 21], we find

$$\chi_f(0) = \chi(CeNi_5) - \chi(LaNi_5)$$
$$= 0.33 \times 10^{-3} \text{ emu/mol Ce.}$$

Equations (5) and (6) now yield T_K = 1470 K and T_{sf} = 1220 K. We see that the estimates of the characteristic temperature T_K (T_{sf}) made in terms of different model approaches [29, 32] correlate satisfactorily with the T_K derived from the thermopower.

Analysis of the present model concepts [2, 33, 34] permits the suggestion that the double-humped $g_{fi}(E)$ structure observed near E_F in the case of the saturated Ce valence is of a coherent nature.

In principle, a double-humped $g_{fi}(E)$ structure of a correlation nature can also be obtained within Anderson's model of the *f* impurity center [29, 30]. At high *f*-state hybridization energies with the band states, where T_K becomes of the same order of magnitude as the spin–orbit splitting energy of the *f* states (Δ_{SO}/k_B = 3000 K), the *f*' state with *J* = 7/2 can be thermally populated. This produces a density-of-states resonant peak $g_{f2}(E)$ lying below E_F. However, as follows from theoretical estimates [29] and inelastic neutron-scattering data [35], the separation between such peaks is $\sim\Delta_{SO}$, which is at odds with the figure $\Delta \sim 400$ K found here.

It is well known that coherent effects in systems with intermediate Ce valence quite frequently produce a double-humped fine structure near E_F with a quasi-gap Δ [1, 2]. Treated in terms of the Kondo and Anderson lattice models, this quasi-gap can have a spin, charge, or quasi-particle nature and assume values of Δ comparable to T_K [33, 34]. Unfortunately, the results obtained in theoretical studies of thermopower within these models are contradictory [28–30] and do not permit a quantitative comparison. The calculated $S_f(T)$ relations obtained in [36] are the closest to those observed experimentally in $Ce(M_xNi_{1-x})_5$ alloys. The model parameters used in the calculation correspond approximately to the case of strong hybridization of the Ce *f* states with itinerant states (high T_K) in metallic systems. However, a negative low-temperature minimum in the thermopower occurs only at a small number of electrons per *f* center, a situation which is not likely to apply to $CeNi_5$.

In conclusion, we note that although the mechanism of formation of the quasi-gap Δ in $CeNi_5$ requires further studies, it is apparently connected with the saturated Ce valence states.

REFERENCES

1. N. B. Brandt and V. V. Moshchalkov, Adv. Phys. **33** (5), 373 (1984).
2. J. W. Allen and R. M. Martin, Phys. Rev. Lett. **49** (15), 1106 (1982).
3. L. Severin and B. Johansson, Phys. Rev. B **50** (24), 17886 (1994).
4. S.-H. Yang, H. Kumigashira, T. Yokoya, *et al.*, Phys. Rev. B **53** (18), R11946 (1996).
5. A. B. Andrews, J. J. Joyce, A. J. Arko, *et al.*, Phys. Rev. B **53** (6), 3317 (1996).
6. P. A. Alekseev, V. N. Lasukov, and I. P. Sadikov, J. Magn. Magn. Mater. **76–77**, 423 (1988).
7. S. Cabus, K. Gloos, U. Gottwick, *et al.*, Solid State Commun. **51** (11), 909 (1984).
8. M. D. Koterlin, B. S. Morokhivskiĭ, R. R. Kutyanskiĭ, *et al.*, Fiz. Tverd. Tela (St. Petersburg) **40** (1), 7 (1998) [Phys. Solid State **40**, 5 (1998)].
9. Y. Naidyuk, M. Reiffers, A. G. M. Jansen, I. K. Yanson, P. Wyder, D. Gignoux, and D. Schmitt, in *Physics of Transition Metals*, Ed. by P. M. Oppeneer and J. Kubler (World Sci., Singapore, 1992), p. 222.
10. R. V. Lutsiv, M. D. Koterlin, O. I. Babich, and O. I. Bodak, Fiz. Tverd. Tela (Leningrad) **26** (4), 1182 (1984) [Sov. Phys. Solid State **26**, 716 (1984)].
11. M. D. Koterlin, O. I. Babich, B. S. Morokhivskiĭ, *et al.*, Fiz. Tverd. Tela (Leningrad) **30** (5), 1512 (1988) [Sov. Phys. Solid State **30**, 873 (1988)].
12. M. D. Koterlin, O. I. Babich, R. V. Lutsiv, *et al.*, Preprint No. 11, IMF (Kiev, 1986).
13. R. V. Lutsiv and M. D. Koterlin, Fiz. Tverd. Tela (Leningrad) **25** (8), 2484 (1983) [Sov. Phys. Solid State **25**, 1426 (1983)].
14. M. D. Koterlin and R. V. Lutsiv, in *Physics and Chemistry of Rare-Earth Semiconductors* (Nauka, Novosibirsk, 1990), p. 18.
15. M. D. Koterlin, O. I. Babich, and R. R. Kutyanskiĭ, Fiz. Tverd. Tela (St. Petersburg) **36** (6), 1610 (1994) [Phys. Solid State **36**, 880 (1994)].
16. M. D. Koterlin, O. I. Babich, and R. R. Kutyans'kiĭ, Dopov. Akad. Nauk Ukr. **3**, 46 (1995).
17. S. K. Malik, F. J. Arlinghaus, and W. E. Wallace, Phys. Rev. B **25** (10), 6488 (1982).
18. L. Nordstrom, M. S. S. Brooks, and B. Johansson, Phys. Rev. B **46** (6), 3458 (1992).
19. M. D. Koterlin, O. I. Babich, B. S. Morokhivskiĭ, *et al.*, Fiz. Tverd. Tela (Leningrad) **29** (3), 943 (1987) [Sov. Phys. Solid State **29**, 542 (1987)].
20. V. A. Shaburov, A. E. Sovestnov, I. A. Markova, *et al.*, Fiz. Tverd. Tela (Leningrad) **23** (8), 2455 (1981) [Sov. Phys. Solid State **23**, 1437 (1981)].
21. H. Flandorfer, P. Rogl, K. Hiebl, *et al.*, Phys. Rev. B **50** (21), 15527 (1994).
22. F. J. Blatt, P. A. Schroeder, C. L. Foiles, and D. Greig, *Thermoelectric Power of Metals* (Plemum, New York, 1976; Metallurgiya, Moscow, 1980).
23. V. E. Zinov'ev, *Thermophysical Properties of Metals under High Temperatures: Reference Edition* (Metallurgiya, Moscow, 1989).
24. A. T. Burkov, E. Bauer, E. Gratz, and R. Resel, in *Physics of Transition Metals*, Ed. by P. M. Oppeneer and J. Kubler (World Sci., Singapore, 1992), p. 387.

25. D. Greig and G. J. Morgan, Philos. Mag. **27** (4), 919 (1973).
26. W. E. Pickett, Phys. Rev. B **26** (3), 1186 (1982).
27. L. M. Noskova, E. V. Rozenfel'd, and Yu. P. Irkhin, Fiz. Tverd. Tela (Leningrad) **26** (9), 2785 (1984) [Sov. Phys. Solid State **26**, 1686 (1984)].
28. K. H. Fischer, Z. Phys. B **76** (3), 315 (1989).
29. N. E. Bickers, D. L. Cox, and J. W. Wilkins, Phys. Rev. B **36** (4), 2036 (1987).
30. D. L. Cox and N. Grewe, Z. Phys. B **71** (3), 321 (1988).
31. J. W. Allen, S. J. Oh, O. Gunnarsson, *et al.*, Adv. Phys. **35** (3), 275 (1986).
32. M. T. Beal-Monod and J. M. Lawrence, Phys. Rev. B **21** (10), 5400 (1980).
33. H. Tsunetsugu, M. Sigrist, and K. Ueda, Rev. Mod. Phys. **69** (3), 809 (1997).
34. K. Ueda, Physica B (Amsterdam) **230–232**, 22 (1997).
35. A. P. Murani, R. Raphel, Z. A. Bowden, and R. S. Eccleston, Phys. Rev. B **53** (13), 8188 (1996).
36. H. Schweitzer and G. Czycholl, Phys. Rev. Lett. **67**, 3724 (1991).

Translated by G. Skrebtsov

Physics of the Solid State, Vol. 44, No. 5, 2002, pp. 831–836. Translated from Fizika Tverdogo Tela, Vol. 44, No. 5, 2002, pp. 799–804.

SEMICONDUCTORS AND DIELECTRICS

A Negatively Charged Silicon Vacancy in SiC: Spin Polarization Effects

T. T. Petrenko, T. L. Petrenko, and V. Ya. Bratus'

Institute of Semiconductor Physics, National Academy of Sciences of Ukraine, Kiev, 03028 Ukraine

e-mail: taraspetrenko@netscape.net

Received July 16, 2001

Abstract—The equilibrium geometry and hyperfine interaction constants of the nearest and next-to-nearest neighbor atoms are calculated for a negatively charged silicon vacancy in the high-spin state in cubic SiC. The calculations are performed within the cluster approach in terms of the density-functional theory (DFT). It is shown that the results of calculations with the use of a 70-atom cluster are in good agreement with experimental data. A detailed consideration is given to spin polarization in the electron subsystem and the applicability of a simple LCAO model that is commonly used in the interpretation of the electron paramagnetic resonance data for semiconductors. The spin density distribution for the defect under investigation is analyzed in terms of localized orbitals. *© 2002 MAIK "Nauka/Interperiodica".*

1. INTRODUCTION

Over the last forty years, the negatively charged vacancy in crystalline silicon has been a subject of extensive theoretical investigation [1]. Originally, the properties of this defect were treated in the framework of the so-called defect molecule model. This model allows for only the interaction between the orbitals of silicon atoms in the first coordination sphere. However, calculations performed in the last few years have demonstrated that a quantitative agreement between the hyperfine parameters and experimental data can be achieved only with clusters or supercells containing at least several hundreds of atoms [2]. It was found that the point symmetry, lattice relaxation, and energy characteristics calculated for a negatively charged vacancy in silicon substantially depend on the size of the system used for simulating this defect. In the general case, it is necessary to answer the question as to how the size of the model cluster affects the calculated properties of the defect under consideration and to choose the appropriate cluster with a minimum size for adequate description of this defect.

As a rule, microscopic models of vacancy defects in semiconductors are based on the analysis of the hyperfine parameters determined by the electron paramagnetic resonance (EPR) and electron–nuclear double resonance (ENDOR) methods. At the same time, first-principles calculations of the hyperfine parameters present considerable difficulties. This is associated with the necessity of applying computational techniques that account for both the electron correlation and relaxation of atoms in the neighborhood of the studied defect and large basis sets for the wave functions.

In recent years, the high efficiency of calculations in terms of the density-functional theory (DFT), which is outside the province of the local-spin-density approximation, has been demonstrated for many characteristics of molecular systems, including hyperfine parameters [3, 4]. In this respect, it is of particular interest to apply the density-functional methods to the calculation of defects in semiconductors (for at least those formed by relatively light elements).

At present, it is established that the ground state of a negatively charged vacancy in tetrahedral semiconductors can have both the spin $S = 1/2$ and spin $S = 3/2$ depending on the exchange interaction in each specific case [5, 6]. Itoh *et al.* [7] studied cubic *n*-SiC after irradiation and identified the negatively charged silicon vacancy V_{Si}^- from the intensity ratio of hyperfine lines in the EPR spectrum. More recently, Wimbauer *et al.* [8] determined the actual value of the spin ($S = 3/2$) for the V_{Si}^- center in 3*C*-SiC from the ENDOR measurements and calculated the hyperfine parameters for atoms of two coordination spheres in the framework of the local-spin-density approximation without regard for lattice relaxation. Subsequently, Torpo *et al.* [9] calculated the relative stability of the spin states $S = 1/2$ and 3/2 for V_{Si}^- in the framework of the local-spin-density approximation, pseudopotential, and supercell approach. It was found that the high-spin state is more energetically favorable. However, the spin densities and hyperfine parameters were not computed.

In the present work, the V_{Si}^- center was considered within the cluster approximation in terms of the density-functional theory. The purpose of this work was to examine the contribution of the spin polarization effects to the observed hyperfine interaction constants and to analyze the applicability of a number of simpli-

1063-7834/02/4405-0831$22.00

fied approaches to the interpretation of experimental EPR data.

2. COMPUTATIONAL TECHNIQUE

The electronic structure of a negatively charged silicon vacancy in 3*C*-SiC was calculated within the cluster approximation. The calculations were performed using the density-functional method with an unrestricted wave function, the 6-311G(*d*) all-electron basis set of Gaussian functions with six *d* functions for silicon and carbon atoms, and the STO-3G basis set for saturating hydrogen atoms [10]. The use of the all-electron basis set stems from the necessity of correctly describing the behavior of the wave function in the vicinity of the nucleus in order to calculate precisely the hyperfine parameters. In the density-functional theory calculations, we used the B3LYP three-parameter functional [11], including local and nonlocal terms. Moreover, for comparison, we carried out the calculation of the electronic structure at the unrestricted Hartree–Fock level with the same basis set. The actual region of the crystal in the vicinity of the defect was simulated by the $C_4Si_{12}H_{36}$ and $C_{16}Si_{18}H_{36}$ tetrahedral clusters (Fig. 1). The geometry was optimized at fixed saturating hydrogen atoms.

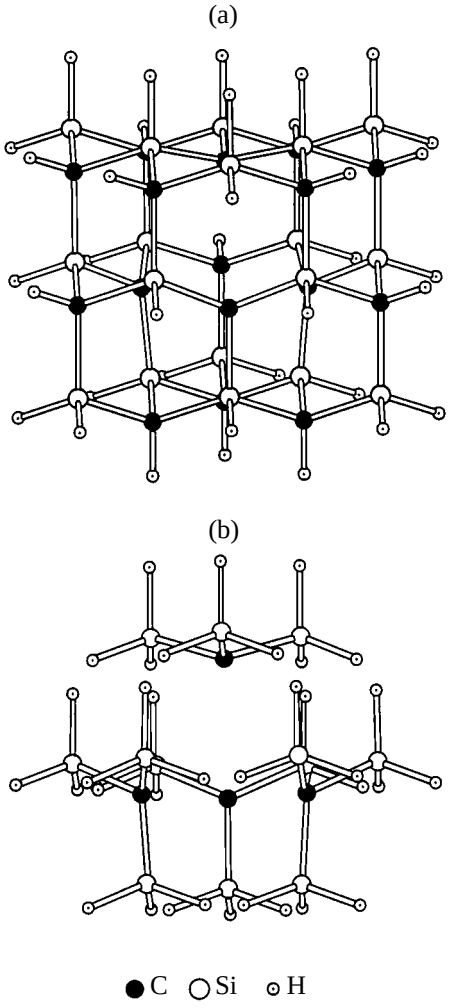

Fig. 1. Schematic representation of the clusters used in the calculations: (a) $C_{16}Si_{18}H_{36}$ and (b) $C_4Si_{12}H_{36}$.

The isotropic hyperfine constant a_{iso} and the components of the spurless tensor T_{ij} for the anisotropic hyperfine interaction with the *N*th nucleus were calculated according to the relationships [12]

$$a_{iso}^{(N)} = \frac{4\pi}{3} g\beta g_N \beta_N \langle S_z \rangle^{-1} \rho^S(R_N), \quad (1)$$

$$T_{ij}^{(N)} = \frac{1}{2} g\beta g_N \beta_N \langle S_z \rangle^{-1} \int \rho^S(r) \tau_{ij}(r - R_N) dr, \quad (2)$$

where $\tau_{ij}(r - R_N) = r_{kN}^{-5}(r_{kN}^2 \delta_{ij} - 3r_{kN,i} r_{kN,j})$, $\rho^S(r)$ is the spin density, and the other coefficients have the universally accepted meaning.

3. RESULTS OF CALCULATIONS

A comparative calculation of the total energies of the negatively charged silicon vacancy V_{Si}^- with spins $S = 1/2$ and 3/2 in SiC was performed using a vacancy defect simulated by the $C_4Si_{12}H_{36}$ cluster. It was found that the gain in total energy ΔE_{tot} for the V_{Si}^- center in the high-spin state is equal to 0.32 eV. This result is consistent with the inferences made by Torpo *et al.* [9]. The point symmetry group at the total energy minimum corresponds to T_d for $S = 3/2$ (which is in good agreement with the experimental data obtained by Wimbauer *et al.* [8]) and C_{3v} for $S = 1/2$. In the ground state, carbon atoms of the first coordination sphere undergo an outward-directed relaxation. As a result, the C–C distance is equal to 3.379 Å (for a perfect lattice, this distance is 3.086 Å) and the displacement of the carbon atoms along the [111] direction is 0.18 Å.

The isotropic hyperfine parameters and components of the anisotropic-hyperfine-interaction tensor for carbon and silicon atoms of the first and second coordination spheres were calculated within different approximations (Table 1). As can be seen from the data presented in Table 1, the accuracy in calculating the hyperfine parameters increases both with an increase in the cluster size and upon changing over to the higher level of the theory used in the calculation (from the unrestricted Hartree–Fock method to the DFT method). This is a quite reasonable result. Good agreement between the calculated hyperfine parameters and the experimental data indicates that the magnetic resonance properties of the V_{Si}^- defect can be adequately described with the use of a 70-atom cluster ($C_{16}Si_{18}H_{36}$) and the B3LYP hybrid functional. Note that silicon atoms of the second coordination sphere are character-

ized by negative spin densities (it should be remembered that, for a ^{29}Si isotope, the magnetic moment $g_N\beta_N$ is negative). According to our calculations, atoms of more distant coordination shells have a zero spin density, which agrees with the ENDOR data [8]. This is another argument in support of the above inference that the cluster of the chosen size is quite suitable for describing the properties of the defect under investigation.

Figure 2 shows the regions with a negative spin density $\rho^S(r)$ in the vicinity of the studied defect. It can be seen that silicon atoms of the second coordination sphere are characterized by negative spin densities, whereas carbon atoms of the first coordination sphere exhibit positive spin densities.

4. THE RELATIONSHIP BETWEEN THE PARAMETERS OF HYPERFINE AND THE WAVE FUNCTION OF UNPAIRED ELECTRONS

Since our cluster calculation has demonstrated good agreement between the theoretical and experimental hyperfine interaction parameters, it is of interest to examine the applicability of a simple LCAO model in terms of higher level methods. As a rule, the hyperfine interaction constants obtained in electron paramagnetic resonance investigations of deep defects in semiconductors are analyzed according to the procedure proposed earlier by Watkins [13] and widely used to date (see [14]). This procedure is based on the representation of the wave function for an unpaired electron in the form

$$\Psi = \sum_i \eta_i(\alpha_i\varphi_{si} + \beta_i\varphi_{pi}). \quad (3)$$

In expression (3), summation is performed over all atoms in the localization region of the unpaired electron. The parameters η are quantitative characteristics of the degree of localization, and the parameters α and β determine the degree of hybridization of the orbitals of the atom under consideration. If the hyperfine interaction parameters a_0 and b_0 are known for the *s* and *p* atomic orbitals, the parameters α, β, and η (for example, for axial symmetry) are determined from the following relationships:

$$\eta_i^2\alpha_i^2 a_0 = a, \quad \eta_i^2\beta_i^2 b_0 = b, \quad \alpha_i^2 + \beta_i^2 = 1, \quad (4)$$

where *a* and *b* are the experimental hyperfine interaction constants.

Within this approximation, it is assumed that all the other electrons are paired electrons and do not contribute to the hyperfine interaction constants. As follows from relationships (4), the signs of *a* and *b* are determined by the signs of the hyperfine interaction parameters a_0 and b_0, respectively. For the atomic orbitals, we can write the relationships $a_0 = (8/3)\pi g\beta g_N\beta_N\varphi_s^2(0)$ and $b_0 = (2/5)g\beta g_N\beta_N\langle r_p^{-3}\rangle$. Hence, in the LCAO approximation, the sign of the hyperfine interaction parameters is governed only by the sign of the nuclear magnetic moment $g_N\beta_N$ and the spin densities on the atomic orbitals are universally positive.

Table 1. Hyperfine parameters (in G) for the V_{Si}^- center with spin $S = 3/2$ in SiC

Cluster type	Atom	Components of the hyperfine interaction tensor	Calculated components of the hyperfine interaction tensor	
			Hartree–Fock method	DFT method (B3LYP)
$C_4Si_{12}H_{36}$	C	a_{iso}	33.80	36.78
		T_1	11.4	9.26
		T_2	–5.7	–4.63
		T_3	–5.7	–4.63
	Si	a_{iso}	4.60	–1.66
		T_1	–0.39	–0.40
		T_2	–0.09	–0.06
		T_3	0.48	0.46
$C_{16}Si_{18}H_{36}$	C	a_{iso}	29.60	15.17
		T_1	11.8	11.8
		T_2	–5.9	–5.9
		T_3	–5.9	–5.9
	Si	a_{iso}	5.50	3.01
		T_1	–0.28	–0.24
		T_2	–0.18	0.06
		T_3	0.46	0.18
Experiment [2]	C	a_{iso}	17.36	
		T_1	11.20	
		T_2	–5.6	
		T_3	–5.6	
	Si	a_{iso}	±2.92	
		T_1	0	
		T_2	0	
		T_3	0	

Note: T_1, T_2, and T_3 are the principal components of the anisotropic-hyperfine-interaction tensor calculated according to formula (2).

It is generally believed that errors in determination of the parameters η_i, α_i, and β_i in the wave function (3) stem from the fact that the atomic functions are modified in crystals. In turn, this leads to changes in the hyperfine interaction parameters a_0 and b_0 compared to those for a free atom. In our calculations, we used the split-valence basis set augmented with *d* orbitals. In this

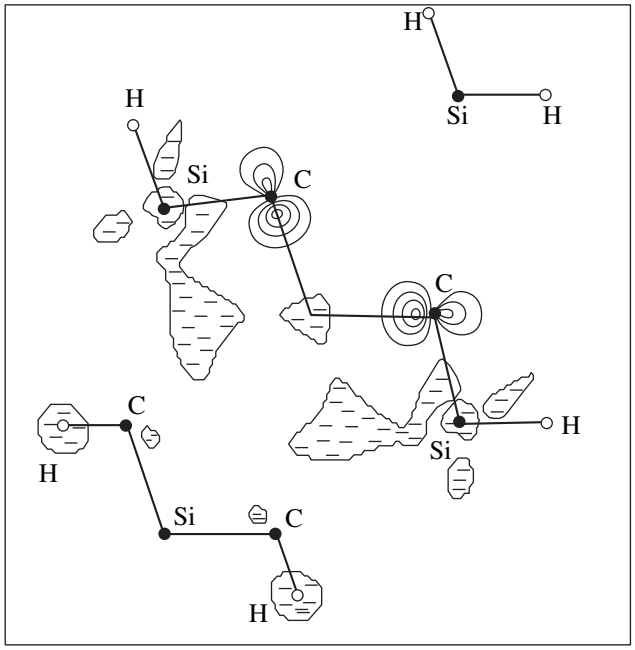

Fig. 2. Spin density distribution for the V_{Si}^- defect in the $C_{16}Si_{18}H_{36}$ cluster in the (110) plane. Hatched regions correspond to negative spin densities. Contours indicate positive spin densities.

case, changes in the size and shape of atomic orbitals in the crystal are automatically taken into account.

The experimental determination of the sign of the hyperfine interaction constants is a very complex problem and, as a rule, can be accomplished only in rare cases. As was noted above, the spin densities calculated for the V_{Si}^- center in 3*C*-SiC are negative in the case of silicon atoms of the second coordination sphere. Illgner and Overhof [15] also obtained the negative spin densities when calculating other point defects in semiconductors. It can be assumed that the occurrence of negative spin densities in a number of coordination spheres is a rule rather than an exception for deep defects in semiconductors. However, according to the simple LCAO model [see relationships (3) and (4)], the spin densities must necessarily be positive. This is direct evidence of the inadequacy of this model.

Table 2. Contributions of the highest canonical molecular orbitals to the total tensor of hyperfine interaction (in G) for the V_{Si}^- center with spin $S = 3/2$ in cubic SiC

Cluster type	Atom	Hyperfine parameter	Computational technique		
			all MOs	3α MOs	(4α + β) MOs
$C_{16}Si_{18}H_{36}$	C	a_{iso}	15.17	1.03	–0.94
		T_1	11.8	16.7	17.6
		T_2	–5.90	–5.6	–6.0
		T_3	–5.90	–11.1	–11.6
	Si	a_{iso}	3.01	–150.1	–141.2
		T_1	–0.24	–0.33	–0.32
		T_2	0.06	0.07	0.03
		T_3	0.18	0.26	0.29

Expressions (1) and (2) for the hyperfine constants can be represented as the sums of the contributions from different occupied molecular orbitals (MOs), that is,

$$T_{jk} = \sum_{i=1}^{N_\alpha} t_{jk}^{(i,\alpha)} - \sum_{i=1}^{N_\beta} t_{jk}^{(i,\beta)}, \quad (5)$$

$$a_{iso} = \sum_{i=1}^{N_\alpha} a^{(i,\alpha)} - \sum_{i=1}^{N_\beta} a^{(i,\beta)}, \quad (6)$$

where N_α and N_β are the numbers of the α and β occupied orbitals with electron spin projections +1/2 and –1/2, respectively.

The partial contributions of the *i*th α orbital to the hyperfine constants have the following form:

$$t_{jk}^{(i,\alpha)} = \frac{1}{2} g\beta g_N \beta_N \langle S_z \rangle^{-1} \sum_{\mu\nu} C_{i\mu}^{(\alpha)} C_{i\nu}^{(\alpha)} \langle \varphi_\mu | \tau_{jk} | \varphi_\nu \rangle, \quad (7)$$

$$a^{(i,\alpha)} = \frac{4\pi}{3} g\beta g_N \beta_N \langle S_z \rangle^{-1} \sum_{\mu\nu} C_{i\mu}^{(\alpha)} C_{i\nu}^{(\alpha)} \varphi_\mu(r_n) \varphi_\nu(r_n). \quad (8)$$

Here, $C_{i\mu}^{(\alpha)}$ stands for the coefficients of the *i*th α orbital defined as

$$\chi_i^{(\alpha)} = \sum_\mu C_{i\mu}^{(\alpha)} \varphi_\mu. \quad (9)$$

Similar expressions can be written for the partial contributions of the β orbitals.

The representation of the wave function in the form of expression (3) implies that, for spin $S = 1/2$, only the terms $t_{jk}^{(i,\alpha)}$ and $a^{(i,\alpha)}$, which correspond to the highest occupied α MO ($i = N_\alpha$), are taken into consideration. When this model is applied to the V_{Si}^- center with spin $S = 3/2$, allowance should be made for three α electrons of molecular orbitals with $i = N_\alpha$, $(N_\alpha - 1)$, and $(N_\alpha - 2)$. In this case, it is assumed that the other terms in relationships (5) and (6) cancel each other or, in other words, that the other electrons are paired electrons. This suggests that the spatial parts of the α and β orbitals coincide with each other; i.e., $C_{i\mu}^{(\alpha)} = C_{i\mu}^{(\beta)}$.

Table 2 lists the hyperfine interaction parameters calculated in terms of the density-functional theory

using three different techniques. The first technique consists in calculating the hyperfine interaction parameters according to formulas (1) and (2) with allowance made for all MOs of the particular cluster. Table 2 also presents the contribution of the three highest occupied α orbitals to the total tensor of hyperfine interaction (the second technique) and the contribution of four α and one β orbitals to the total tensor of hyperfine interaction (the third technique), which were calculated from expressions (5)–(8).

As is well known [13], the one-determinant wave function, one-particle density functions, and two-particle density functions are invariant with respect to a unitary transformation of single-electron MOs. Consequently, in order to choose these functions unambiguously, it is necessary to impose additional constraints on the orbitals. The contributions of the highest occupied MOs (Table 2) correspond to the so-called canonical orbitals [13]. The data presented in Table 2 demonstrate that the partial contribution of several upper MOs to the hyperfine interaction parameters is small compared to the contribution of the other orbitals. Therefore, in the case when the MOs are chosen in the form of canonical orbitals, the hyperfine interaction parameters in the system under consideration are determined by polarization of the all-electron subsystem rather than by only three unpaired α electrons.

The single-electron MOs can be interpreted in a more pictorial form by changing over from the canonical orbitals to the so-called localized orbitals.

5. ANALYSIS OF THE SPIN DENSITY IN TERMS OF LOCALIZED ORBITALS

The invariance of the one-determinant wave function with respect to unitary transformations of single-electron occupied MOs can be used to construct a new set of orbitals that are well localized on a small number of atoms. As a rule, these orbitals correspond to intuitive notions of two-center two-electron chemical bonds. When calculating the localized orbitals, the specific criterion of localization is used as an additional constraint. In order to describe qualitatively the localized MOs, we performed the MO calculations for clusters of different sizes in terms of the density-functional theory [10] and in the valence approximation at the Hartree–Fock level with the GAMESS code [16]. In these calculations, we used three different procedures in accordance with the criteria of localization: (i) the self-repulsion of each electron pair on a particular MO was maximized [17], (ii) the distance between the centers of MO distributions was maximized [18], and (iii) the number of atoms on which the particular MO is localized was minimized [19].

It turned out that all three procedures lead to similar localized orbitals which can be described in the following way. Let us assume that the valence subsystem contains $(2N + 1)$ electrons or, more precisely, $(N - 1)$ β electrons and $(N + 2)$ α electrons. In this case, the localized orbitals obtained in the calculation can be divided into three groups.

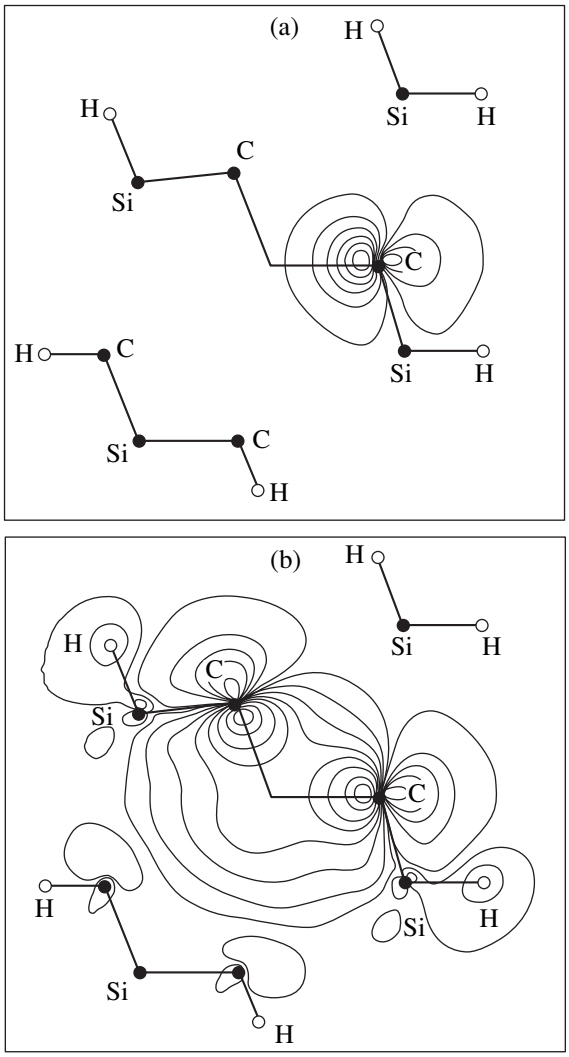

Fig. 3. Density contours for localized orbitals of the V_{Si}^{-} defect in the $C_{16}Si_{18}H_{36}$ cluster in the (110) plane: (a) one of the four α equivalent localized orbitals and (b) the β delocalized orbital.

The first group involves four equivalent one-center orbitals centered on carbon atoms of the first coordination sphere (Fig. 3a). Four α electrons that are not involved in chemical bonds with neighboring atoms and correspond to the concept of dangling bonds are localized on these orbitals.

The second group contains $(N - 2)$ two-center orbitals localized on the neighboring silicon and carbon atoms. The relevant bonds can be considered classical two-electron two-center chemical bonds. However, the spatial parts of the orbitals for the α and β electrons are somewhat different, which gives rise to a low spin density on these orbitals. Nonetheless, the α electrons on

$(N-2)$ two-center orbitals can be treated to be approximately paired with the β electrons.

The third group is represented by one β orbital delocalized over the cluster and transformed according to the A_1 irreducible representation of the T_d group (Fig. 3b).

Therefore, the above choice of the single-electron orbitals provided five unpaired electrons with spatial orbitals that differ drastically from orbitals of the other (paired) electrons. Instead of the expected three unpaired α electrons and $(2N-2)$ paired electrons, we obtained four strongly localized α electrons, one completely delocalized β electron, and $2(N-2)$ virtually paired electrons. In this case, it is incorrect to assert that the measured hyperfine interaction constants can be calculated from the wave function of three unpaired electrons, because the magnitudes and signs of these constants are determined by the spin polarization of the all-electron subsystem. As was noted above, the choice of the single-electron orbitals is not unique. For this reason, these orbitals are mathematical rather than physical objects. However, the many-electron wave function and its related spatial distribution of α and β electron densities have real physical meaning.

6. CONCLUSION

Thus, the equilibrium geometry, spin state, and parameters of hyperfine interaction for a negatively charged silicon vacancy in cubic 3*C*-SiC were calculated in terms of the density-functional theory with the use of a 70-atom cluster. The results of calculations are in good agreement with the experimental data. As follows from the above analysis of the spin density distribution, the simple LCAO model, which is widely applied in experimental works to the interpretation of the hyperfine interaction parameters for deep centers in semiconductors, is inadequate for the V_{Si}^{-} center in SiC and even qualitatively does not describe the real physical situation. This model should be applied with caution to defects in semiconductors, because the spin polarization effects can make a dominant contribution to the observed hyperfine interaction parameters for a number of actual coordination spheres.

REFERENCES

1. S. Ogut, H. Kim, and J. R. Chelikowsky, Phys. Rev. B **56** (18), R11353 (1997).
2. M. J. Puska, S. Poykko, M. Pesola, and R. M. Nieminen, Phys. Rev. B **58** (3), 1318 (1998).
3. P. Lahorte, F. de Proft, F. Callens, *et al.*, J. Phys. Chem. A **103** (50), 11130 (1999).
4. P. J. O'Malley, J. Phys. Chem. A **101** (35), 6334 (1997).
5. J. Isoya, H. Kanda, Y. Uchida, *et al.*, Phys. Rev. B **45** (3), 1436 (1992).
6. T. A. Kennedy, N. D. Wilsey, J. J. Krebs, and G. H. Stauss, Phys. Rev. Lett. **50** (17), 1281 (1983).
7. H. Itoh, N. Hayakawa, I. Nashiyama, and E. Sakuma, J. Appl. Phys. **66** (9), 4529 (1989).
8. T. Wimbauer, B. K. Meyer, A. Hofstaeter, *et al.*, Phys. Rev. B **56** (12), 7384 (1997).
9. L. Torpo, R. M. Nieminen, K. E. Laasonen, and S. Poykko, Appl. Phys. Lett. **74** (2), 221 (1999).
10. M. J. Frisch, G. W. Trucks, H. B. Schlegel, P. M. W. Gill, B. G. Johnson, M. A. Robb, J. R. Cheeseman, T. Keith, G. A. Peterson, J. A. Montgomery, K. Raghavachari, M. A. Al-Laham, V. G. Zakrzewski, J. V. Ortiz, J. B. Foresman, J. Cioslowski, B. B. Stefanov, A. Nanayakkara, M. Challacombe, C. Y. Peng, P. Y. Ayala, W. Chen, M. W. Wong, J. L. Andres, E. S. Replogle, R. Gomperts, R. L. Martin, D. J. Fox, J. S. Binkley, D. J. Defrees, J. Baker, J. P. Stewart, M. Head-Gordon, C. Gonzalez, and J. A. Pople, *Gaussian 94: Revision E1* (Gaussian Inc., Pittsburgh, 1995).
11. A. D. Becke, J. Chem. Phys. **98** (7), 5648 (1993).
12. R. McWeeny and B. T. Sutcliffe, *Methods of Molecular Quantum Mechanics* (Academic, London, 1969).
13. G. D. Watkins, Phys. Rev. **134** (5A), A1359 (1964).
14. A. van Duijn-Arnold, J. Mol, R. Verberk, *et al.*, Phys. Rev. B **60** (23), 15829 (1999).
15. M. Illgner and H. Overhof, Phys. Rev. B **54** (4), 2505 (1996).
16. M. W. Schmidt, K. K. Baldridge, J. A. Boatz, *et al.*, J. Comput. Chem. **14** (11), 1347 (1993).
17. C. Edmiston and K. Ruedenberg, Rev. Mod. Phys. **35** (3), 457 (1963).
18. S. F. Boys, Rev. Mod. Phys. **32** (2), 296 (1960).
19. J. Pipek and P. G. Mezey, J. Chem. Phys. **90** (9), 4916 (1989).

Translated by O. Borovik-Romanova

Physics of the Solid State, Vol. 44, No. 5, 2002, pp. 837–842. Translated from Fizika Tverdogo Tela, Vol. 44, No. 5, 2002, pp. 805–810.

SEMICONDUCTORS AND DIELECTRICS

Hopping Charge-Transfer Mechanism in Quasi-Crystals of Boron and of Its Compounds

O. A. Gudaev and V. K. Malinovskiĭ

Institute of Automation and Electrometry, Siberian Division, Russian Academy of Sciences, pr. Akademika Koptyuga 1, Novosibirsk, 630090 Russia

e-mail: malinovsky@iae.nsk.su

Received June 7, 2001; in final form, August 2, 2001

Abstract—A large array of experimental data on the electrical conductivity of boron and high-boron compounds obtained within a broad temperature range is analyzed. It is shown that there is no need to describe the temperature dependence of the conductivity, as is usually done, by summing numerous exponentials corresponding to different charge-transfer mechanisms from conduction in extended states at high temperatures to hopping between localized states near the Fermi level at low temperatures. The conductivity obeys, within a broad temperature range, either a power law or the inverse Arrhenius relation. The difference is associated with specific structural features of the materials, the depth of the spatial potential relief, and with whether polarons participate in the charge transport or not. A number of compounds exhibit a crossover from the power- to inverse-Arrhenius law dependence with increasing temperature. *© 2002 MAIK "Nauka/Interperiodica".*

1. INTRODUCTION

Physical properties of disordered compounds exhibit a number of specific features compared to single-crystal semiconductors. In optical spectra, this is the Urbach tail. In charge-transfer processes, this is the conduction activation energy, which decreases slowly with decreasing temperature. The smoothness of the $\sigma(T)$ relation permits researchers to draw more than one tangent, whose slope corresponds, by Mott's interpretation [1], to different activation energies and different charge-transfer mechanisms, from conduction in extended states at high temperatures to hopping between localized states near the Fermi level at low temperatures (Fig. 1).

Because of the smoothness of the $\sigma(T)$ curves, the question of how to draw a tangent remains open, which makes calculation of the corresponding activation energies uncertain. At the same time, it is seen from Fig. 1 that when plotted on the inverse Arrhenius scale, the $\sigma(T)$ relation allows linearization over a broad temperature range. The validity and uniqueness of the interpretation put forward in [1] becomes questionable in this case. As shown in [2–4], the conductivity of a number of disordered materials can be described, within a broad temperature range, not by a sum of several exponentials corresponding to different charge-transfer mechanisms but rather by any one relation other than the Arrhenius law.

One more point requiring elucidation is the part played by lattice strain around a carrier in noncrystalline solids. Some researchers have attributed considerable significance to small polarons in charge transfer [1, 5, 6]. At present, there is a wealth of experimental information on transport phenomena in disordered materials. Their interpretation, however, can quite frequently be done both in terms of Mott's model [1] and based on the small-polaron theory [5, 6].

Boron and its compounds represent an interesting subject for use in studying the semiconducting properties of disordered materials [7–9]. Viewed from the crystallographic standpoint, borides are crystals. In their semiconducting properties, they are similar to amorphous materials.

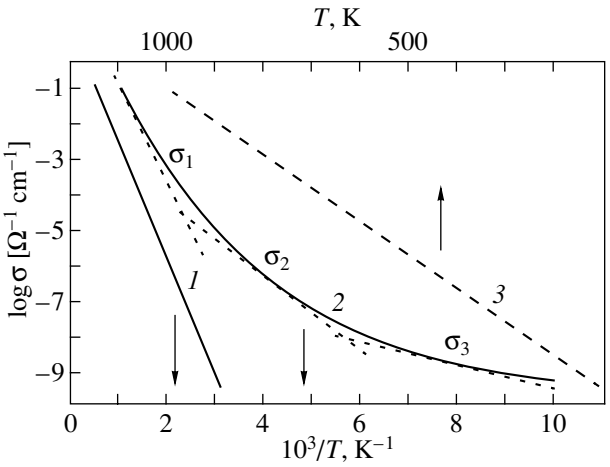

Fig. 1. Typical temperature dependence of conductivity for solids: (*1*) crystal, (*2*, *3*) disordered solids in (*2*) the Arrhenius and (*3*) inverse Arrhenius scaling; σ_1, σ_2, and σ_3 are the conductivities in a band of empty states, in localized band-tail states, and in a localized-state band at the Fermi level, respectively. Arrows specify the horizontal scale.

1063-7834/02/4405-0837$22.00 © 2002 MAIK "Nauka/Interperiodica"

Boron, the fifth element in the Periodic table, has three valence electrons. It forms high-melting compounds ($T_{melt} > 2500$ K), thus permitting one to study their semiconducting properties up to extremely high temperatures. The lattice of boron and of borides is made up of B_{12} icosahedra. Two of the B valence electrons provide intraicosahedral bonding. The third valence electron accounts for the strong covalent bonds in the crystal. In more complex compounds, conglomerates of icosahedra $B_{12}(B_6)_{12}$ and $B_{12}(B_{12})_{12}$ act as building blocks. The number of atoms N in the unit cell varies in the boron and boride series from 12 to 1600. As N increases, atoms can form groups with different coordination numbers. Note also the looseness of the structure of boron and of the borides, i.e., a large number of crystallographic voids in the structure. The space filling for β-B, for instance, is ~36%.

The rhombohedral α boron ($N = 12$), the simplest substance in crystallographic structure in the boride series, is the closest to crystals in its physical properties. However, as N increases, some of the properties of borides approach those of amorphous semiconductors. This is evident from an analysis of IR absorption spectra [10]. Disorder in complex compounds increases through statistical distribution of boron vacancies, interstitial boron, and boron atoms with different coordination numbers, as well as because of a change in short-range order parameters, i.e., in this particular case, of bond lengths in a unit cell.

The so-called "boron impurity in boron" [8] plays a fundamental part in the density-of-states distribution in boron and its compounds. These are boron atoms differing from others in their coordination number. For instance, in β-B, the boron coordination number is six. However, ~13% of the atoms have coordination numbers equal to eight and nine. This gives rise to the formation of a band of localized states ~0.5 eV distant from the valence-band edge (the band gap ~1.4 eV). The Fermi level is pinned at this band. The density of states at the Fermi level is $g(E_F) \approx 10^{19}$–10^{20} eV^{-1} cm^{-3}.

According to present-day concepts [8], conduction in β-B is governed at low temperatures by electrons hopping near the Fermi level. At very low T, variable-range hopping provides a large contribution (Mott's law). At higher temperatures, charge transfer via localized states in the valence-band tail becomes dominant. At still higher T, conduction occurs in extended valence-band states. In metal borides, polaron effects may become significant in conduction. A small-polaron (bipolaron) model has been developed for boron carbide [5, 6].

It thus follows that boron and its compounds are a suitable subject for testing various models of charge transfer in disordered materials, experimental determination of the functional dependence $\sigma(T)$ over a broad temperature range (in some cases, more than one thousand kelvins in width), and learning the role played by polaron effects in charge transfer.

As already mentioned, it has been shown for a group of disordered materials that conductivity lends itself to description over a broad temperature range by any one law except the Arrhenius law. This means that charge transfer in noncrystalline materials can be treated in a frame that would not invoke several activation processes with different activation energies. Models have been proposed for conduction both in the absence of polaron effects and in the case where they are involved. These models describe the experimentally observed relations for $\sigma(T)$ [2–4] and yield the following results.

If the material conductivity is due to electrons hopping from one state to another in a one-phonon process, the transition probability scales with temperature as [1]

$$w \sim \omega \exp(-\omega/kT), \tag{1}$$

where ω is the phonon frequency. In this case, the conductivity σ is described by the inverse Arrhenius law [2–4]:

$$\sigma = \sigma_0 \exp(T/\alpha^{-1}T_0), \tag{2}$$

where α^{-1} and T_0 are parameters, $\alpha \geq 1$, and T_0 determines the density-of-states decay in the exponential region. Such a mechanism is characteristic of nonpolar materials in the case where the polaron effects are insignificant.

In the case of polar materials, where many-phonon polaron transitions from one state to another are dominant, the transition probability at moderately high temperatures scales with temperature as [1]

$$w \sim [kT/\hbar\omega]^n, \tag{3}$$

where n is the number of phonons involved. Now, the conductivity depends on temperature by the law [3, 4]

$$\sigma = \sigma_0 T^n. \tag{4}$$

We will use the concepts developed earlier [2–4] to analyze a large array of experimental data as to the conductivity of boron and its compounds. The results of this analysis suggest some conclusions on the mechanism of charge transfer in these materials, as well as identify manifestations of the polaron conductivity in them.

2. EXPERIMENTAL

The rhombohedral β boron ($N = 105$, $Eg = 1.4$ eV) is the most well studied of the four B crystallographic modifications [7, 8]. Figure 2a displays the temperature dependence of conductivity of β-B measured on several samples. In the range 100–1100 K, it is seen to follow the inverse Arrhenius law closely. In some samples, the conductivity varies over six to seven orders of magnitude. The parameter $\alpha^{-1}T_0$ varies from 20 to 40 K for different samples (depending on the technology of

preparation used). According to published data [7, 8], polaron effects should not operate in β-B.

Metal atoms enter β-B-based interstitial solid solutions as a doping impurity in B voids. Figure 2b plots the conductivity of the β-B : Si and β-B : Mn interstitial solid solutions (impurity content 1–2 at. %). The temperature dependence of the β-B solid-solution conductivity is described well by the inverse Arrhenius law ($\alpha^{-1}T_0$ = 35–40 K).

The situation is different for boron compounds with metals. The B content in this case is, as a rule, ≥90%. In contrast to the β-B and its solid solutions, high-boron compounds exhibit polaron properties. $B_{14}Si$, $B_{22}Mn$, and $B_{24}Cu$ (N = 105) are structural analogs of β-B. In contrast to the β-B : Si and β-B : Mn solid solutions, the temperature dependence of the $B_{14}Si$ and $B_{22}Mn$ compounds follows a power law $\sigma \sim T^n$ (Fig. 3). The value of the parameter n depends on the technology of sample preparation.

IR absorption in borides [10] clearly exhibits a tendency to spectral modification, more specifically, from spectra characteristic of boride crystals with a small N to those typical of the amorphous state of borides with a large N (~1600). No such distinct relationship is observed, however, in the conductivity of borides. Figure 4 plots the temperature dependences of the conductivity for α-AlB_{12} and (Be, Al)B_{12} for which N = 200 and for β-AlB_{12} for which N = 50. In all these cases, the conductivity scales well as $\sigma \sim T^n$ and has comparable values.

Amorphous boron (*a*-B), both in the form of films and in bulk samples, has been recently attracting considerable interest [14, 15]. This interest is connected with the problem of thin nanostructured amorphous semiconducting films, i.e., amorphous films which contain inclusions of nanocrystallites or nanoclusters 1 nm in size distributed in an amorphous host. Amorphous boron is different in that it always contains nanoinclusions from B_{12} icosahedra d = 0.51 nm in diameter to $B_{12}(B_{12})_{12}$ structural blocks with d = 2.3 nm. Figure 5 shows the temperature dependences of the conductivity for amorphous boron. Unlike crystalline β-B, the conductivity of *a*-B follows a power-law relation.

Compounds of the MB_{66} type (N = 1600) are frequently compared with amorphous boron in terms of their physical properties [7, 8]. The structure of these compounds is the most complex of the materials considered here. Figure 5 presents the temperature dependence of the conductivity of YB_{66}. It indeed behaves similar to that of *a*-B. However, the $\sigma(T)$ relation for YB_{66} does not differ qualitatively in behavior from that of other borides with N = 50, 105, and 200.

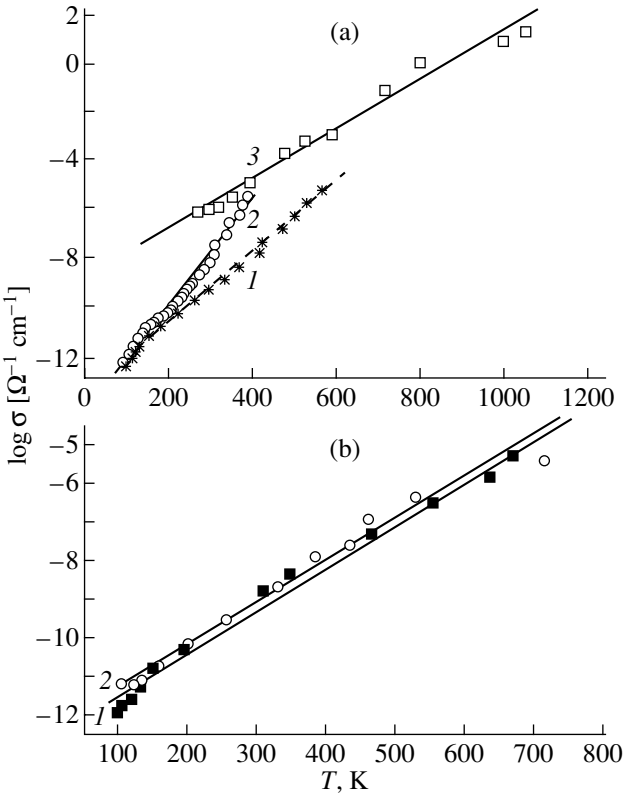

Fig. 2. (a) Temperature dependences of the conductivity of rhombohedral single-crystal β boron. $\alpha^{-1}T_0$ (K): (*1*) 32 [11], (*2*) 20 [12], and (*3*) 43 [7]. (b) Temperature dependences of the conductivity of solid solutions: (*1*) β-B : Mn ($\alpha^{-1}T_0$ = 36 K) and (*2*) β-B : Si ($\alpha^{-1}T_0$ = 36 K) [11].

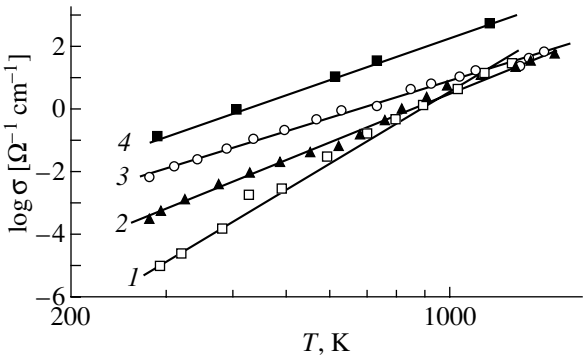

Fig. 3. Temperature dependences of the conductivity of boron compounds (*1*, *4*) $B_{14}Si$ [13], (*2*) CuB_{24} [7], and (*3*) MnB_{22} [7]. The values of n are (*1*) 10, (*2*) 7, (*3*) 5, and (*4*) 6.

3. DISCUSSION

Boron and its compounds are heavily defective crystals. This accounts for the high density of states at the Fermi level and in the band tails (of the order of 10^{19}–10^{20} eV^{-1} cm^{-3}). Therefore, the electronic properties of these compounds resemble those of amorphous materials very closely. In particular, the temperature depen-

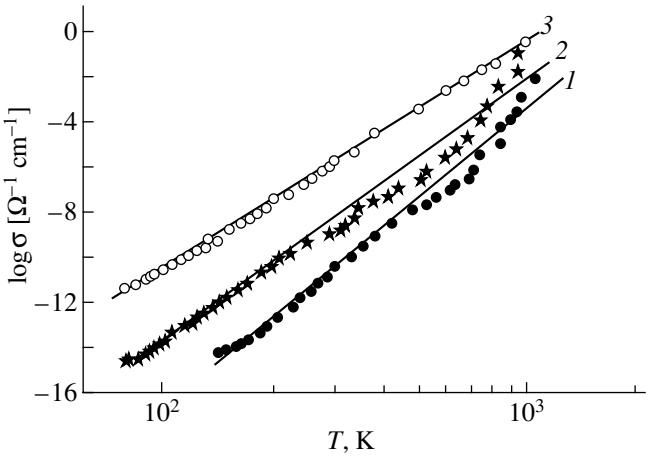

Fig. 4. Temperature dependences of the conductivity of boron compounds (*1*) $(Be_{0.1}Al_{0.9})B_{12}$, (*2*) β-AlB_{12}, and (*3*) α-AlB_{12} [12]. The values of *n* are (*1*) 12 and (*2*, *3*) 10.

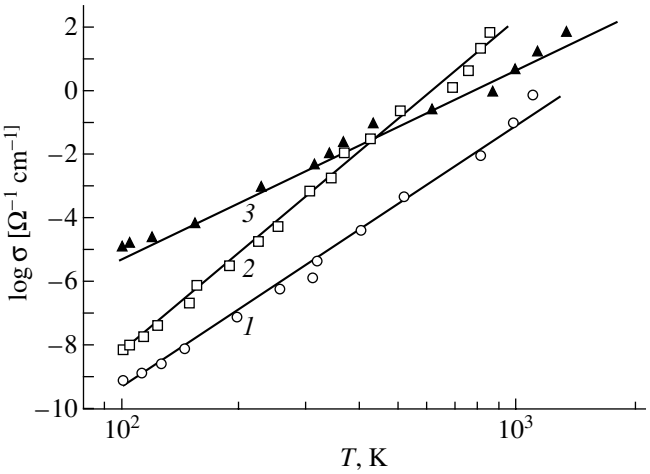

Fig. 5. Temperature dependences of the conductivity: (*1*) bulk *a*-B sample [15], (*2*) *a*-B film [15], and (*3*) YB_{66} crystal [15]. The values of *n* are (*1*) 8, (*2*) 11, and (*3*) 6.

dence of the conductivity of β-B crystals plotted in the Arrhenius coordinates ($\log\sigma \sim 1/T$) differs very little from that of amorphous boron. In both cases, it is a curve with an activation energy varying smoothly with temperature. The temperature dependences of conductivity of all B compounds (with *N* from 50 to 1600) behave similarly. As follows from these data, when experimental results are plotted in the standard Arrhenius coordinates, it is difficult to see whether they have features inherent to charge-transfer mechanisms in boron and its compounds or not. The method employed by us, namely, plotting experimental curves in inverse Arrhenius coordinates, permitted us to establish that the conductivity of crystals of β-B and its solid solutions has a radically different nature than that of *a*-B and the metal borides. At the same time, it was found that the number of atoms in the unit cell of borides is not a crucial factor in the mechanism of conductivity.

Following the concepts developed in [2–4], conductivity of the type $\sigma \sim \exp(T/\alpha^{-1}T_0)$ is characteristic of materials in which polaron effects do not occur and charge transfer is realized through electrons hopping from one state to another in a one-phonon process. By contrast, a temperature dependence of the form $\sigma \sim T^n$ is typical of polaron conduction wherein polaron transitions between states involve a many-phonon process.

The polaron is a conduction electron (or hole) moving slowly in a polar crystal. The electron polarizes and, thus, distorts the ionic lattice in its vicinity. The potential well created by the electron in the polar material can be written as $U_p(r) = e^2/\varepsilon_p r$, where *r* is the distance and ε_p is given by the difference between the high-frequency ε_∞ and static ε dielectric permittivities: $\varepsilon_p^{-1} = \varepsilon_\infty^{-1} - \varepsilon^{-1}$. Hence, the manifestation of polaron effects should be expected in materials with ionic or partially ionic bonding, because the electron–phonon coupling in them is substantially higher than that in covalent crystals [16]. The β-B crystal has covalent bonds, and it does not reveal polaron effects in its conductivity. By contrast, in metal borides, one may expect to see polaron conduction. Polaron conduction occurs in the cases where, for the electron drift velocity and the electron–phonon coupling characteristic of the material, the dielectric relaxation time of ions in the field of an electron is long enough for a structural rearrangement to take place around the electron.

The interstitial solid solutions of β-B with Mn and Si and B compounds with Mn and Si are structural analogs. An analysis of the temperature dependences of the conductivity suggests, however, that charge transfer in boron and its solid solutions occurs by one-phonon electron hopping from one state to another, whereas in the Mn and Si borides, it involves many-phonon polaron hopping. The polaron charge-transfer mechanism turns out to be typical of all metal borides (with *N* from 50 to 1600).

Polaron conduction is also found to be typical of *a*-B. The possibility of small-polaron formation in noncrystalline materials has been considered by a number of authors, in particular, by Emin [17]. The probability of formation of such polarons in a disordered system was shown to increase considerably compared with that in the crystalline state. If a carrier resides near an atomic site long enough to allow displacement of neighboring atoms, a potential well may form and will trap the carrier. The experiments made on β-B crystals and amorphous boron are in agreement with these conclusions. In contrast to the crystalline material, amorphous boron exhibits polaron properties.

It appears crucial to analyze the behavior of conductivity in materials with polaron conduction at high *T*, where one may expect a transition from the power-law

to the inverse Arrhenius relation. It is in the high-melting borides that one may expect this transition to occur. Figure 6 displays the temperature dependence of the conductivity of FeB_{28} in the high-temperature domain. For $T > 400$ K, it follows the inverse Arrhenius relation ($\alpha^{-1}T_0 = 300$ K); i.e., for $T > \alpha^{-1}T_0$, as expected, the conductivity scales as $\sigma = \sigma_0 \exp(T/\alpha^{-1}T_0)$. For lower T, the power law becomes dominant. The $\sigma(T)$ behavior for $FeB_{29.5}$ (an analog of FeB_{28}) was studied in considerable detail in [7, 18]. An analysis of the experimental data reveals that for temperatures $T < \alpha^{-1}T_0$, the temperature dependence of the conductivity is described by a power law with $n \sim 3$.

Figure 6 also presents the temperature dependence of the conductivity of $MgAlB_{14}$ measured in the high-temperature domain. As in the case of FeB_{28}, the conductivity follows the inverse Arrhenius relation for $T > \alpha^{-1}T_0$ ($\alpha^{-1}T_0 \approx 600$ K). Below $\alpha^{-1}T_0$, the $\sigma(T)$ relation deviates from the inverse Arrhenius law. The small number of experimental points available does not permit one to determine the exponent n accurately.

Disorder in a material gives rise to strong fluctuations of the band edge potentials. Density-of-states tails appear as a result of averaging over all possible potential-well configurations. The T_0 parameter, which determines the exponential decay of the density of states, characterizes the effective potential-well depth. For β-B, the parameter $\alpha^{-1}T_0$ is small, 20–40 K. This corresponds to a well depth of a few millielectronvolts. The more structurally perfect a β-B crystal, the smaller the parameter $\alpha^{-1}T_0$.

Polaron wells may have different depths. In some cases, two to five phonons are enough for a carrier to hop, while in others, this number has to be of the order of ten.

In all substances that do not feature polaron effects, the $\alpha^{-1}T_0$ parameter is, as a rule, less than 100 K. As for the polaron wells, they are substantially deeper. As a result, in materials with polaron conduction (FeB_{28}, $FeB_{29.5}$, $MgAlB_{14}$), the inverse Arrhenius law starts to operate only at very high temperatures. According to Mott [1], the polaron transition probability from one state to another at such temperatures is described by an exponential $\exp(-\varepsilon/kT)$.

The parameter $\alpha^{-1}T_0$ can be used to estimate the polaron well depth:

$$U_p = 2z\hbar^2/(m_p a^2). \quad (5)$$

Here, z is the coordination number ($z \sim 6$), m_p is the effective polaron mass, and a is the distance between localized states ($a = 10$ Å).

For $MgAlB_{14}$, we have $U_p = 60$ meV, and for FeB_{28}, $U_p = 30$ meV (to within the magnitude of α, $\alpha \geq 1$). The effective mass of the polaron involved in charge transfer is $m_p = 13m_e$ for $MgAlB_{14}$ (to within α) and $m_p = 6m_e$ for FeB_{28}.

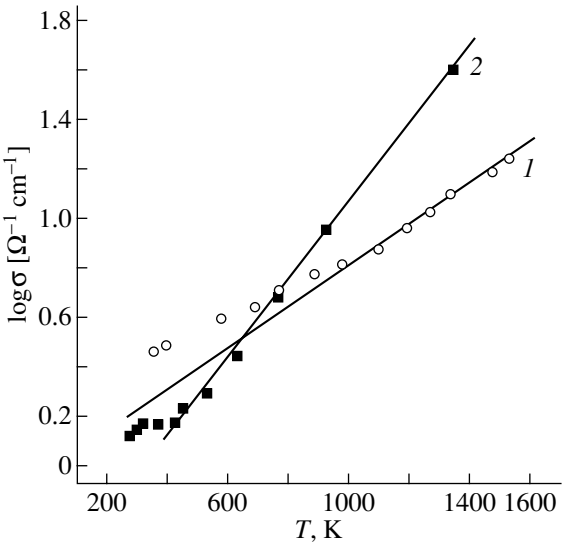

Fig. 6. Temperature dependences of the conductivity: (*1*) $MgAlB_{14}$ (600 K) and (*2*) FeB_{28} (300 K) [7].

4. CONCLUSIONS

The above analysis of experimental data on the temperature dependence of conductivity carried out for a large number of boron compounds has shown that there is no need to describe this dependence by summing numerous exponentials corresponding to different transfer mechanisms. Studied over a broad temperature range, the conductivity obeys either a power-law or the inverse Arrhenius relation. This is associated with the specific structural features of the material involved, the depth of the spatial potential relief, and with whether polarons are involved in charge transfer or not. In the case where electron hopping occurs between shallow potential wells in single-phonon transitions, the conductivity is described by the inverse Arrhenius relation. If self-trapping produces deep potential wells, many-phonon polaron transitions between states become dominant and the conductivity scales with temperature as a power law. When the temperature is increased (above $\alpha^{-1}T_0$), the probability of hopping between deep wells in such materials is described by the formula typical of a one-phonon process and the power law for the conductivity crosses over to the inverse Arrhenius relation.

Thus, the temperature dependence of conductivity permits one to establish the degree of disorder in a material, the role played by polaron effects in charge transfer, the polaron well depth, and the effective polaron mass. It becomes possible to interpret, within a common frame, the behavior of the temperature dependence of conductivity for a large group of materials, its

power-law or inverse Arrhenius scaling, and the crossover from one relation to another at $T \sim \alpha^{-1}T_0$.

ACKNOWLEDGMENTS

This study was supported by the Russian Foundation for Basic Research (project no. 99-02-16697).

REFERENCES

1. N. F. Mott and E. A. Davis, *Electronic Processes in Non-Crystalline Materials* (Clarendon, Oxford, 1979; Mir, Moscow, 1982), Vols. 1, 2.
2. O. A. Gudaev and V. K. Malinovskiĭ, Fiz. Tverd. Tela (St. Petersburg) **37** (1), 81 (1995) [Phys. Solid State **37**, 41 (1995)].
3. O. A. Gudaev and V. K. Malinovskiĭ, Fiz. Tverd. Tela (St. Petersburg) **34** (2), 548 (1992) [Sov. Phys. Solid State **34**, 293 (1992)].
4. O. A. Gudaev and V. K. Malinovskiĭ, Fiz. Khim. Stekla **26** (4), 522 (2000).
5. D. Emin, G. Samara, and L. Azevedo, J. Less-Common Met. **117**, 415 (1986).
6. C. Wood and D. Emin, Phys. Rev. B **29** (8), 4582 (1984).
7. O. A. Golikova, Phys. Status Solidi A **101**, 277 (1987).
8. O. A. Golikova, Usp. Fiz. Nauk **158** (4), 581 (1989) [Sov. Phys. Usp. **32**, 665 (1989)].
9. D. Emin, Phys. Today **40** (1), 55 (1987).
10. O. A. Golikova, Fiz. Tverd. Tela (Leningrad) **29** (9), 2869 (1987) [Sov. Phys. Solid State **29**, 1652 (1987)].
11. O. A. Golikova, N. Amandzhanov, and A. A. Tadzhiev, Izv. Akad. Nauk UzSSR, Ser. Fiz.-Mat. Nauk, No. 1, 85 (1989).
12. O. A. Golikova and S. Samatov, *Boron and Its Semiconductor Compounds* (Fan, Tashkent, 1988).
13. J. M. Dusseau, T. P. Lepetre, J. L. Robert, and B. Pistoulet, J. Less-Common Met. **47**, 135 (1976).
14. O. A. Golikova, Fiz. Tekh. Poluprovodn. (St. Petersburg) **26** (9), 1604 (1992) [Sov. Phys. Semicond. **26**, 900 (1992)].
15. O. A. Golikova, Fiz. Tekh. Poluprovodn. (St. Petersburg) **34** (3), 369 (2000) [Semiconductors **34**, 363 (2000)].
16. C. Kittel, *Introduction to Solid State Physics* (Wiley, New York, 1976; Nauka, Moscow, 1978).
17. *Amorphous Semiconductors*, Ed. by M. Brodsky (Springer-Verlag, Berlin, 1979; Mir, Moscow, 1982).
18. H. Werheit, K. De Groot, and W. Malkemper, J. Less-Common Met. **82**, 163 (1981).

Translated by G. Skrebtsov

Physics of the Solid State, Vol. 44, No. 5, 2002, pp. 843–851. Translated from Fizika Tverdogo Tela, Vol. 44, No. 5, 2002, pp. 811–819.

SEMICONDUCTORS AND DIELECTRICS

Quantum Discreteness Effects and Flicker Fluctuations in Tunneling Conductivity

Yu. E. Kuzovlev*, Yu. V. Medvedev*, and A. M. Grishin**

**Donetsk Physicotechnical Institute, National Academy of Sciences of Ukraine, Donetsk, Ukraine*
e-mail: medvedev@kinetic.ac.donetsk.ua
***Royal Institute of Technology, Stockholm, Sweden*

Received September 13, 2001

Abstract—An analysis of events in the tunneling junction shows that the interaction of one-electron processes in a many-electron system may be a source of scale-invariant low-frequency fluctuations of conductivity (the interaction consists in that the quantum probability of an electron transition depends on fast random changes in the environment in the course of the transition, including the changes caused by analogous transitions). The theory relates flicker fluctuations in the tunneling conductivity to the discrete character of the spectrum of electron states and explains the nonlinearity of the noise–current characteristic observed in nanocomposites. © *2002 MAIK "Nauka/Interperiodica".*

1. INTRODUCTION

Low-frequency flicker noise (noise with a $1/f$ spectrum), observed in a large variety of structures [1–5], is an important problem for both applied and theoretical physics. A special feature of this noise is that it represents fluctuations in the rates of transport and relaxation processes. In electronics, these are primarily the conductivity fluctuations, which are difficult to remove by frequency filtration (or by smoothening in time). As a rule, these fluctuations are much more sensitive with respect to the material structure and the external factors than is the conductivity itself. Therefore, once an adequate theory is created, such fluctuations would provide additional information about the charge transfer mechanisms.

At present, flicker noise is usually related to a large time scale, for example, to slow (rare) thermoactivated fluctuations in the structural disorder, occupation of electron traps, etc. [1, 3, 5–17]. The $1/f$ spectrum is interpreted as a superposition of Lorentzians corresponding to "fluctuators" with various lifetimes, assuming that there is a rather broad and homogeneous distribution of their activation energies [1]. However, such a theory fails to explain some factors, including the $1/f$ fluctuations of the band mobility of carriers in intrinsic semiconductors [2, 18] or the $1/f$ noise in liquid metals [4]. In recent years, extensive investigations have been devoted to noise in the systems with nonmetallic (narrow-band, hopping, tunneling, percolation) conductivity, representing heavily doped and amorphous semiconductors [8, 10–14], defect metal films [5, 9], oxides [7] (including manganites featuring the giant magnetoresistance effect [19–21]), etc. An important part in such systems belongs to the long-range Coulomb interactions, while the role of a slow fluctuator can be performed by charge redistribution in the "Coulomb glass" [6, 8, 14]. However, particular estimates are indicative of a low-frequency saturation of the $1/f$ noise spectrum [13], in discrepancy with the experiment. Apparently, the forecast of Tandon and Bilger [22] that reducing the $1/f$ noise to Lorentzians will be a drawback of the theory comes true.

At all importance of fluctuations of the activation type and of the other "slow" fluctuations, the fundamental $1/f$ noise is worth special attention. This noise originates directly from the "fast" kinetic events (collisions and interactions between particles or between quasi-particles and quanta) responsible for the electric resistance [4, 23–27]. It should be recalled that the phenomena of relaxation and irreversibility in any dynamic system are related essentially to its ability to "forget" the prehistory. Loosing memory of the number and type of kinetic events in the past, the system is incapable of maintaining the "average number (probability) of events per unit time" (more precisely, only a proportion of the events mutually inverse in time is controlled, rather than the difference or sum of such events [23, 26, 27]). In such a case, the probable fluctuations in the number of events (as well as the most probable number of these events) increase in proportion to the time of observation and, hence, no definite time-average number of events exists. In other words, if the fluctuations in the current "number of kinetic events per unit time" (or the "rate of events" in terms of [28]) produce no feedback reaction, then such fluctuations exhibit no relaxation and, hence, possess no characteristic (upper) time scale. This behavior evolves precisely into the scale-invariant $1/f$ spectrum (for more details, see [4, 23, 27]). As a (quite paradoxical) result, the long-lived correlations corresponding to the $1/f$ spectrum reflect

forgetfulness of the system rather than memory of its prehistory (Krylov [28] emphasized that not every statistical correlation reflects causal relationships).

The kinetic theory misses the $1/f$ noise of this nature by postulating strictly determined "probabilities per unit time" (collisional integrals). On the contrary, the gas kinetics constructed on the statistical mechanics without this simplification [24, 27] reveals the $1/f$ fluctuations in the diffusion rate and in the molecular mobilities. These fluctuations are caused by the fact that the system is insensitive to a random distribution of the past collisions of any molecule over the impact parameter (i.e., to the real collision cross section of this molecule) rather than by large relaxation times (absent in the system). The flicker fluctuations of dissipation and light scattering observed in quartz can also be explained as an intrinsic statistical property of the system kinetics (in this case, of the phonon system) [25]. This kinetics cannot be reduced to certain three- or four-particle collisional integrals because the "elementary" kinetic events (decay, merging, and scattering of phonons) are intermixed in time and parametrically mutually influence one another.

Below, we will demonstrate that the "$1/f$ noise due to the loss of memory" in the quantum kinetics of many-electron systems (as well as in the phonon systems) can arise from intermixing of the kinetic events representing electron transitions. The flicker fluctuations of conductivity in such systems are manifested, provided that the real duration of the events and the real quantum discreteness of the energy states of electron are not ignored.

With allowance for the finite duration, every one-electron transition appears as the fragment of a many-body process. Separating this fragment using boson lines, we may consider the quantum amplitude of the transition as formed under the action of effective variable fields reflecting other components of the process. For example, the accomplished electron transitions through a tunneling junction, together with the thermal motion of charges inside the junction sides (banks), induce fast voltage fluctuations across the junctions. The latter fluctuations randomly shift the phases of increments of the quantum amplitude of the forthcoming transition. This mutual influence of one-electron events involving numerous soft photons was studied in the theory of Coulomb blocking and low-temperature anomalies in the current–voltage characteristics of small tunneling junctions [29–31] (a mathematically analogous problem with phonons instead of photons was encountered in the theory of mobility of a tightly bound polaron [32]).

Apparently, this may result both in renormalization of the transport characteristics and in the appearance of specific fluctuations in these characteristics. Since the quantum probabilities of "elementary" electron transitions considered as functionals of the whole system noise (including fluctuations of the electric, magnetic, exchange, and elastic fields) are random, the conductivity of this system is also random. To our knowledge, this effect has never been studied before. It must be well pronounced, provided that the noise correlation time is small as compared to the duration (expectation time) of a typical transition. This situation is natural, in particular, for the tunneling conductivity. Using this example, we will demonstrate how the fast noise becomes a source of low-frequency flicker fluctuations in the conductivity (probably, an additional source of such fluctuations in the case of hopping conductivity is the fast fluctuations of the Coulomb potential induced by local charge redistribution).

For illustrative purposes, we concentrate on the ideal tunneling junction. It should be emphasized that, originating from the thermal noise, the effect under consideration principally differs from the reproducible fluctuations of conductivity caused by a static disorder in the junction [33] observed at low temperatures [34]. As for the $1/f$ noise in real tunneling junctions [16, 35], this process is usually attributed to the structural fluctuators representing two-level systems. The possibilities of the corresponding theory were analyzed in detail by Gal'perin *et al.* [15]. Note also that the interest of researchers in the role played by discreteness of the electron states in tunneling junctions and the many-body processes in these systems has a long history (see, e.g., [36, 37] and references therein).

2. CHARACTERISTIC TUNNELING TIMES

When a small voltage $U < T/e$ (T is the temperature) is applied to a tunneling junction, the average amount of charge transferred over the time interval Δt and the corresponding conductivity can be expressed as follows:

$$\Delta Q = e\frac{Ue}{\delta E}\frac{\Delta t}{\tau_t}, \quad G = \frac{\Delta Q}{U\Delta t} = e^2\nu\gamma, \qquad \nu = \frac{1}{\delta E}, \quad \gamma = \frac{1}{\tau_t}. \tag{1}$$

Here, δE is the average distance between the electron energy levels on the two sides, ν is the density of states, $Ue/\delta E$ is the effective number of "active" levels "loaded" by the charge transport, and τ_t is the average time required for the electron transition from a given level on one boundary to the opposite boundary (more strictly speaking, τ_t is the time of accumulating the quantum probability of a jump on the order of unity, so that the inverse quantity γ plays the role of the jump probability per unit time).

A real tunneling junction is always characterized by a finite capacitance C and a characteristic time $\tau = RC \equiv C/G$. Analogous to the relaxation time of a usual RC chain, this is the correlation time of the thermal fluctuations of charge in the junction (if the Coulomb interaction between the junction sides is manifested in a sto-

chastic form). Let us compare the time scales introduced above:

$$\frac{\tau_t}{\tau_c} = \frac{e^2\nu}{C} = \frac{E_c}{\delta E}. \quad (2)$$

Here, E_c is a characteristic Coulomb energy and, hence, the ratio (2) is merely the number of levels involved in the charge relaxation.

Now, we will demonstrate that tunneling is a slow process, such that

$$\tau_t/\tau_c \gg 1, \quad (3)$$

even if the Coulomb effects are weak in the trivial sense ($E_c \ll T$). For certainty, we consider the case of flat sides with thickness w confining a flat barrier with thickness d and a typical dielectric constant $\epsilon \sim 20$. Using the formula for C of a flat capacitor and the well-known expressions for the electron density of states and the Fermi energy and velocity in a standard metal, we obtain

$$e^2\nu/C \approx \frac{e^2}{\hbar v_F}\frac{4\pi dw}{\epsilon a^2} \approx \frac{dw}{a^2},$$

where a is a characteristic atomic size (on the order of three Ångströms). This result clearly indicates that inequality (3) is always valid and, in this sense, the Coulomb effects are always strong. Therefore, a tunneling electron experiences numerous variations of the voltage $u(t)$ across the junction (fluctuating under the action of other transitions of electrons in both directions).

In terms of a one-electron process, this result implies that the quantum-mechanical probabilities of transitions are random values. From the standpoint of a strict many-body theory, a description of the corresponding excess contribution to the transport current fluctuations would require using at least four-particle Green's functions (determined at four different time instants and not admitting approximate separation into two-particle functions [4]). Since the necessary formalism is not yet developed, we will attempt to formulate the problems in simple terms of a tunneling Hamiltonian and quantum-mechanical nonstationary perturbation theory. We will employ the simplest model, according to which all the tunneling matrix elements are approximately equal: $g_{kq} \approx g$.

We consider the standard tunneling Hamiltonian approximation, initially assuming $u = 0$. Let $p_{kq}(\Delta t, U)$ be the probability of the electron transition from state k on one (left) boundary to state q on the other (right) boundary (or of the reverse transition) during the time interval t. The total probability of jumping left to right from state k is given by a sum of probabilities over q, while the jump duration, in its physical sense, is inverse to the probability of jumping per unit time:

$$\gamma = \tau_t^{-1} = p_k(\Delta t, U)/\Delta t,$$

$$p_k(\Delta t, U) \equiv \sum_q p_{kq}(\Delta t, U)$$

(it will be assumed that these values weakly depend on k). Now, we will employ (which is a usual practice in constructing a kinetic theory) the Fermi golden rule

$$p_{kq}(\Delta t, U) \longrightarrow 2\pi g_{kq}^2 \delta(E_{kq})\Delta t/\hbar,$$

$$E_{kq} \equiv E_q^+ - E_k + eU$$

(where the plus sign refers to the right boundary). This rule provides for the linear increase in the jump probability with time, thus stipulating a certain rate (frequency) of jumps:

$$\gamma = \tau_t^{-1} \approx 2\pi g^2 \nu/\hbar. \quad (4)$$

Application of the golden rule (i.e., the continuum approximation) implies that the time of observation of the evolution of quantum amplitudes (sufficient for an adequate evaluation of the probabilities) falls within the interval $\hbar/T \ll \Delta t \ll \tau_g$, where $\tau_g = 2\pi\hbar/\delta E$ is a characteristic time determined by the discreteness of the energy spectrum. Obviously, the adequate observation time interval necessary for properly taking into account the noise $u(t)$ must be much longer than the noise correlation time; with allowance for condition (3), it is desired that the observation time be comparable to a typical jump duration. Therefore, a standard scheme would have to obey the condition $\tau_g > \tau_t$. However, formulas (1) and (4) yield the relation

$$\frac{\tau_t}{\tau_g} = \frac{R}{R_0} \approx \left(\frac{\delta E}{2\pi g}\right)^2, \quad R_0 = \frac{2\pi\hbar}{e^2}, \quad (5)$$

which indicates that a low-transparent junction features just the opposite situation:

$$\tau_t/\tau_g \gg 1. \quad (6)$$

The physical meaning of this inequality is that the broadening of levels caused by the barrier transparency is small compared to the distance between levels. Thus, in the case of a well-pronounced discreteness, the golden rule is inapplicable and the analysis encounters the problem that the "probabilities of transition per unit time" are undetermined.

We will address the situation in (6), which is essentially the most interesting case, the more so since the method of the tunneling Hamiltonian for $R < R_0$ is formally incompatible with the perturbation theory [38] (unless the contact with $R < R_0$ is equivalent to a parallel connection of autonomous high-ohmic [in the sense of (6)] junctions). Under condition (6), the perturbation theory is undoubtedly applicable, including the case with the voltage noise $u(t)$. This noise, making the transitions inelastic, restores the linear growth of the prob-

ability with time. However, the noise will also render a probability fluctuating with increasing amplitude in proportion to the time of observation.

3. PROBABILITY FLUCTUATIONS

Let us consider the quantum transitions under the action of a variable potential difference $u(t)$ between terminal points. According to the modern theory of quantum chaos, stochastic behavior is typical of quantum systems despite the discreteness of the energy spectrum [39, 40]. In this context, we will interpret $u(t)$ as a classical random process (in strict theory, $u(t)$ is an operator intermixed with the operators of particles). For $\Delta t \sim \tau_t$, it will be sufficient to find an approximate (in terms of the perturbation theory) solution to the Schrödinger equation for the electron wave function. The result can be written as

$$p_{kq} \approx |A_{kq}|^2, \quad A_{kq} \equiv \frac{g_{kq}}{\hbar}\int_0^{\Delta t} \exp(iE_{kq}t/\hbar)Z(t)dt,$$
$$Z(t) = \exp[i\varphi(t)], \quad \varphi(t) = \frac{e}{\hbar}\int_0^t u(t')dt', \tag{7}$$

where $\varphi(t)$ is a diffusively accumulated random phase gain. For $u(t) = 0$, formulas (7) can be reduced to the usual expressions for the probabilities of transitions; otherwise, these formulas describe a chaotic parametric excitation or quenching of the probabilities by the phase breakdown.

Let us introduce a phase correlation function, the corresponding time of coherence of the quantum amplitudes, and the energy equivalent:

$$K(t_1 - t_2) = \langle Z(t_1)Z^*(t_2)\rangle,$$
$$\tau_{coh} = \int_0^\infty |K(\tau)|d\tau, \quad \Delta E = 2\pi\hbar/\tau_{coh}, \tag{8}$$

where the angle brackets denote averaging over $u(t)$. Generally speaking, the multiplicative character of noise $Z(t)$ implies that the calculation of even elementary statistical characteristics of the solution would require extensive information concerning the $u(t)$ statistics. However, for the coherence time that is much smaller than the observation time, the factor $Z(t)$ in the integrand of (7) behaves as complex white noise. Then, the transition amplitudes A_{kq} behave for the most part as (complex) Brownian trajectories and, hence, knowledge of characteristics (8) is quite sufficient.

Now, let us consider the coherence time, assuming for simplicity that the shunting effect of an external chain upon the τ_c is insignificant. Note that $K(t)$ is a characteristic function (in the sense of the probability theory) of the random phase gain. This function can be readily determined (e.g., for $E_c \ll T$) by considering the voltage noise as a Gaussian random process. This yields $\tau_{coh} \sim (\hbar/e)(C/T)^{1/2} \ll \tau_g$. This estimate probably gives a minimum possible value of τ_{coh}. For $E_c > T$, it would be more reasonable to employ a statistical model in which the charge of the capacitor varies by discrete portions and, accordingly, the process $u(t)$ takes values that are multiples of e/C. In this case, the calculation of $K(t)$ with allowance for (6) yields an estimate $\tau_{coh} \sim \tau_c$; as a result, the coherence time can also be comparable to τ_g.

Thus, we have grounds to consider $Z(t)$ to be fast (white) noise and the amplitudes to be Brownian random walk; therefore,

$$\langle p_{kq}^2\rangle = \langle |A_{kq}|^4\rangle \approx 2\langle |A_{kq}|^2\rangle^2 = 2\langle p_{kq}\rangle^2,$$
$$\langle p_{kq}, p_{kq}\rangle \approx \langle p_{kq}\rangle^2. \tag{9}$$

Here, we use the convenient Malakhov cumulant brackets $\langle x, y\rangle \equiv \langle xy\rangle - \langle x\rangle\langle y\rangle$. This result leads to the first interesting conclusion: the probabilities of transitions are completely undetermined for a time exceeding the coherence time. The second conclusion is that the average probabilities increase linearly with time:

$$\langle p_{kq}\rangle \approx \Delta t(g_{kq}/\hbar)^2\int K(\tau)\exp(iE_{kq}\tau/\hbar)d\tau \propto \Delta t. \tag{10}$$

However, we are most interested in determining the total probability of jumping. This probability can be presented in the following form:

$$p_k \equiv \sum_q p_{kq} = \int_0^{\Delta t}\int \Gamma_k(t_1 - t_2)Z(t_1)Z^*(t_2)dt_1dt_2, \tag{11}$$

where the kernel of the integral is

$$\Gamma_k(\tau) = \sum_q \left(\frac{g_{kq}}{\hbar}\right)^2 \exp(i\tau E_{kq}/\hbar).$$

The analytical properties of this kernel, determined by discreteness, are of basic importance. In the continuum approximation, $\Gamma_k(\tau)$ would be an integrable function rapidly and irreversibly tending to zero (e.g., delta function). In fact, this kernel is extremely nonlocal and never decays, while sometimes returning to values on the order of the value at zero (this behavior is a kind of manifestation of the unitarity of the quantum dynamics). Taking for the sake of illustration an equidistant spectrum $E_q^+ - E_k = n\delta E + \varepsilon_k$, where n is an integer, we obtain

$$\Gamma_k(\tau) = \frac{1}{\tau_t}\exp(i\varepsilon_k\tau/\hbar)\sum_n \delta(\tau - n\tau_g). \tag{12}$$

Therefore, the third evident, important circumstance is that the energy band ΔE accessible for the transitions from a given level is determined by the noise (coherence time) rather than by the time of observation. For

this reason, jumps into a discrete spectrum are possible as well as jumps into continuum. For $\Delta E > \delta E$, the average probability of jumping $\langle p_k \approx \Delta t/\tau_t \rangle$ virtually coincides with that employed in the usual kinetics.

Of course, the noise will not make the probabilities more definite. The fourth conclusion is that the discreteness renders the total probability of jumping a random quantity. Owing to the possibility of treating $Z(t)$ as white noise, we can obtain an expression for the variance of this random quantity:

$$\langle p_k, p_k \rangle \approx \int \ldots \int_0^{\Delta t} \Gamma_k(t_1 - t_2)\Gamma_k(t_3 - t_4) \times K(t_1 - t_4)K(t_3 - t_2)dt_1 \ldots dt_4. \quad (13)$$

For $\Delta E > \delta E$, this expression can be evaluated in a more or less general form. Taking into account that only the regions of $t_1 \approx t_4$ and $t_3 \approx t_2$ are significant and the remaining two-dimensional integral contains contributions from the delta functions entering into kernel (12), we obtain

$$\langle p_k, p_k \rangle \approx \frac{\Delta t^2}{\tau_t^2 \tau_g} \int |K(\tau)|^2 d\tau \approx \frac{\tau_{\text{coh}}}{\tau_g} \langle p_k \rangle^2 = \frac{\delta E}{\Delta E} \langle p_k \rangle^2 \quad (14)$$

(here, it is also taken into account that the "width" of the delta functions, equal to the inverse total width of the energy band, is much smaller than τ_{coh}). For the following, it is important to determine the mutual correlation of fluctuations of the probabilities of jumps (charge injection) from various levels. Estimating the cross correlator, we obtain

$$\langle p_{k_1}, p_{k_2} \rangle \approx \langle p_{k_1} \rangle \langle p_{k_2} \rangle \frac{\delta E}{\Delta E} S(E_{k_1} - E_{k_2}), \quad (15)$$

where the function

$$S(E) = \int \exp(iE\tau/\hbar)|K(\tau)|^2 d\tau \Big[\int |K(\tau)|^2 d\tau\Big]^{-1}$$

describes the correlation as depending on the energy distance ΔE between levels. As can be seen, the levels occurring in the same "coherence band" ΔE introduce in-phase contributions to the charge transfer fluctuations.

The above formulas require certain comments. First, these expressions can be readily generalized to the case of violated inequality (6), with allowance for the real nonequidistant character of the energy spectrum. Second, a giant increase in the jump probability fluctuations (100% and above) is possible provided that $\Delta E < \delta E$. In this extreme case, evaluation of the fluctuations depends on the details of the spectrum and requires knowledge of the statistics of the levels. In addition, this is accompanied by a significant renormalization of the average probabilities (and, hence, of the conductivity and the current–voltage characteristic) under the action of noise (even though we are only interested in the case of fluctuations against an approximately linear *I–U* background). Third, expressions (14) and (15) suggest that there is a kind of uncertainty relation, whereby the variances of all jump probabilities are inversely proportional to ΔE, such that a decrease in the probability fluctuations is accompanied by an increase in the correlation of these fluctuations and vice versa. Finally, the random contributions from various parts of the observation period are statistically fully correlated with each other despite being due to independent parts of $u(t)$ (a phenomenological statistics of such random flows of events was considered in [23, 26, 27]).

4. CONDUCTIVITY FLUCTUATIONS

Let us consider fluctuations in the charge transport through a junction between electrodes (connected via an external chain), assuming that the temperature is not very low ($T \gg \delta E$) and the external voltage is not very large ($U < T/e$). Below, ΔQ will denote a random quantity containing two parts, $\Delta Q = \Delta Q_{th} + \Delta Q_{ex}$, where the first term describes the contribution of fast thermal (shot) fluctuations of the transport current related to the random character of the transition moments. This contribution (also present in the state of equilibrium, when $U = 0$) can be readily evaluated using the fluctuation-dissipation theorem $\langle \Delta Q_{th}^2 \rangle \approx 2TG\Delta t$. Now, we are interested in the second term including the average transport current and the excess fluctuations caused by the random quantum probabilities of the transitions.

In terms of statistics, the ΔQ_{ex} value can be defined as the conditional average of ΔQ for fixed p_{kq}. From the elementary thermodynamic considerations, it is evident that this conditional average is of the same sign as U and vanishes when $U = 0$. Thus, we may treat this term as a result of "uncompensated" jumps in one direction (e.g., left to right). Using this circumstance, we can avoid an analysis of correlations between opposite transitions and use the results obtained in the preceding section (without recourse to such correlations). It is important to note that such correlations do not hinder any low-frequency fluctuations of the transport current proceeding with conservation of the internal statistical balance in the junction [23, 26, 27]. We can assume that all correlations are implicitly taken into account in the statistics of $u(t)$ noise. This is a quite reasonable assumption in view of the aforementioned fact that details of the $u(t)$ statistics are insignificant. Without any loss of generality, we may also assume that $p_k(\Delta t, U) \approx p_k(\Delta t, 0)$.

In the first step, we will ignore the mutual correlations in the random arrangement of active levels (from which the excess jumps take place) on the energy scale. According to this model, the second term can be expressed as

$$\Delta Q_{ex} = e\sum_k [f(E_k) - f(E_k + eU)]p_k(\Delta t, U), \quad (16)$$

where $f(E)$ is the Fermi distribution function and it is implied that averaging over the level arrangements (determined by the Fermi statistics of the occupation of states on the sides) is performed. The first term in the sum has the meaning of the probability that an arbitrarily selected level is active. Note that, with neglect of the p_k fluctuations, expression (16) reduces to the well-known formula for the average tunneling current (it should be emphasized that this formula takes into account the Fermi statistics of levels on both sides). The result of averaging (16) coincides with the corresponding formula (1).

Let us consider a variance of the transferred charge and the corresponding fluctuations of the conductivity $G = \Delta Q_{ex}/U\Delta t$ (details of the calculations are omitted). For a sufficiently small coherence time, when $\Delta E > \delta E$ ("large" junction area, dense spectrum, strong noise), a variance of (16) with allowance for (15) can be presented in the following form:

$$\langle \Delta Q_{ex}, \Delta Q_{ex} \rangle \approx (\langle G \rangle U \Delta t)^2 \frac{\delta E}{\Delta E} \times \int W(E')W(E'')S(E' - E'')dE'dE'', \quad (17)$$

where $\langle G \rangle$ is the average conductivity and

$$W(E) \equiv [f(E) - f(E + eU)]/eU \approx -\partial f(E)/\partial E$$

is a function playing the role of a "one-particle" probability distribution density of the active levels with respect to energy. From this we obtain a quite universal result for the conductivity fluctuations:

$$\delta G^2 \equiv \frac{\langle G, G \rangle}{\langle G \rangle^2} \approx \frac{\delta E}{T} \quad (\tau_{\text{coh}} < \tau_g). \quad (18)$$

For a large coherence time, when $\Delta E < \delta E$ ("small" junction area, rare levels, weak noise), the conductivity fluctuations become sensitive to the statistics of (mutually incommensurate) levels on the junction sides and cannot be unambiguously evaluated. In this situation (called extreme),

$$\frac{\delta E}{T} < \delta G^2 < 1 \quad (\tau_{\text{coh}} > \tau_g), \quad (19)$$

potentially "everything is possible" up to relative fluctuations on the order of unity.

As is seen, the discreteness is essentially a measure of relative fluctuations in the conductivity. The factor ΔE is missing from the estimates; this is a correct result, provided that the average number of active levels $N \equiv eU/\delta E$ is small and these levels can be arranged in any manner, even falling within the same coherence band ΔE. However, the latter is impossible for N exceeding the possible number of levels ($\Delta E/\delta E$) in such bands. Therefore, permissible distributions of the active levels with respect to energy for $eU > \Delta E$ are on the average more uniform and, hence, the fluctuations of the probabilities of jumping from these levels are less correlated. This can lead to suppression of the conductivity fluctuations with increasing voltage even at $eU \ll T$ (when the average conductivity is still more or less constant).

The expression for variance (17) shows that this effect is not described by model (16), in which the "two-particle" (pairwise) distribution with respect to the energy is formally factorized in the form $W(E')W(E'')$. In order to make the necessary corrections, let us renumerate the active levels in the order of increasing energy. Then the distance between levels with the number $j > i$ cannot be smaller than $\approx (j - i)\delta E$. Each pair of numbers corresponds to its own pairwise distribution

$$W_{ji}(E', E'') \approx W(E')W(E'')\vartheta(|E'' - E'| - |j - i|\delta E), \quad (20)$$

where ϑ is the Heaviside function. Instead of (16), we use

$$\Delta Q_{ex} = e\sum_{j=1}^{n} p_{k_j}(\Delta t, U), \quad (21)$$

thus passing to the real unity populations of the active levels and considering all possible positions of these levels. In this case, the average value of n is N. Let us calculate a variance of (21) by averaging this expression simultaneously over level positions and random jump probabilities. Since the result for $N \sim 1$ must coincide with that obtained above, it is sufficient to put $N \gg 1$ and $n = N$. Accomplishing simple transformations, we obtain

$$\langle \Delta Q_{ex}, \Delta Q_{ex} \rangle \approx e^2(\gamma \Delta t)^2 \frac{\delta E}{\Delta E} \times \sum_{i,j=1}^{N} \int W_{ij}(E', E'')S(E' - E'')dE'dE'' \quad (22)$$

and the following estimate of the conductivity fluctuations instead of (18):

$$\delta G^2 \approx \frac{\delta E}{T} D(eU), \quad (23)$$

where

$$D(X) = \frac{1}{X}\int_0^X dE \int_E^\infty S(E')dE' \left[\int_0^\infty S(E)dE\right]^{-1} \quad (24)$$

is the function describing the dependence of the fluctuations on the voltage. According to this estimate, the fluctuations at $eU > \Delta E$ decrease approximately in inverse proportion to U. For example, in the case of exponential phase correlation, we obtain

$$K(\tau) = \exp(-|\tau|/\tau_{\text{coh}}),$$

$$D(X) = \frac{1}{X}\int_0^X \left(1 - \frac{2}{\pi}\arctan\frac{E}{\Delta E}\right)dE.$$

Estimate (19) is modified in the same manner.

We can say that, as the voltage increases, the effective number of statistically independent energy channels of electron tunneling grows and the relative fluctuations of the conductivity decrease in inverse proportion to the number of channels. Thus, both the discreteness scale δE and the parameter ΔE characterizing the noise of the environment are directly reflected either in the current–voltage characteristic or in the noise–current characteristic. A strict difference between the roles of these values suggests that these quantities will probably retain their meaning in more rigorous theory.

As for the junction transparency, this parameter is missing from the estimates of relative fluctuations of the conductivity and, hence, is not a small parameter in this respect. Nor is it a small parameter in comparison with the excess fluctuations to the thermal (shot) noise. Although the latter noise contribution to the transport variance is proportional to the first power of transparency, the contribution due to excess fluctuations is proportional to the square of the transparency. While the first contribution increases linearly with time, the second contribution is quadratic and, hence, dominates at sufficiently large times and low frequencies (thus representing a qualitatively different type of noise). It is easy to check that, for $eU \sim T$, this takes place already at a time on the order of one jump duration τ_t. This is confirmed by the experiments with real operating currents. From the formal mathematical standpoint, the transparency cannot be considered a small parameter because the random phase gain $\varphi(t)$ depends on this parameter in a nonperturbative manner.

5. DISCUSSION AND COMPARISON WITH EXPERIMENT

There is a certain parallelism between the theory outlined above and the experimental data reported in [35], where the $1/f$ noise was thoroughly studied in a metal–ceramic composite comprising Ni nanoparticles in an Al_2O_3 matrix. In this system, the parameters of a typical tunneling junction between metal granules were $\delta E \approx 0.2$ meV, $d \approx 2$ nm, $C \approx 5 \times 10^{-6}$ cm, $E_C \sim T$ (at room temperature), and $R \approx 30$ MΩ, which corresponds to $\tau_g \approx 3 \times 10^{-11}$ s, $\tau_c \approx 1.5 \times 10^{-10}$ s, and $\tau_t \approx 3 \times 10^{-8}$ s. The system exhibited giant conductivity fluctuations with a spectral density $S_{\delta G}(f) \approx \alpha/N_g f$, where $\alpha \approx 6 \times 10^{-3}$ and N_g is the number of metal granules in a sample. Since $E_C \sim T$, the N_g value approximately coincides with the number of mobile (simultaneously transferred) electrons in the sample [35]. Therefore, an almost "standard" $1/f$ noise was observed with a "classical" Hooge constant ($\alpha \approx 2 \times 10^{-3}$ [1–4]).

These results correspond to fluctuations $S_{\delta G}(f) \sim \alpha/f$ in a separate elementary junction; since the inequalities (3) and (6) are quite well satisfied, we can assume that the noise is caused by the mechanism described above. To compare the theory to the experiment, let us relate the variance of conductivity fluctuations to the spectrum of fluctuations. For stationary noise, this relationship must include the logarithm of the observation time approximately as $\delta G^2 \approx f S_{\delta G}(f) \ln(\Delta t/\tau_c)$. For $\Delta t \sim \tau_t$ and $\alpha = 0.006$, this yields $\delta G^2 \sim 0.03$. For $\delta E = 0.2$ meV and room temperature, formula (18) gives ≈ 0.008. This is quite a good agreement, since we are basically dealing with the extremal region (19): for the above estimates, $\tau_{coh} \sim \tau_c > \tau_g$ and, hence, ΔE is comparable with δE.

It is interesting to note that the relative fluctuations of the conductivity decreased in approximately inverse proportion to the applied voltage when the latter exceeded a certain threshold value (which was much smaller than the linearity threshold of the current voltage characteristic). It has been noted [35] that the threshold corresponds to a voltage of $\sim \delta E/e$ per elementary contact. This result reveals sensitivity of the $1/f$ noise with respect to discreteness of the electron spectrum of the granules (the current–voltage characteristic was ohmic up to a voltage greater by a factor of $T/\delta E \approx 100$). Taking into account the close values of ΔE and δE, we may conclude that, as far as this effect is considered, the theory is fully consistent with experiment.

In the above example, the discreteness of the levels was determined by the volume of metal nanoparticles. Apparently, in the case of continuous sides, the δE value will also be determined by the volume of a region physically accessible for the jump, that is, by the junction geometry and by the processes of electron interaction and scattering at the junction sides. At not too low a temperature, there is not much freedom for selection: the accessible volume is restricted to the contact area A and the inelastic mean free path of electrons λ in the junction sides (electrodes). In other words, this is a region in which the distance between levels is on the order of their broadening caused by the inelastic relaxation. Of course, now it would be more correct to consider the situation in terms of the statistics of energetic repulsion between the spatially close states [40] (which is operative at a nonzero temperature as well [39]) rather than in terms of strictly fixed levels. Here, the discreteness is a synonym for uncertainty: details of the state depend on the "environment noise" and cannot be controlled to within less than δE.

In accordance with these considerations, this uncertainty limit in a system with sufficiently thick metal sides is $\delta E \sim E_F a^3/A\lambda$, where E_F is the Fermi energy and a is the characteristic atomic size. Relating the λ value to the metal conductivity ($\sigma \sim \lambda/a^2 R_0$) and using (18), we obtain the estimate

$$\delta G^2 \sim \frac{E_F}{T}\frac{a^2}{A}\frac{\sigma_{min}}{\sigma}, \tag{25}$$

where $\sigma_{min} \sim (aR_0)^{-1}$ is the minimum metal conductivity. For example, let the boundary metal be pure such that the phonon relaxation mechanism dominates. Then

[41], $\sigma \sim (\hbar e^2 n_e/m^*T)(T_D/T)^4$ (in standard notation) and we may expect the excess noise at a temperature below the Debye temperature to be proportional to the fourth power of the temperature (in relative units).

In terms of the possible orders of magnitude, the variance of the relative fluctuations of conductivity (related as shown above to $fS_{\delta G}(f)$ for $E_F \sim 5 \times 10^4$ K) is $\delta G^2 \sim (a^2/A)(T/T_D)^4$. For a microjunction with a contact area of $\sim 10^{-9}$ cm^2 (studied in [16]) and $T \sim T_D$, the variance amounts to $\sim 10^{-7}$. This estimate agrees with the results of measurements at 260 K [16]. The above formulas naturally explain the rapid (by almost two orders of magnitude) noise buildup experimentally observed in response to the temperature increase from 100 to 300 K [16]. In order to explain this, the authors of [16] had to assume the presence of a sharp step in the fluctuator activation energy distribution, although the $1/f$ spectrum structure implies that this distribution is smooth. In our opinion, two types of noise were observed in the experiment, representing a structural noise (with an uneven spectrum composed of several Lorentzians) dominating below 100 K and the noise studied in this paper, which dominated at higher temperatures but still gave a residual $1/f$ component with a smooth spectrum as in [16].

In this context, it should be noted that the two types of noise, albeit markedly different, can nevertheless exhibit a mutual influence. For example, the fact that the electrons from metal participate both in the conduction and in the heat transfer (i.e., are involved in low-frequency temperature fluctuations of the conductivity) may lead to a change in the spectrum of flicker fluctuations to $1/f^{\gamma}$ with $\gamma > 1$ [4]. By the same token, the interaction of electrons with structural defects may also influence the flicker noise of the conductivity, while not being a reason for this noise. In particular, the elastic scattering of carriers on the impurities suppresses the flicker fluctuations of mobility [2]. In contrast, the presence of vacancies enhances the flicker noise in metal films [5]. This effect can hardly be explained by the thermoactivated diffusion of vacancies: from the standpoint of an elementary diffusion step, the real scatter of the activation energies is insufficiently broad and the process cannot account for the $1/f$ spectrum. This was established in the case of temperature diffusion (rejected as the hypothetical source of such a spectrum) [1–4]. At the same time, vacancies can favor the inelastic scattering of carriers, thus acting as mediators of the "flicker noise due to a loss of memory."

Thus, according to a theory consistently taking into account the role of quantum discreteness in the process of charge transfer (in contrast to the continuum approximation), the amplitude of elementary quantum transitions (influenced by the whole system noise) may perform Brownian motion, eventually leading to fluctuations in the rate of charge transfer. These fluctuations exhibit no characteristic time scale and are insensitive to the time of averaging and observation, which is a distinctive feature of the flicker noise. Formally speaking, an analysis restricted to the times $\Delta t \sim \tau_t$ led to fluctuations with nondecaying correlations and a spectrum $\sim\delta(f)$ resembling static universal fluctuations of conductivity in disordered conductors [40]. However, in contrast to the "universal" fluctuations suppressed by the random diffusion of quantum phases (decoherence), the fluctuations under consideration are generated due to this random process.

From the basic standpoint, our results follow from the trivial quantum-mechanical rule that (even in the presence of noise and decoherence) the final result of a system evolution is determined by the interplay of amplitudes of the intermediate steps rather than by their probabilities. For this reason, the inelastic boundary processes explicitly included into the theory do not break the pattern (from the standpoint of quantum unitarity and discreteness); therefore, the scale-invariant character of conductivity fluctuations must be retained in a more rigorous many-electron theory considering arbitrarily large times (while the $\sim\delta(f)$ spectrum transforms into that of a $1/f$ type with the same frequency dimensionality). A formal justification of this transformation will be considered separately.

In concluding, we will make several remarks concerning the standard scheme of quantum kinetics, which originates from the well-known Pauli kinetic equation. Van Hove [42] mathematically justified this scheme in the limit of negligibly weak interaction. However, the final model does not leave place for the flicker noise. This seems to be related to the fact that, prior to the limiting transition $g \longrightarrow 0$ (where g is the interaction energy scale), the theory implicitly adopts the transition $\delta E \longrightarrow 0$, leading to a partial loss of the dimensional effects related to discreteness of the quantum evolution. Probably, elimination of the former limiting transition would lead to the kinetic theory of flicker noise.

ACKNOWLEDGMENTS

This study was supported by the Ministry of Education and Science of Ukraine (project no. 2M/71-2000) and by the Royal Academy of Sciences of Sweden.

REFERENCES

1. P. Dutta and P. Horn, Rev. Mod. Phys. **53**, 497 (1981).
2. F. N. Hooge, T. G. M. Kleinpenning, and L. K. J. Vandamme, Rep. Prog. Phys. **44**, 481 (1981).
3. M. B. Weissman, Rev. Mod. Phys. **60**, 537 (1988).
4. G. N. Bochkov and Yu. E. Kuzovlev, Usp. Fiz. Nauk **141**, 151 (1983) [Sov. Phys. Usp. **26**, 829 (1983)].
5. G. P. Zhigal'skiĭ, Usp. Fiz. Nauk **167**, 623 (1997) [Phys. Usp. **40**, 599 (1997)].
6. M. B. Weissman, Rev. Mod. Phys. **65**, 829 (1993).
7. B. Raquet, J. M. D. Coey, S. Wirth, and S. von Molnar, Phys. Rev. B **59**, 12435 (1999).

8. J. G. Massey and M. Lee, Phys. Rev. Lett. **79**, 3986 (1997).
9. M. J. C. van den Homberg, A. H. Verbruggen, P. F. A. Alkemade, *et al.*, Phys. Rev. B **57**, 53 (1998).
10. G. M. Khera and J. Kakalios, Phys. Rev. B **56**, 1918 (1997).
11. M. Gunes, R. E. Johanson, and S. O. Kasap, Phys. Rev. B **60**, 1477 (1999).
12. K. M. Abkemeier, Phys. Rev. B **55**, 7005 (1997).
13. G. Snyder, M. B. Weissman, and H. T. Hardner, Phys. Rev. B **56**, 9205 (1997).
14. V. I. Kozub, Solid State Commun. **97**, 843 (1996).
15. Yu. M. Gal'perin, V. G. Karpov, and V. I. Kozub, Zh. Éksp. Teor. Fiz. **95**, 1123 (1989) [Sov. Phys. JETP **68**, 648 (1989)].
16. C. T. Rogers and R. A. Buhrman, Phys. Rev. Lett. **53**, 1272 (1984).
17. J. P. Hessling and Yu. Galperin, Phys. Rev. B **52**, 5082 (1995).
18. X. Y. Chen, P. M. Koenrad, F. N. Hooge, and J. H. Wolter, Phys. Rev. B **55**, 5290 (1997).
19. A. Lisauskas, S. I. Khartsev, and A. M. Grishin, J. Low Temp. Phys. **117**, 1647 (1999).
20. A. Lisauskas, S. I. Khartsev, and A. M. Grishin, Appl. Phys. Lett. **77**, 756 (2000).
21. V. Podzorov, M. Uehara, M. E. Gershenson, and S.-W. Cheong, cond-mat/9912064.
22. J. L. Tandon and H. P. Bilger, J. Appl. Phys. **47**, 1697 (1976).
23. Yu. E. Kuzovlev and G. N. Bochkov, Izv. Vyssh. Uchebn. Zaved., Radiofiz. **26**, 310 (1983); Izv. Vyssh. Uchebn. Zaved., Radiofiz. **27**, 1151 (1984).
24. Yu. E. Kuzovlev, Zh. Éksp. Teor. Fiz. **94** (12), 140 (1988) [Sov. Phys. JETP **67**, 2469 (1988)].
25. Yu. E. Kuzovlev, Zh. Éksp. Teor. Fiz. **111**, 2086 (1997) [JETP **84**, 1138 (1997)].
26. Yu. E. Kuzovlev, Phys. Lett. A **194**, 285 (1994).
27. Yu. E. Kuzovlev, cond-mat/9903350.
28. N. S. Krylov, *Works on Justification of Statistical Physics* (Akad. Nauk SSSR, Moscow, 1950).
29. Yu. V. Nazarov, Zh. Éksp. Teor. Fiz. **95**, 975 (1989) [Sov. Phys. JETP **68**, 561 (1989)].
30. M. H. Devoret, D. Esteve, H. Grabert, *et al.*, Phys. Rev. Lett. **64**, 1824 (1990).
31. S. M. Girvin, L. I. Glazman, M. Jonson, *et al.*, Phys. Rev. Lett. **64**, 3183 (1990).
32. I. G. Lang and Yu. A. Firsov, Zh. Éksp. Teor. Fiz. **43**, 1843 (1962) [Sov. Phys. JETP **16**, 1301 (1962)].
33. Yu. Nazarov, Zh. Éksp. Teor. Fiz. **98**, 306 (1990) [Sov. Phys. JETP **71**, 171 (1990)].
34. A. van Oudenaarden, M. H. Devoret, E. H. Visscher, *et al.*, Phys. Rev. Lett. **78**, 3539 (1997).
35. J. V. Mantese, W. I. Goldburg, D. H. Darling, *et al.*, Solid State Commun. **37**, 353 (1981).
36. Yu. A. Genenko and Yu. M. Ivanchenko, Phys. Lett. A **126**, 201 (1987).
37. Yu. M. Ivanchenko and Yu. V. Medvedev, Fiz. Nizk. Temp. **2**, 142 (1976) [Sov. J. Low Temp. Phys. **2**, 69 (1976)].
38. Yu. A. Genenko and Yu. M. Ivanchenko, Teor. Mat. Fiz. **69**, 142 (1986).
39. G. Casati and B. Chirikov, *Fluctuations in Quantum Chaos*, Preprint (Budker Institute of Nuclear Physics, Siberian Division, Russian Academy of Sciences, Novosibirsk, 1993).
40. C. W. J. Beenakker, Rev. Mod. Phys. **69** (3), 731 (1997).
41. E. M. Lifshitz and L. P. Pitaevskiĭ, *Physical Kinetics* (Nauka, Moscow, 1974; Pergamon, Oxford, 1981).
42. L. van Hove, Physica (Amsterdam) **21**, 517 (1955).

Translated by P. Pozdeev

Physics of the Solid State, Vol. 44, No. 5, 2002, pp. 852–856. Translated from Fizika Tverdogo Tela, Vol. 44, No. 5, 2002, pp. 820–823.

SEMICONDUCTORS AND DIELECTRICS

Nanocrystalline Cu_2O Prepared under High Pressures

E. G. Ponyatovskiĭ, G. E. Abrosimova, A. S. Aronin, V. I. Kulakov, I. V. Kuleshov, and V. V. Sinitsyn

Institute of Solid-State Physics, Russian Academy of Sciences, Chernogolovka, Moscow oblast, 142432 Russia

e-mail: sinitsyn@issp.ac.ru

Received June 5, 2001; in final form, July 31, 2001

Abstract—The effect of high pressure on the structure of Cu_2O is investigated. Polycrystalline samples are treated during different periods of time at different temperatures and pressures in the vicinity of the kinetic curve of the decomposition $Cu_2O \longrightarrow Cu + CuO$. The structure of the samples subjected to thermobaric treatment is characterized by x-ray diffraction, electron diffraction structural analysis, and electron microscopy at atmospheric pressure. It is found that, upon treatment of Cu_2O at temperatures and pressures close to the decomposition region, the microstructure undergoes a transformation into the nanocrystalline state. © *2002 MAIK "Nauka/Interperiodica".*

1. INTRODUCTION

Over the last several decades, considerable attention has been given to investigations into polymorphic transformations of chemical elements and compounds under pressure and the elucidation of the behavior of solids upon transition from a phase equilibrium between two polymorphic modifications to the metastable region of one of these phases. It has been demonstrated that, at temperatures below the glass transition point T_g when the kinetics of the crystal–crystal polymorphic transformation is frozen, the metastable phase becomes unstable and transforms into the amorphous state.

There are a large number of works dealing with solid-phase amorphization (see, for example, [1–3] and references therein). However, the behavior of materials that are able to decompose into simpler species or even elements under pressure has been studied to a considerably smaller extent. The same is true for both the decomposition reaction at all its stages and the specific features in the behavior of the initial material in the metastable region between the thermodynamic equilibrium and the kinetic decomposition region. As the temperature decreases, the rate of decomposition attended by diffusive motion of atoms should decrease, the metastable region of existence of the initial phase should increase, and thermodynamic stability of the initial phase should decrease away from the thermodynamic equilibrium. From general considerations, we can outline the following possible scenarios for the behavior of materials susceptible to pressure-induced decomposition at temperatures below the glass transition point T_g: (i) polymorphic phase transition to a denser crystalline modification and (ii) amorphization due to a change in the short-range order, as has been observed in a number of experiments (see, for example, [4–6]).

It can be assumed that, at moderate temperatures, the structure and properties of the initial compound exhibit specific behavior in the vicinity of the kinetic decomposition region due to a decrease in the kinetic stability against decomposition. The purpose of the present work was to investigate structural transformations of Cu_2O in the predecomposition region at different temperatures and pressures. The choice of Cu_2O as the object of investigation was made for the following reasons.

(1) In the *P–T* phase diagram, the calculated curve of the equilibrium $Cu_2O \rightleftharpoons Cu + CuO$ (curve *II* in Fig. 1) [7] corresponds to pressures convenient for experimental investigations into decomposition and predecomposition processes.

(2) In the *P–T* phase diagram, the kinetic curve of the decomposition $Cu_2O \longrightarrow Cu + CuO$ (curve *III* in Fig. 1) and the curve of the back synthesis $Cu + CuO \longrightarrow Cu_2O$ (curve *I* in Fig. 1) under pressures are constructed using treatment of the samples at different temperatures and pressures and their subsequent x-ray diffraction investigation at atmospheric pressure [7].

(3) A considerable body of experimental data on the structure and physical properties of Cu_2O over wide ranges of temperatures and pressures is available [8–11].

2. SAMPLE PREPARATION AND EXPERIMENTAL TECHNIQUE

A microcrystalline powder of Cu_2O with 5- to 10-μm grains was produced through the reduction of divalent copper to the univalent state with the use of a weak glucose reductant. The phase composition of the powder prepared was checked using x-ray powder diffraction. The initial Cu_2O powder was placed in a teflon cell 5 mm high and 3 mm in diameter and was then sub-

jected to pressure treatment in a Toroid high-pressure chamber. The pressure treatment of Cu_2O was carried out at temperatures ranging from 80 to 170°C and pressures up to 100 kbar. The sample was allowed to stand at specified temperatures and pressures for different times (from 20 min to 3 days). Then, the temperature was decreased to room temperature and the high-pressure chamber was relieved. The compact samples thus prepared were studied using x-ray diffraction and electron microscopy. X-ray diffraction analysis of cleavages and polished surfaces of the sample was performed on a Siemens D500 diffractometer (CuK_α radiation). The microstructure was examined with a JEM-100CX electron microscope. For electron microscopic investigations, the samples were mechanically polished to a thickness of 0.1–0.2 mm and were then finished to the thickness required on a Gatan Diomill 600 ionic thinning instrument.

3. EXPERIMENTAL RESULTS

As was noted above, the reactions of Cu_2O decomposition and back synthesis under pressures up to 80 kbar were analyzed thoroughly by Belash *et al.* [7]. Figure 1 shows the kinetic curves for synthesis and decomposition of cuprous oxide (curves *I* and *III*, respectively) and the calculated curve for the equilibrium $Cu_2O \longleftrightarrow Cu + CuO$ (curve *II*) according to the results obtained in [7]. Kalliomaki *et al.* [8] performed optical and x-ray diffraction investigations of the phase transformations in cuprous oxide samples with the use of diamond anvils and observed the decomposition of Cu_2O at room temperature and pressure $P > 150$ kbar. Webb *et al.* [9] also observed the decomposition of Cu_2O into CuO and Cu; however, according to their observations, the decomposition of Cu_2O occurs only at temperatures above 500°C. At the same time, Webb *et al.* [9] did not reveal the decomposition of Cu_2O at room temperature under pressures up to 240 kbar. From the aforesaid, it is seen that the data available in the literature on the stability of Cu_2O under high pressures are very contradictory. In this respect, it was necessary to verify experimentally the decomposition of Cu_2O under the same pressure–temperature conditions as were established in [7]. For this purpose, the Cu_2O samples studied in the present work were treated at $T = 170$°C and $P = 70$ kbar (point *1* in Fig. 1). Analysis of the x-ray diffraction pattern of the sample treated under these conditions (Fig. 2) demonstrates that the decomposition of Cu_2O actually occurs in the vicinity of the decomposition curve constructed in [7]. Moreover, it is revealed that, after the decomposition, the sample has a two-phase composition and consists of Cu and CuO. All the subsequent treatments (the region bounded by dashed lines in Fig. 1) were performed at temperatures and pressures below the kinetic curve of decomposition [7].

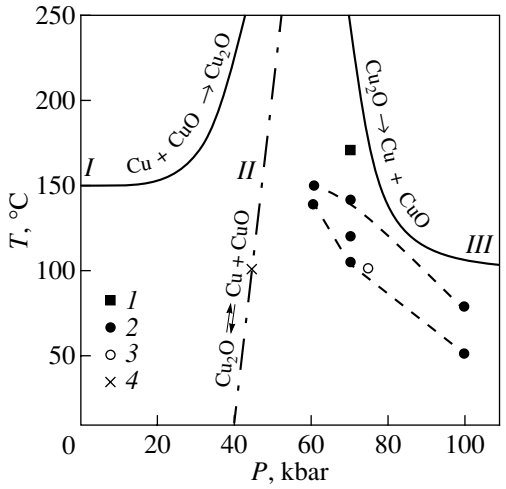

Fig. 1. *P–T* phase diagram: (*I*) the kinetic curve of the synthesis of cuprous oxide (solid line) [7], (*II*) the calculated curve of the equilibrium $Cu_2O \rightleftharpoons Cu + CuO$ (dot-dashed line) [7], (*III*) the kinetic curve of the decomposition of cuprous oxide (solid line) [7], (*1*) decomposition $Cu_2O \longrightarrow Cu + CuO$ (curve *III*), (*2*) formation of a nanocrystalline structure under quasi-hydrostatic pressures, (*3*) formation of a nanocrystalline structure under hydrostatic pressure, and (*4*) retention of the initial microstructure of Cu_2O. The dashed lines bound the *P–T* region corresponding to the formation of the nanocrystalline state.

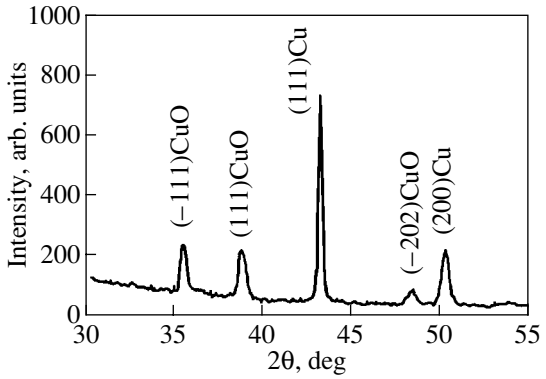

Fig. 2. X-ray diffraction pattern of the sample after decomposition at $P = 70$ kbar and $T = 170$°C.

X-ray diffraction patterns of the samples treated at temperatures and pressures in the vicinity of the kinetic curve of decomposition are depicted in Figs. 3 and 4. For comparison, Fig. 3 shows the x-ray diffraction pattern of the Cu_2O initial sample. It can be seen from Figs. 3 and 4 that, after the treatment, the positions of all the diffraction peaks remain unchanged, whereas their intensities decrease drastically and the half-widths increase considerably. The half-widths of the most intense peaks in the x-ray diffraction pattern of the Cu_2O initial sample are estimated to be $2\theta = 0.1°–0.2°$.

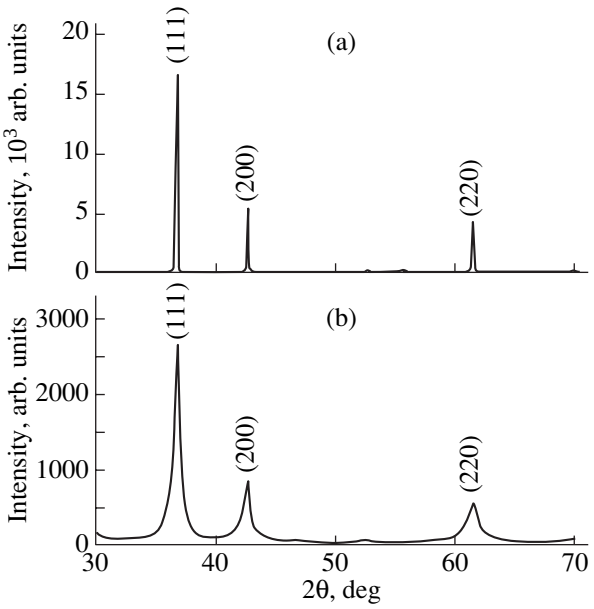

Fig. 3. X-ray diffraction patterns of (a) the initial sample and (b) the sample after heat treatment under pressure.

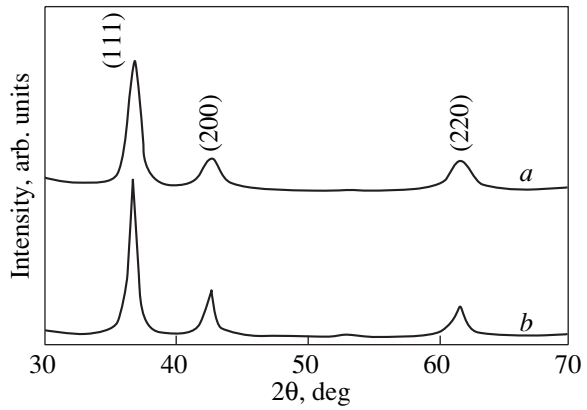

Fig. 4. X-ray diffraction patterns of the samples after heat treatment under pressure: (*a*) P = 70 kbar and T = 100°C (quasi-hydrostatic treatment) and (*b*) P = 72 kbar and T = 90°C (hydrostatic treatment).

After the treatment, we obtained $2\theta = 1.0°–1.5°$. An increase in the heat treatment temperature at the same pressure leads to a broadening of the diffraction peaks. An increase in the pressure at a constant temperature affects the x-ray diffraction patterns in a similar manner. It should be noted that, after heat treatment under pressure both to the left of the curve of the equilibrium $Cu_2O \rightleftharpoons Cu + CuO$ (curve *II* in Fig. 1) and in the immediate curve of thermodynamic equilibrium (point *4* in Fig. 1), the x-ray diffraction patterns of the initial and treated Cu_2O samples virtually coincide and substantial broadening of the diffraction lines is not observed. Therefore, we can assume that heat treatment under pressure leads to either atomic disordering within this structure or a decrease in the crystalline grain size.

The real structure of the sample subjected to heat treatment under pressure was examined with the use of electron microscopy. Figure 5 displays typical bright-field and dark-field images of the Cu_2O sample after heat treatment under pressure (P = 70 kbar and T = 100°C), which were obtained with an electron microscope. As can be seen from these micrographs, the structure involves 5- to 20-nm nanocrystals attributed to the initial phase of the Cu_2O compound. Analysis of the electron diffraction pattern (see inset in Fig. 5a) did not reveal an amorphous phase in the sample. Judging from the initial size of crystalline grains (5–10 μm), we can conclude that, upon heat treatment under pressure, the size of the crystalline grains decreases significantly and the sample attains the nanocrystalline state.

4. DISCUSSION

At room temperature and atmospheric pressure, Cu_2O has a cubic structure (space group $Pn3m$). This structure can be represented in the form of two interpenetrating lattices: one (face-centered) lattice is formed by copper atoms and the other (body-centered) lattice consists of oxygen atoms. Reasoning from this structure, it would be expected that, under pressure, Cu_2O undergoes a transition to a denser crystalline phase. This assumption is also supported by the results of earlier investigations into the elastic properties of Cu_2O [11], according to which an increase in the pressure at room temperature leads to a considerable decrease in the shear moduli C_{44} and C_{11}–C_{12}. This suggests that the formation of a nanocrystalline structure can be considered a consequence of the mechanical instability of the system in the vicinity of the polymorphic phase transition. However, Werner and Hochheimer [10] performed a comprehensive structural investigation and revealed that the first polymorphic phase transition in Cu_2O occurs at P = 100 kbar, whereas the decrease in size of crystalline grains is observed already at $P \geq 50$ kbar.

The nanocrystalline state of materials can be achieved through plastic deformation in different ways (grinding, milling, extrusion, etc.). In the course of powder compacting, the most severe plastic strains arise at early stages of compacting, as a rule, in the pressure range 10–20 kbar. However, we did not reveal noticeable changes in the grain size of cuprous oxide samples in this range of pressures. In our case, a decrease in the crystalline grain size of Cu_2O is observed at pressures above the curve of the equilibrium $Cu_2O \rightleftharpoons Cu + CuO$ (curve *II* in Fig. 1). Hence, we can make the inference that the nanocrystallization observed after the heat treatment under pressure is unrelated to conventional plastic strains. This inference is confirmed by the results obtained for the Cu_2O pow-

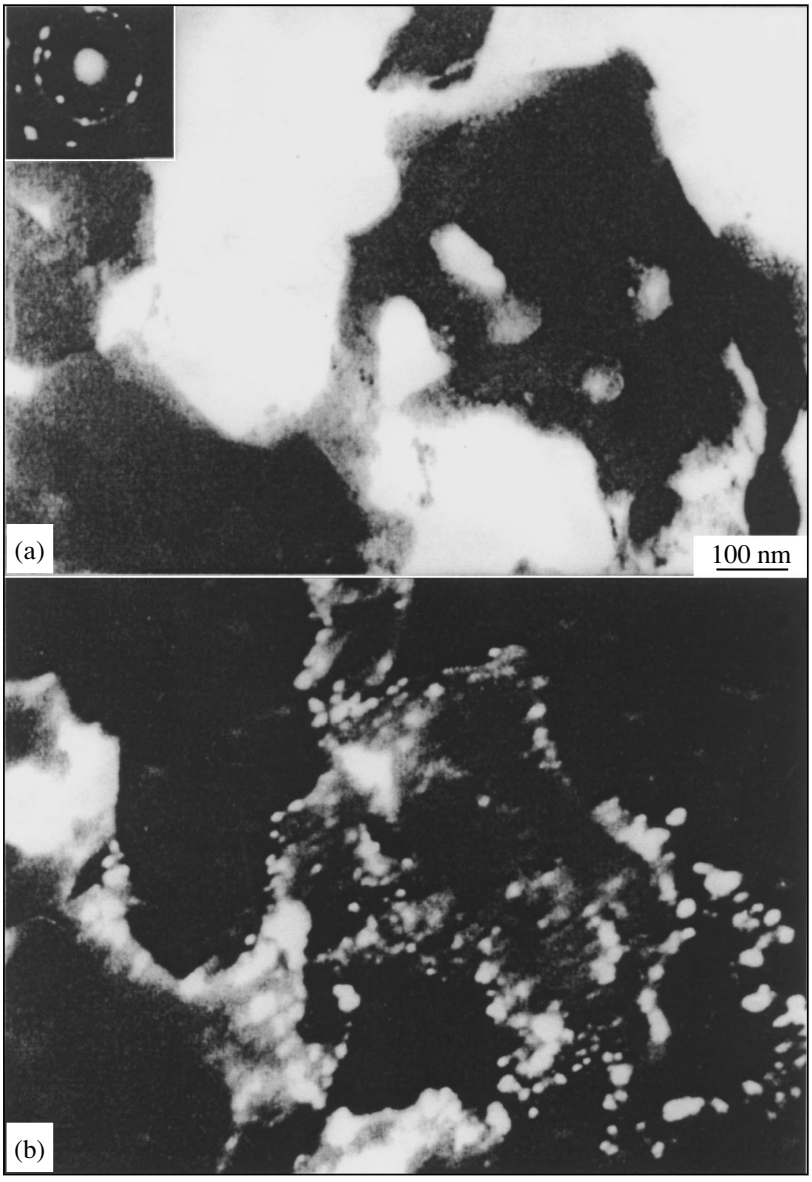

Fig. 5. (a) Bright-field and (b) dark-field images of the Cu_2O sample after nanocrystallization. The inset shows the electron diffraction pattern of the same sample.

der heat treated under pressure in a sealed cell filled with a mixture of ethanol and methanol, i.e., under conditions of actual hydrostatic pressure. Upon treatment of the Cu_2O powder at $P = 72$ kbar and $T = 90°C$ for 10 min, Cu_2O also transforms into the nanocrystalline state (Figs. 1, 4). However, it should be noted that curves *a* and *b* in Fig. 4 differ appreciably. Analysis of the diffraction peaks in curves *a* (quasi-hydrostatic treatment) and *b* (hydrostatic treatment) demonstrates that the crystals in the sample subjected to hydrostatic treatment have different sizes, whereas the size of crystalline grains in the sample subjected to quasi-hydrostatic treatment is characterized by a considerably smaller scatter. The difference observed in the x-ray diffraction patterns of the samples after hydrostatic and quasi-hydrostatic treatments suggests that the nonhydrostatic pressure components appreciably affect the nanocrystallization, even though they cannot be considered a decisive factor responsible for this process.

5. CONCLUSION

Thus, the above investigation demonstrated that the Cu_2O compound has a nanocrystalline structure after heat treatment under pressure in the vicinity of the decomposition curve (curve *III* in Fig. 1). As far as we know, this result has been obtained for the first time. Reasoning from the experimental data, it would be

expected that the microstructure undergoes further transformation until the amorphous phase is formed in the immediate vicinity of the decomposition curve at certain parameters *T* and *P*. However, the experimental verification of this assumption calls for further *in situ* structural investigation under pressure, which will be performed in the near future.

ACKNOWLEDGMENTS

We would like to thank D.V. Matveev for his assistance in performing the electron microscopic investigations.

This work was supported by the Russian Foundation for Basic Research (project no. 99-02-17007) and the Swiss Research Cooperation Program (SCOPE 2000 N 7SUPJ062362).

REFERENCES

1. E. G. Ponyatovsky and O. I. Barkalov, Mater. Sci. Rep. **8**, 147 (1992).
2. S. V. Demishev, Yu. V. Kosichkin, N. E. Sluchanko, and A. G. Lyapin, Usp. Fiz. Nauk **164** (2), 195 (1994) [Phys. Usp. **37**, 185 (1994)].
3. M. Surinder, S. M. Sharma, and S. K. Sikka, Prog. Mater. Sci. **40**, 1 (1996).
4. Y. Fuji, M. Kowaka, and A. Onodera, J. Phys. C **18**, 789 (1985).
5. G. C. Serghiou, R. P. Winters, and W. S. Hammack, Phys. Rev. Lett. **22** (68), 3311 (1992).
6. Ch. Meade and R. Jeanloz, Geophys. Res. Lett. **8** (17), 1157 (1990).
7. I. T. Belash, G. I. Peresada, and E. G. Ponyatovskiĭ, Izv. Akad. Nauk SSSR, Neorg. Mater. **13** (4), 666 (1977).
8. M. Kalliomaki, V. Meisalo, and A. Laisaar, Phys. Status Solidi A **56**, K127 (1979).
9. A. Webb, E. R. Carpenter, L. C. Towle, *et al.*, High Press. Res. **6**, 107 (1990).
10. A. Werner and H. D. Hochheimer, Phys. Rev. B **25** (9), 5929 (1982).
11. M. H. Manghani, W. S. Brower, and H. S. Parker, Phys. Status Solidi A **25**, 69 (1974).

Translated by O. Borovik-Romanova

Physics of the Solid State, Vol. 44, No. 5, 2002, pp. 857–863. Translated from Fizika Tverdogo Tela, Vol. 44, No. 5, 2002, pp. 824–829.

SEMICONDUCTORS AND DIELECTRICS

Heat Transfer in $Kr_{1-\xi}Xe_{\xi}$ Solid Solutions

V. A. Konstantinov*, R. O. Pohl, and V. P. Revyakin***

** Verkin Institute for Low Temperature Physics and Engineering, National Academy of Sciences of Ukraine, pr. Lenina 47, Kharkov, 63103 Ukraine*

*** Laboratory of Atomic and Solid-State Physics, Cornell University, Ithaca, New York 14853-2501, USA*

e-mail: konstantinov@ilt.kharkov.ua

Received July 4, 2001

Abstract—The isochoric thermal conductivity of $Kr_{1-\xi}Xe_{\xi}$ solid solutions (ξ = 0.034, 0.072, and 0.14) is investigated in the temperature range from 80 K to T_m (T_m is the melting temperature) for samples of different densities. It is found that an increase in disordering of the crystal leads to a gradual crossover from the thermal conductivity of a perfect crystal to the lower limit of the thermal conductivity of the lattice. A quantitative description of the results obtained is performed within the Debye model of thermal conductivity and allows for the fact that the mean free path of phonons cannot be less than half the phonon wavelength. © *2002 MAIK "Nauka/Interperiodica".*

1. INTRODUCTION

In dielectric crystals, heat transfer occurs primarily through phonons. An increase in temperature leads to an enhancement of phonon–phonon scattering and a decrease in the phonon mean free path l. However, the phonon mean free path cannot become less than the phonon wavelength λ. At $l \sim \lambda$, the temperature behavior of the thermal conductivity of a crystal should deviate from the dependence $\Lambda \propto 1/T$ and the magnitude of the thermal conductivity should tend to a minimum value permissible for this crystal.

Strong phonon scattering can be caused by structural disordering, defects, etc. The thermal conductivity reaches a lower limit Λ_{min} in glasses and strongly disordered crystals. Phenomenologically, the lower limit of thermal conductivity Λ_{min} can be treated as a lower limit of the mean free path of phonons in the framework of the Debye model. Slack [1] assumed that the lower limit of the mean free path of phonons is equal to the phonon wavelength. Cahill *et al.* [2, 3] showed that the thermal conductivity in a number of amorphous materials and strongly disordered crystals can be adequately described under the assumption that excitations are weakly localized in regions whose size is of the order of half the wavelength $\lambda/2$ and migrate from region to region through diffusion. In this case, the lower limit of the thermal conductivity Λ_{min} can be written as

$$\Lambda_{min} = \left(\frac{\pi}{6}\right)^{1/3} k_B n^{2/3} \sum_i v_i \left\{ \left(\frac{T}{\Theta_i}\right)^2 \int_0^{\Theta_i/T} \frac{x^3 e^x}{(e^x - 1)^2} dx \right\}. \quad (1)$$

Here, the summation is performed over three (two transverse and one longitudinal) vibrational modes, v_i stands for the velocities of sound, $\Theta_i = v_i(\hbar/k_B)(6\pi^2 n)^{1/3}$ is the Debye temperature for each polarization, and n is the number of atoms per unit volume. In the high-temperature limit ($T \geq \Theta_i$), Λ_{min} is temperature independent and its magnitude falls in the range 1–10 mW cm^{-1} K^{-1} for the majority of materials.

The question arises as to whether the lower limit of thermal conductivity Λ_{min} can be achieved in perfect crystals with an increase in temperature due to three-phonon scattering. This problem has been considered in a number of works [1, 4, 5]. According to the estimates made by Roufosse and Klemens [4], noticeable deviations from the dependence $\Lambda \propto 1/T$ for the majority of materials should be observed at temperatures above 1500 K. As follows from the theoretical analysis carried out by Pettersson [5], the thermal conductivity can tend to the lower limit Λ_{min} in alkali halide crystals composed of ions with significantly different masses (NaBr, NaJ, KJ, RbF, etc.). To the best of our knowledge, direct measurements of thermal conductivity in alkali halide crystals have never been performed at temperatures close to the melting point (hereafter, premelting temperatures). The possible minimum of the thermal conductivity in ThO_2 and α-Al_2O_3 at $T > 1500$ K was discussed in [1]. However, the problem of heat transfer by radiation at these temperatures calls for detailed consideration.

In order to choose the most suitable objects for observations of the minimum thermal conductivity in perfect crystals, we compare the thermal conductivities Λ_{meas} for a number of crystals with different types of chemical bonding [1, 5–9] and the minimum thermal conductivities Λ_{min} calculated according to formula (1) at temperatures close to the melting point T_m (Fig. 1). For alkali halide crystals, the thermal conductivity in

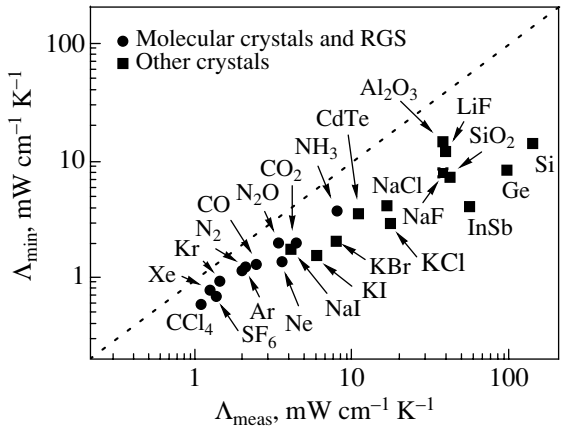

Fig. 1. Comparison of the thermal conductivities Λ_{meas} for a number of crystals with different types of chemical bonding [1, 5–9] and the minimum thermal conductivities Λ_{min} calculated according to formula (1) at temperatures near the melting point.

the vicinity of T_m was estimated by extrapolating the available data with the use of the relationship $\Lambda \propto 1/T$ [5]. The densities and acoustic velocities required for the calculation of Λ_{min} were taken from [7–10]. It can be seen from Fig. 1 that the ratio $\Lambda_{meas}/\Lambda_{min}$ is equal to 1.5–2 for solidified rare gases and simple molecular crystals, 2–5 for alkali halide crystals, and ~10–12 for crystals with diamond-type structures. For diamond, the ratio $\Lambda_{meas}/\Lambda_{min}$ (calculated according to the data taken from [10, 11]) is approximately equal to 30 at temperatures close to the sublimation temperature. These data indicate that the ratio $\Lambda_{meas}/\Lambda_{min}$ increases with an increase in the bond strength. Multicomponent crystals and crystals with a complex structure, as a rule, are characterized by a low thermal conductivity of the order of several mW cm^{-1} K^{-1} [12], which is close to Λ_{min} for the majority of compounds [1–3]. However, exact calculations in this case can be complicated because of the necessity of accounting for the contribution of the optical branches [1]. A similar problem also arises in molecular crystals. For example, the ratio $\Lambda_{meas}/\Lambda_{min}$ is equal to ~1.7 for solidified rare gases and N_2O. The isochoric thermal conductivity of solidified rare gases at premelting temperatures deviates only slightly (by 20–25%) from the law $\Lambda \propto 1/T$ [6], whereas the thermal conductivity of solid N_2O is virtually independent of temperature at $T \approx T_m$ [13]. As was noted above, the thermal conductivity should not depend on temperature at $T \geq \Theta_D$ (where Θ_D is the Debye temperature) in the case when it reaches the lower limit Λ_{min}. The degree of approximation of the isochoric thermal conductivity to a steady-state value [for example, the parameter $(\partial \ln\Lambda/\partial \ln T)_V$] can be used as a criterion for closeness of the thermal conductivities Λ_{meas} and Λ_{min}. In the case of N_2O, it is reasonable to make the inference that the rotational degrees of freedom of molecules in a crystal make an additional contribution to Λ_{min}, which is disregarded in relationship (1). This contribution is determined by the possibility of transferring the rotational energy from site to site, i.e., by the noncentral interaction force.

Therefore, crystals with van der Waals bonding, in particular, solidified rare gases, are the most suitable objects for observations of the effects associated with the attainment of the lower limit of the thermal conductivity due to umklapp processes. Since the melting temperatures for the majority of simple molecular crystals are below room temperature, heat transfer by radiation is ruled out. The ratio $\Lambda_{meas}/\Lambda_{min}$ for these materials at premelting temperatures is equal to 1.5–2. Investigations into the isochoric thermal conductivity of solidified rare gases and simple molecular crystals revealed considerable deviations from the dependence $\Lambda \propto 1/T$ [6, 13, 14].

In the case when the thermal conductivity approaches Λ_{min} with an increase in temperature, the effect of impurities should manifest itself in a specific manner. Impurities cannot considerably decrease the thermal conductivity at premelting temperatures at which the conductivity has already been close to the minimum value. A decrease in temperature should result in an increase in the contribution of impurities to the thermal resistance of crystals $W = 1/\Lambda$. This behavior of the thermal conductivity was observed in solid Kr with a CH_4 impurity [15]. The maximum impurity content was equal to 6.3%, and the thermal conductivity substantially exceeded the lower limit calculated according to relationship (1). In the present work, we elucidated how the Xe heavy impurity affects the thermal conductivity of solid Kr. The thermal conductivity was investigated at a constant density in order to exclude the effect of thermal expansion.

2. EXPERIMENTAL TECHNIQUE

Molecular solids that are characterized by relatively small temperature pressure coefficients $(dP/dT)_V$ can be investigated at a constant volume. If a high-pressure cell is filled with a solid sample of sufficiently high density, the sample can be subsequently cooled at virtually a constant volume and the pressure in the sample decreases rather slowly. In a certain density range, the sample separates from the cell walls at a characteristic temperature T_0 and the condition V = const does not hold. An increase in the sample density leads to a shift in the melting temperature toward the high-temperature range. The deviations from the constant volume due to thermal and elastic deformations of the measuring cell can be easily taken into account.

In this work, the experiments were performed on a coaxial-geometry setup using the stationary method [16]. A beryllium bronze measuring cell 160 mm long and 17.6 mm in inside diameter was rated at a maxi-

mum pressure of 800 MPa. The diameter of the inner measuring cylinder was equal to 10.2 mm. Temperature detectors (platinum resistance thermometers) were placed in special channels of the inner and outer cylinders and did not experience a high pressure. The samples were grown at a temperature gradient of approximately 1 K cm^{-1} along the measuring cell. In order to prepare samples of different densities, the pressure in the capillary during the growth could be varied in the range from 50 to 250 MPa. After the growth, the inlet capillary was blocked by freezing with liquid nitrogen (hydrogen) and the samples were annealed for 5–6 h at premelting temperatures. Upon completion of the measurements, the samples were evaporated into a thin-wall vessel and their mass was determined by weighing. The molar volume of the sample was calculated from the known volume of the measuring cell and the sample mass. The total systematic error in measurements was predominant and did not exceed 5% for thermal conductivity and 0.2% for volume. The purity of the initial gases Kr and Xe used for preparing a solution was no less than 99.98%. The component concentrations were measured by chromatography in the gaseous phase.

3. RESULTS

In this work, the isochoric thermal conductivity of $Kr_{1-\xi}Xe_\xi$ solid solutions (ξ = 0.034, 0.072, and 0.14) was investigated in the temperature range from 80 K to the melting temperature for samples of different densities. The choice of this system, concentrations, and temperature range of measurements was made for the following reasons.

The phase diagram of the $Kr_{1-\xi}Xe_\xi$ solid solution is well known [17]. The liquid and solid phases are characterized by a point of equal concentrations at a temperature of 114.1 K and ξ = 0.15. At temperatures from 75 to 114 K, the components form solid solutions with a face-centered cubic structure in the entire range $1 \geq \xi \geq 0$. When the samples are grown with a temperature gradient along the measuring cell, the phase separation of solid solutions can be observed at $\xi > 0.15$. Therefore, the maximum Xe concentration in the solution was limited by 14%. The scattering factor Γ (see below) for the $Kr_{1-\xi}Xe_\xi$ solid solution is one of the largest among those for rare-gas solutions. Therefore, strong scattering by impurities can be expected.

The smoothed coefficients of the isochoric (Λ_V) and isobaric (Λ_P) thermal conductivities of $Kr_{1-\xi}Xe_\xi$ solid solutions are listed in Table 1. The molar volumes V_m, temperatures T_0 (which correspond to the onset of the satisfaction of the condition V = const in the experiment), temperatures T_m of the onset of melting, and the Bridgman coefficients $g = -(\partial \ln\Lambda/\partial \ln V)_T$ calculated from the experimental data for the studied samples are presented in Table 2. Since the molar volume of the solid solution changes drastically when changing over from Kr to Xe with a variation in ξ, the experimental results are conveniently compared for samples with the same temperature T_0 at which the condition V = const is satisfied. It is rather difficult to choose the growth conditions in such a way as to prepare the samples with identical temperatures T_0. However, if the thermal conductivity is measured for several isochores at the same concentration of the components, the thermal conductivity can be calculated for any temperature T_0 by using the volume dependence of the thermal conductivity in the form $g = -(\partial \ln\Lambda/\partial \ln V)_T$.

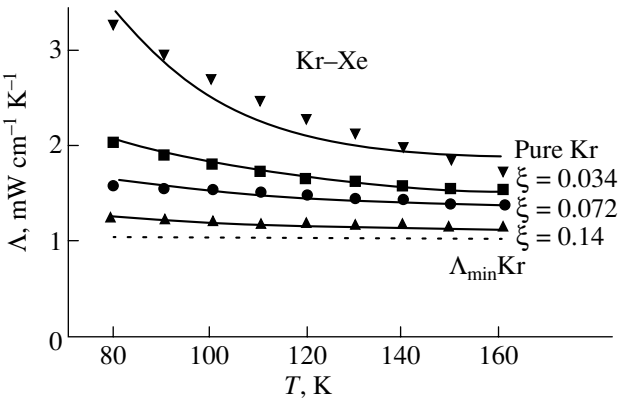

Fig. 2. Smoothed isochoric thermal conductivities of pure Kr [5] and $Kr_{1-\xi}Xe_\xi$ solid solutions (ξ = 0.034, 0.072, and 0.14) for samples whose volume is constant starting from 80 K. Solid lines represent the results of computer fitting. The dashed line indicates the lower limit of the thermal conductivity Λ_{min} of pure Kr for the isochoric case (T_0 = 80 K).

Figure 2 shows the temperature dependences of the isochoric thermal conductivity for pure Kr and $Kr_{1-\xi}Xe_\xi$ solid solutions, which were reduced to T_0 = 80 K. The thermal conductivity of pure Kr was calculated from the semiempirical relationship proposed in [6]. The lower limit Λ_{min} of the thermal conductivity of pure Kr for the isochoric case (T_0 = 80 K) is shown by the dashed line in Fig. 2. The necessary data on the density and velocities of sound for our calculations were taken from [9, 18]. It can be seen that the thermal conductivity of $Kr_{1-\xi}Xe_\xi$ solid solutions decreases and its temperature dependence becomes weaker with an increase in the Xe concentration. At ξ = 0.14, the thermal conductivity virtually coincides with the lower limit calculated by formula (1).

4. DISCUSSION

As was noted above, the lower limit Λ_{min} of the thermal conductivity can be phenomenologically treated as a lower limit of the mean free path of phonons in the framework of the Debye model. Since the mean free path of high-frequency phonons is limited in the case of umklapp processes and Rayleigh scattering, it can be assumed that heat transfer occurs through low-fre-

Table 1. Smoothed coefficients of the isobaric (Λ_P) and isochoric (Λ_V) thermal conductivities (mW cm^{-1} K^{-1}) for $Kr_{1-\xi}Xe_\xi$ solid solutions

T, K	ξ							
	0.034			0.072			0.14	
	Λ_P	Λ_V at V_m		Λ_P	Λ_V at V_m		Λ_P	Λ_V at V_m
		28.95	29.35		29.45	29.9		29.95
80	2.10	2.12		1.60			1.25	
90	1.75	1.98	1.80	1.44	1.55		1.18	1.20
100	1.54	1.90	1.73	1.32	1.52	1.35	1.10	1.17
110	1.35	1.83	1.63	1.21	1.50	1.32	1.03	1.15
120		1.76	1.55		1.45	1.29		1.13
130		1.70	1.50		1.43	1.27		1.11
140		1.66	1.47		1.40	1.25		1.09
150		1.63	1.45		1.38			1.08
160		1.60						

Note: The molar volumes of the studied samples are given in terms of cm^3 mol^{-1}.

quency mobile phonons and modes localized in regions whose size is of the order of $\lambda/2$. The phonon mobility edge is equal to the Debye frequency when the mean free path of each mode is larger than $\lambda/2$ and should shift toward the low-frequency range with an enhancement in scattering. In the limit of a very strong scattering, when all the modes are scattered at a distance of the order of $\lambda/2$, the thermal conductivity reaches the minimum value Λ_{min}. The crossover from weak phonon scattering to strong scattering can be described in the framework of the Debye model. The expression for thermal conductivity can be written in the form

$$\Lambda(T) = 3nk_B v\left(\frac{T}{\Theta_D}\right)^3 \int_0^{\Theta_D/T} l(x)\frac{x^4 e^x}{(e^x-1)^2}dx, \qquad (2)$$

where $\Theta_D = v(\hbar/k_B)(6\pi^2 n)^{1/3}$ is the Debye temperature, v is the polarization-averaged velocity of sound, and $l(x)$ is the mean free path of phonons. At $T \geq \Theta_D$, grain-boundary scattering is relatively weak and the mean free path is predominantly determined by umklapp processes and Rayleigh scattering [19]; that is,

$$l(x) = (l_{Rayl}^{-1} + l_{Umkl}^{-1})^{-1}. \qquad (3)$$

The mean free paths corresponding to different scattering mechanisms can be represented in the following form [19, 20]:

$$l_{Umkl}^{-1} = \frac{CT}{\lambda^2}, \qquad (4)$$

where

$$C = (12\pi^3/\sqrt{2})n^{-1/3}(\gamma^2 k_B/mv^2) \qquad (5)$$

and

$$l_{Rayl}^{-1} = \frac{4\pi^3\Omega_0\Gamma}{\lambda^4}, \qquad (6)$$

where

$$\Gamma = \xi(1-\xi)\left[\frac{\Delta M}{M} + 2\gamma\frac{\Delta\Omega_0}{\Omega_0}\right]^2. \qquad (7)$$

Here, γ is the Grüneisen parameter equal to 2.5 for Kr [9], m is the atomic mass, $M = (1-\xi)M_{Kr} + \xi M_{Xe}$ is the averaged atomic weight per atom of the solid solution, $\Omega_0 = (1-\xi)\Omega_{0Kr} + \xi\Omega_{0Xe}$ is the averaged volume per atom of the solid solution ($\Omega_0 = 6.3\times10^{-23}$ cm^3 and $M = 131$ for pure Xe and $\Omega_0 = 5.0\times10^{-23}$ cm^3 and $M = 83.8$ for pure Kr), $\Delta M = M - M_{Xe}$ is the difference between the averaged atomic weight of the solid solution and the

Table 2. Molar volumes V_m, temperatures T_0 of the onset of the satisfaction of the condition V = const in the experiment, temperatures T_m of the onset of melting, and Bridgman coefficients g for the studied samples

ξ	Sample no.	V_m, cm^3 mol^{-1}	T_0, K	T_m, K	g
0.034	1	28.95	78	165	8.0
	2	28.35	87	150	
0.072	1	29.45	82	169	5.5
	2	29.90	95	150	
0.14	1	29.95	84	160	4.0

atomic weight of the impurity, and $\Delta\Omega_0 = \Omega_0 - \Omega_{0Xe}$ is the difference between the averaged volume of the solid solution and the volume of the impurity.

Relationship (3) is inapplicable when the mean free path $l(x)$ is of the order or less than the phonon wavelength. A similar situation was discussed earlier only for umklapp processes [3]. Let us now consider the combined case of umklapp processes and Rayleigh scattering. It is assumed that the mean free path $l(x)$ is described by relationship (3) at $l(x) \geq \alpha\lambda/2$; otherwise, we have

$$l(x) = \alpha\lambda/2, \tag{8}$$

where α is the numerical coefficient, which is of the order of unity and does not depend on T and λ. Excitations scattered at a distance of the order of $\lambda/2$ are considered to be localized. The phonon mobility edge λ_* can be found from the condition

$$\left(\frac{CT}{\lambda_*^2} + \frac{B}{\lambda_*^4}\right)^{-1} = \alpha\frac{\lambda_*}{2}. \tag{9}$$

Now, we introduce the effective temperature $\Theta_* = h\nu/k_B\lambda_*$ (it is assumed that $\Theta_* < \Theta_D$; otherwise, $\Theta_* = \Theta_D$). Recall that, within the proposed model, the heat is transferred through low-frequency mobile phonons and, above the phonon mobility edge, through the modes localized in regions whose size is of the order of $\lambda/2$. In this case, the thermal conductivity integral is separated into two parts:

$$\Lambda(T) = 3nk_B\nu\left(\frac{T}{\Theta_D}\right)^3\left[\int_0^{\Theta_*/T} l(x)\frac{x^4e^x}{(e^x-1)^2}dx + \int_{\Theta_*/T}^{\Theta_D/T} \alpha\frac{\lambda}{2}\frac{x^4e^x}{(e^x-1)^2}dx\right]. \tag{10}$$

In the high-temperature limit ($T \geq \Theta_D$), when only umklapp processes are involved, the thermal conductivity is represented by the relationship $\Lambda(T) = A_1/T^2 + \Lambda'_{min}$, where A_1 is the numerical temperature-independent coefficient and Λ'_{min} is given by

$$\Lambda'_{min} = 3\alpha\left(\frac{\pi}{6}\right)^{1/3} n^{2/3}k_B\nu\left(\frac{T}{\Theta_D}\right)^2\int_0^{\Theta_D/T}\frac{x^3e^x}{(e^x-1)^2}dx. \tag{11}$$

This expression for Λ_{min} is identical to formula (1), provided the polarization-averaged velocity of sound is used and $\alpha = 1$. For strong phonon scattering, when the heat is predominantly transferred through localized modes ($\Theta_* \ll \Theta_D$), the thermal conductivity is determined by relationships (1) and (11).

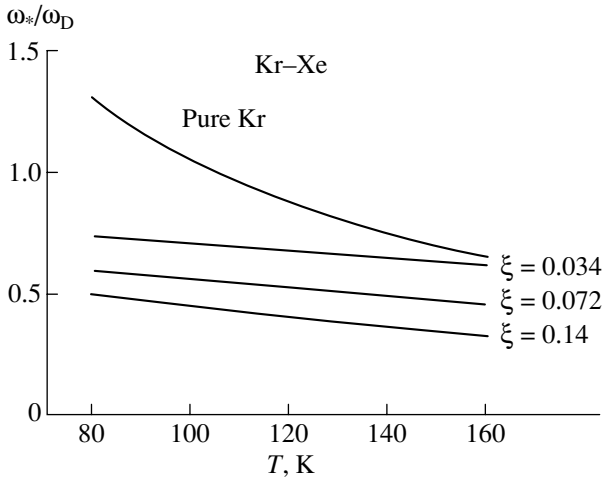

Fig. 3. Temperature and concentration dependences of ω_*/ω_D, where $\omega_* = 2\pi\nu/\lambda_*$ is the phonon mobility edge.

The computer fitting with the use of expression (10) for the thermal conductivity was performed for pure Kr and $Kr_{1-\xi}Xe_\xi$ solid solutions (ξ = 0.034, 0.072, and 0.14) for isochores with T_0 = 80 K. The relevant densities and velocities of sounds were calculated according to the data taken from [9, 18] by assuming a linear interpolation with respect to ξ when changing over from Kr to Xe. In order to decrease the number of variable parameters, the coefficient B describing the Rayleigh scattering was computed using relationships (6) and (7). The results of the fitting are represented by solid lines in Fig. 2. The Debye model parameters (n, ν, Γ) used in the fitting and the coefficients C and α derived by the fitting are given in Table 3. The coefficient C characterizing the intensity of umklapp processes is in good agreement with the low-temperature data (1.5×10^{-9} cm K^{-1}) obtained by Dudkin *et al.* [21]. The parameter α varies from 1.2 to 1.4. This confirms the applicability of relationship (1) to the description of the lower limit of thermal conductivity in solidified rare gases. At the same time, it would make no sense to discuss the validity of the choice of $\lambda/2$ as the lower limit of the phonon mean free path. The simple Debye model

Table 3. Fitting parameters of the Debye model of thermal conductivity for pure Kr and $Kr_{1-\xi}Xe_\xi$ solid solutions

ξ	$n \times 10^{-22}$, cm^{-3}	ν, km s^{-1}	Γ_{calcd}	Variable parameters	
				C, cm K^{-1}	α
0	2.11	0.86	0	1.07×10^{-9}	1.29
0.034	2.07	0.863	0.10	1.17×10^{-9}	1.2
0.072	2.05	0.866	0.19	1.75×10^{-9}	1.19
0.14	2.02	0.87	0.29	3.2×10^{-9}	1.05

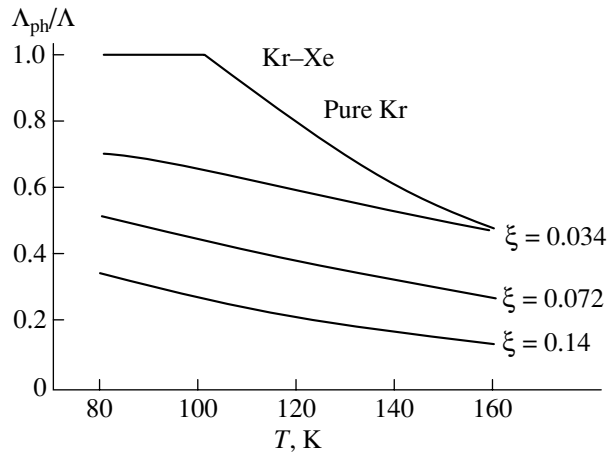

Fig. 4. Relative contributions of low-frequency mobile phonons to the thermal conductivities of pure Kr and $Kr_{1-\xi}Xe_\xi$ solid solutions.

used in our analysis ignores a number of essential factors, primarily of the dispersion and the real density of states. The coefficient α in relationship (8) for the mean free path is an integrated factor accounting for imperfection of the model.

Figure 3 shows the temperature and concentration dependences of the phonon mobility edge ω_*/ω_D, where $\omega_* = 2\pi v/\lambda_*$. The relative contributions of low-frequency mobile phonons to the thermal conductivities of pure Kr and $Kr_{1-\xi}Xe_\xi$ solid solutions are presented in Fig 4. It can be seen that the localization of high-frequency modes in pure Kr occurs at temperatures above 90 K. As the impurity concentration increases, a progressively larger part of the heat is transferred through localized modes. However, even at a maximum impurity concentration ($\xi = 0.14$) and the highest temperature of measurements (160 K), an appreciable part of the heat is transferred through low-frequency mobile phonons.

5. CONCLUSIONS

Thus, in solidified rare gases, unlike crystals with strong interatomic bonds (for example, crystals with a diamond-type structure), the thermal conductivity approaches the lower limit Λ_{min} at premelting temperatures. In this case, impurities cannot substantially decrease the thermal conductivity in the vicinity of the melting temperature T_m; however, at lower temperatures, the introduction of impurities can lead to a noticeable decrease in the thermal conductivity. In $Kr_{1-\xi}Xe_\xi$ solid solutions, a gradual decrease from the thermal conductivity of a perfect crystal to the minimum thermal conductivity is observed as the crystal becomes increasingly more disordered. Since the mean free path of high-frequency phonons is limited in the case of umklapp processes and Rayleigh scattering, the heat is transferred through low-frequency mobile phonons and, above the phonon mobility edge, through the modes localized in regions whose size is of the order of $\lambda/2$. The phonon mobility edge shifts from the Debye frequency toward the low-frequency range as scattering becomes stronger. In the limit of very strong scattering, when all the modes are scattered at a distance of the order of $\lambda/2$, the thermal conductivity reaches the lower limit Λ_{min}. It was demonstrated that the behavior of the thermal conductivity of $Kr_{1-\xi}Xe_\xi$ solid solutions can be described in terms of the Debye model with allowance made for the fact that the mean free path of phonons cannot be less than half the phonon wavelength.

ACKNOWLEDGMENTS

We are grateful to Academician V.G. Manzhelii (National Academy of Sciences of Ukraine) for his continuous interest in this work and helpful discussions of the results.

This work was supported by the Ministry of Education and Science of Ukraine (contract no. 2m/1862-97) and the "Twinning Program 1999–2000" of the National Research Council of the United States.

REFERENCES

1. G. A. Slack, in *Solid State Physics*, Ed. by H. Ehrenreich, F. Seitz, and D. Turnbull (Academic, New York, 1979), Vol. 34, p. 1.
2. D. G. Cahill, S. K. Watson, and R. O. Pohl, Phys. Rev. B **46** (10), 6131 (1992).
3. D. G. Cahill and R. O. Pohl, Solid State Commun. **70** (10), 927 (1989).
4. M. C. Roufosse and P. G. Klemens, J. Geophys. Res. **79** (5), 703 (1974).
5. S. Pettersson, J. Phys.: Condens. Matter **1** (2), 361 (1989).
6. V. A. Konstantinov, V. G. Manzhelii, M. A. Strzhemechnyĭ, and S. A. Smirnov, Fiz. Nizk. Temp. **14** (1), 90 (1988) [Sov. J. Low Temp. Phys. **14**, 48 (1988)].
7. V. G. Manzhelii, A. I. Prokvatilov, V. G. Gavrilko, and A. P. Isakina, *Handbook for Structure and Thermodynamic Properties of Cryocrystals* (Begell House, New York, 1999).
8. *Acoustical Crystals*, Ed. by M. P. Shpol'skiĭ (Nauka, Moscow, 1982).
9. *Rare Gas Solids*, Ed. by M. L. Klein and J. A. Venables (Academic, London, 1977), Vol. II.
10. *Principles of the Physics of Ultrasound*, Ed. by V. A. Shutilov (Leningr. Gos. Univ., Leningrad, 1980).
11. J. R. Olson, R. O. Pohl, J. W. Vandersande, *et al.*, Phys. Rev. B **47** (22), 14850 (1993).
12. D. P. Spitzer, J. Phys. Chem. Solids **31** (1), 19 (1970).

13. V. A. Konstantinov, V. G. Manzhelii, S. A. Smirnov, and A. M. Tolkachev, Fiz. Nizk. Temp. **14** (2), 189 (1988) [Sov. J. Low Temp. Phys. **14**, 104 (1988)].
14. V. A. Konstantinov, V. G. Manzhelii, V. P. Revyakin, and S. A. Smirnov, Fiz. Nizk. Temp. **21** (1), 102 (1995) [Low Temp. Phys. **21**, 78 (1995)].
15. V. A. Konstantinov, V. G. Manzhelii, V. P. Revyakin, and S. A. Smirnov, Physica B (Amsterdam) **291** (1), 59 (2000).
16. V. A. Konstantinov, S. A. Smirnov, and V. P. Revyakin, Prib. Tekh. Éksp. **42** (1), 145 (1999).
17. V. G. Manzhelii, A. I. Prokhvatilov, I. Ya. Minchina, and L. D. Yantsevich, *Handbook of Binary Solutions of Cryocrystals* (Begell House, New York, 1996).
18. P. A. Bezuglyĭ, L. M. Tarasenko, and O. I. Baryshevskiĭ, Fiz. Tverd. Tela (Leningrad) **13** (8), 2392 (1971) [Sov. Phys. Solid State **13**, 2003 (1972)].
19. R. Berman, *Thermal Conduction in Solids* (Clarendon, Oxford, 1976; Mir, Moscow, 1979).
20. L. A. Turk and P. G. Klemens, Phys. Rev. B **9** (10), 4422 (1974).
21. V. V. Dudkin, B. Ya. Gorodilov, A. I. Krivchikov, and V. G. Manzhelii, Fiz. Nizk. Temp. **26** (9–10), 1023 (2000) [Low Temp. Phys. **26**, 762 (2000)].

Translated by O. Borovik-Romanova

Physics of the Solid State, Vol. 44, No. 5, 2002, pp. 864–869. Translated from Fizika Tverdogo Tela, Vol. 44, No. 5, 2002, pp. 830–835.

SEMICONDUCTORS AND DIELECTRICS

EPR of Er^{3+}, Nd^{3+}, and Ce^{3+} Ions in $YAlO_3$ Single Crystals

G. R. Asatryan* and J. Rosa**

**Ioffe Physicotechnical Institute, Russian Academy of Sciences, ul. Politekhnicheskaya 26, St. Petersburg, 194021 Russia*

e-mail: Hike.Asatryan@pop.ioffe.rssi.ru

***Institute of Physics, Czech Academy of Sciences, Division of Solid State Physics, 16200 Prague 6, Czech Republic*

Received July 12, 2001

Abstract—EPR spectra of the Er^{3+}, Nd^{3+}, and Ce^{3+} ions substituting for the Y^{3+} ion in the $YAlO_3$ yttrium orthoaluminate lattice are studied. The EPR spectra of these rare-earth ions are described by a spin Hamiltonian of rhombic symmetry with an effective spin $S = 1/2$. The principal values of the g tensors were determined from an analysis of the angular dependences of the EPR spectra. The orientation of the local magnetic axes of paramagnetic centers relative to the $YAlO_3$ crystallographic directions are shown to depend on the actual rare-earth species. The EPR spectra exhibit a hyperfine structure due to the ^{167}Er, ^{143}Nd, and ^{145}Nd odd isotopes, which permitted unambiguous identification of these spectra. The hyperfine coupling constants for the odd erbium and neodymium isotopes are determined. © *2002 MAIK "Nauka/Interperiodica".*

1. INTRODUCTION

Rare-earth-doped single crystals of yttrium orthoaluminate ($YAlO_3$), also called yttrium aluminum perovskite (YAP), enjoy wide application in quantum electronics [1, 2]. Interest in these materials has been increasing in recent years in connection with the possibility of the use of cerium-doped YAP as fast high-efficiency scintillators [3–7]. For instance, lutecium orthoaluminate $LuAlO_3$ doped with cerium has demonstrated the highest scintillator efficiency, to date, for the detection of positron annihilation, which makes it a potentially promising material for use in positron emission tomography in medicine [8]. Although EPR is widely employed in studies of laser crystals, it has thus far been only scarcely applied to YAP materials. Only a few ions (Cr^{3+}, Fe^{3+}, Gd^{3+}, Ti^{3+}) have been investigated in $YAlO_3$ single crystals by EPR to date [9–16].

We report here on a comprehensive study of EPR spectra of three rare-earth ions (Er^{3+}, Nd^{3+}, Ce^{3+}) in yttrium orthoaluminate. These ions were detected and studied by EPR in $YAlO_3$ for the first time, and the results were published by us in [17].

2. EXPERIMENTAL TECHNIQUES

We studied $YAlO_3$ single crystals doped by cerium, erbium, and neodymium ions to concentrations of up to ~0.3 at. %. The crystals were grown by the Czochralski method and by directed horizontal crystallization at Preciosa Crytur, Ltd (Turnov, Czech Republic), and at the Institute for Raw Materials Synthesis (Aleksandrov, Russia). The EPR spectra were obtained in the 3-cm wavelength range at temperatures from 4 to 50 K on commercial JEOL-JES-PE-3X and ERS-230 radiospectrometers. The samples were oriented by x-ray diffraction to within ±0.5° and cut in the *ab*, *ac*, and *bc* crystallographic planes to form rectangular parallelepipeds measuring $1.5 \times 2 \times 5$ mm. More precise alignment of the principal magnetic axes relative to the external magnetic field was achieved radiospectroscopically, directly in the microwave cavity, by matching the EPR signals due to inequivalent positions. Our samples exhibited, in addition to the EPR response of the Er^{3+}, Nd^{3+}, and Ce^{3+} ions, signals from residual impurities, which made comprehensive investigation of the orientational dependences of the spectra and, in particular, of the hyperfine structure (HFS) due to the odd ^{167}Er, ^{143}Nd, and ^{145}Nd isotopes difficult. It should be pointed out that the EPR spectra of Mo^{3+} ions in yttrium orthoaluminate crystals grown in molybdenum containers were observed for the first time and the results of their detailed investigation will be published separately.

3. EXPERIMENTAL RESULTS

The crystal structure of yttrium orthoaluminate belongs to the D_{2h}^{16}–P_{bnm} orthorhombic space group and has been described in detail in a number of publications (see, e.g., [18–20]). The orthorhombic unit cell of $YAlO_3$ contains four distorted perovskite pseudocells. Therefore, the Y^{3+} and Al^{3+} ions reside in four structurally inequivalent positions. The aluminum ions are surrounded by six oxygen ions, forming a weakly distorted octahedron (local symmetry C_i). The nearest neighbor environment of the Y^{3+} ions is more complex and is more strongly distorted (local symmetry C_s). Figure 1

presents the structure of yttrium orthoaluminate with identification of the positions of the Y^{3+} ions (large hatched circles) substituted by Er^{3+}, Nd^{3+}, and Ce^{3+}. In contrast to the aluminum positions, all ions of oxygen and yttrium are displaced by a few tenths of an angstrom with respect to the ideal perovskite positions. The aluminum sites have only inversion symmetry, and the yttrium sites possess a mirror symmetry plane perpendicular to the *c* axis of the crystal.

One of the principal *g*-tensor axes for the paramagnetic ions localized at the Y^{3+} sites must coincide with the crystal *c* axis, and the two others must lie in the *ab* plane. Moreover, the Y^{3+} ions are related pairwise by inversion site symmetry through the aluminum positions, such that there are only two magnetically inequivalent positions for an arbitrary orientation of an external magnetic field **B**, as well as for **B** rotating in the *ab* plane. If the external magnetic field rotates in the *bc* or *ac* planes, the pattern becomes simplified, because in this case, all four positions are magnetically equivalent and the EPR spectrum has one line only (neglecting the HFS). Thus, one EPR line is also observed when the external magnetic field is parallel to the principal crystal axes.

Figure 2 presents EPR spectra recorded in three principal magnetic-field orientations (**B** ∥ *a*, **B** ∥ *b*, and **B** ∥ *c*) at 12 K for a frequency of 9.24 GHz. One can separate spectra of four types out of the EPR response, which, as will be shown later, belong to the rare-earth ions Er^{3+}, Nd^{3+}, and Ce^{3+}, as well as to the transition element Mo^{3+}. Erbium, neodymium, and molybdenum have odd-number isotopes that possess a nuclear magnetic moment, and their EPR spectra allow unambiguous identification based on the HFS.

3.1. Erbium Ions

The erbium ion Er^{3+} has an electronic configuration $4f^{11}$ with the ground state $^4I_{15/2}$. The energy level diagram of the Er^{3+} ion in $YAlO_3$ single crystals was studied in [1, 2]. The ground-state multiplet $^4I_{15/2}$ is crystal-field split into a number of Stark components, with the lowest of them involved in an EPR transition in the 3-cm range. Because of the large splitting between the ground and the next Stark level (51 cm^{-1}), detection of the excited state in EPR spectra has not been successful. Natural erbium contains, in addition to even isotopes with a zero nuclear spin moment, an odd isotope ^{167}Er with a nuclear spin $I = 7/2$. Its natural abundance is 22.94%. The EPR spectrum of $YAlO_3$ (Fig. 2) agrees fully with the one expected for Er^{3+}. We observed eight nonequidistant lines in it representing the magnetic HFS components due to the odd isotope, whereas the strong central line should be assigned to the even isotopes. The line intensity ratio is in accord with the natural abundance of the erbium isotopes. The EPR spectrum of the Er^{3+} ions in $YAlO_3$ is anisotropic; as the orientation of the external magnetic field relative to the crystal crystallographic axes changes, the EPR lines shift with the magnetic field and the distance between the HFS components also changes; however, their separation remains nonequidistant. The circles in Figs. 3 and 4 refer to the experimental positions of the strong Er^{3+} line of the even erbium isotope obtained with the crystal rotated in a magnetic field in the *ab* and *bc* planes, respectively.

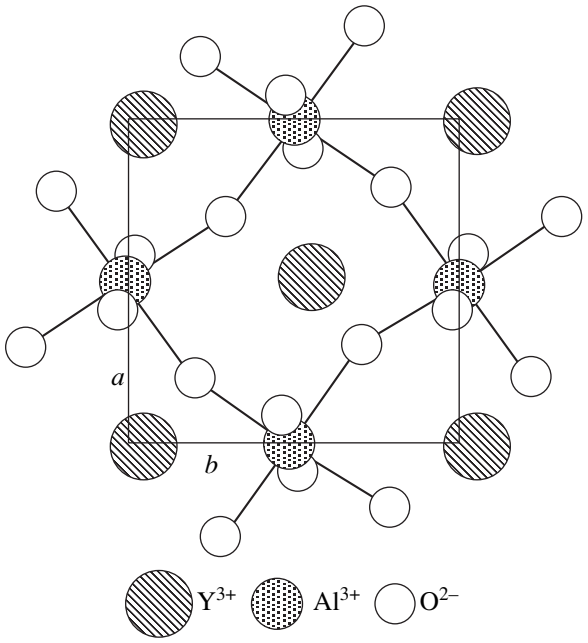

Fig. 1. Projection of the $YAlO_3$ lattice structure on the *ab* plane.

These experimental orientational relations can be described by a rhombic-symmetry spin Hamiltonian,

$$\mathcal{H} = \beta \mathbf{BgS} + \mathbf{SAI}, \quad (1)$$

where the effective spin $S = 1/2$; **g** and **A** are the tensors of the *g* factor and HFS interaction, respectively; and β is the Bohr magneton. The solid lines in Figs. 3 and 4 show the theoretical plots obtained by direct diagonalization of the spin Hamiltonian (1) using the *R*-Spectr code [21]. The *g*-tensor parameters used are as follows: $g_x = 8.98 \pm 0.01$, $g_y = 8.13 \pm 0.01$, and $g_z = 2.73 \pm 0.01$. Note that the principal directions of the Er^{3+} local magnetic axes in yttrium orthoaluminate are oriented so that the *x* axes are along the *c* axis of the crystal and the *y* and *z* axes lie in the *ab* plane. Experimental measurements showed that the local magnetic axis *z* makes an angle of 41.4° with the *a* axis of the crystal in the *ab* plane. The orientational relations of the HFS components yielded the following HFS constants for ^{167}Er: $A_x = 329 \times 10^{-4}$, $A_y = 315 \times 10^{-4}$, and $A_z = 250 \times 10^{-4}$ cm^{-1}.

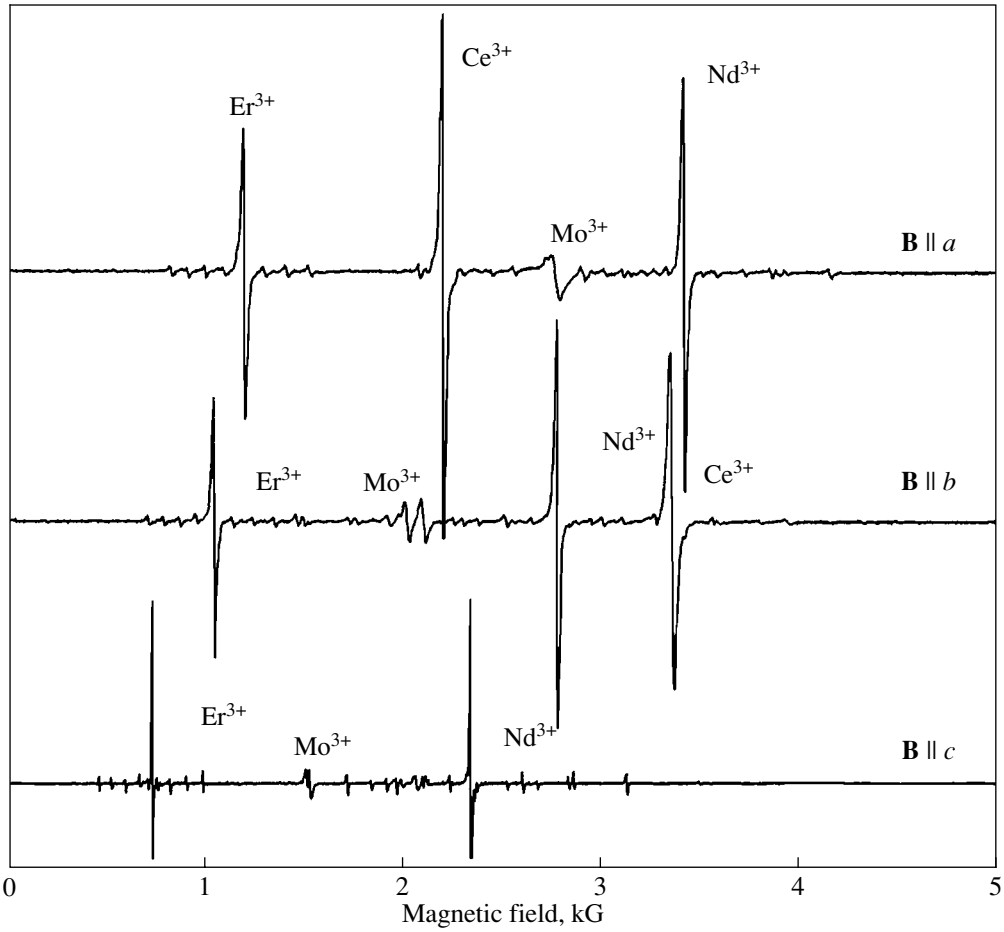

Fig. 2. EPR spectra of Er^{3+}, Nd^{3+}, and Ce^{3+} ions in $YAlO_3$ single crystals obtained for different magnetic-field orientations at ν = 9.24 GHz and T = 12 K.

For the mean g factor, we obtained $\langle g \rangle = (g_x + g_y + g_z)/3 = 6.61$, which agrees quite well with the value of the g factor obtained for the Kramers doublet Γ_7 of Er^{3+} ions in a cubic crystal field, which is quoted to be 6.8 [22].

3.2. Neodymium Ions

The Nd^{3+} ion has an electronic configuration $4f^3$ and ground state $^4I_{9/2}$ [1, 2]. Because of the large splitting between the ground and the first excited Stark components (118 cm^{-1}), the EPR spectra measured in the *X* range can reveal only the ground state. The natural-abundance neodymium has two even and, in addition, two odd isotopes, each having a nuclear spin I = 7/2. The natural abundances of ^{143}Nd and ^{145}Nd are 12.17 and 8.30%, respectively, and their nuclear magnetic moment ratio is 1.609. The observed EPR spectrum Nd^{3+} exhibits two groups of eight nonequidistant lines each, which represent HFS components due to the odd neodymium isotopes; the central strong line derives from the even isotopes. The ratio of the distances between the HFS lines in each group corresponds to the nuclear magnetic-moment ratio for the odd isotopes, and the intensity ratio of the observed EPR lines reflects the natural abundance of these isotopes.

The EPR spectrum of Nd^{3+} ions in $YAlO_3$ is anisotropic. The squares in Figs. 3 and 4 show the experimental values of the resonant magnetic fields corresponding to the position of the strong lines of the even neodymium isotope obtained on a crystal rotated in a magnetic field in the *ab* and *bc* planes, respectively. These experimental orientational relations are described by the spin Hamiltonian (1) with an effective electronic spin S = 1/2 and a nuclear spin I = 7/2. As seen from Figs. 3 and 4, the experimental resonance fields fit well to the calculated curves. The experimental angular dependences of the EPR response yielded the following principal values of the g tensor: $g_x = 2.83 \pm 0.01$, $g_y = 2.58 \pm 0.01$, and $g_z = 1.69 \pm 0.01$. The principal local magnetic axes of the Nd^{3+} ion in yttrium orthoaluminate were found to have the same orientation as those of Er^{3+}. The local magnetic axis z makes an angle of

30.5° with the *a* axis in the *ab* plane. The HFS constants for the ^{143}Nd isotope were derived as $A_x = 295 \times 10^{-4}$, $A_y = 256 \times 10^{-4}$, and $A_z = 192 \times 10^{-4}$ cm^{-1}.

The mean *g* factor $\langle g \rangle = 2.37$ agrees well with that of the Kramers doublet Γ_6 of the Nd^{3+} ion in a cubic crystal field, which was quoted as 2.67 in [22].

3.3. Cerium Ions

The Ce^{3+} ion has the $4f^1$ electronic configuration with the ground state $^2F_{5/2}$. In yttrium orthoaluminate crystals, ions of cerium, as of most rare-earth elements, substitute for Y^{3+}. Natural cerium has only two even isotopes, ^{140}Ce and ^{142}Ce. Because of the absence of odd isotopes, EPR spectra of Ce^{3+} do not have HFS. The single strong line that we assigned to cerium ions was identified by studying $YAlO_3$ samples with different concentrations of these ions, as well as on the basis of the small mean *g* factor $\langle g \rangle$, which is characteristic only of the Ce^{3+} cerium ions. Figures 3 and 4 show (with crosses) the experimental values corresponding to the positions of the Ce^{3+} line obtained by rotating the crystal in a magnetic field in the *ab* and *bc* planes. The strongly anisotropic orientational dependences of the Ce^{3+} EPR spectra in $YAlO_3$ single crystals are described by a spin Hamiltonian of the type of Eq. (1) with an effective electron spin $S = 1/2$. The experimental and calculated curves are seen to be in good agreement. We used the experimental orientational dependences of the EPR spectra to derive the following values for the *g*-tensor parameters: $g_x = 0.395 \pm 0.005$, $g_y = 0.402 \pm 0.01$, and $g_z = 3.614 \pm 0.005$. The principal magnetic axes of the Ce^{3+} ion are oriented so that the *x* axes are along the *c* crystallographic axis and the *y* and *z* axes lie in the *ab* plane. The local magnetic axis *z* makes an angle 31.8° with the crystallographic axis *a* in the *ab* plane. The EPR linewidth of Ce^{3+} in $YAlO_3$ is also anisotropic and varies from 4 to 140 G with the external magnetic field changing orientation from the g_x axis to the g_y axis. The mean *g* factor $\langle g \rangle = 1.47$ agrees well with the *g* factor for the Kramers doublet Γ_6 of the Ce^{3+} ion in a cubic crystal field, which is 1.43 [22].

Ce^{3+} EPR spectra of $YAlO_3$ exhibit two main strong lines due to magnetically inequivalent centers and, in addition, a number of weaker lines (by two to three orders of magnitude). These lines crowd around the main cerium lines and exhibit similar angular and temperature dependences.

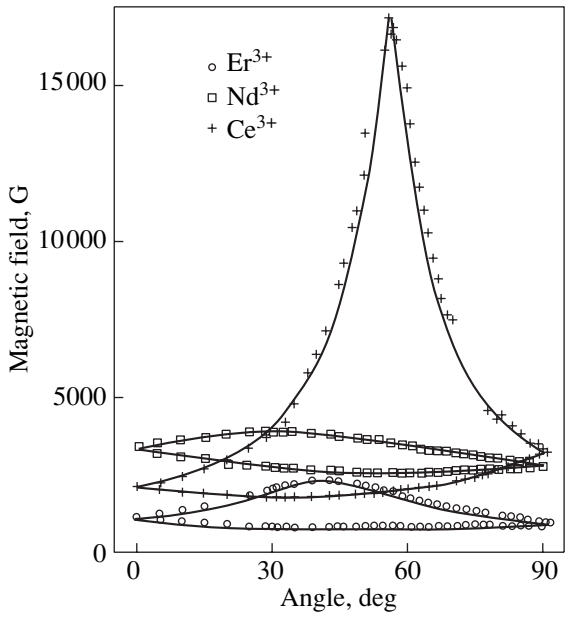

Fig. 3. Calculated (solid lines) and experimental (symbols) angular dependences of the resonant magnetic fields of the Er^{3+}, Nd^{3+}, and Ce^{3+} ions in the *ab* plane of the yttrium orthoaluminate crystal lattice.

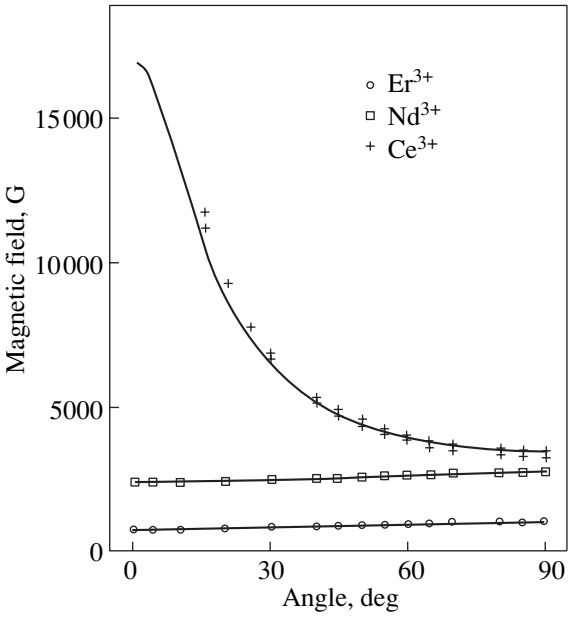

Fig. 4. Calculated (solid lines) and experimental (symbols) angular dependences of the resonant magnetic fields of the Er^{3+}, Nd^{3+}, and Ce^{3+} ions in the *bc* plane of $YAlO_3$.

4. DISCUSSION OF RESULTS

Our EPR study of yttrium orthoaluminate single crystals revealed and unambiguously identified the EPR spectra of the impurity ions Er^{3+}, Nd^{3+}, and Ce^{3+} substituting for Y^{3+}. It was found that the local magnetic axes *z* and *y* of different paramagnetic rare-earth ions residing at equivalent sites are oriented differently with respect to the crystal axes. The direction of the *z* axis relative to the *a* axis in the *ab* plane is 41.1° for Er^{3+}, 30.5° for Nd^{3+}, and 31.8° for Ce^{3+}. Note that an

earlier measurement of this angle for the case of Gd^{3+} substituted for Y^{3+} in $YAlO_3$ yielded 25° [14]. The Y^{3+} ion in $YAlO_3$ crystals is known to be displaced from the ideal perovskite position by a few tenths of an angstrom. Substitution of rare-earth ions with different ionic radii (1.00, 1.06, 1.12, and 1.14 Å for erbium, gadolinium, neodymium, and cerium, respectively) for the Y^{3+} ion [$r_{ion}(Y^{3+}) = 1.02$ Å] distorts the nearest environment of a paramagnetic center differently; it is, therefore, conceivable that the principal local magnetic axes g_z orient differently. The above values of the ionic radii were taken from [1]. The nearest neighbor environment of the paramagnetic rare-earth centers in yttrium orthoaluminate is distorted in such a way that the mirror symmetry plane does not change and, therefore, the magnetic axis *x* directed perpendicular to it (along the *c* crystal axis) does not change its orientation. A difference in the angles between the magnetic axes g_z and the crystallographic directions is also observed to exist for 3*d* transition ions substituting for Al^{3+} in the octahedral sites [9–16]. The difference between the angles for Cr^{3+} and Ti^{3+} in $YAlO_3$ is assigned in [15] to the absence and the presence of the Jahn–Teller effect in the former and the latter cases, respectively.

The absence of odd cerium isotopes with a nonzero nuclear magnetic moment entails some difficulties in the interpretation of the Ce^{3+} EPR spectra. However, the absence of the HFS and the narrowness of the EPR lines permit one to detect very weak EPR signals near the main signal, which is due to Ce^{3+} ions in a regular environment. We also observed weak EPR lines in cerium-doped $YAlO_3$ crystals. Part of these lines, which we call satellites, are crowded near the two main strong cerium lines corresponding to the magnetically inequivalent positions. We assigned these satellite lines to the Ce^{3+} ions, because the values of the *g* factors, the character of the angular dependences of the resonance magnetic fields, and the linewidths correlate with the characteristics of the main EPR signals of the Ce^{3+} ions. Each of these satellites is weaker in intensity than the main line by a factor 100–1000 and exhibits a slight deviation in the direction of the principal magnetic axes, including the axis parallel to the c axis of the crystal. These lines are apparently due to cerium ions whose nearest environment contains a defect distorting the crystal field at the paramagnetic center. These defects are very likely to be the Y^{3+} ions substituting for the Al^{3+} ions in the octahedral sites. This brings about displacements of the nearest neighbor atoms of the paramagnetic center and a change in the symmetry and magnitude of the crystal field on it. The direction of the local magnetic axis oriented along the *c* crystal axis also changes. It is also possible that some of the satellite lines originate from the Ce^{3+}–Ce^{3+} pairs. Similar centers were observed by us in EPR spectra of Ce^{3+} ions in the yttrium-aluminum garnet $Y_3Al_5O_{12}$ [23]. The same complex centers also possibly exist for erbium and neodymium; however, their detection is made difficult by the lower anisotropy of their EPR spectra compared to that of cerium and, hence, by the weaker sensitivity of the EPR line position to changes in the crystal field. The HFS, which is observed in EPR spectra of Er^{3+} and Nd^{3+}, also hampers identification of the satellite lines.

The optical spectra of $YAlO_3$ are known [5] to have additional luminescence peaks due to cerium ions, which may add up in integrated intensity to nearly 10% of the main band. The EPR satellites, which were observed in our experiments and were assigned to Ce^{3+} ions with a defect in the nearest environment associated with off-stoichiometry and to pairs, amount to 1.5–2% of the main lines in integrated intensity.

The strong angular dependence of the Ce^{3+} EPR linewidth in yttrium orthoaluminate, which varies from 4 G for $\mathbf{B} \parallel z$ to 140 G for $\mathbf{B} \parallel y$, is in qualitative agreement with the *g* factor anisotropy and is apparently caused by an unresolved superhyperfine structure due to ligands.

ACKNOWLEDGMENTS

The authors are indebted to J. Kvapil and S.A. Smirnova for providing the cerium-doped yttrium orthoaluminate single crystals, P.G. Baranov for valuable discussions, and V.G. Grachev for the *R*-spectr code for calculation of the spin Hamiltonian parameters by direct diagonalization.

REFERENCES

1. A. A. Kaminskiĭ, *Laser Crystals* (Nauka, Moscow, 1975).
2. A. A. Kaminskiĭ and B. M. Antipenko, *Multilevel Functional Diagrams of Crystalline Lasers* (Nauka, Moscow, 1989).
3. G. Blasse, Chem. Mater. **6**, 1465 (1994).
4. M. Ishii and M. Kobayashi, Prog. Cryst. Growth Charact. Mater. **23**, 245 (1992).
5. J. A. Mares, M. Nikl, C. Pedrini, *et al.*, Mater. Chem. Phys. **32**, 342 (1992).
6. J. A. Mares and J. Kvapil, Cesk. Cas. Fyz. A **38**, 248 (1988).
7. W. Rossner and B. C. Grabmaier, J. Lumin. **48–49**, 29 (1991).
8. J. A. Mares, M. Nikl, J. Chval, *et al.*, Chem. Phys. Lett. **341**, 311 (1995).
9. J. P. van der Ziel, F. R. Merrit, and L. G. van Uitert, J. Chem. Phys. **50**, 4317 (1969).
10. A. Pinto and N. Z. Sherman, J. Magn. Reson. **6**, 422 (1972).
11. R. L. White, G. F. Herrmann, J. W. Carson, and M. Mandel, Phys. Rev. A **136**, 231 (1964).
12. O. F. Shirmer, K. W. Blazey, W. Berlinger, and R. Diehl, Phys. Rev. B **11**, 4201 (1975).
13. N. M. Nizamutdinov, N. M. Khasanova, G. R. Bulka, *et al.*, Kristallografiya **32**, 695 (1987) [Sov. Phys. Crystallogr. **32**, 408 (1987)].

14. N. M. Khasanova, N. M. Nizamutdinov, G. R. Bulka, V. M. Vinokurov, *et al.*, *Physics of Minerals and Their Synthetic Analogues* (Kazans. Univ., Kazan, 1988), p. 73.
15. M. Yamaga, H. Takeuchi, T. P. J. Han, and B. Henderson, J. Phys.: Condens. Matter **5**, 8097 (1993).
16. M. Yamaga, T. Yosida, B. Henderson, *et al.*, J. Phys.: Condens. Matter **4**, 7285 (1992).
17. H. R. Asatryan, J. Rosa, and J. A. Mares, Solid State Commun. **104**, 5 (1997).
18. S. Geller and V. Bala, Acta Crystallogr. **9**, 1019 (1956).
19. P. Coppens and M. Eibshutz, Acta Crystallogr. **19**, 524 (1965).
20. R. Diehl and G. Brandt, Mater. Res. Bull. **10**, 85 (1975).
21. V. G. Grachev, Zh. Éksp. Teor. Fiz. **92**, 1834 (1987) [Sov. Phys. JETP **65**, 1029 (1987)].
22. A. Abragam and B. Bleaney, *Electron Paramagnetic Resonance of Transition Ions* (Clarendon, Oxford, 1970; Mir, Moscow, 1972).
23. H. R. Asatryan, R. A. Babunts, G. Baranov, *et al.*, in *Proceedings of the 10th Feofiliv Symposium on Spectroscopy of Crystals Doped with Transition and Rare-Earth Metal Ions, St. Petersburg, 1995*, p. 283.

Translated by G. Skrebtsov

Physics of the Solid State, Vol. 44, No. 5, 2002, pp. 870–879. Translated from Fizika Tverdogo Tela, Vol. 44, No. 5, 2002, pp. 836–844.

SEMICONDUCTORS AND DIELECTRICS

Optical Properties and Electronic Structure of Fluorite and Corundum

V. V. Sobolev, A. I. Kalugin, V. Val. Sobolev, and S. V. Smirnov

Udmurt State University, Krasnoarmeĭskaya ul. 71, Izhevsk, 426034 Russia

e-mail: sobolev@uni.udm.ru

Received August 20, 2001

Abstract—The complete sets of 12 fundamental optical functions for fluorite crystals in the range 5–39 eV and corundum crystals in the range 2–30 eV are determined from the experimental and theoretical spectra known for certain of these functions. The main features and generalities of these functions are revealed. A theoretical analysis of the optical spectra obtained is performed using the known theoretical band diagrams and the spectra of ε_2. © *2002 MAIK "Nauka/Interperiodica".*

1. INTRODUCTION

Among strongly ionic crystals, fluorite CaF_2 and corundum α-Al_2O_3 are the most convenient model materials. These compounds are widely used in microelectronics, laser materials science, catalysis, radiation dosimetry, and nuclear reactors [1, 2]. In this respect, their electronic structure has been intensively investigated both experimentally ([3–6] for CaF_2 and [7–12] for Al_2O_3) and theoretically ([13–18] for CaF_2 and [19–24] for Al_2O_3) over a wide range of energies.

It is universally accepted that comprehensive data on the specific features in the electronic structure of crystals over a wide range of energies can be obtained from the spectra of 12 fundamental optical functions: the reflection coefficient R, the imaginary (ε_2) and real (ε_1) parts of the permittivity ε, the bulk ($-\mathrm{Im}\varepsilon^{-1}$) and surface [$-\mathrm{Im}(1 + \varepsilon)^{-1}$] characteristic electron energy loss functions, n_{eff}, $\varepsilon_{\mathrm{eff}}$, and others [25]. The experimental spectra of R [3, 4], ε_2, ε_1 [5], and $-\mathrm{Im}\varepsilon^{-1}$ [6] for CaF_2 crystals and the spectra of R [7–12] for Al_2O_3 crystals are available in the literature. In a number of works, the spectra of other optical functions were calculated from the measured spectra. Theoretical optical spectra were obtained only for ε_2 in [17, 18] for CaF_2 and in [22–24] for Al_2O_3 crystals. The experimental data reported in different works were not compared. Theoretical spectra of ε_2 in [17, 18, 23, 24] were compared with the experimental spectra of ε_2 for CaF_2 [5] and the experimental spectra of R for Al_2O_3 [11].

The aim of the present work was to calculate four complete sets of the spectra of the optical functions for CaF_2 and Al_2O_3 crystals with the use of the experimental spectra taken from [3–6] and [8–11], to decompose the spectra of ε_2 and $-\mathrm{Im}\varepsilon^{-1}$ into components, and to compare and discuss the experimental, calculated, and theoretical data.

2. COMPUTATIONAL TECHNIQUES

The most frequently applied techniques of determining the complete set of optical functions involve their calculation from the known experimental reflectance spectrum over a wide range of energies with the use of special programs. As a rule, the computational programs are developed using the Kramers–Kronig integral relationships and formulas for the optical functions. A large number of similar techniques have been devised to date. For the most part, these methods differ in the procedure of extrapolating $R(E)$ to unknown energy ranges [25]. The calculations of the optical functions from the known spectra of ε_2 or $-\mathrm{Im}\varepsilon^{-1}$ are performed in a similar manner.

The calculation procedures we used here for calculating the complete set of optical function and decomposing the integrated spectra of ε_2 and $-\mathrm{Im}\varepsilon^{-1}$ into individual components were described in detail in [25–27] and discussed in [28–30].

3. RESULTS OF CALCULATIONS AND DISCUSSION FOR CaF_2

The reflectance spectra were experimentally measured in the range 6–36 eV at 90 K by Rubloff [3] and in the range 5–21 eV at 4.2 K by Ganin *et al.* [4]. Barth *et al.* [5] recorded the spectra of ε_2 and ε_1 in the range 10–35 eV at 300 K by using the ellipsometric method, and Frandon *et al.* [6] experimentally obtained the spectrum of $-\mathrm{Im}\varepsilon^{-1}$ in the range 8–39 eV at 300 K by characteristic electron energy loss spectroscopy. On the basis of these spectra in the framework of a unified approach, we calculated the sets of fundamental optical functions for CaF_2 in the range 5–39 eV. In the present work, we will briefly dwell only on the spectra of R, ε_2, ε_1, $-\mathrm{Im}\varepsilon^{-1}$, $-\mathrm{Im}(1 + \varepsilon)^{-1}$, n_{eff}, and $\varepsilon_{\mathrm{eff}}$.

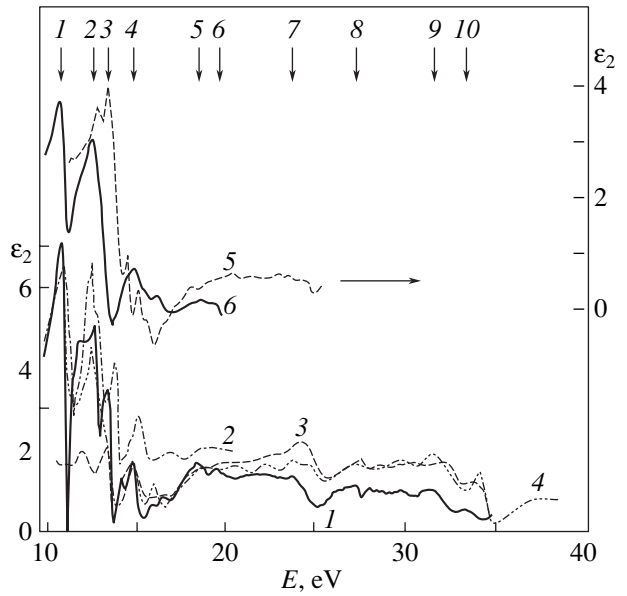

Fig. 1. (*3*) Experimental spectrum $\varepsilon_2(E)$ of the CaF_2 crystal [5], (*1*, *2*) the spectra $\varepsilon_2(E)$ calculated from the experimental spectra $R(E)$ taken from (*1*) [3] and (*2*) [4], (*4*) the spectrum $\varepsilon_2(E)$ calculated from the experimental spectrum $-\mathrm{Im}\varepsilon^{-1}(E)$ taken from [6], and (*5*, *6*) the theoretical spectra $\varepsilon_2(E)$ taken from (*5*) [17] and (*6*) [18]. Arrows and numbers indicate the positions of the maxima in curve *1*.

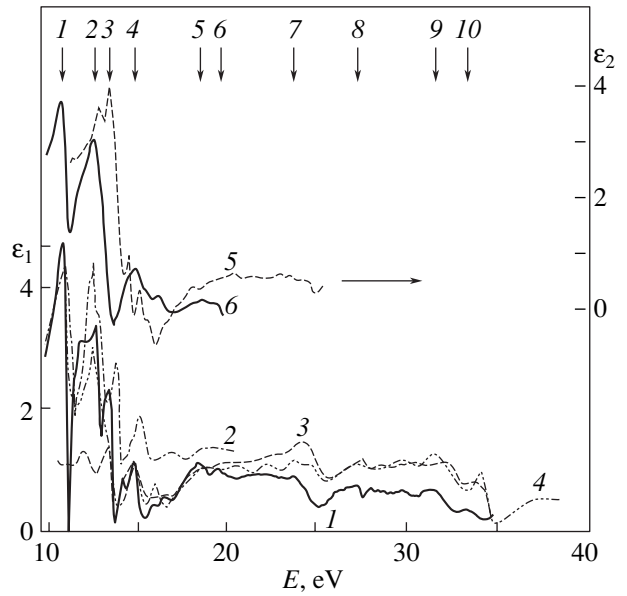

Fig. 2. (*3*) Experimental spectrum $\varepsilon_1(E)$ of the CaF_2 crystal [5], (*1*, *2*) the spectra $\varepsilon_1(E)$ calculated from the experimental spectra $R(E)$ taken from (*1*) [3] and (*2*) [4], (*4*) the spectrum $\varepsilon_1(E)$ calculated from the experimental spectrum $-\mathrm{Im}\varepsilon^{-1}(E)$ taken from [6], and (*5*, *6*) the spectra $\varepsilon_1(E)$ calculated from the theoretical spectra $\varepsilon_2(E)$ taken from (*5*) [17] and (*6*) [18]. Arrows and numbers indicate the positions of the maxima in curve *1*.

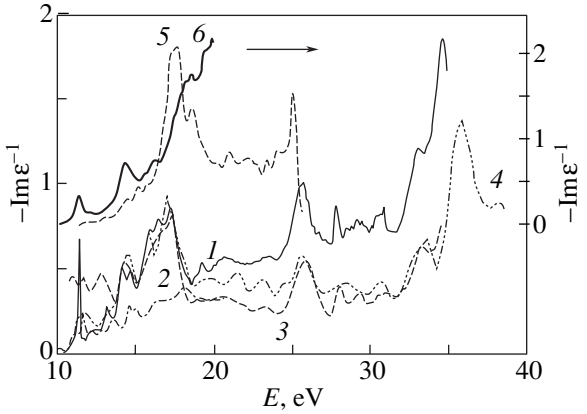

Fig. 3. (*4*) Experimental bulk characteristic electron energy loss spectrum $-\mathrm{Im}\varepsilon^{-1}(E)$ of the CaF_2 crystal [6], (*1*, *2*) the spectra $-\mathrm{Im}\varepsilon^{-1}(E)$ calculated from the experimental spectra $R(E)$ taken from (*1*) [3] and (*2*) [4], (*3*) the spectrum $-\mathrm{Im}\varepsilon^{-1}(E)$ calculated from the experimental spectra $\varepsilon_1(E)$ and $\varepsilon_2(E)$ taken from [5], and (*5*, *6*) the spectra $-\mathrm{Im}\varepsilon^{-1}(E)$ calculated from the theoretical spectra $\varepsilon_2(E)$ taken from (*5*) [17] and (*6*) [18].

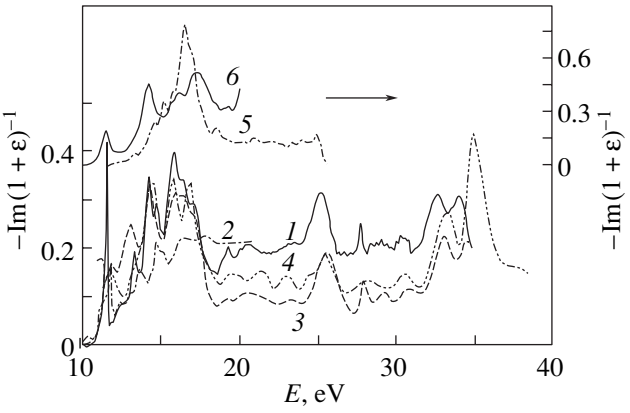

Fig. 4. (*1*–*6*) Surface characteristic electron energy loss spectra $-\mathrm{Im}(1+\varepsilon)^{-1}(E)$ calculated for the CaF_2 crystal from the spectra (*4*) $-\mathrm{Im}\varepsilon^{-1}(E)$ [6] $R(E)$ taken from (*1*) [3] and (*2*) [4], (*3*) $\varepsilon_1(E)$ and $\varepsilon_2(E)$ taken from [5], and $\varepsilon_2(E)$ taken from (*5*) [17] and (*6*) [18].

Let us compare the four reflectance spectra in Figs. 1–4. These spectra have a similar character and contain ten principal intense peaks at 11.15 (peak *1*), 13.05 (peak *2*), 13.8 (peak *3*), 15.55 (peak *4*), 19.1 (peak *5*), 20.3 (peak *6*), 25.05 (peak *7*), 27.7 (peak *8*), 32.75 (peak *9*), and 34.3 eV (peak *10*) [3]. The locations of many maxima in the four spectra $R(E)$ differ by 0.1–0.3 eV. Most likely, this difference is associated with

specific features in the calibrations used in the four works [3–6]. Two main differences should be noted in the spectral structures. First, the most long-wavelength and intense peak *1* manifested itself in [5] as an initial portion of a very weak band; this can be explained by the long-wavelength limit of spectrum recording. Second, peak *2* has a triplet [4] or doublet [3, 5, 6] structure. The differences between the intensity distributions in the four $R(E)$ spectra are much more pronounced. Compared to the data obtained in [3], the relative changes $\Delta R/R$ in the intensities measured in other works are as follows: +0.25 [4] and –0.10 [6] for peak *1*; +0.22 [4], –0.18 [6], and –0.50 [5] for peak *2*; 0.0 [4] and –0.3 [5, 6] for peak *3*; ~–0.1 [4–6] for peak *4*; +0.7 [4], ~–1 [5], and –0.5 [6] for the doublet with peaks *5* and *6*; and ~0.5 [5, 6] for peaks *7* and *8*. It should be noted that the spectra of R in [3] and the spectra of ε_2 and ε_1 in [5] were measured under continuous high-intensity synchrotron radiation, whereas the spectrum of R in [4] was recorded with a laboratory, line, low-intensity light source. In the characteristic electron energy loss spectrum $-\mathrm{Im}\varepsilon^{-1}(E)$, all peaks are very weak compared to the most intense, very broad plasmon excitation band. Barth *et al.* [5] devised a unique ellipsometric technique for recording the spectra of ε_2 and ε_1 in the energy range $E > 6$ eV. They noted that large errors can arise in calculations of ε_2 and ε_1 due to a superposition of diffraction orders of the lattice in the range 8–20 eV. Making allowance for the specific features of the measuring techniques used in [3–6], we can draw the conclusion that the most correct spectrum $R(E)$ of CaF_2 in the range 8–18 eV was obtained in [3]. It is of interest that the experimental spectrum $R(E)$ of the CaF_2 single-crystal cleavage [3] is in close agreement with the $R(E)$ spectrum calculated in our work from the measured spectrum of $-\mathrm{Im}\varepsilon^{-1}$ in thin polycrystals [6]. In the energy range 18–33 eV, the intensity of the $R(E)$ spectrum recorded in [3] is nearly twice as high as that of the spectra measured in [5, 6]. Possibly, this is associated both with the different techniques used in accounting for scattered light in [3, 5] and with the specific features in the calibration of the $-\mathrm{Im}\varepsilon^{-1}$ loss function in [6]. In this respect, the $R(E)$ spectra obtained for the CaF_2 crystal by four essentially different methods were compared for the first time in the present work. This allowed us to reveal and estimate quantitatively the common features and differences in these spectra and to analyze the possible errors in determining the energies and intensities of the maxima corresponding to optical transitions.

The specific features revealed in the $R(E)$ spectra naturally manifest themselves in the spectra of other optical functions (Figs. 1–4). The four spectra $\varepsilon_2(E)$, $\varepsilon_1(E)$, and $-\mathrm{Im}\varepsilon^{-1}(E)$ contain analogs of the ten most intense peaks observed in the spectrum $R(E)$. For $\varepsilon_2(E)$, these peaks either are observed at about the same energies (peaks *1*, *2*, *5*) or are shifted toward the low-energy range by 0.12 (peaks *3*, *6*, *8*), 0.35 (peak *4*), and 0.6 eV (peaks *7*, *9*, *10*). In this case, it is clearly seen that an overestimation of the $R(E)$ values in [4] (underestimation in [5]) leads to an appreciable overestimation (underestimation) of the $\varepsilon_2(E)$ values in the energy range 5–21 eV (10–14 eV). The differences in the position of the peaks observed in the four spectra $\varepsilon_2(E)$ fall in the range 0–0.2 eV (at 10–20 eV). At higher energies, these differences increase to 0.5–1.0 eV.

A comparison of the spectra $\varepsilon_2(E)$ and $-\mathrm{Im}\varepsilon^{-1}(E)$ demonstrates that, compared to the peaks in the spectra $\varepsilon_2(E)$, the loss peaks are shifted toward the high-energy range by ~0.1–0.2 (peaks *1*, *2*, *5*, *8*) and 0.4–0.9 eV (peaks *3*, *4*, *6*, *7*, *9*, *10*). These shifts determine the energies of longitudinal–transverse splittings of the ten strongest transitions in fluorite.

The peaks of the surface loss function $-\mathrm{Im}(1 + \varepsilon)^{-1}$ either coincide with those of the bulk loss function $-\mathrm{Im}\varepsilon^{-1}$ (peaks *1*, *2*, *3*, *5*, *8*) or are shifted toward the low-energy range by ~0.3 (peaks *4*, *6*, *7*), 2.6 (peak *9*), and 1.9 eV (peak *10*).

Analysis of the spectra $R(E)$, $\varepsilon_2(E)$, $\varepsilon_1(E)$, $-\mathrm{Im}\varepsilon^{-1}(E)$, and $-\mathrm{Im}(1 + \varepsilon)^{-1}(E)$ recorded for the CaF_2 crystal with the use of four different techniques shows that the spectrum $R(E)$ measured by the first method in the range 10–33 eV and the spectra of the other functions calculated from this spectrum (curves *1* in Figs. 1–4) should be treated as the most adequate. The results of two other techniques in the range 20–33 eV (curves *3*, *4*) compete with the data obtained by the first method. For this reason, it is expedient to compare the aforementioned data with the theoretical spectra $\varepsilon_2(E)$ derived in [17, 18] and with the spectra of other functions calculated on this basis.

Gan *et al.* [17] calculated the theoretical spectra $\varepsilon_2(E)$ of fluorite in the range 10–27 eV with the use of three methods: the OLCAO self-consistent first-principles method in the LDA approximation without and with due regard for self-interaction corrections (models $G1$ and $G2$, respectively) and with an additional upward shift of the conduction band by ~5.1 eV in order to fit the theoretical value of E_g to the experimental data (model $G3$). Benedict and Shirley [18] performed first-principles calculations in the framework of the LDA and quasiparticle approximation without and with due regard for the electron–hole interaction (models $B2$ and $B1$, respectively) and obtained the spectra $\varepsilon_2(E)$ in the range 8–20 eV. Among the aforementioned five theoretical models, two models ($B1$ and $G2$) are most consistent with the experimental data and the results of calculations from the experimental data (hereafter, these results will be referred to as the experimental–calculated data). For brevity, we will consider the spectra $\varepsilon_2(E)$ derived within models $B1$ and $G2$ and the theoretical–calculated spectra $\varepsilon_1(E)$, $R(E)$, $-\mathrm{Im}\varepsilon^{-1}(E)$, and $-\mathrm{Im}(1 + \varepsilon)^{-1}(E)$ obtained in our work from these $\varepsilon_2(E)$ spectra.

It is generally believed that the longest wavelength peak *1* in the optical spectra is attributed to free excitons. In actual fact, peak *1* is observed in the theoretical spectrum $\varepsilon_2(E)$ only in the case when the electron–hole interaction is taken into account (Fig. 1, curve *6*). This peak is located at 11.1 eV, i.e., at an energy that is only 0.1 eV less than the energy found from our experimental–calculated data on the $R(E)$ spectrum [3] (curve *1*). Such a close agreement between the theoretical and experimental–calculated data was achieved in [18] by increasing the value of E_g from 6.8 to 11.8 eV (i.e., by 5 eV). In this case, the exciton binding energy is equal to 0.7 eV, which is characteristic of strongly ionic crystals. The spectral features predicted theoretically in [18] at higher energies are as follows: a shoulder at 12.0 eV; an unresolved doublet at 13.0 and 13.4 eV; a shoulder at 14.7 eV; three strongly overlapping peaks at 15.4, 15.8, and 16.5 eV; and weak peaks at 18.3 and 19.0 eV. The positions of these features differ from the experimental–calculated data by ~0.2–0.4 eV. The theoretical spectrum $\varepsilon_2(E)$ (within model $B1$) agrees well with the experimental–calculated spectrum not only in structure but also in intensity distribution.

The peaks and shoulders observed in the experimental–calculated spectrum $\varepsilon_2(E)$ are also present in the theoretical spectrum derived in [17] within model $G2$. The differences in position of these features are nearly the same (~0.2–0.4 eV). However, their intensity distributions in both spectra differ significantly in the energy range $E < 13.3$ eV. For the most part, this discrepancy can be artificially decreased by shifting the theoretical spectrum at $E > 12.9$ eV toward the low-energy range by ~1 eV but without a decrease in E_g.

The differences found in the spectral features and intensities of the theoretical (Fig. 1, curves *5*, *6*), experimental (Fig. 1, curve *3*), and experimental–calculated (Fig. 1, curves *1*, *2*, *4*) functions $\varepsilon_2(E)$ are observed in the spectra $\varepsilon_1(E)$ but to a smaller extent (Fig. 2). The positions of the main features *1–4* (*2–4*) in the theoretical spectra coincide accurate to within ±0.1 eV with those in the experimental–calculated spectra without a shift for model $B1$ (or with a shift of ~1 eV toward the low-energy range for model $G2$). The intensities of features *3* (*4*) and *7* appear to be considerably underestimated in the theoretical spectra for model $B1$ ($G2$).

In [18], the theoretical spectrum $\varepsilon_2(E)$ was calculated at 0 K. The energies of the maximum (~11.1 eV) and the half-widths (~0.8 eV) of the longest wavelength exciton reflection band *1* are almost identical in the theoretical and experimental spectra. However, experimental band *1* exhibits a more pronounced dispersion structure: the values of $R(E)$ at a maximum (minimum) are equal to 0.2 (0.02) at 90 K [3] and ~0.15 (0.05) according to our calculations from the theoretical spectrum $\varepsilon_2(E)$ taken from [18]. The inclusion of the exciton–phonon interaction can lead both to an increase in these differences and to a considerable increase in the discrepancy between theory and experiment. In the experimental spectrum obtained in [3], the reflection band in the range 12–15 eV consists of the two narrow intense peaks *2* and *3*, a side weak shoulder, and a side weak peak. In the theoretical spectrum [18], this band is represented by one very broad band with a maximum approximately in the range of peak *3* and a weakly pronounced shoulder approximately in the range of peak *2*. Instead of the experimental intense peak *4* and the subsequent two weak shoulders in the range 15–18 eV, the theoretical spectrum (model $B1$) contains two intense bands with a very complex fine (doublet and quintet) structure. The theoretical spectrum $R(E)$ taken from [17] (model $G2$) can be well fitted to the experimental spectrum according to the positions of the principal peaks and their intensities. The sole exception is peak *1*, which should be shifted toward the low-energy range by approximately 1 eV.

The theoretical spectra $\varepsilon_2(E)$ in [17, 18] were compared with insufficiently correct experimental data taken from [5] without discussing the origin of the peaks. Gan *et al.* [17] considered three models ($G1$, $G2$, and $G3$) of the bands along the ΓL, ΓX, and ΓK directions (Fig. 5). The most adequate model $G2$ underestimates E_g by $\Delta E \approx 3.4$ eV. With due regard for this correction, the energies of the possible most intense interband transitions are estimated at ~12.9 eV for Γ (V_1–C_2) and 13.0 eV for ΓX (V_1–C_1) (peak *2*); 13.5 eV for Γ (V_2–C_1), 13.4 eV for ΓX (V_1–C_2)), and 14.4 eV for ΓL (V_1–C_1) (peak *3*); 15.4 eV for Γ (V_1–C_3), ΓX (V_1–C_3 and V_1–C_4), and ΓL (V_2–C_2) (peak *4*); 17.5 eV for ΓL (V_2–C_3) (peak *5*); 19.5 eV for Γ (V_2–C_3) and ΓL (V_2–C_4) (peak *6*); and 25.4 eV for ΓL (V_2–C_4) (peak *7*). Many peaks in the spectra $\varepsilon_2(E)$ and $R(E)$ can be attributed to metastable excitons. In this case, the peaks are shifted toward the low-energy range with respect to the energies of interband transitions by approximately the binding energy.

The bulk plasmon band is easily identified in the experimental spectrum $-\mathrm{Im}\varepsilon^{-1}(E)$ taken from [6]. The maximum of this band is located at the energy $E_{pv} = 35.8$ eV (Fig. 3, curve *4*). An analog of this band associated with the surface plasmons is observed in the experimental–calculated spectrum $-\mathrm{Im}(1 + \varepsilon)^{-1}(E)$ at the energy $E_{ps} = 35.0$ eV (Fig. 4, curve *4*). According to the plasmon model, these energies should be related by the expression $E_{pv} \approx AE_{ps}$, where $A \approx 1.4$ is the constant factor [31]. For graphite and molybdenum chalcogenides, the value of A is approximately equal to 1.2–1.3 [32]. In our case of fluorite, the A factor proves to be considerably smaller and close to unity ($A \approx 1.02$). This is in sharp contrast with the simplest general plasmon model. The value of E_{pv} can be estimated theoretically from the point of intersection between the curve $\varepsilon_1(E)$ and the energy axis [31], which holds for covalent crystals of the A^4 group. However, this regularity breaks down for the strongly ionic crystal CaF_2.

The intensity of the loss spectra calculated from the theoretical curves $\varepsilon_2(E)$ taken from [17, 18] (Figs. 3, 4,

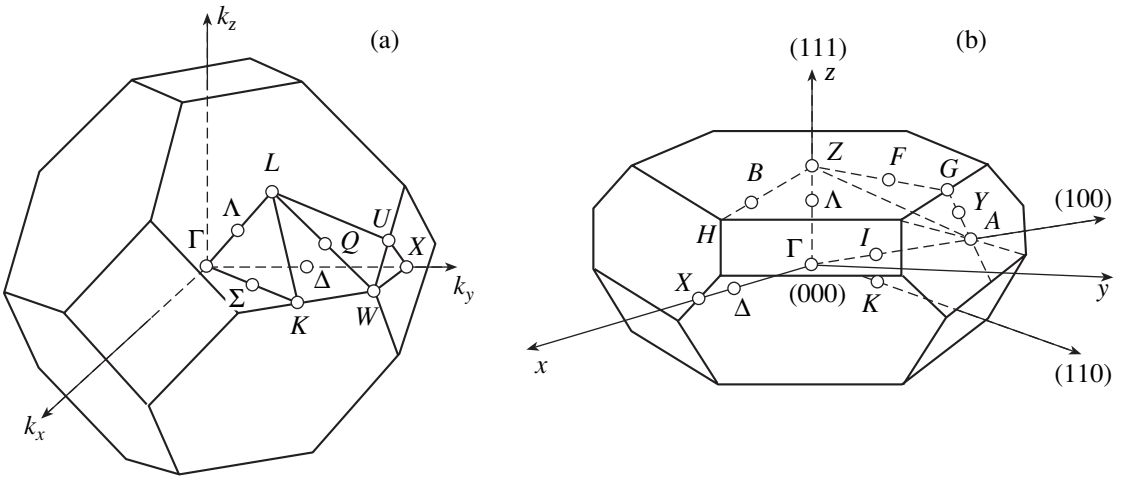

Fig. 5. Brillouin zones for (a) CaF_2 and (b) Al_2O_3 crystals.

curves *5*, *6*) is in poor agreement with the intensity of the experimental and experimental–calculated spectra. The structure of the experimental–calculated spectra agrees with the structure of the spectra calculated using model *B*1 and strongly differs from that obtained within model *G*2.

A considerable overestimation (underestimation) of the reflection coefficients in [4] ([5]) results in the corresponding distortions of the spectra of n_{eff} and ε_{eff}. These spectra are most correctly derived with the use of the experimental spectra $R(E)$ [3] and $-\text{Im}\varepsilon^{-1}(E)$ [6]. In these cases, the inclusion of excitons in the framework of model *B*1 leads to the results close to the experimental–calculated data, whereas the use of theoretical model *G*2 gives the underestimated results.

Twelve electrons of the six upper valence bands of CaF_2 are completely involved in the transitions at the energy $E \approx 27$ eV. At higher energies in the range $E <$ 35 eV, the dependence $n_{\text{eff}}(E)$ smoothly increases without indications of saturation. Most likely, this is associated with the participation of deeper valence bands formed by the Ca^{2+} 3*p* states.

The effective permittivity ε_{eff} at 40 eV is equal to 1.9, and the long-wavelength permittivity ε_0 is ~ 2.0 [2]. The closeness of ε_{eff} (at 40 eV) and ε_0 indicates the validity of the calculations of the optical functions from the experimental reflectance spectra taken from [3].

4. RESULTS OF CALCULATIONS AND DISCUSSION FOR Al_2O_3

The polarized reflectance spectra of α-Al_2O_3 were measured by Tomiki *et al.* [9] (in the range 2–110 eV), Arutyunyan *et al.* [10] (5–25 eV), and Mileshkin *et al.* [7] (5–25 eV) at the polarizations $\mathbf{E} \perp \mathbf{C}$ and $\mathbf{E} \parallel \mathbf{C}$ and also by French *et al.* [11] (5–43 eV) and Abramov *et al.* [8] (7–20 eV), most likely, at the polarization $\mathbf{E} \perp \mathbf{C}$. Since corundum is extremely popular in science and engineering, it is of interest to compare the reflectance spectra obtained in the five different works in the range 5–30 eV. The polarized reflectance spectra were most thoroughly investigated in [9]. According to the data reported in this work (see Table 1, in which the energies of weak peaks and shoulders are parenthesized), the reflectance spectra of the corundum crystal contains weakly polarized peaks *1* and *10* and shoulders *11* and *12*, a strongly polarized peak *6*, and polarized bands with a triplet (peaks *3*, *4*, and *5* at $\mathbf{E} \parallel \mathbf{C}$ and peaks *3*', *4*', and *5*' at $\mathbf{E} \perp \mathbf{C}$ or doublet (peaks *7*, *8* and *9*, *10* at $\mathbf{E} \parallel \mathbf{C}$) structure. The intensity of the reflectance spectra only slightly depends on the polarization, except in the narrow range from 12.5 to 16 eV. The parameters of the polarized reflectance spectra obtained in [9] differ considerably from those determined in [10]:

(1) All the peaks in the spectra measured in [10], specifically in the ranges of the longest wavelength peak *1* and from 15 to 19 eV, are very strongly broadened (by a factor of two or three).

(2) Over the entire energy range, the reflection intensity at the polarization $\mathbf{E} \parallel \mathbf{C}$ is substantially higher than that at the polarization $\mathbf{E} \perp \mathbf{C}$.

(3) The fine structure observed in [9] for bands *3*, *4*, and *7*–*10* was not revealed in [10].

(4) The maxima of bands in the spectra measured in [10] are shifted toward the low-energy range by ~0.3 (peak *1*), 0.6 (peak *4*'), and 0.1 eV (peak *6*) or toward the high-energy range by ~0.45 eV (peak *4*').

The results obtained in [7] also differ appreciably from those reported in [9]:

(1) Peak *1* in the spectra taken from [9] is unpolarized with a high accuracy, whereas this peak in the spectra measured in [7] is strongly polarized and has a higher intensity (by a factor of approximately 1.5 as compared to that observed in [9] at $\mathbf{E} \perp \mathbf{C}$).

Table 1. Energies (eV) of peaks and shoulders in the reflectance spectra of corundum

No.	**E ∥ C**			**E ⊥ C**				
	[9]	[10]	[7]	[9]	[10]	[7]	[11]	[8]
1	8.975	8.65	~8.9	9.057	8.65	9.0	8.85	9.24
2'	–	–	(10.4)	(10.7)	(10.7)	(10.2)	10.4	(10.6)
2	(11.5)	–	11.4	–	–	11.5	(10.7)	–
3'	–	–	–	12.08	–	–	11.8	12.08
3	12.25		–	–	–	–	–	–
		12.65						
4	12.93		–	–	–	–	–	–
4'	–	–	–	13.25	12.70	–	12.8	13.25
5	(13.7)	14.0	14.0	–	–	–	–	–
5'	–	–	–	(13.9)	–	–	–	–
6	–	15.5	–	15.1	~15.0	(14.5)	14.6	15.1
7	(17.1)							
		17.7	16.7	(17.6)	17.7	16.5	17.3	17.2
8	(18.1)							
9'	–	–	–	19.2	–	18.8	19.2	19.0
9	19.45			–	–	–	19.6	–
		20.0	20.3					
10	21.7			21.45	–	–	21.65	–
10'	–	–	(~22.3)	–	22.4	(~22.0)	(22.1)	–
11	(24.2)	–	–	(24.2)	–	–	–	–
12	(26.7)	(26.0)	–	(26.7)	~27	–	~27	–

(2) Instead of the weak and strongly polarized shoulder *2* in [9], a very intense and weakly polarized peak was found in [7]; moreover, a very weak peak was observed in [7] in place of intense peak *6* in the spectrum obtained in [9].

The reflectance spectra, most likely, at one polarization **E** ⊥ **C** were measured in [11] (in the range 6–42 eV) and [8] (4–20 eV). Almost all the spectral features noted in [9] were also observed in [11]; however, they were shifted toward the low-energy range by 0.3–0.5 eV (features *1*, *2*', *3*', *4*', *6*, and *8*). It should be noted that the reflection coefficients determined in the range 8–15 eV in [11] considerably (by ~0.07) exceed the coefficients $R(E)$ obtained in [9]. By contrast, the reflection coefficients measured in [8] are approximately 0.02–0.05 less than those determined in [9]. For the major part, the structures of the spectra $R(E)$ measured in [8, 9] almost coincide.

Thus, the polarized reflectance spectra of corundum in the range 8–30 eV involves 18 peaks and shoulders. The most complete set of these features was obtained in [9], and they are likely characteristic of the most perfect crystals. All the intense peaks with relatively small variations in the energy positions were revealed in all five works. In the range $E < 8.5$ eV, the $R(E)$ spectra recorded in [7, 10] contain intense bands attributed to impurities. Consequently, the discrepancies between the data obtained in these works can be partly explained by the imperfectness of the samples and their spectra $R(E)$ are likely typical of commonly encountered, insufficiently perfect crystals, which is of certain interest in itself. It is difficult to explain the origin of the differences in the reflection intensity in the range 8–13 eV at **E** ⊥ **C** in [9, 11]. One of the possible reasons for the differences observed in the $R(E)$ spectra obtained in the five different works is the use of single crystals grown by different techniques. In this case, the considered $R(E)$ spectra are characteristic of corundum samples that are produced by many existing techniques (including those used in [7, 10]) and have a high concentration of impurities and defects, as is indicated by the presence of intense bands in the energy range $E < 8.5$ eV.

By using the reflectance spectra measured in [8–11], we calculated the complete set of the spectra of the optical functions for the corundum crystal. For brevity, we consider the basic results for the spectra of ε_1 and ε_2 (Fig. 6). Table 2 presents the positions of principal peaks and shoulders (parenthesized) in the spectra $\varepsilon_2(E)$, namely, *A* and *A*', *B* and *B*', *C*, and *D*, which were obtained in our work from the reflectance spectra recorded in [9], [10], [11], and [8], respectively.

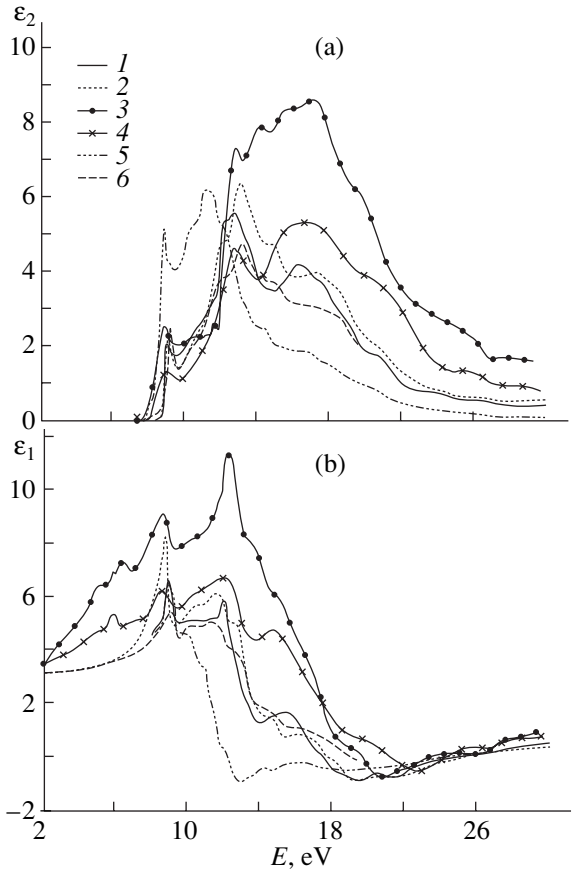

Fig. 6. Theoretical spectra (a) $\varepsilon_2(E)$ and (b) $\varepsilon_1(E)$ calculated for the Al_2O_3 crystal from the experimental reflectance spectra $R(E)$ taken from (*1*, *2*) [9], (*3*, *4*) [10], (*5*) [11], and (*6*) [8]. Polarization: (*1*, *3*) $\mathbf{E} \perp \mathbf{C}$, (*2*, *4*) $\mathbf{E} \parallel \mathbf{C}$, and (*5*, *6*) unpolarized spectra.

The spectra $\varepsilon_2(E)$ calculated from the data obtained in [9], [8], and [10, 11] originate at energies of ~8.5, 8, and 7.5–7.8 eV, respectively. These energies correspond to the location of the long-wavelength fundamental absorption edge. The absorption edge either is rather sharp without a noticeable tail in the low-energy range (spectra *A*, *A*') or is shifted toward the low-energy range and has a substantially smaller slope (spectra *B*, *B*', *C*, *D*), which is explained by the lower degree of perfection of the samples used in [8, 10, 11]. The polarization affects both the energy position of the longest wavelength peak *1* [$E(\mathbf{E} \perp \mathbf{C}) - E(\mathbf{E} \parallel \mathbf{C}) = 0.08$ eV for spectra *A* and *A*' and 0.20 eV for spectra *B* and *B*'] and its intensity [$\varepsilon_2(\mathbf{E} \parallel \mathbf{C}) = 2.08$ for spectrum *A*' and 2.5 for spectrum *B*', and $\varepsilon_2(\mathbf{E} \perp \mathbf{C}) = 2.19$ for spectrum *A* and 1.3 for spectrum *B*]. As the energy increases, the permittivity ε_2 increases first slowly (in the range 9.5–11.0 eV) and then very rapidly to maximum values of ~5.6 for peak *4* at $\mathbf{E} \parallel \mathbf{C}$ and ~6.4 for peak *4*' at $\mathbf{E} \perp \mathbf{C}$. Thereafter, the curve $\varepsilon_2(E)$ (spectra *A*, *A*') falls off steeply to $\varepsilon_2 < 1$ at $E > 24$ eV and exhibits intense peaks *6* and *7* + *8* at $\mathbf{E} \perp \mathbf{C}$ and *7* and *8* at $\mathbf{E} \parallel \mathbf{C}$. For less perfect corundum samples, the intensity ratios of the peaks in the spectra $\varepsilon_2(E)$ (spectra *B*, *B*', *C*) differ significantly from those in spectra *A* and *A*'. It should be emphasized that the peaks and shoulders in the calculated spectra $\varepsilon_2(E)$ for four polarizations $\mathbf{E} \perp \mathbf{C}$ and two polarizations $\mathbf{E} \parallel \mathbf{C}$ appeared to be very close in position. The differences between the positions of the corresponding features are equal to ~0.1–0.5 eV; i.e., they amount to only ~1–5% and less.

In all the cases under consideration, the calculated spectra $\varepsilon_1(E)$ are similar to the reflectance spectra in the energy range $E < 13.5$ eV. At higher energies, the values of $\varepsilon_1(E)$ very rapidly decrease from ~6.0 at 13.5 eV to ~–0.5 at 20 eV and 0.5 at 30 eV.

For an isolated band corresponding to a particular transition, the relative positions of the peaks in the spectra of R, ε_1, and ε_2 follow the universally accepted classical order: $E(\varepsilon_1) < E(R) < E(\varepsilon_2)$ [25]. However, in the case when the bands overlap considerably, this classical inequality can break down for the maxima in the integrated curves. We examined the positions of the peaks in the spectra $R(E)$, $\varepsilon_2(E)$, and $\varepsilon_1(E)$ of corundum. It was found that the classical inequality holds for the longest wavelength band *1*: the energy $E(R)$ is higher than $E(\varepsilon_1)$ by 0.06 eV and is less than the energy $E(\varepsilon_2)$ by 0.12 eV. However, for many peaks in spectrum *A*', the values of $E(\varepsilon_2)$ are less than the values of $E(R)$ by approximately 0.1 eV for peak *4*; 0.3 eV for peak *8*; 0.6 eV for peaks *7*, *9*, and *11*; and 1.1 eV for peak *10*.

For the majority of solids, only experimental reflectance spectra are available. In the absence of the spectra $\varepsilon_2(E)$, the transition energies and band gaps are determined from the peaks in the spectra $R(E)$ under the assumption that $E(R) \sim E(\varepsilon_2)$. Our analysis of the relative position of the peaks in the integrated curves $R(E)$ and $\varepsilon_2(E)$ indicates that the error of this forced assumption can be as large as 1 eV. Moreover, compared to the peak in the spectrum $R(E)$, the peak in the spectrum $\varepsilon_2(E)$ can be located in the low-energy range rather than in the high-energy range. Unfortunately, this circumstance is disregarded in numerous theoretical band calculations in which the fitting parameters are chosen from the energies of reflection peaks.

Traditionally, the longest wavelength peak *1* in the reflectance spectrum of corundum is attributed to Frenkel free excitons with the quantum number $n = 1$ [1, 7–9, 11]. The long-wavelength absorption was experimentally measured only in a narrow range of absorption coefficients up to ~10^3 cm^{-1} and the energy range $E \le 9$ eV [9]. Analysis of this weakly polarized absorption in terms of the Urbach empirical rule led the authors of [9] to the inference that the maximum of the exciton band is located at 9.25 eV for $\mathbf{E} \parallel \mathbf{C}$ and 9.31 eV for $\mathbf{E} \perp \mathbf{C}$ with $\mu \approx 4 \times 10^6$ cm^{-1} for $\mathbf{E} \parallel \mathbf{C}$ and 3×10^7 cm^{-1} for $\mathbf{E} \perp \mathbf{C}$. However, these results can be treated only as approximate. According to our experimental–calculated data, the exciton absorption maxi-

mum is located at 9.17 eV for **E** || **C** and 9.20 eV for **E** ⊥ **C** with $\mu \approx 4 \times 10^5$ for **E** || **C** and **E** ⊥ **C**. Hence, it follows that the use of the Urbach empirical rule in [9] very strongly overestimated the value of μ for the exciton band at a maximum, especially in the case of the polarization **E** ⊥ **C**.

For free excitons in corundum, experimental data for the states with $n > 1$ and the corresponding theoretical calculations are unavailable in the literature and their binding energy E_b is unknown. There are only several rough values of E_g and E_b, namely, $E_g \sim 9.4$ eV [8], $E_g \leq 9.5$ eV [11], $E_b \approx 0.4$ [8], and $E_b \approx 0.1$ eV [11]. The absorption bands associated with the free excitons and interband transitions in corundum overlap significantly. As follows from our data, the minima in the integrated curves $\varepsilon_2(E)$ are located at ~9.5 eV for **E** || **C** and 9.5 eV for **E** ⊥ **C**. Therefore, the values of E_g apparently lie in the range between these energies and the energies corresponding to the exciton maxima, namely, $9.2 < E_g(\mathbf{E} \parallel \mathbf{C}) < 9.5$ eV and $9.3 < E_g(\mathbf{E} \perp \mathbf{C}) < 9.7$ eV. The half-width of the exciton band is equal to ~0.4 eV. These estimates and the specific features in the spectra $\varepsilon_2(E)$ allow us to assume that corundum is characterized by $E_g \sim 9.35$ eV for **E** || **C** and 9.45 eV for **E** ⊥ **C** and $E_b \approx 0.15$ eV.

The other peaks and shoulders in the spectra $R(E)$, $\varepsilon_2(E)$, and other optical functions can be attributed to interband transitions, metastable excitons, and their interference [25]. The theoretical electronic structure of corundum is known only in the framework of the band model without regard for free and metastable excitons. Now, we very briefly dwell on the basic results obtained in theoretical calculations of the bands and the spectra $R(E)$, $\varepsilon_2(E)$, and $\varepsilon_1(E)$.

It is common knowledge that intense absorption peaks are associated with transitions between those pairs of bands that are parallel along the most extended portions of the directions of the Brillouin zone. Within this qualitative model, we considered the energy bands obtained in [20–23] and determined the energies and the origin of the possible most intense interband transitions along the Γ*X*, Γ*Z*, Γ*A*, *AD*, Γ*M*, *MK*, Γ*K*, *AL*, and *AH* directions (Table 3). The theoretical values available in the literature for $E_g(\Gamma)$ are equal to 8 [20], 18 [21], and 6 eV [23]; i.e., they are underestimated by approximately 1.5 eV in [20] and 3.5 eV in [23] and are overestimated by a factor of approximately two in [21]. These corrections were taken into account in our calculations of the interband transition energies. The upper valence band with a width of about 7 eV consists theoretically of 24 subbands, certain of which are degenerate. The intersubband spacings at different points of the Brillouin zone vary from 0.1 to 1.0 eV. Numerous conduction subbands are also spaced very closely. Therefore, the scheme of direct interband transitions along different directions of the Brillouin zone involves several variants of assigning each peak in the spectrum $\varepsilon_2(E)$. The most probable variants are listed in Table 3. The intense bands can be associated with transitions in different regions of the Brillouin zone, which was disregarded in [20–23]. Certainly, the origin of the peaks in the spectrum $\varepsilon_2(E)$ can be treated within an alternative model of metastable excitons [25]. However, no theoretical calculations for corundum were performed in terms of this model.

Table 2. Energies (eV) of peaks and shoulders in the spectra $\varepsilon_2(E)$ of corundum

No.	**E** || **C**		**E** ⊥ **C**			
	A'	*B*'	*A*	*B*	*C*	*D*
1	9.12	8.90	9.20	9.10	8.95	9.30
2'	–	(10.6)	(10.8)	–	(10.4)	(~10.6)
2	(11.55)	(11.75)	–	–	(10.7)	–
3'	–	–	~12.2	–	11.35	12.15
3	12.30	12.85	–	–	–	–
4	12.80		–	–	–	–
4'	–	–	13.15	12.8	12.1	13.2
5	~13.55	~14.25	–	–	–	–
6	–	~15.5	14.90	–	(14.45)	14.9
7	16.4	17.10	17.30	16.5	(16.7)	(17.1)
8	~17.8					
9'	–	–	18.3	–	(~18.5)	–
9	~19.0	19.7	–	–	–	–
10	~20.6		20.5	–	–	–
10'	–	–	–	~20.7	–	–
11	~23.5	–	–	–	–	–
12	–	~25	–	~26	–	–

In [22–24], the spectra of R, ε_2, and ε_1 in the range 0–40 eV were calculated using theoretical band diagrams along the Γ*X*, Γ*Z*, Γ*A*, Γ*D*, *ZA*, and *DA* directions. Unfortunately, the transition probabilities and the bands within the Brillouin zone were ignored in these calculations and the spectra were represented as integrated curves of all transitions without identifying the origin of the peaks. In [23], the theoretical spectra of ε_2 were compared with the curve calculated in [11] from the experimental reflectance spectrum. However, the comparison was carried out without regard for the shift in the theoretical spectrum $\varepsilon_2(E)$ along the energy scale by $\Delta E \approx 3.5$ eV due to the theoretical underestimation of E_g. Naturally, this crude error predetermined the unreliability of the main conclusion drawn in [23] as to good agreement between the theoretical and experimental data on $\varepsilon_2(E)$. A direct comparison of the theoretical spectra $\varepsilon_2(E)$ with our calculated data obtained

Table 3. Theoretical energies (eV) of transitions in corundum and their assignment to the directions of the Brillouin zone

No.	[23] (**E** ∥ **C**)	[23] (**E** ⊥ **C**)	[20]	[21]	[22]
1	–	–	–	–	–
2'	(~10) Γ*X*	(10.6) Γ*X*	11.5 Γ*Z*, Γ*Y*	10.5 Γ*M*	10.6 *L*Γ*Z*
2	13.2 Γ*X*, Γ*Z*, *AD*	–	–	–	12 *L*Γ*Z*
3'	–	(11.5) Γ*X*, *AZ*	12.6 Γ*X*, Γ*Z*, Γ*Y*	12.5 Γ*M*	13 *L*Γ*Z*
3	14.1 Γ*Z*, *AD*	–	–	–	13.7 Γ*Z*
4	14.8 Γ*X*, Γ*Z*, *AD*	–	–	–	14.4 *LZ*
4'	–	13.4 Γ*X*, Γ*Z*, Γ*A*	14.0 Γ*X*, Γ*Z*, Γ*Y*	12.5 Γ*MK*	–
5	15.5 Γ*X*, Γ*Z*, Γ*A*	–	–	–	15 Γ*Z*
6	–	15.7 Γ*X*, Γ*Z*, Γ*A*	15.0 Γ*X*, Γ*Z*, Γ*Y*	16.5 Γ*M*, *MK*, *AL*	15.5 *LZ*
7	16.5 Γ*X*, Γ*Z*, Γ*A*	17.2 Γ*X*, Γ*A*, *AD*	17.3 Γ*X*, Γ*Y*	17.0 Γ*MK*, *AL*	16.5 *LZ*Γ
8	17.8 Γ*X*, Γ*Z*, Γ*A*	(17.9) Γ*X*, Γ*Z*	17.3 Γ*X*, Γ*Y*	17.0 Γ*MK*, *AL*	17.3 Γ*Z*
9'	18.5 Γ*X*, Γ*Z*, Γ*A*	18.7 Γ*X*, Γ*Z*, Γ*A*	18.4 Γ*X*, Γ*Z*, Γ*Y*	~18.0 Γ*MK*, *AL*	19 *LZ*Γ
9	19.0 Γ*X*, Γ*Z*, Γ*A*	–	–	–	–
10	20.0 Γ*X*, Γ*Z*, Γ*A*	19.8 Γ*A*, Γ*X*	19.4 Γ*X*, Γ*Z*	~19.5 Γ*MK*, *AH*	20 *LZ*Γ
10'	–	–	–	–	–
11	22.0 Γ*X*	–	–	–	21.5 *LZ*Γ
12	–	–	–	–	–

from the reflectance spectra taken from [8–11] indicates considerable differences between them both in the structure and intensity ratio of the peaks in the spectra $\varepsilon_2(E)$ and $R(E)$. These problems will be considered in more detail in a separate work.

5. CONCLUSIONS

Thus, the complete sets of the spectra of fundamental optical functions for fluorite and corundum crystals over a wide energy range of fundamental absorption were determined within a unified approach for the first time. The calculations were performed using the experimental spectra $R(E)$ [3, 4], $\varepsilon_2(E)$, $\varepsilon_1(E)$ [5], and $-\mathrm{Im}\varepsilon^{-1}(E)$ [6] of CaF_2 and the experimental spectra $R(E)$ of Al_2O_3 [8–11]. Analysis of the experimental spectra showed that the most correct data were obtained in [3, 9]. The main features in the spectra of the optical functions were revealed. Within the scheme of direct interband transitions, the model assignment of the peaks revealed in the spectra $\varepsilon_2(E)$ of both crystals was proposed reasoning from the recent, most detailed theoretical works. It was demonstrated that, for fluorite crystals, the theoretical spectra $\varepsilon_2(E)$ for models *B*1 in [18] and *G*2 in [17] and the theoretical spectra $\varepsilon_1(E)$ and $R(E)$, for the most part, agree well in structure with the experimental–calculated spectra $R(E)$, $\varepsilon_2(E)$, and ε_1(E). However, the intensities of these spectra are in rather poor agreement. It should be noted that, despite a certain simplicity, the theory allowing for the electron–hole interaction [18] has a great advantage in the entire energy range of fundamental absorption.

The results obtained enabled us to calculate essentially more precise fundamental spectra $\varepsilon_2(E)$, ε_1(E), and $R(E)$ for fluorite and corundum crystals in the range 8–35 eV. This makes it possible to elaborate the theory of electronic structure of fluorite and corundum with inclusion of the excitonic effects over a wide range of energies and to analyze thoroughly the origin of numerous peaks in the spectra $\varepsilon_2(E)$ and $R(E)$.

ACKNOWLEDGMENTS

We would like to thank V.P. Zhukov, V.M. Zaĭnullina, N.V. Starostin, R.A. Évarestov, W.Y. Ching, G.W. Rubloff, J. Frandon, and R.H. French for their reprints.

This work was supported by the Center of Basic Natural Sciences (St.-Petersburg State University).

REFERENCES

1. V. B. Lazarev, V. V. Sobolev, and I. S. Shaplygin, *Chemical and Physical Properties of Simple Metal Oxides* (Nauka, Moscow, 1983).
2. V. V. Sobolev, *Bands and Excitons in Metal Halides* (Shtiintsa, Chisinau, 1988).
3. G. W. Rubloff, Phys. Rev. B **5**, 662 (1972).
4. V. A. Ganin, M. G. Karin, V. K. Sidorin, *et al.*, Fiz. Tverd. Tela (Leningrad) **16**, 3554 (1974) [Sov. Phys. Solid State **16**, 2313 (1974)].
5. J. Barth, R. L. Johnson, M. Cardona, *et al.*, Phys. Rev. B **41**, 3291 (1990).
6. J. Frandon, B. Lahaye, and F. Pradal, Phys. Status Solidi B **53**, 565 (1972).

7. B. N. Mileshkin, V. V. Mikhaĭlov, and V. E. Oranovskiĭ, Tr. Fiz. Inst. Akad. Nauk SSSR **80**, 140 (1975).
8. V. N. Abramov, M. G. Karin, A. I. Kuznetsov, and K. K. Sidorin, Fiz. Tverd. Tela (Leningrad) **21**, 80 (1979) [Sov. Phys. Solid State **21**, 47 (1979)].
9. T. Tomiki, Y. Ganaha, and T. Shficenbaru, J. Phys. Soc. Jpn. **62**, 573 (1993).
10. V. V. Arutyunyan, A. K. Babayan, and V. A. Gevorkyan, Fiz. Tverd. Tela (St. Petersburg) **37**, 443 (1995) [Phys. Solid State **37**, 240 (1995)].
11. R. H. French, D. J. Jones, and S. J. Loughin, J. Am. Ceram. Soc. **77**, 412 (1994).
12. A. K. Harman, S. Ninomiya, and S. Adachi, J. Appl. Phys. **76**, 8032 (1994).
13. V. N. Starostin and M. P. Shepilov, Fiz. Tverd. Tela (Leningrad) **17**, 822 (1975) [Sov. Phys. Solid State **17**, 523 (1975)].
14. R. A. Évarestov, I. V. Murin, and A. V. Petrov, Fiz. Tverd. Tela (Leningrad) **30**, 292 (1988) [Sov. Phys. Solid State **30**, 168 (1988)].
15. L. K. Ermakov, P. A. Rodnyĭ, and N. V. Starostin, Fiz. Tverd. Tela (Leningrad) **33**, 2542 (1991) [Sov. Phys. Solid State **33**, 1435 (1991)].
16. N. C. Amaral, B. Maffeo, and D. Guenzburger, Phys. Status Solidi B **117**, 141 (1983).
17. F. Gan, Y.-N. Xu, M.-Z. Huang, and W. Y. Ching, Phys. Rev. B **45**, 8248 (1992).
18. L. X. Benedict and E. L. Shirley, Phys. Rev. B **59**, 5441 (1999).
19. R. A. Evarestov, A. N. Ermoshkin, and V. A. Lovchikov, Phys. Status Solidi B **99**, 387 (1980).
20. J. P. Batra, J. Phys. C **15**, 5399 (1982).
21. L. Salasco, R. Dovesi, and R. Orlando, Mol. Phys. **72**, 267 (1991).
22. B. Holm, R. Ahuja, Y. Yourdshahyan, *et al.*, Phys. Rev. B **59**, 12777 (1999).
23. W. J. Ching and J.-N. Xu, J. Am. Ceram. Soc. **77**, 404 (1994).
24. Sh.-Di Mo and W. J. Ching, Phys. Rev. B **57**, 15219 (1998).
25. V. V. Sobolev and V. V. Nemoshkalenko, *Methods of Computational Physics in the Solid-State Theory: Electronic Structure of Semiconductors* (Naukova Dumka, Kiev, 1988).
26. V. V. Sobolev, Zh. Prikl. Spektrosk. **63**, 143 (1996).
27. V. V. Sobolev, A. P. Timonov, and V. Val. Sobolev, Fiz. Tverd. Tela (St. Petersburg) **42**, 632 (2000) [Phys. Solid State **42**, 648 (2000)].
28. V. V. Sobolev, in *Proceedings of the International Conference "Optics of Semiconductors"* (Ul'yanovskiĭ Univ., Ul'yanovsk, 1998), p. 3.
29. V. Val. Sobolev and V. V. Sobolev, in *Proceedings of the IV Russia Conference on Physics of Semiconductors, Novosibirsk, 1999*, p. 100.
30. V. Val. Sobolev, L. V. Asylgareeva, and V. V. Sobolev, in *Proceedings of the II International Conference "Amorphous and Microcrystalline Semiconductors," St. Petersburg, 2000*, p. 116.
31. D. Pines, *Elementary Excitations in Solids* (Benjamin, New York, 1963; Mir, Moscow, 1965).
32. A. N. Timoshkin, V. Val. Sobolev, and V. V. Sobolev, Fiz. Tverd. Tela (St. Petersburg) **42**, 37 (2000) [Phys. Solid State **42**, 37 (2000)].

Translated by O. Borovik-Romanova

Physics of the Solid State, Vol. 44, No. 5, 2002, pp. 880–887. Translated from Fizika Tverdogo Tela, Vol. 44, No. 5, 2002, pp. 845–852.

DEFECTS, DISLOCATIONS, AND PHYSICS OF STRENGTH

Transient Optical Absorption of Hole Polarons in ADP ($NH_4H_2PO_4$) and KDP (KH_2PO_4) Crystals

I. N. Ogorodnikov*, V. Yu. Yakovlev, B. V. Shul'gin*, and M. K. Satybaldieva*****

**Ural State Technical University, ul. Mira 19, Yekaterinburg, 620002 Russia*

e-mail: ogo@dpt.ustu.ru

***Tomsk Polytechnical University, Tomsk, 634021 Russia*

****Issyk-Kul State University, Karakol, 722360 Kirghiz Republik*

Received April 16, 2001

Abstract—A study of transient optical absorption of the ADP ($NH_4H_2PO_4$) and KDP (KH_2PO_4) nonlinear crystals in the visible and UV spectral regions is reported. Measurements made by absorption optical spectroscopy with nanosecond-time resolution established that the transient optical absorption (TOA) of these crystals originates from optical transitions in the hole *A* and *B* radicals and the optical-density relaxation kinetics is rate-controlled by interdefect tunneling recombination, which involves these hole centers and the electronic H^0 centers representing neutral hydrogen atoms. At 290 K, hole polarons and the H^0 centers undergo thermally stimulated migration, which is not accompanied by carrier ejection into the conduction or valence band. The slow components of the TOA kinetics with characteristic times from a few tens of milliseconds to a few seconds can be assigned to diffusion-controlled annihilation of hydrogen vacancies associated with impurity or structural defects. © *2002 MAIK "Nauka/Interperiodica".*

1. INTRODUCTION

The tetragonal crystals of potassium and ammonium dihydrophosphate, KH_2PO_4 (KDP) and $NH_4H_2PO_4$ (ADP), respectively (space symmetry group $I\bar{4}2d$), belong to a small class of nonlinear optical materials used in commercial high-power laser systems [1, 2]. Of the presently known crystals possessing high electrooptical coefficients, only the KDP, ADP, and lithium niobate are employed widely for light modulation. The short-wavelength boundary of optical transparency of the ADP and KDP crystals lies in the VUV region, at 176 nm for KDP and 184 nm for ADP [3]. Coupled with their good nonlinear properties, this permits one to use them to advantage for efficient third- and fifth- harmonic generation in high-power YAG : Nd or YLF : Nd picosecond lasers.

Subjecting these crystals to ionizing or high-power laser radiation affects their dielectric properties, optical characteristics, and structural perfection appreciably. The main factor limiting their behavior in this respect is the optical absorption of the crystal, which originates from the formation of intrinsic lattice defects induced by irradiation [4–6]. Among the best studied intrinsic defects in the ADP and KDP crystals, which were reliably identified by EPR, are the *A* radical ($[HPO_4]^-$) representing a hole localized at an oxygen ion near a hydrogen vacancy [7–9]; the *B* radical ($[H_2PO_4]^0$), which is a self-trapped hole (STH) [10, 11]; and the H^0 electronic center based on a hydrogen interstitial [10, 12]. Optical absorption (OA) bands of the *A* and *B* radicals were identified at 10 K [13, 14]. At room temperature, all three defects are metastable. Transient OA (TOA) of the KDP crystals in the visible and near-UV spectral regions was observed under irradiation by a high-intensity laser (λ = 266 nm) in [4, 6], as well as under electron-beam excitation in [15, 16]. However, many fundamental problems bearing on the nature of TOA in the ADP and KDP crystals still remain unclear.

The purpose of this work was to make a detailed study of the transient optical absorption of electron-beam-excited nonactivated ADP and KDP crystals using absorption spectroscopy with nanosecond-scale resolution.

2. EXPERIMENTAL TECHNIQUE

We used ADP and KDP single crystals of high optical quality grown at the Issyk-Kul State University (Karakol, Kirghiz Republik) using the technology described in [17]. The samples were $7 \times 7 \times 1$-mm plane-parallel plates with polished planes perpendicular to the *c* crystallographic axis.

A detailed description of the experimental setup and of the luminescence and absorption spectroscopy with nanosecond-time resolution used in this work can be found in [18]. The induced optical absorption and luminescence in the spectral region 1.2–5.5 eV were measured by the photoelectric method in the total-internal-reflection arrangement with the use of an MDR3 monochromator provided with 1200 and 600 mm^{-1} interchangeable gratings, a FÉU-97 or FÉU-83 PM tube,

and an S8-12 storage oscillograph. Measurements carried out at different wavelengths permitted reconstruction of the total optical absorption (luminescence) spectrum. The excitation source was a nanosecond-pulsed electron accelerator consisting of an Arkad'ev–Marks pulsed-voltage generator, a generator startup system, and an electron beam ejector. The accelerator had the following parameters: average electron energy 0.25 MeV, pulse length adjusted by cutting off the pulse trailing edge within 3–20 ns, current density in the pulse variable from 10 to 1000 A cm^{-2}, and maximum pulse energy 0.16 J cm^{-2}. The pulse energy used for excitation was 23% of the maximum level. The electron beam passed through a ~30-μm-thick aluminum foil directly into an evacuated cryostat with quartz windows, which was connected rigidly to the accelerator exit flange. The probing light sources were an INP-5.50 pulsed lamp for decay times of up to 20 μs and KGM12-100 and DDS-30 lamps powered by a stabilized voltage supply for studies of slower processes.

A YAG : Nd laser with an $LiNbO_3$ frequency doubler served as an additional excitation source. The output parameters of the optical pulse were $\lambda = 532$ nm, $\tau = 30$ ns, and $P = 8$ mJ; the electrical vector was perpendicular to the *c* optical axis of the crystal.

The polarization was analyzed with a Frank–Richter prism. The degree of polarization was estimated from the relation $P = (D_\parallel - D_\perp)/(D_\parallel + D_\perp)$, where the $\parallel$ and $\perp$ indices correspond to the probing-pulse electric vector oriented parallel or perpendicular to the crystal optical axis.

3. RESULTS OF THE EXPERIMENT

Figure 1 presents time-resolved TOA spectra of ADP and KDP measured immediately after the termination of the exciting pulse and 10 μs later. The spectra of both crystals have a similar structure and consist of two groups of partially overlapping bands of Gaussian shape in the regions 1.5–4.5 and 4.5–5.5 eV. Table 1 lists the parameters of these bands. As follows from an analysis of Fig. 1 and Table 1, the TOA in ADP and KDP apparently originates from the same relaxation processes. All the bands in the time-resolved TOA spectra exhibit a slow monotonic decay of the induced optical density. One readily sees, however, that the

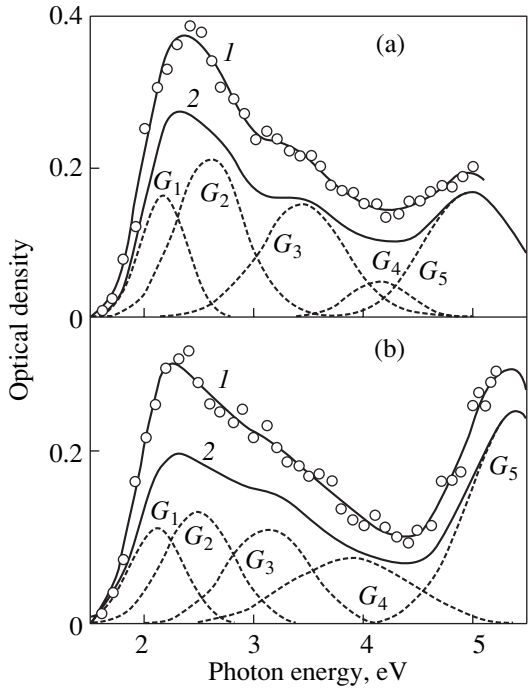

Fig. 1. TOA spectra of (a) ADP and (b) KDP measured at 290 K (*1*) immediately after the end of the excitation pulse and (*2*) 10 μs thereafter. Circles are experimental data, and solid lines are fitting by a sum of Gaussians G_1–G_5.

Table 1. Parameters of TOA spectra of ADP and KDP

Parameter	Crystal				Parameter	Crystal			
	ADP		KDP			ADP		KDP	
	D_{max}	D(10 μs)	D_{max}	D(10 μs)		D_{max}	D(10 μs)	D_{max}	D(10 μs)
E_{m1}	2.15	2.16	2.11	2.11	D_{m3}	0.21	0.15	0.12	0.10
ΔE_1	0.45	0.44	0.46	0.48	E_{m4}	4.09	4.13	3.82	3.89
D_{m1}	0.13	0.09	0.10	0.07	ΔE_4	0.64	0.55	1.09	1.09
E_{m2}	2.56	2.59	2.52	2.49	D_{m4}	0.07	0.03	0.15	0.10
ΔE_2	0.60	0.63	0.64	0.63	E_{m5}	4.95	4.98	5.32	5.40
D_{m2}	0.21	0.17	0.16	0.10	ΔE_5	0.86	0.86	0.88	0.88
E_{m3}	3.33	3.42	3.12	3.12	D_{m5}	0.20	0.18	0.32	0.26
ΔE_3	0.79	0.79	0.75	0.75					

Note: D_{max} and D(10 μs) are TOA spectra measured directly after the end of the excitation pulse and 10 μs thereafter, respectively; E_m, ΔE, and D_m are the position of the maximum (eV), FWHM (eV), and the amplitude of the corresponding constituent band G_1–G_5, respectively.

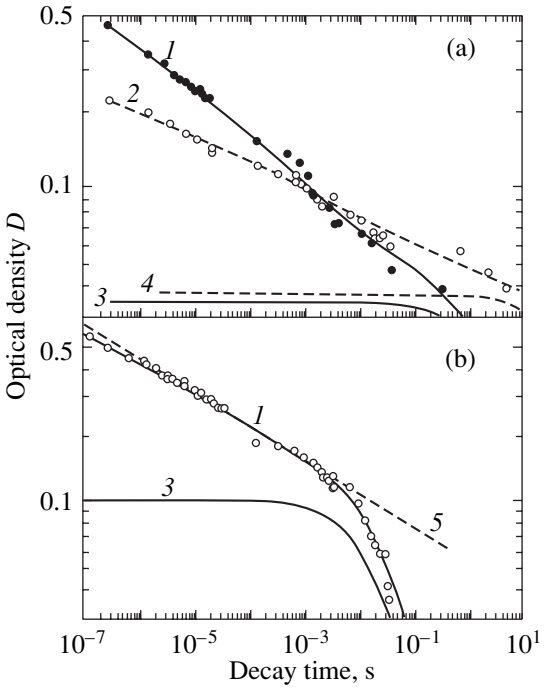

Fig. 2. TOA decay kinetics in the 2.2-eV band of (a) KDP and (b) ADP at 290 K measured after electron-beam excitation (*1*, *3*, *5*) at 23% and (*2*, *4*) 12.3% power levels. Circles are experimental data, solid and dashed lines are theory. Curves *3* and *4* are the calculated contribution from the slow component.

short-wavelength part of the 4.5–5.5 eV spectrum decays slightly slower. This indicates that the TOA in the long- and short-wavelength spectral regions is due to different color centers.

We can use Smakula's relation to estimate the cross section of optical absorption and the concentration $n(t)$ of optically active centers at time t:

$$\sigma = \frac{k(t)}{n(t)} = \frac{n^3}{(2n^2+1)^2}\frac{f\times 10^{-15}}{1.077\Delta}, \qquad (1)$$

where $k(t)$ and Δ are the absorption coefficient at the maximum and the FWHM of the OA band, respectively; f is the oscillator strength; and n is the refractive index. For both crystals, $\sigma \approx 1.04\times 10^{-16} f/\Delta$. Accepting $f = 0.1$, we obtain $\sigma \approx 4.5\times 10^{-17}$ cm^2 as an estimate of the cross section for the longest wavelength OA band in the ADP and KDP crystals. The concentration of the centers and the optical density $D(t)$ at the maximum of the OA band are related through

$$n(t) = \frac{\ln 10}{\sigma l} D(t), \qquad (2)$$

where l is the effective optical path in the layer of induced optical absorption about 50 μm thick. For the 7° measurement geometry, $l = 2 \times 0.05$ mm/sin7° = 0.8 mm. The concentrations of the centers estimated for the long-wavelength OA band in ADP and KDP are given in Table 2. Note that no saturation was observed with increasing electron beam power, which may imply that the color centers involved are of other than extrinsic nature.

Figure 2 displays experimental data on the TOA decay kinetics in ADP and KDP crystals obtained in various excitation conditions. An analysis of these data revealed that the slow monotonic relaxation of the induced optical density occurs at 290 K within a broad time range extending over six to eight decades, while the dynamic range of its variation is comparatively small. One can single out two time regions differing in decay character. In the micro- and millisecond region, the experimental data allow one to make close approximations with a straight line in the log–log coordinates (Fig. 2) and can be formally related by a linear law,

$$-\log D(t) = A + p\log t. \qquad (3)$$

This implies a power-law dependence of optical density on time, $D(t) \sim t^{-p}$. The fitting parameters A and p are given in Table 2, which shows, in particular, that the exponent p depends on crystal type and varies from 0.117 to 0.200 with increasing excitation power. For

Table 2. TOA kinetics parameters for the 2.2-eV band

Parameter	Crystal			Parameter	Crystal		
	ADP	KDP	KDP		ADP	KDP	KDP
Beam power, %	23	12	23	$n(t_0)$, 10^{17} cm^{-3}	3.0	1.3	3.0
A	0.358	0.397	0.677	$D(t_0)$	0.47	0.20	0.47
p	0.155	0.200	0.117	σ_0, THz	54	1000	1000
t_h, s	0.015	60	2	$a_3 \times N$, 10^{-5}	4.30	1.91	3.11
D_h	0.099	0.036	0.034	N, 10^{19} cm^{-3}	4.3	1.9	3.1
t_0, ns	124	114	126				

Note: A and p are fitting parameters used in a formal approximation of the kinetics as $-\log(D) = A + p\log(t)$, where t is the time in μs; t_0 specifies the beginning of kinetics measurement; $n(t_0)$ and $D(t_0)$ are the OA center concentration and optical density at time t_0, respectively; and D_h and t_h are the fitting parameters for the slow component $D = D_h/(1 + t/t_h)$. The parameters of the defect tunneling-recharging model: σ_0 is the prefactor, a is one half of the defect Bohr radius, and N is the defect concentration.

longer decay times, the TOA kinetics can also be approximated with a straight line from Eq. (3) but with $p \approx 1$, which assumes a first-order hyperbolic relation:

$$D(t) = \frac{D_h}{1 + t/t_h}, \quad (4)$$

where D_h and t_h are the initial concentration and the half-life of the defects responsible for the given TOA decay kinetics component. The hyperbolic component is seen most clearly in the ADP crystal for $t > 10$ ms; however, numerical treatment of the TOA kinetics in KDP also reveals the presence of this component (Fig. 2).

Measurements performed in polarized light showed the TOA band to exhibit a comparatively weak optical dichroism at 2.2 eV. The degree of TOA polarization measured immediately after termination of the excitation pulse is approximately –0.1 (ADP) and –0.2 (KDP).

When studying cascade excitation, an additional high-intensity optical pulse was pumped into the 1.9-eV band after a variable delay relative to the end of the electron pulse. The TOA kinetics did not, however, exhibit any change in ADP and KDP under cascade excitation.

Electron-beam excitation of ADP and KDP crystals at 290 K gives rise to a burst of cathodoluminescence with a characteristic decay time of about 20 ns, which is comparable to the excitation pulse length (Fig. 3). The luminescence is unpolarized throughout the spectral region studied. Figure 4 presents pulsed cathodoluminescence (PCL) spectra measured at the peak of this burst. As evident from Fig. 4, the PCL spectra of ADP and KDP are similar in structure and consist of two main bands, at 3.5–3.7 and 4.6–4.9 eV, with an FWHM of 0.9–1.0 and 1.3–1.4 eV, respectively.

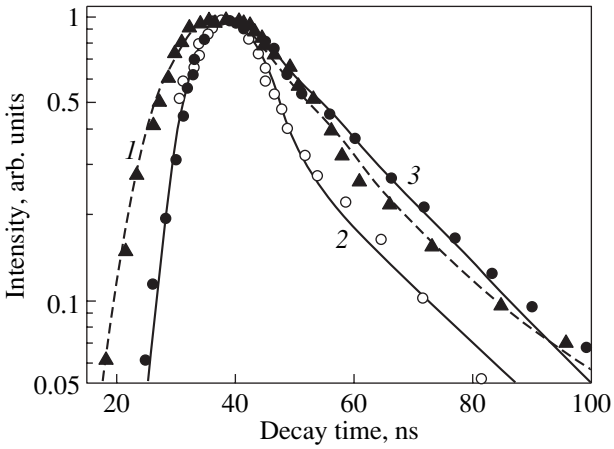

Fig. 3. PCL decay kinetics in the bands at (*1*, *2*) 2.2 eV and (*3*) 4.6 eV in (*1*) KDP and (*2*, *3*) ADP measured at 290 K.

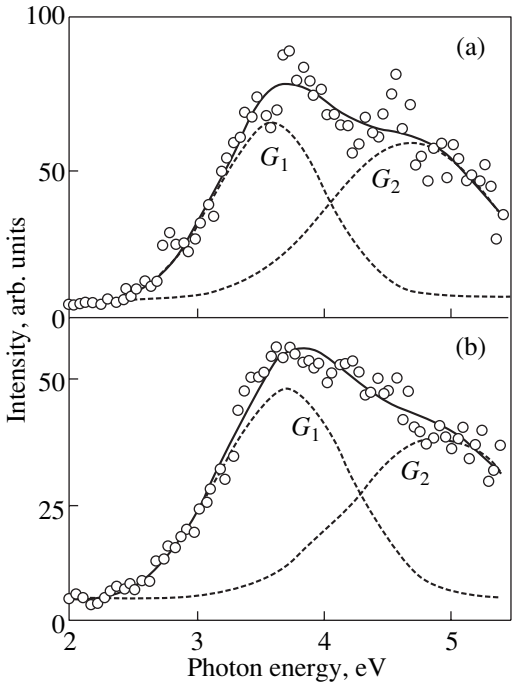

Fig. 4. PCL spectra of (a) ADP and (b) KDP measured at 290 K. Circles are experimental data, and solid lines are their fitting by a sum of Gaussians G_1 and G_2.

4. DISCUSSION OF RESULTS

An analysis of the TOA spectra of ADP and KDP measured at 290 K (Fig. 1) revealed that they are similar to the spectra of the low-temperature stable OA of these crystals [14]. Indeed, unactivated ADP, KDP, and DKDP crystals exhibit, after irradiation by x-ray photons at 10 K, a broad composite OA band in the region 1.5–4.0 eV with a maximum at 2.43 eV (ADP) or 2.26 eV (KDP) and a shoulder at 3.2 eV due to the *A* and *B* hole radicals [13, 14]. The concentration of the *A* and *B* radicals grows monotonically under irradiation; however, the ratio of their concentrations depends neither on the dose nor on the temperature [13]. In both color centers, optical transitions from valence-band (VB) states to the local level of the defect are observed. Viewed from the standpoint of electronic structure [19, 20], the highest occupied molecular orbitals (HOMO) of the H_2PO_4 anion group derive from the antibonding states of oxygen; the VB states derived from the hydrogen orbitals ($E \approx -2.3$ eV) and phosphorus–oxygen orbitals ($E \approx -3.3$ eV) lie lower. The hole produced in the formation of the *A* radical is trapped by the dangling oxygen orbital, pointing toward a hydrogen vacancy [8]. The hole becomes self-trapped (the *B* radical) in the HOMO states. In both cases, the optical transitions are associated with electron transfer to the defect level from the same lower lying occupied states, which assumes a marked similarity between the spectral OA profiles of the *A* and *B* radicals. Their OA spectra differ primarily in polarization; namely, the OA of the *A* rad-

icals is predominantly πpolarized, whereas the *B* radicals provide a major contribution to the σ-polarized OA [14].

All three crystals exhibit a correlation between the thermal-bleaching curves in the OA band of the *A* and *B* radicals [14] and the nonisothermal relaxation of the EPR spectra of these centers [9, 21]. Note that the *B* radicals are annealed (the STHs become mobile) at a temperature of about 70 K, whereas the *A* radicals are annealed near the Curie point T_c = 123 K (KDP) and 148 K (ADP). No stable OA is observed to exist above T_c in the region 1.5–3.5 eV.

The short-wavelength OA bands at 4.7 and 5.4 eV in KDP are attributed to the formation of *L* defects (hydrogen vacancies) associated with impurities (Fe, Cr, Mn, Al) or radiation defects [15, 22–24]. In both cases, the *L* defects form to compensate the excess charge of the main defect. Note that the low-temperature *A* radical represents essentially a hole trapped by a single hydrogen vacancy. The *L* defects associated with impurities form in the course of growth and exist in the crystal before the irradiation, their concentration depending on the impurity content. The *L* defects associated with radiation defects form when the crystal is irradiated by γ photons, neutrons, and ion and electron beams, and their number grows with increasing irradiation dose. The optical transitions occurring in such *L* defects depend only weakly on the actual type of the impurity or radiation defect, which would imply the same spectral response of OA; however, stabilization of *A* radicals by impurities may affect the kinetics and temperature behavior of the optical-density relaxation [15, 22, 25].

We believe that the transient optical absorption of ADP and KDP in the region 1.5–4.0 eV (the G_1–G_3 bands in Fig. 1) is due to optical transitions taking place between VB states and the local level of a hole center (*A* or *B* radical). The comparatively weak polarization of the TOA indicates there are similar contributions from the π and σOA components, i.e., from the optical transitions in both centers. We assign the short-wavelength TOA (4.0–5.5 eV) observed in ADP and KDP crystals under electron-beam irradiation at 290 K (Fig. 1) to the formation and, possibly, recharging of the *L* defects associated with various impurity or radiation defects.

The above analysis of the TOA spectra of ADP and KDP (Fig. 1) suggests that the transient optical absorption in both crystals originates from contributions due to hole centers of several different types. Thus, the comparatively uniform relaxation of the TOA spectra can be accounted for only if the decay of these defects is limited in all cases by the same relaxation process, which is common for both crystals. In this case, the optical-density decay law should reflect the kinetics of this process. We consider the most probable hypotheses on its nature.

It is known that in alkali halide crystals, hole-type centers move above their delocalization temperature through diffusion [26]. The parameters of thermally stimulated STH migration in ADP and KDP are known, namely, the frequency factor ω_0 = 13–19 s^{-1} and the activation energy *E* = 42–45 meV [14]. The characteristic lifetime of the hole centers is given by the relation

$$\tau^1 = \omega_0 \exp(-E/k_B T), \quad (5)$$

where k_B is the Boltzmann constant and *T* is the temperature. One readily sees that for 290 K, τ ≈ 360 ms. This time exceeds the characteristic time of TOA decay in ADP and KDP crystals by three to four orders of magnitude (Fig. 2). One may suggest in this connection that the TOA kinetics in these crystals is rate-limited not by hole polaron transfer but rather by another process, for instance, by electron recombination. This conjecture is indirectly argued for by the absence of cascade excitation effects under excitation into the OA band of the hole center.

We note, first of all, that one should consider only intrinsic lattice defects common for the ADP and KDP crystals to be electronic centers. Indeed, the hole center concentration in unactivated ADP and KDP is fairly high (Table 2) and does not reveal a tendency to saturation with increasing dose. The number of electronic centers in these crystals cannot be less than that of the hole centers. This excludes from consideration the electronic centers associated with residual impurities. Let us discuss the electronic centers involving native ADP and KDP lattice defects.

EPR studies in KDP revealed electronic centers in the form of a molecular PO_3^{2-} ion produced in the capture of an electron by an oxygen vacancy [27]. These centers persist at room temperature for several weeks, and their optical transitions are presumably confined to the region 1000–2000 nm. Obviously enough, the characteristics of these centers do not meet the requirements formulated above.

The most appropriate candidate is the electronic center representing an interstitial hydrogen atom H^0. The H^0 centers form by the following scenario [12]: ionizing radiation or two-photon absorption of laser radiation (λ = 266 nm) generates band electrons and holes. The hydrogen ion H^+ sitting at a lattice site traps an electron to become a neutral hydrogen atom, which, acted upon by thermal vibrations, is ejected from the site. The oxygen atom closest to the vacancy thus formed traps the hole and forms the *A* radical. Interstitial diffusive migration of the neutral hydrogen atom culminates in its localization at the free position of a singly occupied hydrogen bond, a process giving rise to the formation of an $H_3PO_4^{2-}$ group (the *D* defect) [28, 29]. As established by EPR studies [12], the concentrations of the *A* radicals and H^0 centers in KDP crystals irradiated at 77 K are approximately equal and can be as high as 10^{18} cm^{-3}; i.e., there is a common mechanism of formation of these complementary nonimpurity defects. Thermal annealing of the H^0 centers takes

place at temperatures of 80–200 K as a result of their migration and annihilation with hydrogen vacancies.

Diffusive interstitial transport of the H^0 atom is temperature-dependent and has been studied in considerable detail in ADP and KDP by the methods of electrical conductivity [28], NMR [30, 31], and $^3H^0$ tracer diffusion [32]. In particular, the migration activation energy of this defect was determined to be 0.53 eV for KDP and 0.48 eV for ADP. As follows from the theory of diffusion-limited reactions (DLR) [33] with a recombination sphere of radius R_0 and an interdiffusion coefficient D_R, the kinetics of this reaction is quasi-stationary (except the initial stages within $t < R_0^2/D_R$) with the rate constant

$$K = 4\pi D_R R_0(1 + R_0/\sqrt{\pi D_R t}). \quad (6)$$

This rate constant is characterized by a steady-state distribution function of reaction partners over their separation $Y(r) = 1 - R_0/r$ and does not undergo noticeable variations during the process. Assuming $R_0 = 5$ Å and $D_R = 1.3 \times 10^{-11}$ cm^2 s^{-1} [32] and accepting $N_h = 1 \times 10^{17}$ cm^{-3} for the initial defect concentration, we obtain for the characteristic time of DLR kinetics (the half-life) [33]

$$t_h = (KN_h)^{-1} \approx 1.25 \text{ s}. \quad (7)$$

Therefore, the diffusion mechanism of particle migration should not become manifest in the observed TOA kinetics in the microsecond and microsecond ranges (Fig. 2). The comparatively small value of the exponent p obtained in the approximation of the TOA kinetics is also not typical of DLR, for which $p \approx 1$. All this narrows down the scope of acceptable hypotheses bearing on the TOA relaxation mechanisms in ADP and KDP. Only a few post-radiation processes are characterized by a similar asymptotic behavior of the concentration of the relevant defects. In particular, a relatively small exponent p is characteristic of tunneling recharging (TR) of defects, which contributes markedly to the reaction rate constant not only in the low-temperature domain but also at temperatures where the defects become mobile [33]. We believe that the rate-limiting process in the TOA relaxation in ADP and KDP in the microsecond and microsecond ranges is the defect TR.

In the treatment of diffusion-limited TR, the radius R_0 is replaced by the effective recombination radius R_s, which depends on the diffusion coefficient, and the TR reaction is assumed to be confined to a spherical layer of thickness a (a is one half of the Bohr radius of the defect wave function) close to R_s. The TR probability is given by the relation

$$\sigma(r) = \sigma_0 \exp(-r/a), \quad (8)$$

where σ_0 is the prefactor. We consider the case of equal-probability distribution of electronic and hole centers over the crystal. If the concentration of localized electrons N at time zero considerably exceeds that of localized holes n ($t = 0$), the time variation of the hole concentration $n(t)$ under TR is described by the relation [34]

$$n(t) = n(t_0)\exp\left(-\frac{4\pi}{3}a^3 N[\ln^3(\sigma_0 t) - \ln^3(\sigma_0 t_0)]\right), \quad (9)$$

where t_0 is the time starting from which the TOA decay kinetics is analyzed.

For short observation times ($t \le 10^4 t_0$), Eq. (9) transfers to a power-law function,

$$n(t) = n(t_0)\left(\frac{t}{t_0}\right)^{-p}, \quad (10)$$

where $p = 4\pi a^3 N \ln^2(\sigma_0 t_0)$. For typical values of the parameters $\sigma_0 \sim 1000$ THz, $a \sim 1$ Å, $N \sim (2–5) \times 10^{19}$ cm^{-3}, and $t_0 \sim 100$ ns, we obtain $p = 0.085–0.213$. This compares well with our experimental data.

Table 2 lists the TOA kinetics parameters for ADP and KDP at 290 K, which were obtained by fitting the experimental data in Fig. 2 with a sum of two components described by Eqs. (9) and (4). N was estimated by accepting that $a = 1$ Å. As seen from Table 2, for decay times up to 10 ms for ADP and 100 ms for KDP, the TOA asymptotic behavior is well approximated by the theory of TR of randomly distributed fixed defects. The slow component in the TOA decay kinetics originates from the diffusive transport of defects. Let us estimate the radius of the recombination sphere R_s [33]:

$$R_s = a\ln\left(\frac{a^2\sigma_0}{D}\right) \approx 23a. \quad (11)$$

Substituting the recombination sphere radius of Eq. (11) into Eq. (6) for the reaction rate constant and using the numerical values of t_h (Table 2), we obtain the following estimate for N_h from Eq. (7): (1–10) $\times 10^{15}$ cm^{-3} for KDP and about 10^{18} cm^{-3} for ADP. For the KDP crystal, the value of N_h is comparable to the concentration of hydrogen vacancies associated with extrinsic or structural defects. In this case, the slow TOA component could be identified with the TR of these defects (possibly, with their annihilation), which is rate-limited by the diffusive transport of mobile hydrogen atoms. Interpretation of the large value of N_h obtained for the ADP crystal requires separate consideration.

The existence of high carrier concentrations localized at comparatively long-lived defects is favorable for the onset of recombination luminescence. We showed earlier [24] that subnanosecond-scale photoexcitation of KDP at 10 K gives rise to a fast luminescence with a characteristic decay time $\tau < 10$ ns. There is nothing strange, therefore, in the fact that the main part of the luminescence generated under 15-ns-long electron-beam irradiation is confined within the excitation pulse duration and a short time interval after its completion

(Fig. 3). This luminescence originates from electron and hole recombination of band carriers at the corresponding defects (*A* and *B* radicals and the H^0 center). Hole (3.55 eV) and electron (4.77 eV) recombination luminescence bands have been identified in ADP, KDP, and DKDP crystals [14]. It is these bands that are dominant in the fast PCL spectra of ADP and KDP at 290 K (Fig. 4). Obviously enough, at 290 K, the slow thermally stimulated migration of the partners (*A* and *B* radicals and the H^0 center) involved in the interdefect tunneling recombination is not accompanied by ejection of localized carriers into the conduction or valence band. Otherwise, the characteristic recombination luminescence would be observed throughout the TOA decay time range and the decay itself would follow a law different from Eq. (9). It is known [26] that in alkali halide crystals, the interdefect tunneling recombination is usually accompanied by inertial tunneling luminescence. Equation (9) yields, for the tunneling luminescence intensity,

$$I(t) = -\frac{dn(t)}{dt} = 4a^3 Nn(t)\frac{\ln^2(\sigma_0 t)}{t}. \qquad (12)$$

Within the decay time range from 10 ns to 10 s, the expression in the numerator depends comparatively weakly on time. The numerical values of the parameters in Table 2 provide the estimate $I(t) \approx 5 \times 10^{15}/t$, $cm^3\ s^{-1}$. This seems to correspond to a luminescence intensity too weak to be detected in our measurements. Further specific experiments would be required to investigate this.

5. CONCLUSIONS

Thus, our absorption optical spectroscopy study with a nanosecond-scale time resolution has established that the transient optical absorption in ADP and KDP crystals observed in the visible and near-UV spectral regions at 290 K originates from optical transitions in hole polarons representing the *A* and *B* radicals. The optical-density relaxation kinetics is rate-limited by interdefect tunneling recombination, which involves hole polarons and electronic H^0 centers representing neutral hydrogen atoms. At 290 K, the hole polarons and the H^0 centers migrate in a thermally stimulated manner, which is not accompanied by carrier ejection into the conduction or valence band. Slow TOA components with characteristic times from a few tens of milliseconds to a few seconds were assigned to TR or annihilation of hydrogen vacancies associated with extrinsic or structural defects, which is rate-limited by diffusive transport of the hydrogen atoms.

ACKNOWLEDGMENTS

The authors are grateful to V.T. Kuanyshev for his assistance in the measurements and to M.M. Kidibaev for providing the crystals.

REFERENCES

1. V. G. Dmitriev, G. G. Gurzadyan, and D. N. Nikogosyan, *Handbook of Nonlinear Optical Crystals* (Springer-Verlag, Berlin, 1999).
2. W. Koechner, *Solid State Laser Engineering* (Springer-Verlag, Berlin, 1999).
3. W. L. Smith, Appl. Opt. **16** (7), 1798 (1977).
4. G. M. Davis, L. Zhang, P. J. Chandler, and P. D. Townsend, IEEE Photonics Technol. Lett. **5** (4), 430 (1993).
5. S. G. Demos, M. Yan, M. Staggs, *et al.*, Appl. Phys. Lett. **72** (19), 2367 (1998).
6. C. D. Marshall, S. A. Payne, M. A. Henesian, *et al.*, J. Opt. Soc. Am. B **11** (5), 774 (1994).
7. W. E. Hughes and W. G. Moulton, J. Chem. Phys. **39** (5), 1359 (1963).
8. K. Tsuchida, P. Abe, and M. Naito, J. Phys. Soc. Jpn. **35** (3), 806 (1973).
9. J. A. McMillan and J. M. Clemens, J. Chem. Phys. **68** (8), 3627 (1978).
10. J. W. Wells, E. Budzinski, and H. C. Box, J. Chem. Phys. **85** (11), 6340 (1986).
11. K. T. Stevens, N. Y. Garces, L. E. Halliburton, *et al.*, Appl. Phys. Lett. **75** (11), 1503 (1999).
12. S. D. Setzler, K. T. Stevens, L. E. Halliburton, *et al.*, Phys. Rev. B **57** (5), 2643 (1998).
13. E. Diéguez and J. M. Cabrera, J. Phys. D **14** (1), 91 (1981).
14. E. Diéguez, J. M. Cabrera, and F. Agulló López, J. Chem. Phys. **81** (8), 3369 (1984).
15. G. N. Pirogova, Yu. V. Voronin, V. E. Kritskaya, *et al.*, Neorg. Mater. **22** (1), 115 (1986).
16. M. K. Satybaldieva, M. M. Kidibaev, I. N. Ogorodnikov, *et al.*, in *Problems of Spectroscopy and Spectrometry: Interuniversity Collection of Scientific Works* (Ural's. Gos. Tekh. Univ., Yekaterinburg, 2000), Vol. 4, p. 27.
17. A. A. Alybakov, A. A. Abdrazakov, O. M. Arbotoev, and K. Kudabaev, Cryst. Res. Technol. **23** (10–11), 1401 (1988).
18. B. P. Gritsenko, V. Yu. Yakovlev, and Yu. N. Safonov, in *Proceedings of the All-Union Conference "Modern State and Advanced Aspects of High-Speed Photography, Cinematography and Metrology of Fast Processes," Moscow, 1978*, p. 61.
19. S. Saito, K. Wada, and R. Onaka, J. Phys. Soc. Jpn. **37** (3), 711 (1974).
20. I. V. Stasyuk and R. Ya. Stetsiv, Izv. Akad. Nauk SSSR, Ser. Fiz. **55** (3), 522 (1991).
21. G. Volkel, W. Windsch, and W. Urbanowitschins, J. Magn. Reson. **18**, 57 (1975).
22. V. V. Azarov, L. V. Atroshchenko, I. M. Kolybaeva, *et al.*, Fiz. Khim. Obrab. Mater. **5**, 34 (1984).
23. V. T. Kuanyshev, I. N. Ogorodnikov, and M. M. Kidibaev, in *Problems of Spectroscopy and Spectrometry: Interuniversity Collection of Scientific Works* (Ural's. Gos. Tekh. Univ., Yekaterinburg, 1999), Vol. 2, p. 49.
24. I. N. Ogorodnikov, V. A. Pustovarov, B. V. Shul'gin, *et al.*, Opt. Spektrosk. **91** (2), 242 (2001) [Opt. Spectrosc. **91**, 224 (2001)].
25. V. T. Kuanyshev, T. A. Belykh, I. N. Ogorodnikov, *et al.*, Radiat. Meas. **33** (5), 503 (2001).

26. É. D. Aluker, V. V. Gavrilov, R. G. Deĭch, and S. A. Chernov, *Fast Radiation-Enhanced Processes in Alkali Halide Crystals* (Zinatne, Riga, 1987).

27. N. Y. Garces, K. T. Stevens, L. E. Halliburton, *et al.*, J. Appl. Phys. **89** (1), 47 (2001).

28. L. B. Harris and G. J. Vella, J. Chem. Phys. **58** (10), 4550 (1971).

29. A. I. Ryabov, N. S. Stel'makh, G. N. Pirogova, *et al.*, Fiz. Tverd. Tela (Leningrad) **33** (9), 2660 (1991) [Sov. Phys. Solid State **33**, 1502 (1991)].

30. F. E. G. Henn, J. C. Giuntini, and J. V. Zanchetta, Appl. Phys. A **A51**, 455 (1990).

31. J. Dolinsek, M. Karayanni, and G. Papavassiliou, Solid State Ionics **125** (1–4), 159 (1999).

32. J. M. Pollock and M. Sharan, J. Chem. Phys. **51** (8), 3604 (1969).

33. Yu. R. Zakis, L. N. Kantorovich, E. A. Kotomin, V. N. Kuzovkov, I. A. Tale, and A. L. Shlyuger, *Model of Processes in Wide-Gap Solids with Defects* (Zinatne, Riga, 1991).

34. V. N. Parmon, A. F. Khaĭrutdinov, and K. I. Zamaraev, Fiz. Tverd. Tela (Leningrad) **16** (9), 2572 (1974) [Sov. Phys. Solid State **16**, 1672 (1974)].

Translated by G. Skrebtsov

Physics of the Solid State, Vol. 44, No. 5, 2002, pp. 888–892. Translated from Fizika Tverdogo Tela, Vol. 44, No. 5, 2002, pp. 853–857.

DEFECTS, DISLOCATIONS, AND PHYSICS OF STRENGTH

Electronic Structure of a KCl Nanocrystal with an Edge Dislocation

Yu. K. Timoshenko and V. A. Shunina

Voronezh State University, Voronezh, 394693 Russia

e-mail: yury@tim.vsu.ru

Received August 2, 2001

Abstract—The electron structure of a relaxed nanocrystal of potassium chloride with an edge dislocation was calculated in the tight-binding approximation using a procedure self-consistent in effective charges and dipole moments of ions. Total and partial local densities of states were calculated. The effect of relaxation and polarization on the single-electron energy spectrum was calculated. © *2002 MAIK "Nauka/Interperiodica".*

The electron structure of dislocations in ionic crystals has been studied insufficiently, despite the wide use of such crystals in fundamental investigations and applications. To our knowledge, there are only a few works [1–5] in which the dislocation levels have been determined in alkali-halide crystals (AHCs) both experimentally and theoretically. The available experimental data are difficult to interpret adequately, and the results of theoretical works substantially contradict one another. Compare, e.g., theoretical results for KCl crystals. According to [2], the splitting-off of the lowest donor dislocation level from the top of the valence band is a few electron-volts (in any case, it is greater than 4 eV; it cannot be indicated more exactly, since, in our opinion, the data given in the table and in the main text of [2] disagree); the acceptor levels were not considered in [2]. In [3], it was revealed that the donor dislocation band is located in the range 2.47–2.58 eV above the valence band, while the acceptor dislocation band is in the range 1.76–1.96 eV below the bottom of the conduction band. According to [4], the splitting-off of dislocation levels from the top of the valence band is 0.038 eV and that from the bottom of the conduction band is 0.05 eV. In [2, 3], the lattice relaxation caused by dislocation was not considered. In [4], the Madelung fields were calculated proceeding from the ion coordinates in a relaxed lattice with a dislocation that were obtained in [6]. The calculations of the dislocation levels were performed in terms of the one-dimensional perturbation theory, as in [2, 3]. Note that in [2–4] the polarization effects, which necessarily should be taken into account in alkali-halide crystals [7], were completely ignored.

The calculation of the electron structure of a polar crystal with a dislocation with allowance for relaxation and polarization effects is a nontrivial problem. However, the situation is simplified if we restrict ourselves to a nanocrystal. In this paper, we consider an electrically neutral KCl nanocrystal consisting of eight layers. The upper layer is shown in Fig. 1. The total number of ions was 344. As in [2–4], an edge dislocation with a Burgers vector $\langle 110 \rangle$ was located in the glide plane $\{1\bar{1}0\}$.

The relaxation of the nanocrystal was considered in terms of the model of pointlike polarizable ions. In this approximation, the potential energy of interaction of the ions of the system is

$$W = W_C + W_R + W_{VdW} + W_{pol}, \quad (1)$$

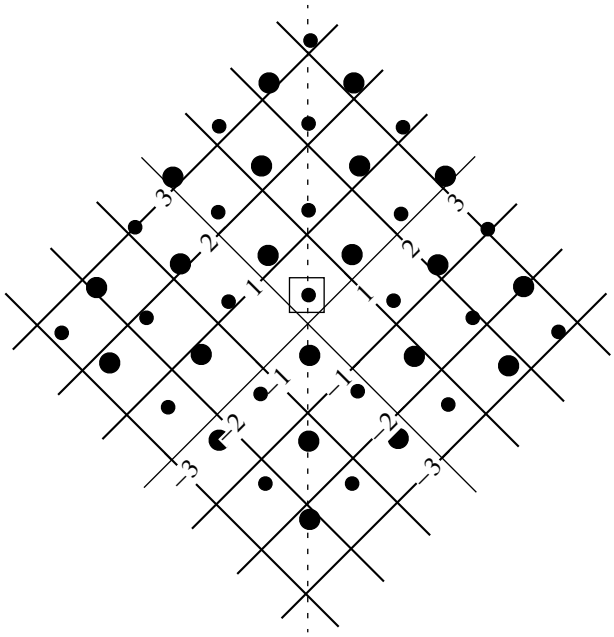

Fig. 1. The upper layer of a nanocrystal with an edge dislocation. The cations are the circles of larger size. Along the axes, coordinates in units of half-lattice-parameter are indicated.

1063-7834/02/4405-0888$22.00 © 2002 MAIK "Nauka/Interperiodica"

where

$$W_C = \sum_{i<j} \frac{q_i q_j}{R_{ij}},$$

$$W_R = \sum_{i<j} b\beta_{ij} \exp\left\{\frac{r_i + r_j - R_{ij}}{\rho}\right\} g(R_{ij}), \quad (2)$$

$$W_{VdW} = -\sum_{i<j} C_{ij} R_{ij}^{-6} g(R_{ij}). \quad (3)$$

W_C is the energy of the Coulomb interaction of the ions; W_R is the energy of repulsion of electron shells; W_{VdW} is the van der Waals energy with allowance for the dipole–dipole interaction; W_{pol} is the polarization term; q_i, the charge of the ith ion; $R_{ij} = |\mathbf{R}_i - \mathbf{R}_j|$ is the spacing between the ith and jth ions; and β_{ij}, r_i, ρ, C_{ij}, and D_{ij} are the parameters of the potential. The $g(R_{ij})$ function has the form [8]

$$g(R) = \begin{cases} 1, & R \le R_b \\ (1-t^3)(1+3t+6t^2), & R_b < R < R_c \\ 0, & R \ge R_c, \end{cases}$$

where $t = (R - R_b)/(R_c - R_b)$, R_c is the cut-off radius, and $R_b < R_c$. The $g(R)$ function ensures a gradual falloff of the potentials W_R and W_{VdW} to zero in the interval $[R_b, R_c]$ and is necessary to prevent jumps in the derivatives on going from W_R to W_{VdW}.

In the model under consideration, each ion represents a point quasi-elastic dipole with an electric moment

$$\mathbf{d}_i = \alpha_i \mathbf{E}(\mathbf{R}_i), \quad (4)$$

where α_i is the polarizability of the ith ion and $\mathbf{E}(\mathbf{R}_i)$ is the strength of the electric field at the point where this ion is located. The term W_{pol} represents the energy of induced quasi-elastic dipoles [9]

$$W_{pol} = -\frac{1}{2}\sum_i \mathbf{d}_i \mathbf{E}(\mathbf{R}_i)$$

in the field produced by point ions and induced dipoles with a strength

$$\mathbf{E}(\mathbf{R}_i) = \mathbf{E}^C(\mathbf{R}_i) + \mathbf{E}^D(\mathbf{R}_i),$$

where

$$\mathbf{E}^C(\mathbf{R}_i) + \sum_{j \ne i} \frac{q_i \mathbf{R}_{ij}}{R_{ij}^3},$$

$$\mathbf{E}^D(\mathbf{R}_i) + \sum_{j \ne i} \left\{\frac{3(\mathbf{d}_j \mathbf{R}_{ij})\mathbf{R}_{ij}}{R_{ij}^5} - \frac{\mathbf{d}_j}{R_{ij}^3}\right\}.$$

Table 1. Parameters of ion interaction for KCl

Parameter	Value
r_e, Å	3.145
r_+, Å	1.330
r_-, Å	1.810
ρ, Å	0.345
β_{++}	1.250
β_{--}	0.750
β_{+-}	1.000
b, eV	0.163
C_{++}, eV Å^6	14.355
C_{--}, eV Å^6	114.219
C_{+-}, eV Å^6	38.947
R_b, Å	4.600
R_c, Å	5.000
Z	0.979
α_+, Å^3	1.33
α_-, Å^3	2.97

Here, the vector $\mathbf{R}_{ij} = \mathbf{R}_i - \mathbf{R}_j$ is directed from the point $\mathbf{R}_j$ to the point of observation $\mathbf{R}_i$. As follows from the above formulas, for each spatial configuration of the ions, the induced dipole moments should be determined in a self-consistent way. The parameters required to calculate (2) are given in Table 1. The magnitude of the effective charge Z was obtained previously in our self-consistent calculations [10], and the other parameters, except for b, R_b, and R_c, were taken from literature data [11–13]. The parameter b was determined by minimizing the potential energy of the ideal infinite crystal using the experimental value of the lattice parameter. The values of the parameters R_b and R_c were taken such that the pair potentials of repulsion of electron shells and the van der Waals potential smoothly tended to zero in an interval (R_2, R_3), where R_k is the radius of the kth coordination shell.

In the zero approximation, all moments of quasi-elastic dipoles were set to zero. Then, in the process of the minimization of the potential energy of the system with respect to ion coordinates, which was performed by the Fletcher–Reeves method [14], the dipole moments were calculated in a self-consistent way. When constructing the initial spatial configuration of a nanocrystal, data on the geometry of the core of an edge dislocation given in [4, 6] were used.

After the calculation of the equilibrium configuration of the nanocrystal, its electron structure was considered. We used the Slater–Koster variant of the tight-binding method modified by one of us [15], in which the self-consistency was performed with respect to the effective charges and dipole moments of the ions. Previously, such a scheme of calculations was successfully

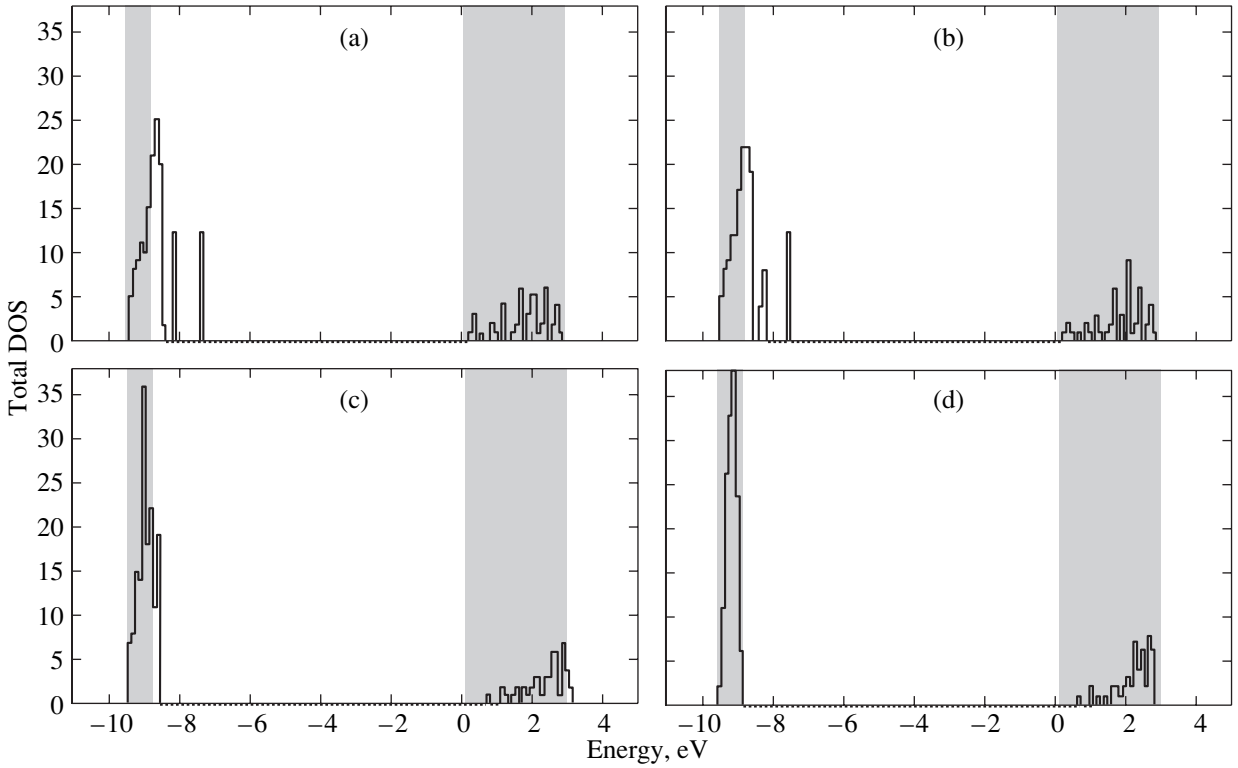

Fig. 2. Histograms of the total densities of states for a nanocrystal consisting of 100 ions calculated in various approximations: (a) non-self-consistent calculation without allowance for relaxation and polarization; (b) self-consistent calculation without allowance for relaxation; (c) self-consistent calculation with allowance for relaxation; and (d) non-self-consistent calculation for a fragment (cluster) of an ideal crystal with matrix elements taken from [18].

applied to studying the electron structure of polar nanocrystals with atomically rough surfaces [10, 16]. The Slater–Koster parameters, as in [17], were taken from [18]. Within this approach, the diagonal matrix elements of the Hamiltonian are calculated by the formula

$$H_{l\alpha,\,l\alpha} = H^0_{l\alpha,\,l\alpha} + \Delta\tilde{W}_l, \tag{5}$$

where

$$\Delta\tilde{W}_l = -|e|\varphi(\mathbf{R}_l) - W^M_l, \tag{6}$$

$$\varphi(\mathbf{R}_l) = \varphi^{\mathrm{C}}(\mathbf{R}_l) + \varphi^{\mathrm{D}}(\mathbf{R}_l), \tag{7}$$

$$\varphi^{\mathrm{C}}(\mathbf{R}_l) = \sum_{j\neq l}\frac{q_j}{|\mathbf{R}_l - \mathbf{R}_j|}, \tag{8}$$

$$\varphi^{\mathrm{D}}(\mathbf{R}_l) = \sum_{j\neq l}\frac{(\mathbf{d}_j, (\mathbf{R}_l - \mathbf{R}_j))}{|\mathbf{R}_l - \mathbf{R}_j|^3}. \tag{9}$$

Here, l is the order number of a site, α is the type of atomic orbital (AO), $\varphi^{\mathrm{C}}(\mathbf{R}_k)$ and $\varphi^{\mathrm{D}}(\mathbf{R}_k)$ are the electrostatic potentials at a site k caused by monopoles and by induced dipoles of the ions, and W^M_k is the Madelung field at the kth site in an ideal crystal. The ionic (inertial) polarization is taken into account in this formalism by using the coordinates of ions in relaxed nanocrystals found in terms of the model of point polarizable ions. The off-diagonal elements of the Hamiltonian for the relaxed nanocrystals were found using the Harrison formula [19]

$$H_{l\alpha,\,l'\alpha'} = \eta_{\alpha\alpha'}\frac{\hbar^2}{md^2_{ll'}}, \quad \alpha, \alpha' = s, p. \tag{10}$$

Here, $l \neq l'$, m is the electron mass, $d_{ll'} = |\mathbf{R}_l - \mathbf{R}_{l'}|$, and $\eta_{\alpha\alpha'}$ is the dimensionless Slater–Koster parameter.

Formulas (5)–(10) make it possible to perform a self-consistent calculation over the effective charges and dipole moments of the ions. The iteration procedure was continued until the maximum deviation of the dipole moments for two neighboring iterations became less than a preliminarily specified δ (in our calculations, $\delta = 10^{-4}$ Debye). In principle, the calculated effective charges and dipole moments could be used to recalculate the parameters entering into formulas (2) and (3) and to refine the coordinates of ions of the relaxed nanocrystal. However, in view of the lack of a reliable algorithm for such a recalculation, we restricted ourselves to the search for the geometry of an equilibrium configuration using only the parameters taken from Table 1.

The allowance for polarization effects in calculations of the electron structure of polar crystals and nanocrystals with defects is of great importance. We consider, using various approximations, the electron structure of a KCl nanocrystal consisting of 100 ions that form a parallelepiped with dimensions of $5 \times 5 \times 4$ ions. Figure 2a displays the histogram of the total density of states (TDOS) for this nanocrystal calculated non-self-consistently, without allowance for relaxation and polarization. It is seen that there are occupied states located in the forbidden band of the ideal crystal. The self-consistency with respect to effective charges but without allowance for relaxation somewhat changes the TDOS (Fig. 2b), but the changes are small. A self-consistent calculation with allowance for both relaxation and polarization leads to qualitative changes in the TDOS. It is seen from Fig. 2c that no deep levels are now present in the region corresponding to the forbidden band of the ideal crystal. For comparison, Fig. 2d shows the TDOS of a cluster consisting of 100 ions of the same shape but simulating the bulk states of an ideal crystal. The hatched regions in the above figures correspond to the valence band and the conduction band of an ideal KCl crystal calculated in terms of the band theory with the same Slater–Koster parameters as in the case of nanocrystals. Thus, the neglect of relaxation and polarization effects leads to an overestimation of the splitting-off of local levels from the band edges. Note also that upon relaxation, the cations and anions located at the centers of faces shift deeper into the nanocrystal. The other ions shift in a similar manner; i.e., on the whole, the nanocrystal shrinks, which qualitatively agrees with the data given in [20].

A self-consistent calculation of the TDOS with allowance for relaxation and polarization for nanocrystals with an edge dislocation shows that in the region corresponding to the forbidden band of an ideal crystal there are occupied levels. The upper occupied level is located above the top of the valence band by about 0.27 eV (Fig. 3). However, it follows from an analysis of orbital coefficients for these levels that the corresponding states are mainly localized near the bordering ions of the nanocrystal rather than in the region of the dislocation line. Calculation of partial local densities of states for ions located at the dislocation line in the bulk of the nanocrystal (Fig. 4) shows that these densities exhibit sharp peaks in the region of band states rather than in the forbidden band. This indicates that the disturbances at the line of dislocation are not too large. Let us turn to Table 2, which lists effective charges, components of the dipole moments, and corrections (6) to diagonal matrix elements of the Hamiltonian for the ions at the line of dislocation ($\Delta\tilde{W}$ was calculated for the relaxed nanocrystal with allowance for polarization, and $\Delta\tilde{W}^0$ was calculated for the starting configuration without allowance for the field of dipoles). The dislocation line goes, as in [4], through an ion located in the square in Fig. 1 and coincides with the axis *OX*. Ions 1 and 8 (Table 2) are located on the opposite surface faces, and ions 4 and 5 are farthest from the surfaces. The nanocrystal has C_{2v} symmetry; therefore, the values listed in the table have no symmetry even in absolute magnitudes with respect to the plane perpendicular to the dislocation line located between the fourth and fifth layers (except for the corrections $\Delta\tilde{W}^0$ corresponding to the unrelaxed crystal). The magnitudes of

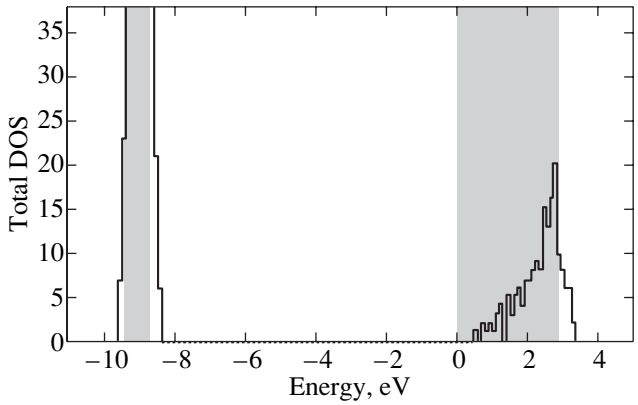

Fig. 3. Histogram of the total density of states of a nanocrystal (consisting of 344 ions) with an edge dislocation.

Table 2. Effective charges, components of dipole moments, and corrections to diagonal matrix elements of the Hamiltonian

No.	Ion	Q, $\|e\|$	d_x, D	d_y, D	d_z, D	$\Delta\tilde{W}$, eV	$\Delta\tilde{W}^0$, eV
1	Cl^-	−0.980	−0.865	−0.197	−0.197	0.344	3.829
2	K^+	0.979	−0.111	0.082	0.082	0.262	–1.037
3	Cl^-	−0.979	−0.251	−0.186	−0.186	0.227	1.812
4	K^+	0.979	−0.036	0.065	0.065	0.157	–1.569
5	Cl^-	−0.979	−0.182	−0.192	−0.192	0.113	1.569
6	K^+	0.979	−0.058	0.055	0.055	0.101	–1.812
7	Cl^-	−0.979	−0.467	−0.210	−0.210	−0.080	1.037
8	K^+	0.981	−0.253	0.067	0.067	0.005	–3.829

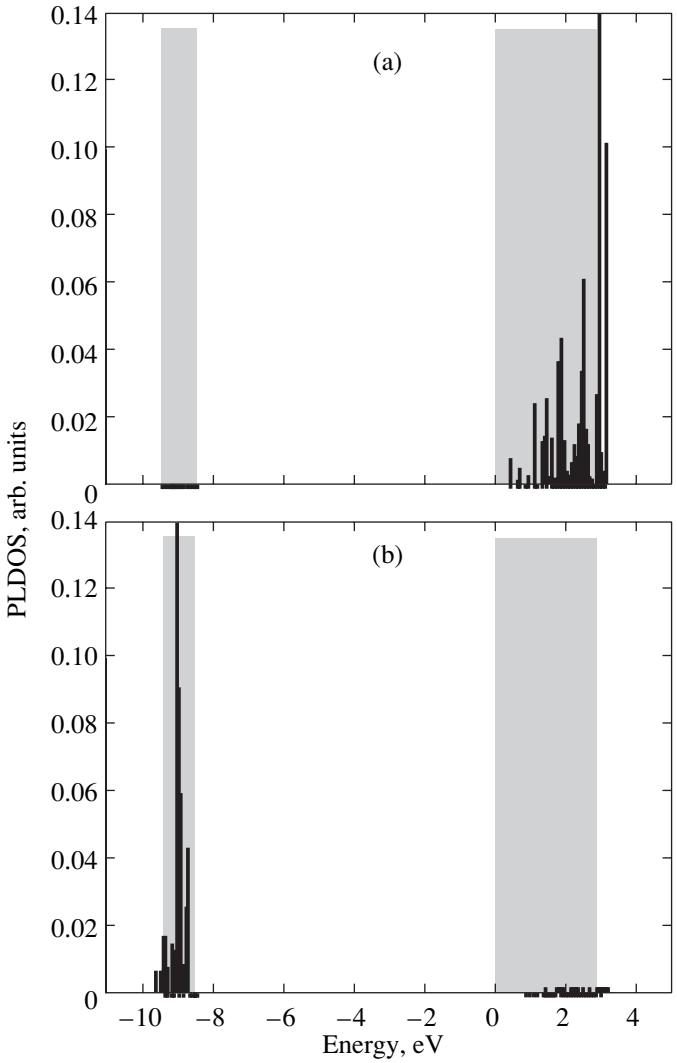

Fig. 4. Partial local densities of states (PLDOSs) for ions at the line of dislocation in the bulk of a nanocrystal: (a) PLDOS for 4*s* orbitals of potassium ions, and (b) PLDOS for 3*p* orbitals of chlorine ions.

the effective charges of surface and bulk ions differ only insignificantly. This is characteristic of the Slater–Koster variant of the tight-binding method, which was already noted in [17]. The dipole moment of the chlorine ion at the site of emergence of the dislocation onto the surface differs weakly from the dipole moment of the chlorine ion at the (100) surface of a sodium chloride crystal [21]. With moving into the depth of the nanocrystal, the dipole moment decreases in absolute value. The corrections to the diagonal matrix elements of the Hamiltonian for the ions of the dislocation line, which arise due to the total effect of the redistribution of the charge density and the appearance of induced dipoles upon relaxation, are quite significant; $\Delta\tilde{W}$ is smaller than $\Delta\tilde{W}^0$ in absolute value by at least an order of magnitude, which explains the shape of the histograms of the partial densities of states in Fig. 4.

Thus, if we extrapolate our results onto an infinite crystal, the states localized at the ions of the dislocation line will most probably be of pseudolocal rather than local type. Our data are most close to those of [4].

REFERENCES

1. S. Z. Shmurak and F. D. Senchukov, Fiz. Tverd. Tela (Leningrad) **15** (10), 2976 (1973) [Sov. Phys. Solid State **15**, 1985 (1973)].
2. A. I. Gubanov, Fiz. Tverd. Tela (Leningrad) **21** (3), 730 (1979) [Sov. Phys. Solid State **21**, 428 (1979)].
3. M. I. Molotskiĭ, Kinet. Katal. **22** (5), 1153 (1981).
4. A. A. Kusov, M. I. Klinger, and V. A. Zakrevskiĭ, Fiz. Tverd. Tela (Leningrad) **31** (7), 67 (1989) [Sov. Phys. Solid State **31**, 1136 (1989)].
5. S. Z. Shmurak, Fiz. Tverd. Tela (St. Petersburg) **41** (12), 2139 (1999) [Phys. Solid State **41**, 1963 (1999)].
6. J. Eisenblatter, Phys. Status Solidi **31** (1), 71 (1969).
7. R. A. Évarestov, E. A. Kotomin, and A. N. Ermoshkin, *Molecular Models of Point Defects in Wide-Gap Solids* (Zinatne, Riga, 1983).
8. J. Mei, J. W. Davenport, and G. V. Fernando, Phys. Rev. B **43** (6), 4653 (1991).
9. I. E. Tamm, *The Priciples of Electricity Theory* (Nauka, Moscow, 1966).
10. W. D. Wilson and K. D. Hatcher, Phys. Rev. **161** (3), 888 (1967).
11. M. J. L. Sangster and M. Dixon, Adv. Phys. **25** (3), 247 (1976).
12. J. Tessman, A. Kahn, and W. Shockley, Phys. Rev. **92** (7), 890 (1953).
13. B. D. Bunday, *Basic Optimisation Methods* (E. Arnold, London, 1984; Radio i Svyaz', Moscow, 1988).
14. J. C. Slater and G. F. Koster, Phys. Rev. **94** (6), 1498 (1954).
15. V. A. Shunina, Author's Abstract of Candidate's Dissertation (Voronezh, 1996).
16. Yu. K. Timoshenko, V. A. Shunina, and A. N. Latyshev, Izv. Akad. Nauk, Ser. Fiz. **61** (5), 961 (1997).
17. Yu. K. Timoshenko, V. A. Shunina, and A. N. Latyshev, Fiz. Tverd. Tela (St. Petersburg) **37** (6), 1569 (1995) [Phys. Solid State **37**, 851 (1995)].
18. G. S. Zavt, N. N. Kristofel', B. V. Shulichenko, and S. Z. Khain, Preprint No. FAI-4, IF AN ÉSSR (Inst. of Physics, Academy of Sciences of Estonia, Tartu, 1970).
19. W. A. Harrison, *Electronic Structure and the Properties of Solids: The Physics of the Chemical Bond* (Freeman, San Francisco, 1980; Mir, Moscow, 1983), Vol. 2.
20. M. Green and M. J. Lee, in *Solid State Surface Science*, Ed. by M. Green (Marcel Dekker, New York, 1969; Mir, Moscow, 1972), Vol. 1, p. 157.
21. T. Yanagihara and K. Yomogita, Surf. Sci. **219** (2), 407 (1989).

Translated by S. Gorin

Physics of the Solid State, Vol. 44, No. 5, 2002, pp. 893–895. Translated from Fizika Tverdogo Tela, Vol. 44, No. 5, 2002, pp. 858–859.

MAGNETISM AND FERROELECTRICITY

Classical Dependence of the Domain Wall Velocity on the Magnetic Field in Garnet Ferrite Films with Orthorhombic Magnetic Anisotropy

V. V. Randoshkin and Yu. N. Sazhin

Magnetooptoelectronics Joint Self-Supporting Laboratory, Institute of General Physics, Russian Academy of Sciences, Mordovian State University, Bol'shevistkaya ul. 68, Saransk, 430000 Russia

Received May 31, 2001; in final form, August 16, 2001

Abstract—The dependence of the domain wall velocity V on the acting magnetic field H is investigated for bismuth-containing single-crystal garnet ferrite films with orthorhombic magnetic anisotropy. It is shown that this dependence includes both the initial linear portion and a saturation portion and exhibits a complex behavior. This behavior is explained within the model of domain wall motion with spin wave radiation. © *2002 MAIK "Nauka/Interperiodica".*

1. INTRODUCTION

Earlier investigations into the dynamics of domain walls in bismuth-containing single-crystal garnet ferrite films of the composition $(Bi,Y,Pr)_3(Fe,Ga)_5O_{12}$ with (210) orientation and orthorhombic magnetic anisotropy have demonstrated that the dependence of the domain wall velocity V on the acting magnetic field H exhibits, at first glance, classical behavior: after the initial linear portion, the $V(H)$ curve shows a small peak followed by a saturation portion in which the differential domain-wall mobility is considerably less than the initial mobility [1–4]. However, high-speed photographic observations of dynamic domains in magnetic fields at approximately the midpoint of the linear portion in the $V(H)$ curve have revealed that dynamic domain walls undergo irregular distortions which are not reproducible from pulse to pulse [5, 6]. This implies that the nonstationary motion of domain walls corresponds to the linear portion of the $V(H)$ curve, which contradicts the theory described in [7].

In the present work, we made an attempt to elucidate the reasons for the above contradiction. For this purpose, the dependence $V(H)$ was measured more thoroughly using high-speed photography [8, 9].

2. SAMPLES AND EXPERIMENTAL TECHNIQUE

The magnetic anisotropy parameters for bismuth-containing single-crystal garnet ferrite films were measured by the phase transition method [10–12]: the azimuthal dependences of the critical bias field $H_b(\varphi)$ and the in-plane magnetic field $H_{in}(\varphi)$ were recorded in the course of homogeneous domain nucleation. As no theory offering simple analytical expressions for magnetic anisotropy in the (210)-oriented films exists, it is impossible to determine the anisotropy constants from these dependences with sufficient accuracy. For this reason, the magnitude of orthorhombic magnetic anisotropy was judged from the maximum (H_{in}^{max}) and minimum (H_{in}^{min}) in-plane magnetic fields in the dependence $H_{in}^{*}(\varphi)$ at which the domain structure disappears.

In order to investigate the dynamics of domain walls, the initial bismuth-containing single-crystal garnet ferrite film was magnetized to saturation with the bias field H_b applied along the normal to the film surface. A pulsed magnetic field H_p was applied in the opposite direction with the use of a pair of pancake coils. The film to be studied was placed in the midplane between the pancake coils. We recorded the image of the reversed domain that nucleated at the point defect. The domain wall velocity was measured in the direction along which it reached a maximum (see Figs. 1a–1c in [6]).

The data reported in this paper refer to a sample with thickness h = 7.3 μm, an equilibrium width of strip domains ω = 16.3 μm, a saturation magnetization $4\pi M_s$ = 59 G, H_{in}^{min} = 2000 Oe, and H_{in}^{max} = 4800 Oe.

3. RESULTS AND DISCUSSION

The field dependences of the domain wall velocity are shown in the figure. Note that the abscissa is both the pulsed magnetic field H_p and the acting magnetic field H [9]:

$$H = H_p - H_b. \quad (1)$$

It can be seen that, unlike the classical dependence of the domain wall velocity on the acting magnetic field,

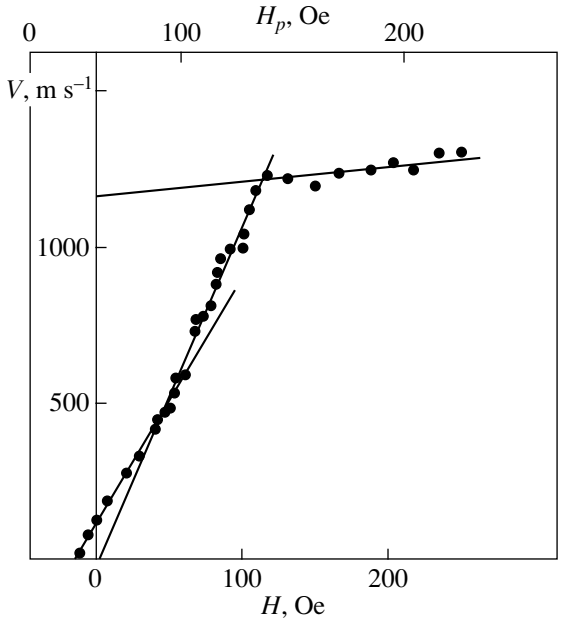

Dependences of the domain wall velocity on the acting magnetic field H and the amplitude of the pulsed magnetic field H_p.

the initial portion of the $V(H)$ curve, which was treated earlier as the initial linear portion, can be divided into two linear portions. The first linear portion is characterized by a slope of 8.3 m s^{-1} Oe^{-1}, and the second portion has a slope of 11.9 m s^{-1} Oe^{-1}. Furthermore, the first portion intersects the abscissa axis at negative H values. It is seen from the figure that, in this case, the bias field H_b is equal to 43 Oe. Direct observations of dynamic domains revealed that the crossover to the second linear portion corresponds to the appearance of spatial distortions of domain walls. Note that the unidirectional anisotropy of the domain wall velocity [3, 13] was observed in the bismuth-containing single-crystal garnet ferrite film under investigation but was not well pronounced.

The results obtained can be explained, according to [14–16], in terms of the spin-wave mechanism of domain wall motion. The crossover to the second linear portion with an increased (by a factor of approximately 1.4) differential mobility is associated with the attainment of a threshold field of spin wave radiation. The spin waves induce a local rotation of the magnetization vector in front of the moving domain wall. In turn, this leads to an increase in the velocity of the front of the reversed domain. The Gilbert attenuation parameter α, which depends on the effective magnetic field in the film plane [14, 16], is sufficiently large due to the relatively high value of H_{in}^{min}. Hence, spin waves attenuate at a small distance from the domain wall and the slopes of the two linear portions of the $V(H)$ curve differ insignificantly. For the same reason, despite the fact that the magnitude of m [16],

$$m = (H_{in}^{max} - H_{in}^{min})/H_{in}^{min}, \quad (2)$$

is more than unity, the unidirectional anisotropy of the domain wall velocity was not well pronounced.

As was noted above, the first linear portion of the $V(H)$ curve does not intersect the H axis at the origin of coordinates. This means that the acting magnetic field cannot be calculated from relationship (1) for bismuth-containing single-crystal garnet ferrite films with (210) orientation in which the localized canting of the easy magnetization axis is significant [17, 18]. For uniaxial bismuth-containing single-crystal garnet ferrite films with (111) orientation, nucleation of reversed domains at points defects has never been observed at negative acting magnetic fields H. At $H_p < H_b$, the magnetization reversal of bismuth-containing single-crystal garnet ferrite films becomes possible. However, in this case, the domain structure intergrows from the sample periphery [19].

It was experimentally found that the width of the image of the moving domain wall exceeds not only the width of the image of the static domain wall but also the domain wall displacement during the course of an emitted pulse (~5 ns). This indicates that the tilts of the static and dynamic domain walls differ from each other. Consequently, the projections of the bias field vector onto the domain wall plane differ for static and dynamic domain walls even though the bias field vector remains unchanged during the experiment. It is because of this circumstance that the first linear portion of the $V(H)$ curve intersects the abscissa axis at a negative H value. This circumstance was ignored when constructing the $V(H)$ curve in the figure.

4. CONCLUSION

Thus, we demonstrated that the appearance of spatial distortions of domain walls in bismuth-containing single-crystal garnet ferrite films with orthorhombic magnetic anisotropy corresponds not to the midpoint of the initial linear portion of the dependence $V(H)$ but to the crossover to the second linear portion characterized by an increased differential mobility. The second linear portion is associated with the spin wave radiation. The spin waves initiate local rotations of the magnetization vector in the vicinity of the moving domain wall.

ACKNOWLEDGMENTS

We thank M.V. Logunov for his assistance in performing the experiment.

REFERENCES

1. V. V. Randoshkin, V. I. Chani, M. V. Logunov, *et al.*, Pis'ma Zh. Tekh. Fiz. **15** (14), 42 (1989) [Sov. Tech. Phys. Lett. **15**, 553 (1989)].

2. V. V. Randoshkin, Thin Films and Beam–Solid Interaction **4**, 267 (1990).
3. V. V. Randoshkin, M. V. Logunov, and Yu. N. Sazhin, Fiz. Tverd. Tela (Leningrad) **32** (5), 1456 (1990) [Sov. Phys. Solid State **32**, 849 (1990)].
4. V. V. Randoshkin, Tr. Inst. Obshch. Fiz. Akad. Nauk SSSR **35**, 49 (1992).
5. V. V. Randoshkin, M. V. Logunov, and Yu. N. Sazhin, in *Proceedings of the XIV All-Russia School-Workshop "Novel Magnetic Materials for Microelectronics," Moscow, 1994*, Part 2, p. 32.
6. I. A. Kolmakov, Zh. Tekh. Fiz. **66** (2), 201 (1996) [Tech. Phys. **41**, 225 (1996)].
7. A. P. Malozemoff and J. C. Slonczewski, *Magnetic Domain Walls in Bubble Materials* (Academic, New York, 1979; Mir, Moscow, 1982).
8. V. V. Randoshkin, M. V. Logunov, and V. B. Sigachev, Prib. Tekh. Éksp., No. 5, 247 (1985).
9. V. V. Randoshkin, Prib. Tekh. Éksp., No. 2, 155 (1995).
10. I. E. Dikshteĭn, F. V. Lisovskiĭ, E. G. Mansvetova, and E. S. Chizhik, Preprint No. 5, IRÉ AN SSSR (Moscow, 1988).
11. I. E. Dikshteĭn, F. V. Lisovskiĭ, E. G. Mansvetova, and V. V. Tarasenko, Mikroélektronika **13** (4), 337 (1988).
12. I. E. Dikshteĭn, F. V. Lisovskiĭ, E. G. Mansvetova, and E. S. Chizhik, in *Proceedings of the XI All-Russia School-Workshop "Novel Magnetic Materials for Microelectronics," Tashkent, 1988*, p. 110.
13. F. V. Lisovskiĭ, A. S. Logginov, G. A. Nepokoĭchitskiĭ, and T. V. Rozanova, Pis'ma Zh. Éksp. Teor. Fiz. **45** (7), 339 (1987) [JETP Lett. **45**, 430 (1987)].
14. V. V. Randoshkin, Pis'ma Zh. Tekh. Fiz. **21** (23), 74 (1995) [Tech. Phys. Lett. **21**, 983 (1995)].
15. V. V. Randoshkin and Yu. N. Sazhin, Zh. Tekh. Fiz. **66** (8), 83 (1996) [Tech. Phys. **41**, 790 (1996)].
16. V. V. Randoshkin, Fiz. Tverd. Tela (St. Petersburg) **39** (8), 1421 (1997) [Phys. Solid State **39**, 1260 (1997)].
17. E. N. Il'icheva, A. V. Dubova, V. K. Peterson, *et al.*, Fiz. Tverd. Tela (St. Petersburg) **35** (5), 1167 (1993) [Phys. Solid State **35**, 594 (1993)].
18. E. N. Il'icheva, Yu. N. Fedyunin, A. G. Shishkov, and A. V. Klushina, Zh. Tekh. Fiz. **63** (11), 143 (1993) [Tech. Phys. **38**, 1005 (1993)].
19. V. V. Randoshkin, L. P. Ivanov, and R. V. Telesnin, Zh. Éksp. Teor. Fiz. **75** (3), 960 (1978) [Sov. Phys. JETP **48**, 486 (1978)].

Translated by N. Korovin

Physics of the Solid State, Vol. 44, No. 5, 2002, pp. 896–898. Translated from Fizika Tverdogo Tela, Vol. 44, No. 5, 2002, pp. 860–861.

MAGNETISM AND FERROELECTRICITY

On the Three-Pulse Excitation of Spin Echo Signals

A. S. Kim

Perm State University, ul. Bukireva 15, Perm, 614600 Russia

e-mail: Irs@psu.ru

Received March 6, 2001

Abstract—Three variants of three-pulse excitation of the quadrupole spin echo are considered. The specific features are determined for each variant of the excitation. © *2002 MAIK "Nauka/Interperiodica".*

1. INTRODUCTION

Earlier, Hahn [1] demonstrated experimentally and theoretically that spin echo signals are observed in a sample exposed to a three-pulse sequence of rf pulses with a pulse-recurrence frequency equal to the resonance frequency of the transition to be excited. This excitation was considered with the following conditions: $t_w < \tau_1$; $\tau_2 < T_2$, T_1; and $T_0 > 6T_1$. Here, t_w is the pulse duration, τ_1 is the time interval between the first and the second pulses, τ_2 is the time interval between the second and the third pulses, T_0 is the repetition period of the pulse sequence, T_2 is the time of spin–spin relaxation, and T_1 is the time of spin–lattice relaxation. The spectrum of excited pulses covers the whole line. Consideration was given to the case $\tau_2 \geq 2\tau_1$.

The present work is dedicated to further investigation into the mechanism of echo signal formation upon three-pulse excitation of a spin system of quadrupole nuclei.

2. THEORETICAL BACKGROUND

We consider the case when the total number of responses of a spin system to three-pulse excitation is equal to 16. In each specific case, the responses are grouped in a different manner.

The calculation was performed in the framework of the density matrix method, as was done by Das *et al.* [2, 3], and led to the following expressions for the amplitudes of nine possible echo signals at the instant of time t:

$$E^{(1)}_{m+1,m}(0) = 2(I'_x)_{m+1,m}\{A_1(x_i)\sin\omega_{m+1,m}(t-0)\}, \quad t = 0 \tag{1}$$

$$E^{(2)}_{m+1,m}(\tau_1) = 2(I'_x)_{m+1,m}\{A_2(x_i)\sin\omega_{m+1,m}(t-\tau_1)\}, \quad t = \tau_1 \tag{2}$$

$$E^{(3)}_{m+1,m}(2\tau_1) = 2(I'_x)_{m+1,m}\{A_3(x_i)\sin\omega_{m+1,m}(t-2\tau_1)\}, \quad t = 2\tau_1 \tag{3}$$

$$E^{(4)}_{m+1,m}(\tau_2) = 2(I'_x)_{m+1,m}\{A_4(x_i)\sin\omega_{m+1,m}(t-\tau_2)\}, \quad t = \tau_2 \tag{4}$$

$$E^{(5)}_{m+1,m}(2\tau_2) = 2(I'_x)_{m+1,m}\{A_5(x_i)\sin\omega_{m+1,m}(t-2\tau_2)\}, \quad t = 2\tau_2 \tag{5}$$

$$E^{(6)}_{m+1,m}(\tau_1+\tau_2) = 2(I'_x)_{m+1,m}\{A_6(x_i)\sin\omega_{m+1,m}(t-[(\tau_1+\tau_2)])\}, \quad t = \tau_1+\tau_2 \tag{6}$$

$$E^{(7)}_{m+1,m}(2\tau_1+\tau_2) = 2(I'_x)_{m+1,m}\{A_7(x_i)\sin\omega_{m+1,m}[t-(2\tau_1+\tau_2)]\}, \quad t = 2\tau_1+\tau_2 \tag{7}$$

$$E^{(8)}_{m+1,m}(\tau_1+2\tau_2) = 2(I'_x)_{m+1,m}\{A_8(x_i)\sin\omega_{m+1,m}[t-(\tau_1+2\tau_2)]\}, \quad t = \tau_1+2\tau_2 \tag{8}$$

$$E^{(9)}_{m+1,m}(2\tau_1+2\tau_2) = 2(I'_x)_{m+1,m}\{A_9(x_i)\sin\omega_{m+1,m}[t-(2\tau_1+2\tau_2)]\}, \quad t = 2\tau_1+2\tau_2. \tag{9}$$

1063-7834/02/4405-0896$22.00

Here, $x_i = \frac{1}{2}(I'_x)_{m+1,m}\gamma H_1^i t_\Delta$; H_1^i and t_Δ are the amplitude and the duration of the ith pulse of an rf field linearly polarized along the X axis of the electric field gradient, respectively (i numbers the pulses in the sequence); γ is the nuclear gyromagnetic ratio; $(I'_x)_{m+1,m}$ is the matrix element of the operator I_x in the representation of the quadrupole Hamiltonian H_q; $A_\kappa(x_i)$ stands for the trigonometric functions of the angular duration of rf pulses (κ numbers the amplitudes of the echo signals); and m is the magnetic quantum number.

Under the assumption that the integrated intensity of one response is taken to be unity, the intensity distribution has the following form:

$$E^{(1)}_{m+1,m}(0) = 1, \quad E^{(2)}_{m+1,m}(\tau_1) = 3, \quad E^{(3)}_{m+1,m}(2\tau_1) = 1,$$

$$E^{(4)}_{m+1,m}(\tau_2) = 2, \quad E^{(5)}_{m+1,m}(2\tau_2) = 1,$$

$$E^{(6)}_{m+1,m}(\tau_1 + 2\tau_2) = 3, \quad E^{(7)}_{m+1,m}(2\tau_1 + \tau_2) = 2,$$

$$E^{(8)}_{m+1,m}(\tau_1 + \tau_2) = 2, \quad E^{(9)}_{m+1,m}(2\tau_1 + 2\tau_2) = 1.$$

3. RESULTS AND DISCUSSION

All these responses can be separated into two types of observed signals: (i) signals of the first type are observed under the excitation conditions considered in [1], and (ii) signals of the second type are generated under the conditions discussed in part in [4–6]. These signals of responses can be observed immediately at the instants of pulses, in the intervals between the pulse sequences, etc. Their common feature is as follows: in order for these signals to be observed, it is necessary to create special conditions for their excitation. For example, in order to observe all the responses at the instants of pulses, the following conditions must be met: (1) the onset of the pulse sequence must be synchronized not at the onset of the first pulse but to the left from it in order to observe the left wing of the response, and (2) the excitation conditions must be changeable over a wide range.

This can be achieved by different methods, for example, by varying the radio pulse duration, the time interval between radio pulses, and the repetition period of the pulse sequence. The location of almost all responses depends on the time intervals τ_1 and τ_2 of the pulse sequence. Figure 1 illustrates three possible variants of three-pulse excitation: $\tau_2 \geq 3\tau_1$, $\tau_1 \geq 3\tau_2$, and $\tau_1 = \tau_2$.

The first variant of three-pulse excitation ($\tau_2 \geq 2\tau_1$) was investigated experimentally and theoretically in [1–3, 7, 8]. According to the calculations, nine echo signals can be observed in this case. In actual fact, only five response signals were observed in the experiments. Under the condition $\tau_2 \geq 2\tau_1$, no echo signal is observed at the instant of time $t = \tau_2$. However, in the case when $\tau_2 \approx 3\tau_1$, the echo signal at the instant $t = \tau_2$ becomes visible.

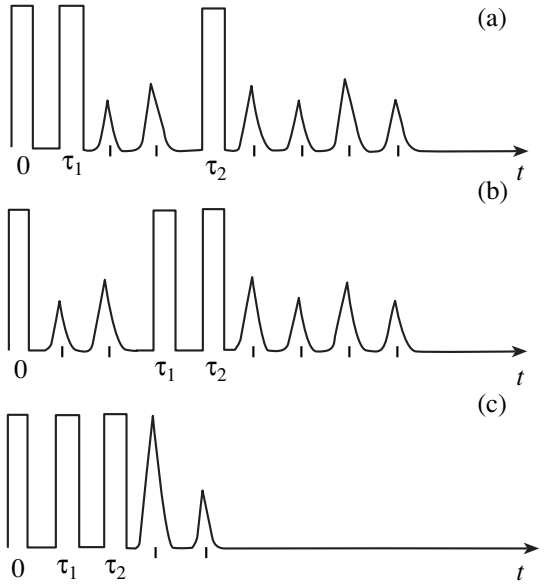

Fig. 1. Variants of three-pulse excitation: (a) $\tau_2 \geq 3\tau_1$, (b) $\tau_1 \geq 3\tau_2$, and (c) $\tau_1 = \tau_2$.

The second variant ($\tau_1 \geq 3\tau_2$) is of chief interest. In this case, observations of nine echo signals are also theoretically possible. Our prime interest here is in the echo signals observed at the following instants of time: $t = \tau_2$, $2\tau_2$, $2\tau_1$, $2\tau_1 + \tau_2$, $\tau_1 + 2\tau_2$, and $2\tau_1 + 2\tau_2$. All these cases are included in the first variant. It is worth noting that the locations of two echo signals ($t = \tau_2$ and $2\tau_2$) are very unusual. These signals are recorded after the first pulse. There arises a paradoxical situation: the earlier signals "know" about the later time interval (this paradox also manifests itself, but not so clearly, in the first variant). Moreover, the envelopes of these signals depend on the time interval τ_2 between the second and third pulses. This paradox comes into existence, because a new pulse, when acting on the sample, gives rise to a reflection of the preceding time interval, i.e., changes its direction. As a result, the new state "forgets" information regarding the preceding time interval. In our case, after the third pulse, we have $(\tau_1 + \tau_2) - \tau_1 = \tau_2$ and $(\tau_1 + 2\tau_2) - \tau_1 = 2\tau_2$. Analysis of the whole set of responses demonstrates that the nuclear spin system "remembers" all that occurred with it but, particularly, sets off the current instant of time. This implies that, at the current instant of time (after the action of a new pulse), the nuclear spin system resides in a new current state.

The third variant ($\tau_1 = \tau_2$) can be obtained from the first two variants. Under the three-pulse excitation, five response signals are formed. The intensity distribution is as follows: $E^{(1)}_{m+1,m}(0) = 1$, $E^{(2)}_{m+1,m}(\tau_1) = 5$,

$E^{(3)}_{m+1,m}(2\tau_1) = 5$, $E^{(4)}_{m+1,m}(3\tau_1) = 4$, and $E^{(5)}_{m+1,m}(4\tau_1) = 1$. This allows for a quantum-type accumulation of nuclear quadrupole resonance signals that can be used for samples containing quadrupole nuclei with a small natural occurrence.

In this work, $KReO_4$ was chosen as the object of investigation (^{187}Re resonance, $J = 5/2$, 5/2–3/2 transition, $\nu_2 = 55.651$ MHz, $T = 77$ K, $T_2 = 390$ μs, $T_1 = 4800$ μs). For $\tau_1 = 150$ μs and $\tau_2 = 50$ μs, we observed six echo signals at the following instants of time: $t_1 = 50$ μs, $t_2 = 100$ μs, $t_3 = 250$ μs, $t_4 = 300$ μs, $t_5 = 350$ μs, and $t_6 = 400$ μs. The amplitude maximum of the echo signals recorded at the instants t_1 and t_2 was observed at $T_0 = \sqrt{T_2 T_1}/2$.

In the case when the duration of the rf pulses changes in the range of $t_w \sim \tau_1$, the responses are observed (the wings of the signals become visible) at the instants of pulse action. The amplitude maximum of these signals cannot be observed experimentally because of the effects of the pulses, but its location can be determined from the signal shapes by varying the location of the midpoint of the line through the change in the duration of each radio pulse.

Thus, different variants of excitation of echo signals in a three-pulse sequence make it possible to extent the range of spectroscopic and technical applications of the pulse method.

REFERENCES

1. E. L. Hahn, Phys. Rev. **80**, 580 (1950).
2. T. P. Das, A. K. Saha, and D. K. Roy, Proc. R. Soc. London, Ser. A **227**, 407 (1955).
3. T. P. Das and E. L. Hahn, in *Solid State Physics*, Suppl. 1 (Academic, New York, 1958).
4. D. I. Kadirov, A. S. Kim, S. G. Kadirova, and I. G. Shaposnikov, J. Mol. Struct. **83**, 97 (1982).
5. M. Kunitomo and T. Hashi, Phys. Lett. A **81**, 299 (1981).
6. A. S. Kim and N. E. Aĭnbinder, Radiospektroskopiya (Perm), No. 17, 327 (1987).
7. V. S. Grechishkin, *Nuclear Quadrupole Interactions in Solids* (Nauka, Moscow, 1973).
8. I. A. Safin and D. Ya. Osokin, *Nuclear Quadrupole Resonance in Nitrogen Compounds* (Nauka, Moscow, 1977).

Translated by O. Moskalev

Physics of the Solid State, Vol. 44, No. 5, 2002, pp. 899–901. Translated from Fizika Tverdogo Tela, Vol. 44, No. 5, 2002, pp. 862–863.

MAGNETISM AND FERROELECTRICITY

On the Velocity of an End Domain Wall in $(Bi,Lu)_3(Fe,Ga)_5O_{12}$ Single-Crystal Films with (210) Orientation

V. V. Randoshkin*, A. M. Saletskiĭ*, N. N. Usmanov*, and D. B. Chopornyak**

** Moscow State University, Vorob'evy gory, Moscow, 119899 Russia*

*** Institute of Nuclear Physics, Moscow State University, Vorob'evy gory, Moscow, 119899 Russia*

Received June 5, 2001

Abstract—The mobility of an end domain wall in $(Bi,Lu)_3(Fe,Ga)_5O_{12}$ single-crystal garnet ferrite films with (210) orientation is determined by the photoresponse method. It is shown that the mobility of end domain walls in these films is considerably higher than that in (111) single-crystal garnet ferrite films free of rapidly relaxing ions. © *2002 MAIK "Nauka/Interperiodica".*

1. INTRODUCTION

The mechanism of magnetization reversal through the motion of an end domain wall makes it possible to increase significantly the speed of controlled magnetooptical transparencies [1, 2]. For the first time, the velocity of an end domain wall V_h was measured in $(Bi,Y)_3(Fe,Ga)_5O_{12}$ bilayer single-crystal garnet ferrite films with the (111) orientation upon transitions of bubble domains from the punched-through state to the floating state and vice versa [3, 4]. It was found that the end domain wall velocity is approximately two times higher than the velocity of a side 180° Bloch wall. Note that the end domain walls of floating bubble in bilayer films have a domed form.

It is known that a planar end domain wall is formed upon pulsed magnetization reversal of inhomogeneous single-crystal garnet ferrite films [5–11]. Specifically, this wall is formed in a layer with a weaker magnetic anisotropy (or at the layer boundary) either through the coalescence of closely located nuclei with reverse magnetization or through the rotation of the magnetization vector. The range of magnetic fields in which end domain walls exist can be taken as a measure of the inhomogeneity of a single-crystal garnet ferrite film.

2. THEORETICAL BACKGROUND

The theory proposed by Khodenkov [12] is based on the assumption that the angle between the magnetization vector inside the end domain wall and the normal to this wall varies in the same manner as in a 180° Bloch domain wall. According to this theory, the relationship for the mobility of an end domain wall has the following form:

$$\mu_h = \alpha\gamma\Delta_h/(1 + \alpha^2). \quad (1)$$

Here, α is the Gilbert dimensionless attenuation parameter, γ is the gyromagnetic ratio,

$$\Delta_h = [A/(K_u - 2\pi M_s^2)]^{1/2}, \quad (2)$$

A is the exchange interaction constant, K_u is the uniaxial anisotropy constant, and $4\pi M_s$ is the saturation magnetization.

The initial mobility of a 180° Bloch domain wall can be determined from the relationship [13]

$$\mu = \alpha^{-1}\gamma\Delta, \quad (3)$$

where

$$\Delta = (A/K_u)^{1/2}. \quad (4)$$

For single-crystal garnet ferrite films free of rapidly relaxing ions, we have $\alpha \ll 1$. Consequently,

$$\mu_h \lll \mu. \quad (5)$$

The dynamics of a planar end domain wall over the entire range of its existence was investigated by Ĭorgov *et al.* [14] for a $(Bi,Y,Lu)_3(Fe,Ga)_5O_{12}$ single-crystal garnet ferrite film with the (111) orientation. It was shown that the experimental mobility of the end domain wall (2.7 ± 0.2 cm s^{-1} Oe^{-1}) agrees closely with the theoretical value (2.2 cm s^{-1} Oe^{-1}) obtained from relationship (1).

It should be noted that Y^{3+} and Lu^{3+} are slowly relaxing ions and do not contribute significantly to the attenuation parameter of the (111) single-crystal garnet ferrite films free of rapidly relaxing ions. However, the attenuation parameter of these films increases drastically provided a constant magnetic field is applied in the plane of the (111)-oriented film [15] or the film has the (110) or (210) orientation when the orthorhombic magnetic anisotropy arises [16, 17].

1063-7834/02/4405-0899$22.00

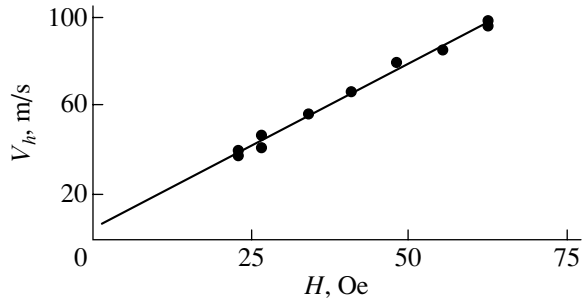

Dependence of the velocity of an end domain wall V_h on the external magnetic field H.

The goal of the present work was to investigate the motion of an end domain wall in $(Bi,Lu)_3(Fe,Ga)_5O_{12}$ single-crystal garnet ferrite films with the (210) orientation. These films exhibit orthorhombic magnetic anisotropy, and the easy magnetization axis is tilted at a sufficiently large angle θ with respect to the normal to the film plane [18]. We report data for a sample with the following parameters: h = 11 μm (film thickness), θ = 46°, $4\pi M_s$ = 43 G, α = 0.0135, and K_u = 1050 erg/cm^3.

3. EXPERIMENTAL TECHNIQUE

The dimensionless attenuation parameter was determined from the width of the ferromagnetic resonance line. Note that the aforementioned value of α can be overestimated because of the inhomogeneity of the single-crystal garnet ferrite film. The value of $H_K - 4\pi M_s$ (where $H_K = 2K_u/M_s$ is the field of uniaxial magnetic anisotropy) was also determined from the ferromagnetic resonance data, specifically from the resonance fields when the external magnetic field is perpendicular and parallel to the film plane. The value of $4\pi M_s$ was calculated from the field of bubble collapse provided the effect of the tilt of the easy magnetization axis was ignored.

The measurements were performed on a universal magnetooptic setup providing high-speed laser photographic observations of magnetization reversal. The Faraday effect was used to visualize the domain structure.

In the initial state, the sample was magnetized with a bias field H_b exceeding the saturation field H_s. The pulsed magnetic field H_p was applied in the opposite direction. During the course of a pulse, the total external field was determined as $H = H_p - H_b$. The widths of the front and the tail of the magnetic field pulse were equal to 7 and 40 ns, respectively.

The motion of the end domain wall was investigated over the entire range of its existence. This range is limited, from below, by the minimum magnetic field in which the end domain wall is formed and, from above, by the minimum field in which the so-called wave of magnetic moment turn-over is generated [19].

The velocity of the end domain wall was determined from the photoresponse signal when the wall was located in the midplane of the film [20].

4. RESULTS AND DISCUSSION

The dependence of the velocity of an end domain wall V_h on the external magnetic field H is shown in the figure. According to the theory proposed in [12], this dependence has a linear behavior; however, the experimental mobility (μ_h = 150 cm s^{-1} Oe^{-1}) is substantially larger than the theoretical value (~2.5 cm s^{-1} Oe^{-1}) obtained from relationship (1). In single-crystal garnet ferrite films of similar composition, the mobility of the end domain wall for the (210) orientation is considerably larger than that for the (111) orientation [14]. This confirms the inference made earlier in [17] that the attenuation parameter in a single-crystal garnet ferrite film increases in the presence of orthorhombic magnetic anisotropy.

Thus, we demonstrated that, in single-crystal garnet ferrite films free of rapidly relaxing ions, the mobility of the end domain wall for the (210) orientation is almost two orders of magnitude higher than that in the case of the (111) orientation.

REFERENCES

1. B. E. McNeal, G. R. Pulliam, J. J. Fernandez de Castro, and P. M. Warren, IEEE Trans. Magn. **MAG-19** (5), 1766 (1983).
2. V. V. Randoshkin, A. M. Saletskiĭ, N. N. Sysoev, and A. Ya. Chervonenkis, Mikroélektronika **30** (3), 91 (2001).
3. A. F. Martynov, L. V. Nikolaev, V. V. Randoshkin, *et al.*, Pis'ma Zh. Tekh. Fiz. **6** (13), 786 (1980) [Sov. Tech. Phys. Lett. **6**, 338 (1980)].
4. V. V. Randoshkin, A. M. Balbashov, Yu. A. Durasova, *et al.*, Fiz. Tverd. Tela (Leningrad) **23** (8), 2520 (1981) [Sov. Phys. Solid State **23**, 1480 (1981)].
5. V. N. Dudorov, M. V. Logunov, and V. V. Randoshkin, Fiz. Tverd. Tela (Leningrad) **28** (5), 1549 (1986) [Sov. Phys. Solid State **28**, 877 (1986)].
6. M. V. Logunov and V. V. Randoshkin, Fiz. Tverd. Tela (Leningrad) **28** (5), 1559 (1986) [Sov. Phys. Solid State **28**, 883 (1986)].
7. V. N. Dudorov, M. V. Logunov, and V. V. Randoshkin, Zh. Tekh. Fiz. **56** (5), 949 (1986) [Sov. Phys. Tech. Phys. **31**, 579 (1986)].
8. D. I. Ĭorgov, O. S. Kolotov, and V. A. Pogozhev, Vestn. Mosk. Univ., Ser. 3: Fiz., Astron. **29** (3), 94 (1988).
9. D. I. Ĭorgov, O. S. Kolotov, and V. A. Pogozhev, Zh. Tekh. Fiz. **59** (3), 120 (1989) [Sov. Phys. Tech. Phys. **34**, 920 (1989)].
10. O. S. Kolotov and V. A. Pogozhev, Vestn. Mosk. Univ., Ser. 3: Fiz., Astron. **32** (5), 3 (1991).
11. V. V. Randoshkin, Defektoskopiya, No. 1, 77 (1996).
12. H. E. Khodenkov, Phys. Status Solidi A **53** (2), 103 (1979).

13. A. P. Malozemoff and J. C. Slonczewski, *Magnetic Domain Walls in Bubble Materials* (Academic, New York, 1979; Mir, Moscow, 1982).

14. D. I. Ĭorgov, O. S. Kolotov, and V. A. Pogozhev, Fiz. Tverd. Tela (Leningrad) **32** (2), 602 (1990) [Sov. Phys. Solid State **32**, 352 (1990)].

15. V. V. Randoshkin, Pis'ma Zh. Tekh. Fiz. **21** (23), 74 (1995) [Tech. Phys. Lett. **21**, 983 (1995)].

16. V. V. Randoshkin and Yu. N. Sazhin, Zh. Tekh. Fiz. **66** (8), 83 (1996) [Tech. Phys. **41**, 790 (1996)].

17. V. V. Randoshkin, Fiz. Tverd. Tela (St. Petersburg) **39** (8), 1421 (1997) [Phys. Solid State **39**, 1260 (1997)].

18. E. N. Il'icheva, A. V. Klushina, N. N. Usmanov, *et al.*, Vestn. Mosk. Univ., Ser. 3: Fiz., Astron. **35** (2), 59 (1994).

19. M. V. Logunov, V. V. Randoshkin, and V. B. Sigachev, Fiz. Tverd. Tela (Leningrad) **29** (8), 2247 (1987) [Sov. Phys. Solid State **29**, 1296 (1987)].

20. O. A. Vasil'ev, D. L. Stolyarov, N. N. Usmanov, and D. B. Chopornyak, in *Proceedings of the XVII International School-Workshop "Dynamics of Domain Boundary," Moscow, 2000*, p. 864.

Translated by O. Moskalev

Physics of the Solid State, Vol. 44, No. 5, 2002, pp. 902–910. Translated from Fizika Tverdogo Tela, Vol. 44, No. 5, 2002, pp. 864–871.

MAGNETISM AND FERROELECTRICITY

Specific Features in Supersonic Nonlinear Dynamics of Domain Walls in Rare-Earth Orthoferrites

A. P. Kuz'menko and V. K. Bulgakov

Khabarovsk State Technical University, Khabarovsk, 680035 Russia

e-mail: kap@tiis.khstu.ru

Received April 18, 2001; in final form, July 12, 2001

Abstract—The dynamics and temperature dependences of the mobility of domain walls in $EuFeO_3$ (from 4.2 to 300 K), $TmFeO_3$ (from 100 to 300 K), $LuFeO_3$ (300 K), $YFeO_3$ (460 K), and $DyFeO_3$ (from 77 to 300 K) orthoferrites are investigated in pulsed magnetic fields H up to 4.8 kOe. It is found that the field dependence of the domain wall velocity $v(H)$ in all these compounds exhibits a nonlinear behavior and consists of discrete portions corresponding to the magnetic field ranges ΔH_i in which the domain wall moves at a constant velocity. The appearance of these features in the ΔH_i ranges is associated with magnetoelastic and flexural oscillations generated by domain walls in a strongly dissipative nonlinear medium. It is revealed that the domain wall dynamics at supersonic velocities has a non-one-dimensional character. At the instant the domain wall breaks through the sound barrier, the domain structures undergo a nonstationary transformation with changes in the fine structure of the domain walls. The interface motion is accompanied by self-organizing processes. © *2002 MAIK "Nauka/Interperiodica".*

1. INTRODUCTION

Owing to the specific features in crystalline and magnetic structures of rare-earth orthoferrites $RFeO_3$ (where R^{3+} is a rare-earth ion), the anisotropy (H_A), exchange (H_E), and Dzyaloshinski–Moriya (H_D) fields induced in these materials are such that the spin flop occurs in anomalously high fields $H_{SF} = -H_D/2 + ((H_D/2)^2 + H_E H_A)^{1/2} \approx 75$ kOe [1]. In lower fields, the domain wall (DW) motion is the main mechanism of magnetization reversal in rare-earth orthoferrites. Experimental and theoretical investigations have revealed that the dynamics of domain walls in the $YFeO_3$ orthoferrite exhibits a nonlinear non-one-dimensional character [2]. For $YFeO_3$, the limiting velocity of stationary domain-wall motion $C \approx 19.74 \times 10^3$ m/s considerably exceeds the velocities of transverse (v_t) and longitudinal (v_l) sound (4.2×10^3 and 7.2×10^3 m/s, respectively). As a rule, the limiting velocity of stationary domain-wall motion C in orthoferrites is estimated from the spin-wave dispersion dependence within the long-wave approximation: $C \sim \gamma(2H_E A/M_0)^{1/2}$, where A is the inhomogeneous exchange constant, M_0 is the sublattice magnetization, and γ is the gyromagnetic ratio [2]. In the case when the velocity of a domain wall in $YFeO_3$ exceeds the velocity of sound, the domain wall bends spontaneously and periodic domain structures in the form of truncated ovals with the same spacing necessarily arise on this domain wall irrespective of the configuration of the applied magnetic field [2]. Adjacent structures of this type are connected via singular points at which the derivatives with respect to spatial coordinates have a discontinuity. It has been demonstrated that, in the course of domain wall motion over a sample, the non-one-dimensional domain structures execute a stationary motion (in the process, their initial shape remains unchanged) and their spacing λ decreases with an increase in the driving magnetic field [2]. For $YFeO_3$ platelike samples, the dependence of the domain wall velocity on the amplitude of the driving magnetic field $v(H)$ exhibits a number of features in the form of horizontal segments in the magnetic field ranges ΔH_i in which the domain wall velocity remains virtually constant. Zvezdin *et al.* [3] proved that the appearance of these features in the dependence $v(H)$ at velocities coinciding with v_t (in the range ΔH_t) and v_l (in the range ΔH_l) is associated with magnetoelastic interactions. The horizontal segments appear in the dependence $v(H)$ at supersonic velocities ($C > v_i > v_{t,l}$) under the parametric resonance conditions when the frequency of natural (wall) flexural oscillations of domain walls coincides with the spatial frequency determined by the size of growth inhomogeneities [4].

Unlike the structure of $YFeO_3$, the structure of orthoferrites $RFeO_3$ involves two magnetic subsystems (Fe^{3+} and R^{3+}) with different properties. As a consequence, the orthoferrite compounds undergo different orientational phase transitions due to changes in temperature, field, or elastic stresses [1, 2]. In rare-earth orthoferrites, the magnetic anisotropy constants are renormalized at the instant the domain wall breaks through the sound barrier when the phase velocities of spin waves in the magnetic and elastic subsystems coin-

cide with each other [2, 3]. In our earlier work [5], we visually observed and examined the separation of a dynamically deformed region from the domain wall in $TmFeO_3$ immediately at the instant the domain wall broke through the sound barrier.

Earlier, the domain wall dynamics in rare-earth orthoferrites was investigated using either a magnetooptical variant of the Sixtus–Tonks induction method or a stroboscopic technique with a low temporal resolution (about 6 ns) in $TmFeO_3$ with an insufficient accuracy in measurements and without control of the domain wall shape during domain wall motion. To our knowledge, the domain wall dynamics in rare-earth orthoferrites at different temperatures has not been examined using double-exposure high-speed photomicrography [2, 4].

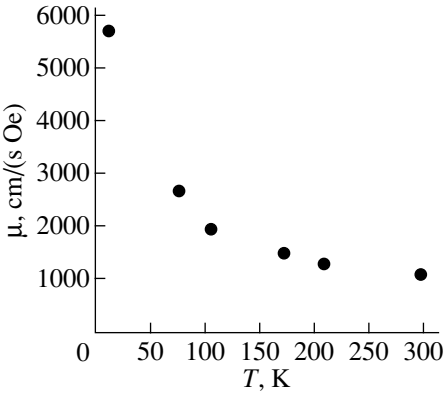

Fig. 1. Temperature dependence of the domain wall mobility in $EuFeO_3$.

2. EXPERIMENTAL RESULTS

All the rare-earth orthoferrite samples were prepared in the form of plates cut out normally to the optic axis. The plate thickness was chosen in such a way as to provide the maximum magnetooptical contrast and did not exceed 1×10^{-4} m. The samples were chemically polished in superheated H_3PO_4 acid with the aim of decreasing the coercivity of the samples. A pulsed magnetic field (induced by two Helmholtz coils 1×10^{-3} m in diameter) with a leading edge of shorter than 20 ns and an amplitude as high as 4.8 kOe was applied to the sample. The pulse frequency was no higher than several hertzs. Prior to motion, a single straight-line domain wall was produced at a distance of 1.5×10^{-4} m from the inner edge of the coil under the action of a gradient magnetic field. The gradient field strength varied depending on the temperature and the rare-earth orthoferrite composition. For example, the domain wall dynamics in $TmFeO_3$ at a temperature of 168 K was investigated in a constant magnetic field with a gradient of 2500 Oe/cm.

The temperature dependences of the domain wall mobility μ can be examined by measuring the relaxation dependences of the domain wall displacement in a high-frequency sinusoidal magnetic field [6]. The maximum mobility μ thus obtained for $TmFeO_3$ samples is observed at a temperature of 168 K and amounts to 860 cm/(s Oe). Below this temperature, the domain wall mobility μ in $TmFeO_3$ decreases with a decrease in the temperature to 100 K. The temperature dependence of the domain wall mobility μ for the $EuFeO_3$ rare-earth orthoferrite is plotted in Fig. 1. As the temperature decreases, the mobility μ in this orthoferrite increases to 5800 cm/(s Oe) at 4.2 K in accordance with a law close to $1/T^2$ [2, 6]. The domain wall mobilities in 25- and 90-μm-thick $DyFeO_3$ samples at room temperature are equal to 343 and 295 cm/(s Oe), respectively. A decrease in the temperature to 77 K results in a decrease in the mobility μ to 50 cm/(s Oe). Single crystals of all these orthoferrites were grown by crucibleless melting with optical heating.

The $LuFeO_3$ orthoferrite sample 1.05×10^{-4} m thick was grown through spontaneous crystallization from a solution in the melt. In this orthoferrite, as in the $YFeO_3$ and $EuFeO_3$ compounds, the spin reorientation is absent in the temperature range covered; i.e., the domain wall mobility μ should increase with a decrease in the temperature. However, as the temperature decreases, the domain wall mobility, which is equal to 350 cm/(s Oe) at room temperature for this sample, decreases and becomes virtually zero at 80 K. This indicates a low quality of the samples grown by the above method.

The dependences $v(H)$ were analyzed using double-exposure high-speed photomicrography [2, 4]. Owing to the improvement in the spatial and temporal resolutions, the error in determining the velocity, the location, and the shape of domain walls at the highest velocity equal to 20×10^3 m/s was reduced to 2% [4, 5]. Typical double dynamic domain walls in $LuFeO_3$ samples at room temperature and in the $YFeO_3$ sample at 460 K are shown in Fig. 2. At supersonic velocities, the domain walls bend with the formation of truncated ovals joined together. The shape and size of these non-one-dimensional structures on the domain walls (Fig. 2c) in the $YFeO_3$ sample at T = 460 K (the Néel temperature is 640 K) at the domain wall mobility μ = 2000 cm/(s Oe) coincide with those observed earlier at T = 100 K on the domain wall with the highest mobility μ = 20000 cm/(s Oe) [2]. The evolution of non-one-dimensional structures on the domain walls in rare-earth orthoferrites (Figs. 2a, 2b, 4a, 4c) also agrees with that observed previously in $YFeO_3$ [2]. The non-one-dimensional structures (with the spacing λ) arise less than in 1 ns after breaking through the sound barrier at any domain wall velocity in the range $C > v_i > v_{t,l}$. This process has a nonstationary character.

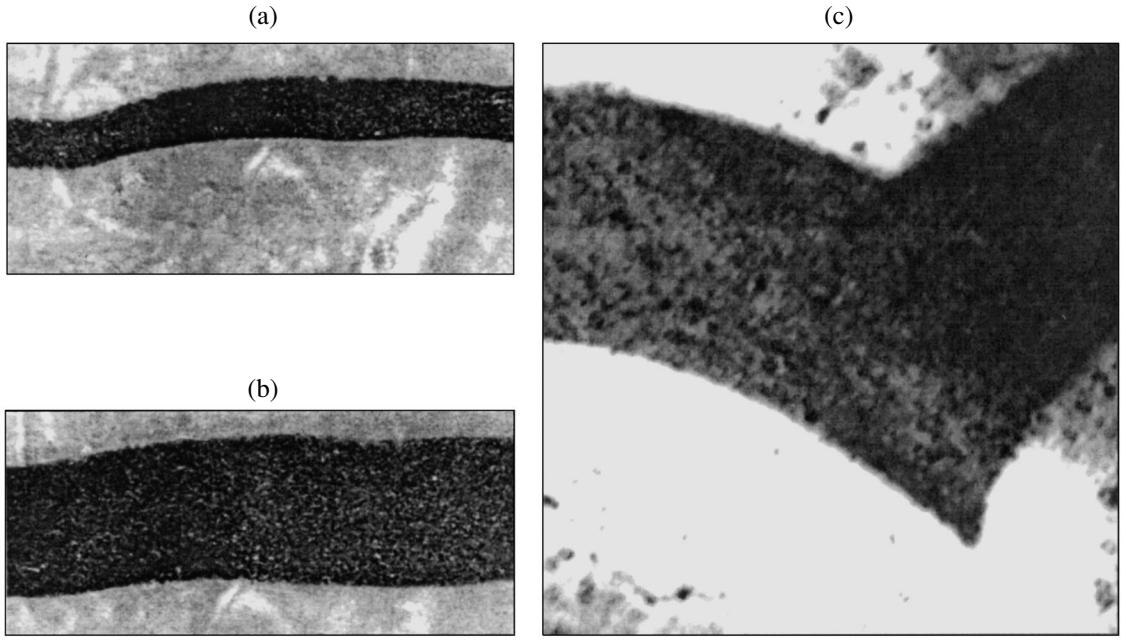

Fig. 2. Micrographs of the double dynamic domain structures in rare-earth orthoferrites (a, b) $LuFeO_3$ at 293 K and (c) $YFeO_3$ at 460 K at different velocities: (a) $v \geq v_t$, (b) 12×10^3 m/s, and (c) 18×10^3 m/s. The time separation between the light pulses is 15 ns. Scale: (a, b) 75 and (c) 60 μm to one centimeter.

The field dependences of the domain wall velocity for $EuFeO_3$ at the liquid-helium temperature, $LuFeO_3$ at room temperature, and $YFeO_3$ at 460 K are displayed in Fig. 3. The domain wall mobility in $YFeO_3$ at this temperature becomes comparable to those in rare-earth orthoferrities. Analysis of the dependences $v(H)$ (Fig. 3) revealed features common to all these dependences.

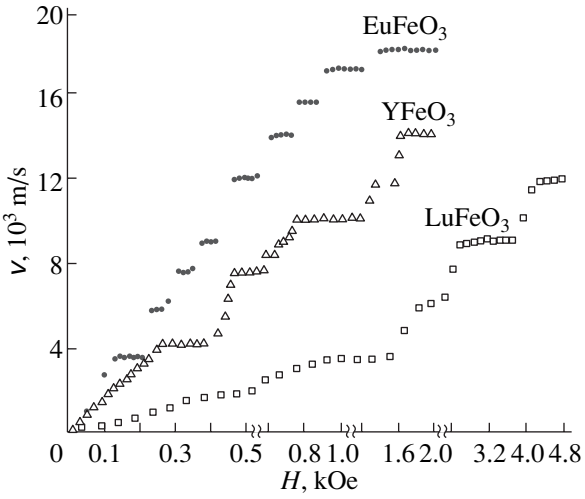

Fig. 3. Field dependences of the domain wall velocity in platelike orthoferrite samples: $EuFeO_3$ at T = 4.2 K, $LuFeO_3$ at T = 300 K, and $YFeO_3$ at T = 460 K.

The dependences $v(H)$ for all rare-earth orthoferrites, as for $YFeO_3$ [4], exhibit a nonlinear behavior and consist of a discrete set of horizontal segments in the magnetic field ranges ΔH_i in which the domain wall velocity is constant. The first two segments in the dependence $v(H)$ in the ranges ΔH_t and ΔH_l correspond to the domain wall velocities coinciding with v_t and v_l. For example, the first two horizontal segments are observed at velocities of 3.5×10^3 and 5.8×10^3 m/s for $EuFeO_3$ and 3.5×10^3 and 6.3×10^3 m/s for $LuFeO_3$, which are equal to the velocities v_t and v_l in these materials. The dependence $v(H)$ for $TmFeO_3$ at transonic domain-wall velocities (3.6×10^3 and 6.2×10^3 m/s) also has horizontal segments in the ranges ΔH_t and ΔH_l.

Apart from the horizontal segments in the ranges ΔH_t and ΔH_l, all the rare-earth orthoferrite samples are characterized by the ranges ΔH_i in which the domain wall motion at supersonic velocities is retarded at different temperatures. For example, the horizontal segments in the dependence $v(H)$ for $EuFeO_3$ are observed at velocities of 3.5×10^3, 5.8×10^3, 7.5×10^3, and 14×10^3 m/s in fields up to 0.5 kOe at the liquid-helium temperature (at the maximum domain-wall mobility μ) and at velocities of 3.5×10^3, 5.8×10^3, 7.5×10^3, 12×10^3, 14×10^3, 15.5×10^3, 17×10^3, and 18×10^3 m/s in fields up to 2 kOe at 77 K (Fig. 3). The dependence $v(H)$ for $TmFeO_3$ in fields as high as 4.8 kOe also involves a number of horizontal segments at domain wall veloci-

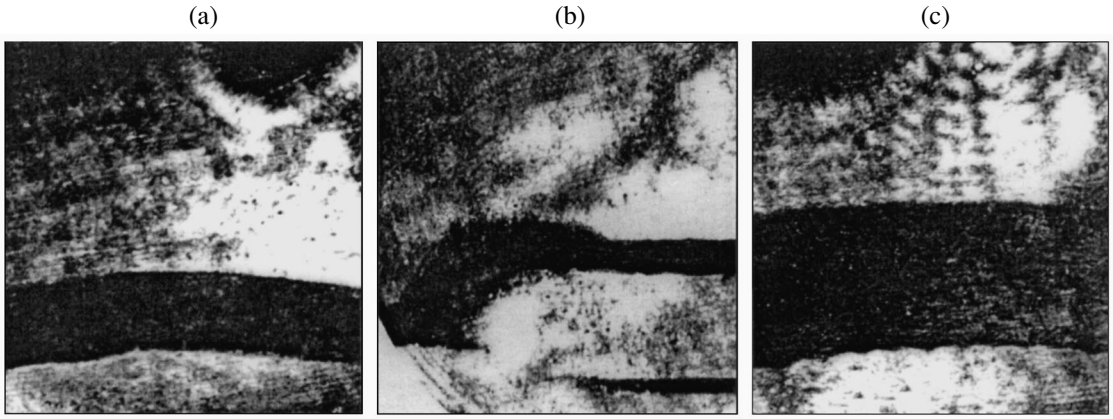

Fig. 4. Micrographs of the double dynamic domain structures in $TmFeO_3$ at 168 K at different velocities v (10^3 m/s): (a) 6.5, (b) 3.6, and (c) 16. The time separation between the light pulses is 15 ns. Scale: 60 μm to one centimeter.

ties of 3.6×10^3, 6.2×10^3, 8×10^3, 11.9×10^3, 13.5×10^3, 15×10^3, and 16×10^3 m/s. Similar horizontal segments in the ranges ΔH_i (in addition to the ranges ΔH_t and ΔH_l) at supersonic domain-wall velocities are revealed for $DyFeO_3$. The dependence $v(H)$ for $LuFeO_3$ in fields up to 4.8 kOe is also characterized by the specific features at supersonic velocities of 9×10^3 and 12×10^3 m/s (Fig. 3). The dependence $v(H)$ for this compound in higher fields was not investigated.

For rare-earth orthoferrites, as in orthoferrite $YFeO_3$ [4], the regularities observed in the behavior of ΔH_i and $v(H)$ are as follows. (1) The dependence $v(H)$ at $v_t < v_l < C$ contains a discrete set of horizontal segments in the ranges ΔH_i whose length and number increase with an increase in the sample thickness. (2) For $v_i \longrightarrow C$, the difference $(v_{i+1} - v_i)$ decreases and the range ΔH_i increases.

The motion of a non-one-dimensional domain wall at supersonic velocities in the field range $H_i < H < H_{i+1}$ is stationary in all the rare-earth orthoferrites under investigation. The spacing of the oval structures on the curved domain wall is retained during motion of this wall in the sample.

Among supersonic horizontal segments in the dependence $v(H)$ for $TmFeO_3$, the horizontal segments at domain wall velocities of 8×10^3, 11.9×10^3, and 16×10^3 m/s are noteworthy. The change-over between these velocities (i.e., at the end of the corresponding horizontal segment over a field range of about 1 Oe) occurs in an irregular manner. At this point, the domain wall velocity increases drastically and the spacing λ of semioval structures decreases jumpwise. Within the ΔH_i range, λ remains constant, whereas the amplitude A of non-one-dimensional structures gradually decreases to zero at the end of the horizontal segment. As can be seen from Fig. 4c, the spacing λ in $TmFeO_3$ at a domain wall velocity of 16×10^3 m/s is equal to 0.4×10^{-4} m. This is clearly seen in the case when the domain wall is illuminated with the first pulse. The values of λ at domain wall velocities of 8×10^3 and 11.9×10^3 m/s are equal to 3.3×10^{-4} and 1.8×10^{-4} m, respectively. For comparison, the smallest spacing λ observed earlier in $YFeO_3$ at a domain wall velocity of 16×10^3 m/s is equal to 2.5×10^{-4} m [2]. The dependence of the spacing λ of non-one-dimensional structures (formed on the domain wall) on the pulsed magnetic field for $TmFeO_3$ is depicted in Fig. 5.

In the $TmFeO_3$ sample (Fig. 4b), the initial two-domain structure undergoes a dynamic transformation when the domain wall breaks through the sound barrier. It is seen from the micrograph in Fig. 4b that the dynamic domain structure becomes more complex. A new magnetic phase moving from right to left is formed at this instant. The region with the initial

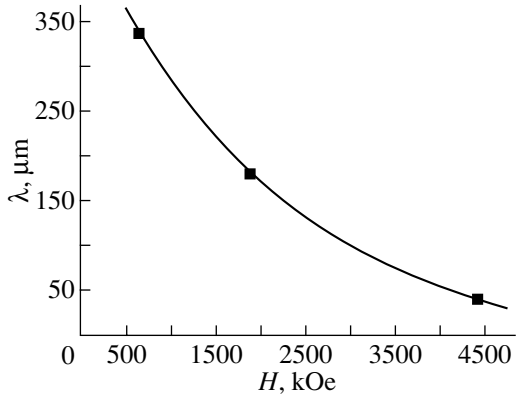

Fig. 5. Dependence of the spacing of non-one-dimensional structures in $TmFeO_3$ on the magnetic field.

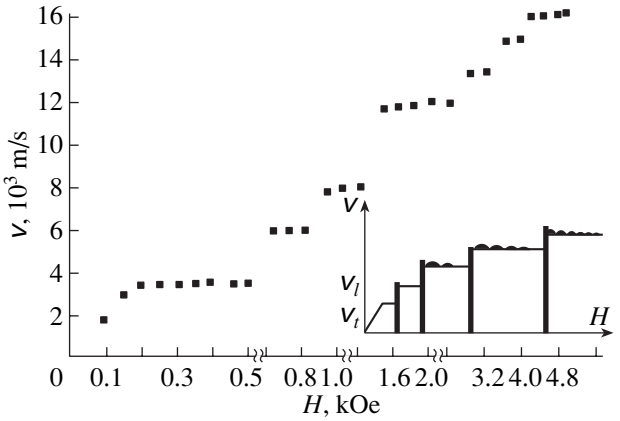

Fig. 6. Field dependence of the domain wall velocity. The inset shows the evolution of non-one-dimensional structures on a domain wall in $TmFeO_3$ at 168 K.

dynamic domain structure is retained in the left part. The domain wall velocity v_t in this region is equal to 3.6×10^3 m/s. The new magnetic phase arising in the right part moves from right to left and is bounded from above and from below by conventional domain walls with well-defined contours. These domain walls move in the original direction with velocities $v_1 = 0.9 \times 10^3$ m/s and $v_2 = 2.7 \times 10^3$ m/s. Their vector sum is equal to v_t. The domain walls at these (transonic) velocities have a straight-line shape. A similar transformation of the domain structure in this orthoferrite occurs when breaking through the sound barrier in the vicinity of v_l. After breaking through the sound barriers (at $v > v_{t,l}$), the domain wall motion becomes stationary and the velocity is uniquely determined by the amplitude of the driving magnetic field (Figs. 4a–4c). The same transformation of the domain structure is observed in $EuFeO_3$ ($T = 4.2$ K) at transonic domain-wall velocities ($v \sim v_{t,l}$).

The velocity of motion v_l of the curved domain wall (from right to left) in the direction normal to the plane of this wall is equal to 6.5×10^3 m/s. The observed domain wall bending coincides in shape with a kink revealed earlier for $YFeO_3$ [2]. The curved domain wall has a diffuse contour. This is clearly seen in the lower part of the dynamic domain structure in the micrograph upon illumination with the second pulse. In this region, unlike the conventional sharp wall observed between dark and bright regions, the magnetooptical contrast is absent. The new magnetic phase moves in two mutually perpendicular directions (Fig. 4b). One of them coincides with the direction of original upward domain-wall motion (along the [100] axis). At the same time, the curved domain wall moves (from right to left) along the [010] axis. The presence of the region with the initial domain structure (the dynamic domain structure on the left of Fig. 4b at a velocity equal to v_t) indicates that all the processes manifesting themselves in this micrograph proceed simultaneously in the period between two light pulses (15 ns). The size of the region occupied by the new magnetic phase is equal to 6.5×10^{-4} m (from right to left) and 1.8×10^{-4} m (from bottom to top), which correspond to velocities of higher than 40×10^3 and 12×10^3 m/s, respectively. The former velocity exceeds the limiting velocity of stationary domain-wall motion in this orthoferrite. The latter velocity coincides with the velocity at which the horizontal segment is observed in the dependence $v(H)$ for this compound (Fig. 6).

Figure 4a shows the micrograph of the stable double domain structure in which the domain wall moves with a velocity equal to the velocity of longitudinal sound $v_l = 6.7 \times 10^3$ m/s. The domain wall has well-defined leading and trailing edges. A new oval-shaped magnetic phase with a spacing of approximately 1.22×10^{-4} m is formed in front of the domain wall at the boundary with the coil. The rate of growth of this structure with a diffuse contour over the period between two light pulses is estimated at 9×10^3 m/s. Moreover, fringes with diffuse edges and a rapidly decreasing intensity are seen in the micrograph. Their spacing is equal to 40 μm. Two structures of the same type at a domain wall velocity of 16×10^3 m/s are also observed in the micrograph in Fig. 4c. In addition to the fringes with the aforementioned spacing, there appear fringes with a spacing of 20 μm. The superposition of the latter fringes is a typical fringe pattern. The location of their origin depends on the domain wall velocity and lies on the normal to the tangent at the point of domain wall bending at the instant the domain wall breaks through the sound barrier.

3. DISCUSSION

The rare-earth orthoferrite samples studied in this work contain trivalent ions R^{3+} of different types: the Dy^{3+} ions belong to Kramers-type ions (with an odd number of electrons and a half-integer spin), whereas the Eu^{3+}, Tm^{3+}, and Lu^{3+} ions are non-Kramers-type ions. In $EuFeO_3$ and $LuFeO_3$, the total quantum number J is equal to zero; hence, the magnetic moment of R^{3+} ions is zero and temperature spin-reorientation transitions are absent. The Dy^{3+} ion is the Ising-type ion. In this case, the magnetic moment is aligned along a particular crystal axis irrespective of the magnetic field orientation. In $DyFeO_3$, the first-order (Morin) phase transition from a weak ferromagnetic state to an antiferromagnetically ordered state G_y is observed at a temperature below 40 K. In $TmFeO_3$, the spin-reorientation transition (a change in the orientation of the weak ferromagnetic vector from the [001] axis to the [100] axis) in the form of two second-order phase transitions $G_xF_z \longrightarrow G_zF_x$ occurs in the temperature range 86–92 K [1].

The dependences $v(H)$ for rare-earth orthoferrites exhibit a pronounced nonlinear behavior and consist of horizontal segments in the specific magnetic-field ranges ΔH_i such that the domain wall velocity changes jumpwise when changing over from one range to another (Fig. 3). The domain wall motion at a velocity coinciding with a phase velocity of excited quasiparticles is accompanied with Čerenkov radiation. This manifests itself in the appearance of horizontal segments in the field ranges ΔH_i in the dependence $v(H)$. The first two horizontal segments in the dependence $v(H)$ are caused by magnetoelastic interactions with transverse (v_t) and longitudinal (v_l) acoustic waves and correspond to the field ranges [2, 3]

$$\Delta H_{t,l} \cong \Delta_0 \delta_{t,l}^2 [1 - (v_{t,l}^2/C^2)]^{1/2}/3M_0\eta_{t,l}v_{t,l}, \qquad (1)$$

where $\eta_{t,l}$ stands for the acoustic damping constants, $\delta_{t,l}$ are the magnetoelastic interaction constants, and Δ_0 is the thickness of the static domain wall. The ranges ΔH_t and ΔH_l for rare-earth orthoferrites are appreciably wider than those for $YFeO_3$ [2, 4]. At the same temperature (77 K) and identical plate thickness (about 10^{-4} m), the ratio $\Delta H_{t\mathrm{EuFeO_3}}/\Delta H_{t\mathrm{YFeO_3}}$ is equal to 100 Oe : 35 Oe. Such a large difference between the values of $\Delta H_{t,l}$ for rare-earth orthoferrites and $YFeO_3$, according to relationship (1), can be associated with the increase in the magnetoelastic interaction constants $\delta_{t,l}$ [2].

All the rare-earth orthoferrite single crystals under investigation exhibit characteristic concentration growth bands that form a periodic relief of magnetic inhomogeneities. The specific features in the dependence $v(H)$ in the ranges ΔH_i for rare-earth orthoferrites at supersonic domain-wall velocities are similar to those observed for $YFeO_3$ [4]. Therefore, the resonance retardation of domain walls by parametrically excited Winter (wall) magnons also occurs in rare-earth orthoferrites. The amplification factor of these oscillations over a wide range of growth inhomogeneity sizes is found to be larger than unity. The appearance of new horizontal segments in the dependence $v(H)$ for rare-earth orthoferrite samples with artificially applied magnetic inhomogeneities confirms the applicability of the proposed model of domain wall retardation. Furthermore, this offers a way to control stationary supersonic domain-wall velocities by varying artificially produced magnetic inhomogeneities.

An increase in the domain wall mobility in $EuFeO_3$ with a decrease in the temperature to 4.2 K (Fig. 1) suggests a low coercivity of the sample. This coercivity was estimated from the dependence $v(H)$ (Fig. 3) at several Oersteds. The highest domain-wall mobility in all the studied orthoferrites is one order of magnitude less than that obtained by Rossol [6] from the relaxation dependences of the domain wall displacement in a high-frequency magnetic field. According to [6], the coercivity of rare-earth orthoferrite samples is less than 1 Oe and the mobility μ increases in the temperature range covered (down to 77 K). Among the samples studied in our work, the $YFeO_3$ orthoferrite has the highest domain-wall mobility, 20×10^3 cm/(s Oe) at 100 K, which is of the same order of magnitude as that found in [6]. The highest mobility μ in $EuFeO_3$ (Fig. 1) proves to be one order of magnitude smaller. The mobility of Néel-type domain walls is defined as $\mu_N \approx \gamma\alpha^{-1}(A/(K + 2\pi M^2))^{1/2}$ [2, 6]. The difference between the dependences $\mu(T)$ for $YFeO_3$ and rare-earth orthoferrites can be explained by the fact that the temperature dependence of K for $RFeO_3$ orthoferrites is more pronounced than those of the Hilbert phenomenological damping constant α and the other quantities (A and M). Moreover, the quantity K is additionally affected by dynamic renormalization of the anisotropy constants at $v \longrightarrow v_{t,l}$ [2–5]. It is under these conditions that the nonstationary transformation of the domain wall is observed in $EuFeO_3$ at 4.2 K and $TmFeO_3$ at 168 K (Fig. 4b).

For orthoferrites $LuFeO_3$ at $T = 300$ K (Figs. 2a, 2b), $TmFeO_3$ at $T = 168$ K (Fig. 4c), and $YFeO_3$ at $T = 460$ K (Fig. 2c), the non-one-dimensional structures, which were revealed earlier only in $YFeO_3$ at the highest mobility [2], are observed at supersonic domain-wall velocities that are multiples of v_t and v_l. The minimum spacing (40 μm) of non-one-dimensional structures on the supersonic domain wall in $TmFeO_3$ is found to be considerably less than that in $YFeO_3$. This can be associated only with the effect of rare-earth ions R^{3+}. All the foregoing indicates that the formation of these structures substantially depends on the temperature and dynamic changes in K and on rare-earth ordering.

A jumpwise change in the spacing of non-one-dimensional structures with an increase in the driving magnetic field (Figs. 5, 6) can be explained in terms of the theoretical inferences following from the probabilistic approach to the description of the nonlinear and non-one-dimensional dynamics of domain walls in orthoferrites. The main tendencies for non-one-dimensional structures to change can be analyzed using the following relationships for their spacing λ and amplitude A [7]:

$$\lambda = (1 - (v/C)^2)^{1/2}(\tau C^2/\mu) \times \int_{-\pi/2}^{\pi/2} (H - H(v\cos\varphi))^{-1}\cos\varphi d\varphi, \qquad (2)$$

$$A = \tau(v^2 - C^2)(v)^{-1}\ln|1 - v/(\mu H)|. \qquad (3)$$

Here, τ is the lifetime of magnetic oscillations and φ is the angle between the normal to the domain wall plane and the direction of the domain wall velocity. The qualitative dependences $\lambda(H)$ and $A(H)$ calculated according to formulas (2) and (3) are depicted in Fig. 5. The

spacing and amplitude of non-one-dimensional structures decrease linearly with an increase in the driving magnetic field. This is in agreement with the experimentally observed dynamic changes in the non-one-dimensional structures on the domain walls.

It is found that jumps in the domain wall velocity bring about changes in the size of non-one-dimensional structures on the domain walls. For example, this size in $TmFeO_3$ varies with jumps in the ith velocity v_i to 8×10^3, 11.9×10^3, and 16×10^3 m/s (Fig. 6). The domain wall acceleration to each velocity v_i necessarily occurs with the domain wall breaking through the sound barrier. When the domain wall motion becomes unstable, the domain wall exhibits a negative differential mobility [3]. This corresponds to a jump $v_i \longrightarrow v_{i+1}$ from one horizontal segment to another horizontal segment ($\Delta H_i \longrightarrow \Delta H_{i+1}$). Note that the difference between the corresponding values of H (the range between ΔH_i and ΔH_{i+1} in Fig. 6) is approximately equal to 1 Oe and is not constant. In this scenario, according to [7], two time scales can be separated in the dynamic behavior of the domain wall. The relaxation of the domain wall toward the state with a local energy minimum after switching off the pulsed magnetic field is a fast process whose time is determined by relaxation in the magnetic subsystem (10^{-9} s). On the other hand, tunneling of the domain wall through the potential barrier produced by an elastic dynamic strain is a slow process. The time of domain wall tunneling through the barrier is two orders of magnitude longer. The observed phenomena of domain structure transformation during supersonic motion of a domain wall in a weak ferromagnet under the conditions of elastic nonlinear excitation and strong dissipation belong to self-organizing processes. The non-one-dimensional structures on the domain wall play the role of an additional channel of the energy dissipation [7]. As the domain wall velocity approaches v_i, the integral in relationship (2) diverges and the ratio A/λ tends to zero; i.e., the two-dimensional solution transforms into the one-dimensional solution. At this instant, the domain wall velocity changes jumpwise and, according to formula (2), the spacing of oval structures increases to infinity; i.e., the domain wall becomes planar.

For each of the aforementioned domain wall velocities (including the velocities v_t and v_l), there is a local minimum of the domain wall energy. The transitions between these minima are similar to tunneling processes [7]. A qualitative pattern illustrating the observed processes is shown in the inset to Fig. 6. The supersonic domain wall tends to transform its own structure in such a way as to provide new additional channels of dissipating the energy acquired by the system. This transformation of dissipative structures on the domain wall impedes an increase in the negentropy in open structures to which the moving domain wall can be assigned [3, 8]. The domain wall energy (with an increase in the driving magnetic field in the range ΔH at sonic and above supersonic velocities) is maximum at the end of the horizontal segment. This is also confirmed by the previously observed increase in the intensity of light scattering by dynamic deformations of domain walls at the end of the range ΔH_t prior to a change-over from v_t to v_l in $YFeO_3$ [9].

Apart from the temperature-induced transitions, orthoferrites can undergo spin-orientation transitions caused by external magnetic fields or elastic stresses [1, 2]. The main magnetic phase (G_xF_z) of the $R FeO_3$ orthoferrites under investigation can involve domain walls of two types, namely, with and without rotation of the weak magnetic vector [10]. The antiferromagnetic vector rotates in the (010) plane at the effective in-plane anisotropy constant $K_{ab} > 0$ and in the (001) plane at $K_{cb} < 0$. In the latter case, the weak ferromagnetic moment vanishes; i.e., the Morin-type first-order phase transition $G_xF_z \longrightarrow G_y$ occurs inside the wall prior to antiferromagnetic ordering throughout the domain. In the case when the domain wall moves in fields far from the spin-flop field ($H \ll H_{SF}$) but has an effective in-plane anisotropy constant that changes upon exposure to temperatures [1], the dynamic renormalization of this constant after the domain wall breaks through the sound barrier can be sufficient to change the sign of the constant. For $TmFeO_3$ at 168 K, the change in sign of the in-plane anisotropy constant ($K_{ab} \longrightarrow K_{cb}$) can lead to the fact that the weak ferromagnetic moment vanishes at the center of the domain wall and that the antiferromagnetic moment vector rotates in the (001) hard magnetic plane.

The dynamics of the Bloch (DW $\perp$ [010]) and Néel (DW $\perp$ [100]) domain walls at transonic velocities differ significantly [3, 4, 7]. For the Bloch domain wall, the dependence $v(H)$ has a horizontal segment in the range ΔH_l, whereas the range ΔH_t is equal to zero. For the Néel wall in the same sample, the horizontal segments are observed in the ranges ΔH_t and ΔH_l; i.e., the sound barrier at v_l is higher than that at v_t [3]. This inference is confirmed by a more complex domain structure in the micrograph in Fig. 4b and a more substantial domain structure transformation observed at the velocity v_l. Moreover, the magnetooptical contrast of the dynamic domain structures (Fig. 4b) allows us to trace their magnetization distribution. The region with an intermediate contrast that is traversed by the new magnetic phase (between the domain structures at domain wall velocities of 0.9×10^3 and 2.7×10^3 m/s) should involve a region of the antiferromagnetic phase G_y in which the weak ferromagnetism is absent. A similar change in the magnetooptical contrast in $DyFeO_3$ in the vicinity of T_M was observed earlier for the static magnetization distribution in the weak ferromagnetic$^+$, antiferromagnetic, and weak ferromagnetic$^-$ metastable phases [11].

In addition to a conventional domain wall motion, Bar'yakhtar *et al.* [2] proposed the soliton mechanism

to offer an explanation of the possible motion of domain walls at velocities above the limiting velocity (the domain wall motion at a velocity of 40×10^3 m/s). A soliton is generated through a fluctuation at the leading edge of a domain wall under the action of a shock wave. As was shown in [2], the soliton free of a topological charge in the magnetic field grows and deforms in different directions. When propagating along the direction of the domain wall motion (Fig. 4b, top and bottom), the soliton annihilates with the domain wall. As a result, the stationary growth rate of the soliton increases to 12×10^3 m/s. At the same time, the domain wall motion at velocities actually higher than the limiting velocity becomes possible in the perpendicular direction due to the strongest longitudinal shock deformations. This motion is highly unstable and, apparently, proceeds through the soliton mechanism. The velocity of the new magnetic phase with the diffuse leading edge (the kink-type domain wall moving from right to left in Fig. 4b) is governed by the transition $G_xF_z \longrightarrow G_y$, which occurs considerably faster than the interface motion [11] and, most likely, is not restricted by the limiting velocity of stationary domain-wall motion. These data indicate the possibility of forming a new magnetic phase with antiferromagnetic ordering.

The formation of new magnetic phases with diffuse boundaries and fringes of the same shape, decreasing intensity, and different spacings can occur in front of the domain wall in different directions along the normals to the non-one-dimensional structures on a domain wall moving at supersonic velocities (Figs. 4a, 4c). This can be explained in terms of the fluctuation mechanism of domain wall breaking through the sound barrier. Note that each subsequent domain-wall breaking through the sound barrier should be accompanied by the generation of a shock wave [5]. The micrographs presented in this work were obtained in real time. This implies that the recorded changes in the magnetooptical contrast and the domain wall motion occur simultaneously. The lifetimes of magnetic and elastic excitations ($\leq 10^{-9}$ s) and the velocities of motion do not provide a satisfactory explanation of the origin of these changes. At the same time, the character and specific features of the changes observed in the magnetooptical contrast and their interrelation with the domain wall breaking through the sound barrier do not rule out the shock wave mechanism. Earlier, Bar'yakhtar *et al.* [2] investigated forced oscillations of domain walls in a strip domain structure in $YFeO_3$ under the same conditions and even observed mechanical fracture of the samples. This directly indicates that the generated shock waves possess a high energy. In a similar situation, Chetkin *et al.* [13] examined a thin plate of the $FeBO_3$ weak ferromagnet upon ultrasonic excitation and observed magnetoelastic waves that led to the modulation in the intensity of the magnetooptical contrast with diffuse boundaries. Apparently, the shock waves are excited at all supersonic domain-wall velocities. However, this process is attended by changes in the profile and distribution of deformations in the domain wall depending on the velocity. Recently, shock waves whose velocity is four times higher than the velocity of sound in condensed media have been recorded with a temporal resolution of 4×10^{-10} s [14]. As applied to our case, the shock wave (leading the domain wall) possibly modulates the intensity of light transmitted through the sample, which is observed in the micrographs (Figs. 4a, 4c).

4. CONCLUSIONS

Thus, we revealed the conditions of the formation of a moving domain wall in the studied orthoferrites and elucidated the mechanisms of dissipation of its energy into magnetoelastic and flexural (Winter) oscillations.

A domain wall moving in a dissipative nonlinear medium is a self-organizing dynamic system. On this basis, the observed evolution of non-one-dimensional supersonic dynamics in rare-earth orthoferrites is in agreement with the theoretical inferences made in [7].

It was demonstrated that, under the conditions of strong dynamic renormalization of the anisotropy constant, the transformation of a *ac*-type domain wall into a *ab*-type domain wall with the formation of an interface region of antiferromagnetic ordering becomes energetically favorable at the instant the domain wall breaks through the sound barrier. The observed nonstationary behavior of the domain wall is described and interpreted qualitatively.

ACKNOWLEDGMENTS

We would like to thank M.V. Chetkin for his continuous interest in this work; V.G. Bar'yakhtar, A.K. Zvezdin, and A.F. Popkov for helpful discussions of the results; and A.M. Balbashov for supplying the rare-earth orthoferrite single crystals used in our investigations.

This work was supported by the Ministry of Education of the Russian Federation, basic research field project no. 97-0-7.0-29.

REFERENCES

1. K. P. Belov, A. K. Zvezdin, A. M. Kadomtseva, and R. Z. Levitin, *Orientational Transitions in Rare-Earth Magnets* (Nauka, Moscow, 1979).
2. V. G. Bar'yakhtar, M. V. Chetkin, B. A. Ivanov, and S. N. Gadetskii, *Dynamics of Topological Magnetic Solitons: Experiment and Theory* (Springer-Verlag, Berlin, 1994), Springer Tracts Mod. Phys., Vol. 129.
3. A. K. Zvezdin, A. A. Mukhin, and A. F. Popkov, Preprint No. 108, FIAN SSSR (Lebedev Institute of Physics, Academy of Sciences of USSR, Moscow, 1982).
4. M. V. Chetkin, A. P. Kuz'menko, A. V. Kaminskiĭ, and V. N. Filatov, Fiz. Tverd. Tela (St. Petersburg) **40** (9), 1656 (1998) [Phys. Solid State **40**, 1506 (1998)].

5. A. P. Kuz'menko, A. V. Kaminskiĭ, E. A. Zhukov, and V. N. Filatov, Fiz. Tverd. Tela (St. Petersburg) **43** (4), 666 (2001) [Phys. Solid State **43**, 692 (2001)].
6. F. C. Rossol, J. Appl. Phys. **40** (3), 1082 (1969).
7. S. V. Gomonov, A. K. Zvezdin, and M. V. Chetkin, Zh. Éksp. Teor. Fiz. **94** (11), 133 (1988) [Sov. Phys. JETP **67**, 2250 (1988)].
8. A. P. Kuz'menko, N. Yu. Sorokin, A. V. Kaminsky, and E. A. Zhukov, in *Abstracts of EASTMAG-2001, Yekaterinburg, 2001*, p. 138.
9. S. D. Demokritov, A. I. Kirilyuk, N. M. Kreines, *et al.*, J. Magn. Magn. Mater. **104** (1), 663 (1992).
10. M. M. Farztdinov, M. A. Shamsutdinov, and A. A. Khalfina, Fiz. Tverd. Tela (Leningrad) **21** (5), 1522 (1979) [Sov. Phys. Solid State **21**, 878 (1979)].
11. V. V. Eremenko, N. F. Kharchenko, Yu. G. Litvinenko, and V. M. Naumenko, *Magnetooptics and Spectroscopy of Antiferromagnets* (Naukova Dumka, Kiev, 1989).
12. I. D. Kim and D. Ch. Khvan, Fiz. Tverd. Tela (Leningrad) **24** (8), 2300 (1982) [Sov. Phys. Solid State **24**, 1306 (1982)].
13. M. V. Chetkin, V. V. Lykov, and V. D. Tereshchenko, Fiz. Tverd. Tela (Leningrad) **32** (3), 939 (1990) [Sov. Phys. Solid State **32**, 555 (1990)].
14. Physics News in INTERNET, Usp. Fiz. Nauk **170** (3), 288 (2000).

Translated by O. Borovik-Romanova

Physics of the Solid State, Vol. 44, No. 5, 2002, pp. 911–919. Translated from Fizika Tverdogo Tela, Vol. 44, No. 5, 2002, pp. 872–880.

MAGNETISM AND FERROELECTRICITY

Effect of an External Electric Field on the Structure of the Magnon Spectrum in a Finite Magnetoelectric Crystal

S. V. Tarasenko

Donetsk Physicotechnical Institute, National Academy of Sciences of Ukraine, Donetsk, 83114 Ukraine

Received April 18, 2001; in final form, July 30, 2001

Abstract—Considering the case of a plate of a centrally antisymmetric tetragonal antiferromagnet for illustration, it is shown that if the tensor of magnetoelectric coupling constants is antisymmetric, then an external electric field causes earlier unknown anomalies to occur in the spectrum of bulk acoustic magnons even in the exchangeless limit. © *2002 MAIK "Nauka/Interperiodica".*

1. INTRODUCTION

From the point of view of spin-wave dynamics, the linear magnetoelectric effect in a magnetic crystal is of special interest when (i) the electric component of an electromagnetic field can excite (through linear coupling) those normal magnon modes in a many-sublattice crystal that are not of the magnetic-dipole type in the quasi-static limit $\omega/c \longrightarrow 0$ (ω is the spin-wave frequency and c is the speed of light) [1, 2] and (ii) the dispersion of spin waves in a magnetically ordered crystal can be intentionally changed using an external static electric field [1].

Such a situation is realized in centrally antisymmetric antiferromagnets (AFMs), for example, in $TbPO_4$, which possesses a fairly high magnetoelectric susceptibility [3]. The linear magnetoelectric coupling in magnetically ordered crystals of this type can be generally written in the form

$$F_{\text{me}} = \hat{\gamma}\mathbf{lmP}, \qquad (1)$$

where $\hat{\gamma}$ is the tensor of magnetoelectric coupling constants and $\mathbf{P}$ is the electric-polarization vector [4–9]. In the two-sublattice AFM model, $\mathbf{m} = (\mathbf{M}_1 + \mathbf{M}_2)/2M_0$ is the ferromagnetism vector, $\mathbf{l} = (\mathbf{M}_1 - \mathbf{M}_2)/2M_0$ is the antiferromagnetism vector, $\mathbf{M}_1$ and $\mathbf{M}_2$ are the sublattice magnetizations, and $|\mathbf{M}_1| = |\mathbf{M}_2| = M_0$. Therefore, for a fixed orientation of the equilibrium ferromagnetism vector $\mathbf{m}$, both the magnitude and character of magnetoelectric coupling in these AFMs can depend critically on the equilibrium orientation of the antiferromagnetism vector $\mathbf{l}$.

Calculations showed that both optical [8] and acoustic modes [9] of the magnon spectrum can be of the electric-dipole type in an antiferromagnetic crystal with the magnetoelectric interaction energy of Eq. (1). In [10–12], the conditions under which a new class of electric-dipole exchangeless spin waves (electrostatic spin waves) can propagate in a plate of a centrally antisymmetric AFM with magnetoelectric interaction (1) were first found. If the magnetoelectric coupling tensor $\hat{\gamma}$ in Eq. (1) is antisymmetric, then magnons of this class are not of the magnetic-dipole type in a certain geometry and, therefore, cannot propagate in the absence of linear magnetoelectric interaction. Physically, the propagation of exchangeless spin waves of this class in a magnetoelectric plate is due to indirect spin–spin interaction via the long-range electrostatic field. In fact, these electric-dipole magnons are Coulombic magnetic TM polaritons (E-type polaritons). As shown in [10–12], under certain conditions, magnetic-dipole and electric-dipole exchangeless spin waves can propagate simultaneously and independently in a finite AFM with an antisymmetric magnetoelectric coupling tensor. Magnetic-dipole magnons (magnetostatic spin waves) are Coulombic magnetic TE polaritons (H-type polaritons). Therefore, by analogy with polariton dynamics, we will refer to magnetic-dipole exchangeless magnons as H magnons and to electric-dipole ones as E magnons in what follows.

For E magnons, it was shown in [10–12] that magnetoelectric interaction in combination with spatial dispersion (due to inhomogeneous exchange interaction) leads to a number of anomalies in the spectrum of this type of dipole exchange spin waves with dispersion relation $\Omega_\nu(k_\perp)$, where $k_\perp$ is the wave number[1] and the mode index $\nu = 1, 2, 3, \ldots$ runs over an infinite discrete set. Among the anomalies under discussion are, in particular, inflection points ($\partial^2\Omega_\nu(k_\perp)/\partial k_\perp^2 = 0$), extremum points ($\partial\Omega_\nu(k_\perp)/\partial k_\perp = 0$, $\partial^2\Omega_\nu(k_\perp)/\partial k_\perp^2 \neq 0$), and crossover points ($\Omega_\nu(k_\perp) = \Omega_\rho(k_\perp)$ for $\nu \neq \rho$). In [10–12], we

[1] In this paper, we ignore the dependence of the magnon spectrum $\Omega_\nu(k_\perp)$ on the direction of the wave vector $\mathbf{k}_\perp$ in the plane of the plate and consider only the dependence on the wave number $|\mathbf{k}_\perp| = k_\perp$.

1063-7834/02/4405-0911$22.00 © 2002 MAIK "Nauka/Interperiodica"

considered, as an example, the collinear phase of a tetragonal AFM ($|\mathbf{l}| = 1$, $|\mathbf{m}| = 0$) with structure $4_z^{\pm}2_x^{\pm}I^-$ in the absence of external magnetic (**H**) and electric (**E**) fields and under the condition that the normal to the film plane **n**, the direction of wave propagation $\mathbf{k}_\perp/|\mathbf{k}_\perp|$, and the equilibrium vector **l** lie in one plane (**l** ∥ **n** or **l** ⊥ **n**).

It was found in [10–12] that the optimal conditions for the existence of the anomalies under discussion in the magnon spectrum are realized if the corresponding electric-dipole-active branch of the spectrum of acoustic spin waves has a low activation energy. For example, this can take place in weakly anisotropic magnetic crystals (in particular, in an easy-plane AFM) or in the case where the magnon mode in question is soft and the crystal is near a phase transition from the given magnetic state.

From the above discussion, it is clear that, when developing a consistent theory of the spectrum of acoustic electric-dipole magnons in a magnetoelectric crystal, one should take into account at least the following two factors: (1) the finite size of the actual magnetic sample and (2) the spatial dispersion due to inhomogeneous exchange interaction. We note that the effect of an external electric field on the spectrum of electric-dipole magnons in a finite centrally antisymmetric AFM has not yet been investigated despite the fact that, due to its low activation energy, the acoustic-magnon spectrum is also sensitive to external fields. As shown in [4–7], even in the collinear phase ($|\mathbf{l}| = 1$, $|\mathbf{m}| = 0$) of a magnetoelectric AFM with structure $4_z^{\pm}2_x^{\pm}I^-$, an external electric field $\mathbf{E} \perp \mathbf{l}$ induces a uniform magnetization $\mathbf{m} \perp \mathbf{E}$, $(\mathbf{ml}) = 0$. As a result, spin waves that are of the electric-dipole type for $|\mathbf{E}| = 0$ become, in addition, of the magnetic-dipole type when $|\mathbf{E}| \neq 0$. However, the features of the spectrum of electric-dipole exchangeless magnons have not yet been investigated in a finite magnetoelectric AFM placed in an external electric field.

The objective of this paper is to find the conditions under which additional anomalies arise in the spectrum of bulk exchangeless spin waves in a finite centrally symmetric AFM when an external electric field **E** is applied to it.

2. BASIC RELATIONS

In the case of $|\mathbf{m}| \ll |\mathbf{l}| = 1$ (relativistic interactions are weak in comparison to the intersublattice exchange), the energy density of a two-sublattice tetragonal magnetoelectric AFM can be written in terms of the ferromagnetism **m** and antiferromagnetism **l** vectors (following [4–7]) in the form

$$\begin{aligned} F &= F_\mathrm{m} + F_\mathrm{me} + F_\mathrm{p}, \\ F_\mathrm{m} &= M_0^2(0.5\delta\mathbf{m}^2 + 0.5\alpha(\nabla\mathbf{l})^2 + 0.5bl_z^2 \\ &\quad + 0.5\beta l_x^2 l_y^2 - \mathbf{mH}), \\ F_\mathrm{p} &= 0.5\kappa^{-1}P_z^2 + 0.5\kappa_\perp^{-1}(P_x^2 + P_y^2) - \mathbf{PE}, \end{aligned} \tag{2}$$

where δ and α are the homogeneous and inhomogeneous intersublattice exchange constants, respectively; b and β are the anisotropy constants; and $\kappa_\perp$ and κ are the dielectric susceptibilities.

As an example (in order to compare the results with those obtained in [10–12]), we will study the spin-wave dynamics of a centrally antisymmetric tetragonal AFM with structure $4_z^{\pm}2_x^{\pm}I^-$. In this AFM, the tensor of the magnetoelectric coupling constants is antisymmetric and the magnetoelectric interaction energy F_me in Eq. (2) can be written in the form [4–7]

$$\begin{aligned} F_\mathrm{me} &= -\gamma_1 m_z(l_x P_y \pm l_y P_x) - \gamma_2 P_z(m_x l_y \pm m_y l_x) \\ &\quad - \gamma_3 l_z(m_x P_y \pm m_y P_x), \end{aligned} \tag{3}$$

where $\gamma_{1,2,3}$ are the magnetoelectric coupling constants. Phenomenologically, the dynamic properties of the model characterized by Eq. (2) is described by a set of coupled dynamic equations composed of magnetostatics and electrostatics equations, Landau–Lifshitz equations for the vectors **m** and **l**, and an effective equation of motion for the electric polarization **P**. In the case under study, the spin-wave frequency satisfies the inequalities [1]

$$\omega \ll g\delta M_0, \quad \sqrt{f/\kappa_\perp}, \quad \sqrt{f/\kappa}, \tag{4}$$

where g is the gyromagnetic ratio, $f \sim z^2/mv_0$, and z and m are the absolute value of the ion charge and the reduced mass of the unit cell of volume v_0, respectively. Therefore, one can reduce the initial set of dynamic equations by eliminating **m** and **P** between them.

In the case of $|\mathbf{E}| = |\mathbf{H}| = 0$, the AFM under study can have either of two equilibrium magnetic phases: the easy-axis one (**l** ∥ z) or easy-plane one (**l** ⊥ z) [4–7]. If the equilibrium antiferromagnetism vector **l** lies in the plane of propagation of the magnetic polariton wave (taken as one of the coordinate planes) and coincides with one of the coordinate axes, then, as analysis reveals, both phases can support propagating magnetic polaritons of the TE and TM types independently. In particular, for **l** ∥ x and $\mathbf{k} \in xy$ (i.e., $k_z = 0$; k is the wave vector), the following (nonzero) components of the vectors **E, H**, $\tilde{\mathbf{l}}$, and **m** are related to one another:[2] H_z, $E_{x,y}$, $\tilde{m}_z$, $\tilde{l}_y \neq 0$ in a spin wave of the electric-dipole

[2] The notation $\tilde{A}$ means that the quantity A performs small-amplitude oscillations about its equilibrium value.

type (magnetic TM polariton) and E_z, $H_{x,y}$, $\tilde{m}_y$, $\tilde{l}_z \neq 0$ in a spin wave of the magnetic-dipole type (magnetic TE polariton). If $\mathbf{l} \parallel x$ and $\mathbf{k} \in xz$ ($k_y = 0$), then the nonzero components of the vectors $\mathbf{E}$, $\mathbf{H}$, and $\mathbf{l}$ are H_y, $E_{x,z}$, $\tilde{m}_y$, $\tilde{l}_z \neq 0$ for the TM polariton and E_y, $H_{x,z}$, $\tilde{m}_z$, $\tilde{l}_y \neq 0$ for the TE polariton. It is easy to verify that analogous conditions for the propagation of magnetic TM and TE polaritons take place in an infinite magnetoelectric AFM not only in the easy-plane phase for $\mathbf{k} \in xy$ ($k_z = 0$) or $\mathbf{k} \in yz$ ($k_z = 0$) but also in the easy-axis phase. For example, if in the equilibrium we have $|\mathbf{m}| = 0$ and $\mathbf{l} \parallel z$, then the magnetic polaritons of the types indicated above can propagate independently for $\mathbf{k} \in xz$ ($k_y = 0$) and for $\mathbf{k} \in yz$ ($k_x = 0$) [9]. It should be stressed that in all these cases, because of the linear magnetoelectric effect, the normal polariton-like modes of both TE and TM types are of a nonreciprocal nature, $\omega(\mathbf{k}) \neq \omega(-\mathbf{k})$, in the case of $(\mathbf{kl}) \neq 0$, and the velocity of electromagnetic waves is finite ($\omega/c \neq 0$).

As shown in [4–7], an external electric field $\mathbf{E}$ can change the equilibrium magnetic configuration of the magnetoelectric AFM with the $(4_z^{\pm}2_x^{\pm}I^-)$ structure even in the absence of an external magnetic field $\mathbf{H}$. In particular, if $\mathbf{E} \perp \mathbf{l}$ and $|\mathbf{H}| = 0$, then $|\mathbf{m}| \neq 0$ ($\mathbf{m} \perp \mathbf{E}$). However, the dispersion of propagating waveguide magnetic polaritons in a finite magnetoelectric crystal in these circumstances has not yet been investigated. In this paper, we consider only the case where the direction of an external electric field $\mathbf{E}$ is such that the electric-dipole magnon corresponding to the Coulombic magnetic TM polariton for $|\mathbf{E}| = 0$ becomes, in addition, of the magnetic-dipole type when $|\mathbf{E}| \neq 0$ and, therefore, the Coulombic magnetic TM polariton is transformed into a Coulombic magnetic EH polariton.

As an example, we consider (following [4–7, 11]) the easy-plane phase of a tetragonal AFM with the $4_z^{\pm}2_x^{\pm}I^-$ structure: $\mathbf{l} \parallel x$, $\mathbf{E} \parallel z$, and $\mathbf{m} \parallel y$. In this case, in the absence of an electric field ($|\mathbf{E}| = 0$), as indicated above, bulk exchangeless magnons of the H and E types can propagate independently with $\mathbf{k} \in xy$ ($k_z = 0$) and $\mathbf{k} \in xz$ ($k_y = 0$) in an infinite magnetoelectric crystal described by Eq. (2). In the presence of an external electric field applied perpendicular to the plane of propagation of such a TM polariton (e.g., $\mathbf{k} \in xy$, $\mathbf{E} \parallel z$), this polariton transforms into a magnetic EH polariton whose spectrum consists of two branches in the Coulombic limit. In order to simplify analytical calculations, we will assume that in the easy-plane AFM described by Eq. (2) (with the easy plane taken as the xy coordinate plane) the following condition is satisfied:

$$b \gg \beta. \tag{5}$$

In this case, the spectrum of normal spin waves for any $\mathbf{k}$ consists of two (high- and low-frequency) branches [12]. In particular, if $|\mathbf{E}| = |\mathbf{H}| = 0$ and $\mathbf{k} \in xy$ ($k_z = 0$), then the magnetic TM polariton is associated with the low-frequency magnon mode ($\tilde{m}_z$, $\tilde{l}_y \neq 0$) and the TE polariton is associated with the high-frequency magnon mode ($\tilde{m}_y$, $\tilde{l}_x \neq 0$).

In the case of $\mathbf{k} \in xz$ ($k_y = 0$) and $|\mathbf{E}| = |\mathbf{H}| = 0$, the high-frequency magnon ($\tilde{m}_y$, $\tilde{l}_z \neq 0$) is of the electric-dipole type and the low-frequency magnon ($\tilde{m}_x$, $\tilde{l}_y \neq 0$) is of the magnetic-dipole type. Naturally, the magnetoelectric effects will be more pronounced in the spectrum of the low-frequency magnon mode. For this reason, in what follows, we will restrict our consideration to those Coulombic magnetic EH polaritons that are associated with the low-frequency magnon spectrum of the magnetoelectric AFM under study ($\tilde{m}_z$, $\tilde{l}_y \neq 0$, in the case of $\mathbf{l} \parallel x$). Furthermore, we will ignore the influence of the high-frequency branch of the magnon spectrum on the low-frequency branch for $\omega^2 \ll \omega_s^2 \delta b$, where $\omega_s \equiv gM_0$. We also restrict our consideration to the case of $\mathbf{E} \parallel z$, $\mathbf{l} \parallel x$, $\mathbf{k} \parallel xy$ ($k_z = 0$), and $\tilde{m}_z$, $\tilde{l}_y \neq 0$, because the low-frequency magnon mode is of the electric-dipole type for $\mathbf{k} \parallel y$ and of the magnetic-dipole type for $\mathbf{k} \parallel x$ when $E_z \neq 0$, $|\mathbf{H}| = 0$, and $\mathbf{l} \parallel x$.

With these restrictions, the dispersion relation for the EH magnons under study in the infinite AFM described by Eq. (2) can be written in the following form in the short-wavelength limit ($\mathbf{k}^2 \equiv k_x^2 + k_y^2$):

$$\omega^2 = (\omega_0^2 + c_m^2\mathbf{k}^2)(1 + A_p k_y^2 \mathbf{k}^{-2}) + \omega_E^2 k_x^2 (\mu k_y^2 + k_x^2)^{-1},$$
$$A_p = 4\pi\gamma_1^2\kappa_\perp^2/(\delta\varepsilon), \quad \mu \equiv 1 + 4\pi/\delta,$$
$$\omega_E^2 \equiv \omega_s^2\gamma_2^2 4\pi\kappa^2 E_z^2/\delta, \tag{6}$$
$$\varepsilon_\perp \equiv 1 + 4\pi\kappa_\perp, \quad c_m^2 \equiv 0.25\alpha\delta\omega_s^2,$$
$$\omega_0^2 \equiv c_m^2\beta/\alpha, \quad \varepsilon \equiv 1 + 4\pi\kappa.$$

In this paper, we study the dynamics of a finite magnetoelectric crystal. Therefore, the set of dynamic equations should be supplemented by boundary conditions. We will assume that the normal $\mathbf{n}$ to the surface of the AFM is directed along one of the coordinate axes (x or y).

If the magnetic moments at the surface of the AFM plate are completely pinned, the boundary (exchange) conditions can be written in the form [13]

$$\tilde{\mathbf{m}} = \tilde{\mathbf{l}} = 0, \quad \zeta = \pm d, \tag{7}$$

where ζ is the coordinate along the normal $\mathbf{n}$ and $2d$ is the thickness of the plate.

The electrodynamic boundary conditions for the magnetostatic potential φ ($\mathbf{H} \equiv \nabla\varphi$) and electrostatic potential ψ ($\mathbf{E} \equiv \nabla\psi$) are assumed to have the following

form (depending on the relative orientation of the normal **n** and the equilibrium direction of the antiferromagnetism vector **l**):

$$\psi + \alpha_* \frac{\partial \psi}{\partial \zeta} = 0, \quad \varphi + \beta_* \frac{\partial \varphi}{\partial \zeta} = 0, \quad \zeta = \pm d, \quad (8)$$

where $\alpha_* = \alpha_*(\mathbf{l}/|\mathbf{l}|)$ and $\beta_* = \beta_*(\mathbf{l}/|\mathbf{l}|)$.

In the specific case where both surfaces of the plate are covered with a superconducting layer, we have $1/\beta_* = 0$ and $\alpha_* = 0$ [14].

3. THE SPECTRUM OF BULK EH MAGNONS

In order to calculate the spectrum of waveguide EH magnons with allowance for the magnetoelectric and inhomogeneous exchange interactions, we use the method developed in [15–17] for calculating the spectrum of dipole–exchange bulk magnons in a thin ferromagnetic film. From the electrostatics and magnetostatics equations (for $\omega/c \longrightarrow 0$) subject to boundary conditions (8), we express the amplitudes of the electrostatic potential ψ and magnetostatic potential φ in terms of the amplitude of the y component of the antiferromagnetism vector $\tilde{\mathbf{l}}$, assuming the spatial variation of this component along the normal to the film to be given and using the Green's function method. Therefore, the problem of determining the magnon spectrum of a finite magnetoelectric crystal is reduced to a boundary-value problem in the form of an integrodifferential equation for $\tilde{l}_y$ with exchange boundary conditions (7) alone. Following the method developed in [15–17], we seek a solution to our boundary problem in the form of an expansion in terms of the eigenfunctions of the exchange boundary-value problem. In the case of boundary condition (7), we have [15–17]

$$l_y(r, t) = \sum_\nu A_\nu \sin(\kappa_\nu \zeta) \exp(i\omega t - i\mathbf{k}_\perp \boldsymbol{\tau}), \quad (9)$$

where $\tau \in xy$, $\boldsymbol{\tau} \perp \mathbf{n}$, and $\kappa_\nu = \pi\nu/d$, with $\nu = 1, 2, \ldots$. Therefore, the dispersion relation that describes the spectrum of waveguide EH magnons under consideration with allowance for the magnetoelectric and inhomogeneous exchange interactions for $\mathbf{k} \in xy$, $\mathbf{n} \parallel x$ or $\mathbf{n} \parallel y$ and boundary conditions (7), (8) can be represented in the form of an infinite set of linear algebraic equations for the unknown amplitudes A_ν.

Since the structure of this set of equations is basically the same for different relative orientations of the vectors **l** and **n** in the chosen plane (xy) of propagation of the polariton wave, we write out the relevant expressions only for the case of $\mathbf{k} \in xy$ and $\mathbf{n} \parallel x$ ($k_x = \kappa_\nu$ and $k_y = k_\perp$):

$$(W_{\nu\nu}(k_\perp) - \omega^2)A_\nu - W_{\nu\rho}(k_\perp)A_\rho = 0,$$
$$\nu \neq \rho, \quad \nu, \rho = 1, 2, \ldots,$$

$$W_{\nu\nu}(k_\perp) \equiv (1 + A_p P_{\nu\nu}(k_\perp))$$
$$\times (\omega_0^2 + c_m^2(k_x^2 + k_y^2)) + \omega_E^2 R_{\nu\nu}(k_\perp),$$
$$W_{\nu\rho}(k_\perp) \equiv A_p P_{\nu\rho}(k_\perp)(\omega_0^2 + c_m^2(k_x^2 + k_y^2)) + \omega_E^2 R_{\nu\rho}(k_\perp),$$

$$P_{\nu\nu}(k_\perp) = k_\perp^2 \int_{-d}^{d} d\zeta \sin(\kappa_\nu \zeta) \int_{-d}^{d} dt G(\zeta, t) \sin(\kappa_\nu t),$$

$$P_{\nu\rho}(k_\perp) = k_\perp^2 \int_{-d}^{d} d\zeta \sin(\kappa_\rho \zeta) \int_{-d}^{d} dt G(\zeta, t) \sin(\kappa_\nu t),$$

$$R_{\nu\nu}(k_\perp) = \kappa_\nu^2 \int_{-d}^{d} d\zeta \cos(k_\nu \zeta) \int_{-d}^{d} dt F(\zeta, t) \cos(k_\nu t), \quad (10)$$

$$R_{\nu\rho}(k_\perp) = \kappa_\nu \kappa_\rho \int_{-d}^{d} d\zeta \cos(k_\rho \zeta) \int_{-d}^{d} dt F(\zeta, t) \cos(k_\nu t),$$

$$G(\zeta, t) \equiv \begin{cases} \sinh(k_\perp(t - d + \zeta_\alpha)) \\ \times \sinh(k_\perp(\zeta + d + \zeta_\alpha))/\Delta_G, \\ -d \le \zeta \le t, \\ \sinh(k_\perp(t + d + \zeta_\alpha)) \\ \times \sinh(k_\perp(\zeta - d + \zeta_\alpha))/\Delta_G, \\ t \le \zeta \le d, \end{cases}$$

$$\tanh(\zeta_\alpha k_\perp) = k_\perp \alpha_*, \quad \Delta_G \equiv k_\perp \sinh(2k_\perp d),$$

$$F(\zeta, t) \equiv \begin{cases} \cosh(ak_\perp(t - d + \zeta_\beta)) \\ \times \cosh(ak_\perp(\zeta + d + \zeta_\beta))/\Delta_F, \\ -d \le \zeta \le t, \\ \cosh(ak_\perp(t + d + \zeta_\beta)) \\ \times \cosh(ak_\perp(\zeta - d + \zeta_\beta))/\Delta_F, \\ t \le \zeta \le d, \end{cases}$$

$$\tanh(a\zeta_\beta k_\perp) = ak_\perp \beta_*,$$

$$\Delta_F \equiv ak_\perp \sinh(2ak_\perp d), \quad a \equiv \sqrt{\mu}.$$

The condition for the existence of a nontrivial solution to the set of equations (10) for the amplitudes A_ν is the vanishing of the determinant of their coefficients. An analysis reveals that if $1/\beta_* = 0$ and $\alpha_* = 0$ in Eq. (8) (perfect superconductor), then we have $W_{\nu\rho} = 0$ for any ν, ρ, and $k_\perp$. In this case, the spectrum of the waveguide EH magnons under study, traveling along the AFM plate, is found from Eqs. (10) to be

$$\Omega_\nu^2(k_\perp) - W_{\nu\nu}(k_\perp) = 0, \quad \nu = 1, 2\ldots. \tag{11}$$

Thus, if we solve Eqs. (10) using the coupled-mode method [18], then, in general, the off-diagonal elements $W_{\nu\rho} \neq 0$ in Eqs. (10) can be considered a perturbation with respect to the zeroth-order approximation in $W_{\nu\rho} \neq 0$ given by Eq. (11). The presence of $W_{\nu\rho} \neq 0$ gives rise to coupling between the waveguide EH-magnon modes with indices ν and ρ. Therefore, if the modes with given indices ν and ρ are degenerate in Eq. (11), then the crossover points will disappear for $W_{\nu\rho} \neq 0$, and in the vicinity of a specific crossover point, which is determined from Eqs. (10) in the case of $W_{\nu\rho} = 0$ by putting $\Omega_\nu(k_\perp) = \Omega_\rho(k_\perp)$ for $\nu \neq \rho$, the spectrum of the bulk EH magnons under study can be found from Eqs. (10) and (11) to be

$$(W_{\nu\nu}(k_\perp) - \omega^2)(W_{\rho\rho}(k_\perp) - \omega^2) - W_{\nu\rho}^2(k_\perp) \approx 0, \quad \nu \neq \rho. \tag{12}$$

A similar calculational technique can also be used in the case of $\mathbf{n} \parallel y$, $k \in xy$. In what follows, we calculate the spectrum of EH magnons for $\mathbf{n} \parallel x$ and $\mathbf{n} \parallel y$ through second order in $W_{\nu\rho} \ll 1$ ($\nu \neq \rho$); that is, we ignore repulsion of the dispersion curves at the crossover point and put $k_x = \kappa_\nu$, $\kappa_y = k_\perp$ for $\mathbf{n} \parallel x$ and $k_y = \kappa_\nu$, $k_z = k_\perp$ for $\mathbf{n} \parallel y$. As a result, we obtain

$$\begin{aligned}
\Omega_\nu^2(k_\perp) &= (\omega_0^2 + c_m^2(\kappa_\nu^2 + k_\perp^2))(1 + A_p k_\perp^2(\kappa_\nu^2 + k_\perp^2)^{-1}) \\
&\quad + \omega_E^2 \kappa_\nu^2(\mu k_\perp^2 + \kappa_\nu^2)^{-1}, \\
&\quad \mathbf{n} \parallel x, \\
\Omega_\nu^2(k_\perp) &= (\omega_0^2 + c_m^2(k_\perp^2 + \kappa_\nu^2))(1 + A_p \kappa_\nu^2(k_\perp^2 + \kappa_\nu^2)^{-1}) \\
&\quad + \omega_E^2 k_\perp^2(\mu\kappa_\nu^2 + k_\perp^2)^{-1}, \\
&\quad \mathbf{n} \parallel y.
\end{aligned} \tag{13}$$

In order to investigate the effect of nonlocal spin–spin interaction on the spectrum of EH magnons traveling along the AFM plate and described by Eqs. (2), (7), and (8), we will analyze Eqs. (13) in the specific case of $\alpha \longrightarrow 0$. This limit corresponds to the exchangeless approximation, which ignores the spatial dispersion due to inhomogeneous exchange interaction and is well known from the theory of magnetic-dipole magnons [13].

4. THE SPECTRUM OF BULK EH MAGNONS IN THE EXCHANGELESS LIMIT

In the case of $\alpha \longrightarrow 0$ and $W_{\nu\rho}(k_\perp) \ll 1$ ($\nu \neq \rho$), as follows from Eqs. (13), the short-wavelength limit of the spectrum of the bulk magnons under study for $\mathbf{k} \in xy$, $\mathbf{E} \parallel z$, and $\mathbf{l} \parallel x$ can be written in the form

$$\begin{aligned}
\Omega_\nu^2(k_\perp) &= \omega_0^2(1 + A_p k_\perp^2(\kappa_\nu^2 + k_\perp^2)^{-1}) \\
&\quad + \omega_E^2 \kappa_\nu^2(\mu k_\perp^2 + \kappa_\nu^2)^{-1}, \\
&\quad \mathbf{n} \parallel x, \\
\Omega_\nu^2(k_\perp) &= \omega_0^2(1 + A_p \kappa_\nu^2(k_\perp^2 + \kappa_\nu^2)^{-1}) \\
&\quad + \omega_E^2 k_\perp^2(\mu\kappa_\nu^2 + k_\perp^2)^{-1}, \\
&\quad \mathbf{n} \parallel y,
\end{aligned} \tag{14}$$

where $k_x = \kappa_\nu$, $k_y = k_\perp$ for $\mathbf{n} \parallel x$ and $k_y = \kappa_\nu$, $k_x = k_\perp$ for $\mathbf{n} \parallel y$. It can be seen from Eqs. (14) that this spin-wave spectrum has condensation points at $k_\perp \longrightarrow 0$ and $k_\perp \longrightarrow \infty$; that is, $|\Omega_\nu(k_\perp) - \Omega_\rho(k_\perp)| \longrightarrow 0$ for the two fixed mode indices ν and ρ. When $|\mathbf{E}| = 0$, then in a centrally antisymmetric AFM described by Eq. (2), the dispersion curves of the spectrum in the exchangeless limit (14) correspond to direct waves ($\partial\Omega_\nu(k_\perp)/\partial k_\perp > 0$) for $\mathbf{n} \parallel x$ and to back waves ($\partial\Omega_\nu(k_\perp)/\partial k_\perp < 0$) for $\mathbf{n} \parallel y$ for any mode index ν and wave number $k_\perp$. For a given value of the wave number $k_\perp$ and a fixed mode index $\nu < \rho$, we have $\Omega_\nu(k_\perp) > \Omega_\rho(k_\perp)$ for $\mathbf{n} \parallel x$ and $\Omega_\nu(k_\perp) < \Omega_\rho(k_\perp)$ for $\mathbf{n} \parallel y$. For any mode index ν, the dispersion curves described by Eqs. (14) have an inflection point ($|\mathbf{E}| = 0$) at some value of $k_\perp \neq 0$ in both cases of $\mathbf{n} \parallel x$ and $\mathbf{n} \parallel y$. When $|\mathbf{E}| = 0$, the dispersion of exchangeless EH magnons under study described by Eqs. (14) is due to magnetoelectric interaction alone ($\Omega_\nu(k_\perp) \neq$ const only if $\hat{\gamma} \neq 0$ [10–12]).

Now, we consider the anomalies in the spin-wave spectrum of Eq. (14) that are due to $E_z \neq 0$. An analysis reveals that in this case, the equation $\partial\Omega_\nu(k_\perp)/\partial k_\perp = 0$ can have a nonzero root for both $\mathbf{n} \parallel x$ and $\mathbf{n} \parallel y$. Therefore, an electric field $\mathbf{E}$ applied along the z axis can cause an extremum to appear at $k_\perp \neq 0$ on the dispersion curve $\Omega_\nu(k_\perp)$ of bulk EH magnons with $\mathbf{k} \in xy$ for $\mathbf{n} \parallel x$ (or $\mathbf{n} \parallel y$). In particular, for $\mu > 1$, an extremum appears at $k_\perp = k_*$ on the dispersion curve described by Eq. (14) for $\mathbf{n} \parallel x$ or $\mathbf{n} \parallel y$ if the following conditions are satisfied:

$$\begin{aligned}
&\omega_0^2 A_p/\mu < \omega_E^2 < \mu\omega_0^2 A_p, \\
&k_*^2 = \kappa_\nu^2(R-1)/(\mu - R), \quad \mathbf{n} \parallel x, \\
&k_*^2 = \kappa_\nu^2(\mu - R/(R-1)), \quad \mathbf{n} \parallel y,
\end{aligned} \tag{15}$$

where $\mathbf{k} \in xy$; $k_x = \kappa_\nu$, $k_y = k_\perp$ for $\mathbf{n} \parallel x$ and $k_y = \kappa_\nu$, $k_x = k_\perp$ for $\mathbf{n} \parallel y$; and $R^2 \equiv \mu_E^2\mu/A_p\omega_0^2$. If the strength of the external field $\mathbf{E} \parallel z$ is such that $\omega_E^2 < \omega_0^2 A_p/\mu$, then for a given mode index ν, the type of the dispersion curve $\Omega_\nu(k_\perp)$ described by Eq. (14) remains the same as in the case of $|\mathbf{E}| = 0$; that is, we have a direct wave [$\partial\Omega_\nu(k_\perp)/\partial k_\perp > 0$] for $\mathbf{n} \parallel x$ and a back wave [$\partial\Omega_\nu(k_\perp)/\partial k_\perp < 0$] for $\mathbf{n} \parallel y$. In the case where the inequality $\omega_E^2 > \omega_0^2 A_p \mu$ is true, as calculation shows, the application of an electric field $\mathbf{E} \parallel z$ reverses the wave

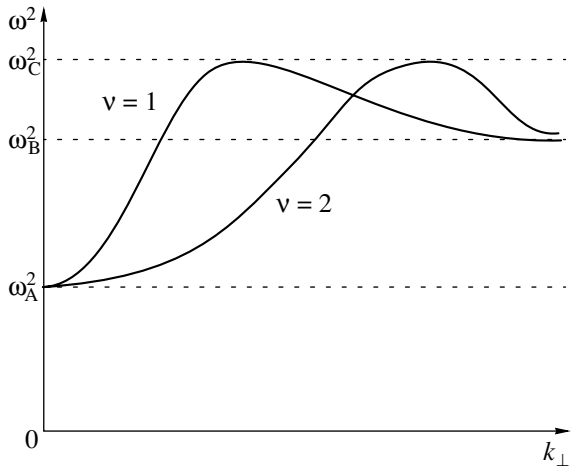

Fig. 1. Spectrum of bulk exchangeless EH magnons given by Eq. (14) for $\mathbf{n} \parallel x$ and, $\omega_0^2 A_p/\mu < \omega_E^2 < \omega_0^2 A_p \mu$, where $\omega_A^2 \equiv \omega_0^2$, $\omega_B^2 \equiv \omega_0^2 (1 + A_p)$, and $\omega_C^2 \equiv \Omega_\nu^2 (k_{\nu *})$, with $k_{\nu *}^2 \equiv \kappa_\nu^2 (R-1)/(\mu - R)$.

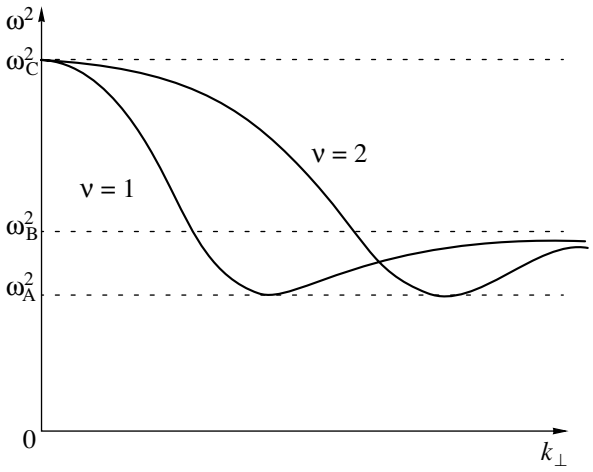

Fig. 2. Spectrum of bulk exchangeless EH magnons given by Eq. (14) for $\mathbf{n} \parallel y$ and $\omega_0^2 A_p/\mu < \omega_E^2 < \omega_0^2 A_p \mu$, where $\omega_A^2 \equiv \Omega_\nu^2 (k_{\nu *})$, $\omega_B^2 \equiv \omega_0^2 + \omega_E^2$, and $\omega_C^2 \equiv \omega_0^2 (1 + A_p)$, with $k_{\nu *}^2 \equiv \kappa_\nu^2 (\mu - R)/(R-1)$.

type in comparison to the case of $|\mathbf{E}| = 0$ for a given mode index ν in Eq. (14) and a given relative orientation of $\mathbf{n}$ and $\mathbf{l}$: we have a direct wave $(\partial\Omega_\nu(k_\perp)/\partial k_\perp > 0$ for $\mathbf{n} \parallel y$ and a back wave $(\partial\Omega_\nu(k_\perp)/\partial k_\perp < 0$ for $\mathbf{n} \parallel x$.

In the case where the conditions of Eq. (15) are satisfied, the modes with indices ν and ρ can have a cross point (crossover) at $k_\perp \neq 0$ for $\mathbf{n} \parallel x$ and $\mathbf{n} \parallel y$. If at some value of $k_\perp \neq 0$ a bulk EH-magnon mode of Eq. (14) has a maximum ($\mu > 1$), then for mode indices $\nu < \rho$ we have $\Omega_\nu(k_\perp) > \Omega_\rho(k_\perp)$ in the vicinity of the long-wavelength condensation point of the spectrum ($k_\perp \longrightarrow \infty$) and $\Omega_\nu(k_\perp) < \Omega_\rho(k_\perp)$ for $k_\perp \neq 0$. If at some value of $k_\perp \neq 0$ a bulk EH-magnon mode of Eq. (14) with a fixed mode index ν has a minimum ($\mu > 1$), then for mode indices $\nu < \rho$ we have $\Omega_\nu(k_\perp) < \Omega_\rho(k_\perp)$ for $k_\perp \longrightarrow 0$ and $\Omega_\nu(k_\perp) > \Omega_\rho(k_\perp)$ for $k_\perp \longrightarrow \infty$ (Figs. 1, 2).

Up to this point, when analyzing dispersion relations (13), we neglected the effects of inhomogeneous exchange interaction (formally putting $\alpha \longrightarrow 0$). However, even in an infinite crystal, the contribution from the inhomogeneous exchange interaction to the energy of a spin wave described by Eq. (6) increases with wave number $k_\perp$. The effect of this mechanism of spatial dispersion on the spectrum of bulk EH magnons under study in a finite centrally antisymmetric AFM described by Eq. (2) is discussed in the following section.

5. THE EFFECT OF INHOMOGENEOUS EXCHANGE INTERACTION

In general, an analysis of Eqs. (13) is difficult to make, but it is significantly simplified if one assumes that for $\mathbf{n} \parallel x$, the strength of the external electric field $E_z \neq 0$ is such that $|R_\nu - 1| \ll 1$, where $R_\nu = \omega_E^2 \mu / A_p \omega_\nu^2$, and $\omega_\nu^2 = \omega_0^2 + c_m^2 \kappa_\nu^2$. In the case of $\mathbf{n} \parallel y$, calculations are also simplified if the electric field $\mathbf{E} \parallel z$ is such that $|R_\nu - \mu| \ll \mu$. Analysis of Eqs. (13) and (14) in this case reveals that if in the exchangeless limit of Eq. (14) we have $\Omega_\nu(k_\perp) > \Omega_\rho(k_\perp)$ for modes with given indices ν and ρ ($\nu < \rho$) in the vicinity of a condensation point, then even for an infinitely small inhomogeneous exchange constant α the condensation point disappears and an additional cross point (crossover) of the dispersion curves $\Omega_\nu(k_\perp)$ and $\Omega_\rho(k_\perp)$ of Eq. (13) arises at some value of $k_\perp \neq 0$.[3] If the above condition in the vicinity of a condensation point of dispersion curves of Eq. (14) is not satisfied and we have $\Omega_\nu(k_\perp) < \Omega_\rho(k_\perp)$ for $\nu < \rho$, then only the disappearance of this condensation point takes place in Eqs. (13) in the case of $\alpha \neq 0$. Furthermore, if in the vicinity of the short-wavelength condensation point ($k_\perp \longrightarrow \infty$) we have $\partial\Omega_\nu(k_\perp)/\partial k_\perp < 0$ for a given mode index ν in the exchangeless approximation ($\alpha \longrightarrow 0$), then in the presence of inhomogeneous exchange interaction ($\alpha \neq 0$) the condensation point disappears and a minimum arises at some value of $k_\perp \neq 0$ on the corresponding dispersion curve $\Omega_\nu(k_\perp)$. The appearance of this minimum on the dispersion curve of Eq. (13) with mode index νdepends critically on the strength of the external electric field $\mathbf{E} \parallel z$ for a given relative orientation of the vectors $\mathbf{n}$ and $\mathbf{l}$ ($\mathbf{k} \in xy$). In particular, the conditions $\partial\Omega_\nu(k_\perp)/\partial k_\perp = 0$ and $\partial^2\Omega_\nu(k_\perp)/\partial k_\perp^2 > 0$ can be satisfied simultaneously for dispersion relation (13)

[3] Here and henceforth, we neglect energy dissipation.

with mode index ν and $k_\perp \neq 0$ if $\omega_E^2 > \omega_\nu^2 A_p \mu$ for $\mathbf{n} \parallel \mathbf{l}$ and $\omega_E^2 < \omega_\nu^2 A_p/\mu$ for $\mathbf{n} \perp \mathbf{l}$.

Thus, the comparison of Eqs. (13) and (14) shows that in the case of $\alpha \neq 0$ and $E_z \neq 0$ an additional cross point of dispersion curves of Eq. (13) for bulk EH magnons appears in comparison to the exchangeless limit of Eq. (14). In particular, in both cases of $\mathbf{n} \parallel \mathbf{l}$ and $\mathbf{n} \perp \mathbf{l}$, two cross points $\Omega_\nu(k_{\nu\rho}) = \Omega_\rho(k_{\nu\rho})$ ($k_{\nu\rho} \neq 0$) can appear for the dispersion curves of Eq. (13) with mode indices ν and ρ. For example, in the case of $\mathbf{n} \perp \mathbf{l}$ ($\mathbf{k} \in xy$), two cross points can arise if condition (15) is satisfied. For $\mathbf{n} \parallel \mathbf{l}$, the spatial dispersion together with an external electric field can also cause an additional extremum (minimum) to appear on a dispersion curve $\Omega_\nu(k_\perp)$ of spin waves described by Eq. (13) at some value of $k_\perp \neq 0$ if in the exchangeless limit ($\alpha \longrightarrow 0$) of Eq. (14) there is only a maximum at $k_\perp \neq 0$ for $\omega_\nu^2 A_p \mu > \omega_E^2 > \omega_\nu^2 A_p/\mu$.

When the quantity $c_m \nu/d$ is sufficiently large, the dispersion curve $\Omega_\nu(k_\perp)$ of EH magnons described by Eq. (13) corresponds to a direct wave ($\partial\Omega_\nu(k_\perp)/\partial k_\perp > 0$) for any value of the wave number $k_\perp$ and has no inflection point ($\partial\Omega_\nu(k_\perp)/\partial k_\perp = 0$) and no crossover [$\Omega_\nu(k_\perp) = \Omega_\rho(k_\perp)$].

It is well known [19] that, when analyzing the reflection and refraction of a bulk normal wave at the boundary of a crystal, the shape of the wave-vector surface of the normal wave is of prime importance. The local geometry of a constant-frequency surface of the normal bulk waves under study in an infinite crystal must significantly affect the spectrum of these waves in a finite crystal, because in the latter case, the spatial dispersion of the amplitude of bulk vibrations is a result of the interference of bulk waves incident on and reflected from the boundaries of the crystal. In the next section, we analyze the combined effect of the magnetoelectric and inhomogeneous exchange interactions on the shape of the wave-vector surface of normal spin waves of the EH type in an infinite AFM and the relationship between the local geometry of this surface and the anomalies in the spectrum of Eq. (13) of bulk EH magnons in a plate of a magnetoelectric AFM.

6. THE SHAPE OF A CONSTANT-FREQUENCY SURFACE AND THE STRUCTURE OF THE WAVEGUIDE EH-MAGNON SPECTRUM

Since in Eqs. (6) and (13) the wave vector of the EH magnon under study is assumed to lie in the xy plane, we should examine, using Eq. (6), the shape of the intersection of the $k_x k_y$ plane and a constant-frequency surface (ω = const) of the normal EH-type spin wave in $\mathbf{k}$ space. The corresponding expression can be written in the form

$$c_m^2 k^2 = [\omega^2 - \omega_E^2 \cos^2\theta(\mu \sin^2\theta + \cos^2\theta)^{-1}] \times (1 + A_p \sin^2\theta)^{-1} - \omega_0^2, \quad (16)$$

where $k_y^2/k^2 \equiv \sin^2\theta$ and $k^2 \equiv k_x^2 + k_y^2$. Analysis of the extremum points of the curves described by Eq. (16) and comparison with the results of the analysis of dispersion relations (13) presented above reveals that a local extremum on the dispersion curve of the waveguide EH magnon in question is associated with the region of $\partial\omega/\partial k_x = 0$ for $\mathbf{n} \parallel y$ or $\partial\omega/\partial k_y = 0$ for $\mathbf{n} \parallel x$ in the corresponding cross section of the wave-vector surface of the normal spin wave of the same polarization as in Eq. (16) propagating in the infinite crystal. Whether this extremum is a maximum or a minimum is determined by the sign of the local Gaussian curvature of the curve described by Eq. (16) at this point. In particular, if $|\mathbf{E}| = 0$ and $\mathbf{n} \parallel y$, an extremum at $k_\perp \neq 0$ on a dispersion curve described by Eq. (13), as well as the region of $\partial\omega/\partial k_x = 0$ in the corresponding cross section of Eq. (16), can appear for $\omega^2 < \omega_0^2 (1 + A_p)^2$ (Fig. 3). In the case of a minimum (maximum) on a dispersion curve of Eq. (13), the Gaussian curvature of the corresponding portion of the wave-vector surface of Eq. (16) will be positive (negative).

In the magnetoelectric AFM in question, the presence of an extremum on a dispersion curve of Eq. (13) of bulk dipole–exchange magnons is determined not only by the frequency ω, mode index ν, plate thickness d, and wave number $k_\perp$ of these magnons but also by the strength of the external electric field E_z. For example, when $\mathbf{n} \parallel x$, $\omega_E^2 > \omega_0^2 A_p \mu$, and $\omega_0^2 (1 + A_p) < \omega^2 < \omega_*^2$, the region of $\partial\omega/\partial k_\perp = 0$ can appear simultaneously on curves of Eqs. (13) and (16) (Fig. 4). The points of intersection of curves of Eq. (16) with straight lines k_y = const or k_z = const carry information about the spectrum of the corresponding waveguide EH magnons with given wavenumber $k_\perp$, frequency ω, and mode index ν, that is, information about curves of Eq. (13). In particular, when the normal to the surface of the plate $\mathbf{n}$ lies in the k_x, k_y plane and is aligned with the axis of ordinates ($\mathbf{n} \parallel y$), then the number of points that the straight line $k_x = k_{\text{perp}}$ and the curve of Eq. (16) have in common is equal to the maximum number of bulk spin-wave modes that can propagate along the x axis through an AFM plate of thickness $2d$ and have the same wave number $k_\perp$ and frequency ω (i.e., the number of crossovers). In the same geometry, the common points of the curve of Eq. (16) and the straight line $k_y = \kappa_\nu$ indicate the wave numbers $k_\perp$ with which the waveguide magnons in question with a fixed mode index ν and frequency ω can propagate through a thin plate of thickness $2d$ of the AFM under study. Since the group velocity of a wave is aligned with the outward normal to the wave-vector surface [19], an investigation of the local

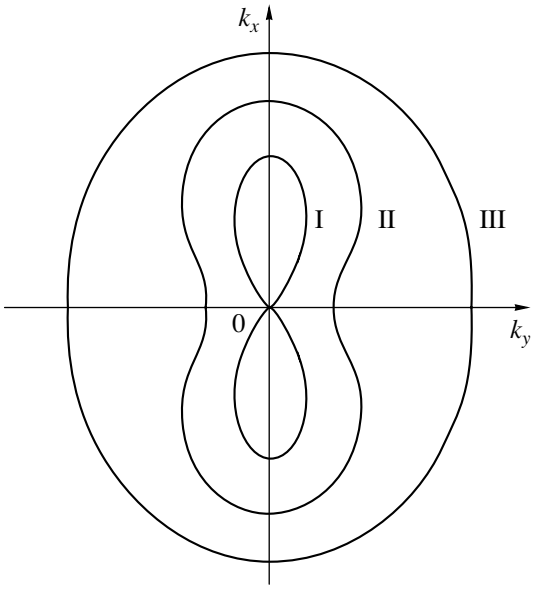

Fig. 3. Cross section of the wave-vector surface of EH magnons described by Eq. (16) for $|\mathbf{E}| = 0$ and different frequencies: (I) $\omega_0^2 < \omega^2 < \omega_0^2(1 + A_p)$, (II) $\omega_0^2(1 + A_p) < \omega^2 < \omega_0^2(1 + A_p)^2$, and (III) $\omega^2 > \omega_0^2(1 + A_p)^2$.

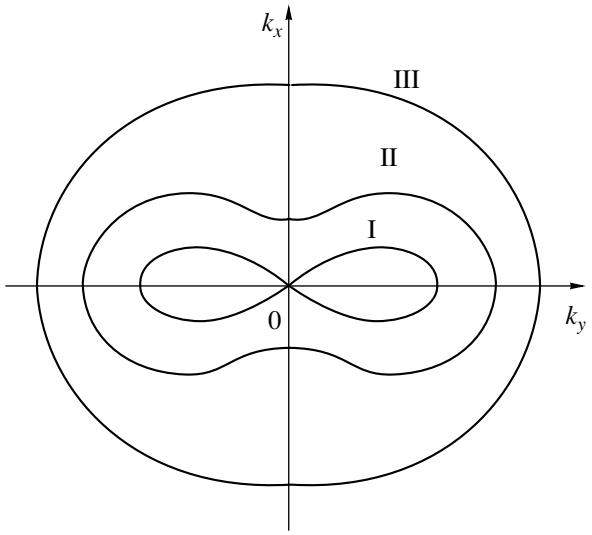

Fig. 4. Cross section of the wave-vector surface of EH magnons described by Eq. (16) for $\omega_E^2 > \omega_0^2 A_p \mu$ and different frequencies: (I) $\omega_0^2 + \omega_E^2 > \omega^2 > \omega_0^2(1 + A_p)$, (II) $\omega_0^2 + \omega_E^2 < \omega^2 < \omega_*^2$, and (III) $\omega^2 > \omega_*^2$, where $\omega_*^2 \equiv \omega_0^2(1 + A_p)^2 - \omega_E^2(1 + A_p)/\mu$.

Gaussian curvature of the cross section of the constant-frequency surface described by Eq. (16) allows one, as an analysis of Eq. (13) reveals, to determine the type (direct or back waves) of bulk EH magnons corresponding to the portion of the dispersion curve of Eq. (13) characterized by given ω, κ_ν, and $k_\perp$. In particular, a bulk spin wave with $\mathbf{k} \in xy$ propagating along a plate with $\mathbf{n} \parallel x$ and described by Eq. (13) will be of the back-wave type if the projection of the outward normal to the wave-vector surface onto the y axis at the point of intersection of this surface and the straight line $k_x = \kappa_\nu$ is negative; if this projection is positive, the corresponding wave will be of the direct-wave type for given $k_\perp$, ω, and κ_ν.

In this paper, we primarily analyzed the zeroth-order approximation in $W_{\nu\rho} \ll 1$ to Eqs. (10) and (11). It should be noted, however, that when dispersion curves of direct waves ($\partial\Omega_\nu(k_\perp)/\partial k_\perp > 0$) and back waves ($\partial\Omega_\nu(k_\perp)/\partial k_\perp < 0$) intersect at a degeneracy point [$\Omega_\nu(k_\perp) = \Omega_\rho(k_\perp)$], then the degeneracy is lifted, according to Eq. (12), and an additional extremum ($\partial\Omega_\nu(k_\perp)/\partial k_\perp = 0$) corresponding to a local maximum or minimum of the dispersion curve appears on each of the two separated branches of the spin-wave spectrum.

7. CONCLUSIONS

Thus, we have considered the case of a plate of a centrally antisymmetric AFM and found the necessary conditions under which the application of a static electric field can lead to earlier unknown anomalies in the spectrum of bulk electric-dipole magnons. Among the features of the spin-wave dynamics caused by a static electric field **E** in a finite magnetoelectric crystal are (1) transformation of a waveguide E magnon into a waveguide EH magnon; (2) the possibility of the bulk EH spin-wave energy flux (group velocity) reversing in comparison to the case of $|\mathbf{E}| = 0$ in a given magnetooptical geometry; (3) the possibility of extremum points appearing on a dispersion curve of the magnon spectrum $\Omega_\nu(k_\perp)$ for $k_\perp \neq 0$ in the presence of spatial dispersion (inhomogeneous exchange interaction), as well as in the exchangeless approximation; (4) the existence of cross points (at $k_\perp \neq 0$) of dispersion curves of modes with indices ν and ρ of the bulk EH spin-wave spectrum $\Omega_\nu(k_\perp)$; and (5) the ability of an external electric field to change the local geometry of a constant-frequency surface of a normal EH spin wave in a centrally antisymmetric AFM; there is a one-to-one correspondence between the local geometry of the wave-vector surface of a normal EH spin wave in an infinite AFM crystal and the structural features of the spectrum of a waveguide mode of the same type in a finite crystal of the AFM.

It should be noted that, when discussing possible experimental observations of the features of the quantized spectrum of bulk magnons investigated in this paper, one should take into account the mode damping. It is not difficult to include energy dissipation phenomenologically. However, since the class of magnetoelec-

tric crystals in question has not been well studied experimentally, we can only make order-of-magnitude estimates. Let ΔH_ν be the linewidth of the bulk normal mode $\Omega_\nu(k_\perp)$ with index ν and let $\Delta\Omega_{\nu\rho}$ be the frequency gap between the bulk normal modes $\Omega_\nu(k_\perp)$ and $\Omega_\rho(k_\perp)$ at their cross point after their degeneracy has been lifted. It follows from Eq. (12) that quantum size effects will be experimentally observable in the spectrum of bulk magnons (far from crossovers) in an AFM plate of thickness $2d$ if the following condition is satisfied:

$$H_E \nu a/2d \gg \Delta H_\nu, \tag{17}$$

where H_E is the exchange field and a is the lattice parameter. The linewidth ΔH_ν can vary considerably with temperature [20]; for example, in MnF_2, it can vary over four orders of magnitude. Putting $\Delta H_\nu \approx 10^3$ Oe, $H_E \approx 10^6$ Oe, and $a \approx 10^{-8}$ cm [20], we obtain from Eq. (17) that $d \ll 10^{-5}$ cm. As for the repulsion between dispersion curves $\Omega_\nu(k_\perp)$ and $\Omega_\rho(k_\perp)$ near their cross point, the criterion for it to be observable, according to Eq. (12), is more stringent than Eq. (17):

$$\Delta\Omega_{\nu\rho} \gg g\Delta H_\nu, \tag{18}$$

where g is the gyromagnetic ratio.

It should also be noted that although the calculations in this paper were carried out for the specific exchange and electrodynamic boundary conditions, the results are of a more general character, because the spectrum of bulk spin waves, which are inhomogeneous across the plate thickness for $\nu > 1$, depends only slightly on the boundary conditions [21]. The sole exception to this may be the conditions for the existence of intersection points of dispersion curves, which were found using boundary conditions (7) and (8).

ACKNOWLEDGMENTS

The author is grateful to V.M. Yurchenko, T.N. Tarasenko, and I.E. Dragunov for their encouragement and helpful discussions.

REFERENCES

1. G. A. Smolenskiĭ and I. E. Chupis, Usp. Fiz. Nauk. **137** (3), 415 (1982) [Sov. Phys. Usp. **25**, 475 (1982)].
2. R. V. Pisarev, Ferroelectrics **162** (1–4), 191 (1994).
3. S. Bluck and H. G. Kahle, J. Phys. C **21** (11), 5193 (1988).
4. E. A. Turov, Ferroelectrics **162** (1–4), 253 (1994).
5. E. A. Turov, V. V. Men'shenin, and V. V. Nikolaev, Zh. Éksp. Teor. Fiz. **104** (6), 4157 (1993) [JETP **77**, 1014 (1993)].
6. E. A. Turov, Zh. Éksp. Teor. Fiz. **104** (5), 3886 (1993) [JETP **77**, 868 (1993)].
7. E. A. Turov and V. V. Men'shenin, Zh. Éksp. Teor. Fiz. **108** (6), 2061 (1995) [JETP **81**, 1124 (1995)].
8. V. N. Krivoruchko and D. A. Yablonskiĭ, Zh. Éksp. Teor. Fiz. **94** (9), 268 (1988) [Sov. Phys. JETP **67**, 1886 (1988)].
9. V. D. Buchel'nikov and V. G. Shavrov, Zh. Éksp. Teor. Fiz. **109** (2), 706 (1996) [JETP **82**, 380 (1996)].
10. S. V. Tarasenko, Opt. Spektrosk. **86** (4), 658 (1999) [Opt. Spectrosc. **86**, 588 (1999)].
11. S. V. Tarasenko, Fiz. Nizk. Temp. **27** (1), 52 (2001) [Low Temp. Phys. **27**, 40 (2001)].
12. S. V. Tarasenko, Fiz. Nizk. Temp. **27** (2), 178 (2001) [Low Temp. Phys. **27**, 130 (2001)].
13. A. G. Gurevich and G. A. Melkov, *Magnetic Oscillations and Waves* (Nauka, Moscow, 1994).
14. V. I. Alshits, A. N. Darinskii, and J. Lothe, Wave Motion **16** (2), 265 (1992).
15. O. G. Vendik and D. N. Chartorizhskiĭ, Fiz. Tverd. Tela (Leningrad) **12** (5), 1538 (1970) [Sov. Phys. Solid State **12**, 1209 (1970)].
16. B. A. Kalinikos, Izv. Vyssh. Uchebn. Zaved., Fiz. **24** (8), 42 (1981).
17. B. A. Kalinikos and A. N. Slavin, J. Phys. C **19** (11), 7013 (1986).
18. A. Yariv and P. Yeh, *Optical Waves in Crystals: Propagation and Control of Laser Radiation* (Wiley, New York, 1984; Mir, Moscow, 1987).
19. Yu. I. Sirotin and M. P. Shaskolskaya, *Fundamentals of Crystal Physics* (Nauka, Moscow, 1979; Mir, Moscow, 1982).
20. A. A. Mukhin, Preprint No. 245, IOF AN SSSR (General Physics Institute, Academy of Sciences of USSR, Moscow, 1984).
21. L. M. Brekhovskikh, *Waves in Layered Media* (Nauka, Moscow, 1973; Academic, New York, 1980).

Translated by Yu. Epifanov

Physics of the Solid State, Vol. 44, No. 5, 2002, pp. 920–926. Translated from Fizika Tverdogo Tela, Vol. 44, No. 5, 2002, pp. 881–887.

MAGNETISM AND FERROELECTRICITY

Electrical Conductivity, Magnetoresistance, and Specific Heat of Oxygen-Deficient $La_{0.67}Ca_{0.33}MnO_{3-\alpha}$ ($0 \le \alpha < 0.4$)

E. I. Nikulin, V. M. Egorov, Yu. M. Baĭkov, B. T. Melekh, Yu. P. Stepanov, and I. N. Zimkin

Ioffe Physicotechnical Institute, Russian Academy of Sciences, ul. Politekhnicheskaya 26, St. Petersburg, 194021 Russia

e-mail: baikov.solid@pop.ioffe.rssi.ru

Received July 30, 2001

Abstract—This paper reports on a first study of the effect of oxygen content in $La_{0.67}Ca_{0.33}MnO_{3-\alpha}$ on the electrical conductivity, magnetoresistance, and specific heat within a broad range of oxygen deficiency variation, $0 \le \alpha < 0.4$. Preparation of a large quantity of stable samples with an easily controllable oxygen deficiency was made possible by using a "soft" hydrogen treatment (870 K, 1–2 kPa). The properties of samples with $0 \le \alpha \le 0.06$ are shown to differ from those with $\alpha \ge 0.1$. For instance, samples studied in the semiconducting phase at 300 K revealed, on the average, $E_g = 0.28$ eV in the first group and $E_g = 0.43$ eV in the second, and only samples of the first group exhibit giant negative magnetoresistance and specific-heat anomalies in the range 150–200 K. The latter anomalies correlate with magnetoresistance peaks observed in all samples of the first group (with $\alpha \le 0.06$). The metal–semiconductor transition was found to disappear abruptly for $\alpha > 0.006$. The effects of a variation in the cation composition and the oxygen content on the physical properties are compared.

1. INTRODUCTION

Perovskite oxides with mixed-valence cations have been attracting interest for a long time because of their physical properties, which are frequently unusual and promising for use in potential device applications. For instance, the ferromagnetic (FM) properties of the $(RE)_{1-x}(AE)_xMnO_3$ solid solutions were discovered more than 50 years ago, the high-temperature protonic conductivity of $(AE)Ce_{1-x}(RE)_xO_3$ has been a subject of intense interest for over 20 years, and the $(RE)Ba_2Cu_3O_{7-\alpha}$ compound was found to be superconducting 15 years ago (*AE* = Ca, Sr, Ba; *RE* = Y, La). Despite the differences in their physical properties, these groups of oxides have, in addition to structural similarities, a number of other common characteristics. Viewed from the chemical standpoint, these are the presence of cations of transition elements (Mn, Cu, Ce) and off-stoichiometric variations both in the cations and in oxygen, which give rise to either a smooth (quantitative) variation of the physical characteristics or to radical changes in the properties. Present-day concepts tend to relate such changes, in many cases, to the behavior of cations in the perovskite position *B*, primarily, to a change in their charge state. The latter can be achieved in more than one way, for instance, indirectly, through a compositional change in the cation position *A* (in manganites); by direct chemical substitution in the cation position *B* (in cerates); and by acting on the anion component (the oxygen sublattice, in cuprates). It should be stressed that although we are actually dealing with the existence and/or formation of a mixed-valence (charge) state of these cations, it would be more appropriate in some cases to examine the change in the oxidation state of the oxygen–transition element subsystem or of the BO_x polyhedra ($2 \le x \le 6$). For instance, in the case of manganites, it is on the manganese mixed valence that one usually focuses attention, more specifically, on the Mn^{3+}/Mn^{4+} ratio, which is governed, in turn, by the ratio of differently charged ions in the *A* position, for instance, La^{3+}/Ca^{2+}. However, one also takes into account the oxygen environment of the *B* position, whose significance in the formation of both the transport properties and magnetic ordering is always stressed even for oxygen-stoichiometric manganites [1, 2].

It appeared, therefore, only natural to choose an experiment to test the corresponding theoretical concepts in which the oxygen content in a solid solution of the lanthanum and calcium manganites could be varied and correlations between the electrical and magnetic properties, on the one hand, and the deviation from oxygen stoichiometry, on the other, could be looked for. Such studies were found very useful in their time in understanding the properties of superconducting cuprates [3, 4]. In contrast to the cuprates, however, manganites are much stabler against oxygen loss. To produce noticeable deviations from the stoichiometric oxygen content (characterized usually as three oxygen atoms per formula unit), temperatures above 1200 K and extremely low partial oxygen pressures are needed. This entails a risk of changing the cation composition

near the surface and even of a partial decomposition of the original sample. Moreover, determination of the amount of extracted oxygen, which is necessary in such cases and should be done with a high enough precision, was carried out in the available publications in an indirect way, from the partial pressure of oxygen equilibrated with the sample, which was measured by ZrO_2-based oxygen sensors. This pressure is connected with the oxygen off-stoichiometry through a complex relation; it was derived for specific samples and did not take into account the technological factors, which are essential here. In our work within the project "Hydrogen and Mixed Valence in Perovskites" supported by the Russian Foundation for Basic Research, we decided to employ, for oxygen removal, reduction by molecular hydrogen, a method which, while being not less efficient, is "softer." The corresponding experience was gained by us in studies with superconducting cuprates [5, 6], and a preliminary work performed with manganites [7] has provided supporting data for the potential of the method.

The present paper describes a study of a series of $La_{0.67}Ca_{0.33}MnO_{3-\alpha}$ samples with $0 \le \alpha < 0.4$. Attention was focused primarily on two aspects, namely, the methodology bearing on the preparation of oxygen-deficient samples by reduction in hydrogen, a most important and original point, and the specifics of the experiment, which are connected with changes in the electrical conductivity, giant negative magnetoresistance, and thermal properties as a function of α, i.e., of the oxygen content for a fixed cation composition, a feature revealed by us, effectively, for the first time. Measurements by differential scanning calorimetry (DSC), a very efficient method of studying phase transformations, including those occurring in other perovskites investigated by us [6, 8], were performed on the same samples that were used in the electrical measurements, thus substantially reducing possible differences among the samples caused by technological factors.

2. EXPERIMENTAL

2.1. Chemical Procedures

The starting material of $La_{0.67}Ca_{0.33}MnO_{3-\alpha}$ composition was prepared by direct cold-crucible rf melting [9]. The composition of the material is specified based on the ratio of the starting oxides. Chemical analysis of such materials shows that the starting cation ratio usually remains unchanged in the samples. A comparative x-ray structural and phase analysis of various parts of the ingot, 200 cm^3 in total volume, showed it to be homogeneous enough, particularly after annealing it in air at 800°C. For the experiments, we chose two pieces cleaved from the same part of the ingot, about 15 mm in diameter. They were used to cut out rectangular samples, $2 \times 2 \times 4$ mm in size, for the electrophysical and subsequent calorimetric measurements. Three more samples measuring $25 \times 10 \times 2$ mm were cut for verification experiments (see below). After cutting and visual selection for the absence of mechanical damage, caverns, cracks, etc., all samples (14 in all) were subjected to preliminary oxidation in air at 800°C to check for the homogeneity and identity of the samples with respect to oxygen content and stability against thermal effects. In this experiment, all 14 samples prepared from the starting material revealed exactly the same relative change in weight, which may be considered as an additional argument for the starting material being homogeneous and for the samples having the same composition. (The small samples weighed 150 ± 20 mg.) After this, all samples were annealed in dry oxygen at 800°C for 48 h. No substantial changes in sample weight were found compared with that measured immediately after the annealing in air; $\Delta\alpha$ was not more than +0.005.

Oxygen was extracted by reacting a sample with hydrogen in a closed reactor, 250 cm^3 in volume, consisting of two parts; one of them, which contained the samples, was heated, and the other was cooled by liquid nitrogen to condense the water vapor formed. These parts of the reactor were separated by a stopcock. After putting the samples in place and evacuating both parts with a fore pump (at room temperature), hydrogen was admitted. The hydrogen pressure was chosen based on the amount of oxygen desired to be extracted and the calibrated reactor volume. Then, the heating and liquid-nitrogen cooling of the corresponding parts of the reactor were activated. The temperature of 600°C, chosen in preliminary experiments, ensured oxygen extraction in a reasonable time (about six hours). Six to ten hours later, the residual pressure in the reactor was measured and, on making sure that the hydrogen had been completely consumed, the two reactor parts were disconnected. The samples were annealed at 1000°C in a residual vacuum of about 1 Pa for 24 h to make sure that the samples became homogeneous in oxygen content. The samples were cooled to room temperature over two to three hours. While the samples thus prepared were weighed to additionally determine the oxygen loss, the basic method remained barometric measurement of both the consumed hydrogen and the water formed. The amount of the water was determined by evaporating it from the trap into a larger volume (480 cm^3) in order to avoid water vapor condensation on the vessel walls. The changes in the oxygen content measured by the three methods coincided within 10% for $\Delta\alpha$ less than 0.03 and within 5% for larger changes in α. The values of α and of the corresponding changes in the oxygen concentration are given in the table.

2.2. Measurements of the Electrical Conductivity

The bar-shaped samples of the above dimensions were placed, after the chemical treatment, into a special fixture providing a sufficiently strong clamping of the copper electrodes to the sample. The measurements were carried out using the dc four-probe arrangement. The fixture with the samples was placed inside a mas-

Main characteristics of the oxygen-deficient $La_{0.67}Ca_{0.33}MnO_{3-\alpha}$ samples

No.	α	Δ_N, 10^{20} cm^{-3}	σ (300 K), S/cm	E_g (300 K), eV	T^*_{part}, K	T_{max}, K	MR, %	Specific heat, J/mol K		Specific entropy at T_{pt}, J/mol K
								110 K	250 K	
1	0	0.0	15.0	0.2 ± 0.03	197	186	45	60.4	102.1	1.96; 185
2	0.006	1.0	12.0	0.30 ± 0.01	185	180	41	59.0	104.9	2.21; 170
3	0.017	2.9	11.4	0.28 ± 0.01	158	158	31	60.3	102.7	1.36; 150
4	0.03	5.3	3.7	0.28 ± 0.01		140	17	62.3	101.9	1.03; 155
5	0.04	6.8	2.8	0.27 ± 0.01		125	18			
6	0.06	10.6	1.24	0.26 ± 0.01	120	120	15	62.3	101.9	0.45; 150
7	0.10	17.0	0.092	0.45 ± 0.02	155					
8	0.16	27.2	0.051	0.42 ± 0.02				63.39	99.84	
9	0.22	37.4	0.028	0.42 ± 0.02				60.62	97.69	
10	0.34	58.0	0.009	0.45 ± 0.02	140			60.75	95.18	

Notes: ΔN is the change in the oxygen ion concentration corresponding to the given α.

T^*_{part} are specific points in the resistivity vs. temperature curves.

T_{max} is the temperature of the maximum magnetoresistance (MR).

T_{pt} is the temperature of the maximum of the anomalous specific-heat peak and, probably, of the paramagnet–ferromagnet phase transition.

sive copper cylinder, whose temperature was varied slowly from room temperature to 78 K (or 20 K). The temperature was measured with a copper–constantan thermocouple. The input resistance of the instruments was 10^{11} Ω, which permitted one to perform studies within a broad range of sample resistances. The resistance measurement reproducibility at various temperatures was not worse than 0.5%.

2.3. Magnetoresistance

The magnetoresistance (MR) of the samples under study is defined as the relative difference between the resistance in a magnetic field H (R_H) and without it ($R_{H=0}$), i.e., $MR(\%) = 100(R_{H=0} - R_H)/R_{H=0}$. The measurements were done in the following order. After the temperature had been stabilized at a given level, the sample resistance was measured just before field application, then in the field, and then immediately after field turnoff. The sample resistance at $H = 0$ was determined as the mean between the values measured before and after application of the field. The magnetic field used in the work was 0.5 T. This field does not saturate the sample magnetization. No relaxation phenomena associated with the application and turnoff of the field were detected.

2.4. Calorimetric Measurements

The temperature dependence of the specific heat $C(T)$ was measured on a Perkin-Elmer DSC-2 differential calorimeter in dry helium in the range 100–270 K. The temperature scale of the instrument was calibrated against the melting points of indium (430 K) and ice (273.1 K); the specific-heat scale, against the specific heat of sapphire. The measurements were done in two steps. First, we recorded the baseline with the empty chambers, after which the sample to be studied was placed into the measuring chamber and the temperature scanning was repeated. The difference between the relations thus obtained yields $C(T)$ of the sample. The scanning in temperature was performed in heating and cooling runs at a rate of 5–40 K/min. The relative error of such specific-heat measurements was less than 1.5%.

To increase the sensitivity and precision of determination of thermal effects in the region of the phase transitions, we used the differential method, in which a second temperature scan of the sample together with a sapphire reference was made, with the latter placed into the calorimeter chamber intended for comparison measurements. The relative error of this method of specific-heat measurement was ~0.5%.

2.5. Effect of Water Vapor

Our procedure of oxygen extraction entails the formation of water vapor, which is condensed in a trap cooled by liquid nitrogen. The equilibrium vapor pressure over ice at this temperature is negligible, and, therefore, the water vapor produced can be considered frozen out. Our experience gained in working with such systems (barium yttrium cuprate [3, 5, 10]) indicates, however, that part of the water may end up trapped by the sample. In this case, the oxygen positions will be occupied by hydroxyl ions rather than by vacancies. While this phenomenon is of interest in itself, it is certainly beyond the scope of the present work. Nevertheless, we performed verification experiments as follows.

First, we ran the reaction with molecular hydrogen without cooling the trap. Second, the oxygen-deficient samples were brought in contact with water vapor (300 Pa at 300–600°C). After these procedures, thermal desorption was studied. No noticeable release of water was detected and, hence, was not absorbed in the course of the experiments, although our experimental conditions were very favorable for dissociative dissolution of water in perovskite cerates [11]; thermodynamic calculations suggest that this process can also take place in manganites [12]. Interestingly, $La_{0.33}Ca_{0.67}MnO_{3-\alpha}$ samples yielded an opposite result [13]. The reason for this is planned for study, but there are grounds to suggest that these differences may be connected with the asymmetry of the electronic subsystem, which was pointed out, e.g., in [14].

3. RESULTS AND DISCUSSION

3.1. Characterization of the Complete Set of Samples

First of all, we stress that these are the first measurements made on melted, high-density (up to 98.5% theoretical level), rather than on ceramic, samples.

The $La_{0.67}Ca_{0.33}MnO_{3-\alpha}$ samples retained the cation composition characteristic of the starting sample. This statement rests on an x-ray phase analysis of a special sample subjected to hydrogen treatment together with the samples to be studied. Only sample 11 revealed weak reflections belonging to foreign phases. These reflections could be assigned to lanthanum oxide; however, they disappeared after a repeated oxidation. Actually, the relatively low temperature of the reaction with hydrogen (600°C) could not have resulted in chemical decomposition of the samples. Literature data suggest that the oxygen content of 2.6 is a critical level for these samples at temperatures above 1200°C [15]. The oxygen off-stoichiometry (column labeled "α"), the measured physical parameters, and the characteristics derived from them are listed in the table.

Because we worked with high-density samples, we had to make sure that they had a uniform oxygen distribution. To do this, we compared the differences in composition between samples of different thickness (2, 4, and 6 mm) but with a larger area (250 mm^2) than the ones typical of this series and, accordingly, of a larger weight, which increased the accuracy of oxygen content determination by weighing. If the depth profile was nonuniform (diffusive) and the anneal time was not sufficiently long, one could expect differences in the relative weight changes between these three samples. No such differences were observed in our experimental conditions.

The lattice parameters of the samples used in the measurements could not be determined; however, measurements performed on the same special sample of a larger size did not reveal any substantial changes in the reflection pattern observed at room temperature; namely, the structure was pseudocubic with a parameter of 0.3884 nm.

3.2. Dependence of the Magnitude and Character of Electrical Conductivity on the Oxygen Content

The resistance vs. temperature plots obtained at temperatures below 300 K for 11 samples with different oxygen contents varying from 3.0 to 2.60 exhibit an increase in the electrical resistivity with decreasing oxygen content; this increase is as high as four orders of magnitude compared to the room-temperature level (see table) and is substantially larger in the low-temperature domain.

The $R(T)$ curves can be clearly separated into two groups. The first group (samples *1, 2*) is characterized by a nonmonotonic variation of R with decreasing T. The second group (samples *4–10*) exhibits a monotonic, exponential-like growth of R with decreasing temperature; this pattern becomes particularly pronounced when plotting the graphs in Arrhenius coordinates, $\ln R$ vs. T^{-1}. Sample *3* shows a nonmonotonic variation of the first derivative of $\ln R$ with respect to T^{-1} that can be classed in either group. The temperature behavior of sample *11* was not studied because of its resistance being too high already at room temperature and of the above-mentioned indications of the presence of foreign phases. The curves are displayed in Fig. 1.

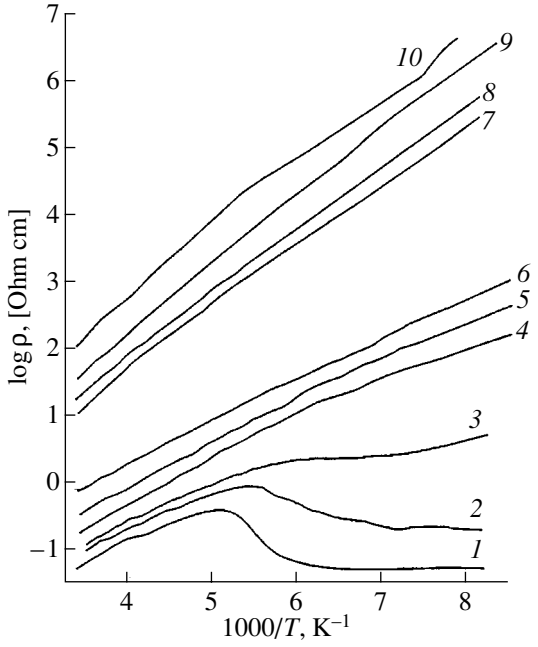

Fig. 1. Temperature dependence of the electrical resistivity of $La_{0.67}Ca_{0.33}MnO_{3-\alpha}$ samples. Oxygen deficiency increases from bottom to top through α = 0, 0.006, 0.017, 0.03, 0.04, 0.06, 0.1, 0.16, 0.22, and 0.34. The figures adjoining the curves are sample numbers in the table.

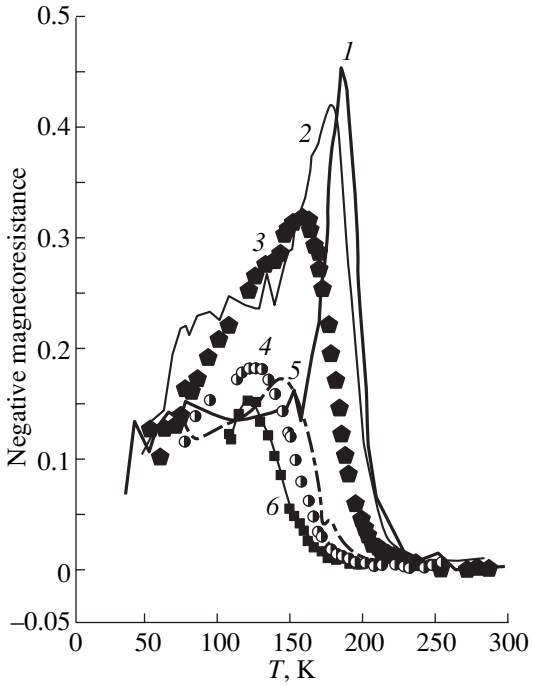

Fig. 2. Temperature dependence of the negative magnetoresistance of $La_{0.67}Ca_{0.33}MnO_{3-\alpha}$ samples. The figures adjacent to the curves are sample numbers in the table.

A more careful analysis of mathematically treated data permitted us to separate some other features in the behavior of the $R(T)$ curves, which appear to be of importance for interpretation of the experimental results. The following points deserve attention in this connection.

(1) In all the curves (*1–10*), there exists a temperature interval near room temperature where the $R(T)$ relation follows, in the first approximation, a semiconducting pattern, can be linearized in the $\ln R$ vs. T^{-1} coordinates (the rms error is less than 0.5%), and allows determination of the band gap E_g from the argument of the exponential (see column 5 in table). As seen from the table, E_g varies relatively weakly for oxygen contents corresponding to $\alpha \le 0.06$ and is approximately 0.28 eV. As the oxygen content is reduced still lower, a growth is observed up to $E_g \cong 0.43$ eV.

(2) One observes an exponential decrease in the sample conductivity with increasing α in the semiconducting phase. This decrease is different for the two intervals of the oxygen deficiency; namely, it is much steeper for $\alpha \le 0.06$ than for $\alpha \ge 0.1$.

(3) After the resistance R of samples *1* and *2* has passed through a maximum, the conductivity acquires a metallic character with a further decrease in the temperature (below 150 K); namely, it grows slightly with decreasing temperature to 25 S cm^{-1} in the former sample and does not change in the latter, remaining equal to 5 S cm^{-1}.

(4) For samples *3–9*, the resistivities plotted in the Arrhenius coordinates are convex-up curves, such that their description would formally require invoking a quadratic dependence of $\ln R$ on T^{-1}, where the coefficient of T^{-2} characterizing the curvature of the $\ln R = f(T^{-1})$ curve would be negative.

Viewed from the standpoint of the present theoretical concepts concerning the mechanism of electric transport in manganites, the above approximation excludes the possibility of charge transfer by small-radius polarons. Indeed, the corresponding relation of the type of $R \sim T\exp(E/T)$, if plotted in the $\ln R$ vs. T^{-1} coordinates, would bring about a curvature of the opposite sign!

3.3. Magnetoresistance as a Function of Temperature and Oxygen Content

Magnetoresistance as a characteristic of manganites is of interest only in the temperature region where it reaches giant levels. By theory, this occurs in a region close to the metal–semiconductor and ferromagnet–paramagnet phase transitions. As seen from the table, in our experiments, a giant MR was observed only for $0 \le \alpha \le 0.06$. The temperature position of the maximum and the maximum magnitude of the effect decrease with decreasing oxygen content. The general pattern of the phenomenon is illustrated in Fig. 2. We clearly see two overlapping maxima of magnetoresistance in the samples studied. This observation will be analyzed in detail in a subsequent publication.

3.4. Specific Heat as a Function of Temperature and Oxygen Content

Figure 3 presents the starting DSC curves used to determine the specific heat of samples *1–8*. As seen from the curves, at temperatures below 190–200 K, the specific heat of samples *1–5* exhibits an anomaly in the form of an endothermic λ-shaped peak whose intensity decreases with increasing α, while the temperature position of the peak T_{max} shifts toward lower temperatures. Experimental isolation of the anomaly ΔC from the overall temperature dependence of the specific heat $C(T)$ does not appear possible for a sample with a fixed α, because the specific heats of samples with different α differ from one another, as well as from those of samples *6–8*, whose specific heats could serve as baselines as they do not exhibit any anomalies.

To isolate the local endothermic peak and derive the specific transition entropy ΔS, we attempted to fit the lattice (phonon) part of the specific heat to the Debye interpolation relation $F_D(T/\Theta)$, with the Debye temperature Θ constant for different samples. In this case, the anomaly ΔC of interest could be found as the difference $\Delta C = C(T) - F_D(T/\Theta)$. It turned out, however, that the lattice specific heat of the $La_{0.67}Ca_{0.33}MnO_{3-\alpha}$ samples with different α cannot be represented in this form. To

describe the lattice specific heat analytically, one would have to use not only Debye's interpolation expression with different Debye temperatures for different samples but also additional components. Without going into details, we present, as an illustration, an experimental $C(T)$ relation and a generalized $F_D(T/\Theta)$ function for the sample with $\alpha = 0$ (Fig. 4). These dependences are seen to coincide for $T > 190$ K, while for $T < 190$ K, the difference between the $C(T)$ and $F_D(T/\Theta)$curves represents the anomaly as an endothermic λ-shaped peak with a specific heat ΔS. The specific heat ΔC thus derived was used to calculate the specific entropy of the peak $\Delta S = \int [\Delta C(T)/T]dT$. The calculated values of ΔS for samples *1–4* and *6* are presented in the table.

3.5. Discussion of the Results

Our analysis of the results related to the three different characteristics of the oxygen-deficient solid solutions of the lanthanum and calcium manganites studied (conductivity, magnetoresistance, and specific heat) revealed a number of points which become evident in inspecting the table.

(1) Coincidence of the oxygen-content intervals within which all three properties investigated undergo quantitative and/or qualitative changes (for $\alpha \le 0.06$: $E_g = 0.28$ eV, MR is observed to exist and there is nonzero entropy of the phase transition; for $\alpha \ge 0.1$: $E_g = 0.43$ eV, there is no MR effect and no specific-heat anomalies are observed in the range 100–300 K).

(2) Coincidence of the temperature intervals within which magnetoresistance and the specific-heat anomaly are observed and their variations follow those in the oxygen content (compare T_{max} of the MR and of the specific heat and the decreases in the MR effect and in the specific entropy of the phase transitions).

(3) A sharp change in the temperature behavior of the conductivity with oxygen loss (within the loss interval from 0.2 to 0.6 at. %, the semiconductor–"dirty" metal transition disappears).

Thus, we have obtained convincing evidence of a substantial role being played by the oxygen subsystem in the physical properties of manganites. Note that the above findings were made in a direct experiment and are in no way associated with the model. At the same time, the present theoretical models, which are quite frequently alternative in nature, consider oxygen to be the component primarily responsible for the electrophysical properties. Its influence is both through the formation of the Mn^{4+}–O–Mn^{3+} chains, supporting electron transfer, and through variation of the carrier concentration. (Note that theoretical models usually consider the stoichiometric concentration of oxygen.)

The same can be said of the theoretical ideas concerning the role of oxygen in the magnetic properties of solid solutions of manganites and the related phase transformations. Nevertheless, the available theoretical models can be used to relate, based on the variation of the Mn^{4+}/Mn^{3+} ratio, the variations in the oxygen content with those in the magnetic properties.

By and large, if one associates the chemical nature of the changes in conductivity and magnetoresistance

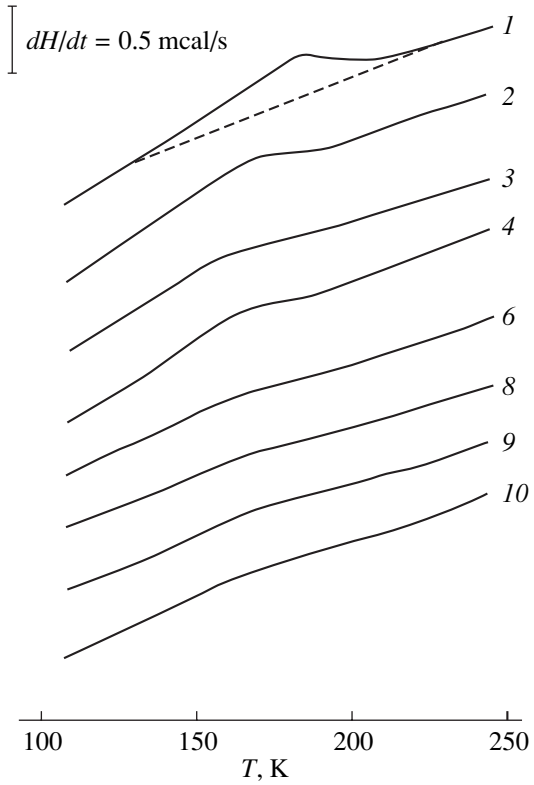

Fig. 3. DSC curves obtained on $La_{0.67}Ca_{0.33}MnO_{3-\alpha}$ samples. Oxygen deficiency increases from top to bottom through $\alpha = 0$, 0.006, 0.017, 0.03, 0.06, 0.16, 0.22, and 0.34. The figures adjoining the curves are sample numbers in the table.

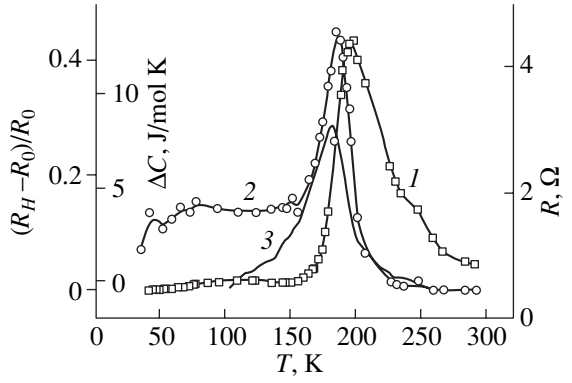

Fig. 4. Temperature dependences of the resistance (R, curve *1*), negative magnetoresistance [$(R_H - R_0)/R_0$, curve *2*], and excess specific heat (ΔC, curve *3*) matched at the point of the semiconductor–metal phase transition for the $La_{0.67}Ca_{0.33}MnO_3$ sample.

with action on the mixed-valence state of the manganese ions only, then variations in the oxygen content and in the La^{3+}/Ca^{2+} ratio should produce the same effect (in this sense, two calcium ions are equivalent to one oxygen ion). These considerations are buttressed qualitatively by the Goodenough diagram [16] for the $La_{1-x}Ca_xMnO_3$ system, according to which the Curie temperature (for the paramagnet–ferromagnet phase transition) decreases from 250 to 140 K with x decreasing from 0.33 to 0.09, a process equivalent to the removal of 0.24/2 = 0.12 oxygen ions per formula unit (in our experiments, this would correspond to $\alpha = 0.12$). According to the same diagram, when x decreases still further, the character of the phase transition is changed to paramagnet–antiferromagnet, with the Néel temperature becoming a characteristic temperature in the diagram. The absence of the MR effect in samples with $\alpha \geq 0.1$ in our experiments can be attributed to such changes, which could also be treated as an abrupt decrease in the fraction of the FM phase (islands of the FM phase in an ocean of the antiferromagnetic phase [2]).

However, current theoretical concepts suggest a conclusion that extraction of oxygen may produce an effect which is not analogous with the variations in the cation composition; indeed, the removal of one oxygen ion breaks one link in the …O–Mn–O–Mn–O… chain. Thus, a change in the concentration of carriers disorganizes the paths of their transport. This is probably why the character of the conductivity changes so abruptly when the oxygen content becomes slightly off-stoichiometric. This is not equivalent to a change in the Curie temperature when the La^{3+}/Ca^{2+} ratio varies near the value of 0.33. Indeed, a decrease in oxygen content by $\Delta\alpha = 0.01$ actually blocks the metal–semiconductor phase transition, while a change in calcium content from 0.33 to 0.31 changes T_c at most by 5–7 K. ($\Delta\alpha = 0.01$ was chosen as the average change of α in going from sample *2* to sample *3*.)

We conclude by stressing once again the unconventional character of our approach to studying the composition–property relation in the family of perovskite manganites, which exhibit the giant magnetoresistance effect in a number of cases. Actually, the phase diagram should be at least three-dimensional, such as, for instance, the phase transition temperature–cation composition–oxygen content phase diagram; however, most studies examine only the same cut of this diagram for a constant oxygen content (an assumption that may not hold). Our approach may be called "perpendicular" in the sense that we examine a cut of the diagram at a constant cation composition. The lanthanum–strontium system will be the next in the series of our studies in this direction.

ACKNOWLEDGMENTS

This study was supported by the Russian Foundation for Basic Research (project nos. 97-03-33466, 00-03-32476) and INTAS (grant no. 00-0728).

REFERENCES

1. J. M. D. Coey and M. Viret, Adv. Phys. **48** (12), 167 (1999).
2. E. L. Nagaev, Usp. Fiz. Nauk **166**, 833 (1996) [Phys. Usp. **39**, 781 (1996)].
3. E. K. Shalkova, Yu. M. Baikov, and T. A. Ushakova, Sverkhprovodimost: Fiz., Khim., Tekh. **5** (1), 22 (1992).
4. T. Hirata, Phys. Status Solidi A **156** (2), 227 (1996).
5. Yu. M. Baĭkov, Sverkhprovodimost: Fiz., Khim., Tekh. **7** (7), 1208 (1994).
6. V. M. Egorov, Yu. M. Baikov, V. A. Bershnein, *et al.*, J. Therm. Anal. **38**, 1123 (1992).
7. Yu. M. Baĭkov, E. M. Nikulin, B. T. Melekh, *et al.*, Pis'ma Zh. Tekh. Fiz. **26** (12), 58 (2000) [Tech. Phys. Lett. **26**, 523 (2000)].
8. V. M. Egorov, Yu. M. Baĭkov, E. F. Kartenko, *et al.*, Fiz. Tverd. Tela (St. Petersburg) **40** (1), 2109 (1998) [Phys. Solid State **40**, 1911 (1998)].
9. B. T. Melekh, V. M. Egorov, Yu. M. Baikov, *et al.*, Solid State Ionics **97**, 465 (1997).
10. Yu. M. Baikov and S. L. Shokhor, Physica C (Amsterdam) **185–189**, 1589 (1991).
11. K. D. Kreuer, Chem. Mater. **8**, 610 (1996).
12. M. S. Islam and M. Cherry, Solid State Ionics **97**, 33 (1997).
13. Yu. M. Baikov, W. Gunther, V. P. Gorelov, *et al.*, Ionics **4** (5/6), 347 (1998).
14. P. V. Vanitha, K. Vijaya Sarathy, A. K. Cheetham, and C. N. R. Rao, Solid State Commun. **115**, 463 (2000).
15. J. Nowotny and M. Rekas, J. Am. Ceram. Soc. **81** (1), 67 (1998).
16. J. B. Goodenough, Aust. J. Phys. **52**, 155 (1999).

Translated by G. Skrebtsov

Physics of the Solid State, Vol. 44, No. 5, 2002, pp. 927–931. Translated from Fizika Tverdogo Tela, Vol. 44, No. 5, 2002, pp. 888–892.

MAGNETISM AND FERROELECTRICITY

Effect of the Disorder Parameter on the Magnetic, Electrical, Galvanomagnetic, Elastic, and Magnetoelastic Properties of $R_{0.55}Sr_{0.45}MnO_3$ Manganites

A. I. Abramovich*, L. I. Koroleva*, A. V. Michurin*, O. Yu. Gorbenko*, A. R. Kaul'*, M. Kh. Mashaev, R. Szymczak***, and B. Krzymanska*****

**Moscow State University, Vorob'evy gory, Moscow, 119899 Russia*
e-mail: abramovich@ofef343.phys.msu.su
***Turkmen State University, Ashkhabad, 744014 Turkmenistan*
****Institute of Physics, Polish Academy of Sciences, Warsaw, 02-668 Poland*

Received July 30, 2001

Abstract—This paper reports on a study of the magnetic, transport, magnetotransport, elastic, and magnetoelastic properties of the $R_{0.55}Sr_{0.45}MnO_3$ ceramics (R = Sm, $Eu_{0.40}Nd_{0.15}$, $Tb_{0.25}Nd_{0.30}$) with the same carrier concentration and identical tolerance factor but which differ in the cation disorder parameter σ^2. It was found that the Curie temperature T_C decreases linearly with increasing σ^2. An increase in σ^2 results in an increase in the maximum electrical resistivity and an increased jump in the temperature dependence of linear thermal expansion near T_C, as well as in a decrease in magnetoresistance and magnetostriction. For $T > T_C$, one observes an abrupt increase in magnetostriction, magnetization, and magnetoresistance in a critical field H_{C1} which grows with increasing temperature. The value of H_{C1} determined at fixed T/T_C decreases with increasing σ^2.

1. INTRODUCTION

The magnetic properties of the $R_{1-x}A_xMnO_3$ manganites with perovskite structure, in which rare-earth R^{3+} and alkaline-earth A^{2+} ions occupy the A positions, are affected by various factors. Among them are, in particular, the carrier concentration, the average radius of the A cation $\langle r_A \rangle$, and the disorder caused by the difference in radii between the cations on the A sublattice, which is defined as $\sigma^2 = \sum x_i r_i^2 - \langle r_A \rangle^2$, where x_i is the concentration of cation i on the A sublattice and r_i is the ionic radius of cation i [1, 2]. For instance, the Curie temperature T_C increases linearly with $\langle r_A \rangle$, except in the case of large $\langle r_A \rangle$, where this linearity breaks down. In addition, it has been found that disorder on the A sublattice substantially reduces T_C for the same value of $\langle r_A \rangle$, with σ^2 remaining related linearly to T_C [2, 3]. It has been shown [4] that increasing σ^2 for fixed $\langle r_A \rangle$ and carrier concentration suppresses magnetic interactions, both ferromagnetic (FM) and antiferromagnetic (AFM), and destabilizes charge ordering (CO). The effect of disorder on the elastic and magnetoelastic properties has not thus far been studied.

2. EXPERIMENTAL RESULTS AND DISCUSSION

In order to study the effect of cation disorder on the magnetic, electrical, galvanomagnetic, elastic, and magnetoelastic properties of manganites, we synthesized $Sm_{0.55}Sr_{0.45}MnO_3$ (composition **1**), $Eu_{0.40}Nd_{0.15}Sr_{0.45}MnO_3$ (**2**), and $Tb_{0.25}Nd_{0.30}Sr_{0.45}MnO_3$ (**3**) ceramics with a constant carrier concentration and the same tolerance factor (t = 0.927) but with different cation disorder parameters $\sigma^2 = 7.85 \times 10^{-3}$, 8.05×10^{-3}, and 8.48×10^{-3} Å for compositions **1**, **2**, and **3**, respectively. To avoid possible influences of the conditions of preparation, all the samples were synthesized at the same time and in the same conditions as described in [5]. This paper reports on a study of the magnetic, electrical, galvanomagnetic, elastic, and magnetoelastic properties of the above samples. The results obtained are presented in Figs. 1–8. The experimental techniques employed are described in [5].

Figure 1 plots the temperature dependence of the initial magnetic susceptibility measured in an ac magnetic field with an amplitude of 1 Oe and frequency of 8 kHz. The Curie points were determined as the temperatures at which the $[\partial\chi/\partial T](T)$ curves pass through a minimum and were found to be T_C = 126, 112, and 76 K for compositions **1**, **2**, and **3**, respectively. The inset to Fig. 1 presents a T_C vs. σ^2 plot, which shows that T_C decreases linearly with increasing σ^2 in accordance with the relation $T_C(\langle r_A \rangle, \sigma^2) = T_C(\langle r_A \rangle, 0) - p_1\sigma^2$ proposed in [2]. The values of $T_C(\langle r_A \rangle, 0) = 750$ K and $p_1 = 8 \times 10^4$ K Å^{-2}, which were derived from the $T_C(\sigma^2)$ relation plotted in the inset to Fig. 1, turned out to be larger

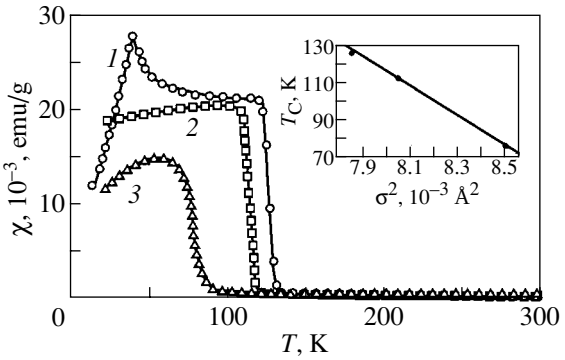

Fig. 1. Temperature dependence of the initial magnetic susceptibility in an ac magnetic field of 1 Oe of frequency 8 kHz obtained on (*1*) $Sm_{0.55}Sr_{0.45}MnO_3$, (*2*) $Eu_{0.40}Nd_{0.15}Sr_{0.45}MnO_3$, and (*3*) $Tb_{0.25}Nd_{0.30}Sr_{0.45}MnO_3$. Inset: T_C vs. σ^2 plot.

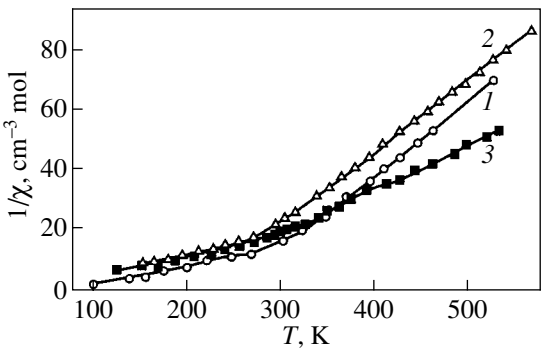

Fig. 2. Temperature dependence of the paramagnetic susceptibility of (*1*) $Sm_{0.55}Sr_{0.45}MnO_3$, (*2*) $Eu_{0.40}Nd_{0.15}Sr_{0.45}MnO_3$, and (*3*) $Tb_{0.25}Nd_{0.30}Sr_{0.45}MnO_3$.

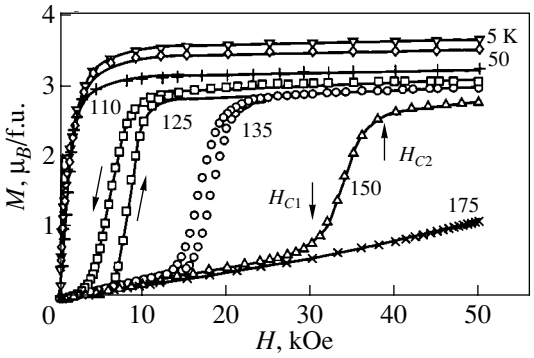

Fig. 3. Isotherms of magnetization of an $Eu_{0.40}Nd_{0.15}Sr_{0.45}MnO_3$ sample.

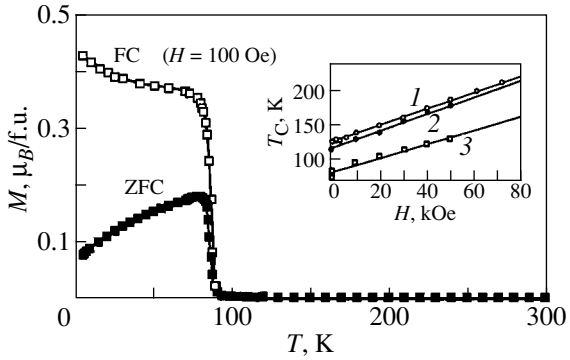

Fig. 4. Temperature dependence of ZFC and FC magnetizations of a $Tb_{0.25}Nd_{0.30}Sr_{0.45}MnO_3$ sample. Inset: T_C plotted against the magnetic field in which it was measured on (*1*) $Sm_{0.55}Sr_{0.45}MnO_3$, (*2*) $Eu_{0.40}Nd_{0.15}Sr_{0.45}MnO_3$, and (*3*) $Tb_{0.25}Nd_{0.30}Sr_{0.45}MnO_3$.

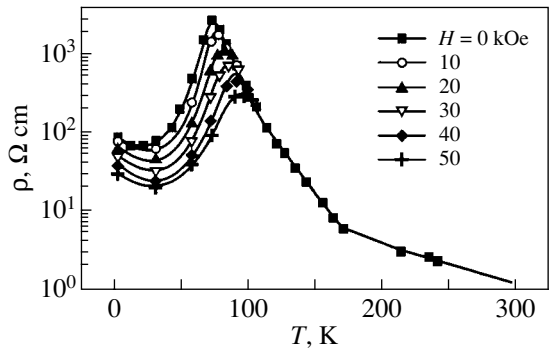

Fig. 5. Temperature dependence of the electrical resistivity of a $Tb_{0.25}Nd_{0.30}Sr_{0.45}MnO_3$ sample measured in different magnetic fields.

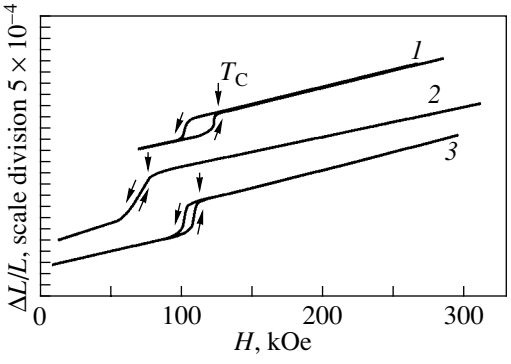

Fig. 6. Temperature dependence of linear thermal expansion of (*1*) $Sm_{0.55}Sr_{0.45}MnO_3$, (*2*) $Eu_{0.40}Nd_{0.15}Sr_{0.45}MnO_3$, and (*3*) $Tb_{0.25}Nd_{0.30}Sr_{0.45}MnO_3$.

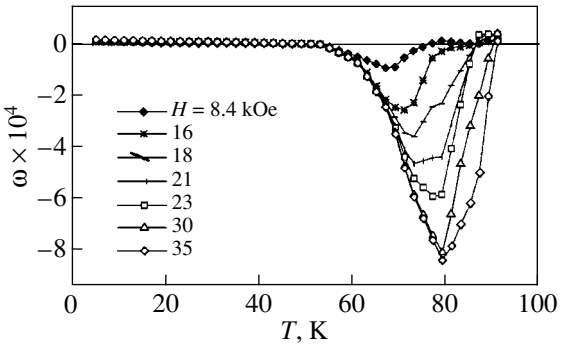

Fig. 7. Temperature dependence of volume magnetostriction measured in different magnetic fields on a $Tb_{0.25}Nd_{0.30}Sr_{0.45}MnO_3$ sample.

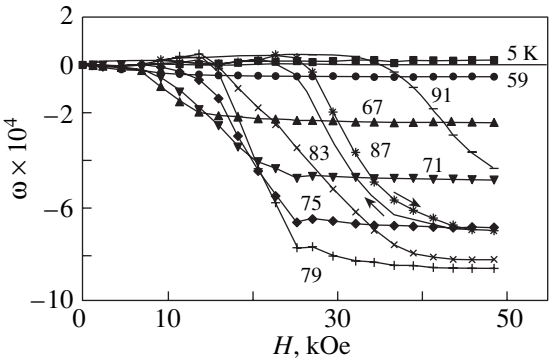

Fig. 8. Isotherms of volume magnetostriction of a $Tb_{0.25}Nd_{0.30}Sr_{0.45}MnO_3$ sample.

than those obtained for $Ln_{0.7}A_{0.3}MnO_3$ [$T_C(\langle r_A\rangle, 0)$ = 400 K, $p_1 = 2.06 \times 10^4$ K Å^{-2}] [2] and for $Ln_{0.5}A_{0.5}MnO_3$ [$T_C(\langle r_A\rangle, 0)$ = 330 K, $p_1 = (2.9–1.9) \times 10^4$ K Å^{-2}] for different $\langle r_A\rangle$ = 1.225–1.237 Å [3]. In addition, we revealed a strong dependence of T_C on the magnetic field H in which the measurements were carried out (inset to Fig. 4). For instance, the change in the Curie temperature $\Delta T_C = T_C(H = 50\ \text{kOe}) - T_C(H = 1\ \text{Oe})$ = 65, 61, and 53 K for compositions **1**, **2**, and **3**, respectively, which indicates that ΔT_C decreases with increasing σ^2. It should be pointed out that although the compounds studied in this work are characterized by a large tolerance factor t and, hence, a large transfer integral, their T_C do not exceed 126 K, which is apparently accounted for by the large value of σ^2. Local distortions determined by σ^2 affect the Mn–O–Mn angle and, hence, reduce T_C; we observed exactly this. Figure 2 displays the temperature dependence of the inverse paramagnetic (PM) susceptibility $1/\chi(T)$ for all the compositions studied. We readily see that at high temperatures, this dependence follows the Curie–Weiss law $\chi = N\mu_{\text{eff}}^2/3K(T - \theta)$ with the PM Curie points θ_1 = 250, 210, and 170 K for compositions **1**, **2**, and **3**, respectively, and with effective magnetic moments μ_{eff} = 5.6, 5.7, and 7.3 μ_B per formula unit, which is slightly in excess of the values calculated taking into account the contribution due to the R^{3+} ions. While the Curie–Weiss law also holds for $T \geq T_C$, the parameters θ_2 and μ_{eff2} are different: θ_2 = 70, 50, and 10 K and μ_{eff2} = 14.8, 11.5, and 11.0 μ_B per formula unit for compositions **1**, **2**, and **3**, respectively. The large values of μ_{eff2} imply the existence of magnetic clusters in this temperature region. Calculations showed that the above magnetic moments correspond to clusters consisting of four Mn ions ($2Mn^{3+}$, $2Mn^{4+}$). The inflection point T^* in the $1/\chi(T)$ curves is apparently the temperature at which clusters start to form. As seen from Fig. 2, T^* = 305, 270, and 210 K for compositions **1**, **2**, and **3**, respectively; i.e., this temperature decreases with increasing σ^2. The fact that $\theta_2 \ll \theta_1$ indicates the existence of AFM coupling at temperatures $T \geq T_C$. This may be associated with the local charge ordering observed to occur for composition **1** above T_C [4, 6, 7].

The isotherms of magnetization of all three compositions behave similarly. For illustration, Fig. 3 shows the isotherms of magnetization of composition **2** with T_C = 112 K for several temperatures. We see that in the PM region, an abrupt increase in magnetization occurs after the magnetic field reaches the level H_{C1}, which increases with temperature. In addition, a hysteresis is observed as the magnetic field is increased and decreased. Note that the width of the hysteresis loop increases with increasing σ^2. The spontaneous magnetization M measured at 5 K is 3.50 μ_B/f.u. for compositions **1** and **2**, which is slightly lower than 3.55 μ_B/f.u., the figure corresponding to FM ordering of the Mn^{3+} and Mn^{4+} ions. For composition **3**, we have M = 4.02 μ_B/f.u.; this large magnetic moment is, however, associated probably not with σ^2 but rather with the magnetic moment of the Tb^{3+} ion. The rate of saturation of the magnetization isotherms depends on σ^2. Indeed, the magnetization saturation of sample **3** occurs much slower than that of compositions **1** and **2**. While the $M(T)$ curves indicate the FM transition at T_C in all the samples, the sample magnetization at low temperatures decreases in magnetic fields $H \leq 10$ kOe (Fig. 4). Such a low-temperature behavior of M is not typical of ferromagnets and indicates the presence of AFM interactions. Moreover, the low-temperature magnetization depends on the actual conditions in which the cooling was carried out. As seen from Fig. 4, the FC magnetization (with the sample cooled in a magnetic field) differs substantially from the ZFC magnetization (with the sample cooled in zero field). The difference between the FC and ZFC regimes disappears in magnetic fields $H > 10$ kOe.

A sharp maximum in the temperature dependence of electrical resistivity $\rho(T)$ is observed near T_C for all compositions. Note that ρ at 4.2 K is close to its room-

temperature value. For illustration, Fig. 5 shows a $\rho(T)$ graph for composition **3**, as well as how it is affected by a magnetic field. The magnitude of ρ_{max} grows with increasing σ^2. For instance, $\rho_{max} = 10^2$ Ω cm for composition **1** and 2.7×10^3 Ω cm for composition **3**. The reason for this lies in that a deviation of the Mn–O–Mn angle from 180° strongly increases the resistivity in regions with local lattice distortions. The magnetoresistance (MR), which forms as a result of the maximum in $\rho(T)$ being suppressed by a magnetic field, peaks near T_C and decreases strongly with increasing σ^2. For instance, MR, defined as $\Delta\rho/\rho = [\rho(H) - \rho(0)]/\rho(0)$, reaches colossal values of 69, 64, and 2.5% for compositions **1**, **2**, and **3**, respectively, in a magnetic field of 10 kOe. Note that a MR of 40% is reached in composition **3** only in a field $H = 50$ kOe (Fig. 5).

Linear thermal expansion $\Delta L/L$ is observed to undergo an abrupt change near T_C for all compositions (Fig. 6). The corresponding volume change $\Delta V/V = 3\Delta L/L$ is 0.06, 0.09, and 0.13% for compositions **1**, **2** and **3**; in other words, $\Delta V/V$ increases with increasing σ^2. Hence, local distortions give rise to an additional contribution to thermal expansion. Application of an external magnetic field suppresses the jump in the $[\Delta L/L](T)$ relation and initiates a negative volume magnetostriction ω, which is small everywhere except in a narrow interval near T_C where the $\omega(T)$ curves pass through a minimum. At the minimum, $|\omega|$ reaches a giant value. This is seen from Fig. 7, which plots the $\omega(T)$dependence for composition **3**. As follows from a comparison of the values of $|\omega|$ in a weak magnetic field obtained on all the samples studied, this quantity decreases with increasing degree of disorder. For instance, in $H = 8.4$ kOe, we have $\omega = 5 \times 10^{-4}$, 4×10^{-4}, and 0.8×10^{-4} for compositions **1**, **2**, and **3**, respectively; i.e., $|\omega|$ of sample **1** is larger by nearly an order of magnitude than that of composition **3**. The volume magnetostriction saturates for all compositions in a field ~50 kOe to about the same level $|\omega| \approx 10^{-3}$. The anisotropic part of the magnetostriction is very small for all compositions throughout the temperature interval covered, increases near T_C, and reverses sign at T_C. The isotherms of volume magnetostriction $\omega(H)$ exhibit a jump in ω at a field H_{C1} in all compositions. This is seen from Fig. 8, which displays $\omega(H)$ curves for composition **3**. Note that the values of H_{C1} derived for the same temperature from the magnetization and magnetostriction coincide only for sample **1**, while for compositions **2** and **3**, the values of H_{C1} determined from the magnetostriction are larger than those calculated from the magnetization. In addition, the values of H_{C1} obtained for a fixed $\mathbf{T}/T_C$ ratio decrease with increasing σ^2.

An analysis of the experimental data obtained in this work shows that the disorder produced by chemical substitution on the *A* sublattice affects the physical properties of the manganites substantially. Many properties of the manganites presently allow interpretation in terms of the model of phase separation [8]. Note that phase separation in manganites has a more complex pattern than that in conventional magnetic semiconductors. In manganites, one has to take into account orbital and charge ordering and the influence of the Jahn–Teller effect and of the disorder stemming from the difference in ionic radii on the *A* sublattice. Computer calculations made with due account of the latter factor have revealed that large metallic and dielectric clusters may coexist in manganites at carrier concentrations close to 0.5 [9]. The size of these clusters depends on the actual degree of disorder; namely, the less the disorder, the larger the clusters. Their distribution can be arbitrary, and the shape is fractal. A percolation mechanism was proposed in [10] to explain the $\rho(T)$ dependence near T_C. For instance, for $T < T_C$, the AFM clusters are arranged in a singly connected network of metallic FM jumpers, so that, on the whole, the sample will behave as a "dirty" metal (Fig. 5). Obviously enough, a magnetic field and temperature will change the volume of the jumpers, producing the effect of large MR (Fig. 5). Neutron diffraction showed that at low temperatures, the $Sm_{1-x}Sr_xMnO_3$ system supports a nonuniform magnetic state including the FM, *A*-type AFM, and AFM CO phases. The FM and *A*-type AFM reflections disappear near T_C, whereas the AFM CO phase is seen to persist above T_C [7]. The size of AFM-ordered CO clusters in a sample with $x = 0.40$, close in composition to sample **1**, was estimated in [8] to be a few hundreds of angstroms. The coexistence of FM and AFM clusters for $T > T_C$ in the samples under study follows from measurements of the paramagnetic susceptibility. After the applied magnetic field has reached H_{C1}, the FM clusters start to grow rapidly at the expense of the AFM clusters, thus bringing about a sharp increase in the magnetization (Fig. 3) and magnetostriction (Fig. 8) and a decrease in the resistivity. This is observed to occur up to the field H_{C2}, where the FM clusters percolate and the above characteristics saturate. The Curie point in the samples under consideration is the temperature at which the FM clusters break down. Therefore, the external magnetic field, in creating the FM clusters destroyed by temperature, should increase T_C. We observed this in our work (see inset to Fig. 4).

3. CONCLUSION

Thus, we have shown experimentally that the magnetic, electrical, galvanomagnetic, elastic, and magnetoelastic properties of the $R_{0.55}Sr_{0.45}MnO_3$ ceramics (R = Sm, $Eu_{0.40}Nd_{0.15}$, $Tb_{0.25}Nd_{0.30}$) with a constant carrier concentration and the same tolerance factor depend on the degree of cation disorder σ^2 on the *A* sublattice. Although the compositions studied have a large tolerance factor $t = 0.927$ and, hence, a large transfer integral, their T_C are not high (126, 112, 76 K). This is

apparently due to the large value of σ^2. Local distortions determined by σ^2 change the Mn–O–Mn angle and, hence, decrease T_C. In the absence of disorder ($\sigma^2 = 0$), their T_C would be 750 K (inset to Fig. 1), i.e., an order of magnitude higher. As follows from measurements of the paramagnetic susceptibility, FM clusters start to form at a temperature T^*, which is substantially higher than T_C and decreases with increasing σ^2 (Fig. 2). The increase in σ^2 gives rise to an increase in the maximum electrical resistivity, which is due to the increasing resistivity in regions with local lattice distortions caused by the Mn–O–Mn angle deviating from 180°. A strong suppression of the MR is observed to occur in our compositions with increasing σ^2. Local lattice distortions provide an additional contribution to thermal expansion, which becomes manifest in an increased jump in the temperature dependence of linear thermal expansion (Fig. 6) and a decrease in magnetostriction near T_C with increasing σ^2. For $T > T_C$, one observes a jump in magnetostriction (Fig. 8), magnetization (Fig. 3), and magnetoresistance at a critical field H_{C1}, which grows with increasing temperature. The magnitude of H_{C1} determined for a fixed T/T_C ratio decreases with increasing σ^2.

ACKNOWLEDGMENTS

This study was supported by the Russian Foundation for Basic Research (project nos. 00-15-96695, 00-02-17810), INTAS (grant nos. 97-open-30253, 97-11954), and NATO-HTECH (grant no. LG 972942).

R. Szymczak and B. Krzymanska also express gratitude for grant no. PBZ/KBN/13/T08/99/19.

REFERENCES

1. B. Raveau, A. Maignan, C. Martin, and M. Hervieu, Chem. Mater. **10**, 2641 (1998).
2. Lide M. Rodrigez-Martinez and J. Paul Attfield, Phys. Rev. B **54**, R15622 (1996); Phys. Rev. B **58**, 2426 (1998).
3. F. Damay, A. Maignan, C. Martin, and B. Raveau, J. Appl. Phys. **81**, 1372 (1997); J. Appl. Phys. **82**, 6181 (1997).
4. C. Martin, A. Maignan, M. Hervieu, and B. Raveau, Phys. Rev. B **60**, 12191 (1999).
5. A. I. Abramovich, L. I. Koroleva, A. V. Michurin, *et al.*, Fiz. Tverd. Tela (St. Petersburg) **42**, 1451 (2000) [Phys. Solid State **42**, 1494 (2000)].
6. V. V. Runov, D. Yu. Chernyshov, A. I. Kurbakov, *et al.*, Zh. Éksp. Teor. Fiz. **118**, 1174 (2000) [JETP **91**, 1017 (2000)].
7. I. D. Luzyanin, V. A. Ryzhov, D. Yu. Chernyshov, *et al.*, Preprint PNPI-2342 (1999).
8. É. L. Nagaev, Usp. Fiz. Nauk **166**, 833 (1996) [Phys. Usp. **39**, 781 (1996)].
9. E. Dagotto, T. Hotta, and A. Moreo, Phys. Rep. **344**, 1 (2001).

Translated by G. Skrebtsov

Physics of the Solid State, Vol. 44, No. 5, 2002, pp. 932–937. Translated from Fizika Tverdogo Tela, Vol. 44, No. 5, 2002, pp. 893–897.

MAGNETISM AND FERROELECTRICITY

Anisotropy of the Spin-Wave Resonance Spectrum in the Case of a Dissipative Mechanism of Spin Pinning

A. M. Zyuzin, S. N. Sabaev, V. V. Radaĭkin, and A. V. Kulyapin

Mordovian State University, ul. Bol'shevistskaya 68, Saransk, 430000 Russia

Received May 14, 2001; in final form, August 6, 2001

Abstract—Mechanisms leading to anisotropy of dispersion curves of the spin-wave resonance spectrum in magnetic multilayer films are investigated experimentally and theoretically. One of the reasons for the considerable increase in the dispersion-curve slope for the static magnetic field directions intermediate between the parallel and normal ones in relation to the film plane is shown to be connected to the alteration of the equilibrium orientation of magnetization. This factor (in addition to the dominant dissipative mechanism of the spin pinning and to the reactive or dispersive properties of a layer with strong damping) is established to affect the wavenumbers of standing spin waves and cause a difference between the dispersion curves for normal and parallel orientations of the dc magnetic field. © *2002 MAIK "Nauka/Interperiodica".*

1. INTRODUCTION

Spin-wave resonance (SWR) spectra allow one to derive a large amount of information concerning the physical properties of magnetic films [1–4]. In addition, these spectra are highly sensitive to the character of the spatial distribution of film properties, which allows them to be determined by analyzing the spectrum evolution occurring when the film thickness is reduced through layer-by-layer etching [5–7]. Such a characteristic of the SWR spectrum as the dispersion curve, along with SWR lines, their number, strengths, and widths, contains very important information [8–10]; e.g., its slope gives the exchange constant A. In order to extract this information, however, one needs a reliable identification of the absorption peaks of spin-ware (SW) modes and knowledge of their wave numbers, which is far from being an easy and uniquely resolvable task.

SWR spectra, whose excitation is caused by the dynamical mechanism of spin pinning or by surface anisotropy, are known to be very anisotropic [2–5, 10]. Depending on the direction of the dc magnetic field **H**, harmonic standing spin waves are excited in different parts (layers) of the film. This leads to a strong modification of the SWR spectrum when the **H** direction is varied. In particular, when the uniform-resonance fields in the layers coincide, the spectrum collapses into a single common zeroth mode.

The dissipative mechanism of spin pinning [8, 11–13] operates in multilayer films with layers differing widely in damping parameter and, unlike the mechanisms mentioned above, does not depend on the **H** direction; i.e., it is isotropic. The reasons for this are, first, that the harmonic part of a standing spin wave at any **H** orientation relative to the film is limited by the layer with low damping and, second, that the damping parameter of garnet ferrite films does not depend on the **H** direction. As follows both from the numerous experimental results obtained by us and from the published data, the magnitude of possible anisotropy of the Gilbert damping parameter $\alpha = \Delta H\gamma/\omega$ (where ΔH is the absorption line half-width, γ is the gyromagnetic ratio, and ω is the cyclic frequency of the microwave field) does not exceed the experimental error, which is less than 6%. At the same time, even in this case, the dispersion-curve slope depends crucially on the orientation of the dc magnetic field **H** relative to the film. The purpose of the present work was to investigate the mechanisms determining the slope of dispersion curves of the SWR spectrum in multilayer films in the case of dissipative mechanisms of spin pinning.

2. EXPERIMENTAL

Experimental investigations were carried out on two- and three-layer films of garnet ferrite single crystals. The films were produced using the liquid-phase epitaxy method by means of consecutive growth of layers on a gadolinium gallium garnet substrate with (111) orientation from various solutions in a melt. The layer closest to the substrate (pinning layer) was made of $(SmEr)_3Fe_5O_{12}$ and had a high value of $\alpha = 0.2$; the saturation magnetization $4\pi M$ was 1330 G, the effective uniaxial anisotropy field $H_k^{\text{eff}} = 96$ Oe, the cubic-crystalline anisotropy field $H_{k1} = -120$ Oe, $\gamma = 1.38 \times 10^7$ Oe^{-1} s^{-1}, and the thickness $h = 1.2$ μm. The following (excitation) layer was made of $Y_{2.98}Sm_{0.02}Fe_5O_{12}$, $\alpha = 0.003$, $4\pi M = 1740$ G, $H_k^{\text{eff}} = -1715$ Oe, $H_{k1} = -82$ Oe, and $\gamma = 1.76 \times 10^7$ Oe^{-1} s^{-1}. In different samples, the thickness of this layer h_1 varied from 0.46 to 0.9 μm. Three-layer films were different from bilayers

1063-7834/02/4405-0932$22.00 © 2002 MAIK "Nauka/Interperiodica"

in their having one more pinning layer. In films of this kind, spins were pinned at both surfaces of the excitation layer (symmetrical boundary conditions). SWR spectra were registered at a frequency of 9.34×10^9 Hz. The magnetic field was measured by an NMR magnetometer. The thickness was determined by the interference method on single-layer analogs of the layers. The thickness of the excitation layer was changed by varying the time of its growth or by etching it chemically. The orientation of the ⟨100⟩ and ⟨111⟩ axes, as well as the values of H_{k1}, was found using the technique described in [14]. It is noteworthy that in recording SWR spectra at a constant microwave frequency ω, the dispersion curve has been assumed, as a rule, to be described by the relation $H_0 - H_n = f(k^2)$, where H_0 and H_n are the resonance fields of the zeroth and nth SW modes and k is the wave number [5, 8, 9, 11]. In this case, the difference $H_0 - H_n$, as well as the SW frequency (at constant H), is a quadratic function of k. When constructing dispersion curves, the wave numbers of the SW modes were taken equal to $(n + 1/2)\pi/h_1$ for two-layer and $(2n + 1)\pi/h_1$ for three-layer films [5]. This indexing scheme implies that a node of a standing spin wave is located at the interface between layers.

Upon the basis of numerous experiments, it was established that SWR spectra have no essential differences in their structure for the perpendicular, parallel, and intermediate orientations of the magnetic field relative to the film if the dissipative mechanism of spin pinning is dominant and the parameter α in the pinning layer is no less than 0.2 (Fig. 1). At excitation layer thicknesses $h_1 \geq 0.9$ μm, the dispersion curves for the perpendicular and parallel orientations of **H** differ only slightly (in slope, Fig. 2). With decreasing h_1, the dispersion curves for both field orientations remain linear, their slopes increase, and, simultaneously, the difference between the curves increases. Spin pinning at both boundaries of the excitation layer (in a three-layer film) leads to an approximately two times greater difference between the curves (Fig. 3), although the mean value of their slopes is approximately the same as in the case of a two-layer film.

In all films studied, the slope of the dispersion curve corresponding to the SWR spectrum for the parallel orientation of **H** exceeded that for the perpendicular orientation. The slope was even greater when the field had an intermediate direction between the normal and parallel ones and the angle θ_H between **H** and the normal to the film lay in the range between ~20° and 80°. As an illustration, Figs. 2 and 3 show dispersion curves of the SWR spectrum for the angle θ_H equal to 45°.

3. CALCULATION OF THE SWR SPECTRA

With the aim of explaining the obtained results, a calculation of the SWR spectra and the corresponding

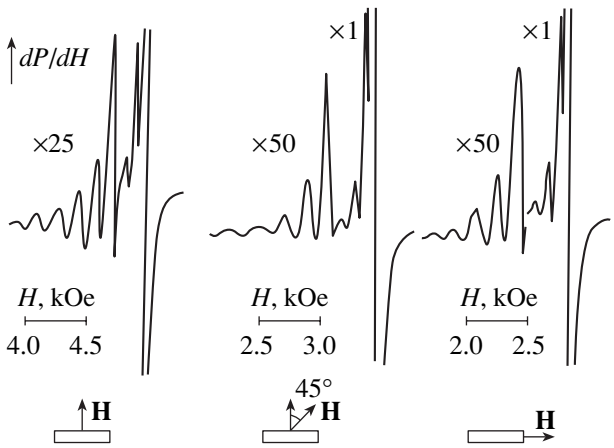

Fig. 1. SWR spectra at different orientations of the field **H** for a film with excitation layer thickness $h_1 = 0.69$ μm.

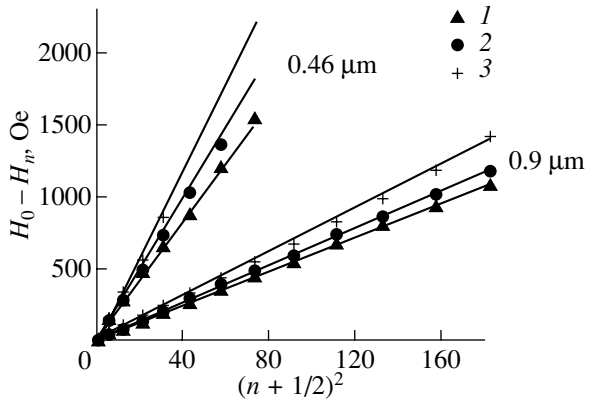

Fig. 2. Dispersion curves $H_0 - H_n = f(n + 1/2)^2$ for two-layer films with thickness h_1 equal to 0.9 and 0.46 μm for different values of θ_H equal to (*1*) 0°, (*2*) 90°, and (*3*) 45°. Dots are experimental data, and lines are the calculation.

dispersion dependences was undertaken. We used the dispersion relation [15]

$$\left(\frac{\omega}{\gamma}\right)^2 = \left[H\cos(\theta_H - \theta_M) + H_k^{\text{eff}}\cos^2\theta_M - H_{k1}a(\theta_M) + \frac{2A}{M}k^2\right]\left[H\cos(\theta_H - \theta_M) + H_k^{\text{eff}}\cos 2\theta_M - H_{k1}b(\theta_M) + \frac{2A}{M}k^2\right], \quad (1)$$

where

$$a(\theta_M) = (3 - 16x - 3y)/16,$$

$$b(\theta_M) = -(x + 3y)/4,$$

$$x = (2^{3/2}\sin 2\theta_M - \cos 2\theta_M)/3,$$

$$y = -(2^{5/2}\sin 4\theta_M - 7\cos 4\theta_M)/9.$$

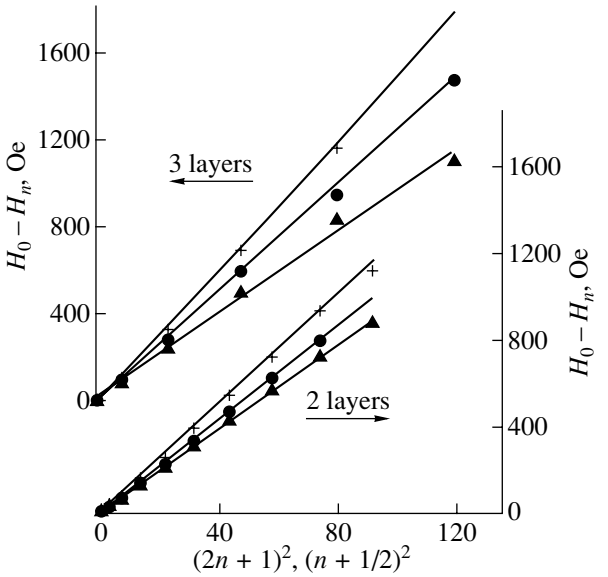

Fig. 3. Dispersion curves $H_0 - H_n = f(n + 1/2)^2$ for a two-layer film (below) and $H_0 - H_n = f(2n + 1)^2$ for a three-layer film (above) with thickness $h_1 = 0.69$ μm; the designations are the same as in Fig. 2. Dots are experimental data, and lines are the calculation.

Equation (1) describes spin-wave dispersion in both the excitation and pinning layers and allows one to find the relation between the wave numbers in the layers. The angle θ_M is found from the condition for the equilibrium orientation of the magnetization **M:**

$$2H\sin(\theta_H - \theta_M) = H_k^{\text{eff}}\sin 2\theta_M + H_{k1}\left[\frac{1}{12}\sin 2\theta_M + \frac{7}{24}\sin 4\theta_M + \sqrt{2}\sin^2\theta_M - \frac{4\sqrt{2}}{3}\sin^4\theta_M\right]. \quad (2)$$

In these equations, θ_M and θ_H are the angles that the normal to the film makes with **M** and **H**, respectively; these angles are measured in the (110) plane from the normal to the film [111] through the shortest path towards the crystallographic direction [001]. We note that the vector **M** lies in the (110) plane if the field **H** is in this plane.

The calculation was made using the exchange boundary conditions at the excitation layer boundaries

$$\left.\frac{\partial m_1}{\partial z}\right|_{z=0} = 0, \quad \left.\frac{m_1}{M_1} = \frac{m_2}{M_2}\right|_{z=h_1}, \quad \left.\frac{A_1}{M_1}\frac{\partial m_1}{\partial z} = \frac{A_2}{M_2}\frac{\partial m_2}{\partial z}\right|_{z=h_1} \quad (3)$$

and additional conditions that take account of the spin-wave damping in the layer with a large value of α (pinning layer):

$$\left.\frac{2A_1}{M_{01}}\frac{\partial m_{1y}}{\partial z}\right|_{z=h_1} + b_{11}\int_{h_1}^{h_1+h_2} m_{2y}dz + b_{12}\int_{h_1}^{h_1+h_2} m_{2x}dz = 0,$$
$$\left.\frac{2A_1}{M_{01}}\frac{\partial m_{1x}}{\partial z}\right|_{z=h_1} + b_{22}\int_{h_1}^{h_1+h_2} m_{2x}dz + b_{21}\int_{h_1}^{h_1+h_2} m_{2y}dz = 0, \quad (4)$$

where

$$b_{11} = H\cos(\theta_H - \theta_M) + H_{k2}^{\text{eff}}\cos 2\theta_M + \frac{i\alpha_2\omega}{\gamma_2};$$
$$b_{22} = H\cos(\theta_H - \theta_M) + H_{k2}^{\text{eff}}\cos^2\theta_M + \frac{i\alpha_2\omega}{\gamma_2}; \quad (5)$$
$$b_{12} = -b_{21} = \frac{i\omega}{\gamma_2},$$

h_1 and h_2 are the thicknesses of the excitation and pinning layers, respectively; and the z axis coincides with the normal to the film.

These conditions were derived by integrating the equation of motion over the region including the pinning layer. We also used the relation between the real and imaginary parts of the wave number in the pinning layer [1]

$$k_2'' = \frac{\alpha_2\omega M_2}{4\gamma_2 A_2}\frac{1}{k_2'} = \frac{\beta}{k_2'}. \quad (6)$$

The spatial configuration of the spin wave was assumed to be harmonic in the excitation layer,

$$m_1(z) = B_1\sin k_1 z + B_2\cos k_1 z, \quad (7)$$

and harmonic and exponentially decaying with distance from the boundaries in the pinning layer,

$$m_2(z) = [C_1\sin k_2'(z - h_1) + C_2\cos k_2'(z - h_1)] \times \exp[-k_2''(z - h_1)]. \quad (8)$$

In these equations, B_i and C_i are constants and $z = 0$ corresponds to the free surface of the excitation layer. The results of calculations are presented in Figs. 2 and 3, and they are in good agreement with experimental data.

4. DISCUSSION OF RESULTS

One of the reasons why the slope of the dispersion curves increases in the case of $20° \le \theta_H \le 80°$ is the alteration of the equilibrium orientation of the magnetization **M**, which is caused by the alteration of H when the SWR spectrum is recorded [16]. The effect of this factor depends on the relative value of the effective anisotropy field $H_k^{\text{eff}}/(\omega/\gamma)$ and is most pronounced in the range of θ_H values mentioned above. However, as has already been stressed, in experiments, a difference

between dispersive curves for the normal and parallel field directions is observed, i.e., when **H** is directed along the hard axis or the easy axis and, therefore, **H** and **M** are parallel to each other.

The dispersion curve anisotropy can also derive from (a) anisotropy of the exchange constant; (b) different magnetic-dipole contributions to the magnitude of resonant fields of SW modes at different orientations of **H**; (c) different spin-wave polarizations (circular at the perpendicular field orientation and elliptical at the parallel one); (d) the transverse wave structure in the former orientation and transverse-longitudinal structure in the latter; and (e) the difference in the spatial phase of harmonic spin waves at either one or both boundaries of the excitation layer, which can be caused by the difference in spin-wave configuration in the pinning layer(s) for the different field orientations.

As for reason (a), garnet ferrite films are known not to have any distinctive anisotropy of the exchange constant. Moreover, we carried out an additional investigation of possible anisotropy of the constant A. This anisotropy should basically reveal itself in the case of **M** orientations along crystallographic axes ⟨100⟩ and ⟨111⟩. For these orientations of **M**, we recorded the SWR spectra and constructed dispersion curves, taking into account the influence of the alteration of the equilibrium magnetization orientation. As the experiment showed, the possible anisotropy of the constant A in the investigated films does not exceed the experimental error (3%) and cannot explain the observed anisotropy of the dispersion curves.

Now, we discuss reasons (b) and (c). The magnitude of the possible contribution due to them to the resonant fields of SW modes can depend on the SW wavelength λ_1 or the corresponding wave number $k_1 = 2\pi/\lambda_1$; however, for the same value of k_1, this contribution should not depend on the excitation layer thickness or on the symmetry of the boundary conditions. For example, for the same value of k_1, the difference in the resonant fields of SW modes for the normal and parallel field directions in a three-layer film (symmetrical boundary conditions) should be the same as for the two-layer film (asymmetrical boundary conditions). At the same time, the experimental data testify to the contrary. Pinning at both surfaces of the excitation layer leads to a double difference between the dispersion curves (Fig. 3). This fact, as well as the thickness dependence of the relative difference between the curves, implies that the observed SWR spectrum anisotropy is due to reason (d); i.e., it relates to the influence of the region(s) of strong SW damping on the phase of a harmonic spin wave excited by the microwave field in the layer with a small value of α and, hence, on the wave numbers of SW modes.

Sets of possible wave numbers for the perpendicular and parallel field orientations found by solving the equations presented above are shown in Fig. 4a. We note that, in all samples studied, the pinning layer is a reactive (elastic) medium for spin waves in the case of

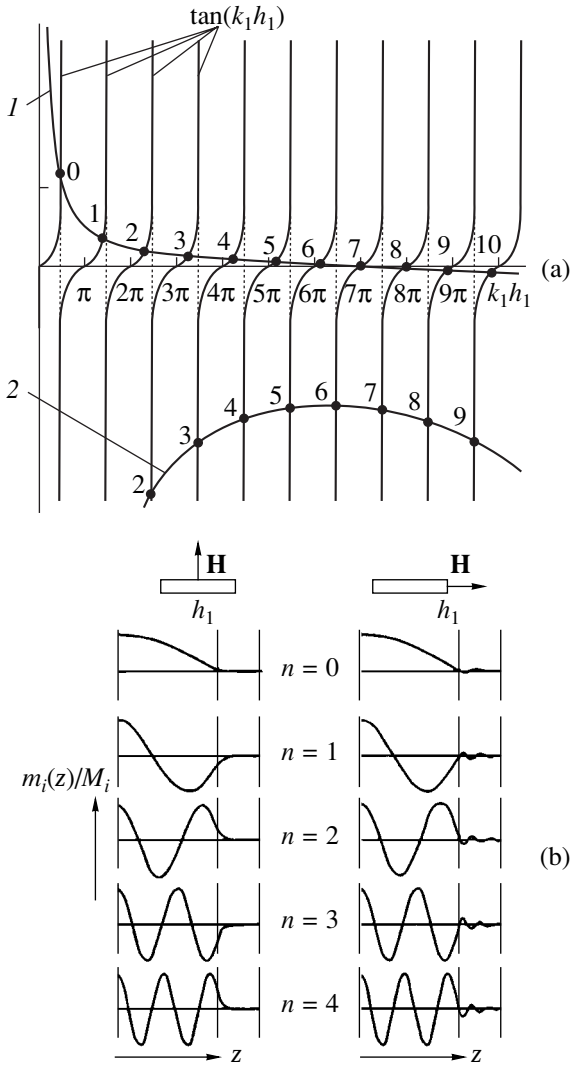

Fig. 4. (a) Graphical representation of a solution of the set of equations (1)–(8) for h_1 = 0.69 μm. Numbers near the intersection points of curve *1* are the values of n for $\theta_H = 0°$, and those of curve *2* are the values of n for $\theta_H = 90°$. (b) The distribution of the normalized magnetization of the ith layer $m_i(z)/M_i$ for the first five SW modes at $\theta_H = 0°$ and 90°.

the perpendicular field orientation and a dispersive medium in the case of the parallel orientation in the magnetic-field range corresponding to the observed SWR spectrum. In the first case, the uniform-resonance field in the pinning layer is less than that in the excitation layer, while in the second case, the situation is reversed. The two different sets of wave numbers, $k_{1n}^{\perp}$ and $k_{1n}^{\parallel}$, determined from the abscissas of intersection points of curves *1* and *2* in Fig. 4a with the family of curves $\tan(k_1 h_1)$ correspond to the two cases discussed above. As follows from Fig. 4a, the zeroth-mode wave numbers for both field orientations are almost

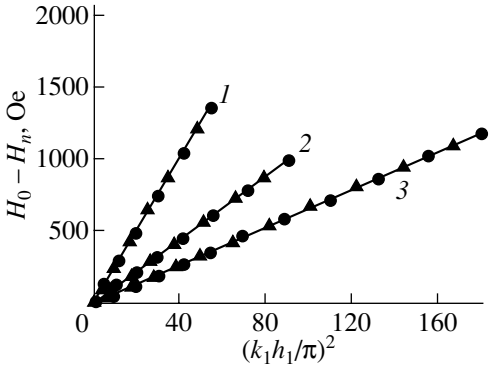

Fig. 5. Dispersion curves $H_0 - H_n = f(k_1h_1/\pi)^2$ for two-layer films with layer thickness h_1 equal to (*1*) 0.46, (*2*) 0.69, and (3) 0.9 μm. k_1 is the calculated wave number. Designations are the same as in Figs. 2 and 3.

identical and close to $\pi/2h_1$. As the index n increases, the difference in the SW mode phases at the excitation layer boundary $\delta = k_{1n}^{\parallel} h_1 - k_{1n}^{\perp} h_1$ (for the same n) increases monotonically. For example, for $n = 8$, this difference is already as large as $\sim\pi/2$. From Fig. 4a, it can also be seen that the values of $k_{1n}^{\parallel} h_1$ are very close to $(n + 1/2)\pi$ and only slightly exceed them for the field **H** parallel to the film (the case where the pinning layer is a dispersive medium). At the perpendicular field orientation (when the pinning layer exhibits reactive properties), the values of $k_{1n}^{\perp} h_1$, on the contrary, noticeably deviate from $(n + 1/2)\pi$ to smaller values. Therefore, as n increases, the spatial phases of the SW modes at the excitation layer boundary vary differently for the different field orientations. First, several mode configurations for a sample with $h_1 = 0.69$ μm are shown in Fig. 4b, illustrating this difference.

Thus, the increase in the spatial-phase difference and, therefore, the increase in the wave-number difference $\delta = k_{1n}^{\parallel} h_1 - k_{1n}^{\perp} h_1$ with increasing mode index n are the reason for the observed difference between the dispersion curves. If we shift the SW mode wave numbers for the perpendicular field orientation by $\Delta k_1 = k_{1n}^{\parallel} - k_{1n}^{\perp} = \delta/h_1$, the dispersion curves for both field orientations will coincide (Fig. 5).

A calculation shows that the difference between wave numbers $k_{1n}^{\parallel} - k_{1n}^{\perp}$ increases as their values increase. Since we have $k_{1n}^{\parallel}$, $k_{1n}^{\perp} \sim h_1^{-1}$, the difference $k_{1n}^{\parallel} - k_{1n}^{\perp}$ increasing with the mode number has to be faster for smaller excitation layer thicknesses δ/h_1; i.e., for the same wave numbers, the relative influence of a change in the standing-spin-wave phase upon $k_{1n}^{\perp}$ and $k_{1n}^{\parallel}$ increases with decreasing thickness h_1. This factor explains the increased difference between the dispersion curves with decreasing excitation layer thickness (Fig. 2).

The approximately double increase in the difference between the dispersion curves in three-layer films in comparison to two-layer films with the same excitation layers is due to the fact that the mechanism described above operates in the former case at two interfaces rather than at one. In this case, SW phase alterations at both boundaries of the excitation layer influence the wave number.

It is necessary to stress that the change in sign of the anisotropy field in the layers would result, according to calculations, in the opposite effect; i.e., the dispersion curve slope for the perpendicular field orientation (the case where the pinning layer is a dispersive medium rather than a reactive one) would be larger than that for the parallel orientation.

5. CONCLUSIONS

Thus, the results obtained above allow one to make the following conclusions:

(1) At an intermediate orientation of the magnetization between perpendicular and parallel (or between the hard and easy directions), the alteration of the equilibrium magnetization orientation taking place in SWR spectrum recording produces an essential increase in the dispersion curve slope.

(2) In addition to the dominant dissipative mechanism of spin pinning, the reactive or dispersive (depending on the field orientation) behavior of the pinning layer causes an alteration of the spatial phases of standing spin waves at the boundary of the excitation layer and, as a result, a difference in the SW mode wave numbers with the same values of n. The last circumstance accounts for the difference between the dispersion curves for the perpendicular and parallel orientations of the static magnetic field with respect to the film.

REFERENCES

1. A. G. Gurevich and G. A. Melkov, *Magnetic Oscillations and Waves* (Nauka, Moscow, 1994).
2. M. Jirsa, Phys. Status Solidi B **187** (125), 187 (1984).
3. N. K. Dan'shin, V. S. Dellalov, A. I. Linnik, and V. F. Shkar', Fiz. Tverd. Tela (St. Petersburg) **41** (8), 1452 (1999) [Phys. Solid State **41**, 1329 (1999)].
4. N. M. Salanskiĭ and M. Sh. Erukhimov, *Physical Properties and Application of Magnetic Films* (Nauka, Novosibirsk, 1975).
5. B. Hoekstra, R. P. van Stapele, and J. M. Robertson, J. Appl. Phys. **48** (1), 382 (1977).
6. C. H. Wilts and S. Prasad, IEEE Trans. Magn. **MAG-17**, 2405 (1981).
7. Z. Q. Han, M. Pardavi-Horvath, P. E. Wigen, and P. DeGasperis, J. Appl. Phys. **61** (8), 4256 (1987).

8. V. A. Ignatchenko and R. S. Iskhakov, Zh. Éksp. Teor. Fiz. **72** (3), 1005 (1977) [Sov. Phys. JETP **45**, 526 (1977)].
9. R. S. Iskhakov, A. S. Chekanov, and L. A. Chekanova, Fiz. Tverd. Tela (Leningrad) **32** (2), 441 (1990) [Sov. Phys. Solid State **32**, 255 (1990)].
10. A. M. Zyuzin, A. G. Bazhanov, and V. V. Radaĭkin, Zh. Tekh. Fiz. **69** (11), 94 (1999) [Tech. Phys. **44**, 1351 (1999)].
11. A. M. Zyuzin and A. G. Bazhanov, Zh. Éksp. Teor. Fiz. **111** (5), 1667 (1997) [JETP **84**, 912 (1997)].
12. A. M. Zyuzin, N. N. Kudel'kin, V. V. Randoshkin, and R. V. Telesnin, Pis'ma Zh. Tekh. Fiz. **9** (3), 177 (1983) [Sov. Tech. Phys. Lett. **9**, 78 (1983)].
13. A. M. Zyuzin, A. G. Bazhanov, S. N. Sabaev, and S. S. Kidyaev, Fiz. Tverd. Tela (St. Petersburg) **42** (7), 1279 (2000) [Phys. Solid State **42**, 1317 (2000)].
14. A. M. Zyuzin, V. V. Radaĭkin, and A. G. Bazhanov, Zh. Tekh. Fiz. **67** (2), 35 (1997) [Tech. Phys. **42**, 155 (1997)].
15. H. Makina and Y. Hidaka, Mater. Res. Bull. **16** (8), 957 (1981).
16. V. N. Van'kov and A. M. Zyuzin, Zh. Tekh. Fiz. **62** (5), 119 (1992) [Sov. Phys. Tech. Phys. **37**, 548 (1992)].

Translated by D. Bayuk

Physics of the Solid State, Vol. 44, No. 5, 2002, pp. 938–945. Translated from Fizika Tverdogo Tela, Vol. 44, No. 5, 2002, pp. 898–905.

MAGNETISM AND FERROELECTRICITY

Spin-Polarized Transport and Submillimetric Microwave Spectroscopy of Solids

A. S. Borukhovich*, N. A. Viglin, and V. V. Osipov****

**Institute of Solid State Chemistry, Ural Division, Russian Academy of Sciences, ul. Pervomaĭskaya 91, Yekaterinburg, 620219 Russia*

***Institute of Metal Physics, Ural Division, Russian Academy of Sciences, ul. S. Kovalevskoĭ 18, Yekaterinburg, 620219 Russia*

Received April 11, 2001; in final form, August 16, 2001

Abstract—The problem of spin transport (spin transfer and localization in space by charge carriers) is considered from the standpoint of implementing this phenomenon in microelectronic devices based on novel physical principles. Experimental data are presented to confirm the possibility of creating extremely-high-frequency solid state microelectronic devices, operating in the millimetric and submillimetric wavelength range, which can be used as the main elements for spin informatics. These devices can be based on ferromagnetic semiconductor–nonmagnetic semiconductor junctions, the output parameters of which are controlled both by the transport current and by an external magnetic field. © *2002 MAIK "Nauka/Interperiodica".*

1. INTRODUCTION

In the beginning of 2000, the *Physics World* journal published a list of the ten currently important and promising directions in physics most intensively developed over the past years. These include the direction pertaining to solid state and semiconductor physics related to the electron spin transfer (spin transport) from a magnetically active (ferromagnetic) material to a paramagnetic material. The field of applications of this phenomenon in microelectronics is called spin electronics (spintronics). The significance of this field in modern science and technology is related, on the one hand, to the creation and development of quantum one-electron logical structures and spin systems for informatics, the so-called spin informatics, in which a memory unit cell is based on the electron spin (one spin representing one bit of information) [1]. These systems will probably reach the limiting possibilities offered by the magnetic data recording.

On the other hand, the spin transport by charge carriers opens new possibilities in solid state electronics. Examples are offered by the phenomenon of spin-polarized luminescence and by the creation of microwave diodes with the output characteristics controlled by an external magnetic field [2, 3]. These possibilities constitute a base for the new generation of narrow-band devices for solid state spin electronics operating in the millimetric and submillimetric wavelength range, including oscillators, amplifiers, receivers, filters, etc. These devices are current-controlled and can be modulated and frequency-tuned by an applied magnetic field. This additional "degree of freedom" (current control) and the possibility of changing the properties of spintronic structures with the aid of an external magnetic field (which is rarely possible in heterostructures based on usual nonmagnetic semiconductors and in related devices) significantly expands the functions of existing and future microelectronic devices [4]. In this way, we can develop and implement in practice solid state spectroscopy in the aforementioned wavelength range and create a solid sate laser operating in this range (which is inaccessible with the existing heterostructures based on nonmagnetic semiconductors). The latter possibility, rarely mentioned in the literature, is specially considered in this paper based on both previously reported data and new experimental results obtained by the authors.

It should be noted that, in principle, binary structures representing junctions of the normal metal–ferromagnet (Me/F) or nonmagnetic semiconductor–ferromagnet (S/F) types allow us to create a magnetically controlled stabilitron, the reverse breakdown voltage of which can be changed by an applied magnetic field. Based on a detailed investigation of the spin transport mechanisms, together with an analysis of basic problems such as the coexistence of superconductivity and ferromagnetism and the possibility of Josephson tunneling through a ferromagnetic barrier, we can actually solve the tasks of localizing and transferring the electron spin in space, expanding the frequency range of solid state spectroscopy and some others. In addition, such investigations, stimulating single crystal and planar techniques and the physics and chemistry of surfaces and contact phenomena, form grounds for the development of advanced technologies.

2. THEORETICAL PREMISES AND EXPERIMENTAL BACKGROUND

Historically, the problem of observing electron tunneling in the classical (single-particle) variant was essentially solved as long ago as in 1961, when L. Esaki

and his coworkers observed a tunneling current between two normal metal electrodes separated by a magnetic dielectric (EuS or EuTe) [5]. This was in fact the first observation of a spin-polarized tunneling current. It should be noted that such magnetically active spacers represent ferromagnetic semiconductors, with localized magnetic moments of Eu^{2+} ions possessing a fully ferromagnetically ordered structure at low temperatures in an external magnetic field. In turn, the ferromagnetic ordering of europium ions leads to a spin polarization of charge carriers by the mechanism of *s–d* (*d–f*) exchange interaction. A record magnetic moment per ion ($\sim 7\mu_B$) for ferromagnets was observed in EuO crystals (this value is due to the $4f^7$ electrons of Eu ions), where the saturation magnetization at $T \approx 0$ K reaches $4\pi\sigma_s = 2.43$ T. As a result, the charge carriers in this ferromagnetic semiconductor exhibit a maximum (close to 100%) spin polarization. It is this circumstance that makes ferromagnetic semiconductors (FSs) rather than ferromagnetic metals promising materials as structures ensuring a high spin polarization of the emission current (in particular, for tunneling and contact structures). It should be recalled that a maximum degree of the spin polarization of charge carriers in ferromagnetic metals is only on the order of 10% [6].

Another remarkable property of FSs is a significant dependence of the optical absorption edge shift (or the gap E_g in the electron energy spectrum) on the degree of magnetic ordering in the structure and on the external magnetic field. A maximum "red" shift for FSs observed on decreasing the sample temperature to 20 K was reported in EuO, where $\Delta E_g = 0.25$ eV ($E_g = 0.16$ eV in EuS and in $LaMnO_3$-based compounds at $T < T_C$, where T_C is the Curie temperature). Application of an external magnetic field increases the ΔE_g value by almost 10%. Thus, by varying this external parameter and thus controlling the concentration and mobility of charge carriers, we can change both the intrinsic and impurity conductivity of FSs at a maximum spin polarization. The use of EuO and EuS in spin filters of spin injectors is restricted to a low temperature region, since the corresponding T_C values are 69 and 16 K, respectively. Somewhat higher Curie points, reaching the region of liquid nitrogen temperature, are known for FSs based on chromium chalcogenide spinels ($Me^{2+}Cr_2Se_4$, *Me* = Cd, Hg) and $LaMnO_3$-based perovskites. Doping the latter compounds with Ca^{2+} or Sr^{2+} ions allows their T_C values to be increased up to room temperature. These FSs are also capable of nearly 100% spin polarization of the intrinsic charge carriers, although the magnetic parameters of these materials are inferior to the aforementioned properties of europium monochalcogenides. Such materials are especially promising for use in spin structures intended for operation without expensive cryogenic systems. In particular, preliminary results show that these FSs can be used in tunneling spintronic structures [7].

It is interesting to note that the aforementioned feature of the ferromagnetically ordered barrier in a multilayer *Me*(S)/F structure (capable of passing one-particle tunneling current of charge carriers with the spin orientation corresponding to magnetization of the ferromagnetic barrier) found an interesting practical application even before the onset of interest in the development of spintronic structures. This application is related to the exchange-induced splitting of the conduction band in a ferromagnetic metal into subbands corresponding to the spin up ($\uparrow$) and spin down ($\downarrow$) states upon spin ordering on the Fermi level. This splitting presents an additional energy barrier for the tunneling quasi-particles possessing a certain spin orientation. In the case of the spin orientation coinciding with the lower spin-split subband of the ferromagnetically ordered barrier, the energy barrier height effectively decreases and the barrier becomes more transparent to these particles than to those with the opposite spin orientation. Thus, the ferromagnetically ordered barrier in a tunneling multilayer *Me*(S)/F structure plays the role of a spin filter.

Under conditions of cryogenic temperatures, high vacuum, and sufficiently high electric field strength, the diode current of spin-polarized electrons, acquiring an azimuthal asymmetry upon scattering from an anode target, found a direct application in research (for example, in experimental atomic physics and high-energy physics) in the study of low-energy electron scattering, parity conservation effects, and some other phenomena [8], which sharply increased the informativity of such processes. In spin-polarized electron emitters based on a W/EuS solid state structure, the degree of particle orientation in an electric field of $E \approx 1$ kV was on the order of 85%. Theoretically, the possible degree of electron spin polarization in such an *Me*/FS solid state emitter may reach up to $P \approx 93$–96% and is limited only by the natural smearing (~4% [10]) of the Fermi distribution function on the tail of the density of states for electrons in an FS. Close properties can be expected for a source of polarized electrons based on an *Me*/EuO structure, which, in contrast to the W/EuS emitter, must be capable of stable operation in high vacuum at temperatures up to liquid-nitrogen temperature [11].

The rectifying effect in a multilayer *Me*/FS structure, related to the Schottky barrier formation in the interfacial region of a ternary FS based on a $CdCr_2Se_4$ phase, in a paramagnetic temperature range ($T > T_C$) was reported for the first time in [12]. For an analogous *Me*/FS heterojunction using a $HgCr_2Se_4$ crystal of the *n* type in the ferromagnetic temperature range ($T < T_C = 120$ K), additional physical possibilities were demonstrated in [13]. These features were related to the exchange-induced splitting of the conduction band of this FS upon ferromagnetic ordering of Cr^{3+} ions with the formation of two subbands by the *s–d* exchange interaction mechanism:

$$\Delta_{sd} = \pm 1/2 A_{sd} S\sigma(T)/\sigma(0).$$

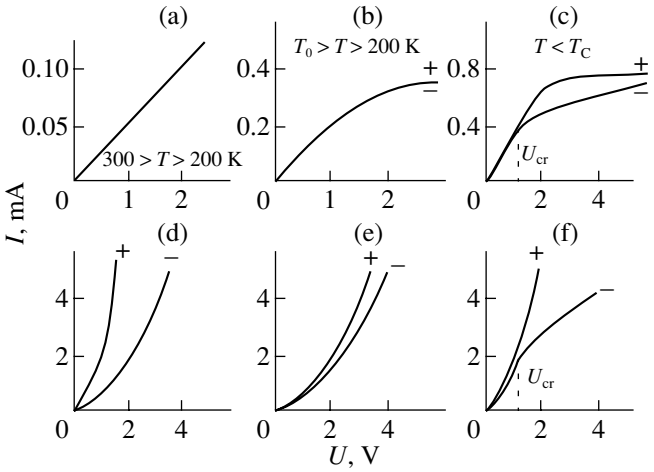

Fig. 1. Rectifying properties of the HgIn/$HgCr_2Se_4$ junction at various temperatures T and pressures P of annealing in Hg vapors: (a–c) P = 0.5; (d–f) P = 10 atm (signs on the curves indicate the bias voltage polarity on FS).

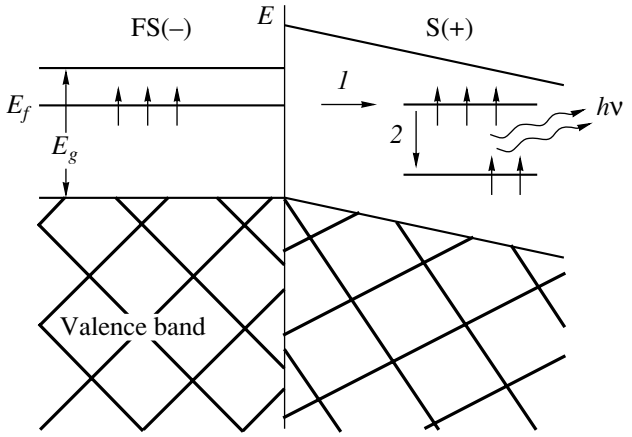

Fig. 2. An energy band diagram of the FS/S junction: (*1*) nonradiative carrier spin transfer from FS to a donor level of S and an increase in the level occupancy in the absence of magnetic field H; (*2*) transition of a charge carrier to a free acceptor level in S at an EPR frequency with radiation from S; E_f is the Fermi level split into sublevels with spins up ($\uparrow$) and down ($\downarrow$) as a result of the spontaneous magnetization.

Here, S is the ion spin, A_{sd} is the s–d exchange integral, and $\sigma(T)$ and $\sigma(0)$ are the FS saturation magnetization at the current temperature T and at $T = 0$ K, respectively. As the electrons pass by tunneling from metal to FS and occupy the upper subband, the electric conductivity of the structure decreases when the applied voltage exceeds a certain critical value ($U > U_{cr}$), which is related to a decrease in the mobility of carriers in the FS as a result of the electron–magnon scattering.

Figure 1 presents the experimental data illustrating this process observed for a HgIn/$HgCr_2Se_4$ junction at various temperatures [13]. The diode (rectifying) properties of the junction decrease when the temperature T decreases from 300 to 200 K (Figs. 1d, 1e) but then increase again for $T < 120$ K and $U > U_{cr}$ (Figs. 1c, 1f). The temperature dependence of the critical voltage $U_{cr}(T)$ for various σ follows the variation in the magnetic gap $\Delta_{sd}(T)$; in this FS, the cut-off voltage always corresponds to a negative potential on the metal side.

In contrast to the above heterostructure, the cut-off voltage in an *Me*/$HgCr_2Se_4$ structure of the *p* type is observed for a positive polarity of the metal, which corresponds to the behavior of classical metal–semiconductor junctions [14]. However, the rectifying properties of this junction disappear at $T < T_C$ and the contact becomes ohmic, whereby the electric resistance varies as that in a metal, by analogy with a FS based on $HgCr_2Se_4$ of the *n* type.

New practical possibilities for realization of the spin transport are related to the physical phenomena in heterojunctions and multilayer FS/S structures. In a wide variety of heterostructures and other multilayer structures based on nonmagnetic semiconductors and metals employed in existing microelectronic devices, the spin orientation of charge carriers is insignificant and does not influence the properties of these devices and the mechanisms determining their operation. The novel possibilities are related to the spin-controlled injection of polarized electrons from FS to S, which can radically change the properties of the latter semiconductor. As indicated above, it is possible to observe the phenomenon of polarized luminescence [2, 3]. The mechanism of this luminescence is different from the theoretically predicted possibility of magnetizing the spin system of charge carriers in a semiconductor illuminated by a nonpolarized light [15]. In both cases, however, the spin orientation of charge carriers in a semiconductor must influence the microwave characteristics in an external magnetic field. For example, this can be manifested at an electron paramagnetic resonance (EPR) frequency $\nu = \mu_B gH/h$, where h is the Planck constant, μ_B is the Bohr magneton, and g is the g-value of conduction electrons in the normal semiconductor. Depending on the degree of population inversion on the Zeeman electron levels as a result of the spin-polarized carrier injection from FS to S, we can observe either increased absorption or an additional radiation with a quantum energy $h\nu = \mu_B gH$ controlled by an external magnetic field H.

The possibility of such generation in an F*Me*(FS)/S structure is illustrated in Fig. 2, which represents an energy band diagram for the spin transfer from F*Me*(FS)/S to the uppermost Zeeman level of the nonmagnetic semiconductor with an electron transported by the electric field E (absorption process) in the absence of an external magnetic field; this can be followed by the transition of carriers at the EPR frequency to a lower vacant level of the semiconductor, accompanied by liberation of the corresponding energy $h\nu$ (radiation process).

The above effects were realized for the first time in the following microjunction heterostructures of the FS/S type: *n*-$HgCr_2Se_4$/*n*-InSb (I), *n*-EuO/*n*-InSb (II), and *p*-$HgCr_2Se_4$/*n*-InSb (III) [16, 17]. The investigation of microwave processes accompanying the passage of current of a certain polarity in structure I revealed a microwave absorption in the millimetric range at the EPR frequency of the free charge carriers in *n*-InSb (Fig. 3) [16]. For the same polarity, heterostructures II and III produced microwave radiation with a magnetic-field-controlled wavelength (Fig. 4) which could be continuously tuned from the centimetric (8 mm) to submillimetric range (0.2 mm) [17]. The transfer of an electron from FS to an upper Zeeman level in S, followed by radiative transition to a vacant lower level, gives rise to electromagnetic radiation at an EPR frequency. The theoretical limit of the output power for this heterostructure is

$$N = \mu_B g H J/e \equiv h\nu J/e,$$

where J is the current passing in the heterostructure and e is the electron charge. According to this formula, N = 156 μW/A for the 8-mm spectral range and 12 mW/A for the 0.1-mm range [18]. Although the experimentally observed values in these intervals are lower by 1–2 orders of magnitude, there exist technical possibilities to increase the output power up to the theoretical limit. Indeed, this heterostructure is capable of bearing a current of up to 10 A.

The above relationship for the radiation emitted from an FS/S heterostructure indicates that the output power is proportional to the frequency and the applied magnetic field strength. This fact suggests that these structures can be used in magnetic-field- controlled generators of millimetric and submillimetric microwave radiation. The magnetic field control cannot be implemented in the existing semiconductor generators, where the output power depends on the frequency as $N \sim \nu^{-4}$. Thus, there is experimental evidence that FS/S heterostructures and microjunctions can serve as a basis for the new generation of narrow-band solid state spintronic devices operating in the millimetric and submillimetric wavelength range. Measurements of the parameters of radiation emitted from structure III in an external field of $H \approx 460$ Oe showed that, for a current of 2 A and T = 77 K, the radiation linewidth was $\Delta H \leq$ 20 Oe (at a pass cavity frequency of 33.4 GHz) [18].

A difference in the energetics of electron spins tunneling from FS to S, which is reflected by occupancies of the upper and lower Zeeman electron energy levels in the nonmagnetic semiconductor, can determine the orientation of spins relative to the applied magnetic field and, hence, can be used as a data bit code. In other words, these structures can be employed in quantum one-electron logical devices for spin informatics. This application is favored by selecting *n*-InSb crystals as a nonmagnetic semiconductor for the FS/S structures, which offers several important advantages. First, an anomalously large g value (about 50) of this semiconductor allows the submillimetric wavelength range to be achieved already with a magnetic field strength as low as $H \approx 4$ kOe. Second, this material provides for a relatively small EPR line width for the conduction electrons ($\Delta H \approx 0.2$ Oe in the 8-mm range for a field strength of $H_0 \approx 450$ Oe and $\Delta H \approx 2$–3 Oe in the 0.8-mm range for $H_0 \approx 5.5$ kOe) at T = 4.2 K. Third, a record level of the charge carrier mobility (reaching up to 10^6 cm^2/V s) together with a large spin–lattice relaxation time allow the charge carriers to be polarized in the *n*-InSb layer with a thickness of 0.1–1.0 cm. The ratio of the spin–lattice relaxation time (10^{-7}–10^{-6} s) to

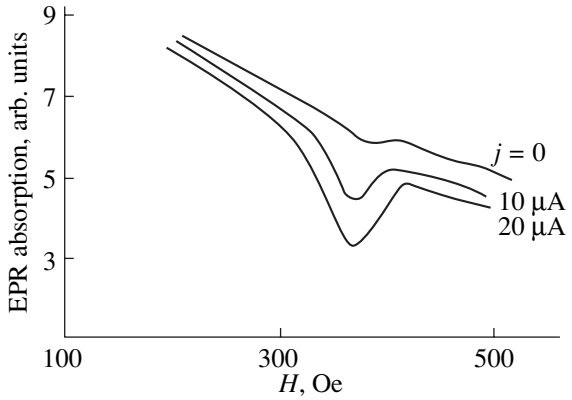

Fig. 3. The intensity of absorption at the EPR frequency (26 GHz) by free carriers in an *n*-$HgCr_2Se_4$/*n*-InSb heterostructure for various currents.

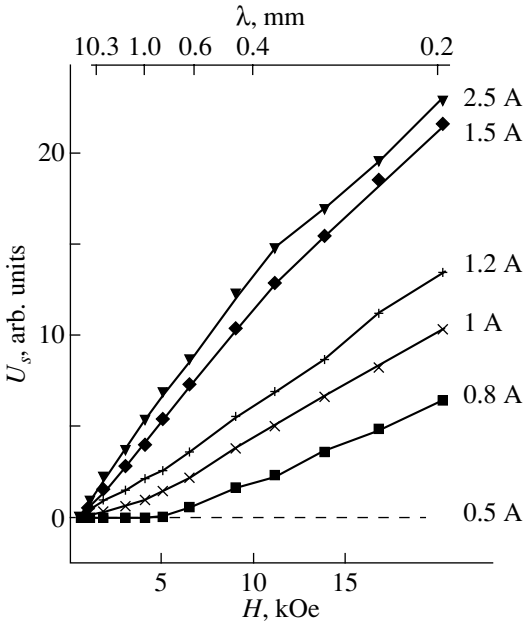

Fig. 4. The magnetic-field-controlled radiation intensity measured for a structure of type III at T = 77 K and various currents.

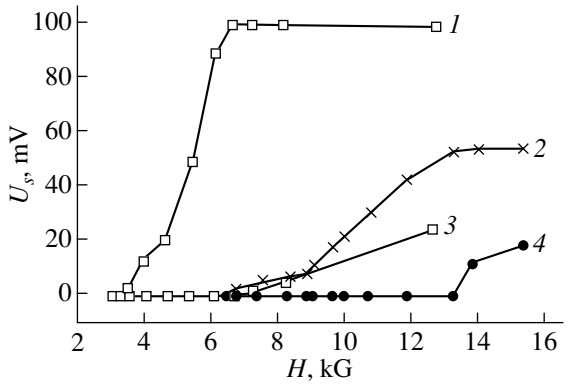

Fig. 5. Microwave radiation intensity of Co_2MnSn/InSb (F/S) structures 1 (curves *2, 4*) and 2 (curves *1, 3*) biased with plus (*1, 2*) and minus (*3, 4*) on the semiconductor component (I = 2 A; T = 4 K; see text for the characteristics of structures 1 and 2).

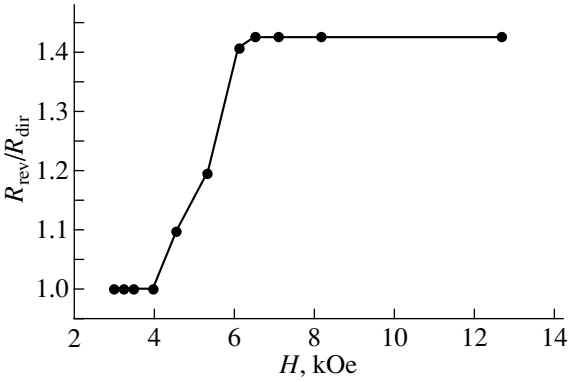

Fig. 6. The plot of R_{rev}/R_{dir} versus magnetic field strength for Co_2MnSn/InSb structure 1.

the carrier free-run lifetime (10^{-12} s) amounts to ~10^5–10^6, which favors a considerable spin localization in time for carriers on the corresponding Zeeman energy levels. The latter circumstance is one of the most important physical requirements for implementation of the FS/S structures as an element for spin informatics.

Figure 4 shows parameters of the magnetic-field-controlled radiation from an FS/S heterostructure with an output power of several tens of microwatts measured at temperatures from 4 to 160 K. It was suggested that this temperature interval of microwave generation is determined by the magnetic properties of FS (EuO or $HgCr_2Se_4$), while the range of magnetic fields depends on the microwave properties of S (InSb). From this it follows that a change in the spin-orienting medium employed in the structure (e.g., use of an FS material possessing a higher Curie temperature) will allow the radiation to be observed at higher temperatures. In order to check for this possibility [19], we studied a structure in which the FS component was replaced by a Geissler alloy with the composition Co_2MnSn possessing T_C = 826 K. This ferromagnet belongs to semimetals and is characterized by a lower degree of the carrier spin orientation as compared to that in the aforementioned FS materials [20].

The experiments were performed with two heterostructures of the Co_2MnSn/*n*-InSb type possessing different carrier concentrations in the semiconductor component: $n = 10^{15}$ cm^{-3} (structure 1) and 7.3×10^{13} cm^{-3} (structure 2). The samples were prepared by vacuum deposition of a preliminarily synthesized Geissler alloy onto a polished semiconductor crystal surface. The main experimental results are as follows.

1. When the current passed from the ferromagnet to the semiconductor, a signal in the detector appeared in a field on the order of 3 kOe, increased with the field strength H, and tended to saturation at H = 7 kOe for structure 2 and at H = 14 kOe for structure 1 (Fig. 5). The current in both structures was maintained on a constant level, since an increase in the field led to a growth in the electric resistance of the InSb crystal. From these data, it follows that the radiation wavelength in both structures was below 2 mm, thus falling outside the standard *Q*-band in which the available 8-mm-range instrumentation was applicable (this corresponds to the frequency range from 24 to 36 GHz). Nevertheless, the presence of microwave radiation could be judged from the shape and character of the pulsed signal rectified by the detector: the output pulse had a rectangular shape repeating that of the current pulse, and the pulse amplitude could be fully suppressed by a resistive microwave attenuator (this proves the absence of a spurious induced electromagnetic signal in the detector).

Since the output power is proportional, as demonstrated above, to the radiation frequency (or the magnetic field strength), while the detector sensitivity drops as ν^{-1} (as a result of the intrinsic capacitance), the experimentally observed signal saturation at $H \geq$ 10 kOe can be explained by both these factors.

2. The fact that the radiation of the Co_2MnSn structures studied is due to the carrier spin transfer from the ferromagnet to the semiconductor is confirmed by a plot of the ratio of sample resistances for the direct (F to S) and reverse (S to F) current (Fig. 6). Assuming that electrons are more strongly spin-polarized in the ferromagnet film than in the semiconductor substrate, we have to conclude that only electrons with the spin polarization corresponding to that in the ferromagnet will enter the film in the case of a reverse bias, while carriers with the opposite spin polarization will accumulate at the F/S interface, thus creating a cut-off layer in the semiconductor. This effect must be magnetic-field-dependent since the energy difference for electrons with different spin orientations increases with the magnetic field strength H.

Figure 6 shows that an increase in the magnetic field strength leads to a buildup of the difference in resistance for the direct and reverse bias polarity. For the same applied voltage, the current from F to S is always greater than that in the reverse direction (from S to F). This effect of the current "rectification" in the magnetic field must be related to the injection of spin-polarized electrons in the heterostructure under consideration. Figure 7 shows the temperature dependence of the output microwave signal amplitude for the two Co_2MnSn/InSb structures studied. As can be seen, the output signal intensity for structure 2 drops at 140 K, while the radiation from structure 1 is detected up to 200 K.

It should be recalled that a drop in the intensity of radiation detected from an EuO/InSb structure was observed at $T = 160$ K [18]. The close values of these temperatures are probably related to the parameters of the semiconductor (InSb) used in the heterostructures studied, rather than to the ferromagnetically ordered sate of the ferromagnet component. These results can also be influenced by a lower degree of polarization of electrons in Co_2MnSn as compared to that in EuO and by some other factors which have to be studied. From this it follows that a solution to the problem of increasing the temperature of microwave generation in spin structures requires further investigations [21, 22].

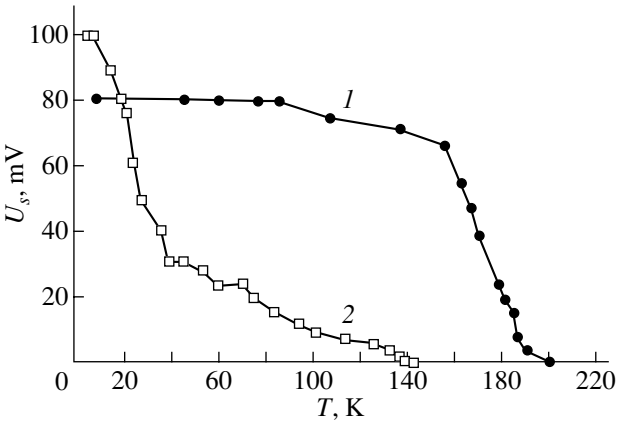

Fig. 7. Temperature dependence of the output microwave signal intensity for Co_2MnSn/InSb structures 1 and 2 (curves *1* and *2*, respectively) measured in a magnetic field of $H = 7$ kOe.

3. PROBLEMS AND PROSPECTS FOR FUTURE INVESTIGATIONS

As can be seen from the above considerations, the apparently simple (at first glance) problem of injecting spin-polarized carriers from one medium to another, in which the carriers would accumulate on an excited level (with the spin orientation retained), in fact separates into several independent problems requiring special approaches to their solution. The least studied of these is the problem of transferring the spin through the boundary between two media without loss of orientation corresponding to injector magnetization. The interface behaves as an energy barrier: not every oriented spin can penetrate through this barrier, and not every one that succeeds can retain the spin orientation in what follows. The spin orientation can be lost under the action of uncontrolled spin defects in the interfacial layers, gases adsorbed at the interface, and nonplanar geometry and/or discontinuity of the junction. Solving this contact problem reduces to the development of technology ensuring the obtainment of stable and reproducible physical results.

The second important problem consists in detecting and measuring the radiation of heterostructures. The electromagnetic wave generated as a result of the interelectron spin transition can be absorbed inside the structure and converted into heat or can lose energy upon reflection from semiconductor crystal faces (including the output surface–vacuum interface). In order to solve this problem, it is necessary to develop the methods of microwave spectroscopy, in particular, the pulsed and modulated techniques.

The third problem is related to the need to match the heterostructure output to the waveguide tract. This, in contrast to the two former problems, is a purely engineering and technical problem.

From the technological standpoint, it is most important to provide for a good electrical contact between the two media constituting the F/S heterostructure, that is, between two crystals, between a crystal and a film, or (in planar film technology) between film components. In the former case, this is achieved by mechanically joining (due to spontaneous adhesion) two optically smooth plane single crystal surfaces, the distance between which must not exceed 10 Å. Then, tight contact is provided by the van der Waals forces, static electric forces, and chemical bonds [23], making the joint strong and vacuum tight. However, this connection requires the preparation of perfectly plane and chemically clean surfaces with a roughness not exceeding a few nanometers, which can be achieved only by using special technologies [24].

In the case of heterostructures fabricated by methods of multilayer (thin film) technology, some of the aforementioned difficulties can be obviated, but the problem of proper preparation of the substrate (crystal) surface for the ferromagnetic layer deposition still remains. It is necessary to ensure that the magnetic characteristics of the ferromagnetic film would not differ significantly from those of the bulk material. The film must retain the ability to increase the degree of spin polarization of electrons (in particular, at elevated temperatures) due to residual magnetization. The development of film deposition techniques for the fabrication of multilayer FS/S structures includes selection of the optimum deposition regimes for each FS and S

material using initial components or preliminary synthesized compounds.

Finding solutions to the above problems is based on experience in creating and characterizing FS/S heterostructures, which is permanently accumulated and enriched by implementing new technologies, novel materials, advanced experimental techniques, computation facilities, and computer simulation methods.

The problem of spin transport in solid state structures is a multifold problem. Although the physical mechanisms pertaining to realization of this transport are more or less clear, the practical implementation of spin injection in real structures encounters both technological difficulties and restrictions posed by a limited set of available materials in which the spin can be transferred only at relatively low temperatures. In this paper, we concentrated on the pathways of extending the study of spin transport toward a new range of high-frequency investigations of solids—millimetric and submillimetric microwaves—offering additional practical possibilities. In particular, there are good prospects for creating a solid state laser operating in the corresponding frequency range and the related development of solid state spectroscopy in this microwave region. The study of spin transport from the standpoint of special features in the manifestation of optical properties of heterostructures and their magnetoresistance behavior is of independent interest. Research and development in the above directions were considered in recent symposia [21, 22].

It should be noted that the wish to control the properties of "classical" MIS heterojunctions by means of external magnetic field led to the need of replacing a nonmagnetic semiconductor by a ferromagnetic semiconductor or metal [25]. Structures of the MIFS (or MIFM) types are capable (in contrast to their precursors) of combining the functions of selecting, amplifying, delaying signals, etc. Since the publication of review [25], where the expected direction of research was formulated to be magnetoelectronics, numerous physicochemical and technological problems in this field have been solved [26]. The concept of spintronics, having methodologically replaced the previous term, is based on new physical knowledge and recent technological achievements. In our opinion, the main distinction of recent investigations [26] from the preceding works is that the spintronic structures involving ferromagnetic semiconductors can be controlled both by applying an external magnetic field and by varying the transport current in the heterostructure using the electron–magnon interaction between mobile spin carriers and magnetization of the ferromagnetic semiconductor.

Since the contribution of lattice oscillations to the spin transport increases with the temperature and can become dominant at elevated temperatures, the observation of room-temperature spin injection can be problematic even with the "high-temperature" ferromagnetic semiconductors. We hope that solving this problem can be facilitated by investigations of the phenomenon of magnetoabsorption in the new structures developed for spintronics. It is probably necessary to search for an FS/S pair characterized by close values of the electron conductivities, a nearly 100% spin polarization of carriers in the FS component, and a large degree of Zeeman level splitting in the semiconductor component (with a g-value exceeding 50). In view of the aforementioned limitations and recent estimates [27], the attempts to use the existing FS/S structures in spintronics are evidently low-effective because of the negligibly small probability of providing for a significant spin transport from ferromagnetic to nonmagnetic semiconductors.

ACKNOWLEDGMENTS

This study was performed within the framework of the Quantum Macrophysics Program of the Russian Academy of Sciences and supported by the Federal Targeted Scientific-Technological Program "Investigations and Developments in Promising Directions of Science and Civilian Technology" (Subprogram "Important Directions in the Physics of Condensed Media," project 26, No. 107-26(00)-P- D01, Contract No. 2.4) and by the Russian Foundation for Basic Research (project no. R-2001-Ural No. 01-02-96429).

REFERENCES

1. G. A. Prinz, Phys. Today **48** (4), 353 (1995).
2. R. Flederling, M. Kelm, G. Reuseher, *et al.*, Nature **402**, 787 (1999).
3. Y. Ohno, K. Young, B. Beschoten, *et al.*, Nature **402**, 790 (1999).
4. A. S. Borukhovich, Usp. Fiz. Nauk **169** (7), 737 (1999).
5. L. Esaki, P. J. Stiles, and S. von Molnar, Phys. Rev. Lett. **19**, 852 (1967).
6. J. Kessler, *Polarized Electrons* (Springer-Verlag, Berlin, 1985; Mir, Moscow, 1988).
7. V. M. Svistunov, Yu. V. Medvedev, V. Yu. Tarenkov, *et al.*, Zh. Éksp. Teor. Fiz. **118** (3), 629 (2000) [JETP **91**, 547 (2000)].
8. V. L. Agranovich, A. V. Glamazdin, V. G. Gorbenko, V. P. Efimov, and I. N. Karnaukhov, *Sources of Polarized Electrons* (TsNIIatominform, Moscow, 1984).
9. E. Kisker, G. Baum, A. N. Mahau, *et al.*, Phys. Rev. B **18**, 2256 (1978).
10. M. I. Auslender and V. Yu. Irkhin, Solid State Commun. **50**, 1003 (1984).
11. A. S. Borukhovich, V. G. Bamburov, L. V. Efimova, *et al.*, USSR Inventor's Certificate No. 1,267,983.
12. V. P. Buzhor, in *Proceedings of the Conference "Ternary Semiconductors and Their Application"* (Shtiintsa, Kishinev, 1983), p. 87.
13. V. V. Osipov, V. I. Mikhaĭlov, A. A. Samokhvalov, and N. M. Chebotaev, Fiz. Tverd. Tela (Leningrad) **31** (9), 37 (1989) [Sov. Phys. Solid State **31**, 1495 (1989)].

14. V. A. Bonch-Bruevich and S. G. Kalashnikov, *Physics of Semiconductors* (Nauka, Moscow, 1977).
15. A. G. Aronov and G. E. Pikus, Fiz. Tekh. Poluprovodn. (Leningrad) **10**, 1177 (1976) [Sov. Phys. Semicond. **10**, 698 (1976)].
16. N. A. Viglin, V. V. Osipov, and A. A. Samokhvalov, Phys. Low-Dimens. Struct. **9/10**, 89 (1996).
17. N. A. Viglin, V. V. Osipov, A. A. Samokhvalov, and O. G. Reznitskikh, Phys. Low-Dimens. Struct. **1/2**, 89 (1997).
18. V. V. Osipov, N. A. Viglin, and A. A. Samokhvalov, Phys. Lett. A **247**, 353 (1998).
19. N. A. Viglin, V. V. Osipov, A. A. Samokhvalov, *et al.*, Phys. Low-Dimens. Struct. **1/2**, 29 (2000).
20. V. Yu. Irkhin and M. I. Katsnel'son, Usp. Fiz. Nauk **164** (7), 705 (1994) [Phys. Usp. **37**, 659 (1994)].
21. A. S. Borukhovich, in *Proceedings of the 17th International School-Workshop "Novel Magnetic Materials for Microelectronics," Moscow, 2000*, p. 648.
22. V. V. Osipov, N. A. Viglin, A. A. Samokhvalov, *et al.*, in *Proceedings of the 1st International Symposium on the Spintronics, FRG, 2000*, p. 18.
23. U. Gozele, Solid State Phenom. **47–48**, 33 (1996).
24. J. Haisma, Appl. Opt. **33**, 1154 (1994).
25. Yu. M. Yakovlev and A. I. Merkulov, in *Reviews on Electronics. Series Materials* (Élektronika, Moscow, 1983), Vol. 9.
26. V. G. Bamburov, A. S. Borukhovich, and A. A. Samokhvalov, *Introduction to the Physics and Chemistry of Ferromagnetic Semiconductors* (Metallurgiya, Moscow, 1988).
27. G. Schmidt, D. Ferrand, L. W. Molenkamp, *et al.*, Phys. Rev. B **62** (8), 4790 (2000).

Translated by P. Pozdeev

Physics of the Solid State, Vol. 44, No. 5, 2002, pp. 946–952. Translated from Fizika Tverdogo Tela, Vol. 44, No. 5, 2002, pp. 906–911.

MAGNETISM AND FERROELECTRICITY

Physical Mechanisms Responsible for the Relaxation Time Distribution in Disordered Dielectrics

V. A. Stephanovich*, M. D. Glinchuk, B. Hilczer***, and E. V. Kirichenko***

** Institute of Mathematics, Opole University, Opole, 45-052 Poland*

*** Frantsevich Institute of Materials Science Problems, National Academy of Sciences of Ukraine, ul. Krzhizhanovskogo 3, Kiev, 03680 Ukraine*

**** Institute of Molecular Physics, Polish Academy of Sciences, Poznan, 61-614 Poland*

e-mail: glin@materials.kiev.ua

Received July 17, 2001

Abstract—The relaxation time distribution function $F(\tau)$ is calculated in the framework of the random-field theory. The function $F(\tau)$ is expressed through the distribution function $f(E)$ of a random electric field E with due regard for the derived dependence of the relaxation time τ on the electric field. The distribution function $F(\tau)$ is calculated in terms of the statistical theory within the random-field approximation. The nonlinear random-field contributions and spatial effects of correlations between randomly distributed electric dipoles are taken into account. The calculations are performed for a mixed ferroelectric glassy phase in which the short-range and long-range polar orders coexist. It is demonstrated that the inclusion of nonlinear contributions of the random field leads to an asymmetric relaxation time distribution function $F(\tau)$, whereas allowance made only for the linear random-field contributions results in a symmetric function $F(\tau)$. A comparison of the calculated functions $F(\tau)$ with empirical functions derived from the Cole–Cole (CC), Davidson–Cole (DC), Kohlrausch–Williams–Watts (KWW), and Havriliak–Negami (HN) laws for the dielectric response shows that these laws correspond to disordered systems in which the long-range and short-range orders coexist. Different forms of the function $F(\tau)$ are determined by either linear (the CC law) or nonlinear (the DC, KWW, and HN laws) contributions of the random field. © *2002 MAIK "Nauka/Interperiodica"*.

1. INTRODUCTION

Disordered ferroelectrics, polymers, and composites are characterized by anomalies in their dynamic properties.

Specifically, strong dispersion of the dynamic magnetic or dielectric susceptibility has been observed for many spin or dipole glasses (see, for example, [1] and references therein). As a rule, the dispersion stems from the fact that disordered systems are characterized by a broad spectrum of relaxation times. This spectrum can be derived from the observed frequency dependence of the susceptibility [2]. For this purpose, it is general practice to use a model of superposition of several relaxation processes with different relaxation times described by the Debye law. Within this model, the dynamic characteristics (frequency dependences of the polarization, the permittivity, etc.) can be calculated by averaging with the use of the relaxation time distribution function $F(\tau)$ under the assumption that concurrent (independent) relaxation processes occur in the system under consideration. The key problem of the above approach is associated with the particular form of the relaxation time distribution function. So far, this function has not been calculated in the framework of an appropriate physical model. Hence, a number of simple empirical expressions derived for $F(\tau)$ have been used in practice to date. One of these expressions was proposed by Fröhlich [3], who assumed that the function $F(\tau)$ is equal to a positive constant in the relaxation time range $[\tau_0, \tau_1]$ and to zero outside this range. However, this function cannot be used to describe the dielectric response which appears to be more complex than that predicted by the Debye law and, as a rule, can be represented by the Cole–Cole (CC), Davidson–Cole (DC), Havriliak–Negami (HN), and other empirical laws [4]. Malecki and Hilczer [5] showed that a non-Debye response can be described using different complex empirical relationships derived for the function $F(\tau)$ [5]. However, it is evident that the distribution functions determined from experimental dielectric responses cannot provide insight into the physical nature of the anomalies observed in the response of disordered systems.

In our recent works, we calculated both the linear [6, 7] and nonlinear [8] dielectric responses in an external dc electric field for ferroelectric relaxors, such as $PbMg_{1/3}Nb_{2/3}O_3$ (PMN), $PbSc_{1/2}Nb_{1/2}O_3$ (PSN), and $Pb_{1-x}La_xZr_{0.35}Ti_{0.65}O_3$ (x = 0.7–0.9, PLZT).

A random electric field induced by a substitutional disorder form lead and oxygen vacancies and other lat-

tice defects was treated as a dominant factor responsible for the specific features in the dynamic properties, because the random field brings about changes in barriers between different dipole orientations. Within this model, we proved that the temperature dependence of the relaxation time obeys the Vogel–Fulcher law and that the time dependence of the polarization is adequately described by the stretched exponential law [6]. Furthermore, we revealed a number of interesting features in the nonlinear susceptibility [8].

In the present work, the random-field method was applied to the calculation of the relaxation time distribution function. Moreover, we analyzed how the random electric field affects the square and parabolic barriers. The relaxation time distribution function was calculated in terms of the random-field distribution function with the inclusion of both the linear [9] and nonlinear random-field contributions and the spatial correlation effects [10].

2. RELATION BETWEEN THE RANDOM-FIELD AND RELAXATION-TIME DISTRIBUTIONS

2.1. General relationships. The random electric field E is a specific feature of disordered systems. In a random electric field, all physical characteristics, including the relaxation time τ, become random quantities and, in particular, $\tau = \tau(E)$. A detailed form of this dependence will be considered below. In our earlier works [9–11], we calculated the random-electric-field and elastic-field distributions in the framework of the statistical theory. With knowledge of the distribution function $f(E)$ and the relationship between the relaxation time τ and the random field E, it is possible to calculate the distribution function for the relaxation time τ according to the standard formulas of the probability theory. In the simplest case, when $\tau(E)$ is a single-valued continuous function of E, the probability theory gives the following expression [12]:

$$F(\tau) = f(E(\tau))\left|\frac{dE(\tau)}{d\tau}\right|, \quad (1)$$

where $E(\tau)$ is the inverse function, which determines the random field E for the given value of τ.

In a more general case, when $\tau(E)$ is a many-valued function [i.e., to each value of τ there correspond several values of E ($E_1, E_2, \ldots, E_n$)], the space of the E values is separated into n regions (involving the given points $E_1, E_2, \ldots, E_n$) in such a way that $\tau(E)$ is the single-valued continuous function in each region. As a result, the function $F(\tau)$ in the whole space of fields can be written as the sum of expressions (1) in the regions of monotonic behavior of $\tau(E)$ [12]; that is,

$$F(\tau) = \sum_{i=1}^{n} f(E_i(\tau))\left|\frac{dE_i(\tau)}{d\tau}\right|. \quad (2)$$

Formula (2) represents the general expression of the distribution function for a single random quantity in terms of the distribution function for another quantity when the relationship between these quantities is known. In particular, formula (2) was used to calculate the random-field distribution function in the case of significant contributions of nonlinear effects and correlations [10].

2.2. The influence of electric field on the relaxation time. Conventional ferroelectric materials (such as $PbTiO_3$ and $BaTiO_3$) with a long-range polar order are characterized by a sole relaxation time that accounts for the recovery rate of macroscopic polarization after disturbance of the system under external action.

Disordered systems, for example, relaxors, exhibit a broad spectrum of relaxation times, because they most probably occur either in the dipole glass state (characterized only by nanometer-sized polar clusters or, in other words, by the short-range polar order) or in the ferroelectric glassy phase in which the short-range and long-range orders coexist. Since the polar order in the disordered systems under investigation is governed primarily by the alignment of electric dipoles, their misorientation can be considered the main mechanism of relaxation. As a rule, the temperature dependence of the dipole misorientation probability is described by the Arrhenius law. In this case, the relaxation rate can be represented in the form

$$\frac{1}{\tau} = \frac{1}{\tau_0}\exp\left(-\frac{U}{T}\right), \quad (3)$$

where U is the height of the barrier between equivalent directions of the dipole.

It is believed that the barrier heights at different points of the studied sample should be different due to changes in the type and number of ions surrounding a particular dipole. These changes in the environment manifest themselves in changes in the local electric field and can be accounted for in the random-field distribution function.

In order to derive the relationship between the relaxation time τ and the random field E, we consider the relaxation dynamics of a dipole with two equivalent orientations in the random electric field. Analysis demonstrates that the relaxation time depends primarily on the form of the potential $U(x)$ in which the dipole executes a motion. In the absence of the random field ($E = 0$), the potential $U(x) \equiv U_0(x)$ has a symmetric form with a maximum at $x = 0$ and $U(x = 0) \equiv U$ corresponds to the barrier height in the conventional Arrhenius law (3). In the presence of the random field, the potential becomes asymmetric and can be written in the following form:

$$U(x) = U_0(x) \pm eE_{\text{loc}}x. \quad (4)$$

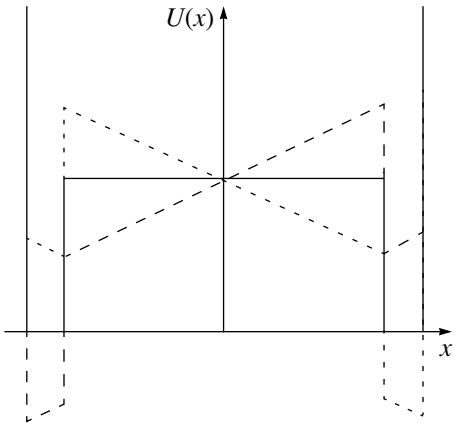

Fig. 1. Effect of the electric field E on the double-well potential $U(x)$ with a square barrier at $E = 0$ (solid line), $E < 0$ (dashed line), and $E > 0$ (dotted line).

The function $U_0(x)$ can be represented as a constant term (square barrier) or as the sum of the potential U and a power series of x whose form is governed by symmetry. It can be seen from Fig. 1 that, for a square barrier, the barrier height is a linear function of the field. It can easily be shown that, for a parabolic barrier, the barrier height varies in proportion to the square of the field. Below, we will consider the square barrier. In this case, the Arrhenius expression can be rearranged as follows:

$$\frac{1}{\tau} = \frac{1}{\tau_0}\exp\left(-\frac{U \pm dE_{\text{loc}}}{T}\right), \tag{5}$$

where d is the dipole moment.

It follows from relationship (5) that the electric field can either decrease the barrier height when the dipole is aligned with the field or increase the barrier height when the dipole is oriented in the opposite direction.

In the final form, the dependence of the relaxation time on the field E can be obtained after averaging function (5) over the possible orientations of the electric dipole. The quantum-static averaging with the Hamiltonian $H = -dE_{\text{loc}}$ gives

$$\langle\tau\rangle = \bar{\tau}_0\frac{\text{Sp}\exp(d^*E/T - H/T)}{\text{Sp}\exp(-H/T)} = \bar{\tau}_0\frac{\cosh(2d^*E/T)}{\cosh(d^*E/T)}, \tag{6}$$
$$\bar{\tau}_0 = \tau_0\exp\left(\frac{U}{T}\right).$$

In expression (6), we made allowance for the equality $dE_{\text{loc}} = d^*E$, where d^* is the effective dipole moment. It follows from expression (6) that the random field leads to an increase in the relaxation time; i.e., it hinders reorientation of the electric dipoles.

3. RELAXATION TIME DISTRIBUTION

3.1. General equations. Formula (6) leads to the following relationship between the electric field and the dimensionless relaxation time $t \equiv \dfrac{\langle\tau\rangle}{\bar{\tau}} \geq 1$:

$$E(t) = kT\,\text{arccosh}\left(\frac{1}{4}(t + \sqrt{t^2 + 8})\right) \equiv kT f_{0\pm}(t). \tag{7}$$

Here, the signs ± correspond to two branches of the function

$$\text{arccosh}(x) = \ln(x \pm \sqrt{x^2 - 1}). \tag{8}$$

These two branches correspond to two values of $i = 1$ and 2 in formula (2), from which it is possible to obtain the relaxation time distribution function by substituting the function $E(t)$ in the form of expressions (7) and (8) into the random-electric-field distribution function. In the simplest case when only the electric dipoles are sources of random fields, this distribution function can be written in the Gaussian form

$$f_l(E) = \frac{1}{\sqrt{2\pi}\Delta}\exp\left(-\frac{(E - E_0L)^2}{2\Delta^2}\right). \tag{9}$$

Here,

$$\Delta = \sqrt{\frac{32\pi}{15}r_c^3 n}\frac{d^*}{\varepsilon_0 r_c^3}, \quad E_0 = \frac{4\pi n d^*}{\varepsilon_0},$$

L is the number of coherently oriented dipoles, n is the dipole concentration, d^* is the effective dipole moment, and r_c and ε_0 are the correlation radius and the static permittivity of the host lattice, respectively [9]. The subscript l in formula (9) indicates that the distribution function is written in the approximation linear with respect to E. Substitution of relationships (9) and (7) into formula (2) gives the relaxation time distribution function

$$F(t) = \frac{b_1}{\sqrt{\pi}}\left\{\left|\frac{df_{0+}}{dt}\right|\exp[-b_2(\upsilon f_{0+}(t) - L(\upsilon, z))^2]\right. \tag{10a}$$
$$\left. + \left|\frac{df_{0-}}{dt}\right|\exp[-b_2(\upsilon f_{0-}(t) - L(\upsilon, z))^2]\right\},$$

$$\frac{df_{0\pm}}{dt} = \pm\frac{1}{\sqrt{2}}\frac{1 + t/\sqrt{t^2 + 8}}{\sqrt{t^2 + t\sqrt{t^2 + 8} - 4}}. \tag{10b}$$

Here, we introduced the following dimensionless parameters convenient for numerical calculations:

$$b_1 = \frac{kT}{2\sqrt{nB}} \equiv \upsilon b_2, \quad b_2 = \frac{E}{2\sqrt{nB}} = \frac{1}{2}\sqrt{15\pi z},$$
$$z = nr_c^3, \quad \upsilon = \frac{kT}{E_0}, \quad B = \frac{16}{15}\pi r_c^3\left(\frac{d^*}{\varepsilon_0 r_c^3}\right)^2. \tag{11}$$

3.2. Relaxation time distribution function in the mean-field approximation. In the paraelectric and ferroelectric phases, all the properties of disordered ferroelectrics, including the relaxation time distribution, can be calculated in the mean-field approximation. Within this approximation, the random-field distribution function can be represented as a delta function or, more precisely, $\delta_{mf}(E) = \delta(E - E_0L)$ in the linear case and $\delta(E - E_0L(1 + \alpha E_0^2 L^2))$ in the nonlinear case, where α is the nonlinearity constant [10]. The number of coherently oriented dipoles is given by $L \neq 0$ in the ferroelectric phase and $L = 0$ in the paraelectric phase. By substituting these functions into formula (1), we obtain the following expression for the linear contribution of the random field:

$$F_{mf}(t) = \delta(E(t) - E_0L)\left|\frac{dE(t)}{dt}\right|. \tag{12}$$

Making allowance for the equations $f(x)\delta(x - a) = f(a)\delta(x - a)$ and $\delta(f(x)) = \sum_k \frac{\delta(x - x_k)}{|f'(x_k)|}$ (see, for example, [12]), where x_k are the real roots of the equation $f(x)|_{x = x_k} = 0$, we can rewrite expression (12) in the form

$$F_{mf}(t) = \delta(t - t_{mf}). \tag{13}$$

Here, t_{mf} is the unique root of the equation $E(t) - E_0L = 0$ for the linear case. Relationship (13) is also valid for the nonlinear case; however, the relaxation time t_{mf} in the mean-field approximation is determined as the root of the equation $E(t) - E_0L(1 + \alpha E_0^2 L^2) = 0$. In the paraelectric phase ($L = 0$), according to formulas (7) and (8), we obtain $t_{mf} = 1$; i.e., $\tau_{mf} = \bar{\tau}_0 = \tau_0\exp(U/kT)$. In the ferroelectric phase ($L \neq 0$), the temperature dependence of the relaxation time exhibits a more complex behavior. Specifically, at $LE_0/kT \gg 1$, we have $\tau_{mf} = \tau_0\exp((U + LE_0)/kT)$ in the linear case and $\tau_{mf} = \tau_0\exp[(U + LE_0(1 + \alpha E_0^2 L^2))/kT]$ in the nonlinear case (where $L = L(T)$ is the order parameter). Note that the terms dependent on L in the exponent account for the effect of the mean field on the barrier height.

3.3. Numerical calculations of the relaxation time distribution function. The relaxation time distribution functions beyond the scope of the mean-field approximation (i.e., for the dipole glass state or the mixed ferroelectric glassy phase) were numerically calculated from formula (10a) in the linear case and from formulas (2) and (7) in the nonlinear case. In the latter case, the nonlinear and correlation effects were taken into account in the random-field distribution function in the same manner as in [10]. Since the disordered systems are characterized by a very broad spectrum of relaxation times ($1 \leq \tau/\bar{\tau}_0 = t < \infty$), we constructed the relaxation time distribution function $F(t)$ on a logarithmic ($\ln t$) scale, as is done in the majority of works. For the same reason, the derivative $df_{0\pm}/dt \sim d\ln t/dt$ was disregarded when constructing the relaxation time distribution curves, because this derivative becomes constant at sufficiently long times t. The relaxation time distribution functions calculated for the linear case are depicted in Fig. 2. In order to exclude the paraelectric phase from our consideration, we chose $\upsilon = T/T_{cmf} < 1$ and two dipole concentrations $z = nr_c^3 = 1$ and 10 (Fig. 2, curves *1* and *2*, respectively). The concentration $z = 1$ is characteristic of the mixed ferroelectric glassy phase, whereas the concentration $z = 10$ corresponds to a sufficiently high degree of long-range order in the system. In this case, the distribution function should approach the delta function, which is illustrated in Fig. 2. Curve *1* can be described by the Gaussian form (9) of the random-field distribution function $f_l(E)$. For other forms of the random-field distribution function $f_l(E)$ (for example, Lorentzian, Holtsmarkian, and other forms corresponding to different sources of random fields), the relaxation time distribution function $F(t)$ in the linear

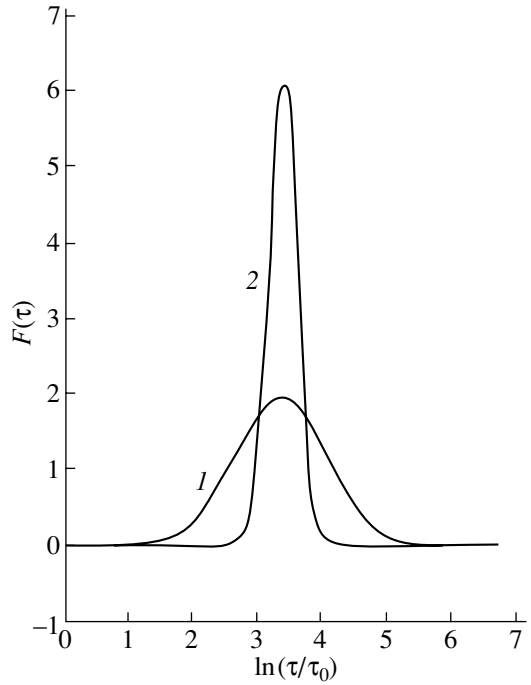

Fig. 2. Relaxation time distribution functions in weak random fields (the linear case). The parameters used in the calculations are as follows: $\upsilon = 0.3$ and (*1*) $z = 1$ and (*2*) $z = 10$.

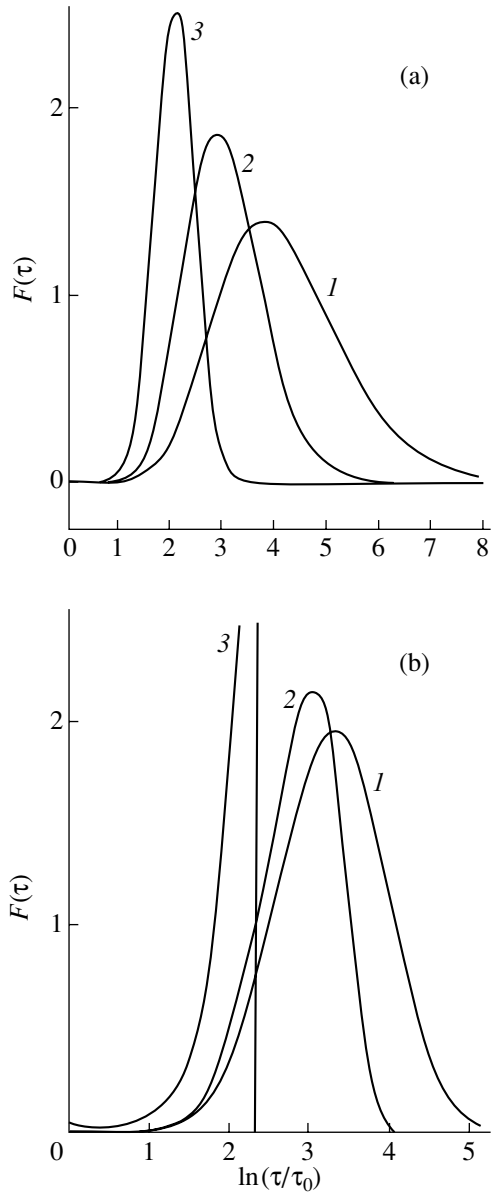

Fig. 3. Relaxation time distribution functions in strong random fields (the nonlinear case) for (a) positive and (b) negative nonlinearity coefficients. The parameters used in the calculations are as follows: (a) $\upsilon = 0.5$; $z = 2$; and $\alpha_0 = (1)$ 1, (*2*) 0.5, and (*3*) 0.1 and (b) $\upsilon = 0.3$; $z = 1$; and $\alpha_0 = (1)$ –0.01, (*2*) –0.1, and (3) –0.3.

case should have the same form as the function $f_l(E)$ in accordance with the probability theory. Since all the above forms of the function $f_l(E)$ are symmetric forms, the relaxation time distribution function should also have a symmetric form in the linear case.

Let us now consider the nonlinear case. As was assumed in the preceding section for systems with the center of inversion in the paraelectric phase, the first term nonlinear in the random field is proportional to $\sim\alpha E^3$. The calculations demonstrated that the form and width of the relaxation time distribution function $F(t)$ are strongly affected by the sign and magnitude of the dimensionless nonlinearity coefficient $\alpha_0 \equiv \alpha E_0^2$ (Fig. 3a for $\alpha_0 > 0$ and Fig. 3b for $\alpha_0 < 0$). It can be seen that, at $\alpha_0 > 0$ (Fig. 3a), the distribution function $F(t)$ broadens and shifts in maximum toward longer times t with an increase in the magnitude of α_0. This behavior can be associated with an increase in the barrier height due to the nonlinear contribution of random fields. As the α_0 coefficient increases, the function $F(t)$ transforms from a totally symmetric to slightly asymmetric form. For example, at $\alpha_0 = 1$, the right wing of $F(t)$ has the Gaussian form, whereas the left wing falls off more steeply than in the case of the Gaussian form.

It turned out that, at $\alpha_0 < 0$, the specific feature of $F(t)$ is a substantially asymmetric form. As can be seen from Fig. 3b, an increase in the magnitude $|\alpha_0|$ leads to an increase in the asymmetry of $F(t)$. The relaxation time distribution function $F(t)$ narrows and shifts in maximum toward shorter times t with an increase in $|\alpha_0|$. This behavior can be explained by the decrease in the barrier height. Judging from the values of z and υ, the curves shown in Figs. 3a and 3b correspond to the mixed ferroelectric glassy phase in which the short-range and long-range orders coexist. The calculations of $F(t)$ for the dipole glass state ($z < z_c$, $z_c = n_c r_c^3$ is the critical concentration [13]) led to a very broad distribution with slowly descending branches even on a ln$t$ scale.

4. COMPARISON OF THE CALCULATED AND EMPIRICAL RELAXATION TIME DISTRIBUTION FUNCTIONS

As a rule, the empirical relaxation time distribution function can be determined from the experimental frequency dependences of the dielectric response. For ordered systems, the dielectric response can be described by the Debye law with a sole relaxation time. A number of empirical functions representing the generalized Debye law were proposed earlier in order to describe the observed dynamic response in disordered ferroelectrics, polymers, and composites (see, for example, [4, 5]). Among these functions, the most well-known are represented by the following expressions:

$$\frac{\varepsilon^*(\omega)-\varepsilon_\infty}{\varepsilon_0-\varepsilon_\infty} = \begin{cases} (1+(i\omega\tau_{CC})^{1-\kappa})^{-1} & (14a) \\ (1+i\omega\tau_{DC})^{-\beta} & (14b) \\ (1+(i\omega\tau_{HN})^{\gamma})^{-\delta}. & (14c) \end{cases}$$

Formula (14a) corresponds to the Cole–Cole function ($0 \le \kappa < 1$), formula (14b) represents the Davidson–Cole function ($0 < \beta \le 1$), and formula (14c) describes the Havriliak–Negami function ($0 < \gamma \le 1$ and $0 < \delta \le 1$).

All these functions are written in the frequency space. In the time space, the decay function has the form $\exp(-t/\tau)$ for the Debye law and, as a rule, is represented in the stretched exponential form, which corresponds to the Kohlrausch–Williams–Watts (KWW) relaxation function; that is,

$$\Phi(t) = \exp\left(-\frac{t}{\tau_{KWW}}\right)^{\alpha}, \quad 0 < \alpha \leq 1. \tag{15}$$

Alvarez *et al.* [4] numerically calculated the Fourier transform of function (15) and demonstrated that this function at a specific parameter ratio ($\gamma\delta = \alpha^{1.23}$) coincides with the Havriliak–Negami function [formula (14c)].

For many years, the empirical functions (14) and (15) were used to describe slow relaxation processes in conventional glasses, polymers, composites, disordered ferroelectrics, etc. The experimental data obtained by different techniques (dielectric spectroscopy, nuclear magnetic resonance, quasi-elastic neutron scattering, etc.) were successfully fitted to formulas (14) and (15). It was assumed that these formulas could be obtained from the Debye function $1/(1 + i\omega\tau)$by including the relaxation time distribution function:

$$\frac{\varepsilon^*(\omega) - \varepsilon_\infty}{\varepsilon_0 - \varepsilon_\infty} = \int_0^\infty \frac{1}{1 + i\omega\tau} F(\tau) d(\ln\tau), \tag{16a}$$

$$\exp\left(-\frac{t}{\tau_{KWW}}\right)^{\alpha} = \int_0^\infty \exp\left(-\frac{t}{\tau}\right) F(\tau) d(\ln\tau). \tag{16b}$$

Expressions (16) make it possible to derive the relaxation time distribution function for all empirical functions (14). The relaxation time distribution functions thus obtained in [5] for the Cole–Cole ($\kappa = 0.2$), Davidson–Cole ($\beta = 0.6$), and Kohlrausch–Williams–Watts ($\alpha = 0.42$) functions are displayed in Fig. 4. In this figure, the vertical straight line (instead of the delta function) shows the distribution function corresponding to the conventional Debye law. It should be noted that, owing to the aforementioned relationship between the Kohlrausch–Williams–Watts and Havriliak–Negami laws, their functions $F(\tau)$ have a similar form (Fig. 4).

For the purpose of elucidating the physical mechanisms responsible for the substantially different behavior of the relaxation time distribution function for different empirical laws (14), we compared the functions $F(\tau)$ represented in Fig. 4 with the calculated functions shown in Figs. 2 and 3. A comparison of the curves in Figs. 3 and 4 shows that curves *2* and *3* in Fig. 3b are similar to the KWW and DC curves in Fig. 4. The coincidence of the time $\tau_{CC}$with the Debye relaxation time τ_D and the considerable difference in width of the distributions $F(\tau)$ for these laws (Fig. 4) are in agreement with the calculated data presented in Fig. 2, according

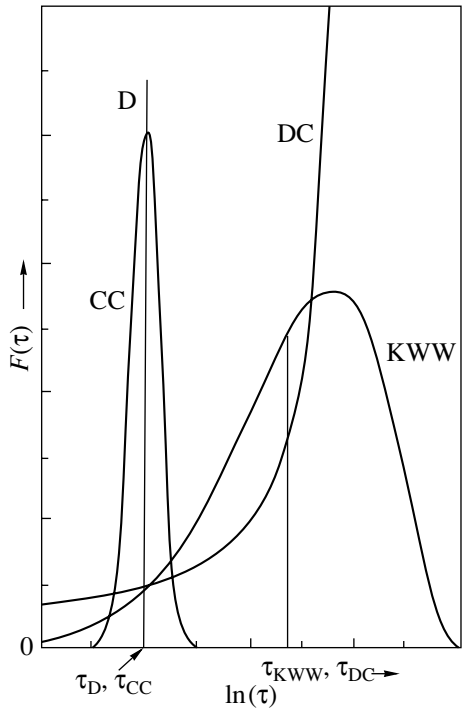

Fig. 4. Relaxation time distribution functions derived in terms of the Debye (D), Cole–Cole (CC), Davidson–Cole (DC), and Kohlrausch–Williams–Watts (KWW) laws [5].

to which curve *2* should transform into the delta function with an increase in the concentration of randomly distributed electric dipoles. The symmetric distribution function representing the Cole–Cole law in Fig. 4 corresponds to the symmetric functions (Fig. 2) calculated in the framework of the linear (with respect to the random field) approximation, which holds at a sufficiently low concentration of random-field sources. The calculated curves in Figs. 2 and 3 correspond to the mixed ferroelectric glassy phase in which the short-range order coexists with the long-range order. Therefore, we can draw the conclusion that the physical mechanisms of relaxation processes described by the aforementioned empirical laws are associated with this coexistence and a weak random field for the Cole–Cole law or a sufficiently strong random field (responsible for the contribution of nonlinear effects at a negative nonlinearity coefficient) for the Kohlrausch–Williams–Watts, Davidson–Cole, and Havriliak–Negami laws. It should be noted that, as was shown earlier in [10], the nonlinear effects at a negative nonlinearity coefficient lead to a decrease in the degree of ordering of the system; as a result, the system becomes more disordered. Under these conditions, the random electric field and its related relaxation time distribution play a decisive role in the specific features of the physical properties of disordered materials.

REFERENCES

1. I. Ya. Korenblit and E. F. Shender, Usp. Fiz. Nauk **157** (2), 267 (1989) [Sov. Phys. Usp. **32**, 139 (1989)].
2. E. V. Colla, E. Yu. Koroleva, N. M. Okuneva, and S. B. Vakhrushev, J. Phys.: Condens. Matter **4**, 3671 (1992).
3. H. Fröhlich, *Theory of Dielectrics* (Oxford Univ. Press, Oxford, 1958).
4. F. Alvarez, A. Alegria, and J. Colmenero, Phys. Rev. B **44** (14), 7306 (1991).
5. J. Malecki and B. Hilczer, Key Eng. Mater. **92–93**, 181 (1994).
6. M. D. Glinchuk and V. A. Stephanovich, J. Appl. Phys. **85** (2), 1722 (1999).
7. M. D. Glinchuk, V. A. Stephanovich, B. Hilczer, *et al.*, J. Phys.: Condens. Matter **11**, 6263 (1999).
8. M. D. Glinchuk and V. A. Stephanovich, J. Phys.: Condens. Matter **10**, 11081 (1998).
9. M. D. Glinchuk and V. A. Stephanovich, J. Phys.: Condens. Matter **6**, 6317 (1994).
10. M. D. Glinchuk, R. Farhi, and V. A. Stephanovich, J. Phys.: Condens. Matter **9**, 10237 (1997).
11. M. D. Glinchuk and I. V. Kondakova, Solid State Commun. **96** (7), 529 (1995).
12. D. J. Hudson, *Statistics for Physicists*, CERN Report (Geneva, 1964; Mir, Moscow, 1967).
13. M. D. Glinchuk and R. Farhi, J. Phys.: Condens. Matter **8**, 6985 (1996).

Translated by O. Borovik-Romanova

Physics of the Solid State, Vol. 44, No. 5, 2002, pp. 953–963. Translated from Fizika Tverdogo Tela, Vol. 44, No. 5, 2002, pp. 912–922.

MAGNETISM AND FERROELECTRICITY

Dynamical Dielectric Susceptibility of Ferroelectric Thin Films and Multilayers

M. D. Glinchuk*, E. A. Eliseev*, and V. A. Stephanovich**

**Institute of Materials Science Problems, National Academy of Sciences of Ukraine, Kiev, 03680 Ukraine*
e-mail: glin@materials.kiev.ua
***Institute of Mathematics, Opole University, Opole, 45-052 Poland*
Received June 7, 2001; in final form, August 6, 2001

Abstract—The thickness dependence of the real and imaginary parts of the dynamical dielectric susceptibility is investigated phenomenologically for a multilayer structure consisting of alternating ferroelectric and paraelectric layers. It is shown that the frequency dependence of the linear dielectric response can be closely approximated by that of a damped harmonic oscillator, with the static susceptibility, relaxation time, and soft-mode frequency depending on the layer thickness and temperature. When the layer thickness and temperature are equal to their critical values corresponding to the onset of a size-driven ferroelectric phase transition, the static susceptibility and the relaxation time become anomalously large and then decrease with further increasing layer thickness. A spectrum of natural polarization oscillations is predicted to exist with thickness-dependent frequencies. This spectrum includes a soft-mode frequency which vanishes at the critical thickness and at the critical temperature. The frequency spectrum lies below the soft-mode frequency of a thick film (in which the gradient of polarization is negligible). The calculations are compared with experimentally measured dispersion of the dielectric response of a $PbTiO_3$–$Pb_{0.72}La_{0.28}TiO_3$ multilayer structure. The agreement between the theory and experiment is found to be good. *© 2002 MAIK "Nauka/Interperiodica".*

1. INTRODUCTION

Considerable recent attention has been focused on ferroelectric thin films and multilayers, because they have considerable application potential in the development of new types of memory devices, capacitors, electromechanical microtransducers, pyroelectric detectors, etc. (see, e.g., [1, 2]). Investigation of the properties of thin ferroelectric films is not only of practical importance but also of much fundamental interest, because it was found experimentally that ferroelectric thin films and multilayers exhibit a number of unusual properties, such as anomalous behavior of the paraelectric–ferroelectric phase transition temperature [3], anomalous growth of multilayers [4], and specific features of their domain structure and vibrational spectra [5].

Of particular interest is the giant dielectric response, which has been recently observed in multilayers composed of layers of ferroelectric $PbTiO_3$ (PT) and paraelectric $Pb_{1-x}La_xTiO_3$ (PLT, $x = 0.28$) grown on single-crystal $SrTiO_3$ substrates [6]. The real and imaginary parts of the dielectric susceptibility of multilayers with spatial periods 400 and 2000 Å were reported in [6] to exhibit frequency dispersion of the Debye type, with the low-frequency susceptibility being equal to 4.2×10^5 and 3.5×10^5 at $T \approx 50$°C, respectively, and increasing up to 7×10^5 at $T = 125$°C in the multilayer with spatial period 400 Å. Recently, it was shown [7] that such behavior of the susceptibility can be due to a size-driven phase transition [8] and, therefore, is a manifestation of size effects in thin ferroelectric films. The giant susceptibility can also be due to domain wall pinning caused by electrodes of a special type [6] and to the contribution from the electronic conductivity (through the Maxwell–Wagner mechanism) to the low-frequency susceptibility [9]; in this case, however, the dispersion must be essentially different from that of the Debye type, which is in contradiction with the experimental data. On the other hand, it is not clear whether the dispersion of the susceptibility is of the Debye or another type in thin ferroelectric films where the size effects, including size-driven phase transitions, depend on the gradient of polarization [8]. Solving this problem is of importance in understanding the mechanisms of the anomalous dielectric response of ferroelectric thin films and multilayers.

In this paper, we calculate the dynamical dielectric susceptibility by using a phenomenological model and analytically solving the Lamé equation. The model adequately describes the experimentally measured dispersion of the real and imaginary parts of the susceptibility of a PT–PLT multilayer.

2. MODEL OF A MULTILAYER

We consider a multilayer (superlattice) consisting of alternating ferroelectric (A) and paraelectric (B) layers (similar to a PL–PLT multilayer). The layers have the same thickness, $l_A = l_B = l$; therefore, the total thickness of the multilayer is $L = 2Nl$, where N is the number of

unit cells in the superlattice, which extends along the z axis from $z = -L/2$ to $L/2$. Since the dielectric susceptibility reaches its maximum when an external field E is applied along the x axis (i.e., when $E = E_x$ and the capacitance of the multilayer is equal to the sum of the capacitances of the layers, which are connected in parallel in this case), we will consider the case where the ferroelectric A layers have an a-domain structure, i.e., where the polarization is subject to the conditions $P_{Ax} = P_{Ay} \equiv P_A \neq 0$ and $P_{Az} = 0$. In the paraelectric B layers, the spontaneous polarization is zero and the field-induced polarization is such that $P_{Bx} \equiv P_B \neq 0$ and $P_{By} = P_{Bz} = 0$. In thin layers, the polarization is nonuniform across the layer thickness, i.e., $P_A = P_A(z)$ and $P_B = P_B(z)$, because there is a gradient of polarization along the z axis. The free-energy functional can be written as

$$F = \sum_{j=0}^{N-1} (F_{Aj} + F_{Bj} + F_{ABj}), \tag{1}$$

$$F_{qj} = \frac{1}{l}\int_{z_{q1}(j)}^{z_{q2}(j)} dz\left[\frac{\alpha_q}{2}P_q^2(z) + \frac{\beta_q}{4}P_q^4(z) + \frac{\gamma_q}{2}\left(\frac{\partial P_q}{\partial z}\right)^2 - EP_q\right] + \frac{\gamma_q}{2\delta_{q1}}P_{q1}^2(z_{q1}(j)) + \frac{\gamma_q}{2\delta_{q2}}P_{q2}^2(z_{q2}(j)). \tag{2a}$$

Here, we have introduced the notation

$$q = A, B; \quad z_{A1}(j) = -\frac{L}{2} + 2jl,$$

$$z_{A2}(j) = z_{B1}(j) = -\frac{L}{2} + (2j+1)l, \tag{2b}$$

$$z_{B2}(j) = -\frac{L}{2} + 2(j+1)l.$$

In Eq. (2a), the last two terms describe the surface energy, where $P_{q1,2}$ are the surface polarizations and $\delta_{q1,2}$ are the extrapolation lengths. The coefficients α_q, β_q, and γ_q differ from the respective coefficients for the free energy of the bulk materials, because the former are renormalized by internal mechanical stresses due to the differences in the lattice constants and in the coefficients of thermal expansion and to growth imperfections [7, 10]. Due to this renormalization, the phase transition of the first order may become a second-order transition [10]; therefore, Eqs. (2) are applicable for describing both first- and second-order phase transitions.

The last term in Eq. (1) describes the interaction between A and B layers and can be approximated by the expression [11]

$$F_{ABj} = Q[P_A(z_{B1}(j))P_B(z_{B1}(j)) + P_A(z_{B2}(j))P_B(z_{B2}(j))]. \tag{3}$$

We note that only the first nonzero terms of the power-series expansions in the surface polarization are retained in Eq. (3) and in the surface energy in Eq. (2a). In considering the dynamical properties, we follow the procedure proposed in [12] and arrive at the equation of motion [7]

$$\rho_q\frac{\partial^2 P_q}{\partial t^2} + \eta_q\frac{\partial P_q}{\partial t} + \frac{\delta F}{\delta P_q} = 0. \tag{4}$$

Here, phenomenological parameters ρ_q and η_q are the mass coefficient and the damping constant of polarization oscillations, respectively. The last term in Eq. (4) is the variational derivative of the free energy of Eq. (1). Taking this derivative of Eq. (1) with allowance for Eqs. (2) and (3) and substituting into Eq. (4) yields

$$\rho_q\frac{\partial^2 P_q}{\partial t^2} + \eta_q\frac{\partial P_q}{\partial t} + \alpha_q P_q + \beta_q P_q^3 - \gamma\frac{\partial^2 P_q}{\partial z^2} = E \tag{5}$$

with the boundary conditions

$$\left[-\frac{\partial P_q}{\partial z} + \frac{1}{\delta_{q1}}P_q + \frac{Q}{\gamma_q}P_{\bar{q}}\right]\Bigg|_{z=z_{q1}(j)} = 0,$$
$$\left[-\frac{\partial P_q}{\partial z} + \frac{1}{\delta_{q2}}P_q + \frac{Q}{\gamma_q}P_{\bar{q}}\right]\Bigg|_{z=z_{q2}(j)} = 0, \tag{6}$$

where $\bar{q} = A, B$ and $\bar{q} \neq q$; i.e., if $q = A$, then $\bar{q} = B$ and vice versa.

The polarization must also be subject to the periodicity conditions

$$P_q(z + 2jl) = P_q(z), \quad j = 0, 1, 2, \ldots, N-1. \tag{7}$$

In the case of a multilayer of A and B layers, the model can be simplified. Since the spontaneous polarization is zero in the B layers, the interaction energy $F_{ABj} = 0$ and the layers can be considered to be independent of one another. Therefore, boundary conditions (6) will not contain the last (cross) terms associated with interaction between the layers. Such boundary conditions imply that zero surface polarization corresponds to zero extrapolation lengths; therefore, for the paraelectric layers, we have $\delta_{B1} = \delta_{B2} = 0$ [13]. In what follows, we consider the simple case where, for the A layers, we also have $\delta_{A1} = \delta_{A2} = 0$ and, hence, $P_A|_{z_{1,2j}} = 0$. Physically, this model corresponds to the case of 180° domain walls present on the surfaces of the ferroelectric layers. In this model, the dynamical polarization can be found by solving Eq. (5) for P_A and P_B with boundary conditions

$$P_A|_{z=z_{1,2j}} = 0, \quad P_B|_{z=z_{1,2j}} = 0. \tag{8}$$

3. THE THICKNESS DEPENDENCES OF THE DYNAMIC POLARIZATION AND OF THE SOFT MODE

3.1. The Ferroelectric Phase

Let us consider the spontaneous polarization $P_s \equiv P_{As}$. We represent P_s in the ferroelectric layer $0 \le z \le l$ as the sum of two terms, one of which describes the stationary distribution of the spontaneous polarization, while the other describes time variations of the polarization in the absence of an external field ($E = 0$):

$$P_s(z, t) = P_{s0}(z) + e^{\mu t}\delta P(z). \quad (9)$$

Here, the parameter μ characterizes the time dependence of the polarization and can be found by solving Eq. (5) with boundary conditions (8).

The steady-state component $P_{s0}(z)$ satisfies the following equation and boundary conditions:

$$\alpha P_{s0} + \beta P_{s0}^3 - \gamma\frac{\partial^2 P_{s0}}{\partial z^2} = 0, \quad P_{s0}\big|_{z=0} = 0, \quad P_{s0}\big|_{z=l} = 0. \quad (10)$$

Here, $\alpha \equiv \alpha_A$, $\beta \equiv \beta_A$, $\gamma \equiv \gamma_A$, and $\alpha = \alpha_0(T - T_c)$, where T_c is the ferroelectric phase transition temperature in thick films. A solution to this equation can be expressed in terms of elliptic functions [14]. In the case of $\alpha < 0$ (i.e., $T < T_c$), a finite solution to Eq. (10) subject to zero boundary conditions has the form

$$P_{s0}(z) = P_{st}\sqrt{\frac{2m}{1+m}}\,\mathrm{sn}\left(\frac{z}{l_0\sqrt{1+m}}; m\right). \quad (11)$$

We have introduced the following notation in Eq. (11): $P_{st} = \sqrt{-\alpha/\beta}$ is the spontaneous polarization in a thick film, $l_0 = \sqrt{-\gamma/\alpha}$ is the correlation length, and $\mathrm{sn}(u; m)$ is the elliptic sine [14], whose parameter m is determined from the equation

$$l = 2l_0\sqrt{1+m}K(m), \quad (12)$$

where $K(m)$ is a complete elliptic integral of the first kind [14]. In Eq. (12), the parameter m varies from zero to unity; otherwise, the spontaneous polarization of Eq. (11) becomes a complex quantity. As follows from Eq. (12), the limit $m \longrightarrow 1$ corresponds to the case of a thick film ($l \gg l_0$), while the limit $m \longrightarrow 0$ corresponds to $l \longrightarrow l_0\pi$. Thus, there is a critical layer thickness $l_c = \pi l_0$ at which the spontaneous polarization vanishes [see Eq. (11)]; for layer thicknesses smaller than this critical value, the spontaneous polarization does not occur. Therefore, a decrease in the layer thickness at a fixed temperature lower than the phase transition temperature T_c for a thick film can give rise to the occurrence of a phase transition from the ferroelectric ($P_s \ne 0$) to the paraelectric ($P_s = 0$) phase (size-driven phase transition).

On the other hand, in a film whose thickness exceeds the critical value, the phase transition occurs when the temperature is varied, because both the correlation length and the critical length are temperature-dependent through the relation $l_0 = \sqrt{\gamma/\alpha_0(T_c - T)}$. The phase transition temperature in a thin layer T_{cl} can be found from the condition $l = \pi l_0(T = T_{cl})$, which gives

$$T_{cl} = T_c\left[1 - \left(\frac{l_c(0)}{l}\right)^2\right], \quad l_c(0) = \pi\sqrt{\frac{\gamma}{\alpha_0 T_c}}, \quad (13)$$

where $l_c(0)$ is the critical layer thickness at $T = 0$. For $l \le l_c(0)$, we have $T_{cl} \le 0$; that is, the layer is in the paraelectric phase at any temperature.

An equation for the time-dependent component of the polarization is obtained by substituting Eq. (9) into Eq. (5). Assuming that deviations from the stationary polarization distribution are small and using Eq. (10) for the stationary polarization, we obtain the equation

$$[\rho\mu^2 + \eta\mu + \alpha + 3\beta P_{s0}^2(z)]\delta P(z) - \gamma\frac{d^2(\delta P(z))}{dz^2} = 0, \quad (14)$$

which should be subject to the zero boundary conditions $\delta P(z)|_{z=0,\,l} = 0$. Using Eq. (11) and introducing a new variable $u = z/l_0\sqrt{1+m}$, we represent Eq. (14) and the boundary conditions for it in the form

$$\frac{d^2(\delta P)}{du^2} + \left((1+m)\left(1 + \frac{\eta\mu + \rho\mu^2}{\alpha}\right) - 6m\,\mathrm{sn}^2(u; m)\right)\delta P = 0, \quad \delta P|_{u=0} = \delta P|_{u=2K(m)} = 0. \quad (15)$$

Since Eq. (15) and the boundary conditions for it are homogeneous, the problem has a nontrivial solution only if the parameter $q_m = (1+m)[1 + (\eta\mu + \rho\mu^2)/\alpha]$ is equal to one of the eigenvalues of the boundary-value problem (15), whose solution can be expressed in terms of Lamé functions of the first kind [15]. The lowest and next-to-lowest eigenvalues and the corresponding eigenfunctions are

$$q_{m1} = 1 + 4m, \quad \delta P(u) = \mathrm{sn}(u; m)\mathrm{dn}(u; m), \quad q_{m2} = 4 + m, \quad \delta P_2(u) = \mathrm{sn}(u; m)\mathrm{cn}(u; m), \quad (16)$$

where $\mathrm{dn}(u; m)$ and $\mathrm{cn}(u; m)$ are the delta amplitude and the elliptic cosine, respectively [14]. The other eigenvalues are higher than those in Eq. (16), and their eigenfunctions are of a more cumbersome form.

Knowing the discrete set of eigenvalues q, one can calculate the corresponding values of μ. Using the eigenvalues in Eq. (16), we easily find that either μ is purely imaginary (and the time-dependent polarization

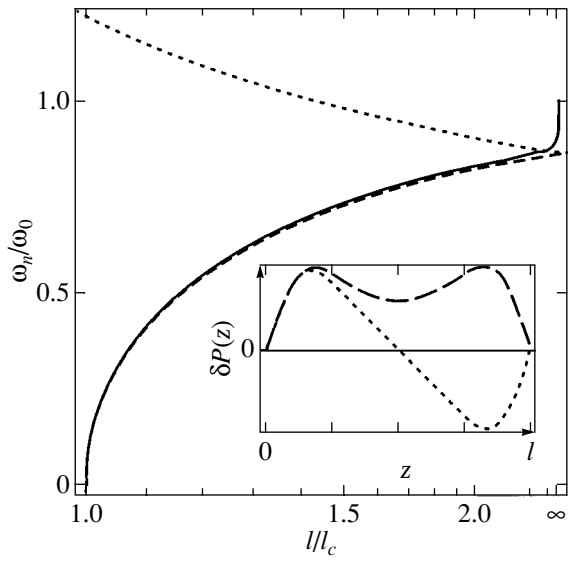

Fig. 1. Dependence of the two lowest frequencies of natural polarization oscillations (dotted and dashed curves) on the thickness of the ferroelectric layer. The solid curve is the calculated frequency involved in approximate expression (29) for the low-frequency susceptibility. The inset shows the amplitudes of these two oscillation modes calculated from Eq. (16) for $m = 0.9$.

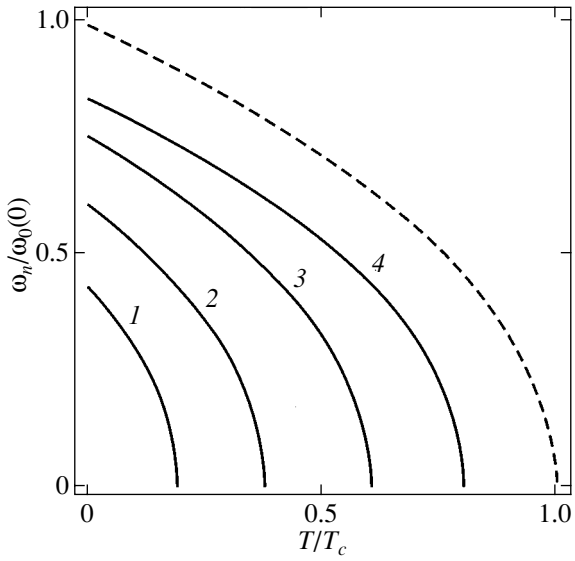

Fig. 2. Temperature dependence of the soft-mode frequency of a thin ferroelectric layer of thickness $l/l_0(0)$ equal to (*1*) 3.5, (*2*) 4, (*3*) 5, and (*4*) 7 and of a thick film (dashed curve).

component is an undamped standing wave) or the real part of μ is negative and, therefore, deviations from the stationary polarization distribution decay in time, being either oscillatory or aperiodic in character. For each specific eigenvalue, the character of polarization variations in time depends on the relationship between the material constants involved in the power-series expansion of the free-energy functional in Eq. (2a) and the damping constant in Eq. (4).

In order to find an explicit solution for the time-dependent polarization component, one should take into account the initial polarization distribution; its expansion in terms of the eigenfunctions δP_i allows one to determine the contribution from each oscillation mode to the polarization of Eq. (9).

The dependences of the polarization oscillation frequencies corresponding to the eigenvalues $q_{1,2}$ of Eq. (16) on the layer thickness and temperature are shown in Figs. 1 and 2 for the case of low damping ($\eta \approx 0$). The inset to Fig. 1 shows the space-coordinate dependence of eigenfunctions (16).

As seen from Fig. 1, the frequency that corresponds to the lowest eigenvalue q_{m1} vanishes at the critical layer thickness $l = l_c$ and, therefore, corresponds to the soft mode associated with the size-driven phase transition. The variation in the polarization oscillation amplitude across the layer thickness for this soft mode is shown in the inset to Fig. 1. The temperature dependence of the soft-mode frequency is shown in Fig. 2 for different layer thicknesses. The frequency can be seen to vanish at the size-driven phase transition temperature $T = T_{cl}$ given by Eq. (13). For comparison, the dashed line in Fig. 2 represents the soft-mode frequency in a thick film, which is always higher than that in thin layers. At a fixed temperature, the frequency of the soft mode decreases with decreasing thickness (Fig. 1). As $T \longrightarrow T_{cl}$ for a fixed layer thickness, the soft-mode frequency vanishes at $l = l_c$, as well as at $T = T_{cl}$ (Figs. 1, 2).

We note that the frequencies are represented in Figs. 1 and 2 in units of the soft-mode frequency of a thick film in the ferroelectric phase: $\omega_0 = \sqrt{2\alpha_0(T_c - T)/\rho} = \omega_0(0)\sqrt{1 - T/T_c}$.

3.2. The Paraelectric Phase

In paraelectric layers, as well as in ferroelectric layers of an arbitrary thickness at $T > T_{cl}$ ($\alpha > 0$) and of a thickness $l < l_c$ at $T < T_c$ ($\alpha < 0$), there is no spontaneous polarization and only the dynamic polarization is nonzero and given by Eq. (14), in which $P_{s0}(z)$ should be put equal to zero. The boundary-value problem for this equation can easily be solved, which gives a set of values of the parameter μ whose real and imaginary parts determine the damping and frequency of polarization oscillations, respectively. In particular, in the absence of the gradient term ($\gamma = 0$) and damping ($\eta = 0$), one can find that $\mu = i\omega_0$, where $\omega_0 = \sqrt{\alpha_0(T - T_c)/\rho}$ is the soft-mode frequency of a thick film in the paraelectric phase.

In thin layers, there is a set of oscillation frequencies, rather than one frequency, and these frequencies depend on temperature and layer thickness. For a layer

of an arbitrary thickness at $T > T_c$ ($\alpha > 0$), the values of μ can be found to be

$$\mu_n = \left\{-\tau_0 \pm \sqrt{\tau_0^2 - \frac{4}{\omega_0^2}\left[1 + \left(\frac{nl_p}{l}\right)^2\right]}\right\}\frac{\omega_0^2}{2}, \qquad (17)$$

where $n = 1, 2, 3, \ldots$, $\tau_0 = \eta/\alpha$ is the relaxation time of the soft mode for a thick film in the paraelectric phase and $l_p = \pi\sqrt{\gamma/\alpha}$ is a parameter characterizing the correlation length. It can be seen that we always have $\mathrm{Re}(\mu) < 0$, which corresponds to damped oscillations; if damping is low ($\tau_0 \approx 0$), there is a set of natural oscillation frequencies $\omega_n = \omega_0\sqrt{1 + (nl_p/l)^2}$ which collapses into one (soft-mode) frequency ω_0 in the case of a thick layer ($l \gg nl_p$). In the case of fairly thin layers ($l \ll l_p$), the oscillation frequencies are temperature-independent.

For a ferroelectric layer of a thickness less than its critical value ($\alpha < 0$, $l < l_c = \pi\sqrt{-\gamma/\alpha}$), the parameter μ is given by Eq. (17), in which the quantities ω_0, τ_0, and l_p are defined by the same expressions as before, except that $\alpha(T)$ is replaced in them by $-\alpha(T)$, with the result that, for example, l_p turns into the critical thickness l_c. In the case of $\tau_0 \approx 0$, the natural oscillation frequencies are $\omega_n = \omega_0\sqrt{(nl_c/l)^2 - 1}$. Therefore, the lowest frequency (corresponding to $n = 1$) tends to zero as $l \longrightarrow l_c$, i.e., when the layer thickness approaches its critical value. This size effect is the distinctive feature of the thin ($l < l_c$) ferroelectric *A* layers in the paraelectric phase in comparison with the paraelectric *B* layers.

4. DIELECTRIC SUSCEPTIBILITY

Now, we consider the linear (with respect to an external field) dielectric response of the ferroelectric layers. In this case, the field-induced polarization is small in comparison with the spontaneous polarization and the total polarization can be written as

$$P(z, t) = P_s(z, t) + \chi(z, t)E(t), \qquad (18)$$

where P_s is the spontaneous polarization satisfying Eq. (5) with $E = 0$ and $\chi(z, t)$ is the linear dielectric susceptibility.

An equation for the susceptibility χ can be found by substituting Eq. (18) into Eq. (5); we assume that the external field E varies in time as $E(t) = E\exp(-i\omega t)$, where ω is the frequency of the external field. We consider the simple case where the time-dependent component of the spontaneous polarization can be neglected; this component is only a small correction (decaying in time) and makes a negligible contribution to the linear susceptibility.

In this case, the time dependence of the field-induced polarization is determined by that of the external field alone; therefore, the susceptibility does not vary in time. If $E = E_x$, all layers are connected in parallel and the susceptibility of the multilayer is the sum of the susceptibilities of the individual layers:

$$\chi_{xx} = \frac{1}{L}\sum_{j=0}^{N-1}\left[\int_{z_{A1}(j)}^{z_{A2}(j)}\chi_{xxA}(z)dz + \int_{z_{B1}(j)}^{z_{B2}(j)}\chi_{xxB}(z)dz\right], \qquad (19a)$$

where $z_{1,2}$ are given by Eq. (2b). Since the layers are independent of one another, Eq. (19a) can be rewritten as

$$\chi_{xx} = \frac{1}{l}\int_0^l(\chi_{xxA}(z) + \chi_{xxB}(z))dz. \qquad (19b)$$

First, we consider the susceptibility of the ferroelectric layers $\chi_{xxA} \equiv \chi$. This susceptibility obeys an equation similar to Eq. (14), with $-i\omega$ replacing μ and with unity in place of zero on the right-hand side. Using the variable u introduced above, this equation and the boundary conditions for it can be written as

$$\frac{d^2\chi(u)}{du^2} + [(1 + m)(1 + 2w) - 6m\,\mathrm{sn}^2(u; m)]\chi(u) = -2(1 + m)\chi_0, \qquad (20)$$

$$\chi|_{u=0} = \chi|_{u=2K(m)} = 0.$$

Here, $w = \chi_0(\rho\omega^2 + i\eta\omega)$, where $\chi_0 = 1/(-2\alpha)$ is the static susceptibility of a thick film at a temperature $T < T_c$ (i.e., $\alpha < 0$). Equation (20) is an inhomogeneous Lamé equation [15]. We seek a solution to this equation in the form of the following trigonometric series, each term of which satisfies the boundary conditions:

$$\chi(u) = \chi_0\frac{8}{\pi}(1 + m)\sum_{n=1}^{+\infty}B_n\sin(n\,\mathrm{am}(u; m)), \qquad (21)$$

where $\mathrm{am}(u; m)$ is the elliptic amplitude [14]. Substituting the series of Eq. (21) into Eq. (20) and equating the coefficients of $\sin(n\,\mathrm{am}(u; m))$ to zero, we obtain a set of algebraic equations for the unknown coefficients B_n. Since this set of equations is infinite, it is impossible to obtain exact expressions for B_{2k-1} for $k > 1$. However, we can find an approximate solution by assuming that only the first several coefficients are nonzero.

The accuracy of such a solution can be controlled by increasing the number of coefficients taken into account and by then calculating the changes in these coefficients. Reasonable accuracy was attained in the case where the first four coefficients (B_1, B_3, B_5, B_7) were assumed to be nonzero (i.e., $B_n = 0$ for $n > 7$).

It should be noted that this number of terms taken into account in the series of Eq. (21) does not allow one to obtain a reasonably smooth space-coordinate dependence for the dynamical susceptibility; however, the oscillations will be smoothened out when calculating the averaged susceptibility of Eq. (19b) (see [16]).

Having taken the integral of the first term in Eq. (19b), the averaged susceptibility $\langle\chi\rangle$ can be represented in the form

$$\langle\chi\rangle = \chi_0\frac{8}{\pi}(1+m)\sum_{k=1}^{\infty}B_{2k-1}(mw)I_{2k-1}(m),$$
$$I_n = \frac{1}{2K(m)}\int_0^{2K(m)}\frac{\sin(n\varphi)d\varphi}{1-m\sin(\varphi)^2}. \quad (22)$$

The dominant contribution comes from the first term of the sum in Eq. (22), for which $B_1 = 1/[3m - 2(1 + m)w]$ and $I_1(m) = \ln[(1 + \sqrt{m})/(1 - \sqrt{m})]/2\sqrt{m}K(m)$. We note that it is the first term of the sum in Eq. (22) that contains the contribution from the soft mode. Explicit expressions for the functions $I_1(m)$ and $B_n(m, w)$ for $n = 3, 5, 7$ are written out in the Appendix.

Equation (22) describes the dependence of the averaged layer susceptibility $\langle\chi\rangle$ on the external-field frequency and material parameters of the layer, because the parameter m is unambiguously determined by the layer thickness l, temperature T, and expansion coefficients of the free energy in Eq. (2a) through Eq. (12).

The solution to Eq. (20) becomes significantly simpler in some physically interesting extreme cases.

As seen from Eq. (12), the parameter m tends to unity for layer thicknesses $l \gg l_0$. In this case, the solution to Eq. (20) is independent of the space coordinate (in regions sufficiently far from the layer boundaries) and has the form

$$\chi_T = \frac{\chi_0}{1-w} = \frac{\chi_0}{1 - i\omega\tau_0 - (\omega/\omega_0)^2}. \quad (23)$$

Thus, the susceptibility of a thick film χ_T is similar to that of a damped harmonic oscillator with frequency $\omega_0 = 1/\sqrt{\chi_0\rho}$ and relaxation time $\tau_0 = \chi_0\eta$. Another physically interesting case is that of high frequencies, where $\omega \gg \omega_0$ or $\omega\tau_0 \gg 1$ and, therefore, $|w| \gg 1$. In this case, Eq. (20) can be reduced to an algebraic equation. From the solution to that equation, it follows that the high-frequency susceptibility χ_H is independent of the coordinate z and layer thickness l and has the form

$$\chi_H = -\frac{\chi_0}{w} = -\frac{\chi_0}{i\omega\tau_0 + (\omega/\omega_0)^2}, \quad (24)$$

which is identical to the susceptibility of a thick film χ_T of Eq. (23) at high frequencies.

It should be stressed that the free-energy functional (2a) with critical $\alpha(T)$ dependence takes into account the contribution from the ionic subsystem alone and ignores the effect of the electronic subsystem, which makes the dominant contribution to the high-frequency susceptibility. Therefore, Eq. (24) describes only the ionic-subsystem contribution to the linear susceptibility, which decreases considerably with increasing frequency. At optical frequencies, the ionic polarization can be considered to be static in the adiabatic approximation for the much lighter electronic subsystem. Therefore, the effect of the ionic polarization is similar to that of an external electric field, which gives rise, through the quadratic electrooptic effect, to the appearance of an additional term proportional to $P_s^2(z)$ in the optical refractive index. We note that the refractive-index profiles recently observed in PZT films [13] can be approximated closely by the $P_s^2(z)$ dependence given by Eq. (11).

At low frequencies, the behavior of the susceptibility is determined by the ionic subsystem. First, we consider the static susceptibility (in static external fields, $\omega = 0$), which can be found in a closed form [7]. The solution to Eq. (20) for $\omega = 0$ has the form [15]

$$\chi|_{\omega=0}(u) = C_1\chi_1(u) + C_2\chi_2(u) + \chi_3(u),$$
$$\chi_1(u) = \mathrm{cn}(u; m)dn(u; m), \quad \chi_2(u) = \chi_1(u)\int_0^u\frac{d\tilde{u}}{\chi_1^2(\tilde{u})}, \quad (25)$$
$$\chi_3(u) = -2(1+m)\chi_0\frac{1+m-2m\,\mathrm{sn}(u; m)^2}{(1-m)^2},$$

where C_1 and C_2 are constants to be determined by the boundary conditions in Eq. (20). A solution for an arbitrary nonzero frequency can be found by the method of variation of constants $C_{1,2}$ in Eq. (25). By expanding the coefficients $C_{1,2}$ in powers of the small parameter $\varepsilon = 2(1 + m)w$, one can find the susceptibility at low frequencies in a closed form. We drop cumbersome calculations and only present the final expression for the averaged low-frequency susceptibility $\langle\chi_L\rangle$:

$$\langle\chi_L\rangle = \chi_S(m)[1 + \tau(m)w], \quad (26)$$

where χ_S is the averaged static susceptibility, which can be derived from Eqs. (19b) and (25) to be

$$\chi_S(m) = \frac{2\chi_0}{K(m)}\frac{1+m}{1-m}\left(K(m) - \frac{2E(m)}{1-m} + \frac{1+m}{1-m}\frac{1}{g(m)}\right),$$
$$g(m) = E(m) - \frac{1-m}{1+m}K(m), \quad (27)$$

with $E(m)$ being the complete elliptic integral of the second kind [14], and $\tau(m)$ is the dimensionless relaxation time

$$\tau(m) = 2(1+m)[(1 + 7m + 7m^3 + m^4)E(m)$$
$$-(1 + 2m - 3m^2 + 4m^3 - 4m^4)K(m)$$
$$-6m(3 + 2m + 3m^2)g(m) + 3m(4(1+m)E(m)$$
$$-(1 + 2m - 3m^2)K(m))g(m)^2 \quad (28)$$

$$+ (1+m)^3 g(m)^3]/9m(1-m)^2 g(m)$$

$$\times \{1 + m + [(1-m)K(m) - 2E(m)]g(m)\}.$$

The low-frequency susceptibility of Eq. (26) increases indefinitely with frequency, in contrast to the high-frequency susceptibility of Eq. (24); therefore, it is desirable to find an approximate expression that reduces to Eqs. (26) and (24) in the respective limits. Approximating Eq. (26) by rational fractions or using the Padé approximant method [16], we arrive at the expression

$$\chi_A = \frac{\chi_S(m)}{1-\tau(m)w} = \frac{\chi_S(m)}{1-\tau(m)(i\omega\tau_0 + (\omega/\omega_0)^2)}. \quad (29)$$

This expression goes over into Eq. (26) at low frequencies and is qualitatively similar to Eq. (24) at high frequencies. We also note that Eq. (29) is identical to the susceptibility of a damped harmonic oscillator of Eq. (23) with χ_S in place of χ_0 and with renormalized relaxation time $\tau_R = \tau(m)\tau_0$ and natural oscillation frequency $\omega_R = \omega_0\sqrt{\tau(m)}$.

The dependence of this renormalized frequency on the layer thickness is shown by the solid line in Fig. 1. It can be seen that if the layer thickness is several times the critical thickness l_c, the frequency ω_R equals the lowest frequency of natural polarization oscillations (dashed line in Fig. 1). The difference between these frequencies for larger thicknesses is due to the fact that, as the layer thickness increases and the parameter m approaches unity, the eigenfunctions δP_i become degenerate and the frequency spectrum is changed: different frequencies are mixed due to the nonlinear term in Eq. (5).

The dependencies of the real and imaginary parts of the susceptibility on the external-field frequency ω are shown in Figs. 3a and 3b, respectively, for the case of a purely relaxative response ($\rho = 0$). As seen from Fig. 3a, there are three frequency ranges in which the behavior of the dynamical susceptibility is essentially different. At low frequencies ($\tau_0\omega \ll 1$), the layer susceptibility calculated from Eq. (22) and shown by solid curves in Fig. 3 is closely approximated by Eq. (29) derived for the low-frequency susceptibility (represented by crosses). At high frequencies $\tau_0\omega \gg 1$ (inset to Fig. 3a), the susceptibility coincides with that of a thick film given by Eq. (23) and represented by the dashed line; a considerable difference (by several times) is observed between the susceptibility calculated from Eq. (22) and that calculated at low frequencies. At frequencies close to the inverse relaxation time ($\tau_0\omega \approx 1$), the behavior of the averaged susceptibility of Eq. (22) noticeably changes: a crossover is observed from the low-frequency dependence, characterized by thickness-(parameter-m-)dependent relaxation time (28) and static susceptibility (27), to the high-frequency dependence, which is the same for different layer thicknesses (curves *1–4* merge together).

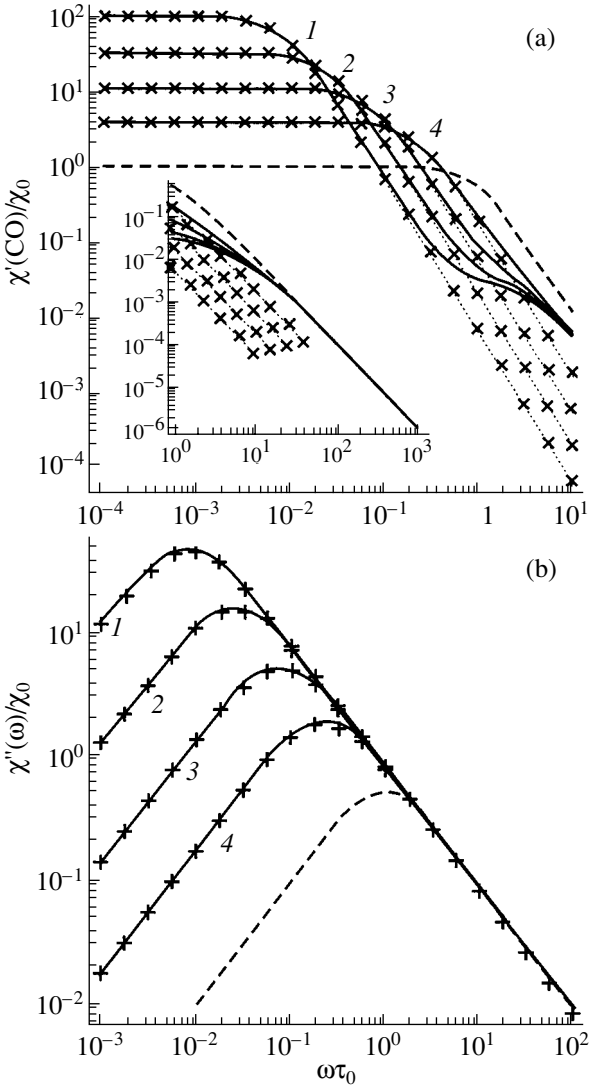

Fig. 3. Frequency dependences of (a) the real and (b) imaginary parts of the susceptibility of ferroelectric layers in the case of a purely relaxative response. Crosses are calculations by Eq. (29) for different values of m: (*1*) 0.0054, (*2*) 0.0171, (*3*) 0.054, and (*4*) 0.1709; dashed curves represent the susceptibility of a thick film calculated from Eq. (23). The inset to (a) shows the high-frequency susceptibility.

The distinctions between calculations of the imaginary part of the susceptibility from different formulas represented in Fig. 3b are qualitatively similar to those for the real part discussed above, although in the region of intermediate and high frequencies, these distinctions are not so pronounced in this case. It is notable that at frequencies $\omega < 1/\tau_0$, the susceptibility of thin layers is always higher than that of a thick film (dashed curves in Figs. 3a, 3b).

We emphasize once again that at low and high frequencies, the dynamical layer susceptibility of Eq. (22)

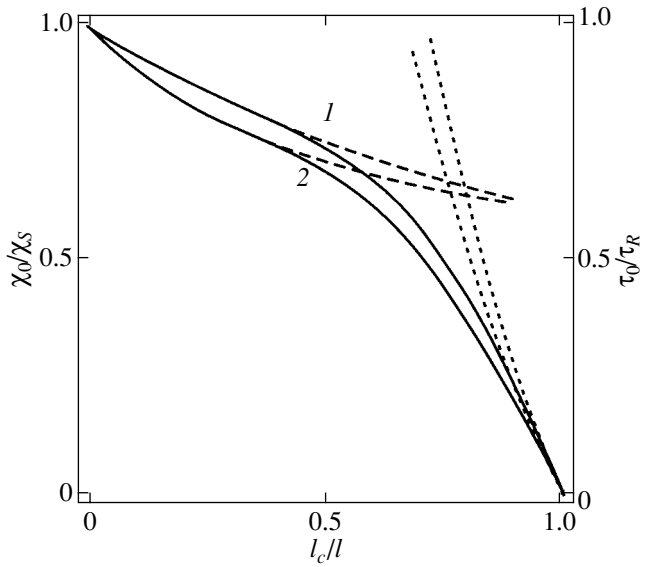

Fig. 4. Dependences of (*1*) the static susceptibility and (*2*) relaxation time on the inverse layer thickness calculated from Eqs. (27) and (28), respectively, as well as from approximate expressions (30) and (31) (dotted and dashed curves, respectively).

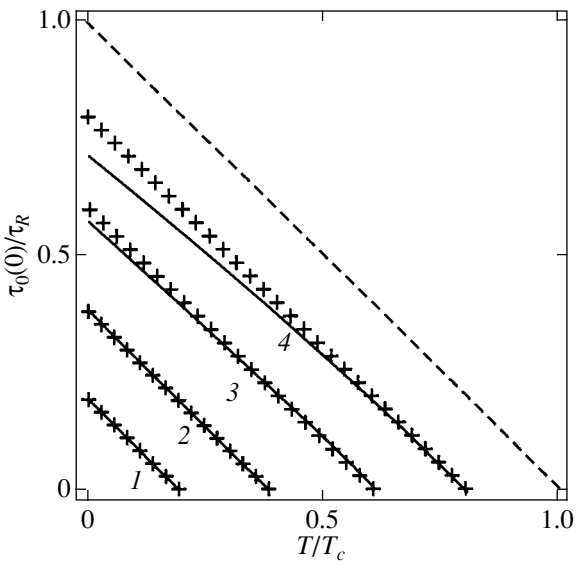

Fig. 5. Temperature dependence of the relaxation time calculated from Eq. (28) (solid lines) and from approximate formula (32) (crosses) for different values of l/l_0: (*1*) 3.5, (*2*) 4, (*3*) 5, and (*4*) 7. The dashed line is the relaxation time of a thick film $\tau_0(T)$.

is closely approximated by the susceptibility of a damped harmonic oscillator of Eqs. (29) and (23), respectively, but with essentially different parameters: the relaxation time and static susceptibility are thickness-dependent only at low frequencies.

The cumbersome expressions for the relaxation time τ_R and static susceptibility χ_S can be simplified in two extreme cases: near the size-driven phase transition (i.e., for fairly thin layers) and for thick layers. Expanding Eqs. (12), (27), and (28) in powers of $m \longrightarrow 0$ and of $m \longrightarrow 1$, one can obtain approximate expressions for layer thicknesses close to the critical thickness,

$$\chi_S \approx \frac{4\chi_0/\pi^2}{l/l_c - 1}, \quad \tau_R \approx \frac{\tau_0/2}{l/l_c - 1}, \quad l - l_c \ll l_c \qquad (30)$$

and for fairly thick layers,

$$\chi_S \approx \chi_0\left(1 + \frac{3}{\sqrt{2}}\frac{l_0}{l}\right),$$
$$\tau_R \approx \tau_0\left(1 + \frac{59/12}{3 + \sqrt{2}l/l_0}\right), \quad l \gg l_0. \qquad (31)$$

Using the expansions mentioned above and Eq. (13), one can also obtain expressions that describe the behavior of the static susceptibility and relaxation time near the phase transition temperature:

$$\chi_S \approx \frac{4/(\pi^2\alpha_0)}{T_{cl} - T}, \quad \tau_R \approx \frac{\eta/(2\alpha_0)}{T_{cl} - T}, \quad T_{cl} - T \ll T_c. \quad (32)$$

Equations (32) are qualitatively similar to the temperature dependences of the static susceptibility $\chi_0 = 1/2\alpha_0(T_c - T)$ and relaxation time $\tau_0 = \eta/2\alpha_0(T_c - T)$ for a thick film.

As seen from the formulas presented above, the static susceptibility and relaxation time for layers of a finite thickness diverge at the size-driven phase transition point; as the layer thickness increases, these quantities tend to the values corresponding to a thick film. Figure 4 shows the thickness dependences of the static susceptibility and relaxation time and the dependences given by approximate expressions (30) and (31). It can be seen from Fig. 4 that the approximate expressions adequately describe the static susceptibility and relaxation time over a fairly wide range of layer thicknesses. The temperature dependences of the relaxation time τ calculated from Eq. (28) and approximate formula (32) and of the relaxation time $\tau_0(T)$ for a thick film are shown in Fig. 5. It can be seen that the approximate formula adequately describes the relaxation time and that the relaxation time for a thick film is shorter than that for thin layers over the entire temperature range. The relaxation time diverges at $T = T_{cl}$ for thin layers and at $T = T_c$ for a thick film; we note that $T_{cl} < T_c$ according to Eq. (13).

In the paraelectric phase, the linear susceptibility $\chi(z)$ can be found from the following equation, which is derived from Eq. (5):

$$(-\rho\omega^2 - i\eta\omega + \alpha)\chi - \gamma\frac{d^2\chi}{dz^2} = 1. \qquad (33)$$

A solution to this equation can be written as a sum of trigonometric functions, and the averaged susceptibility in this case has the form

$$\chi(l) = \chi_A(l) + \chi_B(l), \tag{34a}$$

$$\chi_{A,B}(l) \equiv \frac{1}{\alpha_{A,B} + i\eta_{A,B}\omega + \rho_{A,B}\omega^2} \times \left[\frac{2(1-\cos(q_{A,B}l))}{q_{A,B}l\sin(q_{A,B}l)} - 1\right], \tag{34b}$$

where $q^2 = (\rho\omega^2 + i\eta\omega - \alpha)/\gamma$.

In the ferroelectric *A* layers, the paraelectric phase occurs when $l < l_c$ and $T < T_c$ ($\alpha < 0$) or when $T > T_c$ ($\alpha > 0$), while in the paraelectric *B* layers, the paraelectric phase exists either at any temperature (in incipient ferroelectrics) or at $T > T_c$ ($\alpha > 0$).

The frequency dependence of the dielectric susceptibility of the ferroelectric layers in the paraelectric phase ($l < l_c$) is shown in Fig. 6 for the case of low damping ($\omega_0\tau_0 = 0.2$). The natural oscillation frequency spectrum (see Section 3) is seen to manifest itself in the susceptibility as a set of peaks in the high-frequency region (inset to Fig. 6). The height of these peaks decreases with increasing frequency, and the dielectric response is closely approximated by the high-frequency expression $\chi(\omega) \approx -1/(\rho\omega^2 + i\eta\omega)$. This high-frequency susceptibility is independent of the layer thickness and significantly decreases with increasing ω, which is consistent with the fact that the contribution from the ionic subsystem is negligible at high frequencies.

We note that in Eq. (34a), for the case of *A* layers in the ferroelectric phase ($l > l_c$) and of paraelectric *B* layers, one should take $\chi_A(l)$ in the form of either Eq. (22) or approximate expression (29) and $\chi_B(l)$ in the form of Eq. (34b) for $\alpha > 0$.

5. COMPARISON WITH EXPERIMENT AND DISCUSSION

Our calculations showed that the dielectric susceptibility of thin ferroelectric layers is adequately described by Eq. (29), which has the form of the susceptibility of a damped harmonic oscillator whose oscillation frequency, static susceptibility, and relaxation time depend on the layer thickness and temperature, as shown in Figs. 1, 2, 4, and 5. In the case of a purely relaxational response ($\omega_0 \longrightarrow \infty$), Eq. (29) becomes identical to the Debye formula with thickness-dependent parameters. In particular, the static susceptibility and relaxation time increase as the layer thickness decreases and approaches its critical value. Such behavior was indeed observed in PL–PLT multilayer structures *S*-10 and *S*-2 with a layer thickness of 200 and 1000 Å, respectively [6]. The static susceptibility was as high as 4.2×10^5 for *S*-10 and 3.5×10^5 for *S*-2 at $T \approx$ 50°C. The relaxation time, as estimated from the position of the peak of $\chi''(\omega)$, was roughly 10^{-4} and 10^{-5} s for the *S*-10 and *S*-2 samples, respectively.

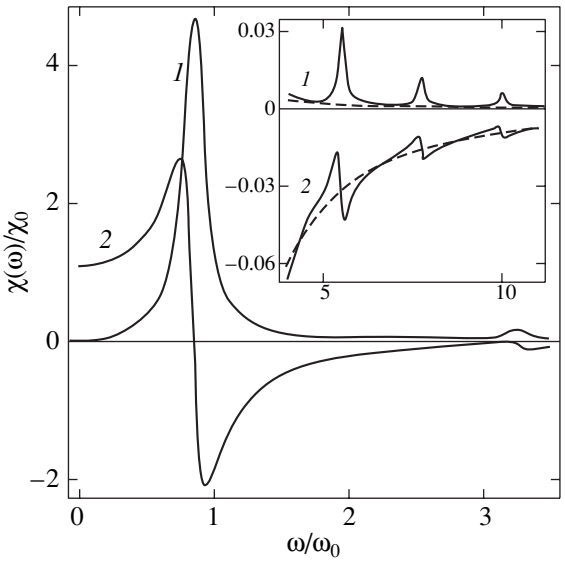

Fig. 6. Frequency dependences of (*1*) the real and (*2*) imaginary parts of the dielectric susceptibility of ferroelectric layers in the paraelectric phase of thickness $l = 2l_c/\pi$ for low damping ($\omega_0\tau_0 = 0.2$). The inset shows the same dependences at high frequencies; the dashed curves are calculated from the formula corresponding to the high-frequency limit.

Figure 7 shows the frequency dependence of the dielectric response calculated theoretically and observed in the *S*-2 and *S*-10 samples of a PT–PLT multilayer structure. The experimental data are seen to be adequately described by the theory in both low-frequency and high-frequency (of the order of a megahertz; crosses in Fig. 7) regions.

The absence of dispersion in the range 1–10^3 kHz in samples *S*-40 (whose layer thickness 50 Å was shown in [7] to be less than the critical value) can be due to the fact that in the paraelectric phase, which exists when $l < l_c$, the relaxation time is very short, $\tau \ll 10^{-6}$ s, and the relaxation term is negligible in the frequency range indicated above.

The prediction that the soft-mode frequency in a thin layer is always lower than that in a thick film (Fig. 2) agrees with the experimental data on Raman scattering in a $BaTiO_3$–$PbTiO_3$ multilayer [5]. In particular, the peak corresponding to the E_{TO} mode was shifted to lower frequencies with decreasing spatial period of the superlattice. We note, however, that the multilayer studied in [5] did not contain paraelectric layers and, therefore, the data presented in [5] can be considered only as an illustration of the predicted behavior.

The theory also predicts some specific features in the frequency dependence of the dielectric response of multilayers (in particular, in the paraelectric phase)

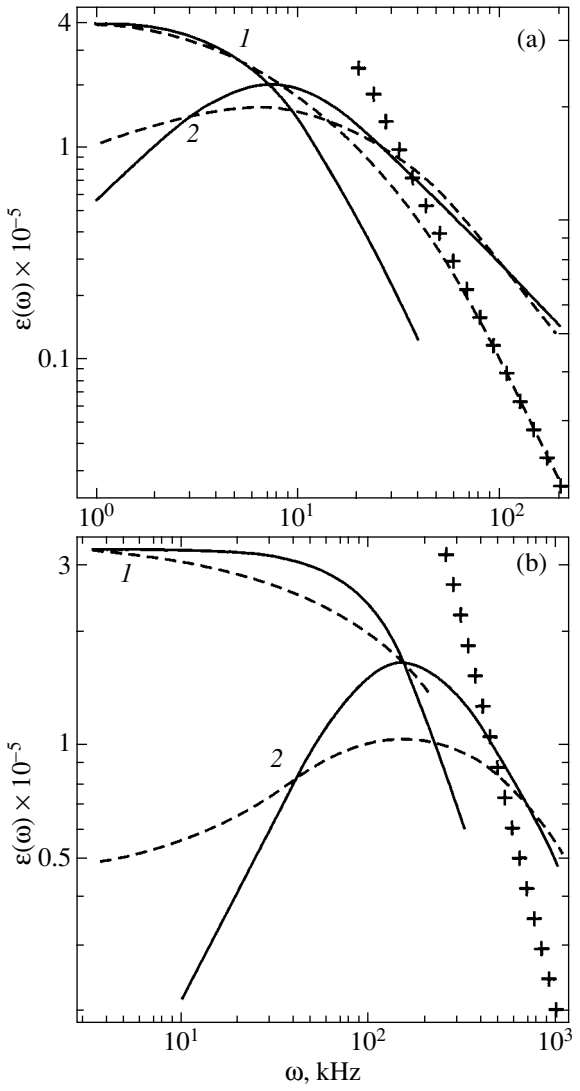

Fig. 7. Frequency dependence of (*1*) the real and (*2*) imaginary parts of the dielectric constant of a PL–PLT multilayer for samples (a) *S*-10 and (b) *S*-2. Solid curves are calculated from the formula $\varepsilon(\omega) = \varepsilon_0/(1 - i\omega\tau)$ for a purely relaxative response with $\varepsilon_0 = 4.1 \times 10^5$ and $\tau = 1.4 \times 10^{-4}$ s for sample *S*-10 and $\varepsilon_0 = 3.3 \times 10^5$ and $\tau = 6.7 \times 10^{-6}$ s for sample *S*-2. Dashed curves are experiment, and crosses represent calculations of the high-frequency limit $\varepsilon_B/(\omega\tau_B)^2$, where $\varepsilon_B/\tau_B^2 = 2 \times 10^{11}$ s^{-2}.

which should be observed near the frequencies of natural polarization oscillations in the layers (Fig. 6). However, the additional peaks of the susceptibility are seen to be much smaller than the main low-frequency peak (at $\omega \sim \omega_0$) of the imaginary part of the susceptibility and their experimental observation may prove to be a problem.

In closing, we note that, since one of the two layers of the multilayer unit cell under study is in the paraelectric phase at any temperature and, therefore, the layers can be considered to be independent of one another, the results obtained in this paper are relevant to both multilayers and isolated single films. In the latter case, however, the boundary conditions can differ from those in multilayers and calculations for ferroelectric films should be carried out for an arbitrary extrapolation length in much the same manner as the static dielectric susceptibility was calculated in [17]. The calculations performed in [17] showed that the main feature of the case of zero extrapolation length is that the critical thickness $l_c = kl_0$ reaches its maximum, $k_{\max} = \pi$, whereas in the case of a nonzero extrapolation length, we have $k < \pi$; for example, if $\delta = 0.6l_0$, then $k = 2$.

Otherwise, all dependences on the layer thickness and temperature are similar for different extrapolation lengths. Therefore, the dependences of the dynamical susceptibility on layer thickness and temperature calculated in this paper can be believed to hold for both multilayers and isolated single films.

APPENDIX

$$B_3 = \frac{B_1}{30\Delta}(160h^3 - 24(240 - 97m)h^2 + 36(1280 - 792m + 43m^2)h - 27m(5120 - 4864m + 945m^2)),$$

$$B_5 = \frac{B_1}{70\Delta}(224h^3 - (6272 - 3464m)h^2 + 24(896 - 708m + 45m^2)h - 9m(3584 - 5520m + 1725m^2)),$$

$$B_7 = 8\frac{B_1}{35\Delta}(10h^3 - 4(40 - 23m)h^2 + 3(160 - 96m + m^2)h - 9m(80 - 88m + 35m^2)).$$

Here, we introduced the notation $h = (1 + m)w$ and

$$\Delta = 16h^3 - 4(160 - 71m)h^2 + 6(1152 - 992m + 173m^2)h - 9(2048 - 2496m + 848m^2 - 75m^3).$$

The integrals $I_n(m)$ can easily be represented as a sum of standard integrals as presented, e.g., in [14]. After straightforward algebra, one can find the integrals of interest:

$$I_3(m) = \frac{m-2}{m}I_1(m) + \frac{2}{mK(m)},$$

$$I_5(m) = \frac{m^2 - 6m + 6}{m^2}I_1(m) - \frac{6 - 4m}{m^2K(m)},$$

$$I_7(m) = \frac{m^3 - 12m^2 + 30m - 20}{m^3}I_1(m) + \frac{18m^2 - 70m + 60}{3m^3K(m)}.$$

REFERENCES

1. S. L. Swartz and V. E. Wood, Condens. Matter News **1** (5), 4 (1992).
2. H. Tabata and T. Kawai, Appl. Phys. Lett. **70**, 321 (1997).
3. E. D. Specht, H.-M. Christen, D. P. Norton, and L. A. Boatner, Phys. Rev. Lett. **80** (19), 4317 (1998).
4. J. C. Jiang, X. Q. Pan, W. Tian, *et al.*, Appl. Phys. Lett. **74**, 2851 (1999).
5. F. Le Marrec, R. Farhi, M. El. Marssi, *et al.*, Phys. Rev. B **61**, R6447 (2000).
6. Y. Kim, R. A. Gerhardt, and A. Erbil, Phys. Rev. B **55** (14), 8766 (1997).
7. M. D. Glinchuk, E. A. Eliseev, V. A. Stephanovich, *et al.*, cond-mat/0004258.
8. Y. Ishibashi, H. Orihara, and D. R. Tilley, J. Phys. Soc. Jpn. **67** (9), 3292 (1998).
9. D. O. Neill, R. M. Bowman, and J. M. Gregg, Appl. Phys. Lett. **77** (10), 1520 (2000).
10. N. A. Pertsev, A. G. Zembrilgotov, and A. K. Tagantsev, Phys. Rev. Lett. **80** (9), 1988 (1998).
11. B. D. Qu, W. L. Zhong, and R. H. Prince, Phys. Rev. B **55** (17), 11218 (1997).
12. V. G. Vaks, *Introduction to the Microscopic Theory of Ferroelectrics* (Nauka, Moscow, 1973).
13. A. Deineka, M. D. Glinchuk, L. Jastrabik, *et al.*, Phys. Status Solidi A **175**, 443 (1999).
14. I. S. Gradshteyn and I. M. Ryzhik, *Table of Integrals, Series, and Products* (Fizmatgiz, Moscow, 1963; Academic, New York, 1980).
15. *Heigher Transcendental Functions (Bateman Manuscript Project)*, Ed. by A. Erdelyi (McGraw-Hill, New York, 1955; Nauka, Moscow, 1967), Vol. 3.
16. R. W. Hamming, *Numerical Methods for Scientists and Engineers* (McGraw-Hill, New York, 1962; Mir, Moscow, 1968).
17. M. D. Glinchuk, E. A. Eliseev, and V. A. Stephanovich, cond-mat/0103083.

Translated by Yu. Epifanov

Physics of the Solid State, Vol. 44, No. 5, 2002, pp. 964–971. Translated from Fizika Tverdogo Tela, Vol. 44, No. 5, 2002, pp. 923–929.

LATTICE DYNAMICS AND PHASE TRANSITIONS

Negative Longitudinal Expansion and the Amplitude of Longitudinal Vibrations in Poly(ethylene) Crystals

A. I. Slutsker*, V. L. Gilyarov*, G. Dadobaev*, L. A. Laĭus, I. V. Gofman**, and Yu. I. Polikarpov*****

** Ioffe Physicotechnical Institute, Russian Academy of Sciences, Politekhnicheskaya ul. 26, St. Petersburg, 194021 Russia*

*** Institute of Macromolecular Compounds, Russian Academy of Sciences, Bol'shoĭ pr. 31, St. Petersburg, 199004 Russia*

**** St. Petersburg State Technical University, Politekhnicheskaya ul. 29, St. Petersburg, 195251 Russia*

e-mail: Alexander.Slutsker@pop.ioffe.rssi.ru

Received June 19, 2001

Abstract—The experimental temperature dependences of the thermal expansion coefficient and the mean-square amplitude of atomic vibrations in the longitudinal direction (along the axes of chain molecules) in poly(ethylene) crystals of different sizes are measured using x-ray diffraction in the temperature range 5–350 K. Theoretical calculations of the temperature dependences of the thermal expansion coefficient and the mean-square amplitude of atomic vibrations in poly(ethylene) crystals are carried out. It is shown that the results of calculations are in good agreement with experimental data. The temperature ranges in which the quantum character of lattice dynamics affects the thermal expansion coefficient and the mean-square amplitude of vibrations are determined. It is revealed that the shear longitudinal modes play an important role in the lattice dynamics of crystals with a chain structure. © *2002 MAIK "Nauka/Interperiodica".*

1. INTRODUCTION

Molecular dynamics in polymer crystals has attracted the particular attention of many researchers by virtue of the specific features associated with strong anisotropy of the elastic characteristics in these materials. This anisotropy stems from a chain structure of crystals in which the rigidity of interatomic bonds in the longitudinal direction (along the molecular axes) is several orders of magnitude higher than the flexural and torsional rigidities and the rigidity of bonds in the transverse direction, i.e., between the chain molecules.

It is well known that the aforementioned anisotropy is responsible for the negative sign of the longitudinal thermal expansion coefficient $\alpha_\parallel$ [1]. The negative longitudinal thermal expansion in like crystals has been analyzed in a number of works [2–5]. For the classical temperature range, Chen *et al.* [4, 5] calculated the linear thermal expansion coefficient along the axis of a chain polymer molecule with the inclusion of flexural and torsional transverse vibrational modes. It turned out that the longitudinal thermal expansion coefficient $\alpha_\parallel$ calculated for poly(ethylene) at room temperature agrees closely with the experimental data. However, as far as we know, theoretical calculations of the longitudinal thermal expansion coefficients over a wide range of temperatures (beginning with the lowest temperature at which quantum effects manifest themselves) or comparison of the calculated coefficients with the corresponding experimental data have never been performed. Furthermore, such an important dynamic characteristic as the mean-square amplitude of atomic vibrations in the longitudinal direction has not been considered to date.

The purposes of the present work were as follows. (1) Measurements of the temperature dependences of the thermal expansion coefficient and the mean-square amplitude of atomic vibrations in the longitudinal direction over a wide temperature range (5–350 K) for poly(ethylene) crystals. (2) Calculation and theoretical analysis of the temperature dependences of these quantities for poly(ethylene) in the same temperature range. (3) A comparison of the calculated and experimental results.

2. EXPERIMENTAL TECHNIQUE

The experiments were performed with samples of oriented poly(ethylene) of two types: (i) samples with poly(ethylene) large-sized crystalline grains (PEL) and (ii) samples with poly(ethylene) small-sized crystalline grains (PES).

The PEL samples were prepared by annealing of preliminarily oriented plates under high pressure.[1]

[1] We are grateful to Yu.A. Zubov (Karpov Research Institute of Physical Chemistry) for supplying the samples used in our investigations and for many pieces of helpful advice.

1063-7834/02/4405-0964$22.00 © 2002 MAIK "Nauka/Interperiodica"

According to x-ray diffraction measurements, the linear sizes of crystalline grains are equal to 90–100 nm along the molecular axes and 50–60 nm in the transverse direction.

The PES samples were produced through a conventional fivefold orientational extension of a poly(ethylene) film at a temperature of 350 K. The crystalline grain sizes in the longitudinal and transverse directions were equal to 12–14 and 16–18 nm, respectively.

The choice of poly(ethylene) samples containing crystalline grains of two significantly different sizes was made from theoretical estimates (see below), according to which the thermodynamic characteristics depend on the crystalline grain size (especially in the longitudinal direction).

The temperature dependences of the thermal expansion coefficient and the mean-square vibration amplitude for crystal lattices in the longitudinal direction were determined from changes in the parameters of meridional (i.e., along the orientation axis of the sample) x-ray reflections with temperature.

The angular difference between the centers of gyration of the reflection at different temperatures T was used to determine the thermal expansion $\varepsilon_\parallel$ of the lattice and the longitudinal thermal expansion coefficient $\alpha_\parallel$:

$$\alpha_\parallel(T) = \frac{d\varepsilon_\parallel(T)}{dT}.$$

The temperature dependence of the mean-square amplitude of atomic vibrations $\langle\delta_\parallel^2\rangle(T)$ in the longitudinal direction was calculated from the temperature dependence of the reflection intensity $I(T)$ according to the standard expression for the Debye–Waller factor [6].

In order to determine the parameters $\alpha_\parallel$ and $\langle\delta_\parallel^2\rangle$ more reliably, the diffraction measurements were performed with the use of filtered radiation at two wavelengths: CuK_α radiation ($\lambda = 0.154$ nm) and MoK_α radiation ($\lambda = 0.071$ nm). In the case of MoK_α radiation, we used reflections of two orders. The measurements were performed on a DRON-1.0 x-ray diffractometer equipped with a thermocryostat attachment, which made it possible to change the sample temperature from ~5 to 350 K.

3. EXPERIMENTAL RESULTS

Figure 1 illustrates the temperature behavior of the (002) meridional reflection (CuK_α radiation) for the PEL sample at the lowest and highest temperatures. Similar results are obtained using CuK_α and MoK_α radiation types for PEL and PES samples at intermediate temperatures.

For CuK_α radiation with a longer wavelength, it was possible to measure only the first-order reflection (002).

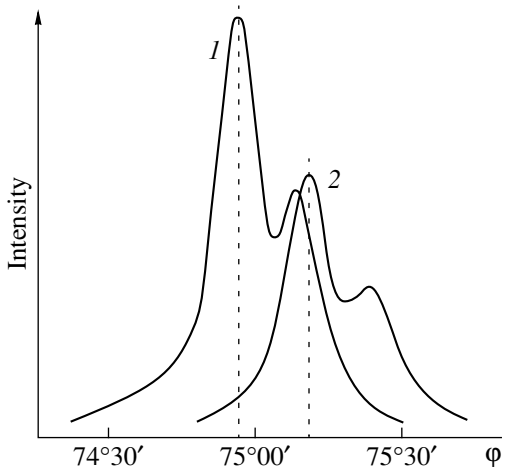

Fig. 1. The (002) meridional reflection (CuK_α radiation) at temperatures of (*1*) 5 and (*2*) 350 K.

The first-order (002) and second-order (004) meridional reflections were measured for MoK_α radiation.

The splitting of the (002) reflection shown in Fig. 1 is associated with the presence of two radiation components, namely, Cu$K_{\alpha1}$ and Cu$K_{\alpha2}$. In the case of MoK_α radiation, the splitting is more pronounced, specifically at lower temperatures. This splitting will be used for analyzing the reflection intensity (see below).

Examination of the angular widths of meridional reflections of two orders demonstrated that the crystal lattices in PEL and PES samples exhibit a very low degree of distortion ($<10^{-4}$) in the longitudinal direction and that the crystalline grain sizes in the longitudinal direction are equal to 90–100 nm for PEL and 12–14 nm for PES.

According to our analysis of the angular widths of equatorial reflections (their contours are not presented in this work), the crystalline grain sizes in the transverse direction are 50–60 nm for PEL and 16–18 nm for PES.

3.1. Negative longitudinal expansion of crystalline grains. As can be seen from Fig. 1, an increase in the temperature brings about a shift of the reflection toward the large-angle range. It should be noted that a similar shift toward the large-angle range was observed in all the diffraction measurements.

For longitudinal lattice strains, differentiation of the Bragg equation gives the following relationship:

$$\varepsilon_\parallel = \frac{\Delta d}{d} = -\frac{\Delta\varphi}{2\tan\varphi_m/2}, \quad (1)$$

where d and Δd are the interplanar distance and its change, respectively, and φ_m and $\Delta\varphi$ are the angular position of the reflection and its angular difference, respectively. This implies a lattice contraction in the longitudinal direction at the positive difference $\Delta\varphi$.

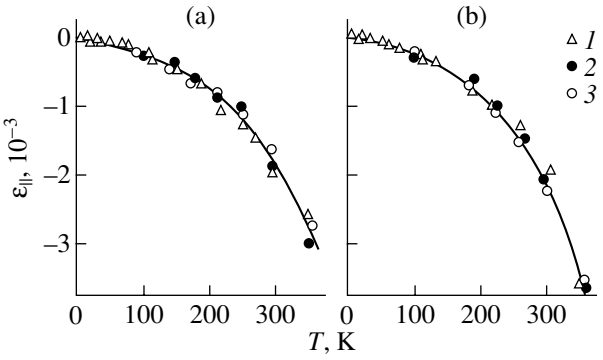

Fig. 2. Temperature dependences of the longitudinal thermal contraction for (a) PEL and (b) PES crystal lattices: (*1*) CuK_α radiation, (*2*) MoK_α radiation (first-order reflection), and (*3*) MoK_α radiation (second-order reflection).

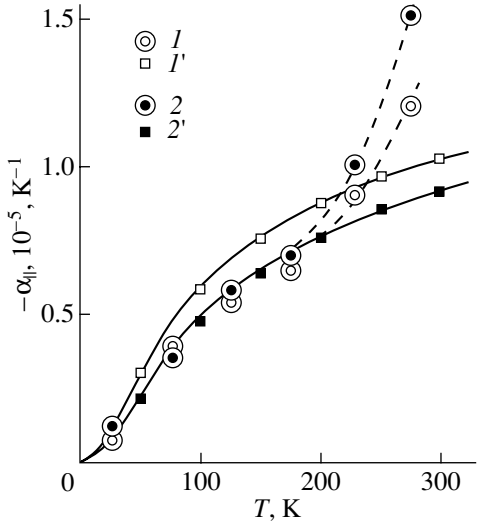

Fig. 3. (*1*, *2*) Experimental and (*1*', *2*') calculated temperature dependences of the negative longitudinal thermal expansion coefficient for (*1*, *1*') PEL and (*2*, *2*') PES crystal lattices.

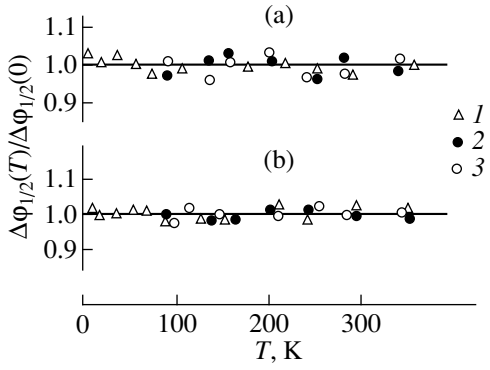

Fig. 4. Constancy of the angular width of the meridional reflection with variations in temperature for (a) PEL and (b) PES: (*1*) CuK_α radiation, (*2*) MoK_α radiation (first-order reflection), and (*3*) MoK_α radiation (second-order reflection).

By using relationship (1) and the experimental dependences $\Delta\varphi(T)$, we obtain the dependences $\varepsilon_{\|}(T)$ for PEL and PES crystal lattices in the temperature range 5–350 K (Fig. 2). It is seen from Fig. 2 that, for each poly(ethylene) sample, the points attributed to different radiation types and reflections of different orders lie along the same curve. This indicates that the dependence $\varepsilon_{\|}(T)$ is determined with a high degree of accuracy.

Differentiation of the dependences $\varepsilon_{\|}(T)$ gives the temperature dependence of the thermal expansion coefficient in the longitudinal direction (Fig. 3):

$$\alpha_{\|}(T) = \frac{d\varepsilon_{\|}(T)}{dT}.$$

First and foremost, we should note that the dependences $\alpha_{\|}(T)$ for PEL and PES crystal lattices can be considered to be virtually coincident with due regard for the spread of points with respect to the approximating curves in Fig. 2.

The main result obtained from the analysis of the temperature dependences $\alpha_{\|}(T)$ resides in the fact that the negative longitudinal thermal expansion coefficient $\alpha_{\|}$ strongly depends on the temperature; more specifically, $\alpha_{\|}$ changes from 0 at $T = 0$ to $\sim -1.5 \times 10^{-5}$ at $T =$ 300 K. Earlier, this circumstance escaped proper attention and was not analyzed theoretically in a quantitative way. This analysis will be carried out below.

3.2. Amplitudes of longitudinal vibrations in crystalline grains. The vibration amplitudes were determined from the data on the temperature behavior of the meridional reflections (Fig. 1).

It can be seen from Fig. 1 that, apart from the angular difference, the reflection is characterized by a decrease in the intensity with an increase in temperature. A similar change in the reflection intensity is observed in all the diffraction measurements. It should be emphasized that, in this case, the angular width of reflections ($\Delta\varphi_{1/2}$) remains virtually constant. This can be judged from the data presented in Fig. 4 for the PEL and PES samples, CuK_α and MoK_α radiation types, and reflections of two orders.

The constancy of the angular width of the reflections under investigation allows us to use the peak intensity when calculating the Debye–Waller factors [6]. The temperature dependence of the peak intensity of the meridional reflection is depicted in Fig. 5.

As follows from the theory of diffraction, a decrease in intensity of crystalline reflections is caused by the spreading of Bragg planes in the crystal lattice. For the (002) reflection of poly(ethylene), this spreading is associated with thermal vibrations of carbon atoms in the direction perpendicular to the (002) plane, i.e., along the axes of chain molecules. By designating the

mean-square amplitude of these vibrations as $\langle \delta_{\parallel}^2 \rangle$, we can write, according to [6], the following expression:

$$I(T) = I(0)\exp\left(-n4\pi^2\frac{\langle \delta_{\parallel}^2\rangle}{d^2}\right), \quad (2)$$

where $I(0)$ and $I(T)$ are the peak intensities of the reflection at $T = 0$ and $T > 0$, respectively, and n is the order of the reflection.

For correct application of expression (2), the following conditions should be met when processing the experimental data.

(i) The crystalline component should be separated from the measured reflection intensity; i.e., it is necessary to eliminate the instrument background and the thermal diffuse scattering intensity which increases with a rise in the temperature. This separation can be efficiently accomplished using the doublet splitting of the reflection for which the ratio between the crystalline components $I(K_{\alpha 1})$ and $I(K_{\alpha 2})$ is known [6]. This provides a means of determining the actual intensities of the crystalline reflections.

(ii) The component attributed only to the lattice dynamics should be separated from the temperature dependence of the intensity of the crystalline reflection; i.e., it is necessary to eliminate the decrease in the reflection intensity, for example, due to amorphization at the crystalline grain boundaries with an increase in the temperature, which leads to a decrease in the coherence volume. This separation can be achieved with reflections of two orders. From expression (2), we obtain

$$\langle \delta_{\parallel}^2\rangle(T) = \frac{d^2}{12\pi^2}\left\{\ln\left[\frac{I'(T)}{I''(T)}\frac{I''(0)}{I'(0)}\right]\right\}, \quad (3)$$

where $I'(0)$ and $I'(T)$ are the intensities of the first-order crystalline reflection at $T = 0$ and $T > 0$, respectively, and $I''(0)$ and $I''(T)$ are the intensities of the second-order crystalline reflection at $T = 0$ and $T > 0$, respectively.

The experimental data on the temperature dependences of the reflection intensity were processed according to formula (3). As a result, we obtained the temperature dependences of the mean-square amplitude of longitudinal vibrations $\langle \delta_{\parallel}^2 \rangle$ for PEL and PES crystal lattices (Fig. 6). As can be seen from Fig. 6, these dependences exhibit similar behavior. It is worth noting that the values of $\langle \delta_{\parallel}^2 \rangle$ for the PEL crystal lattice are substantially larger than those for the PES crystal lattices.

With the aim of interpreting the magnitudes and temperature dependences of the longitudinal thermal expansion coefficient and the mean-square amplitude of longitudinal vibrations, we carried out a theoretical analysis.

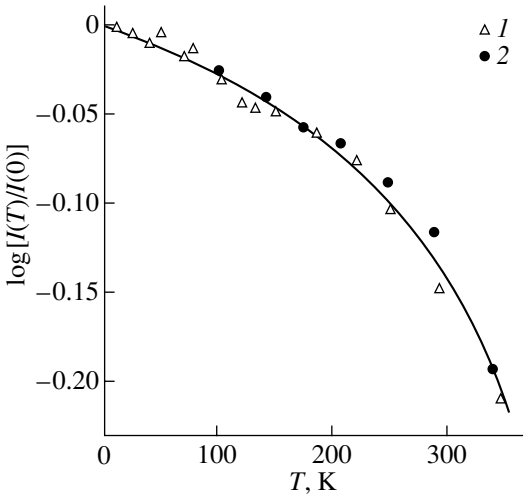

Fig. 5. Temperature dependence of the intensity of the meridional reflection for PEL: (*1*) CuK_α radiation and (*2*) MoK_α radiation (first-order reflection).

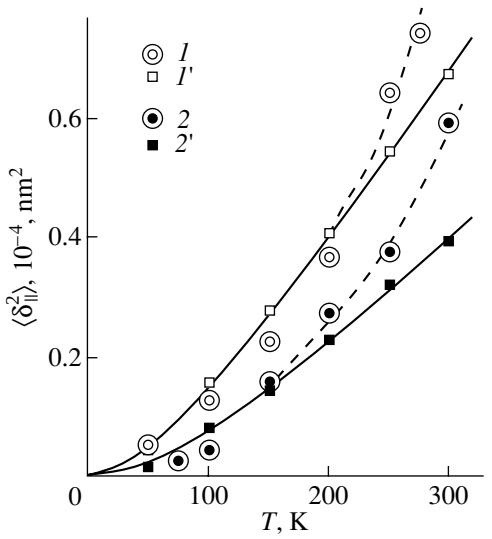

Fig. 6. (*1*, *2*) Experimental and (*1*', *2*') calculated temperature dependences of the mean-square amplitude of longitudinal vibrations for (*1*, *1*') PEL and (*2*, *2*') PES crystal lattices.

4. THEORETICAL ANALYSIS

4.1. Calculation of the longitudinal thermal contraction in poly(ethylene) crystals. The Stockmayer–Hecht model was chosen as a model of a polymer crystal (Fig. 7a). This model includes the characteristics required for describing the dynamic effects, makes it possible to calculate the amplitudes of longitudinal and

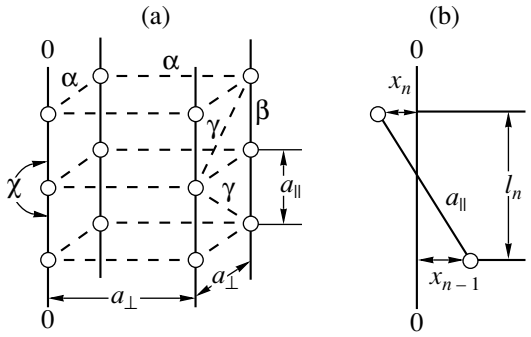

Fig. 7. (a) Stockmayer–Hecht model of a polymer crystal with a chain structure (α, β, γ, and χ are the force elastic constants) and (b) dynamics of a nonstretchable skeletal bond.

transverse vibrations, and, what is particularly important, accounts for the effect of flexural rigidity of the lattice (the coefficient γ). It is also significant that the phonon spectrum is known for the Stockmayer–Hecht model [7]. Thus, the thermodynamic parameters under investigation can be numerically calculated from the general principles of solid-state physics.

Since the longitudinal rigidity of the carbon-chain skeleton of a macromolecule is very high [for poly(ethylene), the modulus of longitudinal elasticity is approximately equal to 250 GPa and, correspondingly, the rigidity β is ~300 N m^{-1}], the poly(ethylene) molecule can be considered to be thermally nonstretchable when calculating the longitudinal thermal expansion coefficient. Chen *et al.* [4, 5] demonstrated that the longitudinal thermal expansion coefficient of a polymer crystal can be represented as an asymptotic expansion in terms of the parameter 1/β in which the main contribution is determined by a term independent of β. In this case, the change in the axial length of the studied molecule (the projection of the molecular contour onto the molecular axis) with a variation in temperature is governed primarily by transverse vibrations of the skeleton atoms. This model was accepted earlier in [3, 4] and is illustrated in Fig. 7b. Within this model, the projection of each link ($a_\parallel$ is the link length) onto the macromolecular axis is determined by the square of the difference between the transverse displacements of the neighboring atoms, that is,

$$l_n \approx a_\parallel - \frac{(x_n - x_{n-1})^2}{2a_\parallel}. \tag{4}$$

The addition term to $\langle l_n \rangle$ due to the proper elongation of $a_\parallel$ at the expense of a finite rigidity β appears to be $\sim l/\beta$, whereas the second term in relationship (4) considerably exceeds this quantity [4, 5].

Consequently, the longitudinal thermal expansion coefficient can be represented in the following form:

$$\alpha_\parallel = \frac{1}{a_\parallel}\frac{d\langle l_n \rangle}{dT} = -\frac{1}{2a_\parallel^2}\frac{d\langle (x_n - x_{n-1})^2 \rangle}{dT}. \tag{5}$$

Therefore, in order to calculate the longitudinal thermal expansion coefficient, it is necessary to determine the transverse-displacement correlator in relationship (5).

For convenience of calculations, it is expedient to change over from vibrations of individual atoms to normal lattice vibrations (phonons).

The mean-square amplitude $\langle u_n^2 \rangle_i$ of atomic vibrations along the *i*th axis is defined by the expression [8]

$$\langle u_n^2 \rangle_i = \frac{1}{N}\sum_n u_{i,n}^2 = \sum_{q,a} U_{q,\alpha}^2. \tag{6}$$

Here, $U_{q,\alpha}$ are the amplitudes of normal modes of the αth branch with the wave vector *q*, which make a contribution to the mean-square amplitude $\langle u_n^2 \rangle_i$, and *N* is the number of atoms in the crystal. For transverse vibrations, we have $u_n = x_n$.

In the case when the interaction between polymer chains is relatively weak (the force elastic constant γ is very small), the phonon spectrum within the Stockmayer–Hecht model [7] is split into three acoustic branches, namely, two transverse branches and one longitudinal branch. Hence, the thermodynamic characteristics can be calculated by omitting the summation over branches in formula (6) and choosing precisely the spectral branch which makes a dominant contribution to the calculated parameter. It should be noted that, in the general case, this separation cannot be accomplished, because the displacements in the longitudinal and perpendicular directions are correlated and the normal modes of the system involve both the longitudinal and transverse displacement components.

According to Ziman [8], we can write the relationship

$$|U_q|^2 = \frac{\langle E_q \rangle}{Nm\omega_q^2}, \tag{7}$$

where *m* is the atomic mass, which is taken equal to the mass of a CH_2 group; *Nm* is the mass of the crystal; and $\langle E_q \rangle$ is the mean energy of the mode (i.e., the energy of a set of phonons with the wave vector *q*). Since the mean energy can be represented by the expression [9]

$$\langle E_q \rangle = \hbar\omega_q\left[\left(\exp\frac{\hbar\omega_q}{k_B T} - 1\right)^{-1} + \frac{1}{2}\right],$$

from relationship (7), we obtain

$$U_q(\omega_q, T) = \frac{\hbar}{Nm\omega_q}\left[\left(\exp\frac{\hbar\omega_q}{k_BT} - 1\right)^{-1} + \frac{1}{2}\right]. \quad (8)$$

The dispersion dependence for the transverse mode has the following form [7]:

$$\omega_\perp^2 = \frac{2}{m}\left[\frac{\alpha}{2}(1 - \cos\varphi_1) + \gamma(2 - \cos\varphi_1\cos\varphi_2 - \cos\varphi_1\cos\varphi_3) + \chi(1 - \cos\varphi_3)^2\right]. \quad (9)$$

Here, α, β, γ, and χ are the force elastic constants given in Fig. 7. The quantities φ_1 and φ_2 are related to the wave vector **q** of the transverse vibrations by the formulas

$$\varphi_1 = q_i a_\perp = 2\pi\frac{i}{N_\perp}, \quad -\frac{N_\perp}{2} \le i \le \frac{N_\perp}{2},$$

$$\varphi_2 = q_j a_\perp = 2\pi\frac{j}{N_\perp}, \quad -\frac{N_\perp}{2} \le j \le \frac{N_\perp}{2}.$$

The quantity φ_3 and the wave vector in the longitudinal direction are related by the expressions

$$\varphi_3 = q_k a_\parallel = 2\pi\frac{k}{N_\parallel}, \quad -\frac{N_\parallel}{2} \le k \le \frac{N_\parallel}{2},$$

where $a_\parallel$ and $a_\perp$ are the interatomic distances and $N_\parallel$ and $N_\perp$ are the numbers of atoms in the transverse and longitudinal directions, respectively. Therefore, the summation over wave vectors in relationships (6), (8), and (9) reduces to the summation over the indices *i*, *j*, and *k*.

It follows from expression (5) that the longitudinal thermal expansion coefficient is determined by correlator (6) rather than by the mean-square vibration amplitude, because the displacements of neighboring atoms are not statistically independent. This correlator can easily be calculated in normal coordinates and has the form

$$\langle(x_n - x_{n-1})^2\rangle = 4\sum_q U_q^2(1 - \cos\varphi_3). \quad (10)$$

This relationship makes allowance for two vibrational modes in the transverse direction.

With due regard for relationships (8) and (9), the expression for numerical calculations of correlator (10) takes the form

$$\langle(x_n - x_{n-1})^2\rangle(T) = 32\sum_{i=1}^{N_\perp/2}\sum_{j=1}^{N_\perp/2}\sum_{k=1}^{N_\parallel/2} U_q^2[\omega_1(q), T](1 - \cos\varphi_3). \quad (11)$$

In calculations for poly(ethylene), we used the force elastic constants α = 3.2 N m^{-1}, β = 300 N m^{-1}, γ = 0.16 N m^{-1}, and χ = 35 N m^{-1} [4] and the interatomic distances $a_\parallel$ = 0.13 nm and $a_\perp$ = 0.4 nm.[2] In accordance with the experimental sizes of crystalline grains, the following numbers of atoms were taken for calculations: $N_\parallel$ = 800 and $N_\perp$ = 140 for the large-sized crystal and $N_\parallel$ = 100 and $N_\perp$ = 40 for the small-sized crystal.

The temperature dependence of the longitudinal thermal expansion coefficient was obtained by differentiating expression (11) with respect to temperature.

The calculated and experimental dependences $\alpha_\parallel(T)$ for both crystals are compared in Fig. 3. This comparison revealed the following features.

(i) The calculated dependences $\alpha_\parallel(T)$ also indicate that the longitudinal thermal expansion coefficient substantially changes with a variation in temperature in the range below 200 K.

(ii) The calculated longitudinal thermal expansion coefficients for the large-sized and small-sized crystals differ only slightly. The estimates demonstrate that correlator (11) weakly depends on the crystal size in the transverse direction at $N_\perp > 20$ and is virtually independent of the crystal size in the longitudinal direction at $N_\parallel > 100$.

(iii) The calculated and experimental dependences $\alpha_\parallel(T)$ almost coincide in the range $T < 200$ K. As the temperature increases above 200 K, the experimental values of the negative longitudinal thermal expansion coefficient $\alpha_\parallel$ become increasingly higher than the calculated values. This can be explained by the fact that the Stockmayer–Hecht model is no more than a rough approximation for poly(ethylene) crystals (the skeletons of poly(ethylene) molecules have the form of a planar zigzag whose planes are perpendicular to each other in a unit cell of the poly(ethylene) crystal [10]) which disregards torsional vibrations and anharmonicity of intermolecular interactions. It seems likely that all these factors are of little significance at low temperatures but begin to play an increasingly important role with a rise in temperature ($T >$ ~200 K).

4.2. Calculation of the mean-square amplitude of longitudinal vibrations in poly(ethylene) crystals. The particular interest expressed in this parameter is associated with its unexpectedly high values observed in experiments (Fig. 6). Indeed, the classical expression $\langle\delta_\parallel^2\rangle \approx kT/\beta$ gives an obviously overestimated amplitude of longitudinal vibrations of the skeleton atoms in the poly(ethylene) chain molecule: $\langle\delta_\parallel^2\rangle \approx 0.1\times10^{-4}$ nm^2 at T = 300 K. This value is overestimated because, owing to the high characteristic temperature (~1000 K), the longitudinal vibrations are not completely excited at room temperature and, hence, their mean amplitude should be appreciably less than the classical amplitude. At the same time, it is clearly seen from Fig. 6 that the

[2] The choice of the flexural constant χ, which is equal to the rigidity upon a change in the bond angle, will be discussed below.

value of $\langle \delta_n^2 \rangle$ at $T = 300$ K is approximately equal to 1.0×10^{-4} nm^2; i.e., it is approximately one order of magnitude larger than the aforementioned estimate. Therefore, the amplitude of longitudinal vibrations of the skeleton atoms in the poly(ethylene) crystal is determined by vibrational modes other than internal longitudinal vibrations of atoms in the poly(ethylene) molecule.

The amplitude of longitudinal atomic vibrations in the poly(ethylene) lattice is calculated from formula (6). In contrast with the calculation of the thermal expansion coefficient, in this case, there is a need to use the longitudinal branch of the phonon spectrum. The dispersion relationship for this branch can be written in the form [7]

$$\omega_\parallel^2 = \frac{2}{m}\left[\frac{\beta}{2}(1-\cos\varphi_3) + \gamma(2-\cos\varphi_3\cos\varphi_1-\cos\varphi_3\varphi_2)\right]. \quad (12)$$

Here, the designations are the same as in the above formulas. Note that relationship (12) includes neither the flexural constant χ nor the constant α of the transverse interaction between the nearest neighbors in the adjacent chains.

The computational formula for the mean-square amplitude of longitudinal vibrations has the form

$$\langle \delta_\parallel^2 \rangle(T) = 8\sum_{i=1}^{N_\perp/2}\sum_{j=1}^{N_\perp/2}\sum_{k=1}^{N_\parallel/2} U_q^2[\omega_\parallel(q), T]. \quad (13)$$

The constants entering into expression (13) are taken equal to those used in the above calculations.

The calculated values of $\langle \delta_\parallel^2 \rangle$ for crystalline grains of both sizes are given in Fig. 6. It should be noted that the component related to zero-point vibrations ($\sim 0.2 \times 10^{-4}$ nm^2) is subtracted from the calculated amplitudes.

The results obtained can be summarized as follows. (1) The calculated amplitudes $\langle \delta_\parallel^2 \rangle$ for both the large-sized and small-sized crystals differ noticeably. The estimates indicate that the mean-square amplitude of longitudinal vibrations is virtually independent of the crystal size in the transverse direction at $N_1 > 20$ ($N_2 > 20$). Therefore, the observed difference in $\langle \delta_\parallel^2 \rangle$ is associated with the difference in crystal sizes in the longitudinal direction. (2) The calculated and experimental dependences of the mean-square amplitude $\langle \delta_\parallel^2 \rangle$ virtually coincide in the temperature range below 200 K. As the temperature increases above 200 K, the discrepancy between the calculated and experimental data increases progressively but remains less pronounced than in the case of the longitudinal thermal expansion coefficient (Fig. 3). The reasons for this discrepancy are most likely the same as those for the longitudinal thermal expansion coefficient (see above). The force elastic constant γ of the diagonal interaction between atoms in the adjacent chains (Fig. 7a) makes the main contribution to the calculated amplitudes $\langle \delta_\parallel^2 \rangle$. The proper longitudinal rigidity of the molecules (the force elastic constant β in Fig. 7a) is very high, and, hence, the intramolecular longitudinal atomic vibrations contribute insignificantly to the mean-square amplitude of longitudinal vibrations (see above). On the other hand, the shear longitudinal displacements of atoms in the adjacent chains becomes possible owing to the low value $\gamma \sim 0.16$ N m^{-1} [4]. This can lead to the observed spreading of the (002) Bragg planes.

Thus, it can be assumed that the shear vibrations (the longitudinal displacements of chains with respect to each other) play an important role in the dynamics of the lattice with a chain structure. Earlier, the contribution of these vibrations to the lattice dynamics was ignored.

A close agreement between the calculated and experimental dependences $\alpha_\parallel(T)$ and $\langle \delta_\parallel^2 \rangle(T)$ over a wide range of temperatures (from 0 to ~200 K) indicates that the lattice dynamics in poly(ethylene) crystals is adequately described in the framework of the proposed model.

A theoretical analysis of the strong dependence $\alpha_\parallel(T)$ in the temperature range from 0 to ~200 K revealed a significant role played by quantum effects, viz., gradual defreezing of modes in the spectrum of longitudinal vibrations. Judging from the calculated dependence $\alpha_\parallel(T)$, the Debye temperature of the transverse vibrations can be estimated at ~100 K. This estimate agrees with those given in [1].

The theoretical model considered above is not entirely consistent with the real geometry of poly(ethylene) crystals. A real molecule of poly(ethylene) has a planar transzigzag structure [11] and is characterized not only by the flexural vibrational mode associated with changes in the bond angles but also by the torsional transverse vibrational mode (twisting of a planar ribbon—the so-called transzigzag). Chen *et al.* [5] analyzed the influence of the torsional mode on the longitudinal thermal expansion coefficient of the poly(ethylene) lattice in the classical temperature range. It was shown that the contribution from this mode is close to the contribution from either of the two components of the flexural vibrations in the Stockmayer–Hecht model. Consequently, the longitudinal thermal expansion coefficient of the tetragonal lattice under consideration proves to be close to the longitudinal thermal expansion coefficient of the real poly(ethylene) molecule, which is determined by flexural and torsional vibrations.

For the mean-square amplitude of longitudinal vibrations, the calculated temperature dependence becomes linear at temperatures above ~50 K, which is

consistent with the classical dependence [11]. To put it differently, the quantum effects are significant at $T <$ 50 K. This can be explained by the fact that the constant of longitudinal shear vibrations is small and the characteristic temperature of these vibrations is low (estimated at 20–30 K).

In this work, we analyzed the experimental and calculated data for only one polymer, namely, poly(ethylene). This polymer is characterized by relatively weak forces of the interchain interaction (van der Waals bonds). The effect of the negative longitudinal thermal expansion is inherit in all polymers with a chain structure [1]. It is clear that the magnitudes of the longitudinal thermal expansion coefficient, the mean-square amplitude of longitudinal vibrations, and the characteristic temperatures (the ranges in which quantum effects manifest themselves) should depend on the intermolecular interaction.

ACKNOWLEDGMENTS

This work was supported by the Russian Foundation for Basic Research, project no. 00-03-33064a.

REFERENCES

1. Yu. K. Godovskiĭ, *Thermal Physics of Polymers* (Khimiya, Moscow, 1982).
2. I. M. Lifshitz, Zh. Éksp. Teor. Fiz. **22** (4), 475 (1952).
3. K. N. Kan, *Problems of Thermal Expansion of Polymers* (Leningr. Gos. Univ., Leningrad, 1975).
4. F. C. Chen, C. L. Choy, and K. Young, J. Polym. Sci., Polym. Phys. Ed. **18** (12), 2313 (1980).
5. F. C. Chen, C. L. Choy, S. P. Wong, and K. Young, J. Polym. Sci., Polym. Phys. Ed. **19** (6), 971 (1981).
6. A. Guinier, *Theorie et Technique de la Radiocristallographie* (Dunod, Paris, 1956; Fizmatgiz, Moscow, 1961).
7. W. H. Stockmayer and C. E. Hecht, J. Chem. Phys. **21** (11), 1954 (1953).
8. J. M. Ziman, *Principles of the Theory of Solids* (Cambridge Univ. Press, London, 1964; Mir, Moscow, 1966).
9. C. Kittel, *Introduction to Solid-State Physics* (Wiley, New York, 1976; Nauka, Moscow, 1978).
10. C. W. Bunn, Trans. Faraday Soc. **35**, 482 (1939).
11. J. Frenkel, *Kinetic Theory of Liquids* (Clarendon, Oxford, 1946; Akad. Nauk SSSR, Moscow, 1975).

Translated by O. Borovik-Romanova

Physics of the Solid State, Vol. 44, No. 5, 2002, pp. 972–977. Translated from Fizika Tverdogo Tela, Vol. 44, No. 5, 2002, pp. 930–934.

LATTICE DYNAMICS AND PHASE TRANSITIONS

Phonon Spectra and Thermodynamic Properties of Rare-Earth Hexaborides

N. N. Sirota*, V. V. Novikov, I. M. Sirota*, and T. D. Sokolovskiĭ*****

** Moscow State University of Nature-Oriented Activity, Moscow, Russia*

*** Bryansk State Pedagogical Institute, Bezhitskaya ul. 14, Bryansk, 241036 Russia*

e-mail: tcopr@bgpi.bitmcnit.bryansk.su

**** Institute of Solid-State and Semiconductor Physics, Belarussian National Academy of Sciences, ul. Brovki 17, Minsk, 220072 Belarus*

Received August 23, 2001

Abstract—The phonon spectra $g(\nu)$ of rare-earth hexaborides $Me B_3$ are calculated both in the approximation $Me B^* + B$ ($B^* = B_6$) without regard for bonding between metal and boron atoms and in the approximation making allowance for this bonding. The temperature dependences of the heat capacity are calculated from the dependences $g(\nu)$, and the results obtained are compared with the experimental data in the range 5–300 K. It is found that stretching vibrations in the metal and boron sublattices and between these sublattices variously affect the thermodynamic functions of hexaborides at low and high temperatures. *© 2002 MAIK "Nauka/Interperiodica".*

1. INTRODUCTION

A unit cell of rare-earth hexaborides has a body-centered cubic structure of the CsCl type in which the cube vertices are occupied by rare-earth atoms and the atomic group B_6 plays the role of a centering pseudoatom.

As an illustration, Fig. 1 shows the structure of lanthanum hexaboride with the distances between metal atoms (*Me*–*Me*), boron atoms (B–B) inside the B_6 (B*) pseudoatom centering the unit cell, and boron atoms (B–B) in the adjacent unit cells.

The distinctive feature of the unit cell of rare-earth hexaborides is that it involves the atomic group B_6 in which the B–B distances are somewhat longer than the bond between boron atoms of the adjacent unit cells.

When analyzing the lattice dynamics of rare-earth hexaborides, allowances are made for the following bonds: (i) bonds between the neighboring metal atoms (*Me*–*Me*), bonds between the metal atom and pseudoatom (*Me*–B_6), bonds inside the B_6 pseudoatom (B–B), and bonds between B_6 groups of the adjacent unit cells (B–B). The ratio of the total bonding energies for bonds between the metal atoms (*Me*–*Me*), the boron atoms (B–B), and the metal and boron atoms (*Me*–B) is of crucial importance. The atomization energy of rare-earth hexaborides can be considered as the sum of the atomization energies of the metal and boron sublattices and the energy of the *Me*–B bond. The table presents the reference values of atomization energies for rare-earth metals, boron, and B_6 and the formation energies for $Me B_6$ per mole of the relevant hexaboride [1, 2]. As follows from the table, the formation energy of the $Me B_6$ compound per gram-atom, which is referred to the standard states of the metal and boron, is substantially less than the atomization energy for the rare-earth element and boron. The relative fractions of bonding energies of the *Me*–*Me* bonds with respect to the *Me*–B and B–B bonds involved in the $Me B_6$ compounds are also given in the table.

Without going into detail on particular interatomic bonds in the unit cell of rare-earth hexaborides, we will analyze the lattice heat capacity and other thermodynamic properties of hexaborides in the framework of two macroscopic approaches. First, let us consider two sublattices, namely, the metal and boron sublattices, in the approximation of two Debye solids with a parabolic phonon spectrum in the case when bonds between these solids are ignored. As the second approximation, we consider the phonon spectrum of the metal–pseudoatom B* (B_6) compound with a CsCl-type structure and complement this spectrum with the density function of vibrational states inside the B_6 pseudoatom.

2. PHONON SPECTRUM OF HEXABORIDES AS A SUPERPOSITION OF DEBYE SPECTRA OF THE METAL AND BORON SUBLATTICES

The Debye spectrum of vibrational states $g(\nu) = dn/d\nu$ is uniquely determined by the Debye characteristic temperature Θ:

$$g(\nu) = (9N/\Theta^3)(h/k)^3\nu^2. \quad (1)$$

Here, N is the number of particles in the system, h is the Plank constant, and k is the Boltzmann constant.

The overall spectrum of the MeB_6 compound is determined as a superposition of the partial Debye spectra of the metal and boron, that is,

$$g_{MeB_6}(\nu) = g_{Me}(\nu) + g_B(\nu). \quad (2)$$

The characteristic temperatures for sublattices of rare-earth elements (Θ_{Me}) and boron (Θ_B) are listed in the table. These temperatures were determined recently by Novikov [3] from an analysis of the temperature dependences of the heat capacity for rare-earth hexaborides. Figure 2 shows the overall phonon spectrum of lanthanum hexaboride as a superposition of the partial spectra calculated for the characteristic temperatures of the corresponding sublattices (Θ_{La} = 205 K and Θ_B = 1230 K). The function $g_{LaB_6}(\nu)$, which was calculated earlier by Kunii [4] from the spectroscopic data, is given in Fig. 2 for comparison. It can be seen from Fig. 2 that, despite certain minor differences, these spectra exhibit similar behavior.

The phonon spectra of all the isostructural rare-earth hexaborides under investigation were obtained by the superposition of the Debye spectra of boron and the relevant metal and had a similar shape. The heat capacities $C_p(T)$ calculated for these hexaborides from the phonon spectra in the temperature range 300–1000 K differ from the experimental values by no more than 3–7% [3].

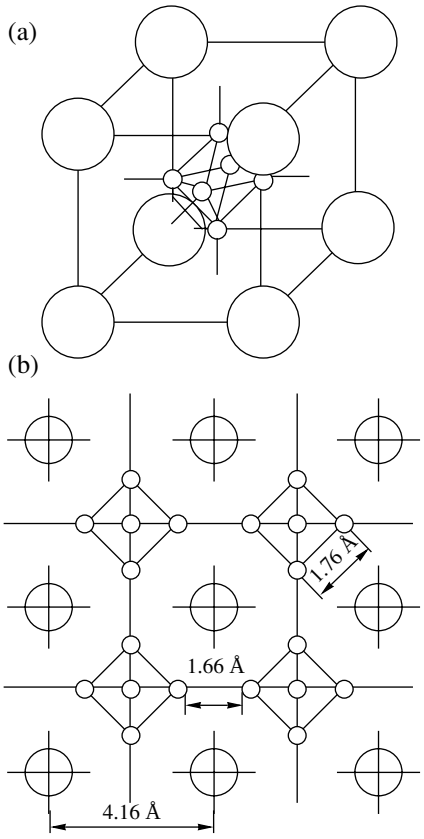

Fig. 1. Crystal structure of lanthanum hexaboride: (a) LaB_6 unit cell and (b) projection of the structure onto the $X0Y$ plane.

3. PHONON SPECTRA OF HEXABORIDES AS A SUPERPOSITION OF BORN–KÁRMÁN SPECTRA OF *Me*B*-TYPE STRUCTURES AND A BORON SPECTRUM

In the second approximation, the phonon spectra of rare-earth hexaborides are treated as spectra of rare-earth compounds with a CsCl-type structure in which the chlorine site is occupied by the B* (B_6) pseudoatom. Moreover, these spectra are complemented with the phonon spectra of boron atoms (within the approximation $MeB^* + B_6$). The molar mass m_{B^*} of the B* pseudoatom in this structure is equal to 64.86 g/mol, which amounts to approximately half the atomic mass of the rare-earth element.

Characteristics of rare-earth hexaborides for the calculation of the phonon spectra

Compound	U_{0Me}, kJ/mol	U_{MeB_6}, kJ/mol	U_0, kJ/mol	Fractions of bonding energies			Θ_{Me}, K	Θ_B, K	Lattice parameter a, Å	Molar volume of MeB^*, V_0, cm^3	$\beta\times10^6$, K^{-1}	m	n
				η_1	η_2	η_3							
LaB_6	431	470.4	535	1	1.23	1.31	205	1230	4.1563	43.2	15	4	12
CeB_6	423	340.2	517	1	1.22	1.33	203	1293	4.1396	42.7	16.5	4	12
PrB_6	455.6	418.3	489	1	1.38	1.58	210	1218	4.1327	42.5	16.8	4	12
NdB_6	427.6	431.8	475.9	1	1.45	1.72	200	1170	4.1266	42.3	15	4	12
SmB_6	208.7	456.1	417.2	1	2.0	2.70	210	1200	4.1334	42.5	13.5	4	12
EuB_6	175.3	471.2	402.5	1	2.30	3.21	198	1383	4.1844	43.9	12	4	6
GdB_6	397.5	481.7	514.4	1	1.29	1.42	212	1254	4.1066	41.92	17.4	4	12
TbB_6	388.7	494.8	510.9	1	1.31	1.45	207	1025	4.1052	41.55	18	5	12
DyB_6	290.4	504	462.4	1	1.59	1.94	208	1074	4.1008	41.4	18.6	5	14
B	562.7												

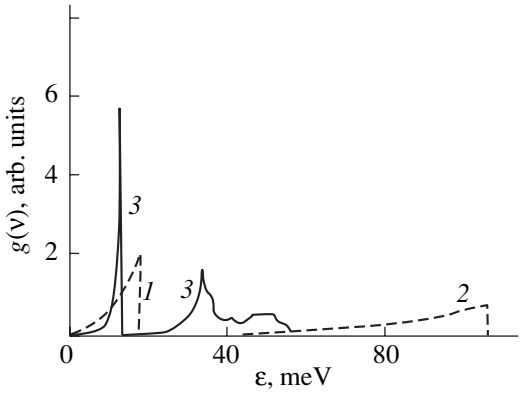

Fig. 2. Phonon spectrum of LaB_6: (*1*) the Debye phonon spectrum of the lanthanum sublattice $g_{La}(\nu)$, (*2*) the Debye phonon spectrum of the boron sublattice $g_B(\nu)$, and (*3*) the phonon spectrum of LaB_6 taken from [4].

The phonon spectra of *Me*B* compounds can be calculated according to the Born–Kármán–Delaunay method via solving the secular equation

$$\left|D(q) - M\omega^2 L\right| = 0. \quad (3)$$

Here, M is the atomic mass, L is the unity matrix, and $D(q)$ is the dynamic matrix specified by vector $\mathbf{q}$ [5–7].

The following three types of bonds in the CsCl-like lattice of *Me*B* should be considered in the calculation of the phonon spectrum: (i) j_1 is the bond between the metal atoms (*Me*–*Me*), (ii) j_2 is the bond between the metal atom and the B* (B_6) pseudoatom (*Me*–B*), and (iii) j_3 is the bond between the B* pseudoatoms (B*–B*). Each *Me*B* compound can be characterized by an expression relating the proportionality coefficients of the aforementioned bonding energies and the total atomization energy of the *Me*B* compound per gram-atom.

For the LaB_6 compound, the proportionality coefficients can be expressed in terms of the j_1 bond (*Me*–*Me*) as follows: $\eta_j = U_{0Me}/U_{0j}$. For the bonds j_1 (*Me*–*Me*), j_2(*Me*–B*), and j_3 (B*–B*), we obtain $\eta_1 = 1$, $\eta_2 = 1.23$, and $\eta_3 = 1.31$, respectively. We introduce the following notation: U_{0Me} is the atomization energy of the metal per gram-atom, U_{0B} is the atomization energy of boron, and U_{MeB_6} is the formation energy of the MeB_6 compound, which is referred to the standard state of the components.

These coefficients are introduced into the program to calculate the phonon spectra of *Me*B* crystals with a CsCl-type structure. The atomization energy per gram-atom of the *Me*B* compound can be determined from the relationship

$$U_0 = \frac{1}{2}(U_{0Me} + U_{0B} + U_{MeB_6}). \quad (4)$$

The Delaunay force constants were taken into account in the computation of four coordination spheres: $i = 1\ldots 4$. Their values are proportional to the second and first derivatives of the atomization energy in the function of distances between the nearest-neighbor atoms, which are taken at the points corresponding to the ith coordination spheres for each bond type j [5]:

$$\alpha_{ij} = (\partial^2 U_j)/\partial r^2)_{r_{ij}}, \quad (5)$$

$$\beta_{ij} = (-1/r)(\partial U_j)/\partial r)_{r_{ij}}. \quad (6)$$

The bonding energy as a function of the distance between the nearest-neighbor atoms can be conveniently expressed in the analytical form using the approximation of $U_j(r)$ in the form of the Mie–Grüneisen potential [8]

$$U_j = -(\alpha/r^m) + (\beta/r^n). \quad (7)$$

From the condition $(\partial U_j/\partial r)_{r_0} = 0$, we obtain

$$U_j = (U_0 mn/(n-m))[(1/m)(r_0/r)^m - (1/n)(r_0/r)^n]. \quad (8)$$

Consequently, the Delaunay force constants take the following form:

$$\alpha_{ij} = \frac{mn(m+1)U_{0j}k_i^{m+2}}{(n-m)^2}\left[1 - \frac{n+1}{m+1}k_i^{n-m}\right], \quad (9)$$

$$\beta_{ij} = -\frac{mnU_{0j}}{(n-m)r_0^2}k_i^{m+2}[1 - k_i^{n-m}], \quad (10)$$

where $k_i = r_0/r_i$ is the ratio of the radius of the first coordination sphere to the radius of the ith sphere.

The exponents n and m in relationships (7)–(10) are calculated according to the procedure described in [8]. In this case, the change in the interatomic distances r determines the change in the mole volume and depends on the presence of different-type atoms.

The $(m + n)$ value can be determined from the bulk modulus B [9], the bulk thermal expansion coefficient β [10], and the nomogram taken from [8]:

$$g = V_0\beta B/R, \quad (11)$$

where V_0 is the volume per gram-atom, β is the bulk thermal expansion coefficient, and R is the universal gas constant. The product mn can be calculated from the atomization energy of the hexaboride U_0, the volume per gram-atom V_0, and the bulk modulus B; that is,

$$mn = 9V_0B/U_0. \quad (12)$$

The characteristics of rare-earth hexaborides, which are used for calculating the exponents m and n, are given in the table.

The calculated phonon spectra of *Me*B* rare-earth compounds (*Me* = La, Ce, Nd, Pr, Sm, Eu, Gd, Tb, and Dy) for $m = 4$ and $n = 12$ are shown in Fig. 3.

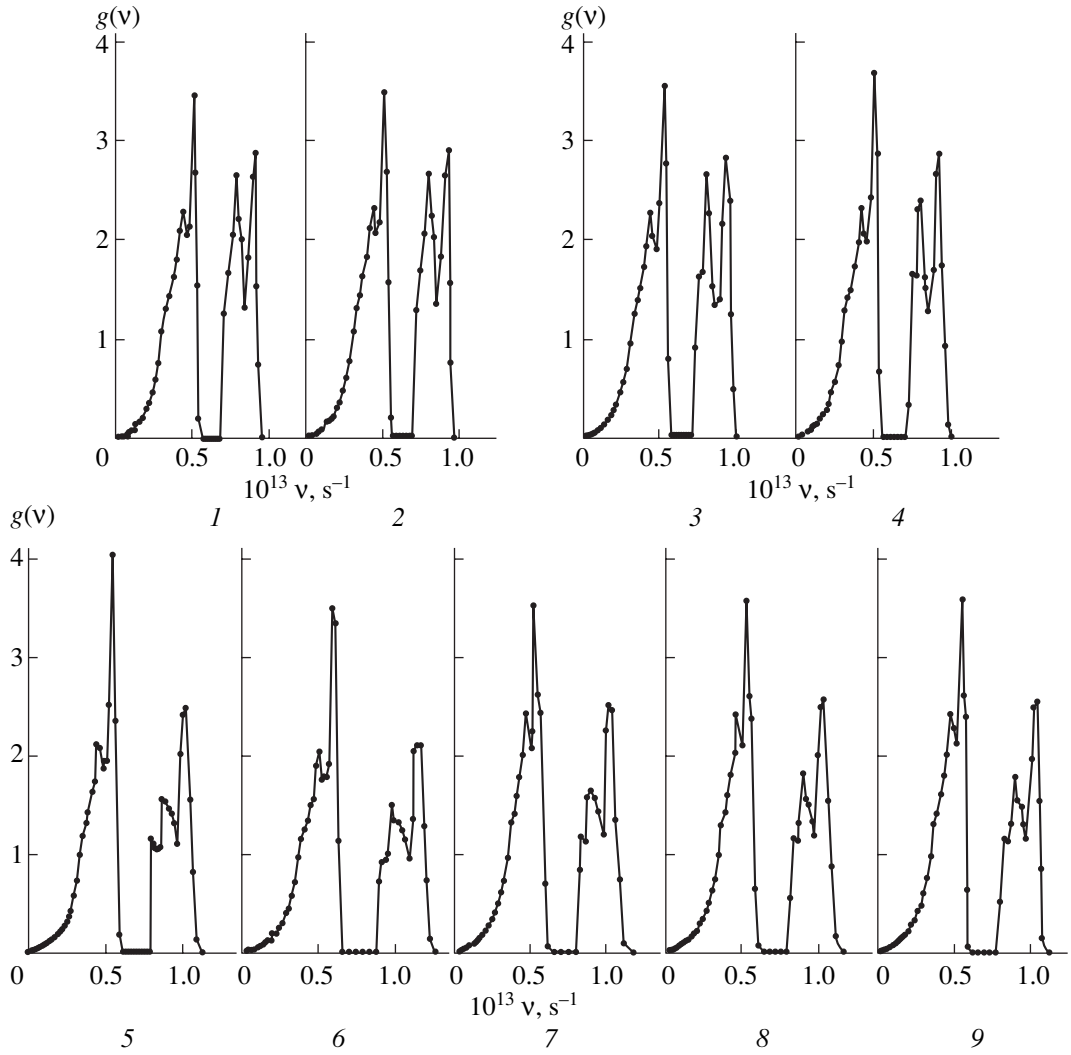

Fig. 3. Phonon spectra of *Me*B* structures: (*1*) LaB*, (*2*) CeB*, (*3*) PrB*, (*4*) NdB*, (*5*) SmB*, (*6*) EuB*, (*7*) GdB*, (*8*) TbB*, and (*9*) DyB*.

The second component of the overall phonon spectrum of MeB_6 hexaborides is the phonon spectrum of vibrational states of boron atoms inside the B* (B_6) pseudoatom. This component for all the hexaborides under investigation is approximated by the Gaussian function

$$g_B(\nu) = Ae^{-((\nu-\nu_0)/\nu)^2}, \quad (13)$$

which is cut off at the highest frequency ν_0. The frequency ν_0 is determined from the characteristic temperature for elemental amorphous boron $\Theta_B = 1217$ K [11]. The calculated phonon spectrum of boron atoms is shown in Fig. 4.

The overall phonon spectrum of MeB_6 hexaborides,

$$g_{MeB_6}(\nu) = g_{MeB^*}(\nu) + g_B(\nu), \quad (14)$$

is normalized to $3N_A$ (N_A is the Avogadro number).

4. LATTICE HEAT CAPACITY OF RARE-EARTH HEXABORIDES

The heat capacities of *Me*B* compounds $C_{MeB^*}(T)$ and boron $C_B(T)$ per gram-atom are calculated from the phonon spectra $g(\nu)$ by numerical integration:

$$C_v = \int_0^{\nu_m} g(\nu)(d\varepsilon/dT)d\nu, \quad (15)$$

where ν_m is the cutoff phonon frequency.

The molar lattice heat capacities of rare-earth hexaborides are calculated from the relationship

$$C_{MeB_6}(T) = 2C_{MeB^*}(T) + 5C_B(T). \quad (16)$$

The coefficient 2 of the first term accounts for the contribution of the *Me*B* diatomic pseudomolecule. The coefficient 5 of the second term allows for the contribu-

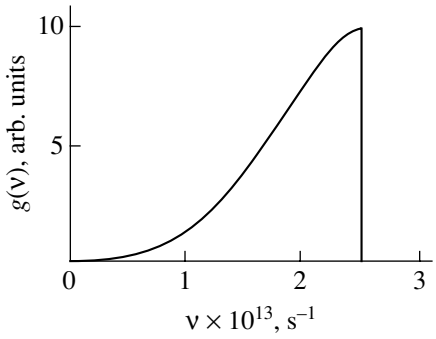

Fig. 4. Phonon spectrum of boron.

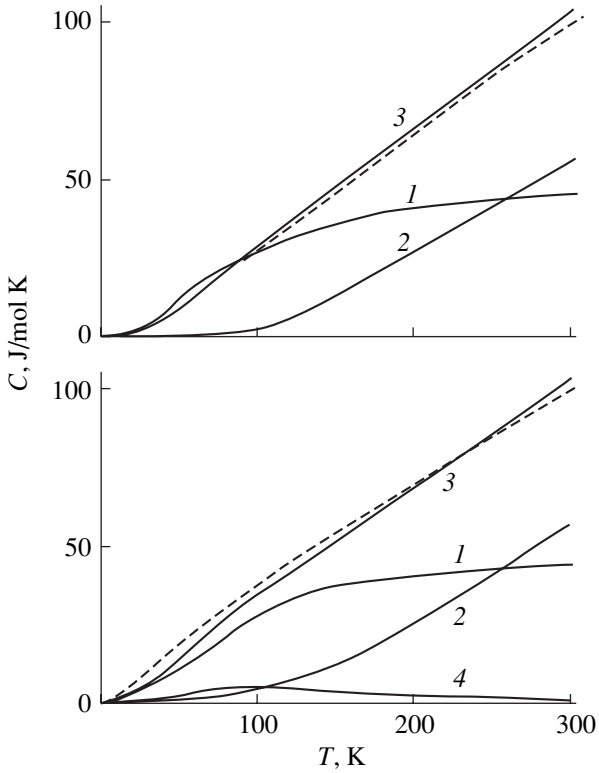

Fig. 5. Heat capacities calculated for hexaborides of (a) lanthanum and (b) neodymium from the phonon spectra and available data on the splitting of the energy levels: (*1*) $2C_{MeB^*}$, (*2*) $5C_B$, (*3*) $C = 2C_{MeB^*} + 5C_B$, and (*4*) $C_{Schottky}$. Dashed lines represent the experimental dependences.

tion of the boron atoms involved in the B_6 octahedron, except for one boron atom taken into account in the first term.

Figure 5 depicts the calculated dependences of the total heat capacity for hexaborides of lanthanum and neodymium in the temperature range 20–300 K. For NdB_6, the contribution of the Schottky heat capacity is taken into account in addition to the lattice contribution. For the greater part of the temperature range covered, the calculated and experimental values are in reasonable agreement. The electronic components of the heat capacity and contributions from anharmonicity are small in the temperature range under consideration and, hence, are disregarded.

Analysis of the calculated phonon spectra and lattice heat capacities of rare-earth hexaborides demonstrates that the (*Me*B* + B) model allows for the metal–boron bond and leads to a more realistic phonon spectrum compared to the model of independent sublattices. On the other hand, the (*Me* + B) model of independent sublattices agrees satisfactorily with the experimental data in the temperature range 5–300 K. The isobaric heat capacities $C_B(T)$, which were calculated from this model, are close to the heat capacities calculated from the (*Me*B* + B) model and agree with the experimental data [3].

At low temperatures (below 60–80 K), the lowest frequency vibrations among the possible vibrations are efficient, whereas the high-frequency vibrations are partially frozen. This explains the good agreement between the experimental heat capacities $C_{lat}(T)$ and the calculated values in the model of independent sublattices, including the range of a certain anomaly in the lattice heat capacity at T = 40–80 K.

At higher temperatures, the role of *Me*–B* and B–B high-frequency vibrations increases. Consequently, the *Me*B* model in the temperatures range 60–300 K gives results that are in close agreement with the experimental data. At temperatures above 100–200 K, the vibrations of boron atoms play a decisive role.

A satisfactory quantitative description of the temperature dependence of the lattice heat capacity $C_{lat}(T)$ at temperatures of 50–300 K and above in both the (*Me*B* + B) model and the approximation of independent sublattices can be explained as follows. (1) The characteristic temperature Θ_{Me} in the model of independent sublattices is lower than the temperature Θ_{MeB^*} by a factor of approximately three, whereas the mass of the B* (B_6) pseudoatom considerably exceeds the atomic mass of boron but is less than that of the metal by a factor of approximately 2.5; as a result, the bonding energies for the *Me*–*Me* and *Me*–B* bonds are close to each other. (2) At temperatures below T = 100 K, the heat capacity is determined primarily by the low frequencies of metal atom vibrations, which are close in magnitude in both models. (3) The characteristic temperatures of boron in both models are close to each other. (4) The curve $C_{lat}(T)$ is weakly affected by the specific features of the phonon spectrum.

Although the (*Me* + B) model of independent sublattices and the (*Me*B* + B) model lead to close results, the latter model is more general. In addition to the *Me*–*Me* bonds, the (*Me*B* + B) model makes allowance for the *Me*–B bond, which naturally exists in hexaborides. This bond is ignored in the former model

because of its relative insignificance. In a number of thermodynamic works [12–15], it is accepted that the metal–metal bond in higher borides is immaterial. The results of our investigation have demonstrated that, at high temperatures, the metal–metal bond in rare-earth hexaborides is of little importance. However, at low temperatures (below 100 K), the contribution of this bond is predominant.

REFERENCES

1. J. Emsley, *The Elements* (Clarendon Press, Oxford, 1989; Mir, Moscow, 1993).
2. G. V. Samsonov, T. I. Serebryakova, and V. A. Neronov, *Borides* (Atomizdat, Moscow, 1975).
3. V. V. Novikov, Fiz. Tverd. Tela (St. Petersburg) **43** (2), 289 (2001) [Phys. Solid State **43**, 300 (2001)].
4. S. Kunii, J. Phys. Soc. Jpn. **57**, 361 (1998).
5. J. Delaunay, Solid State Phys. **2**, 219 (1956).
6. S. L. Upadhyaya, J. L. Upadhyaya, and R. Shyam, Phys. Rev. B **44** (1), 122 (1991).
7. N. N. Sirota, I. M. Sirota, T. M. Soshnina, and T. D. Sokolovskiĭ, Dokl. Akad. Nauk **373** (6), 750 (2000) [Dokl. Phys. **45**, 380 (2000)].
8. R. Furth, Proc. R. Soc. London, Ser. A **193**, 87 (1994).
9. S. Nakamura, T. Goto, S. Kunii, *et al.*, J. Phys. Soc. Jpn. **67** (2), 623 (1994).
10. N. N. Sirota, V. V. Novikov, and A. V. Novikov, Fiz. Tverd. Tela (St. Petersburg) **42** (11), 2033 (2000) [Phys. Solid State **42**, 2093 (2000)].
11. *Physicochemical Properties of Elements: A Handbook*, Ed. by G. V. Samsonov (Naukova Dumka, Kiev, 1965).
12. L. A. Reznitskiĭ, Zh. Fiz. Khim. **61** (7), 1800 (1987).
13. S. V. M. Meshel and O. J. Klepa, J. Alloys Compd. **221**, 37 (1995).
14. L. A. Reznitskiĭ, Zh. Fiz. Khim. **68** (5), 945 (1994).
15. L. A. Reznitskiĭ, Zh. Fiz. Khim. **71** (4), 765 (1997).

Translated by N. Korovin

Physics of the Solid State, Vol. 44, No. 5, 2002, pp. 978–984. Translated from Fizika Tverdogo Tela, Vol. 44, No. 5, 2002, pp. 935–941.

LATTICE DYNAMICS AND PHASE TRANSITIONS

Nonlocal Effects in Diffusive Propagation of Heat Pulses in Systems with Trapping Centers of Nonequilibrium Phonons

E. I. Salamatov

Physicotechnical Institute, Ural Division, Russian Academy of Sciences, ul. Kirova 132, Izhevsk, 426000 Russia
e-mail: salam@oft.fti.udmurtia.su

Received June 26, 2001; in final form, August 30, 2001

Abstract—The propagation of heat pulses in systems with defects as trapping centers of nonequilibrium phonons is investigated theoretically. Among these defects are point defects involving two-level systems (TLSs) of different nature. It is demonstrated that, in addition to the principal signal, one more signal can be detected by the bolometer due to reemission of the nonequilibrium TLS energy at a certain ratio of relaxation times in the phonon and TLS subsystems. The temperature and concentration dependences of the time of signal arrival at the bolometer are analyzed. The results of theoretical investigations are compared with experimental data on the propagation of weakly nonequilibrium thermal phonons in solid solutions of the $Y_{3-x}Er_xAl_5O_{12}$ rare-earth yttrium aluminum garnets. *© 2002 MAIK "Nauka/Interperiodica".*

1. INTRODUCTION

The technique based on analyzing the propagation of weakly nonequilibrium phonons injected by a "warm" generator at $S/T \ll 1$ (where S is the difference between the generator temperature and the thermostat temperature T) is widely used in structural investigations of systems (such as mixed crystals, amorphous materials, and ceramics) with strong phonon scattering by defects [1–4]. Despite a large number of theoretical works dealing with the propagation of weakly nonequilibrium phonons in real materials (see, for example, [5–8]), this problem remains unsolved. In particular, the mechanisms responsible for anomalous retardation of weakly nonequilibrium phonons (by two orders of magnitude) in solid solutions of the $Y_{3-x}R_xAl_5O_{12}$ rare-earth yttrium aluminum garnets (where R = Er, Ho, and Tb) are not clearly understood.

The main difficulties encountered in theoretical investigations of this phenomenon stem from the fact that the propagation of a short heat pulse is essentially a nonstationary process. In the case when the studied system involves low-energy two-level systems (TLSs), this nonstationarity can result in its spatial inhomogeneity associated with the dependence of the TLS state on the coordinate. It is known that nonstationary energy exchange with a thermostat in a system consisting of subsystems characterized by different relaxation times can differ appreciably from stationary exchange. Kumenkov and Perel' [9] demonstrated that the cooling of an electron–hole plasma in semiconductors under dynamic conditions (after flash plasma heating) can be described by two significantly different characteristic relaxation times ($\tau_1 \ll \tau_2$). The former time characterizes plasma cooling and heating of optical phonons up to equalization of their effective temperatures, and the latter time accounts for slow cooling of the system as a whole. As will be shown below, similar processes can be observed during the propagation of a short heat pulse in dielectrics with a sufficiently high TLS concentration, which is responsible for the anomalous dependence of the phonon propagation time in these systems.

2. BASIC EQUATIONS

The propagation of a heat pulse will be described in terms of the following kinetic equations (they formally coincide with the equations used in [9]):

$$\frac{\partial n_q}{\partial t} + (\Gamma_{tq} + \Gamma_L)n_q = \Gamma_L n_{q0} + \Gamma_{tq} n_{q0}, \quad (1)$$

$$\frac{\partial E}{\partial t} = \left(\frac{1}{2\pi}\right)^3 \int \omega_q \Gamma_{tq}(n_q - n_{t0}) d^3q. \quad (2)$$

Here, n_{q0} and n_{t0} are the equilibrium filling numbers of phonons at the thermostat temperature and the TLS effective temperature, respectively; E is the TLS energy; Γ_{tq} is the scattering rate of phonons by TLSs; and Γ_L is the rate of energy exchange between phonons and the thermostat. Within the approximation linear in the deviations S_q and S_t of the subsystem temperatures from the thermostat temperature T ($S_i = T_i - T$), the set of equations (1) and (2) can be rewritten in the form

$$\frac{\partial S_q}{\partial t} + (N\Gamma + \Gamma_L)S_q = N\Gamma S_{ti}, \quad (3)$$

$$\frac{\partial S_t}{\partial t} = \Gamma \frac{c_{\rm ph}}{c_{\rm TLS}}(S_q - S_t), \quad (4)$$

where $c_{ph} = 4\pi^4(T/T_D)^3/5$ is the heat capacity of phonons, $c_{TLS} = (\Delta/T)^2\exp(-\Delta/T)/(1 + \exp(-\Delta/T))^2$ is the heat capacity of TLSs, N is the concentration, Δ is the TLS parameter, and T_D is the Debye temperature. Relationships (3) and (4) were derived by ignoring the dependence of Γ_{tq} on q and using the approximation linear in the defect concentration N under the assumption that $\Gamma_{tq} = N\Gamma$, where Γ is the scattering rate of phonons per defect.

3. THE SPATIALLY HOMOGENEOUS CASE

Before proceeding to the spatially inhomogeneous problem, we consider a simpler case. Let us assume that, at the initial instant of time, all excess energy in a spatially homogeneous system is contained in the TLS subsystem; i.e., $S_t(0) = S(0)$ and $S_q(0) = 0$. This situation can be observed experimentally upon energy pumping of a subsystem of paramagnetic levels with a short microwave pulse [10]. By applying the Laplace transform with respect to the time variable, it is easy to obtain the following expression for the effective temperature of the TLS subsystem:

$$S_q(t) = S(0)(A_1e^{p_1t} + A_2e^{p_2t}). \quad (5)$$

Here, the reciprocals of the relaxation times $-p_1$ and $-p_2$ are the solutions to the quadratic equation

$$p^2 + p[N(1 + c_{ph}/Nc_{TLS}) + \Gamma_L] + c_{ph}\Gamma\Gamma_L/c_{TLS} = 0 \quad (6)$$

and the coefficients A_1 and A_2 have the form

$$A_1 = 1 - A_2 = \frac{(p_1 + \Gamma_L + \Gamma c_{ph}/c_{TLS})}{(p_1 - p_2)}.$$

The solution of Eq. (6) is conveniently analyzed when one of the terms in the square brackets is considerably larger (smaller) than the other term. In this case, we have

$$-p_1 = 1/\tau_1 = \Gamma N(1 + c_{ph}/Nc_{TLS}) + \Gamma_L,$$

$$-p_2 = 1/\tau_2 = \frac{c_{ph}}{c_{TLS}}\frac{\Gamma\Gamma_L}{(\Gamma N(1 + c_{ph}/Nc_{TLS}) + \Gamma_L)}.$$

Upon fast heat exchange between phonons and the thermostat, i.e., at $\Gamma_L \gg \Gamma N(1 + c_{ph}/Nc_{TLS})$, no narrow phonon bottleneck arises. Hence, the TLS relaxation rate within the above approximation is independent of the TLS concentration; that is,

$$1/\tau_1 = \Gamma_L, \quad 1/\tau_2 = \Gamma c_{ph}/c_{TLS}.$$

In the presence of a narrow phonon bottleneck, at $\Gamma_L \ll \Gamma N(1 + c_{ph}/Nc_{TLS})$, the relaxation times become dependent on the defect concentration and can be written as

$$1/\tau_1 = \Gamma N(1 + c_{ph}/Nc_{TLS}) = \frac{c_{ph}}{c_{TLS}}\frac{\Gamma}{C}, \quad (7)$$

$$1/\tau_2 = \frac{c_{ph}}{c_{TLS}}\frac{\Gamma_L}{N(1 + c_{ph}/Nc_{TLS})} = \Gamma_L C, \quad (8)$$

where $C = c_{ph}/(Nc_{TLS} + c_{ph}) < 1$.

The time τ_1 characterizes the fast process of equalizing the temperatures of the TLS subsystem and phonons involved. This process is governed by the cross section for phonon scattering by TLSs. After equalizing the temperatures, the whole system undergoes slow relaxation with the characteristic time τ_2. This process is controlled by the interaction of phonons with the thermostat, does not depend on Γ in the approximation used for deriving expression (8), and is determined only by the rate of energy exchange between phonons and the thermostat. As a rule, the inequality $c_{ph}/Nc_{TLS} \ll 1$ holds in experiments and expression (8) coincides with the Altshuler relationship [11].

In the case when the characteristic time of energy exchange between phonons and the thermostat is determined only by the time of diffusive propagation of phonons over the bulk of a sample with a characteristic linear size L, it is easy to obtain the relationship for the relaxation time τ_2:

$$1/\tau_2 = AL^2/(DC), \quad (8a)$$

where D is the phonon diffusion coefficient and A is the numerical coefficient (of the order of unity), which depends on the sample geometry. Then, the condition for a narrow phonon bottleneck can be written in the form $L^2 > L_0^2 = D\tau_1/A$.

As will be shown below, the parameters characterizing the energy relaxation of the TLS subsystem and phonons in the presence of a narrow phonon bottleneck in the spatially homogeneous case also play an important role in describing the propagation of heat pulses in these systems.

4. HEAT-PULSE PROPAGATION

Now, we consider the problem of propagation of a δ-like heat pulse from the origin of coordinates into an infinite one-dimensional sample. In this case, Γ_L in Eq. (1) should be taken as the diffusion term: $\Gamma_L = -D_0\partial^2/\partial z^2$, where D_0 is the phonon diffusion coefficient, which depends solely on elastic scattering of phonons by defects. (Here, heat exchange between the sample and the thermostat is ignored.) The spatial Fourier transform of the function $S_q(t, k)$ formally coincides with relationship (5); that is,

$$S_q(t, k) = S(0)(A_1(k)e^{-k^2D_1(k)t} + A_2(k)e^{-k^2D_2(k)t}).$$

Here, $S(0)$ is the power of the heat pulse, $D_i(k) = -p_i(k)/k^2$ stands for the effective diffusion coefficients

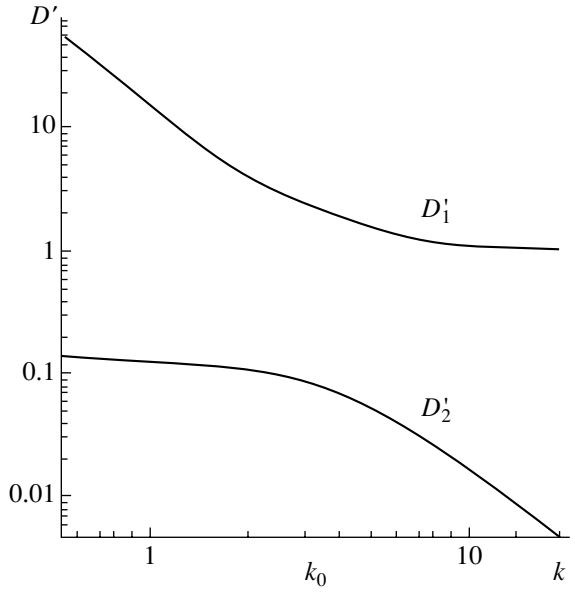

Fig. 1. Spatial dispersion of the effective diffusion coefficients.

of phonons, and $p_i(k)$ are determined from the quadratic equation similar to Eq. (6); that is,

$$A_1 = 1 - A_2 = (p_1 + D_0k^2 + \Gamma c_{ph}/c_{TLS})/(p_1 - p_2). \quad (9)$$

Let us introduce the dimensionless variables $k' = kL$, $D_i'(k) = D_i(k)/D_0$, and $t' = t/t_0$, where L is the coordinate of the point at which the temperature is measured (the sample length) and $t_0 = L^2/2D_0$ is the characteristic time of phonon propagation, which is calculated with allowance made only for elastic scattering of phonons by defects. For the effective diffusion coefficients, we have

$$D_{1,2}'k^2 = (k_0^2 + k'^2 + \sqrt{(k_0^2 + k'^2)^2 - 4k'^2k_0^2C})/2. \quad (10)$$

Expression (10) involves the parameters $C = c_{ph}/(c_{ph} + Nc_{TLS}) < 1$ and $k_0^2 = (L/L_0)^2$, which were introduced for the one-dimensional case ($A = 1$) in the preceding section. From relationships (9) and (10), we obtain $D_1' = 1$ and $A_1 = 1$ at $k' \gg k_0$ and $D_2' = C$ and $A_2 = C$ at $k' \ll k_0$.

The spatial dispersion of the diffusion coefficients $D_i'(k')$ is shown in Fig. 1, from which the physical meaning of the introduced parameters becomes clear. At $k_0 \gg 1$, the narrow phonon bottleneck arises in the system and the time of signal arrival at the bolometer is determined by slow processes: $t_2 = L^2/(2D_0C)$ in accordance with formula (8a). At $k_0 \ll 1$ (in the absence of the phonon bottleneck), the phonon system has no time to respond to changes in the TLS subsystem and the signal propagation time is independent of the TLS state: $t_1 = t_0 = L^2/(2D_0)$.

At intermediate values of k_0, the expression for this parameter can be conveniently written in the equivalent form $k_0 = \sqrt{2t_0/\tau_1}$. From this expression, it follows that k_0 increases with an increase in the number of phonons that have already managed to interact inelastically with TLSs in the presence of a narrow phonon bottleneck. The other phonons do not undergo inelastic scattering by TLSs, and their propagation is governed by the D_0 coefficient. The results of numerical calculations of $S_q(t')$ at the point L for different values of k_0 and C are displayed in Fig. 2. It is seen from the dependences depicted in this figure that the height and position of the first maximum depend primarily on the k_0 parameter, whereas the shape and position of the second maximum are determined by the C parameter.

For an approximate description of the dependences of the position and shape of the maxima on the parameters of the problem, we restrict our consideration to the limit $C \ll 1$. In this case, we can write the relationships

$$A_1(k) = 1 - A_2(k) \simeq 1 - C, \quad k < k_0,$$

$$A_1(k) = 1 - A_2(k) \simeq 1, \quad k > k_0$$

and derive the approximate relationships for the position and shape of the peaks. For the first peak, we obtain

$$S_1(t) \simeq e^{-k_0^2t/t_0}e^{-L^2/4D_0t}\sqrt{\frac{\pi}{4D_0t}}.$$

As follows from this expression, the time it takes for the first peak to arrive at the bolometer is determined by the expression

$$t_1 = \frac{\sqrt{4k_0^2 + 1} - 1}{2k_0^2}t_0. \quad (11)$$

The approximate relationship for the position and shape of the second peak can be derived at sufficiently large values of k_0; that is,

$$S_2(t) \simeq C\sqrt{\frac{\pi}{4D_0Ct}}e^{-L^2/4D_0Ct}, \quad t_2 = t_0/C. \quad (12)$$

Note that, in the limit under consideration, the conditions for a narrow phonon bottleneck are satisfied and the signal propagation time is independent of τ_1.

We now turn to the discussion of the temperature and concentration dependences of the heat-pulse propagation. Unfortunately, as far as we know, experimental data on the spin-lattice relaxation in these systems in the presence of a narrow phonon bottleneck are unavailable. Hereafter, k_0 will be treated as a fitting parameter of the model. For definiteness, we assume that the temperature dependence of the relaxation rate $\Gamma(T)$ in formula (7) is described by an exponential law [11]: $\Gamma(T) = \Gamma_0\exp(-\Delta/T)$. As will be shown below, the

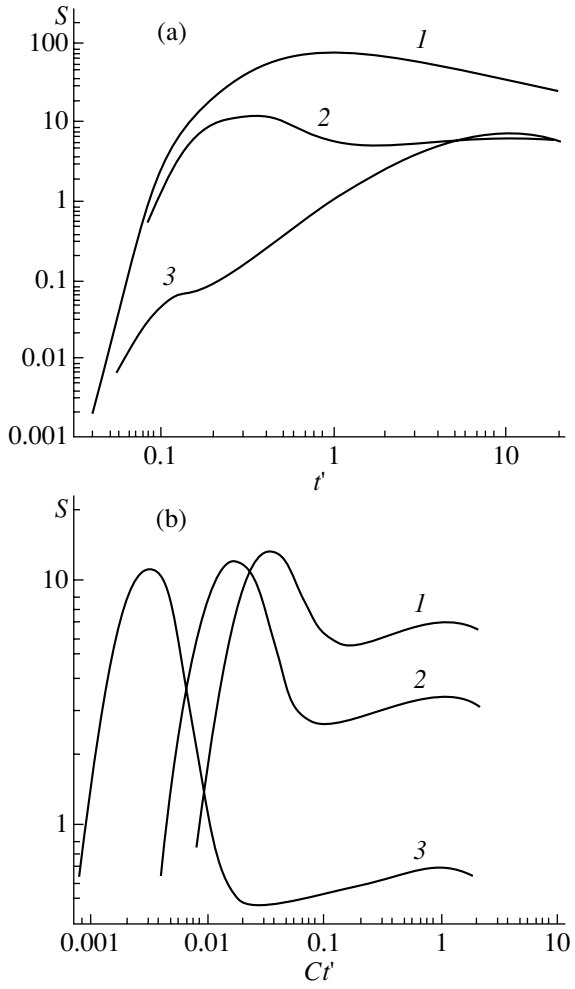

Fig. 2. Shapes of the phonon nonequilibrium signals as functions of the parameters (a) k_0 and (b) C. (a) $C = 0.1$ and $k_0 =$ (*1*) 0, (*2*) 3, and (*3*) 10 and (b) $k_0 = 3$ and $C =$ (*1*) 0.1, (*2*) 0.05, and (*3*) 0.01.

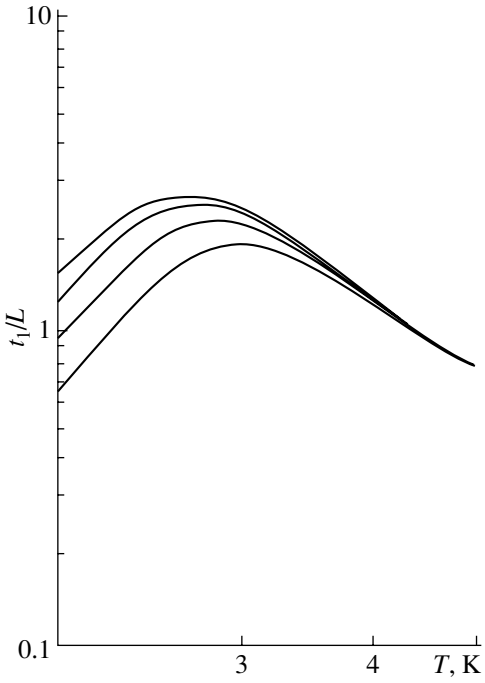

Fig. 3. Normalized (to the sample length) arrival times of the first maximum at $L = 4$, 6, 8, and 10 mm (from bottom to top).

theoretical results obtained for this temperature dependence are in reasonable agreement with the experimental data. Under the assumption that the diffusion coefficient D_0 is determined by the Rayleigh scattering of phonons from defects ($D_0 \sim 1/NT^4$), we found that the parameter k_0 increases with an increase in both the temperature and the defect concentration ($k_0 \sim NLT^2\Gamma^{1/2}$). At $k_0 \geq 1$, from relationship (11), it follows that the time t_1 is concentration independent and increases linearly with an increase in the parameter L. In other words, the time t_1 behaves as a signal of ballistic phonons but decreases with an increase in the temperature. Since, at small k_0, the time t_1 is proportional to T^4, the dependence $t_1(T)$ exhibits a maximum whose position is determined by the temperature dependence $\Gamma(T)$. Figure 3 displays the dependences $t_1(T)/L$ calculated from expression (11) at different parameters L and constant values of N and Γ_0. The behavior of these dependences agrees qualitatively with the available experimental data [4]. Special experimental investigations into the temperature and concentration dependences of t_1 at different L were not carried out. However, Ivanov *et al.* [10] noted that the behavior of the first peak is similar to that of the ballistic signal.

The temperature and concentration dependences of the arrival time of the second peak will be analyzed under the conditions when $k_0 \gg 1$. These conditions can always be satisfied with a sufficiently long sample. Note that the contribution of the first peak to the signal at the bolometer can be disregarded. The arrival time of the second signal is represented by the relationship

$$t_2(T, N) \sim \frac{L^2}{2D_0(T, N)C(T, N)}.$$

The temperature dependences of t_2/N at $D_0 \sim 1/NT^4$ and different defect concentrations are plotted in Fig. 4. It can be seen from this figure that, at a sufficiently high defect concentration, when the inequality $Nc_{TLS} \gg c_{ph}$ holds at temperatures in the vicinity of Δ, the dependence $t_2(T)$ exhibits a nonmonotonic behavior. At $T < 0.5\Delta$, the time t_2 increases exponentially. At $T > 0.5\Delta$, when $c_{TLS} \sim 1/T^2$, the time t_2 decreases as $1/T$. In the other temperature ranges (in which the inequality $Nc_{TLS} \ll c_{ph}$ is satisfied) and at low defect concentrations, the dependence $t_2(T)$ exhibits conventional behavior: $t_2(T) \sim T^4$. As regards the concentration dependence $t_2(N)$, the

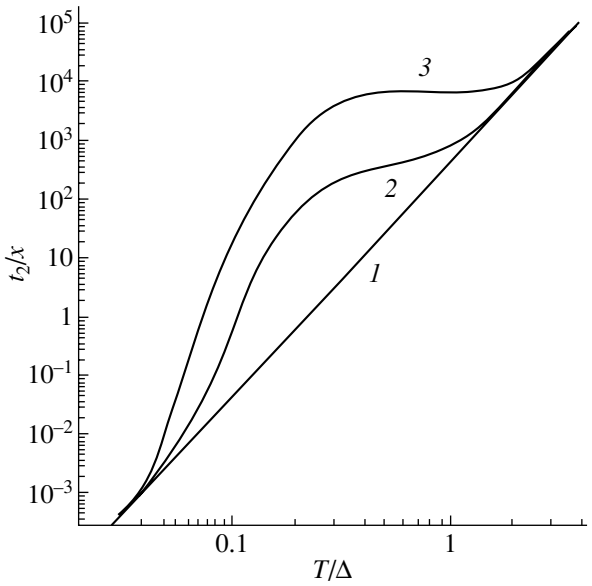

Fig. 4. Normalized (to the concentration) arrival times of the second maximum at $\Delta/T = 0.01$ and different x: (*1*) 0, (*2*) 0.05, and (*3*) 0.5.

time t_2 is proportional to N_2 in the temperature range where $c_{tls} \gg c_{ph}$.

The above analysis has demonstrated that the proposed model qualitatively describes the experimental temperature and concentration dependences of the phonon nonequilibrium signal shape for $Y_{3-x}R_xAl_5O_{12}$ (R = Er, Ho, and Tb) yttrium aluminum garnets.

5. COMPARISON WITH EXPERIMENT

The phonon dynamics in $Y_{3-x}Er_xAl_5O_{12}$ solid solutions has been investigated experimentally in sufficient detail. It is found that, at $x > 0.2$, the phonon nonequilibrium signal has the second maximum and the propagation of phonons is retarded appreciably. In this case, the temperature dependence of the arrival time of the second signal at the bolometer on the concentration of erbium impurity atoms and the sample length has a complex character. At low concentrations of impurity atoms ($0.2 < x < 0.6$), the time t_2 increases very rapidly (exponentially, according to [10]) with an increase in the temperature. At high concentrations x, the temperature dependence $t_2(T)$ is characterized by the negative derivative. At intermediate concentrations x, the sign of the derivative of $t_2(T)$ is predominantly determined by the sample size.

From the above consideration, it is clear that, within the proposed model, the observed behavior of $t_2(T)$ as a function of the concentration can be explained solely under the assumption that the system involves two TLS subsystems with different energy parameters $\Delta_1 < T < \Delta_2$. The solution of the problem with two TLS subsystems does not differ radically from the solution considered above but leads to qualitatively new results (for example, the appearance of the third maximum in the phonon nonequilibrium signal curve observed experimentally in [4]) and calls for separate treatment. In the present work, we restrict our consideration to the limit of large values of the parameter k_0 (or, more precisely, an analog of this parameter). In this case, it is easy to obtain the physically obvious result that the arrival time of the second maxima is determined by the parameter $C = c_{ph}/(c_{ph} + N_1c_{TLS,1} + N_2c_{TLS,2})$, where N_i and $c_{TLS,i}$ are the concentration and the heat capacity of the ith TLS subsystem, respectively.

According to the experimental data on the low-temperature heat capacity [12], doubly degenerate paramagnetic levels with $\Delta_2 = 38.9$ K reside in the $Y_{3-x}Er_xAl_5O_{12}$ system. As can be seen from Fig. 4, it is these TLSs that can lead to a very steep increase in the time t_2 with an increase in the temperature. Experimental investigations into spin-lattice relaxation in this system revealed low-energy paramagnetic levels with $\Delta_1 \simeq 4$ K [10]. At the temperatures used in the experiments, we have $c_{TLS,1} \gg c_{TLS,2}$. Under these conditions, the contribution of the second TLS subsystem dominates when the concentration of high-energy TLSs at $x \le 0.6$ considerably exceeds the concentration of low-energy TLSs ($N_2 \gg N_1$). This becomes possible in the case when the low-energy level is associated with the particular atomic configuration rather than with each impurity atom. At low impurity concentrations, the probability of forming these configurations is small; i.e., $N_1 \ll N_2$. Most likely, it is this situation that is observed at low impurity concentrations in the $Y_{3-x}Er_xAl_5O_{12}$ system. For this reason, in the subsequent discussion (except for the specified case), we will ignore the contribution of low-energy TLSs and consider the case of low concentrations ($x \le 0.6$).

In order to solve the formulated problem, it is necessary to determine the diffusion coefficient D_0 and the parameters C and k_0. The diffusion coefficient D_0 for the system with TLSs cannot be determined directly from experiments. Hence, in the absence of TLSs, this coefficient is assumed to be approximately equal to the diffusion coefficient for the $Y_{3-x}Lu_xAl_5O_{12}$ system: $D_0 = (3.4/T)^4(0.2 + x_0)/(x + x_0)$ mm^2/μs, where $x_0 = 0.025$ is the residual concentration of impurities [4]. When calculating the C parameter, the Debye temperature of the solid solution was determined from the formula $T_D = T_{DY}(M_Y/M_s)^{1/2}$, where $T_{DY} = 750$ K is the Debye temperature of yttrium garnet, M_Y is the molar mass of yttrium garnet, and M_s is the molar mass of the solid solution [12, 13]. The parameters k_0 were obtained from the approximate relationship (11). By comparing the calculated [from formula (11)] temperature dependence of the arrival time of the first maximum and the experimental dependence (Fig. 1 in [4]), we found that Γ_0 is equal to 6.78×10^{-5} μs^{-1} per formula

unit of defects. The dependences $t_{1,2}(T)$ calculated using the above parameters for 6.8-mm-long samples with impurity concentrations of 0.2 and 0.6 formula units are plotted in Fig. 5 (curves *1–3*). Figure 6 shows the phonon nonequilibrium signals for $Y_{3-x}Er_xAl_5O_{12}$ (solid lines) and $Y_{3-x}Lu_xAl_5O_{12}$ (dashed lines) samples at two temperatures T = 3.85 and 2.7 K. The theoretical data presented in Figs. 5 (curves *1–3*) and 6 are in reasonable agreement with the experimental dependences (Figs. 1, 3 in [4]).

Curves *4* and *5* in Fig. 5 are qualitative in character and illustrate changes in the slope of the dependence $t_2(T)$ when the concentration of low-energy TLSs with $\Delta_1 < T$ in the system reaches a certain value. The calculations were performed at x = 1.0 and $N_1 = 0.1\ N_2$ for different temperature dependences of the diffusion coefficient $D_0(T)$. Curve *4* was calculated under the assumption that the diffusion coefficient D_0 is determined by the Rayleigh scattering of phonons from defects. It follows from expression (12) that, in this case, the exponent α in the relationship $t_2(T) \sim T^\alpha$ cannot be less than –1, whereas the experiments revealed a stronger dependence $t_2(T)$ with the negative derivative [4].

It can be assumed that, at sufficiently high concentrations of impurity atoms in the $Y_{3-x}Er_xAl_5O_{12}$ system, the primeval diffusion coefficient D_0 of phonons is governed primarily by phonon scattering from interfaces. In actual fact, the $Y_{3-x}Er_xAl_5O_{12}$ solid solutions are prone to phase separation. In turn, this brings about the formation of regions that have a characteristic size equal to 20–100 nm and are either depleted or enriched with impurity atoms [14]. It is known that, in the case when phonons propagate in systems with well-developed interfaces, the temperature dependence of the phonon diffusion coefficient cannot be determined from the Rayleigh scattering but depends in a complex way on the interface structure (see, for example, [15]). As an illustration of this situation, curve *5* in Fig. 5 was calculated by assuming that $D_0(T)$ = const. As a result, the calculated dependence $t_2(T)$ agrees qualitatively with the experimental dependence (see Fig. 1 in [4]).

It should be noted that the experimental strong temperature dependence $t_2(T)$ with the negative derivative can be explained in terms of the spectral composition of propagating phonons, which was ignored in our simplified treatment. In the case of long propagation times for phonon nonequilibrium signals, a significant role can be played by decay processes [16]. In the framework of the model considered in the present work, the maximum delay of the phonon nonequilibrium signal should be observed in the $Y_{3-x}Tb_xAl_5O_{12}$ system for which the energy parameter of the TLS associated with each impurity atom is equal to 2.45 cm^{-1} [17]. For this system, under usual experimental conditions ($T \simeq 3.5$ K, $x \simeq 0.5$, and $L \simeq 1$ cm), the time t_2 is of the order of 5×10^{-3} s, which is comparable in magnitude to the time of decay processes.

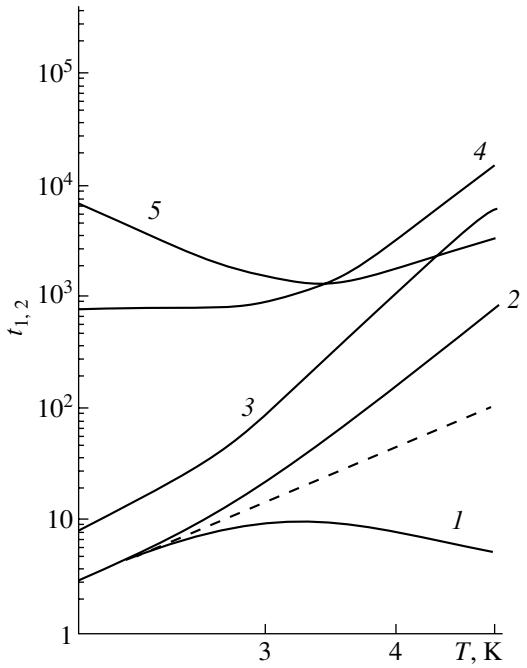

Fig. 5. Temperature dependences of the arrival time (μs) of the (*1*) first and (*2–5*) second maxima for the $Y_{3-x}Er_xAl_5O_{12}$ system at x = (*2*) 0.2, (*3*) 0.6, and (*4, 5*) 1.0. The dashed line represents the temperature dependence of the arrival time of the maximum for the TLS-free system at x = 0.2.

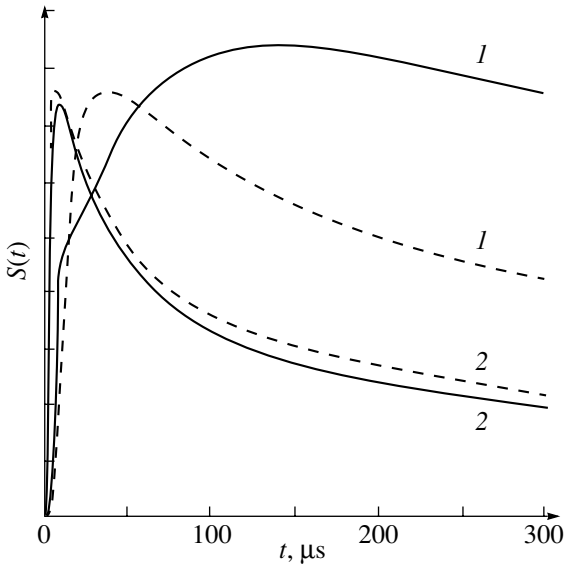

Fig. 6. Phonon nonequilibrium signals in the $Y_{2.8}Er_{0.2}Al_5O_{12}$ (solid lines) and $Y_{2.8}Lu_{0.2}Al_5O_{12}$ (dashed lines) systems at temperatures T = (*1*) 3.85 and (*2*) 2.7 K. L = 6.8 mm.

6. CONCLUSION

A sufficiently simple theoretical model that includes two basic parameters—the ratio C of the phonon heat capacity to the heat capacity of the whole system and the ratio k_0 of the diffusive phonon propagation time to the TLS relaxation time—has been proposed. These two parameters suffice to describe the main anomalies in the temperature and concentration dependences of the propagation of weakly nonequilibrium phonons in systems involving trapping centers. Consideration of more subtle effects observed in experiments calls for further improvement of this model (for example, inclusion of the spectral composition of injected phonons and several TLS subsystems in the analysis outside the province of the linear approximation).

ACKNOWLEDGMENTS

I am grateful to S.N. Ivanov for his helpful discussions and valuable remarks and E.N. Khazanov for providing an opportunity to look through unpublished experimental results.

This work was supported by the Russian Foundation for Basic Research, project no. 00-02-17426.

REFERENCES

1. S. N. Ivanov, E. N. Khazanov, and A. V. Taranov, Pis'ma Zh. Éksp. Teor. Fiz. **40** (1), 20 (1984) [JETP Lett. **40**, 743 (1984)].
2. S. N. Ivanov and E. N. Khazanov, Zh. Éksp. Teor. Fiz. **88** (1), 294 (1985) [Sov. Phys. JETP **61**, 172 (1985)].
3. S. N. Ivanov, A. V. Taranov, and E. N. Khazanov, Zh. Éksp. Teor. Fiz. **99** (4), 1311 (1991) [Sov. Phys. JETP **72**, 731 (1991)].
4. S. N. Ivanov, A. G. Kozorezov, A. V. Taranov, and E. N. Khazanov, Zh. Éksp. Teor. Fiz. **100** (5), 1591 (1991) [Sov. Phys. JETP **73**, 880 (1991)].
5. I. B. Levinson, Zh. Éksp. Teor. Fiz. **79** (4), 1394 (1980) [Sov. Phys. JETP **52**, 704 (1980)].
6. A. G. Kozorezov, Zh. Éksp. Teor. Fiz. **100** (5), 1577 (1991) [Sov. Phys. JETP **73**, 872 (1991)].
7. V. I. Kozub and A. M. Rudin, Fiz. Tverd. Tela (St. Petersburg) **38** (2), 337 (1996) [Phys. Solid State **38**, 189 (1996)].
8. Cz. Jasinkiewicz and P. Paszkievicz, Z. Phys. B **77**, 209 (1989).
9. S. E. Kumenkov and V. I. Perel', Zh. Éksp. Teor. Fiz. **94** (1), 346 (1988) [Sov. Phys. JETP **67**, 193 (1988)].
10. S. N. Ivanov, A. V. Taranov, E. N. Khazanov, *et al.*, Zh. Éksp. Teor. Fiz. **94** (5), 274 (1988) [Sov. Phys. JETP **67**, 1021 (1988)].
11. S. A. Altshuler and B. M. Kozyrev, *Electron Paramagnetic Resonance* (Academic, New York, 1964; Nauka, Moscow, 1972).
12. S. R. Arutyunyan, Kh. S. Bagdasarov, A. P. Dodokin, and A. M. Kevorkov, Fiz. Tverd. Tela (Leningrad) **27** (8), 2299 (1985) [Sov. Phys. Solid State **27**, 1380 (1985)].
13. E. P. Steigmeier, Appl. Phys. Lett. **3** (2), 6 (1983).
14. O. V. Karban', S. N. Ivanov, E. I. Salamatov, and S. G. Bystrov, Neorg. Mater. **37** (1), 1 (2001).
15. S. N. Ivanov, A. G. Kozorezov, A. V. Taranov, and E. N. Khazanov, Zh. Éksp. Teor. Fiz. **102** (2), 600 (1992) [Sov. Phys. JETP **75**, 319 (1992)].
16. B. A. Danil'chenko, S. N. Ivanov, D. V. Poplavskiĭ, *et al.*, Zh. Éksp. Teor. Fiz. **112** (1), 325 (1997) [JETP **85**, 179 (1997)].
17. U. V. Valiev, L. L. Gorbunova, M. M. Turganov, *et al.*, Fiz. Tverd. Tela (St. Petersburg) **37** (4), 1176 (1995) [Phys. Solid State **37**, 639 (1995)].

Translated by O. Borovik-Romanova

Physics of the Solid State, Vol. 44, No. 5, 2002, pp. 985–988. Translated from Fizika Tverdogo Tela, Vol. 44, No. 5, 2002, pp. 942–944.

LATTICE DYNAMICS AND PHASE TRANSITIONS

Effect of Electron Irradiation on the Heat Capacity of $[NH_2(CH_3)_2]_2 \cdot CuCl_4$ in the Phase Transition Region

T. I. Dekola, A. U. Sheleg, and N. P. Tekhanovich

Institute of Solid State and Semiconductor Physics, National Academy of Belarus, ul. Brovki 17, Minsk, 220072 Belarus

e-mail: sheleg@ifttp.bas-net.by

Received July 20, 2001

Abstract—The specific heat of crystalline $[NH_2(CH_3)_2]_2 \cdot CuCl_4$ in the ferroelectric phase, both nonirradiated and irradiated by electrons, was measured calorimetrically. The temperature region of existence of the ferroelectric phase was shown to broaden under electron irradiation. The existence of an incommensurate phase above the Curie point T_{c1} in the crystal was confirmed. The phase-transition sequence observed in $[NH_2(CH_3)_2]_2 \cdot CuCl_4$ is shown to be described by a phenomenological model for A_2BX_4-type ferroelectrics with an organic cation.

Dimethylammonium chlorocuprate $[NH_2(CH_3)_2]_2 \cdot CuCl_4$ $[(DMA)_2CuCl_4]$ is a representative of a large class of A_2BX_4 crystals with the common formula $[NH_2(CH_3)_2]_2 \cdot MeCl_4$ (*Me* = Co, Zn, Cu, Cd). The $(DMA)_2CuCl_4$ crystal undergoes two first-order phase transitions (PTs), at T_{c1} = 279.5 K and T_{c2} = 253 K, between which a ferroelectric phase (FEP) exists [1, 2]. A study of the temperature dependence of the birefringence of $(DMA)_2CuCl_4$ suggests an indirect conclusion [3] that an incommensurate phase (IP) exists in this crystal in the 296–279.5 K interval. In [4], we studied the effect of γ irradiation on the heat capacity of $(DMA)_2CuCl_4$ and showed that the region of the IP existence increases with γ-irradiation dose, which is at odds with the results obtained on the effect of γ irradiation on the Curie temperature T_{c1} in other ferroelectric crystals. The PT temperature T_{c1} usually decreases with increasing γ irradiation [5–8]. It was, therefore, of interest to investigate the effect of electron irradiation on the PT in $(DMA)_2CuCl_4$ and analyze the results obtained.

The heat capacity measurements were performed on an UNTO setup providing computer-controlled temperature variation in a vacuum adiabatic calorimeter with discrete heat injection into the sample (m = 4.559 g). The sample heating rate was 0.01–0.08 K/min. The heat capacity was measured in steps of 0.2–1.5 K to within 0.3%. The electron irradiation was carried out at room temperature on a 6-MeV electron accelerator in a flux of 10^{15} electrons/cm^2.

Figure 1 presents the temperature dependence of the specific heat of a $(DMA)_2CuCl_4$ sample unirradiated (curve *1*) and electron-irradiated (*2*). We readily see that the $C_p(T)$ curve exhibits anomalies in the form of peaks in the PT region at T_{c2} = 256 K and T_{c1} = 281 K. In the electron-irradiated sample, the anomaly at T_{c2} = 256 K shifts toward lower temperatures and the anomaly at T_{c1} = 281 K shifts toward higher temperatures, with both peaks decreasing in amplitude and broadening; this effect is similar to the one observed under γ irradiation [4]. The specific-heat peak at T_{c1} = 281 K is asymmetric; more specifically, the specific heat falls off more slowly above the IP–FEP phase transition point. It is known that the incommensurate (sinusoidal) phase transfers to the soliton mode as one approaches T_{c1}, where the polarization distribution represents actual commensurate regions separated by domain walls (solitons). Considered in the single-harmonic approximation, the anomalous part of the specific heat does not undergo significant changes with decreasing temperature (in the region $T > T_{c1}$) [9]. Nevertheless, the specific heat should increase, as one approaches T_{c1}, as $\Delta C_p \sim (T - T_{c1})^{-1}\ln^2(T - T_{c1})$ because of the domain-like soliton structure [10]. The dependence of $(\Delta C_p)^{-1}$ on $(T - T_{c1})$ plotted in Fig. 2 for $(DMA)_2CuCl_4$ is linear in the interval T_{c1} + 0.1 K < T < T_{c1} + 0.8 K, which agrees with theory. Therefore, a comparison of the experimental data obtained for $(DMA)_2CuCl_4$ with theory argues for the incommensurate nature of the phase observed at temperatures $T > T_{c1}$.

A theoretical description based on the Landau theory was developed in [11] for the PT sequence in A_2BX_4 crystals with an organic cation, more specifically, for the $(TMA)_2ZnCl_4$ crystal, where TMA stands for the $N(CH_3)_4$ tetramethylammonium ion. The phenomenological model proposed does not differ radically from the one elaborated for A_2BX_4 crystals with a metal cation, which has been applied to a number of representatives of the family, namely, K_2SeO_4, Rb_2ZnCl_4, and Rb_2ZnBr_4. Using the free-energy expansions for ferroelectric phase III F_{III} and ferroelastic phase IV F_{IV} given

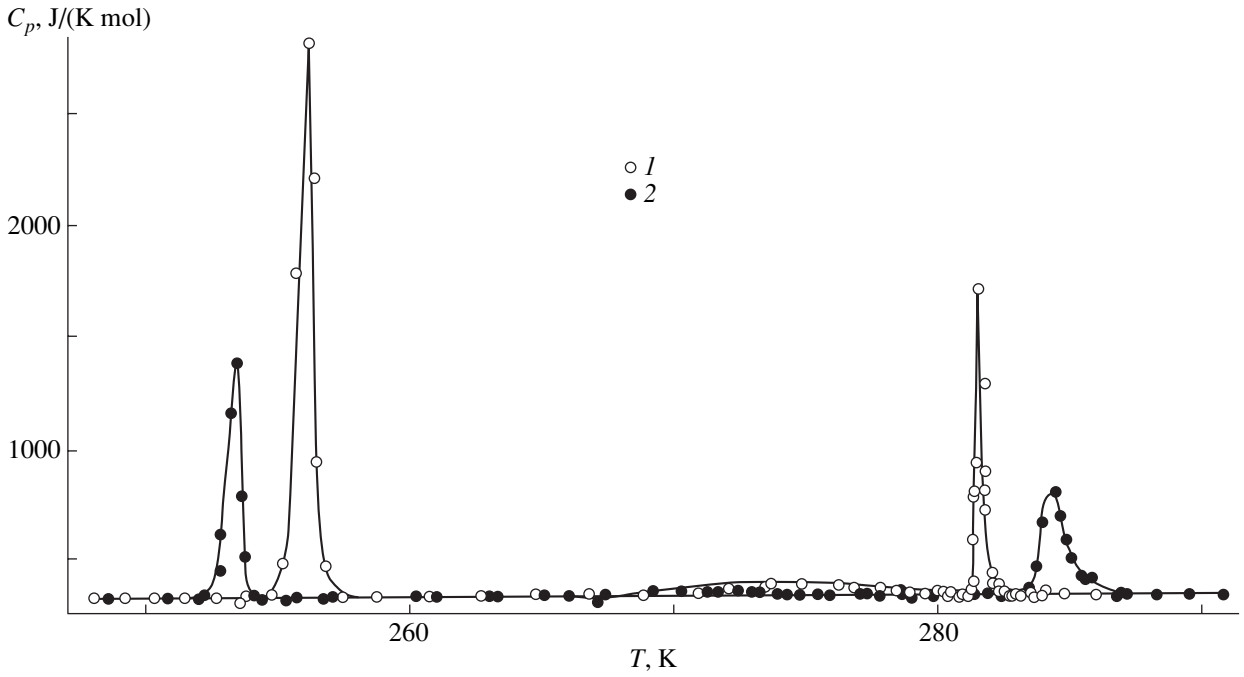

Fig. 1. Temperature dependence of the specific heat of $[NH_2(CH_3)_2]_2 \cdot CuCl_4$ (*1*) before irradiation and (*2*) after irradiation.

in [12] (the notation is retained), one can analyze the temperature dependence of the free energy of the crystal under study. Figure 3 plots the temperature dependence of the free energy of $(DMA)_2CuCl_4$ in units of R, which was derived from the measured values of the specific heat (the origin was placed at $T_i = 296$ K, which is the PT temperature in the IP quoted in [3]). It is seen that the theoretical least squares fits F_{III} and F_{IV} calculated within the temperature regions of existence of the corresponding phases from the model used by us describe the experimental $F(T)$ dependences fairly well. The deviations of experimental points from the phenomenological relations in the PT region show that the Landau model becomes inapplicable in the immediate vicinity of the PT point.

As seen from Fig. 1, electron irradiation shifts the Curie point of $(DMA)_2CuCl_4$ toward higher temperatures, as was reported in [4] for γ irradiation of the same crystal and in [13] for Rb_2ZnBr_4. It is known that the ferroelectric PT temperature in ferroelectrics usually

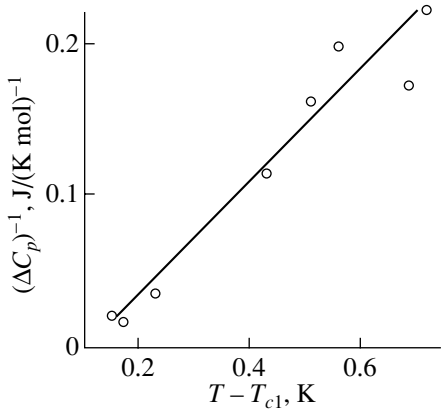

Fig. 2. $(\Delta C_p)^{-1}$ vs. $T - T_{c1}$ plot for an $[NH_2(CH_3)_2]_2 \cdot CuCl_4$ crystal.

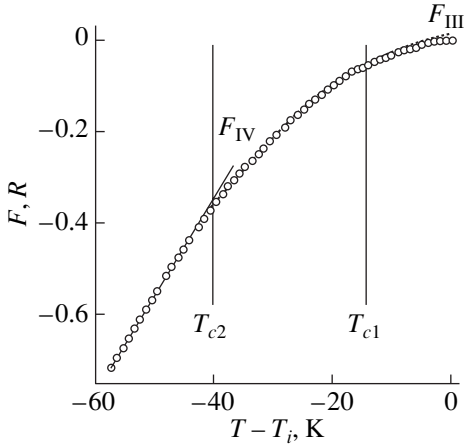

Fig. 3. Temperature dependence of the free energy of an $[NH_2(CH_3)_2]_2 \cdot CuCl_4$ crystal.

decreases as a result of suppression of the ferroelectric properties by irradiation. The deterioration of the ferroelectric state in $(DMA)_2CuCl_4$ with increasing irradiation dose manifests itself in a decrease in the specific-heat anomalies (Fig. 1), i.e., in a decrease in the energy associated with the PT, which implies a decrease in spontaneous polarization, because, as follows from thermodynamic considerations [14], the change in transition energy is proportional to P_s.

It is known that near T_{c1}, polar regions with mutually opposite directions of spontaneous polarization, separated by domain walls (phase solitons), become nucleated in the IP. This accounts for the complex character of the IP-to-FEP transformation. The IP–FEP transition is governed in this case by the thermodynamics of the solitons, which are semimacroscopic objects [15]. According to the phase soliton model, the transition to the FEP at T_{c1} occurs as the polar regions grow continuously through soliton motion [16]. The period of this soliton lattice increases as the temperature approaches T_{c1}. The parameter of the IP–FEP transition is the soliton density (or modulation period), which tends to zero for $T \longrightarrow T_{c1}$. Nevertheless, in real crystals, the soliton density may remain large enough for $T < T_{c1}$, which was observed in a number of crystals. In the FEP, the width of the polar IP regions may grow to a size as large as that of a usual ferroelectric domain ($\geq 10^4$ Å) [17]. The additional specific-heat peak observed by us in the FEP of $(DMA)_2CuCl_4$ at $T \approx 275$ K is apparently due to the relaxation motion of the solitons that did not decay below T_{c1}. Note that a nonlinearity in the relative elongation as a function of temperature and a weak specific-heat anomaly were observed in [1] within the same temperature interval.

Thermodynamic equilibrium in a real crystal is established through the creation, annihilation, and diffusion of solitons. However, if solitons are pinned by defects and impurities, these processes break down and the formation of the period of the equilibrium structure corresponding to the incommensurate wave of atomic displacements is delayed. The metastable state thus formed persists until the system overcomes the pinning energy (as a rule, such states are fairly stable and relax very slowly to the equilibrium state) [15].

The effect of soliton pinning by the crystal lattice, defects, and impurities becomes most manifest near T_{c1}, where the amplitude of the incommensurate modulation reaches saturation, the distance between the solitons is sufficiently large, and the interaction between them is weak. The kinetics of the IP–FEP transformation in a crystal with defects can be conceived as follows. The positions of the solitons separating commensurate-phase regions, into which the crystal breaks down near T_{c1}, are fixed by defects. The polarization distribution in this case is determined by the spatial distribution of defects. The transition to the FEP with decreasing temperature takes place in the low-temperature region of the IP, where the influence of defects becomes dominant because of the weak interaction between the solitons. The temperature of this transition is apparently the point where the energy of intersoliton interaction becomes equal to that of the soliton pinning by defects. As the temperature increases, interaction between solitons becomes a dominant factor. As the concentration of defects grows, they pin the soliton structure more strongly. For the equilibrium state (depinning) to set in, the intersoliton interaction energy must be increased; this is reached through an increase in the transition temperature and is observed experimentally.

Thus, as one approaches the IP–FEP transition in the region $T < T_{c1}$, the interaction of the local fields of the irradiation-induced defects with the incommensurate displacement wave becomes a dominant factor, which gives rise to soliton pinning on defects. As a consequence, the T_{c1} transition temperature for $(DMA)_2CuCl_4$ increases with increasing defect concentration. The same effect is observed to occur in Rb_2ZnBr_4 and $(DMA)_2CuCl_4$ crystals [4, 13] under γ irradiation. Such a behavior of the IP–FEP transition temperature is apparently typical of other ferroelectric crystals with an incommensurate phase and different defect concentrations, which is accounted for by there being soliton interaction with lattice defects.

As seen from Fig. 1, the anomaly at $T \approx 275$ K disappears under electron irradiation. The broadening of this anomaly is apparently associated with the soliton mobility decreasing because of their pinning at defects, which brings about a decreased contribution to $C_p(T)$. A similar effect has been observed under γ irradiation of the same crystal [4].

ACKNOWLEDGMENTS

The authors are indebted to N.F. Kurilovich for his assistance in sample irradiation.

REFERENCES

1. Z. A. Bobrova and V. M. Varikash, Dokl. Akad. Nauk BSSR **30** (6), 510 (1986).
2. Z. A. Bobrova, V. M. Varikash, A. I. Baranov, and L. A. Shuvalov, Kristallografiya **32** (1), 255 (1987) [Sov. Phys. Crystallogr. **32**, 148 (1987)].
3. O. G. Vlokh, V. B. Kapustyanyk, and I. I. Polovinko, Izv. Akad. Nauk SSSR, Ser. Fiz. **54** (6), 1143 (1990).
4. A. U. Sheleg, T. I. Dekola, and N. P. Tekhanovich, Fiz. Tverd. Tela (St. Petersburg) **43** (6), 1086 (2001) [Phys. Solid State **43**, 1124 (2001)].
5. B. A. Strukov, S. A. Taraskin, and A. B. Suvkhanov, Izv. Akad. Nauk SSSR, Ser. Fiz. **55** (3), 539 (1991).
6. B. A. Strukov, S. A. Taraskin, V. A. Fedorikhin, and K. A. Minaeva, J. Phys. Soc. Jpn. **49**, 7 (1980).
7. A. U. Sheleg, T. I. Dekola, N. P. Tekhanovich, and E. F. Andreev, Neorg. Mater. **36**, 4 (2000).

8. A. U. Sheleg, T. I. Dekola, and N. P. Tekhanovich, Fiz. Tverd. Tela (St. Petersburg) **42** (5), 922 (2000) [Phys. Solid State **42**, 950 (2000)].
9. A. P. Levanyuk and D. G. Sannikov, Fiz. Tverd. Tela (Leningrad) **18** (6), 1927 (1976) [Sov. Phys. Solid State **18**, 1122 (1976)].
10. V. A. Golovko, Zh. Éksp. Teor. Fiz. **94** (2), 182 (1988) [Sov. Phys. JETP **67**, 316 (1988)].
11. H. Mashiyama, J. Phys. Soc. Jpn. **49** (6), 2270 (1980).
12. A. Lopez-Echarri, I. Ruiz-Larrea, and M. J. Tello, Phys. Status Solidi B **154**, 143 (1989).
13. A. U. Sheleg, T. I. Dekola, and N. P. Tekhanovich, Fiz. Tverd. Tela (St. Petersburg) **40** (6), 1106 (1998) [Phys. Solid State **40**, 1009 (1998)].
14. S. A. Taraskin, B. A. Strukov, V. A. Fedorikhin, *et al.*, Fiz. Tverd. Tela (Leningrad) **19** (10), 2936 (1977) [Sov. Phys. Solid State **19**, 1721 (1977)].
15. P. Prelovsek and A. Levstik, Phase Transit. **16/17**, 325 (1989).
16. A. Levstik, P. Prelovsek, C. Filipic, and B. Zeks, Phys. Rev. B **25**, 3416 (1982).
17. K. Hamano, Y. Ikeda, T. Fujimoto, *et al.*, J. Phys. Soc. Jpn. **49** (8), 2278 (1980).

Translated by G. Skrebtsov

Physics of the Solid State, Vol. 44, No. 5, 2002, pp. 989–993. Translated from Fizika Tverdogo Tela, Vol. 44, No. 5, 2002, pp. 945–949.

LOW-DIMENSIONAL SYSTEM AND SURFACE PHYSICS

Variation of the Electronic and Adsorption Properties of GaAs(100) in the Transition from an As- to Ga-Rich Surface

G. V. Benemanskaya*, D. V. Daĭneka*, and G. É. Frank-Kamenetskaya**

** Ioffe Physicotechnical Institute, Russian Academy of Sciences, ul. Politekhnicheskaya 26, St. Petersburg, 194021 Russia*

*** St. Petersburg State Technological University, Zagorodnyi pr. 49, St. Petersburg, 198013 Russia*

Received July 12, 2001

Abstract—This paper reports on a threshold photoemission study of the variation of electronic properties occurring as Cs is adsorbed on GaAs(100) and the surface transfers gradually from the As- to Ga-rich state. The ionization energy and integrated photoemission current are studied as functions of the Cs coverage. The minimum of ionization energy and the corresponding Cs dose are established to differ substantially for the As- and Ga-rich GaAs(100) surfaces. The first observation is reported of anomalous curves with two ionization-energy minima, which are characteristics of surfaces in an intermediate state, with Ga and As dimers present. The sticking coefficient of Cs to the surface enriched in As is found to be several times smaller than that for the Ga-rich surface. © *2002 MAIK "Nauka/Interperiodica".*

1. INTRODUCTION

The interest presently expressed in studies of the GaAs(100) surface stems from its broad application potential, in particular, for the development of semiconductor nanostructures using molecular-beam epitaxy. The atomic structure and stoichiometric composition of GaAs(100) surfaces obtained with various growth technologies and heat treatments are dealt with in numerous publications. Atomically clean GaAs(100) surfaces are obtained, as a rule, in ultrahigh vacuum after thermal removal of the oxide or arsenic cap layer. It has been established that the As cap layer disappears when the sample is annealed up to T = 320–350°C, which results in the surface being coated by a (1×1) As monolayer [1–3]. By increasing the annealing temperature gradually, one can obtain various dimer-reconstructed surfaces, from As- to Ga-rich ones. Annealing at $T \sim$ 400–450°C results in a (2×4) or $c(2 \times 8)$ (As-rich) reconstruction with As dimers in the upper layer. The dimers occupy ~70% of the surface. Further increasing the anneal temperature gives rise to the appearance of Ga dimers, i.e., to a decrease in the As/Ga dimer ratio on the surface. When the sample is annealed up to ~570–590°C, the surface becomes Ga-rich with the (4×2) or $c(8 \times 2)$ reconstruction. The surface thus reconstructed is occupied to ~70% by Ga dimers in the top layer. The transformation from an As- to Ga-rich surface is accompanied by a decrease in the work function by ~0.4 eV, which is connected with there being a positive charge on the Ga dangling bonds and a negative charge on the As dangling bonds [2].

These results were obtained by low-energy electron diffraction (LEED) and x-ray photoemission (XPS) and Auger spectroscopy, which characterize macroscopic regions on the surface. Obviously enough, if a surface has microregions that differ in their properties, the resultant signal measured by these techniques will be determined by the dominant regions. Scanning tunneling microscopy (STM) studies made at the atomic level revealed that between the stablest (2×4) As-rich and (4×2) Ga-rich reconstructions there are various transition phases, for instance, (3×6), (4×6), and disordered systems, which are observed to exist in samples annealed at intermediate temperatures T = 470–550°C [3, 4]. The size of domains of different phases is typically estimated to be ~300 Å [3]. Photoemission measurements also indicate the existence of domains of two types on the GaAs(100) surface [1].

The processes involved in alkali-metal adsorption and the mechanisms governing interface formation, in particular, Cs/GaAs(100), have been studied actively for the Ga-rich surface [5–8]. By contrast, data on the electronic properties, the character of adsorption, the sticking coefficient, and the decrease in the work function and ionization energy for the As-rich Cs/GaAs(100) interface as a function of Cs coverage are practically lacking.

The ionization threshold is as fundamental a characteristic of semiconducting surfaces as the work function. The change in the work function and ionization energy entailed in the formation of the metal–semiconductor interface is directly related to the local interaction of adatoms with the active surface dangling bonds; it is the strongest in the initial stage of adsorption, at submonolayer coverages. An increase in the surface concentration of metal adatoms brings about modification of the surface-state spectrum. Saturation of the

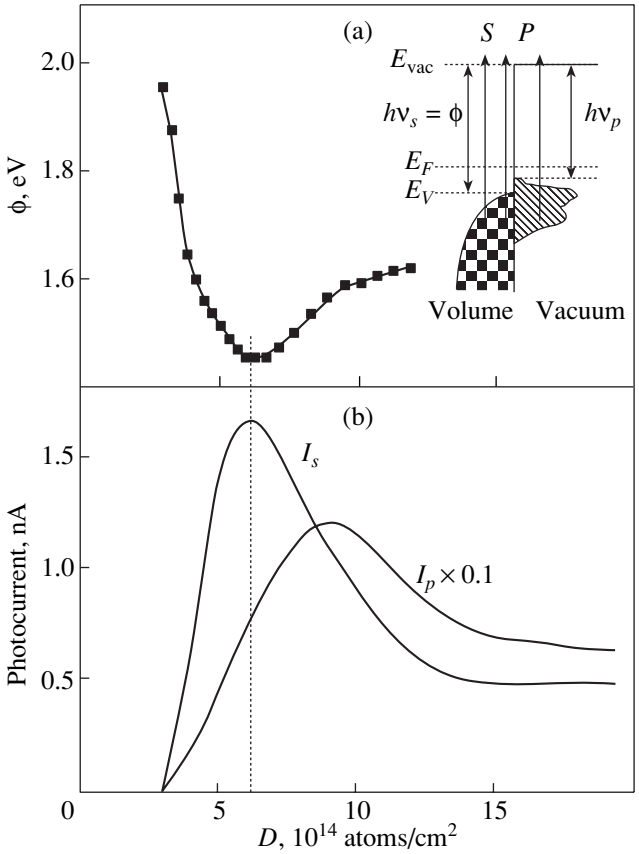

Fig. 1. (a) Ionization energy and (b) photocurrents I_s and I_p measured under excitation by *s*- and *p*-polarized light $h\nu$ = 1.96 eV, respectively, for the Ga-rich Cs/GaAs(100) system and plotted as a function of cesium dose. The inset is a scheme of the excitation of photoemission from the semiconductor by *s*- and *p*-polarized light in the threshold region.

dangling bonds results, as a rule, in stabilization of the work function and of the ionization energy [9, 10].

The present study deals with Cs adsorption on a GaAs(100) surface whose reconstruction and stoichiometric composition were varied gradually *in situ* from As-rich to Ga-rich by annealing at 450–580°C. Measurement of the integrated photoemission current as a function of the Cs dose directly in the course of deposition (the so-called concentration relation) was applied for the first time to study semiconductor surfaces. This method was shown to provide an efficient and fast analysis of the surface condition. It was found that the ionization energy curves for the Cs/GaAs(100) As-rich and Cs/GaAs(100) Ga-rich interfaces differ substantially both in the lowest values of the ionization energy and in the Cs dose required to reach them. It was established that the Cs sticking coefficient for an As-rich surface is several times smaller than that for a Ga-rich one. Anomalous curves with two ionization energy minima obtained as a function of the Cs dose were found for the first time to exist for intermediate reconstructions of the GaAs(100) surface, more specifically, for the case where both the As and Ga dimers are present. Analysis revealed the existence of domains of two types, namely, of Ga-rich and As-rich ones, on such surfaces. The adsorption properties of the domains were observed to be substantially different; as a result, adsorption occurs initially on domains enriched in Ga, to shift subsequently to As-rich domains. Annealing the sample at ~580°C gives way to a complete transition to the Ga-rich surface, with the domain structure disappearing altogether. The density of surface states in the band gap is extremely low for all the interfaces studied.

2. EXPERIMENTAL TECHNIQUE

The photoemission studies were performed *in situ* in an ultrahigh vacuum, $P \sim 5 \times 10^{-11}$ Torr, at room temperature. An atomically clean surface of a GaAs(100) sample (*n* type, 10^{18} cm^{-3}) was obtained after the removal of the As cap layer. The sample annealing temperature was measured with a thermocouple and an IR pyrometer. The error of temperature determination was ~10°C. Atomically pure cesium was deposited on the sample surface from a standard source. The Cs flux was derived using a W(110) reference sample by the technique described in [11]. The error in determining the cesium dose *D* deposited on the GaAs(100) surface did not exceed 10%.

The method employed was threshold photoemission spectroscopy, by which photoemission is excited by *s*- and *p*-polarized light striking a sample at 45° [11, 12]. The photoemission excitation processes in the threshold region are illustrated schematically in the inset to Fig. 1a. The *s*-polarized light excites volume states of the substrate, such that the photoemission threshold $h\nu_s$ corresponds in energy to the valence band top; i.e., $h\nu_s = \phi$, where ϕ is the ionization energy. In the case of *p* polarization, photoemission is excited both from the volume and from the surface through interaction with the normal component of the electric vector of light. If there are filled surface states in the gap, the threshold for *p*-polarized light $h\nu_p < h\nu_s$. We studied the spectral response of photoemission $I_s(h\nu)$ for different Cs doses, as well as the dependence of the photoemission current on the Cs dose, the so-called concentration relations $I_s(D)$ and $I_p(D)$, under excitation by a He–Ne laser with $h\nu$ = 1.96 eV and P = 2 mW. The photoemission currents in the range 10^{-8}–10^{-13} A were measured with an error of 1 to 10%, respectively.

3. EXPERIMENTAL RESULTS AND DISCUSSION

Figure 1a plots the variation of the ionization energy obtained under Cs deposition on a Ga-rich GaAs(100) surface, and Fig. 1b shows the corresponding concentration dependences of the photoemission, $I_s(D)$ and $I_p(D)$. The symbols on the curve of Fig. 1a ($h\nu_s = \phi$) correspond to the approximation of the $I_s(h\nu)$ spectral

response curves measured for each Cs dose. The curves in Fig. 1b were taken under continuous Cs deposition and at a fixed excitation energy $h\nu = 1.96$ eV. The minimum of the ionization energy curve is seen to coincide in position with the maximum of the $I_s(D)$ concentration dependence. These results show that only the $I_s(D)$ relation properly reflects the variation of the ionization energy and, thus, offers a possibility of determining, with a high accuracy, the dose corresponding to the lowest ionization energy from the position of the maximum on this curve. The course of the $I_p(D)$ photoemission curve is governed not only by the variation of ϕ but also by the modification of the surface-state spectrum. The maximum of this curve can differ in position from the ionization energy minimum (Fig. 1b). Hence, this method of express analysis can be employed only under conditions which preclude excitation of the surface states. This means that in order to excite photoemission at nonzero (off-normal-) incidence angles, one should use *s*-polarized radiation, which does not have an electric vector component normal to the surface.

Figure 2 presents curves relating the ionization energy to Cs dose for various conditions of the GaAs(100) surface occurring in going from an As-rich to Ga-rich surface. Curve *1* corresponds to an As-rich surface obtained after complete removal of the As cap layer and a short (10 min) annealing of the sample at 450°C. Curve *2* was measured on a sample surface annealed at an intermediate temperature $T = 490$°C, and curve *3* was obtained on a Ga-rich surface after long (~1-h) annealing of the sample at $T = 590$°C. For comparison, curve *4* in Fig. 2 shows the variation of the ionization energy for a Ga-rich Cs/GaAs(100) system, where the Ga-rich surface was obtained by removing the protective oxide layer [13]. Curves *3* and *4* are seen to agree well, in particular, in the position of the minimum of ionization energy.

As seen from Fig. 2, the minima in curves *1* and *3* differ in depth and in position, corresponding to different Cs doses being deposited. Curve *1* for the As-rich surface passes through a minimum $\phi_{min} = 1.53$ eV positioned at $D \sim 1.4 \times 10^{15}$ atoms/cm^2. Adsorption of Cs on a Ga-rich surface reduces the ionization energy to $\phi_{min} \sim 1.4$ eV at $D \sim 6.5 \times 10^{14}$ atoms/cm^2. When annealing a sample within the temperature interval 470–550°C, we observed, for the first time, anomalous ionization-energy curves with two minima. Their depth varies with increasing anneal temperature in such a manner that curve *1* (As-rich surface) transforms practically smoothly to curve *3* (Ga rich). Curve *2* in Fig. 2 displays such an anomalous dependence with two minima, $\phi^1_{min} = 1.65$ eV and $\phi^2_{min} = 1.57$ eV, obtained at doses of 6.5×10^{14} and 1.6×10^{15} atoms/cm^2, respectively. The character in which the ionization energy curves vary with increasing sample anneal temperature suggests that the anomalous curve with two minima is actually a superposition of two components. Because

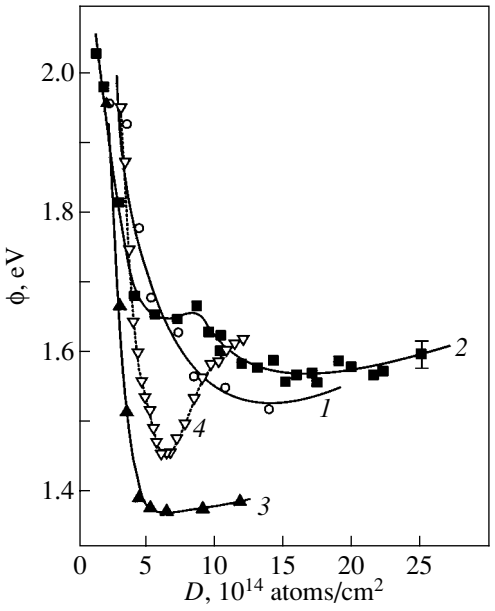

Fig. 2. Ionization energy of the Cs/GaAs(100) system plotted vs. Cs dose. The GaAs(100) sample was annealed at (*1*) 450, (*2*) 490, and (*3*) 590°C. Curve *4* is data for the Ga-rich GaAs(100) surface from [13].

annealing of a sample at 450°C produces an As-rich surface with As dimers in the uppermost layer [3], the minimum at $D = 1.3 \times 10^{15}$ atoms/cm^2 can be assigned to the interaction of Cs adatoms with the As-dimer dangling bonds. On the other hand, after annealing at the maximum temperature, i.e., for a Ga-rich surface, one also observes a minimum at a substantially lower dose, $D \sim 6 \times 10^{14}$ atoms/cm^2, which is apparently connected with Cs adsorption on the Ga dimers. Observation of both minima at intermediate temperatures can be accounted for by the simultaneous existence of domains enriched in As and in Ga on the surface. The modification of the curves with increasing anneal temperature reflects surface reconstruction with an increase in the fraction of Ga-rich domains in the intermediate phase until the surface becomes Ga-rich.

Figure 3 presents concentration dependences of the photoemission current I_s obtained for the same GaAs(100) surface conditions for which the ionization energy curves in Fig. 2 were measured. The transformation of the ionization energy curves and the sharp changes that the integrated photocurrent curves undergo are seen to be qualitatively similar. For the As- and Ga-rich surfaces, the concentration curves have one maximum. The corresponding Cs doses, however, differ more than twofold. As already mentioned, the concentration dependence technique provides the most accurate rapid analysis of the presence of an ionization energy minimum and determination of the corresponding adsorbate dose. For instance, for an As-rich Cs/GaAs(100) system, a maximum of ~0.2 nA is

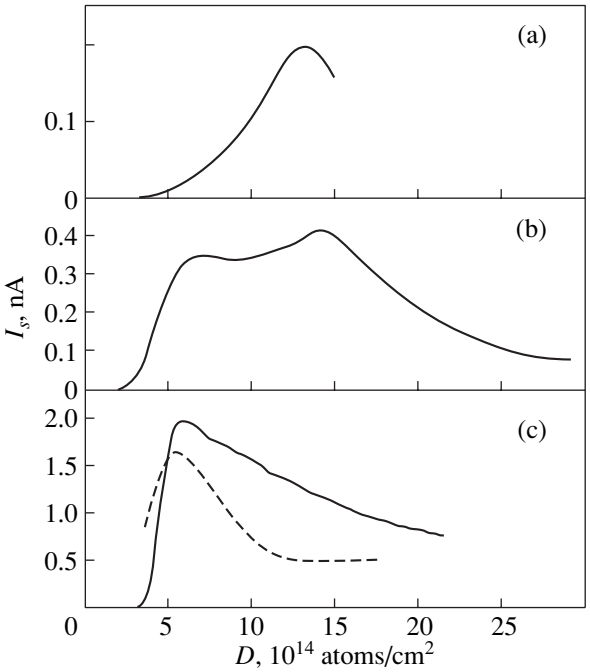

Fig. 3. Concentration dependences of photocurrent $I_s(D)$ for the Cs/GaAs(100) system obtained under excitation by *s*-polarized light of energy $h\nu = 1.96$ eV. The GaAs(100) sample was annealed at (a) 450, (b) 490, and (c) 590°C. Dashed line relates to a Ga-rich GaAs(100) surface obtained by removing the oxide cap layer.

observed to occur for a dose $D \sim 1.3 \times 10^{15}$ atoms/cm^2 (Fig. 3a). The Ga-rich Cs/GaAs(100) system exhibited an order-of-magnitude higher intensity of the maximum, ~2 nA, for $D \sim 6 \times 10^{14}$ atoms/cm^2 (Fig. 3c). The concentration curve obtained for an intermediate surface condition with As and Ga dimers present has two clearly pronounced maxima (Fig. 3b).

These results show that the interaction of Cs adatoms with As and Ga dimers differs considerably in character. Because the dangling bonds of the Ga dimers are not occupied, a Ga-rich surface may be expected to be more adsorption-active. Indeed, adsorption of Cs on a Ga-rich surface brings about a larger decrease in the ionization energy, which corresponds to lower Cs doses than in the case of an As-rich surface. The presence of two minima (Fig. 2) or two maxima (Fig. 3) suggests that Cs adatoms present on a GaAs(100) surface in intermediate phases interact initially with the Ga dangling bonds, and only after their saturation is reached do the Cs adatoms transfer to the As dangling bonds.

One of the most important parameters characterizing the initial processes of the metal–semiconductor interface formation is the extent of submonolayer coverage (or the surface concentration of the metal adatoms). Determination of the coverage is a complex problem, because it requires knowledge of both the dose and the adatom sticking coefficient for the surface under study. Data obtained by Auger spectroscopy for the Ga-rich Cs/GaAs(100) system show that at room temperature, the adsorption proceeds in a layer-by-layer manner. The sticking coefficient is $S \sim 1$ until a 0.5-ML coverage is reached, after which it decreases to one half this value, to practically disappear at a close-to-monolayer coverage [5–8]. The interpretation of these results has been made on the assumption that saturation of the Cs Auger signal occurs upon completion of the first monolayer and that the sticking coefficient changes at 0.5 ML. It should be pointed out that, in the above studies, one understands a Cs monolayer to be the coverage at which the number of adsorbed atoms in direct contact with the surface is the largest. Quantitative estimates of this coverage vary from 4×10^{14} atoms/cm^2 [6, 14] to 7.9×10^{14} atoms/cm^2 [7]. We shall use the traditional determination of the monolayer, 1 ML = 6.3×10^{14} atoms/cm^2. This corresponds to a Cs coverage at which the concentration of adatoms is equal to that of atoms on the unreconstructed GaAs(100) 1×1 surface. As follows from the above data, the cesium dose required to form a monolayer coverage on a Ga-rich GaAs(100) surface is ~9.3×10^{14} atoms/cm^2 and the coverage corresponding to the minimum ionization energy is ~0.7 ML.

Information on the variation of ionization energy and on the sticking coefficient for the As-rich GaAs(100) surface is lacking. The above results show that the ionization energy reaches a minimum at considerably larger Cs doses, ~1.3×10^{15} atoms/cm^2. Because the coverage corresponding to the minimum ionization energy cannot exceed 1 ML, the maximum sticking coefficient for an As-rich surface can be estimated at $S \sim 0.5$ throughout the submonolayer coverage range studied. It should be stressed that the sticking coefficient should vary with increasing coverage. A comparison of the results obtained for the As- and Ga-rich surfaces shows that the sticking coefficient for the As-rich surface is smaller, on the average, by at least a factor of two than that for the Ga-rich surface. Hence, the dose needed to form a monolayer Cs coverage on an As-rich surface is ~1.8×10^{15} atoms/cm^2 and, accordingly, the lowest value of the sticking coefficient can be estimated at $S \sim 0.3$.

ACKNOWLEDGMENTS

The authors are indebted to D. Paget for providing the GaAs(100) sample and to K.E. Rovinskiĭ for technical assistance.

This study was supported by the Russian Foundation for Basic Research (project no. 01-02-16802) and the Ministry of Industry, Science, and Technology (grant no. 1-107).

REFERENCES

1. M. Vitomirov, A. D. Raisenen, A. C. Finnefrock, *et al.*, J. Vac. Sci. Technol. B **10**, 1898 (1992).

2. W. Chen, M. Dumas, D. Mao, and A. Kahn, J. Vac. Sci. Technol. B **10**, 1886 (1992).
3. V. Chizhov, G. Lee, R. F. Willis, *et al.*, Surf. Sci. **419**, 1 (1998).
4. K. B. Bielgelsen, R. D. Bringans, J. E. Northrup, and L.-E. Swartz, Phys. Rev. B **41**, 5701 (1990).
5. D. Rodway, Surf. Sci. **147**, 103 (1984).
6. G. Vergara, A. Herrera-Gomez, and W. E. Spicer, Surf. Sci. **436**, 83 (1999).
7. M. Kamaratos and E. Bauer, J. Appl. Phys. **70**, 7564 (1991).
8. D. Paget, B. Kierren, and R. Houdre, J. Vac. Sci. Technol. A **16**, 2350 (1998).
9. B. Reihl, R. Dudde, and L. S. O. Johansson, Appl. Surf. Sci. **56–58**, 123 (1992).
10. G. V. Benemanskaya, D. V. Daineka, and G. E. Frank-Kamenetskaya, Surf. Rev. Lett. **5**, 91 (1998).
11. A. Liebsch, G. V. Benemanskaya, and M. N. Lapushkin, Surf. Sci. **302**, 303 (1994).
12. G. V. Benemanskaya, M. N. Lapushkin, and M. I. Urbakh, Zh. Éksp. Teor. Fiz. **102**, 1664 (1992) [Sov. Phys. JETP **75**, 899 (1992)].
13. G. V. Benemanskaya, D. V. Daineka, and G. E. Frank-Kamenetskaya, Solid State Commun. **114**, 285 (2000).
14. D. Heskette, T. Maeda Wong, A. J. Smith, *et al.*, J. Vac. Sci. Technol. B **7**, 915 (1989).

Translated by G. Skrebtsov

Physics of the Solid State, Vol. 44, No. 5, 2002, pp. 994–1002. Translated from Fizika Tverdogo Tela, Vol. 44, No. 5, 2002, pp. 950–957.

LOW-DIMENSIONAL SYSTEM AND SURFACE PHYSICS

Simulation of the Process of Deformation-Induced Destruction of Long-Range Order in Alloys with an $L1_2$ Superstructure

V. A. Starenchenko, O. D. Pantyukhova, and S. V. Starenchenko

Tomsk State University of Architecture and Civil Engineering, Solyanaya pl. 2, Tomsk, 634003 Russia

e-mail: dekan@oof.tisi.tomsk.su

Received March 15, 2001; in final form, August 31, 2001

Abstract—Plastic-deformation-induced destruction of long-range order in alloys with an $L1_2$ superstructure is considered. A mathematical model is suggested which takes into account the following mechanisms that lead to the destruction of long-range order: generation of superdislocations, generation of single dislocations, multiplication of antiphase boundaries (APBs) upon the conservative motion of dislocations, multiplication of APBs upon dislocation climb, formation of APB tubes on superdislocations, generation of point defects, and thermal ordering. A mathematical model of deformation strengthening and long-range order destruction with allowance for the change in the type of shear-forming dislocations from superdislocations to single dislocations is formulated. © *2002 MAIK "Nauka/Interperiodica".*

1. INTRODUCTION

Plastic deformation of alloys can be accompanied by changes in both the defect structure of crystals and phase composition of the alloy. Experimental investigations of alloys with an $L1_2$ superstructure subjected to plastic deformation under various conditions (uniaxial deformation, rolling, ball milling) show the presence of changes in the degree of long-range order in these alloys. This follows both from indirect data on the changes in the dislocation substructure [1] and magnetic properties of the alloys [2] and from direct measurements of the degree of long-range order by x-ray diffraction [3–5]. Detailed investigations of the long-range order by X-ray diffraction methods were performed recently for various ordered alloys in [6–10].

To explain the phenomenon of destruction of long-range order under the effect of plastic deformation, various mechanisms were considered [7, 11] related to the motion and accumulation of deformation-induced defects.

In our previous works [12–14], we constructed special models of the destruction of long-range order related to the accumulation of superdislocations [12], generation of antiphase boundaries (APBs) by moving dislocations [13], generation of APB tubes, generation of deformation point defects [13, 14], and climb of edge dislocations [13, 15].

This paper represents an attempt to construct a model that reduces all these particular mechanisms into a single mathematical model.

Recent experimental investigations indicate the heterogeneous character of the deformation-induced order–disorder phase transition [7–10]. This circumstance is considered in the final part of our paper, where we suggest a model of destruction of long-range order with allowance for transition from the motion of superdislocations to the motion of single dislocations.

2. MECHANISMS OF DESTRUCTION OF LONG-RANGE ATOMIC ORDER

It follows from experimental works that, during plastic deformation of ordered alloys, the accumulation of deformation defects leads to a decrease in the degree of ordering of the material [3–10], which is accompanied by an increase in the area of APBs [6–10] and the appearance of regions of a disordered phase.

A decrease in the average (over the material volume) long-range order parameter η with increasing degree of deformation ε and the appearance of a disordered phase can be caused by the following factors.

First, there occurs a disturbance of the long-range atomic order in the bulk of antiphase domains due to the mutual annihilation of point defects generated upon the alloy deformation as a result of nonconservative motion (drag) of jogs by shear-forming dislocations of screw orientation.

The change in the parameter of long-range order inside antiphase domains caused by the mutual annihilation of point defects can be written, as will be shown below, in the form

$$\frac{d\eta_*}{d\varepsilon} = -\eta_* \frac{1}{\dot{\varepsilon}} \mu_r D_0 \exp(-E_i^m/kT) C_i C_v, \qquad (1)$$

where $\dot{\varepsilon}$ is the rate of deformation, μ_r is the temperature-independent coefficient of recombination, D_0 is the preexponential factor, E_i^m is the activation energy for migration of interstitial atoms, k is the Boltzmann constant, T is the deformation temperature, and C_i and C_v

are the concentrations of interstitial atoms and vacancies, respectively. Here, $\frac{1}{\dot{\varepsilon}}\mu_i D_0 \exp(-E_i^m/kT) C_i C_v$ determines the number of point defects that are mutually annihilated inside antiphase domains [13].

Second, an increase, because of deformation, in the area of APBs having a nonzero thickness leads to a reduction of the parameter of long-range order.

The rate of variation of the average long-range order parameter determined from x-ray radiation scattering can be written as a function of deformation in the form [13]

$$\frac{d\eta}{d\varepsilon} = -\frac{1}{2\eta}\eta_*^2(1-k_0^2)\delta\frac{dS^*}{d\varepsilon}. \quad (2)$$

Here, η_* is the average degree of long-range order inside an antiphase domain, $k_0 \in (0, 1)$ is a constant specified by the law of variation of the long-range order parameter in the APB, δ is the thickness of APBs (magnitude of their smearing), and S^* is the area of APBs per unit volume of the crystal.

It is seen from Eq. (2) that the rate of variation of the long-range order parameter is determined by the rate of accumulation of the APB area and by the degree of ordering inside antiphase domains. Thus, the change, in the process of deformation, of the long-range order parameter related to the change in the degree of long-range order inside antiphase domains and the rate of accumulation of the area of APBs will be described by Eqs. (1) and (2).

Note that the change in the area of APBs occurs for various reasons; in particular, their area can increase due to the accumulation of both superdislocations and single dislocations. A conservatively moving shear-forming dislocation upon the intersection of an APB creates steps in it. The formation of tubes of APBs due to the conservative motion of jogs along screw dislocations favors the accumulation of APBs. In addition, part of the interstitial atoms and vacancies accumulated in the process of plastic deformation annihilate at dislocations, thereby causing their climbing, which increases the total area of APBs in the material under deformation. All above mechanisms are related to dislocations generated during deformation.

It is known [1] that under certain conditions upon deformation of alloys with an $L1_2$ superstructure, the type of shear-forming dislocations can change from superdislocations to single dislocations. Depending on which dislocations (single dislocations or superdislocations) are carriers of shear at a degree of deformation ε, different mechanisms of destruction of long-range atomic order can be realized.

2.1. Condition for a Changeover of the Type of Shear-Forming Dislocations

The accumulation of superdislocations in a deformed ordered material will occur until the resistance to motion of superdislocations becomes greater than the resistance to motion of single dislocations; i.e., until the condition [16]

$$\frac{\zeta}{b} < (\alpha_2 - \alpha_1) Gb\rho^{1/2} + \tau_f \quad (3)$$

is fulfilled. Here, ζ is the APB energy; b is the Burgers vector; α_1 and α_2 are the parameters that characterize the intensity of interaction of single and superstructure shear-forming dislocations with forest dislocations, respectively; G is the shear modulus; ρ is the dislocation density; and τ_f is the friction stress, which is determined by the formation of Kear–Wilsdorf barriers at screw dislocations and the trapping of point defects by edge dislocations [17]. The parameters that describe shear processes upon slip of single dislocations will be labeled by indices 1 and I, and the analogous parameters referring to the superdislocations will be denoted by indices 2 and II. When condition (3) is fulfilled, dislocation sources that emit single dislocations start operating.

In ordered materials, the APB energy can be determined as a certain effective energy $\zeta = \zeta_0\eta^2$, where ζ_0 is the energy of APBs in a completely ordered material [1].

In what follows, we assume that the energy of APBs of different types depends on an effective parameter of long-range order which is determined by all the mechanisms of deformation-induced destruction of long-range order considered in our paper. Thus, the condition that determines the type of shear-forming dislocations will depend on the effective parameter of long-range order as follows:

$$\frac{\zeta_0\eta^2}{b} < (\alpha_2 - \alpha_1) Gb\rho^{1/2} + \tau_1. \quad (4)$$

2.2 Mechanisms of Destruction of Long-Range Atomic Order Related to the Motion of Superdislocations

First, we obtain an equation that determines the variation of the long-range order parameter in $L1_2$ alloys in the process of plastic deformation under the condition that only sources that emit superdislocations are operative in the deformed material. In this case, all of the above-mentioned deformation mechanisms of destruction of long-range atomic order take place.

(1) Rate of accumulation of the APB area as a result of generation of superdislocations. Let superdislocations be generated in an ordered material. Then, the long-range order parameter will decrease because of the accumulation of APBs due to an increase in the concentration of superdislocations. The area of APBs per unit volume, when sources of superdislocations are

operative, is directly proportional to the length of dislocations and their width (spacing between superpartial dislocations): $S^* = \rho h$, where ρ is the density of superdislocations and $h = Gb^2/2\pi\zeta_0\eta^2$ is the width of superdislocations.

The extent of splitting of the shear-forming superdislocation (their width) is determined by the effective energy of APBs and, therefore, depends on the degree of ordering in the deformed material (on the effective parameter of long-range order). Earlier [12, 13], we supposed that the splitting of superdislocations is independent of the presence of APBs in the material. Under the assumptions made in [12, 13], the spacing between the superpartials depended on the presence of deformation-induced point defects which could annihilate in a random manner, thereby decreasing the long-range atomic order in the bulk of the deformed alloy. In what follows, we will assume that the splitting of superdislocations depends on both the presence and accumulation of point defects and the presence and accumulation of APBs; i.e., the spacing between the superdislocations will depend on the effective parameter of long-range order. With these assumptions, the rate of accumulation of the area of APBs as a result of generation of superdislocations, $dS^*_{(1)}/d\varepsilon$, can be written as

$$\frac{dS^*_{(1)}}{d\varepsilon} = \frac{Gb^2}{2\pi\zeta_0\eta^2}\left[\frac{d\rho_{II}}{d\varepsilon} - 2\rho\frac{1}{\eta}\frac{d\eta_{II}}{d\varepsilon}\right]. \quad (5)$$

(2) Rate of accumulation of the APB area as a result of intersection of APBs by moving superdislocations. In their conservative motion, superdislocations can intersect interdomain APBs; as a result, steps arise in the latter. This leads to an increase in the total area of APBs. In this case, for the area of APBs, we obtain the following relationship, which describes the greatest of the possible rates of accumulation of the APB area [13]:

$$\frac{dS^*_{(2)}}{d\varepsilon} = \frac{1}{d_0\chi}\exp\left(\frac{\varepsilon}{\omega\chi}\right), \quad (6)$$

where d_0 is the initial average dimension of antiphase boundaries, ω is a constant that determines the shape of antiphase domains, and χ is the Schmid factor.

(3) Rate of accumulation of the APB area due to the formation of APB tubes. The formation of APB tubes as a result of the conservative motion of jogs along superdislocations of screw orientation, along with the previous mechanisms, leads to an increase in the total area of APBs. For this case, the equation that describes the accumulation of the area of APBs is obtained in the form [13]

$$\frac{dS^*_{(3)}}{d\varepsilon} = \frac{1-t_1}{2\Gamma b\chi}\left[4b + \frac{Gb^2}{\pi\zeta_0\eta^2}\right]\rho^{1/2}, \quad (7)$$

where t_1 is the fraction of jogs that generate point defects and Γ is a factor that takes into account the shape of the shear zone.

Since APB tubes are formed as a result of a conservative motion of edge jogs along shear-forming dislocations of screw orientation, the rate of accumulation of the area of APBs is proportional to the dislocation density and the fraction of jogs that generate APBs and is determined by the perimeter of the APB tubes. With allowance for the fact that the width of splitting of superdislocations is determined by the degree of deformation, the perimeter of APB tubes will depend on the effective parameter of long-range order.

(4) Rate of accumulation of the area of APBs caused by the climb of edge dislocations. The rate of accumulation of APB area (per unit volume of the deformed material) caused by climbing edge superdislocations $dS^*_{(4)}/d\varepsilon$ can be written as follows [13]:

$$\frac{dS^*_{(4)}}{d\varepsilon} = \frac{1}{\dot\varepsilon}\frac{a_l^3 D_0}{\chi kTb}\left[\exp(-E_i^m/kT)C_i + \exp(-E_v^m/kT)C_v\right]\tau_2\rho\theta, \quad (8)$$

where a_l is the lattice parameter, E_v^m is the activation energy for migration of vacancies, τ_2 is the flow stress in the case of generation of superdislocations, and θ is the fraction of edge dislocations.

Thus, the total increase in the area of APBs upon deformation of ordered $L1_2$ alloys is determined by the action of all of the above-mentioned mechanisms. The rate of accumulation of the area of APBs of various types per unit volume of the crystal can be represented in the linear-summation approximation as follows:

$$\frac{dS^*_{II}}{d\varepsilon} = \frac{dS^*_{(1)}}{d\varepsilon} + \frac{dS^*_{(2)}}{d\varepsilon} + \frac{dS^*_{(3)}}{d\varepsilon} + \frac{dS^*_{(4)}}{d\varepsilon}. \quad (9)$$

Correspondingly, the equation that describes the change in the effective parameter of long-range order in the case where surface superdislocation sources are operative will have the form

$$\frac{d\eta_{II}}{d\varepsilon} = \frac{-2\pi\zeta_0\delta(1-k_0^2)\eta_*^2\eta^4}{4\pi\zeta\eta_0^5 - 2\delta Gb^2(1-k_0^2)\rho\eta_*^2\eta}\frac{dS^*_{II}}{d\varepsilon}. \quad (10)$$

(5) Destruction of long-range atomic order by deformation-induced point defects. Upon motion of dislocations with jogs, both vacancies and interstitial atoms can be generated [1, 18], which can lead, in ordered alloys, to a decrease in the degree of long-range order. This circumstance is related to the fact that the probabilities of trapping of interstitial atoms at vacant sites usually depend only slightly on which sublattice a vacant site belongs to and on which type of interstitial atom is to be trapped in the site, since the energy liber-

ated upon the annihilation of an interstitial atom with a vacancy is much greater than the energy of ordering. In this connection, to a first approximation, we can assume that the trapping of interstitial atoms at vacant sites occurs randomly. It is shown in [13] that the rate of variation of the long-range order parameter in the bulk of the deformed material caused by the mutual annihilation of point defects has the form

$$\frac{d\eta}{da} = -\eta\frac{dC_i}{da}. \tag{11}$$

Here, dC_i/da determines the number of interstitial atoms per unit volume trapped per unit time by vacant sites.

We assume that the rate of mutual annihilation of point defects inside antiphase domains is proportional to their concentrations, i.e., to $k_i C_i C_v$. The proportionality coefficient k_i can be related to the coefficient of diffusion D_i of interstitial atoms as follows [19]: $k_i = D_i\mu_r$. Taking into account that $D_i = D_0\exp(-E_i/kT)$, the rate of variation of the long-range order parameter inside an antiphase domain caused by the mutual annihilation of point defects can be written as

$$\frac{d\eta}{da} = -\eta\frac{1}{\dot{\varepsilon}}\mu_r D_0\exp(-E_v^m/kT)C_iC_v. \tag{12}$$

2.3. Destruction of the Long-Range Order Caused by the Motion of Single Dislocations

In the case where sources that emit single dislocations are operative, no APB tubes arise in the crystal, since the APB tubes are formed only by superdislocations. The area of APBs that are accumulated due to the generation of single dislocations by operative sources is determined by the area swept by single dislocations as they slip in the crystal. In this case, under the assumption that the single dislocations move independently of one another, we have $dS^*/d\varepsilon = 1/\chi b$.

The rate of variation of the area of APBs caused by the action of all various mechanisms of destruction of long-range atomic order under the condition that sources of single dislocations are operative can be written as

$$\frac{dS_\mathrm{I}^*}{d\varepsilon} = \frac{1}{\dot{\varepsilon}}\frac{a_l^3 D_0}{\chi kTb}[\exp(-E_i^m/kT)C_i + \exp(-E_v^m/kT)C_v]\tau_1\rho\theta + \frac{1}{\chi b}, \tag{13}$$

where τ_1 is the flow stress for the case of generation of single dislocations. The equation that describes the variation of the effective parameter of long-range order will have the form

$$\frac{d\eta_\mathrm{I}}{d\varepsilon} = -\frac{1}{2\eta}\eta_*^2(1-k_0^2)\delta\left\{\frac{1}{\dot{\varepsilon}}\frac{a_l^2 D_0}{\chi kTb}[\exp(-E_i^m/kT)C_i + \exp(-E_v^m/kT)C_v]\tau_1\rho\theta + \frac{1}{\chi b}\right\}. \tag{14}$$

3. MODEL OF THE KINETICS OF DEFORMATION-INDUCED ORDERING AND DESTRUCTION OF LONG-RANGE ORDER

First, we obtain the equations of the balance of deformation-induced defects for the case where sources of superdislocations and single dislocations are operative. The equation that describes the accumulation of superdislocations in the process of plastic deformation can be written as [18, 20]

$$\frac{d\rho_\mathrm{II}}{d\varepsilon} = C_1\frac{(\alpha Gb)^2\rho}{\tau_2} + \frac{C_2 e^{-U_1/kT} + C_3 e^{-U_2/kT}}{Gb\rho^{1/2}} - \frac{1}{\dot{\varepsilon}}\min\left(r_a, [\theta\rho]^{-\frac{1}{2}}\right)\frac{a_l^3 D_0}{\chi kTb}[\exp(-E_i/kT)C_i + \exp(-E_v/kT)C_v]\tau_2\rho^2\theta^2, \tag{15}$$

where $r_a = \dfrac{Gb}{4\pi(\tau_f^0 + \tau_f)}\dfrac{(2-\nu)}{(1-\nu)}$ is the effective radius of capture for superdislocations upon their annihilation, τ_f^0 is the friction stress connected with the overcoming of the Peierls barrier, and ν is Poisson's ratio. The first two terms in Eq. (15) represent the rate of generation of superdislocations, which is determined by the rate of accumulation of superdislocations at the periphery of the shear zone (first summand) and the rate of the formation of Kear–Wilsdorf barriers inside the shear zone (second summand). The annihilation of superdislocations occurs as a result of the climb of their edge components; the rate of annihilation is determined by the last summand in Eq. (15). The meaning of the parameters entering into Eq. (15) has been discussed in detail in [18, 20]. The authors of [18, 20] assume that the annihilation of edge dislocations is possible if dislocations are separated by distances at which the force of interaction between them exceeds the friction stress $(\tau_f^0 + \tau_f)$. The distance between such dislocation segments is determined by the effective capture radius r_a [18, 20]. At high dislocation densities, when the spacing between dislocations is less than r_a, we may assume that the distance between dislocation segments capable of annihilating is equal to the average distance between them $[\theta\rho]^{-\frac{1}{2}}$. Thus, the dislocation spacing at which

the annihilation of edge dislocations is possible may be determined as the smaller of the values r_a or $[\theta\rho]^{-\frac{1}{2}}$, which is designated as $\min(r_a, [\theta\rho]^{-\frac{1}{2}})$ in Eq. (15).

If condition (4) is fulfilled, sources emitting single dislocations begin operating in the deformed material. In this case, the rate of generation of single dislocations will be determined by the intensity of their accumulation at the boundary of the shear zone. No Kear–Wilsdorf barriers will be formed since this process only takes place upon the motion of superdislocations. The rate of annihilation of single dislocations may be obtained in the same manner as for superdislocations, but with allowance for the fact that in this case, the effective radius of trapping single dislocations is determined as

$$r_a^* = \frac{Gb}{4\pi(\tau_f^0 + \zeta_0\eta^2/b)}\frac{(2-\nu)}{(1-\nu)}.$$

Thus, the equation that describes the accumulation of single shear-forming dislocations will have the form

$$\frac{d\rho_{\mathrm{I}}}{d\varepsilon} = C_1\frac{(\alpha Gb)^2\rho}{\tau_1} - \frac{1}{\dot{\varepsilon}}\min\left(r_a^*, [\theta\rho]^{-\frac{1}{2}}\right)\frac{a_l^3 D_0}{\chi kTb} \times [\exp(-E_i/kT)C_i + \exp(-E_v/kT)C_v]\tau_1\rho^2\theta^2. \quad (16)$$

The equations of the balance of deformation-induced point defects are written as follows:

$$\frac{dC_i}{d\varepsilon} = \frac{1}{30\ldots60}p_j\xi B\frac{\tau}{G} - \frac{1}{\dot{\varepsilon}}\frac{a_l^3 D_0}{\chi kT}\exp(-E_i/kT)C_i\tau\rho\theta - \frac{1}{\dot{\varepsilon}}\mu_r D_0\exp(-E_i/kT)C_iC_v, \quad (17)$$

$$\frac{dC_v}{d\varepsilon} = \frac{1}{30\ldots60}p_j\xi B\frac{\tau}{G} - \frac{1}{\dot{\varepsilon}}\frac{a_l^3 D_0}{\chi kT}\exp(-E_v/kT)C_i\tau\rho\theta - \frac{1}{\dot{\varepsilon}}\mu_r D_0\exp(-E_i/kT)C_iC_v. \quad (18)$$

In these relationships, the first term describes the generation of point defects by moving dislocations [21], the second term corresponds to the annihilation of point defects at dislocations [18], and the third term stands for the mutual annihilation of point defects.

Equations (17) and (18) in the case of accumulation of superdislocations and single dislocations will differ in the expressions for the flow stress; we represent them in the following form:

$$\tau_2 = \tau_f^0 + \tau_f + \alpha_2 Gb\rho^{1/2}, \quad (19)$$

$$\tau_1 = \tau_j^0 + \frac{\zeta_0\eta^2}{b} + \alpha_1 Gb\rho^{1/2}. \quad (20)$$

Formulas (1), (10), (15), (17)–(19) and (1), (14), (16)–(18), (20) represent mathematical models of the kinetics of strengthening and destruction of long-range order for the cases where superdislocation sources and sources emitting single dislocations are operative, respectively.

Now, we introduce a function ψ, which takes into account the change of the type of shear carriers, as follows:

$$\psi = \begin{cases} 1, & \dfrac{\zeta_0\eta^2}{b} \geq (\alpha_2 - \alpha_1)Gb\rho^{1/2} + \tau_f \\ 0, & \dfrac{\zeta_0\eta^2}{b} < (\alpha_2 - \alpha_1)GB\rho^{1/2} + \tau_f. \end{cases} \quad (21)$$

The mathematical model of strengthening and destruction of long-range atomic order with allowance for the change in the type of shear-forming dislocations from superdislocations to single dislocations may be written in the form

$$\frac{d\rho}{d\varepsilon} = \frac{d\rho_{\mathrm{II}}}{d\varepsilon}\psi + \frac{d\rho_{\mathrm{I}}}{d\varepsilon}(1-\psi), \quad (22)$$

$$\frac{dC_i}{d\varepsilon} = \frac{dC_{i\mathrm{II}}}{d\varepsilon}\psi + \frac{dC_{i\mathrm{I}}}{d\varepsilon}(1-\psi), \quad (23)$$

$$\frac{dC_v}{d\varepsilon} = \frac{dC_{v\mathrm{II}}}{d\varepsilon}\psi + \frac{dC_{v\mathrm{I}}}{d\varepsilon}(1-\psi), \quad (24)$$

$$\frac{d\eta}{d\varepsilon} = \frac{d\eta_{\mathrm{II}}}{d\varepsilon}\psi + \frac{d\eta_{\mathrm{I}}}{d\varepsilon}(1-\psi), \quad (25)$$

$$\tau = \tau_{\mathrm{II}}\psi + \tau_{\mathrm{I}}(1-\psi). \quad (26)$$

Experimental data show that single dislocations are observed already at moderate degrees of deformation and their fraction increases with increasing deformation [22]. This fact indicates that already at small deformations, regions exist in the alloy which are deformed as a disordered material. This also follows from the results of x-ray diffraction investigations [6–10]. Therefore, we assume that in the deformed material, which is initially ordered, a disordered phase arises as a result of a heterogeneous order–disorder transition [6–10]. We designate the fraction of the remaining ordered phase as $C^*(\varepsilon)$. In the general case, the type of the $C^*(\varepsilon)$ dependence is unknown; however, experimental data [10] indicate that, within good approximation, this dependence can be assumed to be linear: $C^*(\varepsilon) = 1 - \varepsilon/\varepsilon_k$. Here, ε_k is the critical degree of deformation at which the alloy passes into a completely disordered state. The degree of deformation ε_k can be determined by numerically solving the set of differential equations (22)–(26) as that corresponding to the deformation at which the long-range order parameter vanishes. Under the above assumptions, the set of equations of the balance of defects and deformation-induced

strengthening of $L1_2$ alloys that allows for the heterogeneous order–disorder phase transition can be written as

$$\frac{d\rho}{d\varepsilon} = \frac{d\rho_{II}}{d\varepsilon}C^* + \frac{d\rho_I}{d\varepsilon}(1-C^*), \quad (27)$$

$$\frac{dC_i}{d\varepsilon} = \frac{dC_{iII}}{d\varepsilon}C^* + \frac{dC_{iI}}{d\varepsilon}(1-C^*), \quad (28)$$

$$\frac{dC_v}{d\varepsilon} = \frac{dC_{vII}}{d\varepsilon}C^* + \frac{dC_{vI}}{d\varepsilon}(1-C^*), \quad (29)$$

$$\frac{d\eta}{d\varepsilon} = \frac{d\eta_{II}}{d\varepsilon}C^* + \frac{d\eta_I}{d\varepsilon}(1-C^*), \quad (30)$$

$$\tau = \tau_{II}C^* + \tau_I(1-C^*). \quad (31)$$

It is known that, in the process of plastic deformation at enhanced temperatures, restoration of the long-range atomic order can occur in ordered alloys under the effect of large concentrations of point defects. An analysis of various kinetic models of thermal strengthening of alloys was performed in [23]. The kinetics of atomic ordering in $L1_2$ alloys based on migration of deformation-induced vacancies is described by the Zee–Wilkes model, according to which the rate of ordering has the form [23]

$$\frac{d\eta}{dt} = 21\nu_d C_v \exp(-E_v^m/kT) \times \{3(1-\eta)^2 - \exp(-V_0\eta/kT)[16\eta + 3(1-\eta)^2]\}, \quad (32)$$

where V_0 is the energy of ordering.

With allowance for the process of restoration of long-range atomic order, Eq. (30) is written as follows:

$$\frac{d\eta}{d\varepsilon} = \frac{d\eta_{II}}{d\varepsilon}C^* + \frac{d\eta_I}{d\varepsilon}(1-C^*) + \frac{1}{\dot{\varepsilon}}21\nu_d C_v \exp(-E_v^m/kT) \times \{3(1-\eta)^2 - \exp(-V_0\eta/kT)[16\eta + 3(1-\eta)^2]\}. \quad (33)$$

The set of equations (1), (27)–(29), (31), and (33) represents a model of the variation of the effective parameter of long-range order with allowance for the transition from the motion of single dislocation to the motion of superstructure dislocations and the model of the kinetics of deformation strengthening of alloys with an $L1_2$ superstructure.

4. NUMERICAL REALIZATION OF THE MODEL

In terms of the model developed, we calculated the degree of long-range order, stress-strain curves, dislocation densities, and concentrations of point defects as functions of the degree of deformation ($\eta(\varepsilon)$, $\tau(\varepsilon)$, $\rho(\varepsilon)$, and $C_k(\varepsilon)$, respectively). The calculations were performed for alloys with a high energy of APBs (to this end, parameters characteristic of the Ni_3Ge alloy were used) and for alloys with a low APB energy (in this case, parameters typical of the Ni_3Fe alloys were employed).

The values of the parameters necessary for solving the set of equations (1), (25)–(27), (29), and (31) for the Ni_3Ge alloy were taken as follows [20, 24]: $C_1 = 6 \times 10^4$ N/m^2, $C_2 = 5 \times 10^{16}$ N/m^4, $C_3 = 10^{23}$ N/m^4, $U_1 = 0.0094$ eV, $U_2 = 0.72$ eV, $\tau_0^{(1)} = 300$ MPa, $\tau_0^{(2)} = 1700$ MPa, $\chi = 0.48$, $\alpha_0 = 1.9$, $\beta = 1.8 \times 10^{-3}$, $\tau_f^0 = 50$ MPa, $G = 8 \times 10^{10}$ N/m^2, $b = 2.5 \times 10^{-10}$ m, $\alpha_1 = 0.7\alpha_2$, $p_j = 0.5$, $\xi = 0.5$, $B = 340$, $\eta_0 = 1$, $k_0 = 0.5$, $\delta = 0.5$ nm, and $\zeta_0 = 0.2$ J/m^2.

The parameters for Ni_3Fe were borrowed from [25]: $\zeta_0 = 0.05$ J/m^2, $\tau_f^0 = 42$ MPa, $\alpha_0 = 1.2$, and $\beta = 4.2 \times 10^{-4}$.

The results of numerical calculations [with initial conditions $\rho(0) = 10^{10}$ m^{-2}, $C_i(0) = \exp(-E_i^0/kT)$, and $C_v(0) = \exp(-E_v^0/kT)$, where E_i^0 and E_v^0 are the energies of formation of an interstitial atom and a vacancy, respectively, and $\eta_*(0) = 1$ and $\eta(0) = 1$] are given in Figs. 1–4.

(1) Alloys with a low ordering energy. Figure 1 displays the dependence of the long-range order parameter on deformation for various deformation temperatures calculated for the Ni_3Fe alloy. It is seen that the long-range order parameter in the low-temperature and moderate-temperature ranges (77–423 K) is virtually

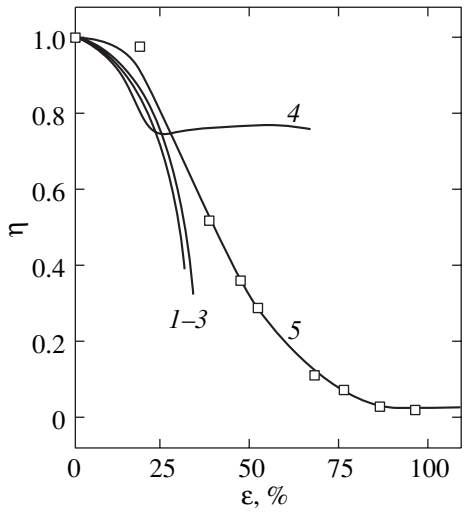

Fig. 1. Dependence of the effective parameter of long-range order on deformation at various deformation temperatures in Ni_3Fe: (*1*) 77, (*2*) 293, (*3*) 423, and (*4*) 573 K; (*5*) experimental curve obtained at room temperature by X-ray diffraction [26, 27].

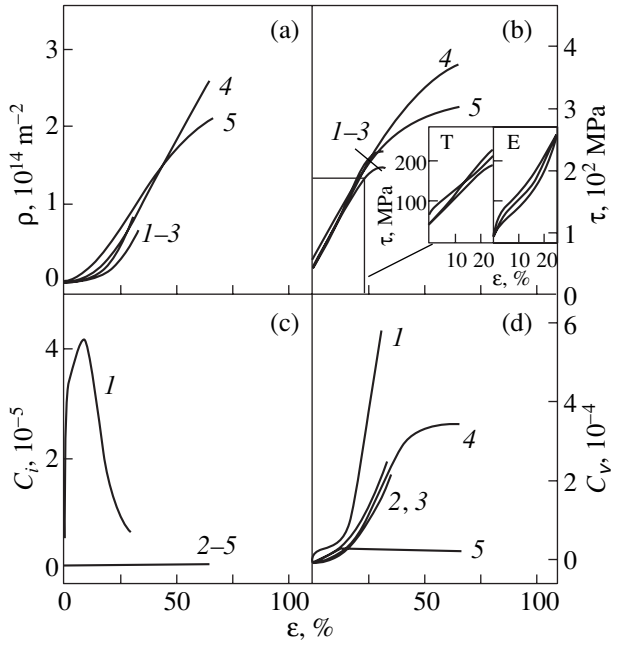

Fig. 2. Dependence of (a) the dislocation density, (b) flow stress, (c) concentration of interstitial atoms, and (d) concentration of vacancies on the degree of deformation at various temperatures in Ni_3Fe: (*1*) 77, (*2*) 293, (*3*) 423, (*4*) 573, and (*5*) 673 K. In the inset, a comparison of experimental (E) [28] and theoretical (T) dependences of the flow stress τ on the degree of deformation ε for the Ni_3Fe alloy calculated on the basis of the model suggested is given.

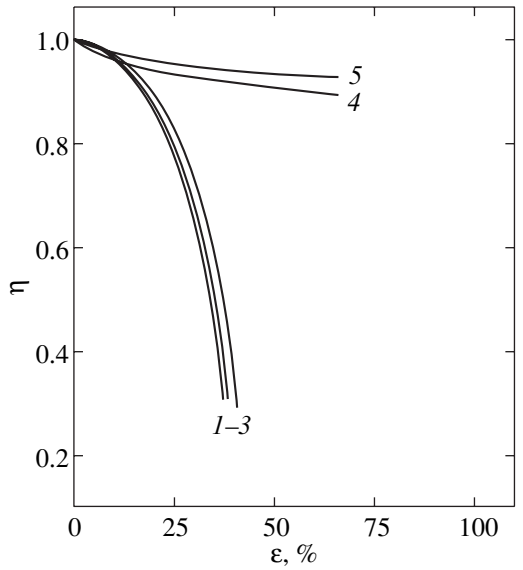

Fig. 3. Dependence of the effective parameter of long-range order on the degree of deformation for various deformation temperatures in the Ni_3Fe alloy: (*1*) 77, (*2*) 293, (*3*) 423, (*4*) 573, and (*5*) 673 K.

independent of the temperature and is determined by the degree of deformation, reaching zero at relative deformations of 30–40%. At enhanced temperatures, a restoration of long-range order is observed in the deformed material. Thus, at 573 K, the long-range order begins restoring at a degree of deformation equal to 25%; the effective parameter of long-range order first increases (a partial ordering of the material occurs until the relative deformation reaches 38%); then, it remains almost unaltered; and, beginning from 50%, a slow decrease in the long-range order parameter occurs with a further increase in deformation.

Curve *5* in Fig. 1 represents the results of experimental measurements of long-range atomic order performed on Ni_3Fe single crystals that had been deformed by rolling at 293 K [26, 27]. A comparison with calculations shows satisfactory agreement up to deformations of 30–40%. Substantial discrepancies at higher deformations may be due to, primarily, specific features of short-range order in this alloy, i.e., to difficulties in the methodological character related to the experimental resolution of the effects of X-ray radiation scattering by long-range and short-range order inhomogeneities at the degrees of long-range order $\eta < 0.2$. Therefore, a comparison of the experimental $\eta(\varepsilon)$ curve with calculations at deformations $\varepsilon > 30$–40% makes no sense without introducing some parameters that would characterize the alloy short-range order in the model.

The dislocation density and the flow stress (strengthening curves) as functions of the degree of deformation for the Ni_3Fe alloy are given in Figs. 2a and 2b. In the inset to Fig. 2b, theoretical (T) and experimental (E) strengthening curves for Ni_3Fe are compared [28].

Figures 2c and 2d display the dependences of the concentrations of point defects (interstitial atoms and vacancies, respectively) on the degree of deformation for various deformation temperatures. It is seen that, with increasing deformation temperature, the concentration of point defects decreases. At a certain degree of deformation, the concentration of point defects at 77 K turns out to be higher than that at 673 K; in the case of interstitial atoms, they even differ by orders of magnitude. The high concentration of point defects in a deformed material at low and moderate temperatures (77–423 K) is natural, since the annihilation of vacancies and interstitial atoms at dislocations and their mutual annihilation occur less intensely at low temperatures.

(2) Alloys with a high ordering energy. Figure 3 displays the dependence of the long-range order parameter on deformation for various deformation temperatures for the Ni_3Ge alloy. As in the case of alloys with a low APB energy, in the temperature range of 77–423 K, there is observed only a weak temperature dependence of the long-range order parameter on the temperature and on the degree of deformation. The restoration of long-range order at enhanced temperatures occurs

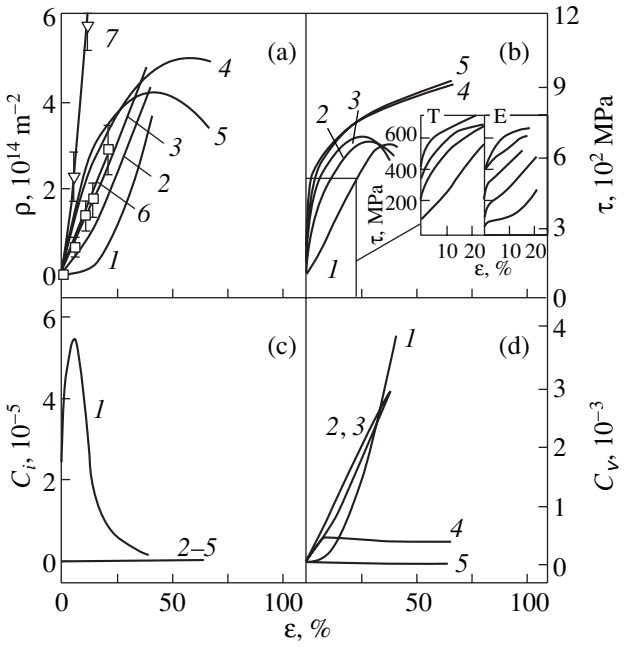

Fig. 4. Dependence of (a) the dislocation density, (b) flow stress, (c) concentration of interstitial atoms, and (d) concentration of vacancies on the degree of deformation for various deformation temperatures in Ni_3Ge: (*1*) 77, (*2*) 293, (*3*) 423, (*4*) 573, and (*5*) 673 K. Curves *6* and *7* in Fig. 4a correspond to experimental data obtained by transmission electron microscopy of thin Ni_3Ge foils for 293 and 673 K, respectively [20, 24]. In the inset, a comparison of experimental (E) [20, 24] and theoretical (T) dependences of the flow stress τ on the degree of deformation ε for the Ni_3Ge alloy calculated on the basis of the model suggested is given.

almost from the very beginning of plastic deformation; as a result, the long-range order parameter changes with deformation relatively slowly. The restoration of long-range order in alloys with both high and low APB energies occurs at almost the same rate. At enhanced temperatures, the long-range order parameter in the alloys with a high APB energy only weakly depends on the deformation temperature. A substantial dependence of the long-range order parameter on temperature is possible at degrees of deformation exceeding hundreds of percent.

Figures 4a and 4b display the dependence of the dislocation density on deformation and the ordering curves, as well as experimental data for the density of dislocations at temperatures of 293 K (curve *6*) and 673 K (curve *7*) for the Ni_3Ge alloy. It is seen from Fig. 4a that the dislocation density substantially depends on temperature. At 77–423 K, the dislocation density increases with both the temperature and the degree of deformation. At enhanced temperatures, the dislocation density at certain degrees of deformation (different at different temperatures) decreases, which is due to a more intense annihilation of dislocations as a result of their climb.

The dependences of concentrations of point defects on the degree of deformation for various temperatures are given in Figs. 4c and 4d. As in the case of Ni_3Fe, there is observed an increase in the concentration of point defects with decreasing temperature. The accumulation of point defects, their mutual annihilation, and annihilation at dislocations occur more intensely in the alloys with a high APB energy, which follows from a comparison of Figs. 2d and 4d.

A comparison of theoretical and experimental [24] strengthening curves for Ni_3Ge is given in the inset to Fig. 4b to show satisfactory agreement between the calculated and experimental data.

5. CONCLUSION

Thus, in terms of the assumptions made, we can satisfactorily describe the experimentally observed regularities of the destruction of long-range atomic order and deformation strengthening in alloys with an $L1_2$ superstructure possessing various ordering energies. A simulation of the process of destruction of long-range atomic order shows that, in alloys with the $L1_2$ structure, a substantial disturbance of long-range atomic order at low and moderate temperatures is observed at deformations of about 30%. Under the assumptions made, the APB energy virtually does not affect the intensity of variation of the long-range order parameter in this temperature range. The effect of the APB energy becomes substantial at enhanced deformation temperatures, where both qualitative and quantitative differences in the η(ε) curves are observed depending on the APB energy. The phenomenon of destruction of long-range order described in this paper (as well as the process of deformation strengthening) apparently cannot be related to the manifestation of only one certain mechanism of destruction of long-range order but is a result of the simultaneous action of a number of mechanisms related to the multiplication of both APBs and point defects and dislocations.

ACKNOWLEDGMENTS

This work was supported in part by the INTAS, grant no. 97-31994.

REFERENCES

1. L. E. Popov, N. A. Koneva, and I. V. Tereshko, *Strain Hardening of Ordered Alloys* (Metallurgiya, Moscow, 1979).
2. A. E. Ermakov, T. A. Sorokina, V. A. Tsurin, *et al.*, Fiz. Met. Metalloved. **48** (6), 1180 (1979).
3. M. M. Dadras and D. G. Morris, Scr. Metall. Mater. **28**, 1245 (1993).
4. D. G. Morris, M. M. Dadras, and M. A. Morris, Acta Metall. Mater. **41** (1), 97 (1993).
5. A. R. Yavari and P. J. Desre, Mater. Sci. Forum **88–90**, 43 (1992).

6. S. V. Starenchenko, N. R. Sizonenko, V. A. Starenchenko, and É. V. Kozlov, Fiz. Met. Metalloved. **81** (1), 84 (1996) [Phys. Met. Metallogr. **81** (1), 57 (1996)].
7. S. V. Starenchenko, I. P. Zamyatina, V. A. Starenchenko, and É. V. Kozlov, Fiz. Met. Metalloved. **85** (2), 122 (1998) [Phys. Met. Metallogr. **85** (2), 201 (1998)].
8. S. V. Starenchenko, N. R. Sizonenko, I. P. Zamyatina, *et al.*, Poroshk. Metall., Nos. 3/4, 33 (1997).
9. S. V. Starenchenko, I. P. Zamyatina, V. A. Starenchenko, and É. V. Kozlov, Fiz. Met. Metalloved. **90** (1), 79 (2000) [Phys. Met. Metallogr. **90** (1), 75 (2000)].
10. S. V. Starenchenko, I. P. Zamyatina, V. A. Starenchenko, and É. V. Kozlov, Izv. Vyssh. Uchebn. Zaved., Fiz., No. 8, 3 (2000).
11. S. V. Starenchenko and V. A. Starenchenko, in *Scientific Works of I International Likhachev Workshop "Topical Problems of Strength" and XXXIII Workshop "Topical Problems of Strength," Novgorod, 1997*, Vol. 2, Part 2, p. 313.
12. V. A. Starenchenko, O. D. Pantyukhova, S. V. Starenchenko, and S. N. Kolupaeva, Izv. Vyssh. Uchebn. Zaved., Fiz., No. 12, 29 (2000).
13. V. A. Starenchenko, O. D. Pantyukhova, S. V. Starenchenko, and S. N. Kolupaeva, Fiz. Met. Metalloved. **91** (1), 90 (2001) [Phys. Met. Metallogr. **91** (1), 85 (2001)].
14. V. A. Starenchenko, O. D. Pantyukhova, S. V. Starenchenko, and S. N. Kolupaeva, Izv. Vyssh. Uchebn. Zaved., Chern. Metall., No. 12, 54 (2000).
15. V. A. Starenchenko, O. D. Pantyukhova, S. V. Starenchenko, and S. N. Kolupaeva, Vestn. Tambov. Gos. Univ. **5** (2–3), 270 (2000).
16. L. E. Popov, L. N. Buĭnova, V. A. Starenchenko, and V. S. Kobytev, Metallofizika **7** (5), 56 (1985).
17. V. A. Starenchenko and Yu. A. Abzaev, Fiz. Met. Metalloved. **79** (1), 147 (1995) [Phys. Met. Metallogr. **79** (1), 102 (1995)].
18. S. N. Kolupaeva, V. A. Starenchenko, and L. E. Popov, *Instability of Plastic Deformation* (Tomsk. Univ., Tomsk, 1994).
19. K. P. Gurov and A. B. Tsepelev, J. Nucl. Mater. **182**, 240 (1991).
20. V. A. Starenchenko, Yu. V. Solov'eva, and Yu. A. Abzaev, Fiz. Tverd. Tela (St. Petersburg) **41**, 454 (1999) [Phys. Solid State **41**, 407 (1999)].
21. V. A. Starenchenko, S. V. Starenchenko, S. N. Kolupaeva, and O. D. Pantyukhova, Izv. Vyssh. Uchebn. Zaved., Fiz., No. 1, 66 (2000).
22. N. A. Koneva, É. V. Kozlov, L. E. Popov, *et al.*, Izv. Vyssh. Uchebn. Zaved., Fiz., No. 2, 136 (1973).
23. L. Ya. Pudan, I. A. Terent'eva, V. A. Starenchenko, and L. E. Popov, Izv. Vyssh. Uchebn. Zaved., Fiz., No. 5, 113 (1989).
24. V. A. Starenchenko, Yu. V. Solov'eva, Yu. A. Abzaev, and B. I. Smirnov, Fiz. Tverd. Tela (St. Petersburg) **38**, 3050 (1996) [Phys. Solid State **38**, 1668 (1996)].
25. V. A. Starenchenko, Yu. A. Abzaev, and L. G. Chernykh, Metallofizika **9** (2), 22 (1987).
26. S. V. Starenchenko, I. P. Zamyatina, and V. A. Starenchenko, in *Scientific Works of IV International Likhachev Workshop "Topical Problems of Strength," Staraya Russa, Novgorod, 2000*, Vol. 2, p. 97.
27. S. V. Starenchenko, I. P. Zamyatina, and V. A. Starenchenko, in *Proceedings of XXXVI Workshop "Topical Problems of Strength," Vitebsk, 2000*, p. 103.
28. N. A. Koneva, L. A. Teplyakova, V. A. Starenchenko, *et al.*, Fiz. Met. Metalloved. **49**, 620 (1980).

Translated by S. Gorin